Hydrogen Embrittlement of Automotive Ultra-High-Strength Steels:

Mechanism and Minimisation

James Alexander Lelliott

Submitted to Swansea University in fulfilment of the requirements for the Degree of Doctor of Engineering

Swansea University

2021

Abstract

Automotive manufacturers are increasingly using ultra-high-strength steels in vehicle components to facilitate mass reduction via downgauging. Unfortunately, as the strength of steels increases, so does susceptibility to 'hydrogen embrittlement', a process in which ductility is significantly impaired by ingress of hydrogen. Mechanisms and environmental conditions by which this degradation occurs are not fully understood.

In this work, 2 fully-ferritic, 2 fully-martensitic boron, and 2 ferrite-martensite dual-phase, ultra-high-strength steels, were assessed for susceptibility to hydrogen embrittlement via 3 key characteristics: firstly, with particular regard to hydrogen evolution under corrosion conditions, through well-established open circuit potential and potentiodynamic polarisation experiments. Exacerbation of hydrogen evolution through galvanic corrosion of a zinc coating was assessed by scanning vibrating electrode technique (SVET), and an attempt made to quantify increased risk of hydrogen evolution during crevice corrosion through a novel time-lapse photography experiment. Secondly, hydrogen diffusivity was assessed via permeation experiments. Finally, degradation in mechanical properties due to diffusing hydrogen was evaluated through slow strain rate tests (SSRT), whereby susceptibility to embrittlement was equated to reduction in ductility of hydrogen-charged test specimens.

The fully-ferritic steels showed the greatest resistance to mechanical degradation, attributed to micro-alloy nano-precipitates within their microstructure acting as 'traps', leading to lower diffusivity compared to dual-phase steels of equivalent strength. Indeed, lower diffusivity showed a strong correlation with lower levels of embrittlement across all steels. 1000 MPa dual-phase steel showed the greatest degradation in mechanical properties, with fully-martensitic boron steels also found to be particularly susceptible. 1000 MPa dual-phase steel also showed the largest increase in hydrogen evolution reaction in response to polarisation, thought to result from the inherent potential difference between ferrite and martensite phases. Galvanic corrosion of a damaged zinc coating was found to polarise the exposed steel substrate, triggering sufficient hydrogen evolution to reach critical concentrations for embrittlement.

Declarations

This work has not previously been accepted in substance for any degree and is not being concurrently submitted in candidature for any degree.

Signed.....[redacted].....

Date.....01/01/2022.....

This thesis is the result of my own investigations, except where otherwise stated. Other sources are acknowledged by footnotes giving explicit references. A bibliography is appended.

Signed.....[redacted].....

Date.....01/01/2022.....

I hereby give consent for my thesis, if accepted, to be available for photocopying and for inter-library loan, and for the title and summary to be made available to outside organisations.

Signed.....[redacted].....

Date.....01/01/2022.....

The University’s ethical procedures have been followed and, where appropriate, that ethical approval has been granted.

Signed…….  …….

Date……..01/01/2022……..

Table of Contents

Acknowledgements

Firstly, I have to thank my primary supervisors, Dr Elizabeth Sackett and Dr Douglas Figueroa-Gordon, for supporting me throughout my studies. Their input has been essential to the completion of this thesis, and I will always be grateful for their ideas and their feedback.

Secondly, I would like to thank some of the other people in the University who have provided enormous assistance. Professor Neil McMurray and Professor Geraint Williams have helped me no end with understanding some of the finer (and broader) points of electrochemistry, as well as assisting me with some of the more mundane activities around laboratory access during a pandemic. I am grateful also to Peter Davies and his team within the AIM facility, who have been extremely helpful over the last 4 years with my microscopy work. A very special thanks must go to my colleagues who have assisted me in my experiments, in particular Alexandra Reynolds, Rachel Board, Chris Griffiths, Mathew Burnell, Dane Hardwicke, and Ria Mitchell.

Thanks also must go to everyone in the Materials and Manufacturing Academy (M2A). Their work is not always easy, but they always seem to take to it with good humour, and without them there would not have been a research project for me to study.

I must of course thank Tata Steel for their sponsorship, and in particular Dr Laura Baker, for allowing me to go and work on this project, and Peter Evans, Andrew Brown, Lee Jones, Geraint Gladwyn, and Thomas Griffith for their help with laboratory hot-stamping, and their support for me to get this thesis written.

I would like to give a special thank you to my mother and father, Margaret and Andrew Lelliott, and my in-laws Valerie and Geraint Rowlands, for all of the moral and practical support they have given me over the years, both during and prior to my studies.

Finally, I have to give the biggest thanks of all to my wonderful wife Gemma, and beautiful, delightful children Ivy and Oscar, who have kept me sane and given me the energy to keep going. It is to them that this work is dedicated.

Table of Figures

List of Tables

Abbreviations and acronyms

α	ferrite
α'	martensite
γ	austenite
σ_y	yield stress
µA	microamps
µm	micrometres / microns
µN	micronewtons
2D	2-dimensional
3D	3-dimensional
A/m^2	amps per square metre
A_{50}	total plastic elongation
AFM	atomic force microscope (or microscopy)
A_g	uniform plastic elongation
AHSS	advanced high-strength steel
AIDE	adsorption-induced dislocation emission
APT	atom probe tomography
bcc	body-centred cubic
bct	body-centred tetragonal
BEV	battery electric vehicle
BH	bake hardening
BiW	body-in-white
BOF	basic oxygen furnace
CAPL	continuous annealing and processing line
CCD	charge coupled device
CCT (diagram)	(in metallurgical context) continuous cooling transformation
CCT	(in corrosion context) cyclic corrosion test

CE	counter electrode
CEV	carbon equivalent value
CFB	carbide free bainite
cm	centimetres
CP	complex phase
CR	(in corrosion context) corrosion rate
CR	(in metallurgical context) cold reduction
CT	computed tomography
DD	ductile dimples
D_{eff}	effective diffusion coefficient
DFT	density functional theory
DP	dual-phase
EBSD	electron backscatter diffraction
EBSP	electron backscatter pattern
EDM	electro-discharge machining
EDS	energy dispersive (X-ray) spectroscopy
EI	embrittlement index
ELC	extra-low carbon
FB	ferrite-bainite
fcc	face-centred cubic
FEG	field emission gun
FEM	finite element method (or model)
g	grams
GA	galvanneal
GI	galvanised iron
GUI	graphical user interface
HDC	hot-dip coated
HDG	hot-dip galvanised (or galvanising)

HDPE	high density polyethylene
HEDE	hydrogen-enhanced decohesion
HEI	hydrogen embrittlement index
HELP	hydrogen-enhanced localised plasticity
HER	hydrogen evolution reaction
HESIV	hydrogen-enhanced strain-induced vacancies
HF	hot forming
HMT	hydrogen microprint technique
HSLA	high-strength low-alloy
HSM	hot strip mill
IG	intergranular
IP	inter-phase
K	Kelvins
kV	kilovolts
m^2	square metres
MD	molecular dynamics
mm	millimetres
mol	moles
mol.H	moles of hydrogen
mol/cm^2	moles per square centimetre
$mol/cm^2/s$	moles per square centimetre per second
MPa	mega-pascals
mV	millivolts
MVC	microvoid coalescence
nA	nanoamps
nm	nanometres
^oC	degrees Celsius
OCP	open circuit potential

OR	orientation relationship
ORR	oxygen reduction reaction
P&O	pickled and oiled
pA	picoamps
PHS	press-hardenable steel
PLS	positron lifetime spectroscopy
ppm	parts-per-million
PTFE	Polytetrafluoroethylene
PγGB	prior austenite grain boundary
PγGS	prior austenite grain size
Q	charge (in Coulombs)
Q&P	quench and partitioned
QC	quasi cleavage
RC	river-like cleavage
RE	reference electrode
RHF	reheat furnace
R_m	ultimate tensile stress
$R_{p0.2}$	0.2% proof stress
SCE	saturated calomel electrode
SEM	scanning electron microscope
SF	shear fracture
SIMS	secondary ion mass spectrometry
SKP	scanning Kelvin probe
SKPFM	scanning Kelvin probe force microscope (or microscopy)
SLR	single lens reflex
SM	shear microvoids
SSCCT	salt spray cyclic corrosion test
SSRT	slow strain-rate test

SVET	scanning vibrating electrode technique
TDA	thermal desorption analysis
TEM	transmission electron microscope
TG	transgranular
TLP	time-lapse photography
TR	tear ridge
TRIP	TRansformation Induced Plasticity
TTF	time to failure
TWB	tailor-welded blanks
TWI	The Welding Institute
TWIP	TWinning Induced Plasticity
UHSS	ultra-high-strength steel
UHT	un heat-treated
ULC	ultra-low carbon
UTS	ultimate tensile strength
V	Volts
WE	working electrode
wt.%	weight-percent
XRD	X-ray diffraction
YS	yield strength
ZM	zinc-magnesium

1 Introduction

Between 1920 and 1926 the portion of steel-framed automobiles being manufactured in the United States grew from 15% to 70% [1]. Since then developments within the automotive manufacturing sector and the steel industry have been inextricably linked, and demands from the automotive industry have seen or seeded the development of novel classes of steel products, many of which have had applications in other industries. Modern automobile designs utilise a variety of steel grades and dimensions to optimise for the mass and function of the various parts, and over the last two decades legislative and commercial pressure to reduce tailpipe CO_2 emissions and improve fuel efficiency has led to a constant endeavour to reduce the mass of vehicles, whilst improving safety performance, particularly in the event of accidents [2].

Steel's relatively high density of 7.8 g/cm^3 is a significant drawback when compared to competitor materials where mass reduction is concerned. Despite this, steel is still the overwhelming choice of metallic material, accounting for around 60% of the total mass of an average vehicle, and being significantly cheaper to produce than competitor materials it is well placed to maintain a dominant position if the correct developments in steel technology are undertaken [2]. In current designs it can be seen that the amount of mild steel being utilised has been lowered to less than 3%, and it is clear that increasing use of advanced high-strength (AHSS) and ultra-high-strength steels (UHSS) (steels with ultimate tensile strength > 780 MPa [3]) is required to fulfil downgauging and crash protection requirements, particularly in 'anti-intrusive' crash protection structures or 'safety cage', in the face of increasing legislative and commercial pressure to reduce greenhouse gas emissions [4].

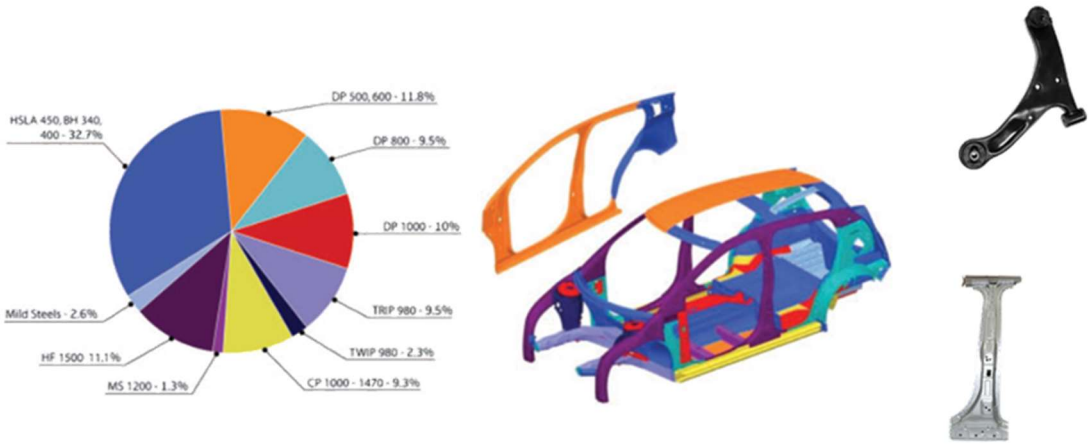

Figure 1.1 Bottom right: characteristic b-pillar; top left and centre: FutureSteelVehicle Body-in-white utilisation and distribution [4] of dual-phase (DP), complex-phase (CP), transformation-induced plasticity (TRIP), twinning-induced plasticity (TWIP), martensitic (MS), and high-strength low-alloy (HSLA) steels; top right: characteristic suspension arm.

The significant drawback with using steels of increasing strength, either throughout the body or within chassis and suspension applications is that this makes them more susceptible to a phenomenon known as 'hydrogen embrittlement', whereby ingress into the steel of atomic hydrogen greatly lowers the strength, ductility, and toughness of the steel, causing it to fail under loads well below that expected when in service. This becomes an increasingly problematic issue as strength levels increase [5], and can be categorised by the embrittlement index (EI, or HEI), defined as:

$$EI\% = \frac{Elongation\ in\ air\ - Elongation\ when\ charged}{Elongation\ in\ air}$$

The exact mechanisms of this phenomenon are still not fully understood [6], for example, whether or not it is truly an 'embrittlement' mechanism or simply facilitates plastic processes at lower stress levels [7,8]. However, certain aspects of this phenomenon have been recognised from the very beginning, such as the key role of hydrogen diffusion, and the increase in susceptibility with increasing strength levels [9].

The purpose of this work is to characterise a range of UHSS in terms of microstructure and mechanical properties, and discern how microstructural differences affect

properties of hydrogen evolution, hydrogen diffusion, and degradation of mechanical properties, both in severity and mechanism, in the steels in question. This is achieved utilising a range of techniques to measure key microstructural, electrochemical, diffusion, and mechanical properties characteristics. Data collected is then analysed with reference to the existing literature, with discussion on how differences in the responses of different microstructures may be utilised when designing UHSS with minimised susceptibility to the deleterious effects of hydrogen in service. This allows conclusions to be drawn about the comparative strengths and weaknesses of different microstructures, how to use these findings to assist design against hydrogen embrittlement in these steels, and the relative merits or shortcomings of some of the investigative techniques.

2 Literature Review

As automotive manufacturers move to increasingly higher strengths of steels to construct their vehicles, the phenomenon of hydrogen embrittlement becomes of increasing concern for this sector. Many factors can influence the degradation incurred by steels of various microstructures, but an understanding of the performance demands, microstructural characteristics of steels designed to meet these demands, and the uptake and diffusion characteristics of hydrogen are crucial to designing steel microstructures that not only fulfil mechanical property requirements, but also resist the deleterious effects of hydrogen. This Literature Review assesses these property requirements, the characteristics of steels designed to meet these requirements (where ultimate tensile strength levels typically exceed 780 MPa), possible sources of hydrogen in service, current understanding of how hydrogen interacts with different microstructural features and the methods employed to understand these characteristics, and assesses what is currently known about hydrogen's interactions with a number of the most commonly used automotive steels.

2.1 Automotive steels

2.1.1 Background

As described in the Introduction, current automobile designs tend to utilise a variety of steel grades and dimensions to optimise for the mass and function of the various components, and legislative and commercial pressure to reduce tailpipe CO_2 emissions and improve fuel efficiency has engendered a significant drive to reduce the mass of vehicles, whilst improving safety performance [2].

2.1.2 Mass reduction

The simplest way of achieving mass-reduction is to reduce the thickness of the steel being utilised. This however presents the drawback of a reduction in physical performance: thinner parts made from the same steels will have lower stiffness and toughness, both critical properties when talking about crash performance or passenger ride comfort. To address these issues, a variety of steel products have been developed with higher strengths and toughness than the mild steel or high-strength low-alloy steels (HSLA) typically utilised in automotive structures for the majority of the twentieth century [4,10]. These ‘new’ steels are typically referred to as ‘advanced high-strength steels’ (AHSS), and if they have ultimate tensile strength (UTS) over 980 MPa, ‘ultra-high-strength steels’ (UHSS) or ‘giga-pascal steels’. Often possessing a multi-phase microstructure, they will typically have yield strength (YS) and UTS significantly higher than the more ‘traditional’ steels that these products are developed to replace [11,12]. Use of a given steel product is, of course, dependent on the demands of the specific application within the vehicle.

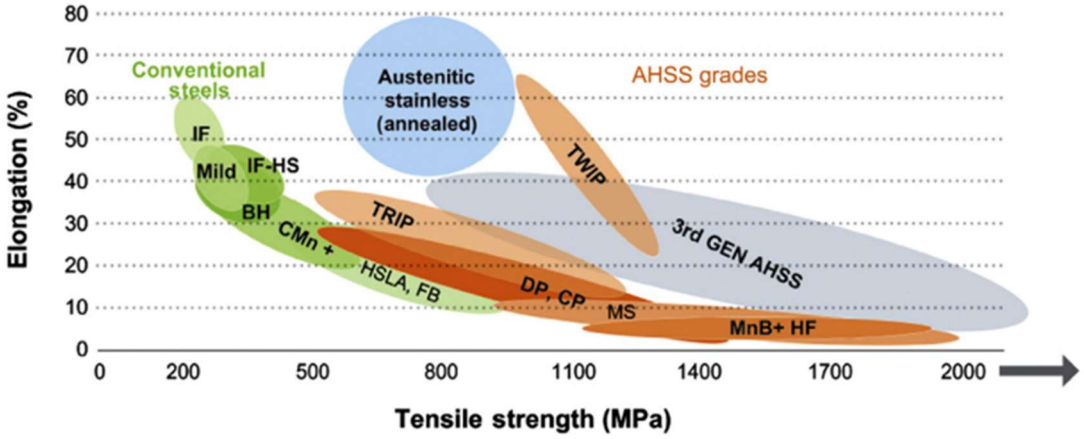

Figure 2.1 Strength-ductility 'banana' diagram showing improved combinations of properties from AHSS (orange) such as transformation-induced plasticity (TRIP), twinning-induced plasticity (TWIP), dual-phase (DP), complex-phase (CP), martensitic (MS), and hot-forming (HF) steels [11].

2.1.3 Applications: chassis and suspension

Whilst there may be substantial overlap in property requirements of steels for different functions within an automotive structure, some clear differences can be drawn between the demands on steels operating within chassis and suspension applications, and those operating within the body-in-white (BiW).

Typically thought of as one combined group of components, chassis and suspension parts can be thought to play a ‘skeletal’ role within the automotive design, providing the vehicle with a sturdy load-bearing frame, without which all other structural components would struggle to function (excluding genuine monocoque vehicle designs).

Designs for chassis and suspension structures vary depending on parameters such as vehicle mass, engine position (if present), or in the case of battery electric vehicles (BEV), location of battery housing, which increasingly is being designed as part of the frame structure itself [13]. However, the range of loads that vehicles will be subjected to is wide-ranging, and often complex, encompassing bending, torsion, lateral, and longitudinal loading, often in combination, and static, transient, or cyclical in nature [14]. This makes component design extremely challenging, both in optimising performance in service, and in facilitating a practicable manufacturing method. As a

consequence, a number of AHSS/UHSS have been developed for use in these applications.

2.1.3.1 Ferrite-bainite (FB) steels

Ferrite-bainite (FB) steels, consisting of up to 0.18 wt.% carbon and up to 2.0 wt.% manganese, are typically used where high stretch flangeability, as measured by hole expansion ratio, is a requirement. This is borne out of their microstructure consisting of a fine ferrite matrix imbued with hard, 'second phase' bainite [15](). This also imparts good fatigue properties, and with a typically higher strain hardening exponent (n-value) and total elongation than conventional high-strength low-alloy (HSLA) or ferrite-martensite dual-phase (DP) steels of similar strength [16], FB steels are ideal for use in parts such as lower control arms (Figure 2.3), rims, and twist beams.

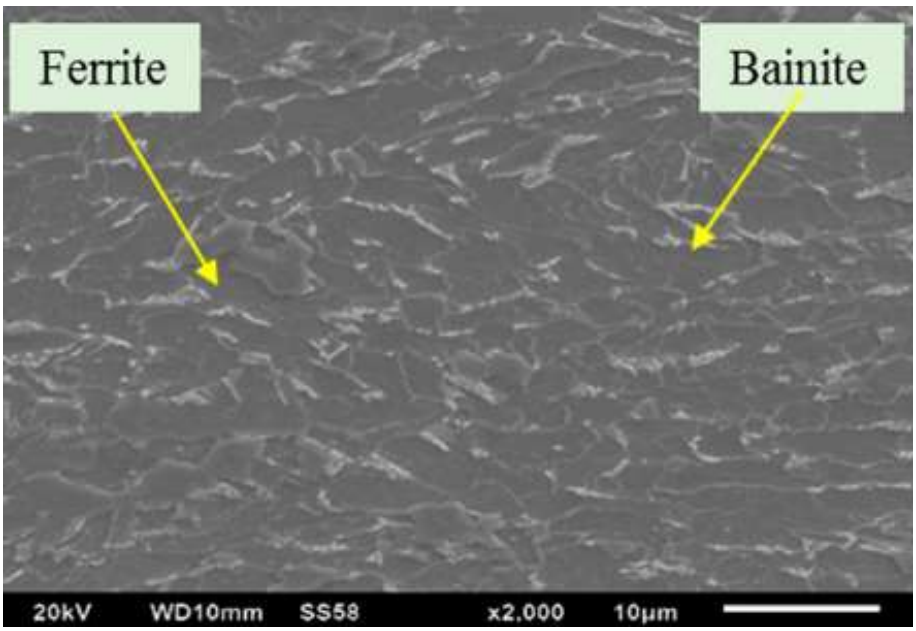

Figure 2.2 SEM micrograph of ferrite (dark grains)-bainite ('lighter' grains) microstructure [17].

Figure 2.3 Lower control arm [18].

This microstructure is achieved through rapid cooling on the run-out-table immediately after finishing rolling at a relatively low ~ 860 ^{o}C in the hot strip mill, ensuring that cooling is sufficiently high speed that transformation from austenite to ferrite (or pearlite) is incomplete and hence there is sufficient quantity of untransformed austenite to allow a significant volume fraction of bainite to form at ~ 450 ^{o}C, at which temperature the strip is coiled. These steels are not typically cold rolled, so are generally sold to manufacturers (or stockholders) in the pickled and oiled (P&O) condition.

2.1.3.2 Ferritic-nanoprecipitate (XPF) steels

Competing with FB steels for use in the lower control arm are the nanoprecipitate-strengthened, single-phase ferrite steels, referred to hereafter by their Tata Steel product name of 'XPF' steels.

These steels have a fine-grained microstructure that is nominally 100% ferrite. Within this ferrite matrix are precipitated carbides and carbonitrides of Nb, Ti, V, and (optionally) Mo.

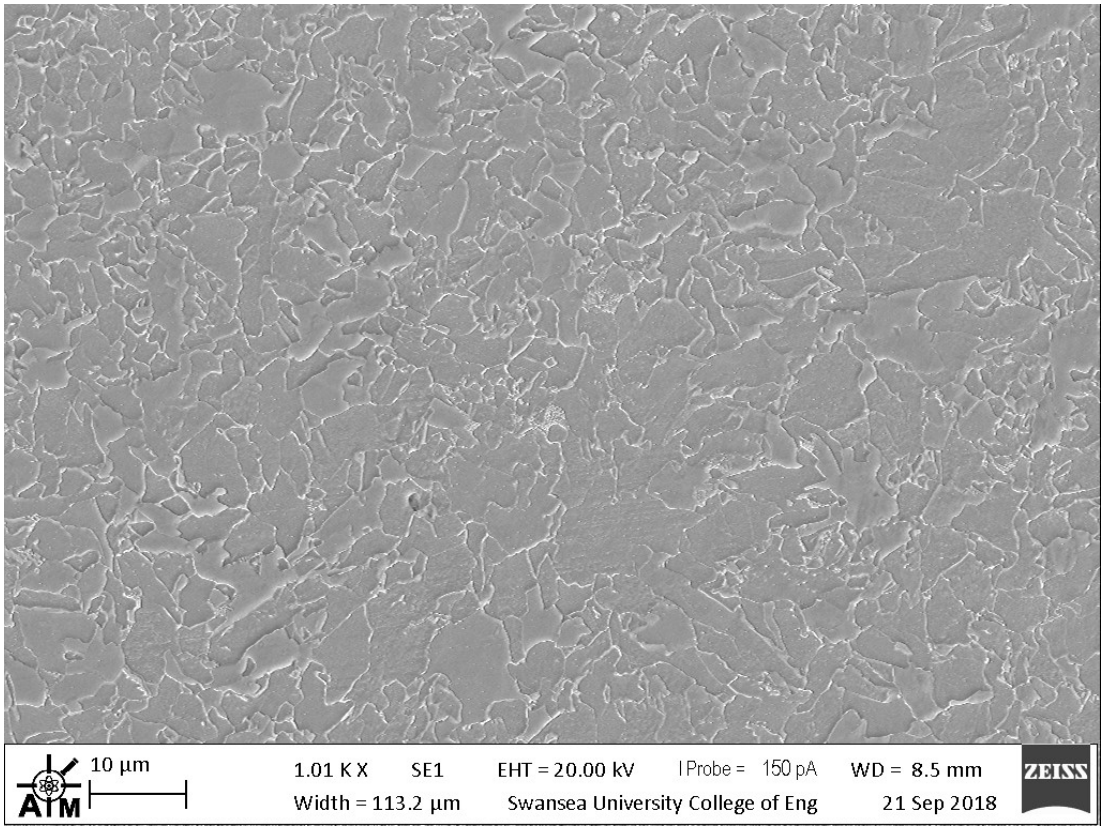

Figure 2.4 SEM micrograph of 800 MPa UTS XPF steel

Like conventional HSLAs, XPF steels benefit from 3 strengthening mechanisms. Firstly, there is the substitutional solid-solution strengthening provided by the addition of alloying elements with atomic diameters that are either larger or smaller than Fe atoms, in this case Mn and Si. In steels, these elements do not form carbides or nitrides, and hence take their place within the atomic lattice, 'substituting' for an Fe atom, according to Hume-Rothery rules [5]. The difference in size between these atoms and the 'native' Fe atoms distorts the lattice and induces a stress field, restricting dislocation motion within the vicinity of the distortion, i.e. it increases the shear stress required for dislocation motion, as any motion of dislocations away from this region would increase the energy of the system overall. In XPFs, the uplift (in MPa) that substitutional alloying elements can impart to the yield strength can be estimated using equation (1), derived by Pickering [19]:

$$32.3 \times wt.\%[Mn] + 83.2 \times wt.\%[Si] + 678 \times wt.\%[P] \qquad (1)$$

The second strengthening mechanism utilised in these steels is that of grain refinement. In XPFs, as in all HSLAs, additions of certain microalloying elements such as Nb and Ti are utilised to refine the austenite grain size. When cast slabs receive high soak temperatures (> 1200 ºC) in the reheating furnace of the hot-strip mill, Nb and Ti (and any already-formed carbides, nitrides, or carbonitrides of these elements) are taken fully into solid solution. As the temperature drops, firstly during rough rolling, then during finishing rolling, solubility of these carbides and carbonitrides decreases and they begin to precipitate. As the austenite grains are deformed during rolling (a thermomechanical process), they undergo 'dynamic recrystallisation', refining the grain size repeatedly through nucleation of 'new' grains at regions of high strain due to the imparted deformation ('static' recrystallisation occurs during thermal treatments such as annealing, rather than thermomechanical processes involving deformation above the recrystallisation temperature). With the carbides and carbonitrides precipitated in the austenite, these act as barriers to growth of the recrystallised austenite grains by increasing the strain required for recrystallisation to proceed, and restricting the motion of recrystallised grain boundaries, further refining the grain size [20]. If finishing rolling takes place at a sufficiently low temperature, recrystallisation may cease and ferrite transformation will occur directly from deformed austenite grains. Assuming rolling takes place above the γ/α transition temperature, by rapid cooling on the run-out-table immediately after finishing rolling, the transformation may occur 'sub-critically', obtaining very fine grain sizes (< 8 μm).

Grain size dictates how far dislocations have to travel before they 'pile up' at grain boundaries – the larger the grain, the more dislocations available to accumulate in these pile ups. As the shear stress at the head of a dislocation pile up is proportional to the number of dislocations involved, this increasing stress in an adjacent grain can in turn initiate dislocation motion in this adjacent grain, propagating the yielding process. Smaller grains necessarily have fewer dislocations (and potentially more neighbouring grains), decreasing opportunities for this propagation effect [20]. Grain size, d, is therefore directly related to yield stress, σ_y, through the Hall-Petch equation, below [21],

$$\sigma_y = \sigma_0 + k_y d^{-\frac{1}{2}} \quad (2)$$

where k_Y is a constant, and σ_0 is the lattice friction stress, (taken as 53.9 MPa in these steels [22]).

Due to the relatively high finishing rolling temperature of 900 ºC, the benefits from grain refinement are not fully-realised in these steels as much as they are in 'conventional' HSLA steels, trading some of the grain size benefits in favour of a third strengthening mechanism, that of 'precipitation strengthening' (or 'dispersion' strengthening), whereby fine precipitates of (typically) microalloy carbides, nitrides, or carbonitrides impede the motion of dislocations (through dislocation 'looping' around the precipitates), and hence resisting plastic deformation [23].

The lack of hard second phases limits void nucleation and suppresses fracture during loading, offering an advantage over multi-phase AHSS [24]. These steels ensure that they are free of Fe_3C by additions of microalloying elements in quantities that are at, or greater than, stoichiometric quantities to ensure they fully combine with available carbon [22]. Whilst some of these microalloys precipitate to be utilised as agents of grain refinement, a substantial amount of strength from precipitation strengthening is gained from the remaining carbonitrides.

The degree of precipitation strengthening, $\Delta\sigma$, can be estimated from the precipitate fraction, f, and diameter, d, through the Ashby-Orowan mechanism [24],

$$\Delta\sigma = \frac{K}{d} f^{-\frac{1}{2}} \ln\frac{d}{b} \tag{3}$$

where K is a constant 5.9 N/m, and b is the Burgers vector, 0.246 nm. This shows that increasing volume fraction or decreasing the diameter of precipitates will increase their effect upon the strength. In the case of XPF steels, Mo and N increase the thermal stability of the precipitates, constraining any precipitate coarsening during hot-rolling, and minimising the d parameter in equation (3) [25]. This facilitates a large volume of nanometre-sized precipitates throughout the ferrite microstructure, imparting a substantial uplift to the yield stress [26].

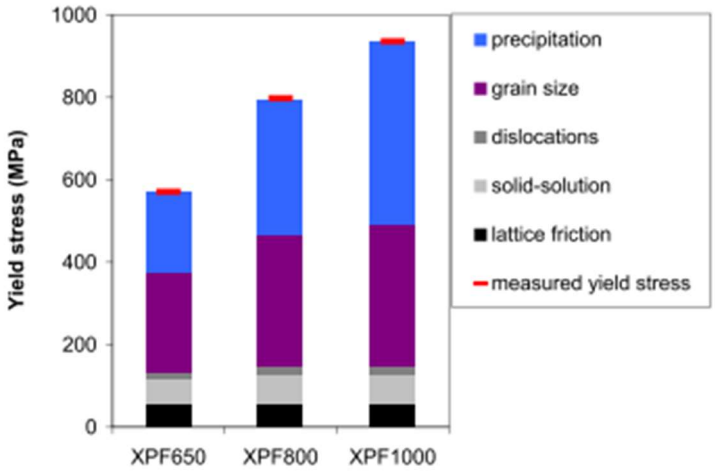

Figure 2.5 Comparison between measured yield stress and calculated yield stress comprising contributions of different strengthening mechanisms [22]. 'XPF' is the Tata Steel brand name for ferrite + nanoprecipitate steels with guaranteed minimum ultimate tensile strengths of 650, 800, and 1000 MPa, for XPF650, XPF800, and XPF1000, respectively.

2.1.3.3 Complex-phase (CP) steels

Complex phase (CP) steels, as the name implies, consist of a complex microstructure containing a ferrite/bainite matrix with small amounts of, martensite, pearlite, and retained austenite (though Kuziak [3] argues that they do not typically contain more than trace amounts of retained austenite). They typically have high levels of grain refinement, and benefit from precipitation strengthening, usually from additions of Nb, Ti and/or V [11,27].

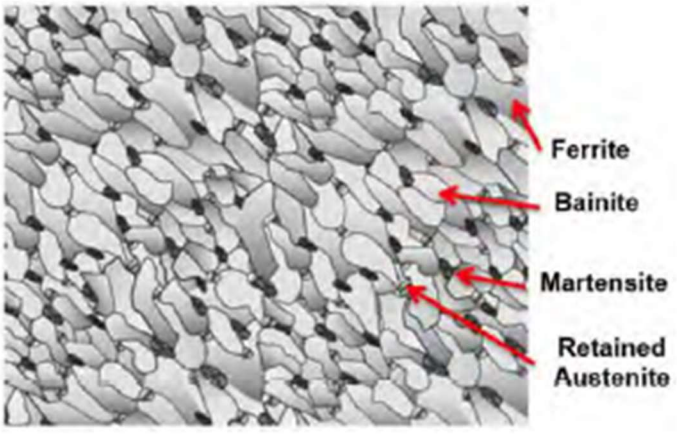

Figure 2.6 Schematic of a CP microstructure [11].

As the presence of retained austenite is not essential, these steels are typically cooled on the run-out-table of the hot strip mill (HSM) in two distinct regimes, with the first

a rapid cool immediately after finishing rolling to a temperature within the ferrite transformation region, whereby the strip is held at this temperature for sufficient time to allow significant ferrite formation, and enriching the untransformed austenite with carbon. In the second regime, the steel is then cooled rapidly for coiling at temperatures above the martensite start temperature, M_S, allowing formation of a fine bainite structure with significant precipitation of microalloy carbides (and carbonitrides) to facilitate precipitation strengthening [28].

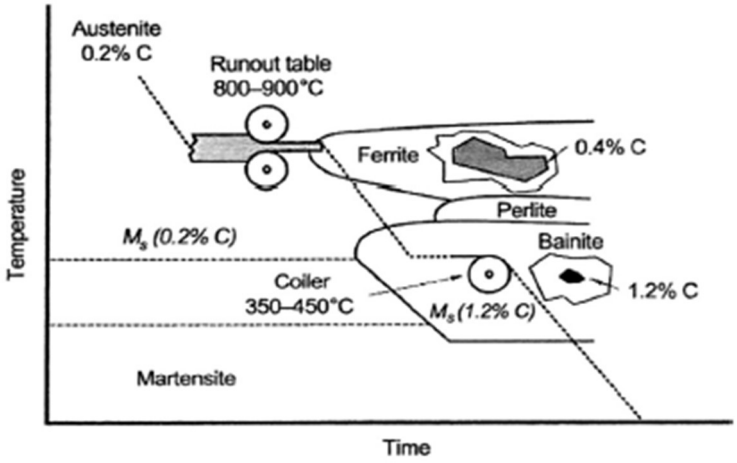

Figure 2.7 Hot-rolling cooling schedule for CP steel [29].

CP steels show very high strength and moderate ductility, as well as high hole expansion coefficients. Furthermore, they have a very high yield strength to ultimate tensile strength ratio, meaning they resist deformation more readily than e.g. dual-phase steels. This combination of properties makes them useful for a wide range of chassis and suspension or body-in-white parts where complex geometry or deep drawing are not requirements, or as anti-intrusion crash protection parts. However, concerns around welding limit the alloying additions that can be made, and mills with constrained run-out-table distance may find the production of hot-rolled CP steels difficult [27].

2.1.3.4 Summary of parts and utilised steels

Below is a summary table of the types of AHSS/UHSS used in chassis and suspension and body-in-white (BiW) applications. Of course, many of these steels find use in other automotive structures, and there are others that are used in chassis and suspension

applications, such as twist beams fabricated using 22MnB5 (which is outlined shortly), and conventional HSLAs.

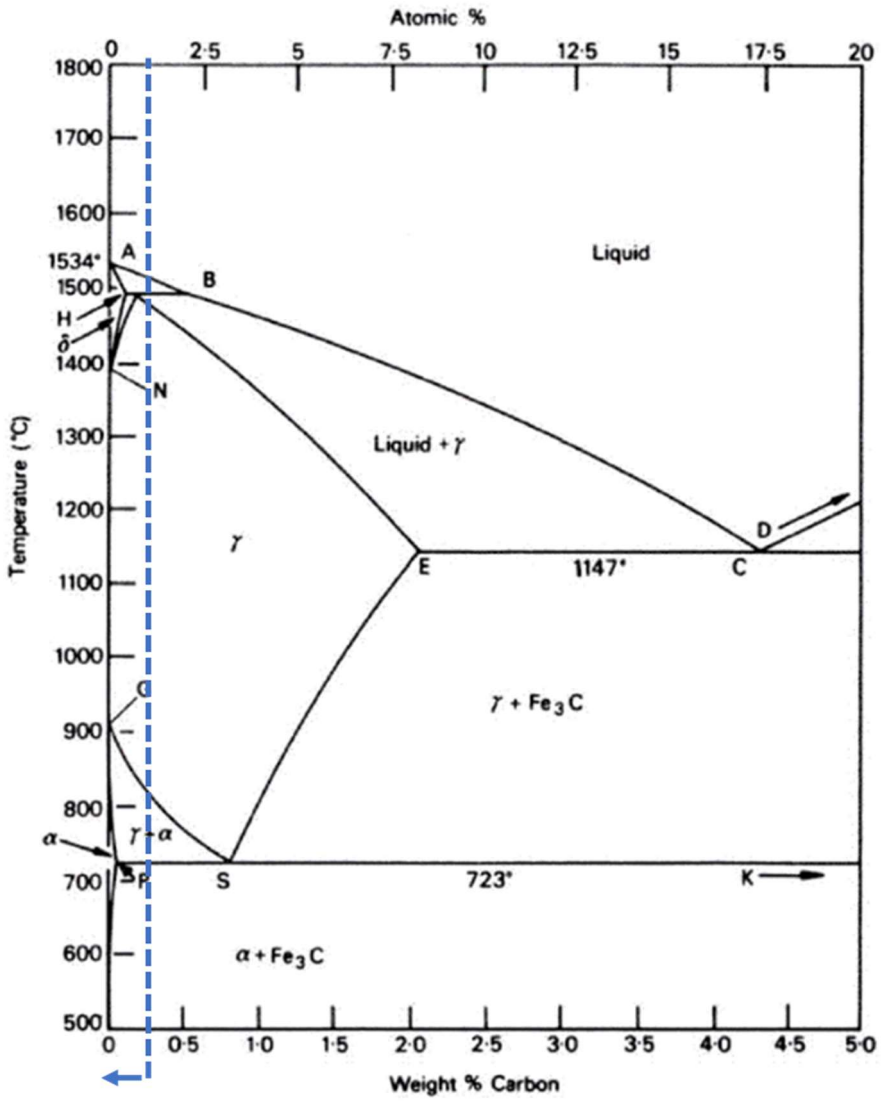

Figure 2.8 Iron-carbon equilibrium phase diagram [20]. All steels studied in this work have carbon levels to the left of the dashed line.

Table 2-1 Typical uses for steels in automotive parts (compiled from information in [11]).

Part	Steel	Part	Steel
A-pillar	22MnB5	Frame rails	CP780
	26MnB5		CP900
	27MnB5		TRIP600
	36MnB5	Front rails	TRIP980
BEV Battery housing	DP1000	Hood outer	DP600
Body side inner	DP800	Lower control arm	FB590
Body side outer	DP500		XPF800
	DP600		XPF1000
B-pillar	22MnB5	Package tray	DP500
	26MnB5	Quarter panel inner	DP800
	27MnB5	Rail reinforcements	TRIP600
	36MnB5	Rear frame rail reinforcements	CP1000
B-pillar reinforcements	CP900	Rear rails	DP800
B-pillar upper	DP1180		TRIP980
	TRIP980	Rear shock reinforcements	DP800
Brake pedal arm	FB450	Rear suspension brackets	CP1000
Bumper beams	CP1470	Rear twist beam	FB590
	FB590		XPF800
Chassis components	CP780	Rim	FB450
	FB590		FB590
Cowl	DP600		XPF800
Crash box	TRIP700	Rocker outer	CP1000
Cross beam	22MnB5	Rocker panels	CP1470
	26MnB5	Roof outer	DP500
	27MnB5	Roof rails	DP1000
	36MnB5		TRIP800
Dash panel	TRIP800		TRIP980
Door outer	DP500	Seat cross member	FB450
Engine cradle	TRIP980	Seat frame	TRIP980
Fender	DP600	Side rail	TRIP700
Fender beam	CP1000	Suspension arm	FB450
Floor panel	DP500	Transverse beams	CP780
	DP600	Tunnel stiffener	CP900
Floor reinforcements	DP1000		

2.1.4 Applications: body-in-white (BiW)

2.1.4.1 Dual-phase (DP) steels

Dual-phase (DP) steels, widely used in safety cage components, outer body, and floor panels (Figure 2.9) consist of an array of second-phase martensite embedded in a ferrite matrix [15], with strength levels increasing as the volume fraction of martensite increases, and exhibiting no sharp yield point [11,30]. This dual-phase ferrite-martensite microstructure also improves the work hardening exponent through concentration of strain within the soft ferrite phase [11], increasing resistance to localised thinning, and allowing more challenging shapes to be formed than is possible with more traditional HSLA steels [31].

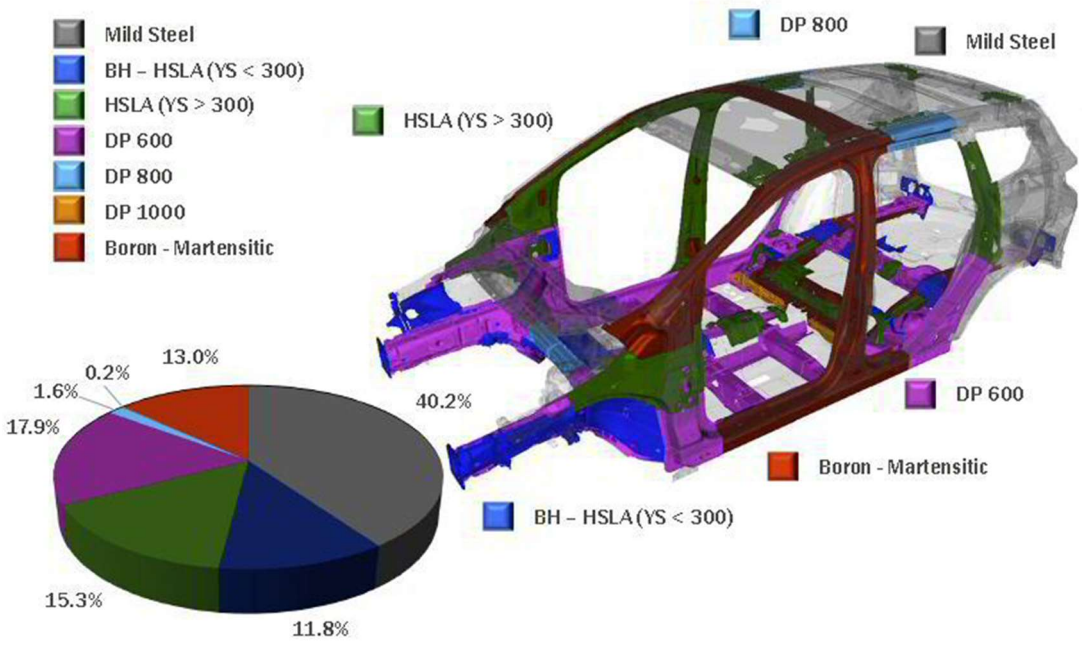

Figure 2.9 Usage of dual-phase (DP) steels in automotive [32].

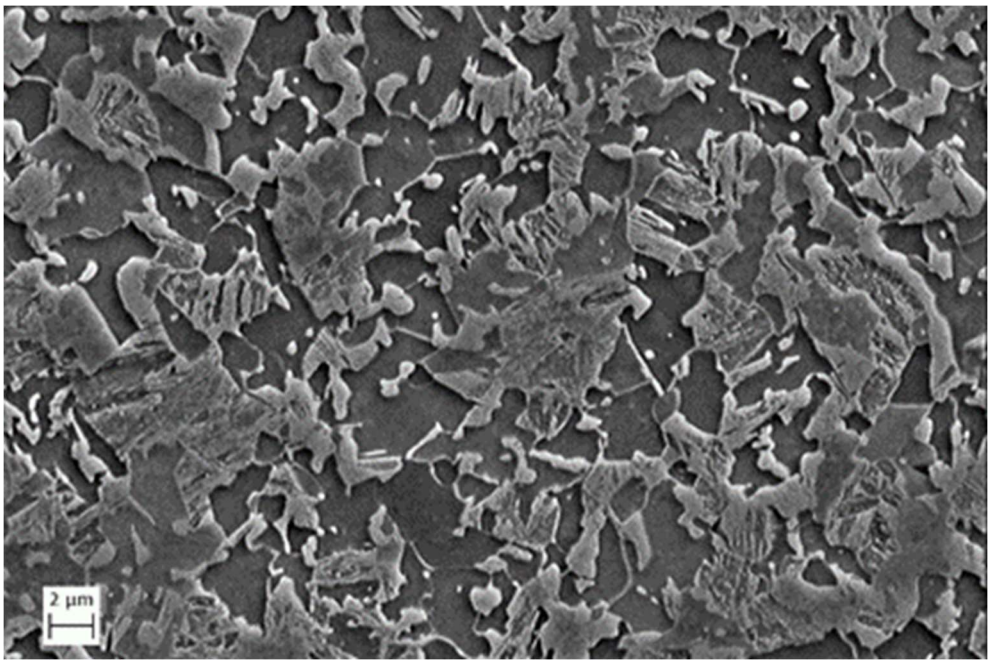

Figure 2.10 SEM micrograph of a typical DP1000 microstructure with approximately 50% ferrite (darker regions), and 50% martensite (lighter regions) (phase fractions estimated using Weka trainable segmentation plugin to ImageJ software).

Whilst the dual-phase microstructure can be achieved with a 'two-step' cooling regime on the HSM run-out-table, DP steels are more typically produced by cold rolling and annealing, either via a continuous annealing (and processing) line (CAPL), or via a continuous hot-dip galvanising line, where the part is required to be zinc-coated. The annealing soak temperatures can be in the fully austenitic region, or more usually 'intercritical', i.e. in the $\gamma + \alpha$ region between A_{c1} and A_{c3}. A 'slow' cool upon exit from the soak region allows for formation of a portion 'new' ferrite grains from the intercritical austenite, and remaining austenite is enriched with carbon that has vacated the newly-formed ferrite grains [33,34]. Allied to alloying additions of Cr to increase hardenability (and retard pearlite formation) and Mn, this carbon enrichment has the effect of stabilising the austenite to lower temperatures, and a subsequent 'rapid' cool inhibits further ferrite formation due to temperatures being too low for the reconstructive ferrite transformation.

Depending on the desired properties, the rapid cool may target a temperature in the bainite-formation region if there is a requirement for increased bake-hardening or hole expansion (or there is a requirement to maintain strip temperature for entry into a zinc pot), followed by a gradual drop in temperature below the martensite start temperature, M_s, to form martensite, or the strip may be cooled directly to the region below M_s, to

form a genuine ferrite-martensite dual-phase microstructure [35]. Example annealing cycles are shown in Figure 2.11 and Figure 2.12, below.

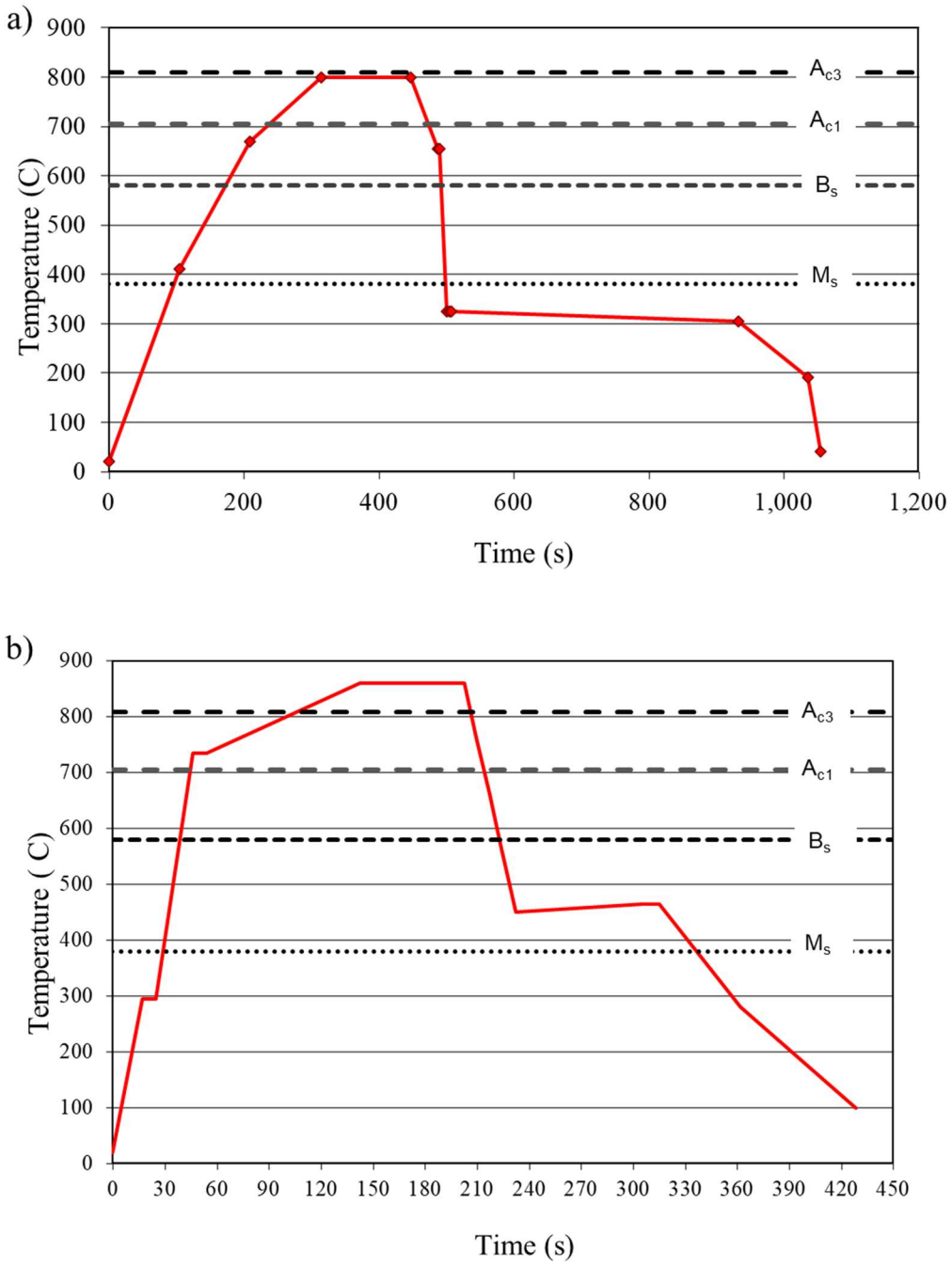

Figure 2.11 Example annealing cycles for dual-phase steels a) intercritical soak temperature with genuine ferrite-martensite final microstructure, b) cooling from the fully-austenitic region to the bainite formation region before final cooling below M_s.

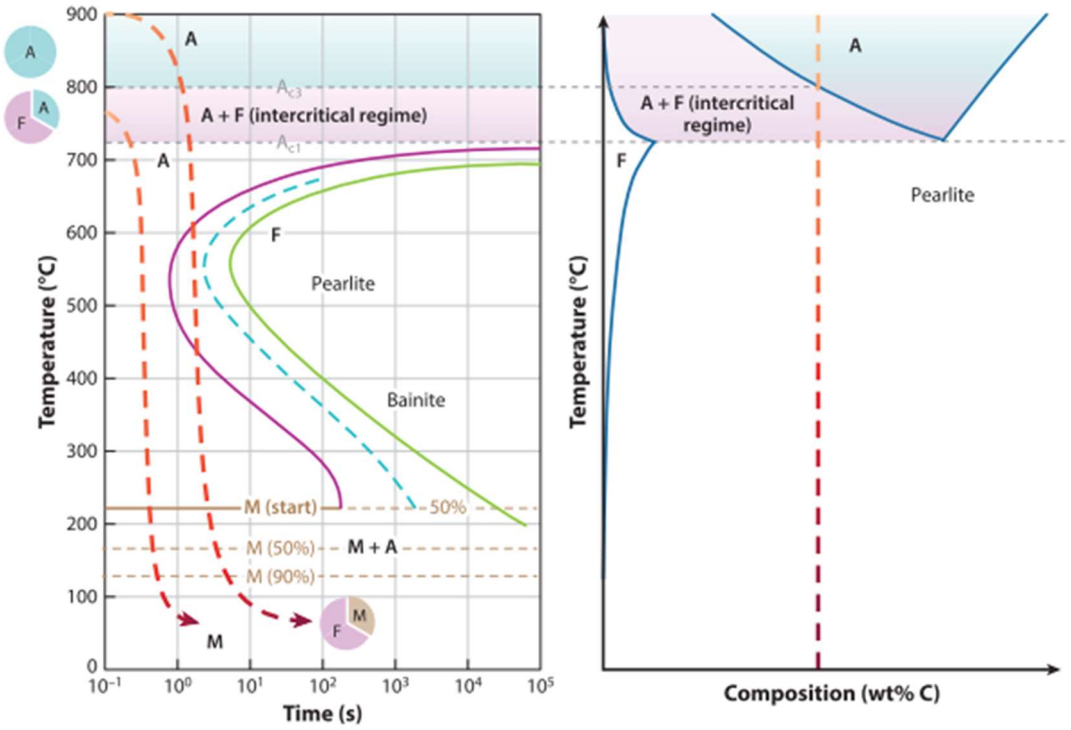

Figure 2.12 Schematic showing potential heat treatment regimens to obtain a DP ferrite-martensite microstructure [32].

The bake hardening response in DP steels allows for an increase in apparent yield strength after undergoing paint curing at 150-200 °C, and unlike in conventional bake hardening steels, is not diminished with increasing pre-strain from deformation during part forming [15], and is in fact dependent on there being an adequate amount of forming strain [11]. In this instance 'bake hardening' refers to the difference (increase) between the measured tensile stress at a given 'pre-strain' level (commonly taken to be 2% plastic strain), and the measured 0.2% proof stress (or offset yield stress) after the pre-strained specimen has been 'baked' for 20 minutes (or however long is specified in the test standard). The difference between the post-bake proof stress and the maximum stress during pre-strain is known as the 'bake hardening index', and is representative of changes in mechanical properties that can be incurred as a result of part-forming, followed by paint curing during manufacture, and is thought to be useful for keeping press loads low whilst benefitting from higher strength in the finished part.

In 'conventional' extra-low carbon (ELC) or ultra-low carbon (ULC) bake hardening (BH) steels, the bake hardening response can lead to an increase in yield stress of up

to 10%, and largely follows a two-stage process [36]. In the first stage, forming of a part either through stamping or pressing leads to typically between 2 and 5 % strain being imparted to the steel, with an accompanying increase in the density of fresh mobile dislocations. Diffusion of solute carbon atoms (nitrogen would also fulfil a similar role, but is removed through alloying with Al ('killing') and microalloying elements such as Ti and Nb to avoid room temperature aging) to these newly-formed dislocations leads to the formation of 'Cottrell' atmospheres, whereby solute carbon (or nitrogen if not fully 'killed') atoms diffuse to dislocation cores, reducing the residual stress associated with a dislocation, and hence pin the dislocations in place (i.e. preventing dislocation motion through increasing the energy required for dislocation motion). Likewise, once the solute atoms are in place at the dislocation core, they too will remain pinned. It is these solute atoms at the dislocation core that form the Cottrell atmosphere. The degree to which dislocations are pinned has been shown to vary linearly with time (to the power $\frac{2}{3}$) according to equation (4) [37],

$$\frac{N(t)}{N_s} = n_0 b^3 \left(\frac{\pi}{2}\right)^{\frac{1}{3}} \left(\frac{ADt}{kT}\right)^{\frac{2}{3}} \tag{4}$$

where $\frac{N(t)}{N_s}$ is the fraction of pinning that is complete, n_0 is the solute (carbon) density in the matrix, b is the Burger's vector, k is Boltzmann's constant, T is absolute temperature, D is the diffusion coefficient of carbon in the matrix, and A is the 'interaction parameter' (analogous to the binding energy of the solute carbon atom to the dislocation) [38]. This adequately describes bake hardening behaviour up to about 30% aging, but has been shown to be limited by neglecting retardation of diffusion due to depletion of solute atoms. Through development of these ideas [39,40], De [41] proposed the following equation to describe the aging kinetics:

$$\frac{\Delta\sigma}{\Delta\sigma_{atm}} = K_1 + K_2 \left(\frac{Dt}{T}\right)^{\frac{2}{3}} \tag{5}$$

where $\Delta\sigma$ is the difference between upper yield stress post pre-straining and baking and the flow stress at end of straining, $\Delta\sigma_{atm}$ is the maximum increase in the yield stress when atmospheres reach saturation, t is aging time, T is the absolute again temperature, D is the diffusion coefficient, and K_1 and K_2 are constants dependent on test condition [38]. Figure 2.13 demonstrates the basic kinetics of this process.

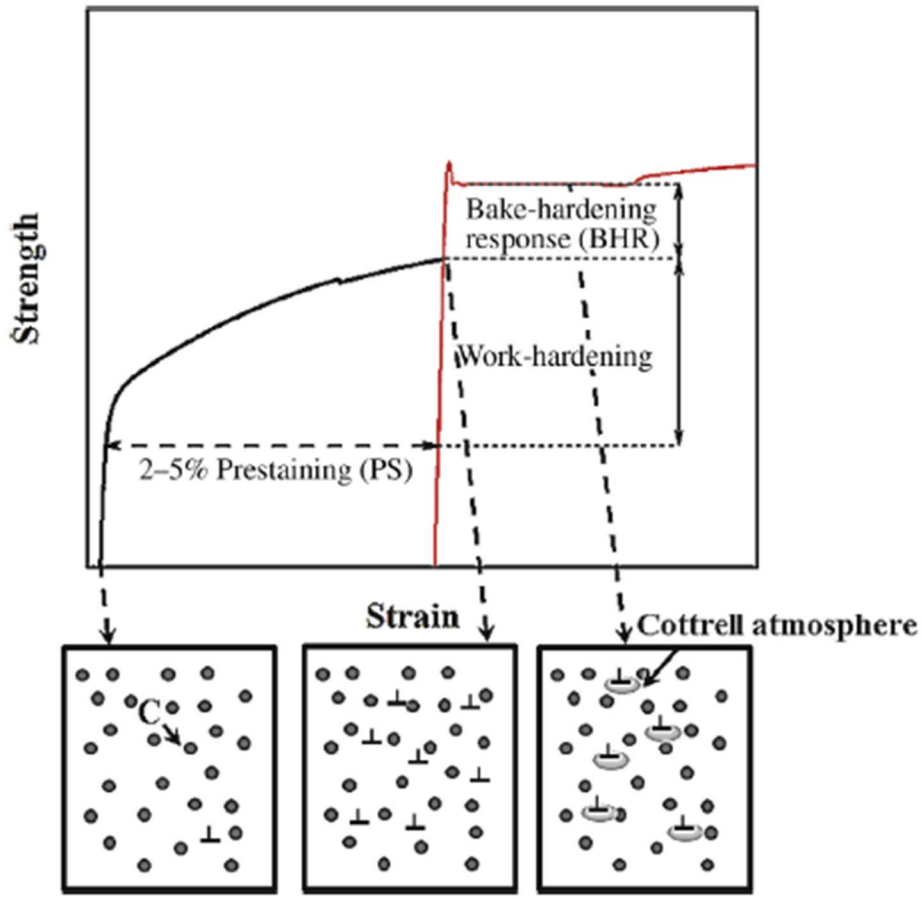

Figure 2.13 Schematic of bake hardening response and associated carbon distribution for an ultra-low-carbon (ULC) ferritic steel [38].

In the second stage, if all dislocation cores are occupied and the Cottrell atmospheres 'condensed', carbon begins to segregate to planar defects, leading to nucleation of coherent carbides at vacancies and dislocations [42].

For the above process to occur, certain criteria must be met. Firstly, there must be a high density of fresh mobile dislocations, without which there can be no 'atmospheres'. Secondly, the rate of dislocation recovery during the baking treatment must remain low. Finally, there must be sufficient concentration of mobile solute atoms to pin the dislocations, in turn requiring alloy chemistry to be carefully tailored to avoid tying up available carbon [43].

For multi-phase AHSS, the situation is complicated further by the very presence of multiple phases. In DP steels, the transformation of intercritical austenite to martensite leads to a high density of mobile dislocations in the adjacent ferrite, enabling rapid

formation of Cottrell atmospheres within the ferrite phase. During baking, carbon segregates to martensite lath boundaries, preventing migration of new dislocations and leading to formation of intermediate carbides and ε-carbide. Where bainite is present, its high dislocation density and supersaturation of carbon atoms accelerates dislocation pinning, explaining the increased bake hardening response in DP steels in the presence of significant volume fractions of bainite [38].

DP steels show a good combination of strength, ductility, and work hardening, and allied to the relative ease with which they can be welded, they are increasingly used in a range of automotive parts, both internal and external to the vehicle, as seen from Figure 2.9.

2.1.4.2 TRansformation Induced Plasticity (TRIP) steels

TRansformation Induced Plasticity (TRIP) steels show the best combination of strength and ductility of any of the '1st generation' AHSS, very high levels of work hardening, and substantial energy-absorption properties [44]. First produced commercially in the early 1990s by the Nippon Steel Corporation, TRIP steels' microstructure have a ferritic-bainitic matrix with embedded dispersions of retained austenite (γ_{ret}), primarily induced in cold reduced strip during an 'austempering' isothermal heat-treatment within the bainite-formation range of temperatures. This follows rapid cooling from annealing soak temperatures within the intercritical ($\gamma+\alpha$) region to avoid formation of new ferrite or pearlite. At the bainite transformation temperature, austenite grains decrease in size, and carbon atoms partition to the austenite from the newly-formed bainite, further enriching the austenite with carbon (and increasing its stability). Once the free energy of bainite-formation exceeds that of austenite, this reaction ceases and the austenite persists to room temperature [45]. An example annealing cycle is shown in Figure 2.14.

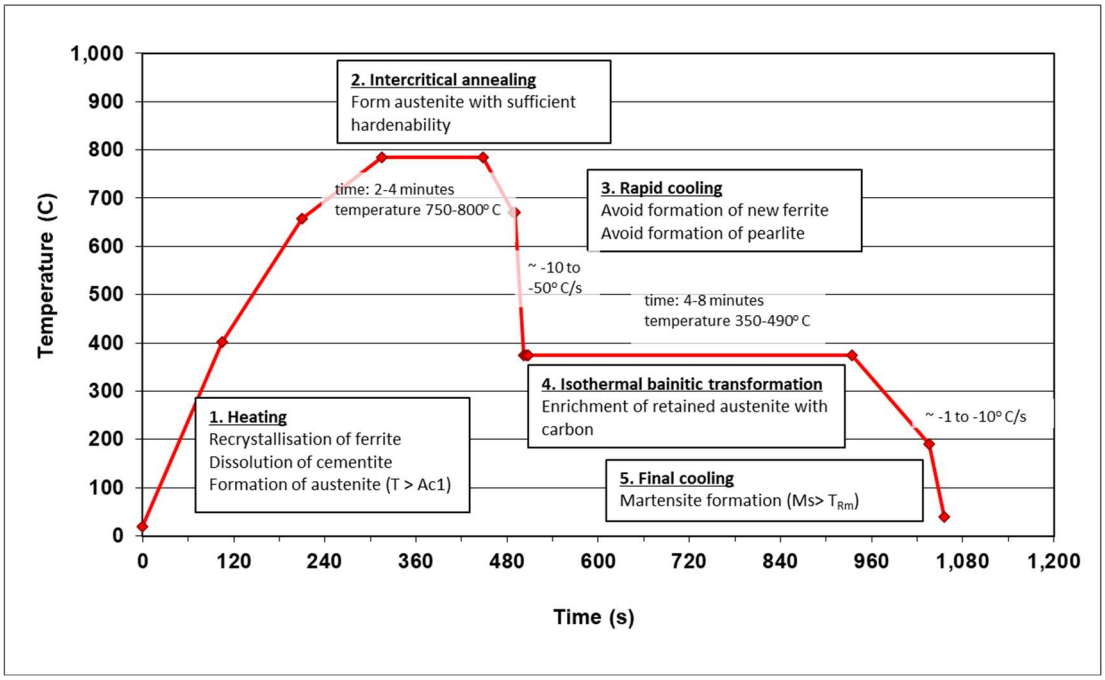

Figure 2.14 Example continuous annealing cycle for cold-rolled, intercritically annealed TRIP steel (adapted from [45]).

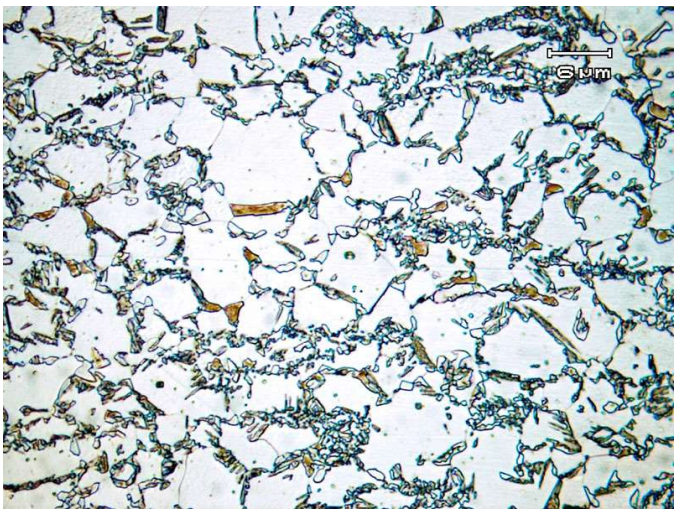

Figure 2.15 Optical micrograph of TRIP steel. Microstructure contains metastable austenite (white) and associated bainite (dark grey needles alongside austenite), martensite (straw coloured) within matrix of ferrite (grey). Microstructure revealed using 2-step etching process of 4% picral and 10% aqueous sodium metabisulfite solution [46].

Excellent work hardening in TRIP steels arises not only from the dispersion of hard second phases within a ferrite matrix (deformation takes place primarily in the soft ferrite phase whilst martensite remains relatively unaffected), as in DP steels, but also from the presence of retained austenite, which progressively transforms to martensite as strain is increased (often referred to as the 'TRIP effect'), the level of which is

determined by carbon content, i.e. unlike DP steels which show greater work hardening earlier on during loading, in TRIP steels work hardening persists to higher levels of strain [11].

Despite the increased bake hardening response seen in multi-phase AHSS, it has been found (e.g. [47]) that work hardening is (>2×) more significant than bake hardening in both TRIP and DP steels when it comes to crash performance as measured by crush force (though this could also apply to part formation more generally). In essence, the work hardening exponent (n-value) is the measure of how a material gains strength during deformation (increasing strain), and can be obtained from the slope of the true stress versus true strain curve, when plotted on a logarithmic scale.

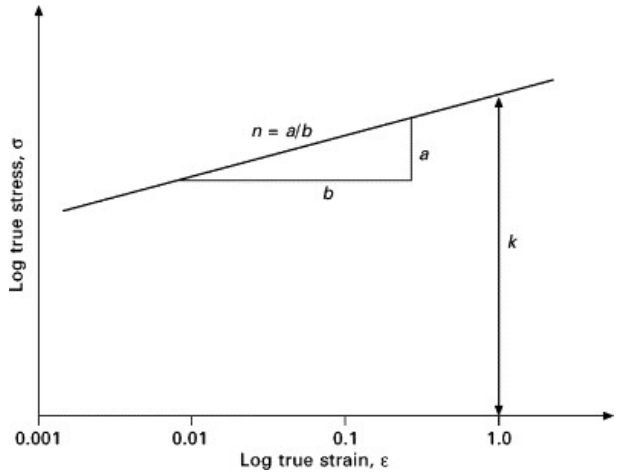

Figure 2.16 Logarithmic plot of true stress versus true strain. n represents the work hardening exponent [48].

This relationship between stress and strain is expressed in the equation

$$\sigma = k\varepsilon^n \tag{6}$$

where σ is true stress, ε is true strain, k is a constant, and n the work hardening exponent [48].

High work hardening permits greater opportunity for stretch forming due to increased resistance to localised thinning, and control of carbon levels determines whether retained austenite transforms during part-forming (lower carbon), or persists into service (higher carbon), making TRIP steels excellent for tailoring for either ease of part manufacture with high strength in the as-manufactured part, or high work hardening during a crash event [45]. Despite this, use of TRIP steels is constrained by

difficulties utilising resistance spot welding as a joining technique due to their additional alloying requirements (higher Si, C, Al etc.) compared to e.g. DP steels [11].

2.1.4.3 Boron Hot-forming (HF) / Press-hardenable steels (PHS)

Also used in agricultural, lifting and excavating, and petrochemical industries, hot-forming (HF), or press-hardening (PHS) boron steels (hereafter referred to simply as 'boron steels') are typically utilised in anti-intrusive 'safety cage' parts of the BiW structure, such as A- and B-pillar, roof- and bumper-reinforcements, and floor. The anti-intrusive nature of the safety cage is borne out of the very high strengths of these steels, with 0.2% proof strength typically ~ 1200 MPa, and UTS typically ~ 1500 MPa [49].

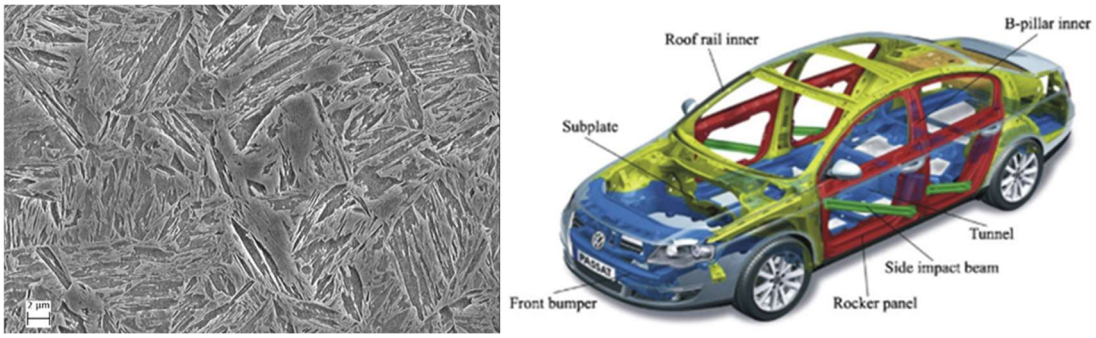

Figure 2.17 Left: SEM image of quenched microstructure for 22MnB5, the most commonly used boron hot-forming steel (author's image); Right: Typical parts constructed from hot-forming boron steels [50].

This remarkably high strength for a low-alloy steels is realised due to the (nominally) fully-martensitic microstructure, achieved during forming of the part at elevated temperatures in a process commonly referred to as 'hot-stamping' [50].

In the direct hot-stamping process, prepared blanks, typically with ferrite-pearlite or ferrite-segregated carbide microstructures and UTS ~ 600 MPa, are austenitised at 900 – 950 ºC for 3 – 10 minutes in a furnace. Upon exit from the furnace, the blanks are transferred by robot to a water-cooled die where it is formed into shape, with the part quenched at a sufficient rate to avoid formation of any ferrite or pearlite, achieving a fully-martensitic microstructure (and accordingly high strength). As transformation

from austenite to martensite occurs entirely within the press/die, and a reduction of flow stress due to forming taking place at elevated temperatures, very little springback is encountered once the formed part is extracted from the tool, and relatively complex parts can be realised [49,51]. In the indirect hot-stamping process, the part is cold-formed in the as-annealed condition before being subjected to a heat-treatment analogous to that used in the direct hot-stamping cycle, whereby the formed part is transferred after soak to a 'calibration' die, where the part is formed to its final shape and simultaneously quenched, as per the direct process [11].

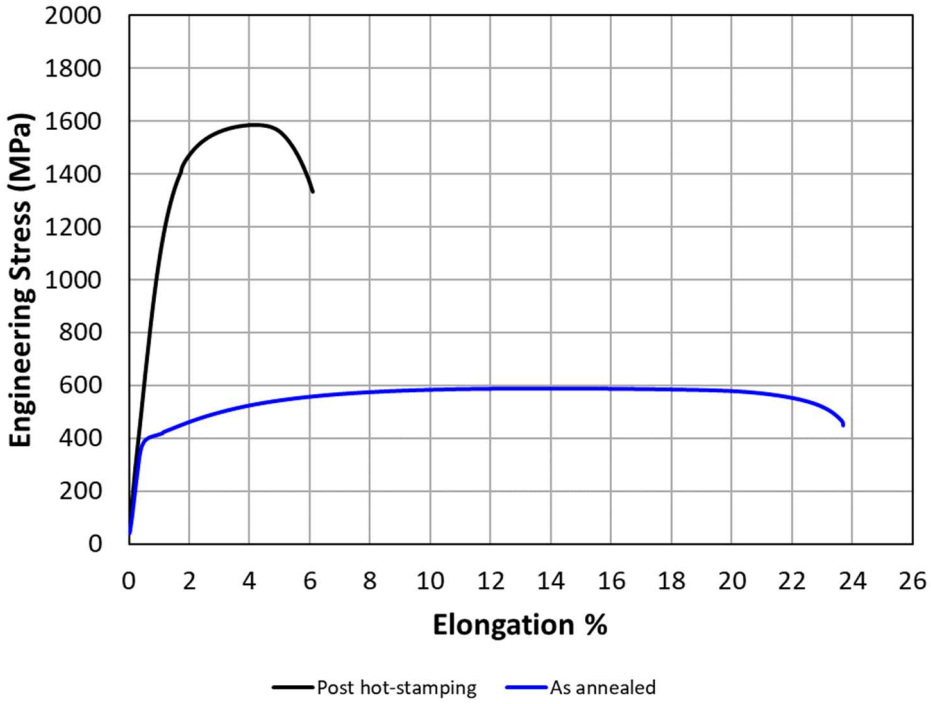

Figure 2.18 Tensile properties of 22MnB5 in the 'as annealed' (blue line) and post hot-stamping (black line) conditions.

In steels, the martensitic transformation is displacive, rather than reconstructive, meaning there is a high level of shear to the austenite lattice, with no associated atomic diffusion. Newly-formed (tetragonal) martensite and the 'parent' austenite therefore have an orientation relationship (OR), which in the steels described here is shown to follow that first described by Kurdjumov and Sachs [52]. The high degree of shear induces a high dislocation density to the martensite, and in tandem with the supersaturation of carbon in the martensite lattice, imparts very high strength and hardness to the martensitic microstructure, as well as an accordingly low formability [20].

Critical to martensite formation in low alloy steels is the ability to achieve cooling rates sufficient to avoid formation of ferrite, pearlite, or bainite. Whilst alloying additions such as manganese and chromium can increase hardenability, it has been found that without the addition of boron it would be very difficult to achieve the fully-martensitic microstructure using the water-cooled dies currently used in the hot-stamping process [53]. Boron greatly increases hardenability, even when only present in minute amounts (of the order of 10ppm), by effectively slowing the rate at which the ferritic transformation proceeds by inhibiting nucleation of proeutectoid ferrite at austenite grain boundaries [54]. This has the effect of pushing the ferrite 'nose' to substantially longer times (without affecting M_s, A_{r3}, or A_{r1}) on the continuous cooling diagram (CCT), and permitting avoidance of reconstructive phase transformations with cooling rates that are practicable in an industrial setting. An illustration of this effect of boron on hardenability can be seen from the CCT curves in Figure 2.19, plotted with a nominal 22MnB5 composition with and without a 10 ppm boron addition.

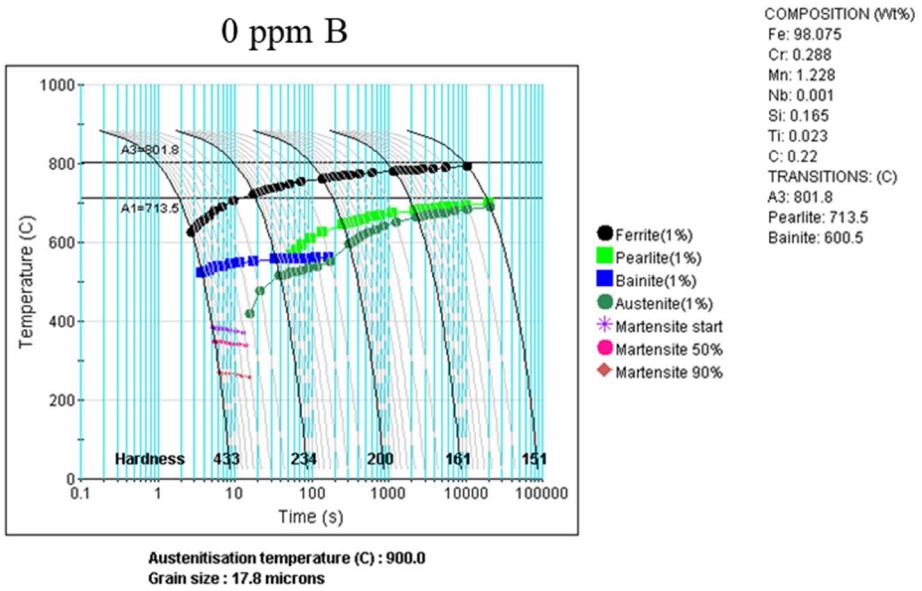

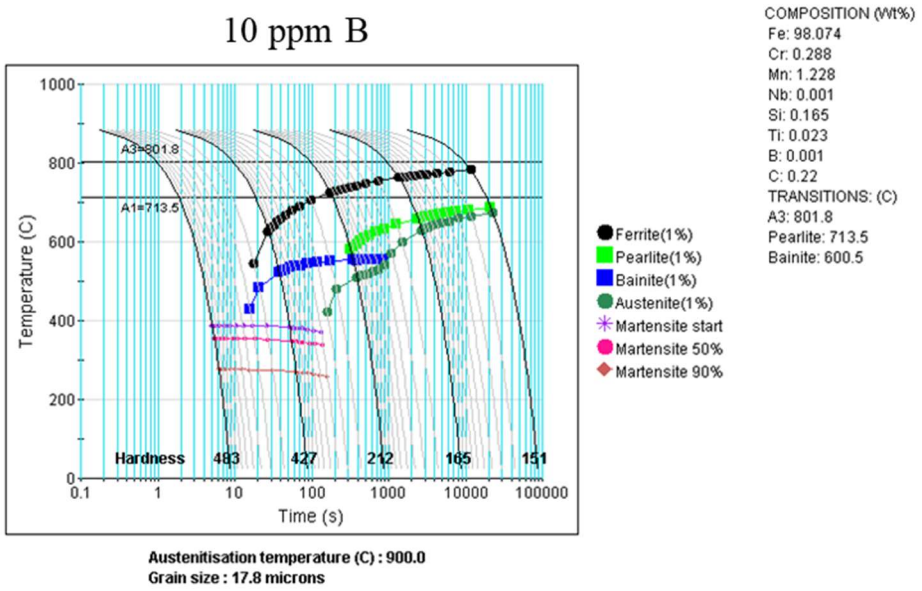

Figure 2.19 CCT curves plotted using JMatPro software illustrating the effect of a 10ppm boron addition on the hardenability of a hot-stamping steel (courtesy of colleague Dane Hardwicke). Alloy chemistry based on actual alloy chemistry of 22MnB5 sample used in this thesis.

The high-strength boron steels are often used in association with lower-strength boron steels developed by a number of steel producers, typically in the form of tailor welded blanks (TWB). The lower-strength boron steels (~ 500 MPa UTS) do not achieve a fully-martensitic microstructure, and consequently they show much higher elongation (~20% total elongation) after hot-stamping than the high-strength version. Furthermore, their lower carbon equivalents permit ease of welding in comparison to the high-strength boron steels, enabling the TWBs to be joined to other components more readily than if utilising the high-strength boron steels alone [55].

2.1.4.4 Other considerations

All of the steels described above belong to what is considered to be the '1st generation' AHSS, usually used to describe steels that utilise both careful alloying and thermomechanical processing to achieve combinations of strength and ductility that were not achievable on an industrial scale prior to their development. They are widely utilised in automotive components today.

'2nd generation' AHSS such as TWinning Induced Plasticity (TWIP) steels and austenitic stainless steels exhibit remarkable combinations of strength (up to ~1100

MPa) and ductility (up to 70% total elongation), but their use thus far has been limited, primarily due to the high alloying costs (e.g. TWIP steels typically contain ~20% Mn), and associated difficulties with processing (e.g. welding) due to the high alloy content [15].

To remedy this, a '3rd generation' of AHSS, a group that includes Carbide-Free Bainite (CFB) and Quench and Partitioning (Q&P) [56] steels has been developed that attempts to combine the low alloy content of the 1st generation AHSS with the enhanced properties of the 2nd generation AHSS. This is achieved largely through use of novel heat-treatment cycles that involve the partitioning of carbon from a hard second-phase/microconstituent (bainite or martensite) to a retained austenite phase that remains stable to room temperature, thus retaining much of the strength from the hard phase whilst increasing formability (and diminishing the mismatch in hardness between phases)[57]. Whilst these steels are producible on an industrial scale using existing facilities, their use is not yet widespread. Discussion of both 2nd and 3rd generation AHSS is beyond the scope of this thesis.

2.2 Sources of hydrogen

There are numerous opportunities for automotive steels to encounter hydrogen, both during manufacture and in service. The following pages provide background to some of the more fundamental considerations, particularly around corrosion, and assesses some of the existing data for automotive steels.

2.2.1 Corrosion

Although there are several potential sources of hydrogen that a steel may encounter during manufacture (some of which are assessed later on in the chapter), it is in-service aqueous corrosion reactions that are of primary concern when considering hydrogen embrittlement in automotive parts – everything else is within the control of the manufacturers.

2.2.1.1 Fundamentals

Corrosion fundamentally is an electrochemical process entailing two half-reactions, involving the transfer of an electron from an oxidised surface at an anodic site to a reduced surface at a cathodic site. For steels, room temperature aqueous corrosion involves the following anodic reaction [58],

$$Fe \rightarrow Fe^{2+} + 2e^{-} \tag{7}$$

and, simultaneously, at least one of the following cathodic reactions,

$$H_2O + e^{-} \rightarrow H + OH^{-} \tag{8}$$

$$H_2O + ½O_2 + 2e^{-} \rightarrow 2OH^{-} \tag{9}$$

$$2H^{+} + ½O_2 + 2e^{-} \rightarrow H_2O \tag{10}$$

$$2H^{+} + 2e^{-} \rightarrow H_2 \tag{11}$$

where reactions (8) and (9) primarily occur in neutral or alkaline solutions, and reaction (10) and (11) primarily occurring in acidic (low pH) conditions.

Thermodynamically, favourability for these reactions depends upon the instantaneous changes in Gibbs free energy within the cell, according to

$$\Delta G = -zFE \tag{12}$$

where ΔG is the change in Gibbs free energy, z is the (stoichiometric) number of electrons exchanged in the reaction, F is Faraday's constant, and E is the cell potential. The corrosion reaction will proceed when $\Delta G < 0$ (with the reverse reaction occurring if $\Delta G > 0$, and equilibrium if $\Delta G = 0$)[59].

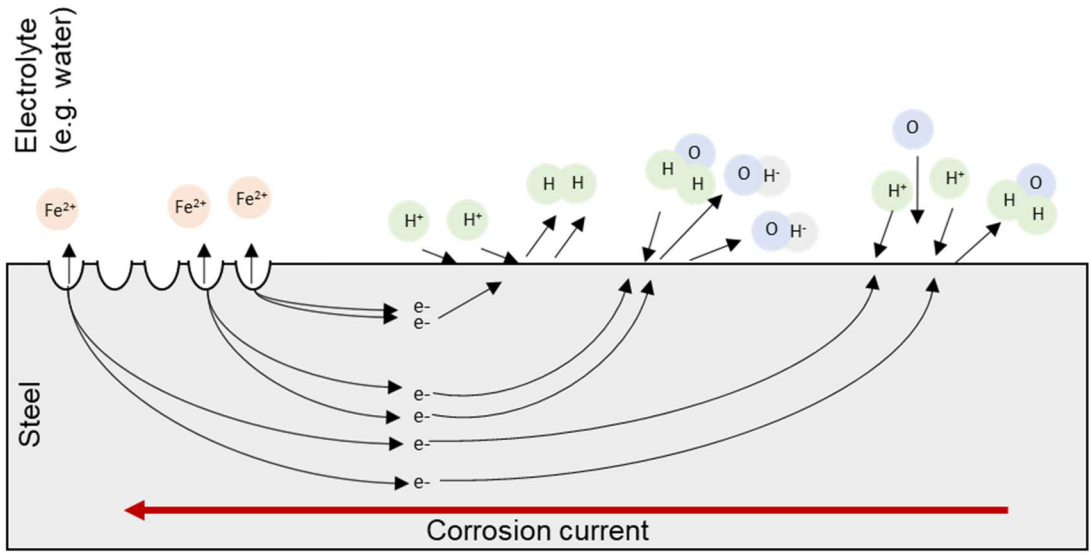

Figure 2.20 Schematic of the basic corrosion reactions at a steel surface in water.

To calculate the cell potential, Nernst took (12) a stage further to derive

$$E_{cell} = E^0_{cell} - \frac{RT}{zF} \ln Q_r \qquad (13a)$$

or

$$E_{cell} = E^0_{cell} - \frac{2.303RT}{zF} \log_{10} Q_r \qquad (13b)$$

where E_{cell} is the cell potential, E^0_{cell} is the *standard* cell potential, R is the universal gas constant (8.314 K^{-1} mol^{-1}), T is the absolute temperature (in Kelvins), and Q_r is the 'reaction quotient' of the cell, calculated by

$$Q_r = \frac{a}{b} \qquad (14)$$

where a and b represent the activity of product and reactants, respectively [60]. For the cathodic reactions above (8,9,10,11), the Nernst equation can be used to calculate the equilibrium potentials as a function of pH, which can be represented graphically in a potential-pH, or Pourbaix, diagram for steels in water (Figure 2.21)[61], where

oxygen reduction equilibrium reaction represents the upper boundary and hydrogen evolution equilibrium reaction the lower boundary of the range where water is stable, with both having slope -0.0592 V/pH × (no. H^+ ÷ no. e^-). This is also important when considering polarisation (discussed later), as it allows calculation of an overpotential, η, with respect to the applied potential and the equilibrium potential.

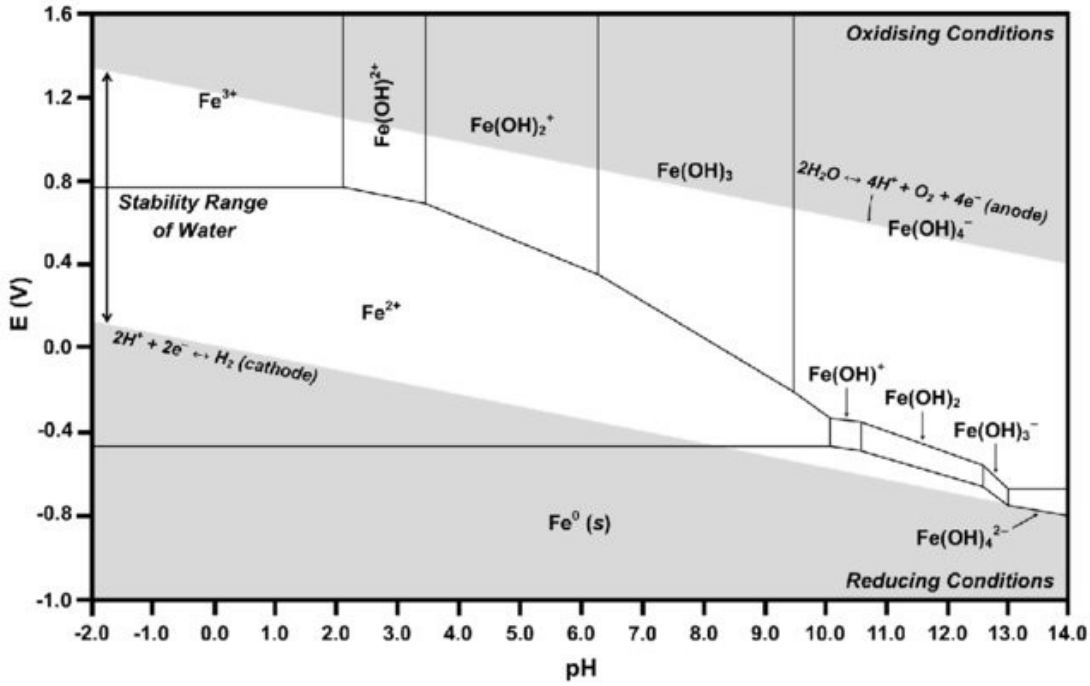

Figure 2.21 Potential-pH diagram for the Fe-H_2O system [62].

The kinetics of corrosion reactions can be inferred using 'Evans' diagrams. These show the synergy between current density (plotted as the logarithm of the current density) and potential for both the oxidation and reduction reactions. In a freely corroding system, all electrons lost in the oxidation reaction are consumed in the reduction reaction, therefore corrosion occurs only where the oxidation and reduction curves intersect, from which we can obtain the free corrosion potential, E_{corr}, and corrosion current, I_{corr} [63].

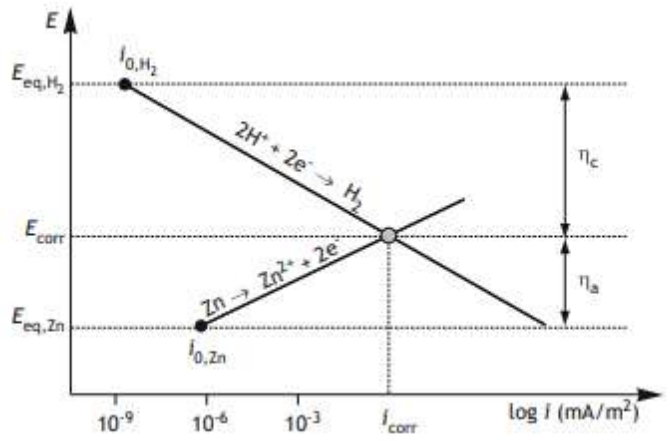

Figure 2.22 Evans diagram of zinc in acid solution [64].

As electron flux determines reaction rate (though may not strictly be the 'rate-limiting' parameter), corrosion rate (or mass loss) can be calculated using I_{corr} in:

$$CR = \frac{I_{corr} M t}{F z \rho} \tag{15}$$

where M is atomic mass (g/mol), t is time (in seconds – value depends on duration over which calculation is undertaken), z is number of electrons in oxidation reaction, F is Faraday's constant, and ρ is mass density (in g/cm^3) [64].

When studying corrosion in automotive steels, the conditions that are primarily of interest involve aqueous environments containing chloride ions, typical of coastal environments or where roads are treated to avoid formation of ice during winter. Sea water is ~ 3.5 wt% NaCl, plus a variety of dissolved metal ions, and as such has a higher electrical conductivity than fresh water, accelerating corrosion processes. Nonetheless, even in characteristically non-marine conditions, atmospheric humidity, rain, and surface spray can provide an additional aqueous source to any accumulation of salts [65]. In this context, it was found by Ootsuka [66] that travel by road after a period of rain provides a source of water that re-dissolves previously dried salts, and increasing the corrosion current at specific locations on the vehicle structure, before a gradual 'rinsing' effect lowered the concentrations of dissolved salts, in turn lowering the corrosion current.

In practice, apart from the general problems of corrosion due to environmental factors, vehicles in service may encounter a range of specific corrosion mechanisms, often in parallel.

2.2.1.2 Galvanic corrosion

Galvanic corrosion occurs where two metals (or conductive non-metals) of differing corrosion potential are in contact, both electrically and electrolytically (i.e. both in contact with an electrolyte), where the less 'noble' metal suffers accelerated corrosion [67].

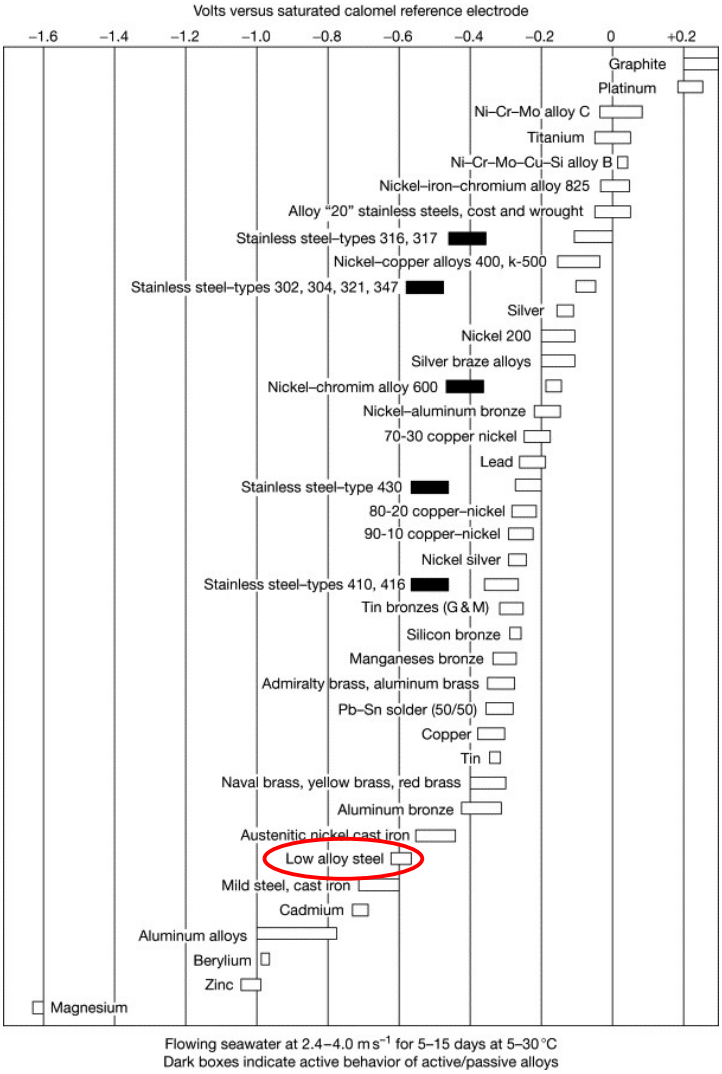

Figure 2.23 Galvanic series for metals in seawater with moderate flow [67]. Metals, conductive non-metals, and alloys are more 'noble' (less reactive) the higher they appear in the table, and more reactive the lower they appear in the table. The steels studied here can all be considered as 'low alloy steels', circled red.

When metals with 'dissimilar' corrosion potentials are in contact, they are each forced to a common potential between their individual corrosion potentials. The further apart their individual potentials, the greater the driving force for galvanic corrosion (the opposite is also true). Although in practical terms consideration must be given to the relative surface areas of cathodic and anodic regions, the notion of 'driving force' for galvanic corrosion is illustrated when considering the Evans diagram for galvanically-coupled iron and zinc, modified to account for ohmic drop incurred in the electrolyte as a result of the galvanic coupling (Figure 2.24). Here point 1 signifies the free corrosion of iron before coupling, and point 2 the free corrosion of zinc; points 3 and 4 represent the corrosion potentials after coupling of iron and zinc, respectively [64]. Calculation of the potential difference between the two metals (driving potential for galvanic corrosion) is given by:

$$\Delta V = E_{cath} - E_{an} = IR \cong i_c \rho \left(\frac{S_c}{kS_a}\right)^2 \quad (16)$$

where ΔV is the driving potential of the cell, E_{cath} and E_{an} are the corrosion potentials of the cathodic and anodic metals *after* coupling, I is current, R is resistance, i_c is cathodic current density, ρ is electrolyte resistivity, S_c and S_a are the surface areas of cathodic and anodic regions, respectively, and k is a constant [64].

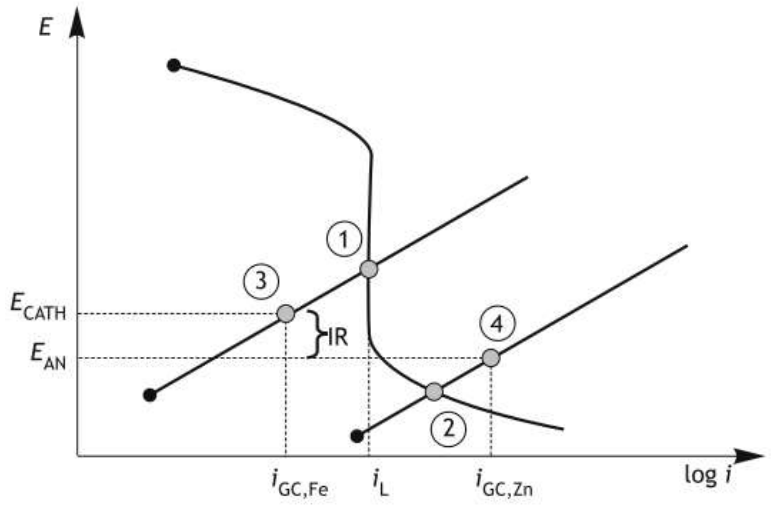

Figure 2.24 Simplified Evans diagram for galvanic coupling of Fe–Zn in a neutral aerated solution, accounting for ohmic drop [64].

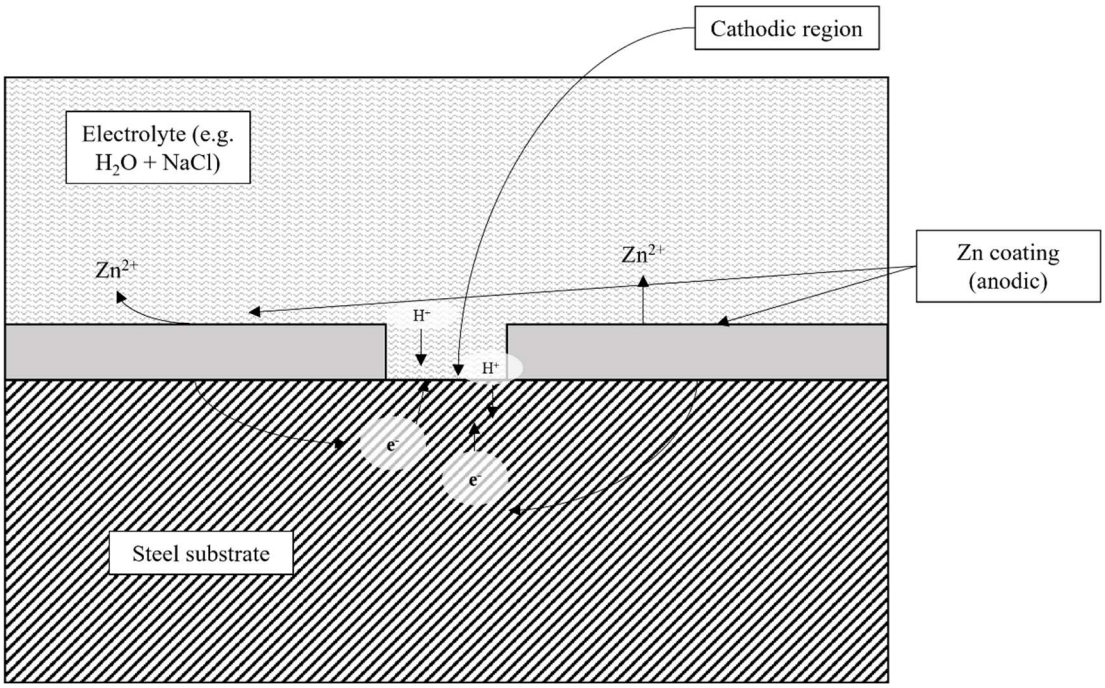

Figure 2.25 Schematic of galvanic corrosion of zinc coating on a steel substrate.

In certain situations, galvanic corrosion can occur even when metals appear to be similar enough that this would not be a concern as found by Wint [68]. When assessing the corrosion properties of heat-treated, fully-martensitic 22MnB5 welded to a 315 MPa yield strength HSLA steel, through use of scanning vibrating electrode technique (SVET) alongside traditional electrochemistry techniques, although they are both nominally low-alloy steels, their free corrosion potentials were sufficiently different (-0.2 V lower in 22MnB5) to drive galvanic corrosion in an aerated 0.017 M NaCl solution. In this instance the martensitic steel corroded as the anode over the predominantly ferritic HSLA. Furthermore, galvanic corrosion has been observed to occur within the same dual-phase steel, where a galvanic couple was initiated between the ferrite and martensite phases. In this case, the ferrite phase corroded anodically, and the martensite phase suffered less corrosion, although when a zinc coating was added to the system, the coating corroded sacrificially, and a hydrogen evolution reaction at the steel surface caused the diffusion of hydrogen into the steel itself [69]. This presents a significant concern when choices are being made about material usage during automotive design.

2.2.1.3 Crevice corrosion

Differences in concentrations of ions, particularly oxygen, in the electrolyte solution can also lead to occurrence of corrosion, due to formation of a concentration cell. This is a particular problem where component design imparts 'crevices' to particular regions of the part, or where dirt can accumulate. In such crevices, electrolyte can stagnate, depleting it of oxygen as free corrosion proceeds. The electrons lost are conducted to an adjacent region external to the crevice, where they are reduced (usually to hydroxyl, OH^-, ions). Dissolution of positively-charged metal ions to the electrolyte continues, but the absence of oxygen induces negatively-charged ions such as chloride (Cl^-) to migrate to the crevice, exacerbating the corrosion reaction. Metal chlorides (apart from those of alkali metals), hydrolize in water, dissociating into insoluble hydroxide and a free acid [70]:

$$M^+Cl^- + H_2O \rightarrow MOH \downarrow + H^+Cl^- \quad (17)$$

Chloride and hydrogen ions accelerate dissolution of most metals (hydrogen reduces any passive films), increasing the migration of Cl^- and H^+, rapidly accelerating the corrosion process, massively increasing the local chloride concentration, and severely decreasing the local pH. Regions external to the crevice incur an increased rate of oxygen reduction, cathodically protecting them from further attack [70,71].

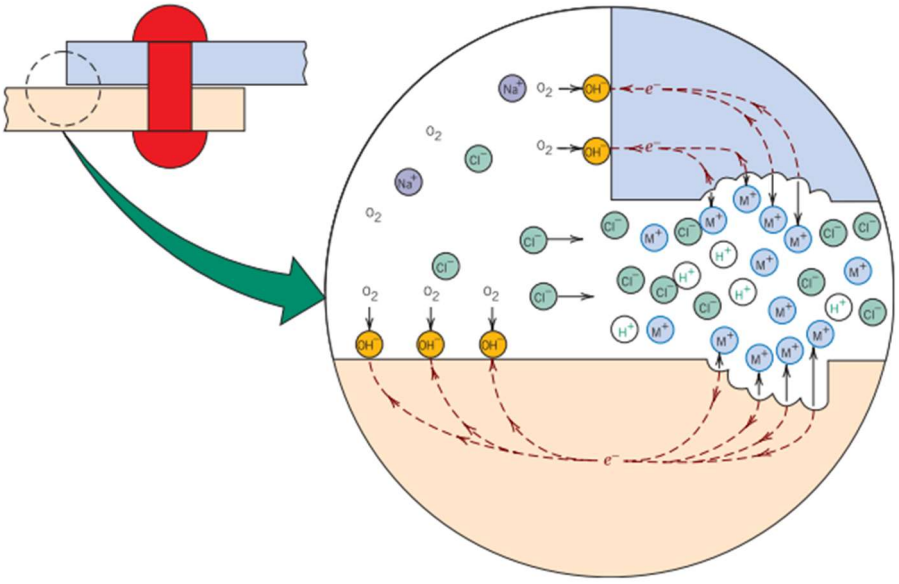

Figure 2.26 Crevice corrosion mechanism between two riveted sheets [70], via [5].

Part geometry is therefore an essential consideration to mitigate against the possibility of crevice corrosion, as it can cause rapid failure and may be difficult to detect. Furthermore, if a galvanic cell is also in situ, the rate of corrosion is further accelerated, as found by Wu [72]. Where crevice corrosion occurs, Liu [73] found that it imparts up to three times more hydrogen to the underlying steel than under (non-crevice) freely-corroding conditions. It is imperative that the formation of crevices narrow enough to permit the stagnation of any possible electrolyte is avoided.

2.2.1.4 Pitting

Related to crevice corrosion in mechanism is pitting corrosion, whereby highly localised 'holes' form in a metal, generally with an equivalent diameter and depth. Often difficult to detect, there is little mass loss to indicate this mode of degradation, making it a particularly problematic form of environmental damage [5].

Corrosion pits are encountered in oxidising chloride-containing environments. The penetration rate can affect the entire thickness of a part in a very short time due to the high cathode-to-anode area ratio. Like the crevice corrosion mechanism, the internal region of a pit acts as the anode, and the region external to the pit as the cathode, a passive region with high rates of oxygen reduction [64].

There appears to be no definitive agreement on what initiates pitting [64,70,74], although there does appear to be agreement that there is a critical anodic potential below which pitting will not initiate [75], although once initiated, the pit can continue to grow even after the apparent potential has decreased [76]. It has been suggested by Evans that initiation of a pit proceeds during general corrosion when dissolution of metal at a particular point is momentarily high, causing an increase in migration of (typically) Cl^- ions to this point, and stimulating further dissolution at this locality [77]. Subsequent reactions proceed in much the same way as seen in crevice corrosion (equation (17)), with migration of H^+ ions to the pit for hydrolysis of the metal chloride salt, with the difference being that pitting corrosion typically proceeds under the effects of gravity, that is, initiating from a horizontal surface and penetrating downwards [70]. The potential within the pit is highly anodic, whilst the surface adjacent to the pit is highly cathodic [78]. Chloride concentrations within the pit are

massively higher than the electrolyte away from the pit, and likewise, electrolyte pH is much lower within the pit than in the bulk electrolyte [74].

2.2.1.5 Corrosion in hydrogen research

Numerous researchers have assessed the impact of corrosion processes on hydrogen uptake in steels, often with novel methods. Li *et al*. [79] studied hydrogen uptake under simulated corrosion conditions using cyclic corrosion tests (CCT), and found that hydrogen content increases with CCT cycle number, with a corresponding decrease in fracture stress observed. This last aspect is important as it demonstrates that a critical hydrogen content for degradation of properties can be achieved in atmospheric conditions (albeit re-created in a laboratory), without applied polarisation for hydrogen charging. To test the impact of real-world corrosion conditions on hydrogen content, Ootsuka *et al*. [66] utilised hydrogen permeation apparatus mounted to a vehicle in real-world conditions, and was able to adjust for differences in temperature. They found that hydrogen uptake correlated well with mass-loss due to corrosion, and that this was exacerbated when chloride levels were increased. Furthermore, when salt deposits on the sample surface became wet from travelling during periods of rain, following a sharp increase due to acceleration in corrosion processes from the high-chloride aqueous environment, hydrogen uptake decreased even if humidity and temperature increased. This was attributed to a gradual 'rinsing' effect from moving on wet roads gradually reducing the chloride concentration. Their findings imply that during winter months, when highways are gritted with salt to prevent ice forming on the road surface, a constant supply of chloride to exposed steel parts from gritted road surfaces has the potential to cause significant issues with hydrogen ingress. This assertion is supported by results of salt-spray cyclic corrosion tests (SSCCT) coupled with permeation undertaken on pure Fe undertaken by Akiyama *et al*. [80], who found that as the number of cycles increased the permeation current rose by more than could be expected from the reduction in membrane thickness due to mass loss. This indicates that there is an enhancement to hydrogen entry as the chloride concentration increases, i.e. an increase in hydrogen concentration at the corroding surface.

Further confirmation that in service corrosion can be sufficient to cause significant hydrogen ingress to steel parts comes from Liu *et al*. [73], who also demonstrated that crevice corrosion conditions could increase hydrogen permeation by a factor of 3, attributed to the depletion of oxygen within the crevice leading to metal dissolution and an associated reduction in pH. Liu also showed that an application of a Zn coating, by far the most common coating on automotive steels, could protect a steel from corroding, but once the coating becomes damaged or corroded under service conditions to expose the steel substrate, more hydrogen can enter the steel than if the steel was uncoated. This was attributed to a cathodic polarisation on the steel surface induced by the corrosion of Zn, which increased the hydrogen reduction reaction and decreased corrosion of the steel. Of all the 'freely corroding' conditions tested in this paper, the dissolution of zinc coating induced the highest hydrogen permeation rates within the steel.

2.2.2 Manufacturing sources of hydrogen

Welding (in the presence of moisture), electroplating (discussed later in context of coating), and even annealing (dependent upon hydrogen-content of the furnace atmosphere) can provide opportunities for hydrogen ingress to steels, though as all 3 occur at elevated temperatures, hydrogen concentrations may be depleted rapidly [81].

Another process that practically all automotive steels will encounter, whether they are used in the hot-rolled or cold-rolled-annealed (or coated) condition, is that of pickling. Pickling steels to remove oxide scale is undertaken in a strong acid, typically HCl, according to reactions (18) – (20)[82]:

$$Fe_2O_3 + Fe + 6HCl \rightarrow 3FeCl_2 + 3H_2O \quad (18)$$

$$Fe_3O_4 + Fe + 8HCl \rightarrow 4FeCl_2 + 4H_2O \quad (19)$$

$$FeO + 2HCl \rightarrow FeCl_2 + H_2O \quad (20)$$

HCl also reacts with the steel itself according to (reaction 21):

$$Fe + 2HCl \rightarrow FeCl_2 + H_2 \quad (21)$$

Inhibitors are usually added to the pickling solution to try to limit the effects on the base steel and allowing preferential attack on the oxides, but hydrogen ions present in the low-pH solution can present a problem if adsorbed to the steel surface. For

‘continuous’ processes typically utilised for strip steels, however, exposure times for the steels to pickling solutions are typically low, restricting potential embrittlement issues due to hydrogen ingress during pickling. As much of the supply of steels to the automotive industry is cold reduced following pickling, and no issues are currently reported in the literature, it is unlikely that pickling of automotive steels is currently leading to embrittlement. Furthermore, as cold-rolled steels subsequently undergo an annealing process, any absorbed hydrogen could be expected to be ‘baked out’ prior to any forming operations.

2.2.3 Hot-dip galvanised coatings (GI/GA)

To protect against the damaging effects of corrosion, and to a certain extent, mitigate against general wear, coatings are often employed on steels used in automotive structures. Most of these are zinc-based, which as we have seen, presents its own set of concerns with regards to galvanic corrosion.

The most widely-used coating on automotive steel parts is a zinc coating applied via a hot-dip galvanising (HDG) process. In the continuous HDG process, the (usually, but not always cold-rolled) steel strip is first welded to the previous strip, before passing through a cleaning section. It is subsequently annealed via a continuous annealing process to achieve the desired microstructure and mechanical properties, before cooling to ~ 460 ^{o}C, at which temperature the strip passes through a molten zinc bath, whereby the molten zinc adheres to the steel surface. The coating thickness is then adjusted and any dross is removed via the use of air knives [83]. Subsequent processing may include a further annealing step (to produce a ‘galvanneal’, GA coating), but will certainly include temper rolling and tension levelling, both to remove any sharp yield point that may have been reintroduced during annealing, and to impart the desired surface texture to the coated strip, dependent on customer specifications for surface roughness, waviness, and lubricity [84].

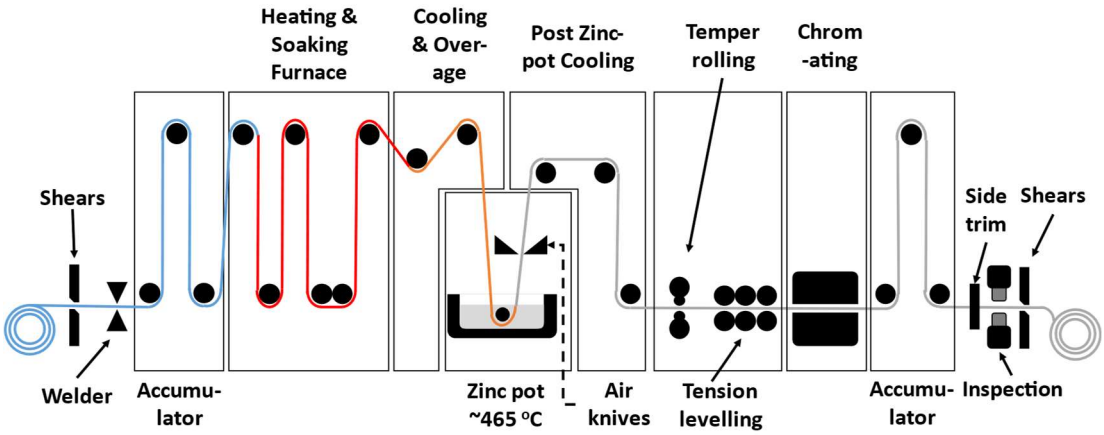

Figure 2.27 Schematic of a continuous hot-dip galvanising line.

In a 'GI' (galvanised iron) coating, the molten zinc bath contains up to 0.3% aluminium (though practically this is kept around 0.1%) to facilitate the formation of an 'interfacial' Fe_2Al_5 intermetallic layer between the steel substrate and zinc coating [85], and thus delaying the formation of brittle $FeZn_{13}$ intermetallic compounds [83,86,87].

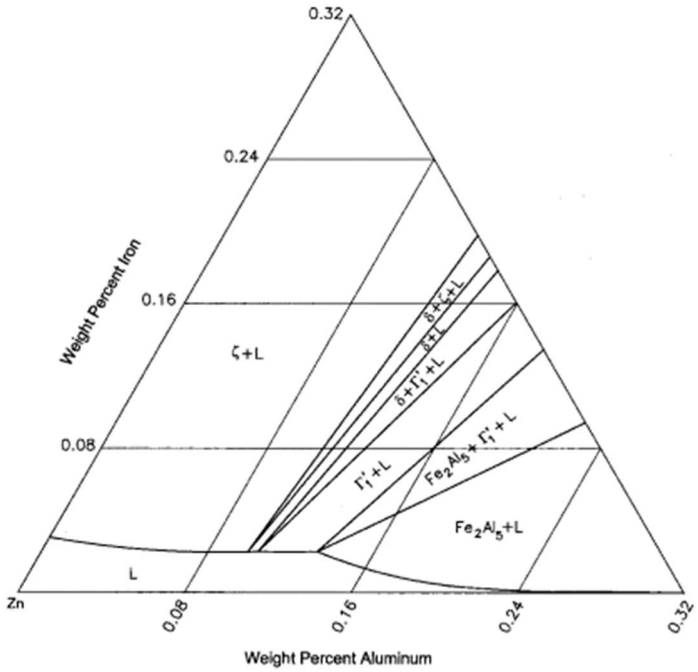

Figure 2.28 Zn-rich corner of Fe-Zn-Al ternary equilibrium diagram phase diagram (460 °C), showing intermetallic formations [88], via [89].

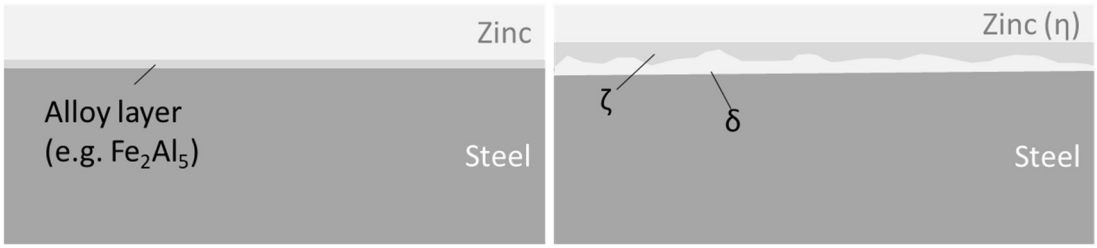

Figure 2.29 Left: schematic of typical GI zinc coating with Fe_2Al_5 barrier layer (based on Fig. 2.E-2 in [11]); right: schematic of Zn coating without inhibitor layer showing formation of various Fe-Zn intermetallics (based on Fig. 3a in [87]).

Whilst GI coatings are the most widely applied coatings for strip steels utilised in the automotive industry, the process itself imposes constraints on the alloy chemistry of the steel. This is a particular issue for steels that may contain high levels of silicon, such as TRIP steels [90], which have surface oxides that inhibit the adhesion between the steel surface and molten zinc, though in this case, redesigning the alloy with increased aluminium, rather than silicon, can allow TRIP steels to be galvanised [45]. Furthermore, the necessity to maintain the strip temperature at or slightly above 460 ^{o}C to allow coating by the molten zinc (and prevent decrease in temperature of the zinc pot) limits the formation of lower-temperature microstructures, particularly martensite phase, and as such it is unusual to find GI coated steels with UTS > 1000 MPa [11].

A variation on the GI coating is the 'galvanneal', or GA coating. This is created with a post-coating heat-treatment, whereby the coated steel is reheated up to ~ 500 ^{o}C immediately after exiting the pot, encouraging diffusion between the steel substrate and zinc coating, and forming a variety of Fe-Zn intermetallic compounds depending on temperature and dwell time (i.e. line speed). The increased Fe content in the coating improves weldability, but can be detrimental to part-forming due to the increased friction of the coating surface, and the differences in ductility between the different intermetallic layers [83].

A good example of the reaction steps occurring is shown in Figure 2.30, below [91].

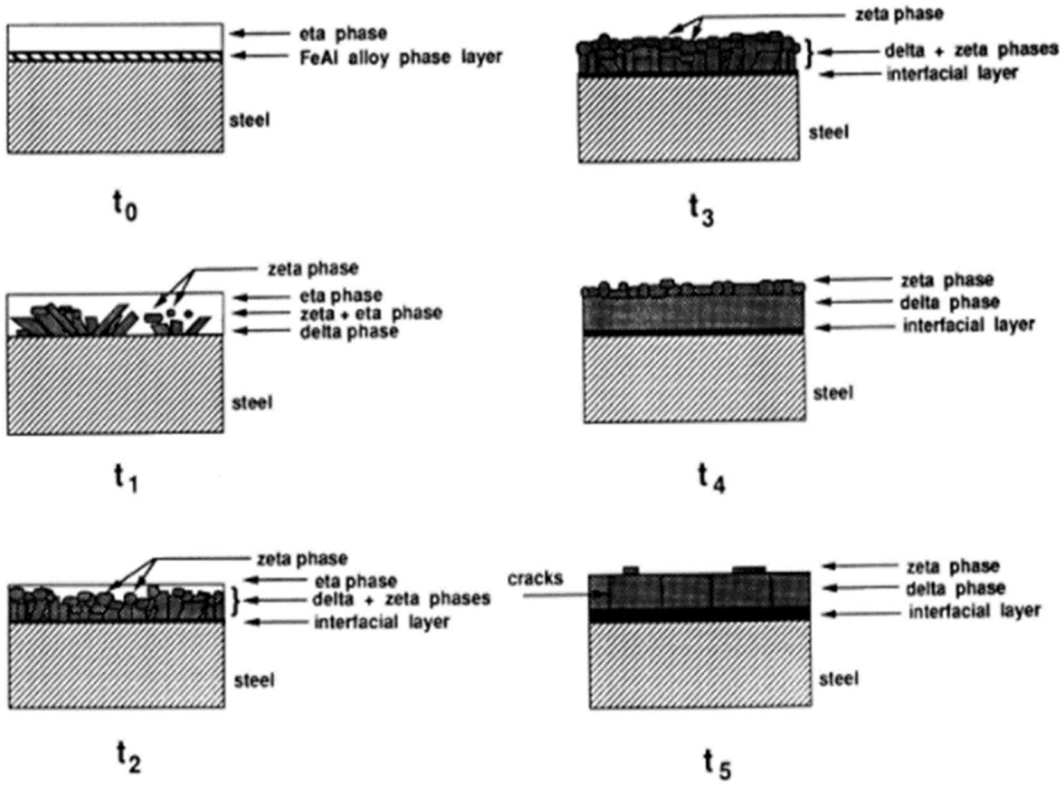

Figure 2.30 Schematic of the galvanneal morphology development [91]. t_0 corresponds to zero time of the as-galvanized structure, i.e. on exit from the zinc bath.

In this instance, the Fe_2Al_5 alloy layer's suppression of Fe-Zn reactions ($\mathbf{t_0}$) is only transient, and the 'barrier' breaks down via an 'outburst' mechanism, whereby the liquid Zn (eta (η) phase) bursts through the inhibitor layer to interface with the steel substrate ($\mathbf{t_1}$), leading to formation of 2 new Fe-Zn intermetallics, zeta (ζ) and delta (δ) phase (properties of which are summarised in Table 2-2), with δ phase forming at coating-substrate interface. Columnar growth of δ phase proceeds, and ζ phase begins transforming to δ phase at $\mathbf{t_2}$, with a new interfacial gamma (Γ) phase forming at the coating-substrate interface. As soak time proceeds ($\mathbf{t_3}$), η phase becomes completely consumed at the coating surface, and diffusion of Fe increases concentration in the coating, increasing the thickness of the δ phase (with ζ phase displaced to the coating surface). At $\mathbf{t_4}$, soak time is such that δ phase continues to grow, Γ remains a fairly stable 1 μm thickness, and ζ becomes increasingly consumed into the δ phase. Should the soak time persist to $\mathbf{t_5}$, δ phase will reach the coating surface and Γ phase will begin to grow at its expense. Furthermore, cracks will begin to appear in the δ surface parallel to the coating-substrate interface. This would constitute an 'over-alloyed' (with Fe) coating [83,92].

Table 2-2 Properties of GA coating phases (adapted from [87]).

Phase	Chemistry	Fe content (wt.%)	Crystal structure	Characteristics
η	Zn	< 0.03	Hexagonal	Ductile
ζ	$FeZn_{13}$	5.7 - 6.3	Monoclinic	Brittle
δ	$FeZn_7$	7.0 - 11.0	Hexagonal	Ductile
Γ	Fe_3Zn_{10}	20.0 – 27.0	Cubic	Brittle

Environmental corrosion has been shown to provide an adequate source of hydrogen to cause embrittlement, exacerbated in the presence of a 'crevice', and typical zinc-based coatings applied to steels have been shown to enhance hydrogen generation at the steel surface when sufficiently damaged to expose the substrate. How this can be resolved whilst maintaining the beneficial effects of these coatings remains a significant challenge, though it should be noted that the number of steel components of sufficient strength to be embrittled that are exposed to a corrosive environment may be somewhat limited by the fact that they are likely to be within the BiW structure, which has several further coatings deposited upon the steel parts, each providing a different protective function. Care must also be taken during design to avoid potential hotspots for crevice corrosion. Surface damage to 'exposed' parts due to wear and tear also needs to be addressed as soon as possible to avoid potential issues with hydrogen embrittlement. For this reason, coatings need to be selected carefully according to their function to ensure that they provide sufficient protection/lubricity/abrasion resistance/paint adherence whilst avoiding augmenting hydrogen evolution, either through the galvanic effects when the coating is damaged, or through the process of applying the coating itself.

2.3 Hydrogen embrittlement

The drive for ever-increasing strength in automotive steels has presented the automotive industry with a new problem. First identified in 1875 [9], hydrogen embrittlement (or hydrogen assisted degradation) is a phenomenon whereby atomic hydrogen enters a steel (or other high-strength alloy) part and causes a degradation in mechanical properties, particularly toughness, leading to often catastrophic failures at relatively low loads, loading cycles or forming severity, often without prior warning signals that failure is imminent. Known to the aerospace industry for a number of years due to failures in landing gear 'maraging steels' [93], hydrogen embrittlement has been shown to increase in severity with increase in strength (e.g. [8,9]). As the automotive industry moves to ever-increasing strengths of steels, hydrogen embrittlement will necessarily become of rising concern [94].

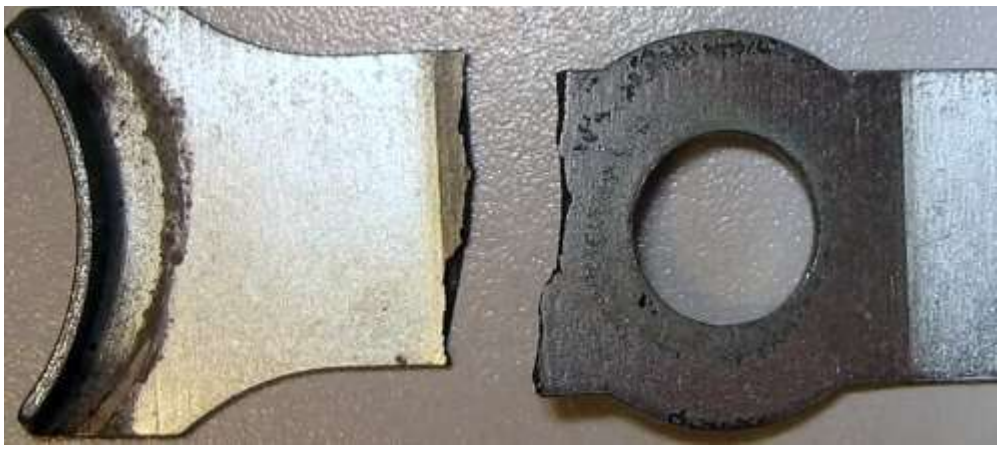

Figure 2.31 Steel leaf spring component that has suffered failure due to hydrogen embrittlement [95].

2.3.1 Evolution and ingress

For steels, hydrogen evolution proceeds via the reaction given in equation (8), essentially according to 7 steps depicted in Figure 2.32.

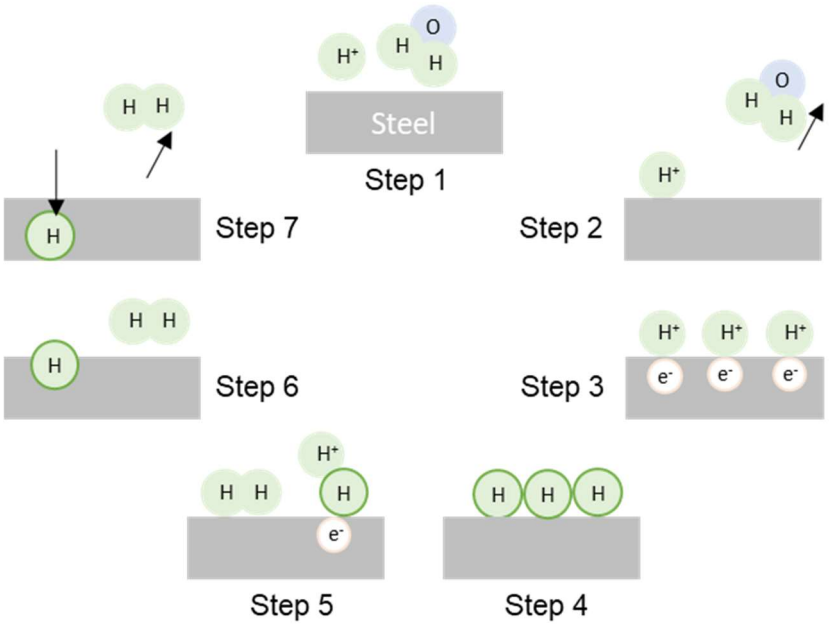

Figure 2.32 Hydrogen evolution and ingress at a steel surface (adapted from [96]).

In step 1 of Figure 2.32, a hydrated proton (H_3O^+) transports to the iron-electrolyte interface (electrical double layer). This hydration is then lost at the double layer (step 2), allowing the proton to be adsorbed to the steel surface (step 3), where it is discharged as an adsorbed hydrogen atom. In step 5 chemical combination between atoms may form molecular hydrogen (H_2) in the Tafel reaction, or an adsorbed proton can combine with an adsorbed atom and be simultaneously reduced by an electron from the steel (electrochemical recombination, the Heyrovsky reaction). The adsorbed hydrogen atom may be absorbed into the steel, or desorb as a bubble of molecular hydrogen (H_2) gas if chemically combined (step 6), either diffusing away from the steel surface through the bulk of the steel, or evolving as hydrogen gas (hydrogen evolution reaction, HER) into the electrolyte (step 7) [96,97]. In this mechanism, the rate-limiting reactions are those occurring at step 5, but these reactions even occur above the reversible hydrogen electrode potential, as above this potential there is still a net rate of generation of hydrogen atoms dependent on the rate of transfer of combined H_2 away from the steel-electrolyte interface, and the rate of hydrogen atom absorption [97].

The coupled discharge-recombination mechanism (Tafel/Heyrovsky) has been shown by Bockris [98] to follow the following sequence at the cathode, when overpotential, η, and hydrogen surface coverage, θ, are low:

$$H_3O^- + e^- + Fe \xrightarrow{k_1} FeH_{ads} \begin{cases} \xrightarrow{+FeH_{ads}} 2\,FeH_{ads} \xrightarrow{k_2} H_2 + 2Fe \\ \xleftrightarrow{k_3} FeH_{abs} \end{cases} \quad (22,23)$$

where FeH_{ads} is adsorbed hydrogen at the steel surface, FeH_{abs} is absorbed hydrogen (directly beneath the metal surface), and k_1, k_2, and k_3 are the rate constants of the reactions depicted.

2.3.2 Embrittlement mechanisms

There are a variety of theories proposed as to the exact mechanism by which steels may suffer mechanical degradation due the ingress of hydrogen. Many are synergistic, or subtle variations of each other, and none are mutually exclusive. Nevertheless, most are derived as explanations for features that appear on fracture surfaces, or as calculations from first principles. Several proposed mechanisms, such as hydride-induced cracking [99], and internal pressure theory [100] have been shown to either not be applicable to steels (as in the case of hydride-formation), or have simply been superseded as the amount of data gathered on the topic has increased, and are better explained by alternative mechanisms.

Broadly speaking, the remaining proposed mechanisms that are invoked to interpret hydrogen-related failure in steels are either based on lattice decohesion, where interaction with diffusing hydrogen weakens the bonds between lattice atoms, or through a hydrogen-mediated plasticity mechanism, where hydrogen diffusing through the bulk lowers the stress required for formation of crystal imperfections commonly associated with plastic deformation. The following sub-chapters give a brief description of the most widely invoked of these mechanisms.

2.3.2.1 Hydrogen-enhanced decohesion (HEDE) mechanism

Whilst versions of this theory had been outlined by Petch and Stables as far back as 1952 [101], the theory as it persists today can be traced primarily to works by Troiano [102] and Oriani [103].

In essence, the theory describes how interstitial diffusion of hydrogen causes interference between the (dissociated) s-band electrons of the diffusing (atomic) hydrogen, and those in the d-band of the lattice atoms. As interatomic distances within the lattice of transition metals, such as iron, is determined by the overlapping of the d-bands, any increase in repulsive forces (i.e. from an increase in the number of electrons due to the presence of hydrogen) reduces the cohesive strength between the lattice atoms. As hydrogen accumulates in regions of high stress triaxiality ahead of a crack tip, the greatest weakening of interatomic bonds occurs in this region, facilitating the propagation of said crack at a considerably reduced magnitude of applied stress [102].

However, despite the magnitude of the stress concentration ahead of the crack tip being 3× the yield stress of the material, Oriani [103] concluded that this was insufficient to facilitate the required hydrogen concentration for crack propagation in this fashion. Instead, Oriani proposed that the hydrogen accumulated 'a few atomic distances' ahead of the crack tip, and that the stress concentration is balanced with the cohesive force per unit area at the crack tip, leading to propagation of the crack in a brittle, but continuous, fashion, with the rate of propagation dependent on the diffusivity (and accumulation) of hydrogen.

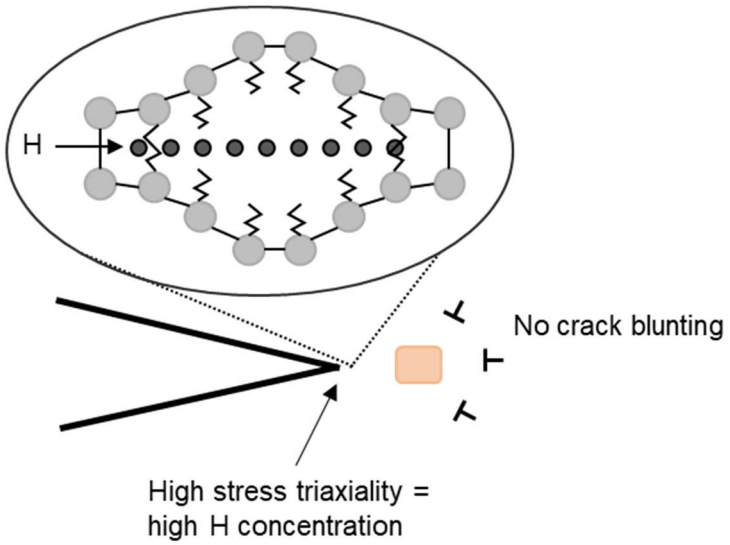

Figure 2.33 Schematic of the HEDE mechanism [102,103].

A further variation on the HEDE mechanism is proposed by Song and Curtin [104]. Simplistically, they calculated via a molecular dynamics (MD) method that hydrogen

accumulated near a crack tip suppresses dislocation emission or motion ahead of the crack tip, in turn preventing blunting of the crack tip, leaving brittle cleavage as the only remaining mechanism of crack propagation that can reduce the free energy.

Evidence in support of these theories has tended to come from first-principles calculations, e.g. density functional theory (DFT) (e.g. [105]), molecular dynamics (e.g. [106]), which support the notion that bonds between lattice atoms are weakened by hydrogen, leading to decohesion. However, as pointed out by Lynch, it has proven difficult to obtain direct experimental data in support of these theories due to a lack of techniques for observing atomic-scale interactions in bulk material [107].

2.3.2.2 Hydrogen-enhance localised plasticity (HELP) mechanism

First proposed by Beachem [7], and now relatively widely utilised for interpretation of results, the HELP mechanism describes a process by which the presence of accumulated hydrogen enables dislocation motion, and hence facilitates a characteristically plastic mode of failure, rather than a 'brittle cleavage'.

Beachem derived the theory to interpret the appearance of dimples characteristic of microvoid coalescence (MVC) on the fracture surface of hydrogen-charged specimens when these features were not apparent during the fast fracture of the same material in air [7]. As such, the appearance of MVC dimples on fracture surfaces has invoked the HELP mechanism as an explanation in numerous articles ever since.

The HELP process begins in much the same way as the HEDE mechanism, with the accumulation of hydrogen ahead of a crack tip due to hydrostatic stress. This accumulated hydrogen then lowers the activation energy required for dislocation motion. Crack growth should therefore proceed in a localised, stepwise manner via MVC not seen in non-hydrogen-rich conditions. In this case, crack propagation could be transgranular or intergranular depending on where the highest concentrations of hydrogen reside.

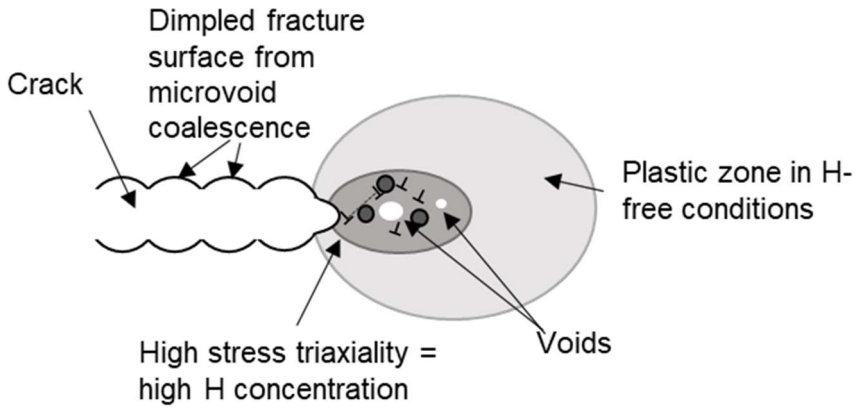

Figure 2.34 Schematic of HELP mechanism (adapted from [108]).

The most significant evidence in favour of this mechanism has come from *in situ* transmission electron microscope (TEM) observations made by Robertson [109] of dislocation motion under the influence of gaseous hydrogen charging. Robertson conducted deformation studies on electron-transparent foils in an environment-cell-equipped TEM flooded with hydrogen gas. This showed that not only could the introduction of hydrogen increase the velocity of dislocation motion, but that at the high hydrogen fugacities obtained due to the interaction between the electron beam and the hydrogen gas, dislocation motion could be induced even in the complete absence of a displacement load, an effect that was subsequently negated upon venting of the hydrogen gas from the TEM chamber. This is direct evidence of enhanced dislocation motion. Furthermore, during nanoindentation experiments featuring *in situ* hydrogen charging, Barnoush [110] observed a decrease in 'pop-in' (an unstable elastic/plastic transition, often taken to be analogous to the yield stress) load and time for hydrogen-charged single-crystal nickel samples, compared to the pop-in load observed for the un-charged samples. This was interpreted as a reduction in the shear modulus and dislocation nucleation in the region of the sample immediately beneath the indenter due to solute hydrogen.

Robertson, Nagao, and co-workers [8,111,112] have gone on to conclude that not only are dislocation processes enhanced in the presence of hydrogen, but hydrogen-dislocation interactions determine the local distribution of hydrogen and the local stress state, inferring that even when ultimate failure is by decohesion (which is conceded for the case of intergranular fracture), the conditions are facilitated by these hydrogen-dislocation interactions.

2.3.2.3 Adsorption-induced dislocation emission (AIDE) mechanism

A second dislocation-mediated plasticity-based mechanism of hydrogen embrittlement is the AIDE mechanism, first proposed by Lynch [113] based on similarities observed between hydrogen- and liquid-metal-embrittled materials. This theory describes a process by which hydrogen adsorbed on to a crack surface both nucleates dislocations and facilitates their motion away from the crack tip, leading to microvoid formation, sub-critical crack propagation, and hence lower ductility [114].

It is in the nucleation that hydrogen is critical, as applied stress is then responsible for the movement away from the crack tip [107]. Nucleation proceeds by simultaneous creation of a dislocation core and 'surface step' by the breaking and re-forming of atomic bonds. It is in this aspect that AIDE shares similarities with the HEDE mechanism, as adsorbed hydrogen is facilitating the decrease in cohesive strength of lattice atoms over several atomic distances [115]. As the stresses required for dislocation emission are high, general dislocation activity ahead of crack tips leads to formation of microvoids, particularly within the plastic zone. These microvoids in turn can sharpen cracks, and dislocation emission from crack tips can lead to crack propagation.

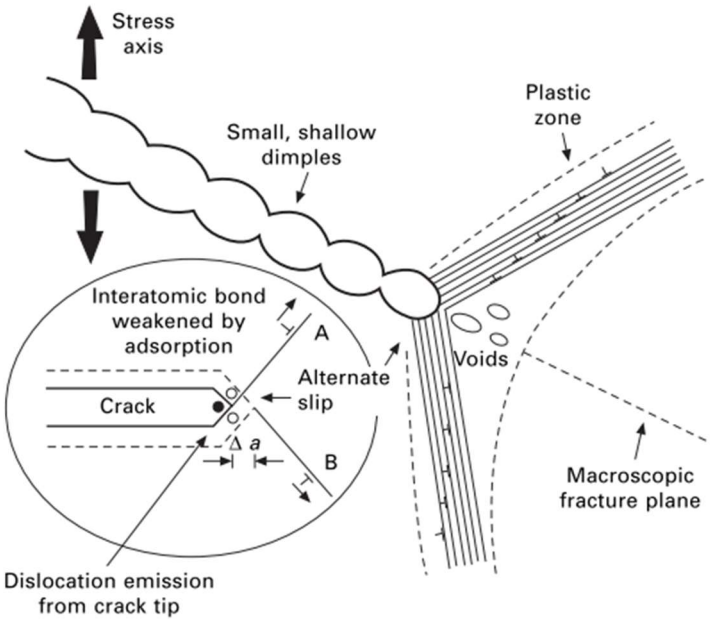

Figure 2.35 Schematic of the AIDE mechanism [107].

Support for this mechanism in literature is largely inferred either indirectly from the high hydrogen concentrations at crack surface sites [116,117], or from the results of atomistic modelling [118,119].

2.3.2.4 Hydrogen-enhanced strain-induced vacancy (HESIV) mechanism

The HESIV mechanism outlines how hydrogen lowers the energy required for vacancy formation ahead of a crack tip during straining, as opposed to dislocation nucleation or movement, and it is the presence of these vacancies that facilitates crack propagation at apparently lower loads than would typically be expected without the presence of hydrogen

First proposed by Nagumo [120], the mechanism is derived partly to explain the results of thermal desorption analysis (TDA) where a secondary higher temperature peak in the hydrogen desorption is observed after straining, as well as a lower-temperature one associated with dislocations [121]. This has been supported by results from Sakaki [122] using positron lifetime spectroscopy (PLS), and more recently Sugiyama [123], who observed how the higher temperature TDA peak (interpreted as vacancies) is enhanced when the specimen is strained in the presence of hydrogen, whereas the lower temperature peak (commonly interpreted as dislocations) is not. Whilst the HESIV mechanism is not a mechanism based on dislocation motion in the same way as HELP or AIDE, strain-induced vacancy-formation does occur via the interactions of dislocations which have been localised in regions tending towards grain boundaries [123], and hence this mechanism still falls into the category of a ‘plasticity-based’ mechanism. However, it also maintains the advantage of not precluding the actions of other mechanisms, whether they are decohesion-based or plasticity-based, as pointed out by Djukic [124].

2.3.2.5 Defactant theory

First applied as a mechanism of 'solute-defect interaction' by Kirchheim [125], and applied as a mechanism of hydrogen embrittlement shortly after [126], the 'defactant' concept provides a thermodynamic framework to explain the hydrogen embrittlement phenomena.

The concept itself is analogous to the concept of 'surfactants' in liquids that can stabilise large surface area features such as foams. Likewise, defactants stabilise large area lattice defects such as grain boundaries, vacancies, and dislocations. The theory builds upon the Gibbs Adsorption Isotherm to demonstrate how adsorption of impurities reduces the energy requirement for the formation of lattice imperfections, such as voids and dislocations (and stabilises those already formed)[125]. It was shown [126] that this concept can be used to add validity to the HELP, AIDE, and HESIV mechanisms (i.e. the mechanisms based on plasticity) in terms of a reduction of free energy, and has since been used to interpret results from nanoindentation experiments [127,128]. Furthermore, whilst this theory is essentially an enhanced plasticity model, it does not preclude decohesion in the same way as much of the literature around the HELP mechanism (e.g. [8]), allowing for a more synergistic interpretation between plasticity-based and decohesion-based theories to explain experimental results (e.g. [124]). Alongside this, it provides an opportunity of adding a thermodynamic basis to more mechanistic ideas.

It is clear is that 'hydrogen embrittlement' is a catch-all term that encompasses a number of different mechanisms that may be synergistic or in competition, depending upon the concentration of hydrogen, the magnitude and nature of an applied load, and the strength of the material in question. Evidence in literature for the applicability of all of the mechanisms outlined above is plentiful, and as seen with the Defactant theory it can be argued that all of them may be valid, depending on test (or field) conditions.

2.3.3 Characterising mechanical degradation

At the ‘macro’ scale, hydrogen-related mechanical degradation can manifest in a variety of ways, from ‘blistering’ at very high hydrogen fugacity typically found in ‘sour’ (high H_2S) environments (e.g. [129,130]), to a ‘delayed failure’ observed in mechanical components at relatively low hydrogen concentrations (e.g. [80,131]). Selecting the appropriate method for assessing the relative risks associated with the in service conditions that steels will encounter is, therefore, a key consideration.

As we are only taking into account conditions experienced by automotive parts which are highly unlikely to be as severe as that experienced in oil and gas pipelines operating in sour environments, only techniques for assessing degradation in strip steels at low hydrogen concentrations need be considered appropriate.

Of those techniques that look at effects operating at the micron or sub-micron scale, one technique that has been found to be extremely useful, and hence become widely adopted, is that of electrochemical nanoindentation. First described by Barnoush and colleagues [110,132], this technique shares similarities with the well-established micro-hardness tests, in that it is utilising an indenter to apply a load to the surface of a metallographically-prepared specimen to yield mechanical property data. Unlike micro-hardness tests, however, nanoindentation is able to yield considerably more detail about the mechanical properties of the specimen than simply hardness, as it generates a load-displacement curve in much the same way as may be encountered in conventional tensile or compression tests. From this curve a variety of mechanical property data can be derived, including identification of a characteristic ‘pop-in’, whereby the load-displacement curve suddenly ‘jumps’ along the displacement axis (i.e. deformation occurs without extra load being applied), observed in materials that typically exhibit a sharp yield point. Furthermore, nanoindentation probes regions that are typically much smaller than can be tested via micro-hardness experiments, allowing for much higher detail to be obtained in terms of microstructural differences. When this technique is combined with electrochemical hydrogen charging, either *in situ* or *ex situ*, and coupled with atomic force microscopy (NI-AFM), Barnoush [132] showed that effects of hydrogen upon individual grains could be probed in regions that had a statistically high probability of being defect-free, i.e. the technique was able to probe the degradation in performance of mechanical properties that were approaching the ‘theoretical’ properties of the material.

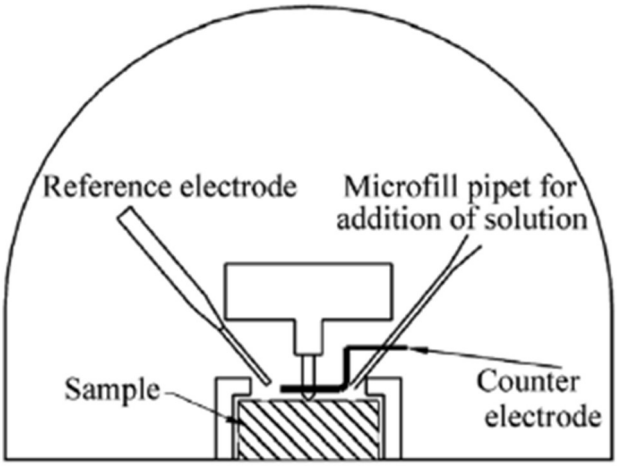

Figure 2.36 Barnoush and colleagues' experimental nanoindentation setup [132].

Electrochemical nanoindentation is therefore a very powerful tool for discerning hydrogen-material interactions at the microstructural scale, and has led to the development of similar techniques, such as 'micro-pillar compression tests' [133], or 'micro-cantilever bend tests' [134] on pre-charged specimens. However, whilst nanoindentation and its related techniques are able to discern fine detail about microstructural interactions with hydrogen, the scale of these tests means that they do not yield comparable information on how materials may perform at the macro scale (i.e. in use), and due to the nature of the tests themselves with very low loads, a range of environmental variables, such as temperature, humidity, and vibration, can have a disproportionate effect on the data that is produced. As such these techniques can only be performed under extremely tightly controlled conditions.

For testing degradation of mechanical properties due to hydrogen at a more representative scale of the real-world, a range of experimental setups have been utilised by coupling them with hydrogen charging (typically prior to testing rather than *in situ*), such as 3- or 4-point bend tests [135–137], and cupping tests [138], with varying levels of success depending on control of charging conditions and strain-rate.

However, a popular choice among researchers for assessing hydrogen-related failure in low-alloy strip steels is the slow strain-rate test (SSRT) (e.g. [139–141]). Essentially a variation on a conventional tensile test (often abbreviated in the context of hydrogen research to CSRT, or 'conventional strain-rate test'), this involves running a tensile test upon a prefabricated and hydrogen-charged specimen at a strain-rate sufficiently

low to allow hydrogen atoms to diffuse to high-stress regions, with a resultant loss of ductility and premature failure. Hydrogen charging can be performed in gaseous hydrogen [141], under atmospheric corrosion conditions [139,142], or, commonly, under imposed electrochemical charging conditions [136,140,143], and can be performed *in situ* during straining, or *ex situ*, prior to charging, or with a combination of both. Quantifying embrittlement is typically done via an assessment of the reduction in ductility during hydrogen-charged tests, such as decreases in total elongation at failure, reduction in cross-sectional area of the fracture surface, or the reduction in area under the tensile curve (absorbed energy), or may be assessed through the resultant decrease in test time-to-failure as a result of hydrogen ingress.

Despite some criticism that SSRT is potentially non-representative of automotive forming stresses, strip steels are commonly assessed for suitability in automotive applications via specified tensile test parameters (e.g. minimum yield strength, work hardening exponent etc.) – this is the release test for automotive customer orders upon strip steel manufacturers. Furthermore, the combination of ability to finely control the test conditions (atmosphere, temperature, charging conditions and duration, strain-rate etc.), and options when assessing influence on performance, make SSRT a powerful and versatile means for assessing the macro-level performance of materials, allowing for relatively straightforward comparisons to be made between different alloys or microstructures, in terms of performance when encountering hydrogen ingress.

When considering choice of technique for assessing mechanical degradation due to hydrogen, selection has to be based on a range of factors, including the mundane considerations of time, material, and equipment availability. Ideally, a combination of techniques for probing hydrogen-related degradation at different scales would be utilised, with the aim of integrating these data to glean maximum understanding of the processes involved at every level. However, in practical terms where decisions have to be taken around the considerations highlighted, the control and repeatability of the slow strain-rate test makes it a logical choice to gain data that can allow useful comparisons to be made between steels at a scale approaching the in-service conditions that would be encountered.

2.4 Hydrogen diffusion

It was shown in the very first paper on the subject [9] that it is diffusible hydrogen that causes degradation, as when hydrogen is effused from a material, it's mechanical properties recover. The single aspect that unites all theories of hydrogen embrittlement outlined previously is that the mobility of hydrogen atoms within the microstructure is crucial [6]. Certain microstructures will have phases present that impart more tortuous diffusion paths [144], or contain hydrogen 'traps' which hinder the diffusion of hydrogen atoms within a microstructure sufficiently to render them immobile (e.g. [6,145–148]), preventing them from causing degradation in properties. There is strong evidence that higher hydrogen diffusivity leads to higher susceptibility to degradation where strength levels are similar [93]. It is therefore appropriate to be able to quantify relative differences between steels with regards to hydrogen diffusion [149].

2.4.1 Microstructural considerations

When considering differences in diffusion characteristics, it is important to recognise that differences between basic lattice structures themselves can greatly affect diffusivity [150]. As hydrogen atoms traverse the body-centred-cubic (bcc) lattice of ferrite, they are thought to favour tetrahedral interstitial sites [151], with the octahedral sites being occupied by carbon atoms. Whilst this interstitial carbon does cause some lattice dilation, the transformation from austenite to ferrite proceeds via diffusion, minimising strain on the lattice and in turn limiting the numbers of vacancies and dislocations retained within the lattice [20], each of which could act as possible trap sites. It follows that where alloy chemistry is the same, the path through ferrite grains for diffusing hydrogen atoms should be comparatively straightforward when compared to a more complex structure, such as martensite. Hydrogen diffusivity in ferrite is also several orders of magnitude higher than that for the face-centred cubic (fcc) lattice of austenite (Figure 2.37), which in turn has a much higher hydrogen solubility than ferrite.

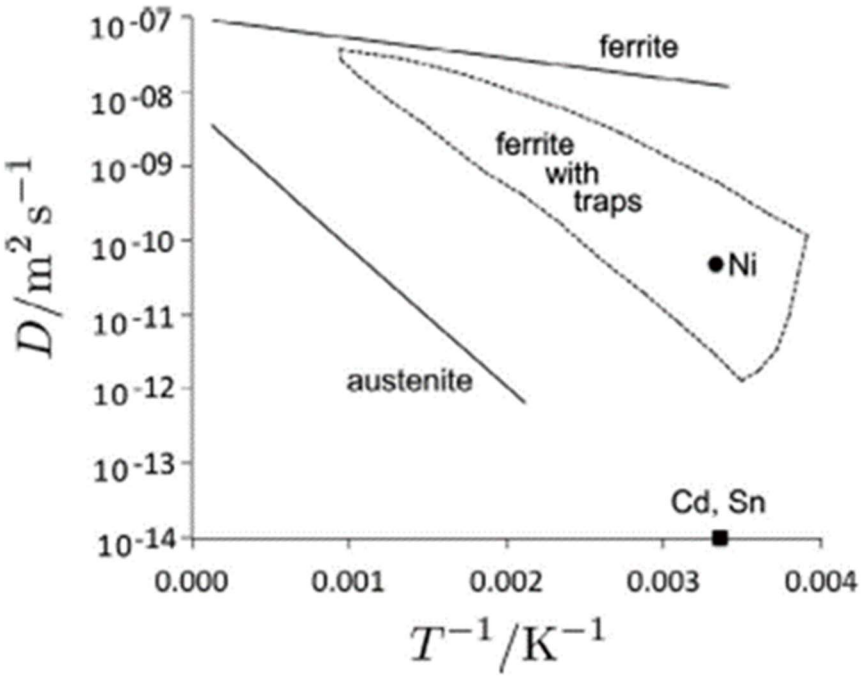

Figure 2.37 Hydrogen diffusion coefficients in ferrite and austenite [6].

Solubility is the determining factor for hydrogen concentration in steels, and the relative phase fractions and presence of microstructural 'features' that may enhance or diminish solubility will determine solubility. In iron, solubility of hydrogen follows Sievert's Law ($C_H = \sqrt{Kp_{mol}}$, where C_H is hydrogen concentration, p_{mol} is partial pressure of the hydrogen gas at the steel surface, and K is the equilibrium constant)[152], with an equilibrium atomic ratio as low as 2×10^{-8} at room temperature (and atmospheric pressure) [121].

With higher solubility and much lower diffusivity of austenite compared to ferrite, austenite can be considered as a strong hydrogen trap when present in a predominantly ferritic microstructure [93]. Whilst the presence of austenite may therefore seem beneficial, it does however pose a problem for the application of transformation induced plasticity (TRIP) steels. Typically used in automotive structures such as roof rails, crash boxes, and b-pillar uppers, TRIP steels have relatively high carbon and silicon additions, enabling the production of a microstructure containing 5%-20% retained, (meta-stable) austenite (γ) embedded in a ferrite (α) matrix, as well as the presence of some harder martensite (α') or bainite, depending on the strength of the product. This retained austenite progressively transforms to martensite during forming with increasing strain, imparting a high work-hardening exponent (n-value) that

persists beyond the levels of deformation where dual-phase (DP) steels of equivalent strength begin to see a drop-off, and enabling more severe forming applications [11,27]. The high solubility of hydrogen in austenite, coupled with low diffusivity, means the retained austenite in TRIP steels can act as a hydrogen sink. Laureys et al. [44] and Lovicu et al. [153] observed that transformation after hydrogen charging led to the formation of martensite that was then supersaturated with hydrogen and failed quickly. Whilst in practice this is unlikely to be observed during forming, not all of the retained austenite is fully transformed during forming operations, and if this becomes enriched with hydrogen during service, it could lead to potential problems during a crash event – martensite has been shown to suffer from the degrading effects of hydrogen in numerous studies (e.g. [44,153]).

The martensite lattice has a nominally body-centred tetragonal (bct) structure induced by the displacive, rather than diffusive, nature of the $\gamma \rightarrow \alpha'$ transformation which occurs at a rate which does not permit the carbon atoms solute in austenite sufficient time to form Fe_3C, as they would for a eutectoid (pearlite) reaction. As the ferrite lattice has a much lower solubility for carbon than austenite, the carbon atoms remain in situ, supersaturating the transformed bcc lattice, which becomes elongated along the c-axis (and contracted along the a- and b-axes) to accommodate these 'extra' carbon atoms. In practice, for the carbon levels in A/UHSS used in automobile construction, the lattice parameters are only slightly affected (on the order of 0.01 to 0.02 Å) [20], making this tetragonality difficult to characterise with conventional diffraction-based techniques. Consequently martensite in plain carbon or low-alloy strip steels is often considered as a bcc lattice with supersaturated carbon, and martensitic 'grains' are formed essentially within the boundaries of the 'parent' austenite grains according to specific orientation relationships.

In 'fully' martensitic steels such as the hot-forming boron-bearing steels typically used for a-pillars, b-pillars, and cross beams [11], this adjustment in the orientation relationship between martensite and the parent austenite, coupled with tetragonality induced in the bcc lattice from super-saturation of carbon atoms, leads to significant strain residing within the lattice [20] and an accompanying high dislocation density [154]. This makes lattice hydrogen diffusion in a martensitic microstructure inherently more complex than diffusion in ferrite. Dislocations have been shown to act as

‘reversible’ hydrogen traps, whereby hydrogen atoms become trapped at dislocations with a characteristic binding energy, such that when the concentration of hydrogen in the lattice decreases (or there is an increase in thermal energy in the system), trapped hydrogen is released back into the lattice once more [147,155], maintaining an equilibrium between reversibly-trapped hydrogen and hydrogen in the lattice [156]. Van den Eeckhout et al. [157] and Iino [158] show that in hydrogen permeation experiments the presence of reversible traps has the effect of making the transient curve more shallow, and reduces the steady-state maximum flux. It follows that the desorption profile is also more shallow, and a relatively high hydrogen concentration can persist in the lattice due to this equilibrium even after a charging source is negated. This is a particular problem for steels in the fully-martensitic condition, which have proven to be highly susceptible to hydrogen embrittlement [153], often due to their inherently very high strength (low formability), and the propensity for defects within the microstructure providing stress concentrations, simultaneously acting as reversible traps capable of maintaining a high hydrogen concentration in potential crack nucleation sites (e.g. [159,160]).

The propensity for martensite to be embrittled by hydrogen extends to steels that do not have fully-martensitic microstructures. Dual-phase (DP) steels, typically used in safety cage components, outer body, and floor panels consist of an array of second-phase martensite embedded in a ferrite matrix, with strength levels increasing as the volume fraction of martensite increases [11,30]. This second-phase martensite also improves the work hardening exponent, allowing more challenging shapes to be formed than is possible with more traditional HSLA steels [31]. This means, however, that DP steels suffer from similar hydrogen susceptibility problems as single-phase martensitic microstructures, as found by Takashima et al. [161]. Several researchers (e.g. [162,163]) have found that DP steels typically have slightly lower hydrogen diffusivity than single-phase steels of equivalent strength, attributed by Schaffner et al. to the higher homogeneity of the single-phase microstructure [162]. This lower diffusivity does not necessarily translate to a lower susceptibility, and DP steels have been observed to suffer a higher degradation in properties than single-phase martensitic steels, as found by Loidl et al. [141]. Takashima et al. [161] propose that the interfaces between lower-strength ferrite and higher-strength martensite can lead to ‘anomalous’ behaviour, and that preferential deformation in the softer, ferrite phase

lowers resistance to crack propagation in this phase, decreasing the time to fracture [164]. This is supported by Koyama et al. [165], who found that in DP steels hydrogen not only decreased critical strain for crack initiation in the martensite phase, but "promotes ferrite/martensite cracking, ferrite/martensite boundary sliding and cracking of the ferrite grains."

2.4.2 Diffusion measurement

As noted previously, for steels to become embrittled it is widely recognised that there is a requirement for hydrogen to be diffusible within the microstructure to allow it to agglomerate at regions of high stress, and that where strength levels are similar, the steel with the higher diffusivity is likely to incur the greater degree of mechanical degradation [166]. For this reason, knowledge of the diffusion characteristics of a steel can be critical for assessing its susceptibility to hydrogen-related degradation. A number of the techniques that have been utilised for this task are described in the proceeding sub-chapters.

2.4.2.1 Hydrogen permeation

The method utilised most frequently to determine hydrogen diffusion coefficients is the hydrogen permeation method. First described by Devanathan and Stachurski [167], this powerful technique typically involves mounting a thin sample between two 3-electrode electrochemical cells (e.g. [73,93,168])(Figure 2.38), with the sample acting as the working electrode in both cells. In one cell, a fixed potential (potentiostatic charging) or fixed current density (galvanostatic charging) is maintained to promote hydrogen evolution on the surface of the sample, whilst in the other cell, a fixed potential is maintained that will ensure oxidation of any hydrogen that has been transported through the sample from the 'generation' cell. As hydrogen is oxidised, a current is generated, and this current (over and above the background current) is directly equivalent to the permeating hydrogen flux. Permeation flux proceeds towards a maximum steady-state, J_∞, which corresponds to the lattice diffusion rate, and from this maximum flux (or time taken to achieve a certain percentage of the maximum flux) an 'effective' diffusion coefficient can be calculated, and in turn, an estimate for the hydrogen concentration at the charging surface [169].

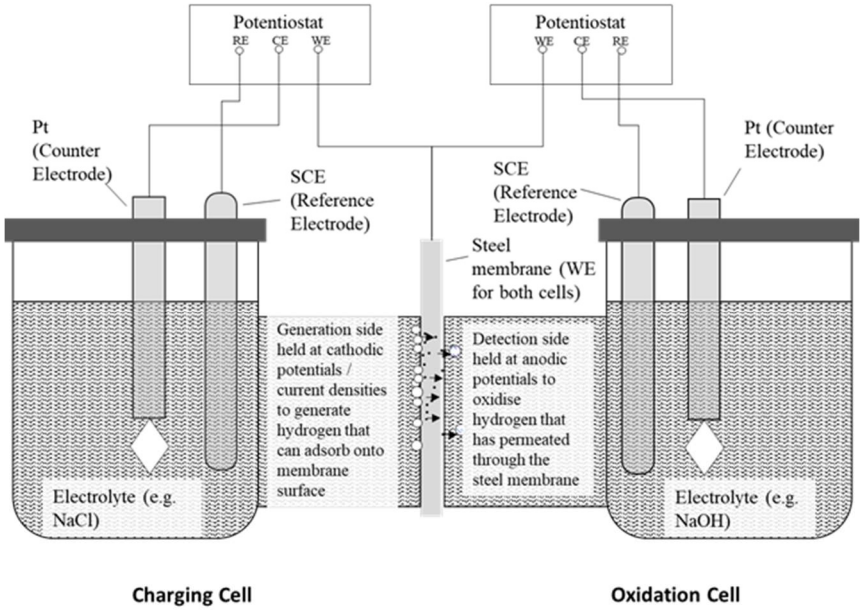

Figure 2.38 Schematic of a typical hydrogen permeation cell.

Under ideal conditions of steady-state 'lattice diffusion', with no effects of tortuosity or trapping, diffusion through the sample membrane is described by Fick's first law:

$$J = -D\frac{\partial C}{\partial x} \tag{24}$$

where J is the hydrogen flux (in mol/cm^2/s), $\frac{\partial C}{\partial x}$ is the concentration gradient of hydrogen through the membrane (i.e. from charging surface to desorption surface, in mol/cm^3), and D is the diffusion coefficient (mol/cm^2) [170]. This shows that the driving force for diffusion is the concentration gradient, and the rate determined by the diffusion coefficient, i.e. there is no change in flux with time.

In practice, ideal lattice diffusion is not the condition under which diffusion is taking place, and concentration gradients are changing across the membrane. This describes the conditions during the initial stages of a permeation experiment, during which the concentration of hydrogen within the membrane has not reached a maximum value, and it is described by Fick's second law [170]:

$$\frac{\partial C}{\partial t} = -D\frac{\partial^2 C}{\partial x^2} \tag{25}$$

Solutions for Fick's first and second laws are dependent on boundary conditions, which are determined by the method of charging – whether potentiostatic or galvanostatic.

2.4.2.1.1 Potentiostatic charging

Potentiostatic charging is commonly regarded as corresponding to a fixed hydrogen concentration at the charging surface, and is recommended as more representative of real-world conditions [150], and found by Akiyama to be more repeatable in the laboratory due to an increased stability of the permeation current density than with galvanostatic charging [171,172]. By applying a fixed potential between the reference electrode and steel membrane in the charging cell, the charging surface of the membrane (x=0) is kept at a constant hydrogen concentration, C_0. In the desorption cell, the potential between the reference electrode and the membrane is maintained at a constant potential such that all of the hydrogen that is desorbing is fully oxidised, effectively meaning that the concentration at x=L, the desorption surface of the membrane, is also fixed at a constant concentration of C_L, which as all desorbing hydrogen is fully-oxidised, C_L=0. The membrane itself has an initial concentration, C_i, which is also usually taken to equal 0. These conditions are represented in the following:

$$C = C_0; \qquad x = 0 \qquad t > 0$$

$$C = C_i; \qquad 0 \leq x \leq L \qquad t = 0$$

$$C = C_L; \qquad x = L \qquad t \geq 0$$

where C is concentration at time t, x is a distance through the membrane thickness, and L is the membrane thickness. The period of time prior to reaching steady-state flux sees a change in the hydrogen concentration gradient according to equation (26) [170].

$$C - C_0 = (C_L - C_0)\frac{x}{L} + \frac{2}{\pi}\sum_{n=1}^{\infty}\frac{C_L\cos(n-\pi) - C_0}{n}\sin\frac{nx\pi}{L}exp\left(\frac{-Dn^2\pi^2t}{L^2}\right) + \cdots\frac{4C_i}{\pi}\sum_{m=1}^{\infty}\frac{1}{2m+1}\sin\frac{(2m+1)\pi x}{L}exp\left(\frac{-D(2m+1)^2\pi^2t}{L^2}\right) \quad (26)$$

At the beginning of a permeation experiment, C_i and C_L are typically zero as hydrogen concentration within the membrane is zero, and the concentration at the depletion surface is also maintained at effectively zero. This simplifies the solution to:

$$C - C_0 = -C_0\frac{x}{L} + \frac{2}{\pi}\sum_{n=1}^{\infty}\frac{C_L\cos(n-\pi) - C_0}{n}\sin\frac{nx\pi}{L}\,exp\left(\frac{-Dn^2\pi^2 t}{L^2}\right) \qquad (27)$$

As time approaches infinity (steady-state condition), the exponential in equation (27) disappears, and hydrogen concentration becomes linear (Figure 2.39).

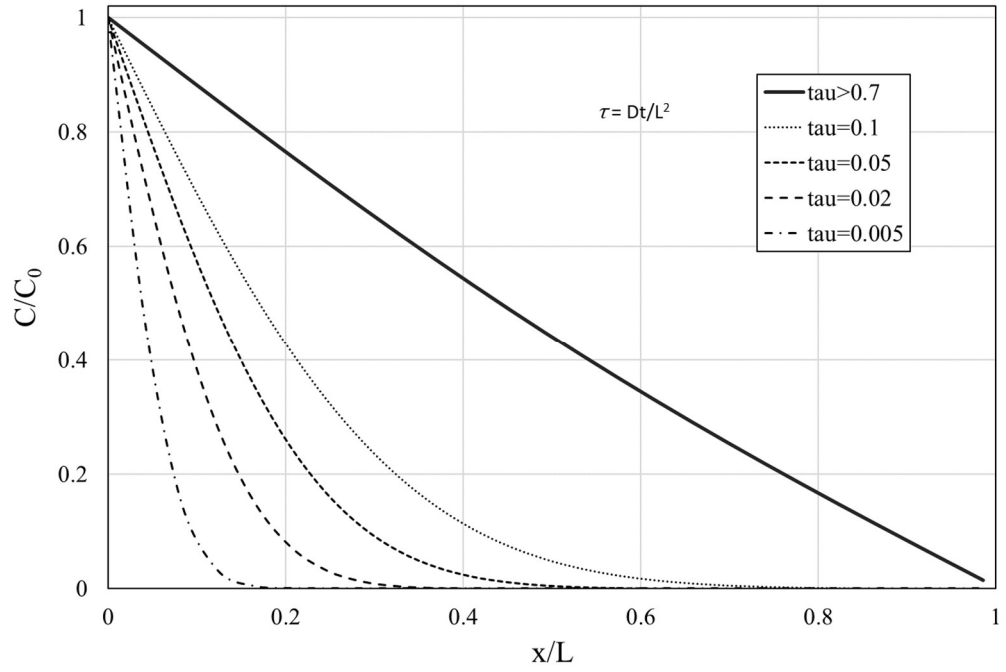

Figure 2.39 Normalised concentration profiles during a potentiostatic permeation experiment.

Hydrogen effuses from the desorption surface of the membrane at $x = L$, and this hydrogen flux corresponds to the characteristic permeation transient, an example of which is given in Figure 2.40, where 'breakthrough' time, t_b, is the time taken for the first hydrogen to be detected on the desorption cell, the 'lag' time, t_{lag}, is the time taken to reach 0.63 × the steady-state flux (as specified in BS EN ISO 17081:2014), which is represented as J_∞.

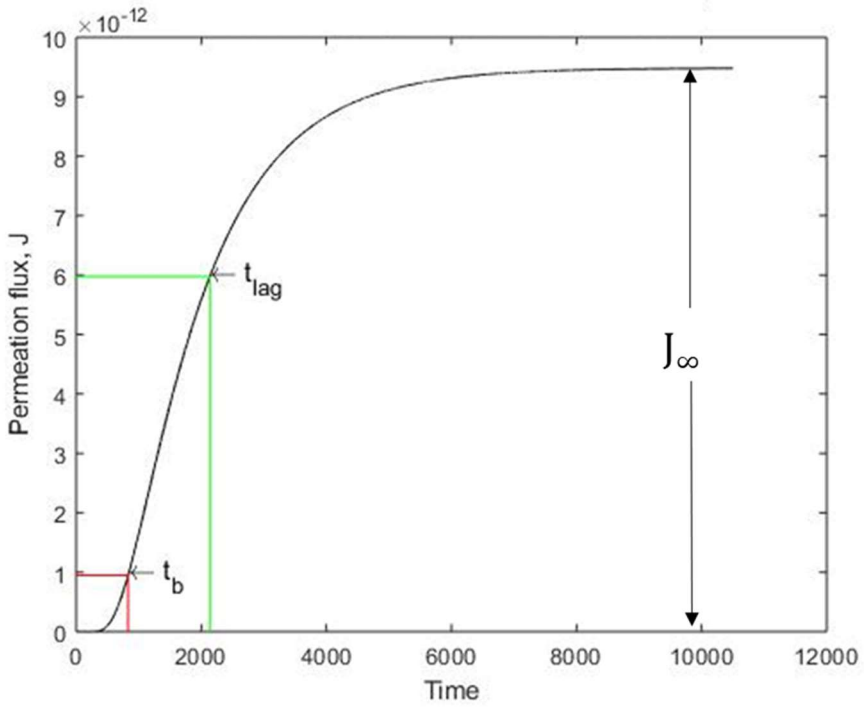

Figure 2.40 Example of hydrogen permeation transient.

The permeation transient shown in Figure 2.40 is calculated by differentiating equation (27) with respect to x, on the basis that when time → ∞, the flux J, becomes $J_\infty = DC_0/L$:

$$J = \frac{DC_0}{L}\left\{1 + 2\sum_{n=1}^{\infty} cos(\pi n) Exp\left(\frac{-Dn^2\pi^2 t}{L^2}\right)\right\} \quad (28)$$

Strictly speaking, determination of breakthrough time and lag time require the calculation of the total amount of diffusing hydrogen, Q_t, through the membrane in time, t, achieved by integrating equation (26) with respect to time:

$$Q_t = D(C_0 - C_L)\frac{t}{L} + \frac{2L}{\pi^2}\sum_{n=1}^{\infty}\frac{C_0\cos(n-\pi) - C_L}{n^2}\left\{1 - exp\left(\frac{-Dn^2\pi^2 t}{L^2}\right)\right\} +$$
$$\cdots\frac{4C_i L}{\pi}\sum_{m=1}^{\infty}\frac{1}{(2m+1)^2}\left\{1 - exp\left(\frac{-D(2m+1)^2\pi^2 t}{L^2}\right)\right\} \quad (29)$$

As described previously, C_i and C_L are zero, and as time →∞ the exponential parts of equation (29) disappear, to simplify to:

$$Q_t = \frac{DC_0L}{L}\left(t - \frac{L^2}{6D}\right) \tag{30}$$

which as a function intercepts the time axis at t_{lag}. Furthermore, t_{lag} can be calculated using the following:

$$t_{lag} = \frac{L^2}{6D} \tag{31}$$

Plotting Q_t/LC_0 against Dt/L^2 when C_i and C_L are zero shows steady-state flux occurs when $Dt/L^2 = 0.5$. Furthermore, the breakthrough time is approximated when $Dt/L^2 = 0.0654$. Breakthrough time is therefore:

$$t_b = \frac{L^2}{15.3D} \tag{32}$$

Lag time and breakthrough time can be graphically obtained from permeation transients, where t_b is approximated by extrapolation of the linear portion of the rising transient prior to steady-state (or first inflection point in rising transient), and t_{lag} is taken as the time when the flux has reached 0.63 × the steady-state flux, J_∞.

2.4.2.1.2 Galvanostatic charging

Galvanostatic hydrogen charging maintains a constant current density at the charging surface, and is commonly considered to represent application of a constant hydrogen flux, J_0, at the charging surface. The boundary conditions for solution of Fick's laws therefore become [173]:

$$C = 0; \qquad x = L \qquad t > 0$$

$$C = 0; \qquad 0 \leq x \leq L \qquad t = 0$$

$$J_0 = J_\infty = \frac{C_0FD}{L}; \qquad x = 0 \qquad t = \infty$$

The solution to equation (25) under constant charging flux conditions is therefore:

$$C = \frac{J_0}{FD}(L - x) - \frac{8J_0L}{FD\pi^2}\sum_{n=1}^{\infty}\frac{(-1)^n}{(2n+1)^2}\sin\frac{(2n+1)(L-x)\pi}{2L}exp\left(\frac{-D(2n+1)^2\pi^2t}{4L}\right) \quad (33)$$

Permeation flux under condition of constant charging flux is given by:

$$J_t = J_0\left\{1 + \frac{4}{\pi}\sum_{n=0}^{\infty}\frac{(-1)^n}{(2n+1)}exp\left(\frac{-D(2n+1)^2\pi^2t}{4L^2}\right)\right\} \quad (34)$$

And breakthrough time and lag time are calculated by equations (35) and (36), respectively:

$$t_b = \frac{L^2}{12.98D} \quad (35)$$

$$t_{lag} = \frac{L^2}{2D} \quad (36)$$

Whilst this test is extremely useful for making comparisons between bulk diffusion characteristics of different alloys under the same conditions, it does however have some limitations. Turnbull [97] points out that to truly glean bulk diffusion characteristics, repeat tests on membranes of increasing thickness should be carried out to ensure concentrations at the charging surface reach equilibrium, but this is not always possible due to material availability, particularly when assessing strip steels. Furthermore, although repeat transients can yield data on the presence of traps, this is not always practical, and analysis on single transients using Fick's laws does not yield any quantitative information about diffusion path tortuosity, or numbers and binding energies of any traps present. To overcome this, many researchers (e.g. [97,144,156,168,174,175]) have developed expansions to Fick's laws to account for these parameters, adjusting parameter values to achieve better fits to the experimental data. However, as with any fitting of models to data, a certain degree of uncertainty will always remain.

Furthermore, dimensions of the test membrane, or the relationship between the charging surface and depletion surface areas [176], are important considerations. Kittel [177] has shown that if permeation membranes drop below a certain thickness, the equilibrium concentration, C_0, at the charging surface will never be reached as hydrogen will be depleted from this region too rapidly by the exit flux in the oxidation cell. Turnbull [97] also recommends ensuring membranes are sufficiently thick to ensure bulk diffusion, rather than surface characteristics or the particular test conditions, is the dominant parameter affecting permeation flux, though there is recognition that selection of membrane thickness is very much dictated by the application of the material being studied.

2.4.3 Trapping

Throughout discussions on microstructural aspects of hydrogen diffusion, it is apparent that the role played by hydrogen traps is crucial in determining diffusivity and overall susceptibility (though this is disputed by Dadfarnia et al. [178] in conditions of continuous hydrogen supply). There have been few attempts, however, to perform comprehensive characterisation of trap binding energies or the effects of morphology on trap efficacy. Much of this will be down to the differences in specific activation energies for lattice diffusion between steels, which would in turn directly affect trap binding energy (see Figure 2.41). Despite this, several authors (e.g. [6,179]) have tried to collate published trap binding energies for steels calculated from data collected by various methods, and from this, some general ‘consistencies’ emerge:

1. Dislocations, microvoids, and grain boundaries can usually be considered to be relatively ‘shallow’ traps;

2. Vacancies, MnS, microalloy (Ti, Nb, V, Mo) carbides, and oxides (and the interface with the matrix) can be considered to be relatively ‘deep’ traps;

3. The beneficial effect of trapping hydrogen is dependent both on charging conditions (i.e. constant source of hydrogen or periodic charging), and processing of the alloy (e.g. tempered microstructure, finer grain size, smaller precipitate size);

4. Where amount of hydrogen charging is large, the presence of traps actually increases hydrogen uptake.

This implies that designing steels to be resistant to hydrogen embrittlement is rather complex. Bhadeshia [6] points out that as embrittlement is not observed to occur below a critical hydrogen concentration, $C_{Hcrit.}$, it is this parameter that needs to be maximised, whether that is achieved by means of embedding of traps or otherwise. This must also be balanced with functional performance. For example, MnS inclusions are known to initiate ductile cracks under ordinary service conditions, and are not usually deliberately engineered into steels for this reason [180]. Added to this, premature fatigue failure has been shown to be exacerbated through hydrogen accumulated around MnS trap sites [181]. This provides a small illustration of how designing against hydrogen embrittlement in steels is far from straightforward, even with copious data on diffusion characteristics.

2.4.4 Other techniques for characterising diffusion

To alleviate some of the uncertainty from curve fitting and gain more 'direct' measurements of trap density and binding energies (and an alternative way of computing diffusion coefficient), thermal desorption analysis (TDA) is often used (e.g. [131,141,182]). This utilises a heating chamber coupled with a mass spectrometer to detect effused hydrogen from pre-charged specimens as they are gradually heated at specific heating rates. Each peak in hydrogen measured at specific temperatures represents hydrogen released from traps of a specific binding energy, which can then be directly calculated from the peak temperature [183–185]. This has proven useful for characterising specific binding energies of various precipitates and lattice defects (see aggregated data in [6]), but does rely on prior characterisation being comprehensive enough to provide some certainty as to what features are actually trapping the hydrogen atoms. Furthermore, this does not distinguish between traps that are considered 'reversible' (those that maintain equilibrium with the hydrogen that is freely diffusing in the lattice [156]) or 'irreversible' (those that bind hydrogen to them even after all the freely diffusing hydrogen has been depleted [149]). Therefore, whilst binding energies may be characterised for various trap sites, it is left to the researchers

to determine whether these traps are of particular benefit or not with regards to prevention of hydrogen's ability to embrittle.

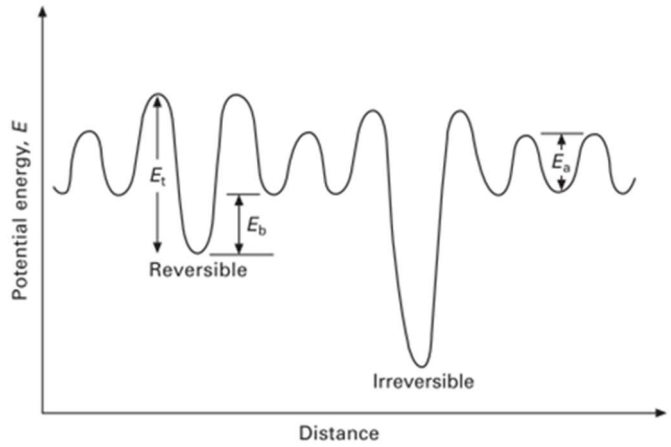

Figure 2.41 Illustration of potential energy associated with lattice diffusion sites of activation energy E_a, and trap sites with binding energy E_b and activation energy E_t [150].

Recently, a number of papers have utilised atom probe tomography (APT) for directly observing hydrogen atoms trapped at specific precipitates [186] and e.g. [187]. Secondary ion mass spectrometry (SIMS) has also been used to identify trapping sites, although in these instances it is often deuterium, rather than H^+, that is the trapped species [188]. Neither of these techniques is able to quantify binding energies, however, so TDA or repeat permeation transients are still necessary.

What neither permeation nor TDA provide is data on preferential diffusion paths. To overcome this, many researchers (e.g. [189–191]) have utilised a hydrogen 'microprint' technique (HMT). This involves the coating of a sample surface in an AgBr emulsion, which is then reduced by effusing hydrogen atoms according to equation (37):

$$AgBr + \frac{1}{2}H_2 = Ag^0 + H^+ + Br^- \quad (37)$$

After removal of any unreacted AgBr via a fixing solution, a system of residual Ag particles remains on the sample surface where hydrogen has preferentially diffused from the sample (Figure 2.42). Upon examination in a scanning electron microscope (SEM) this provides a good indication of the microstructural features favoured by diffusing hydrogen.

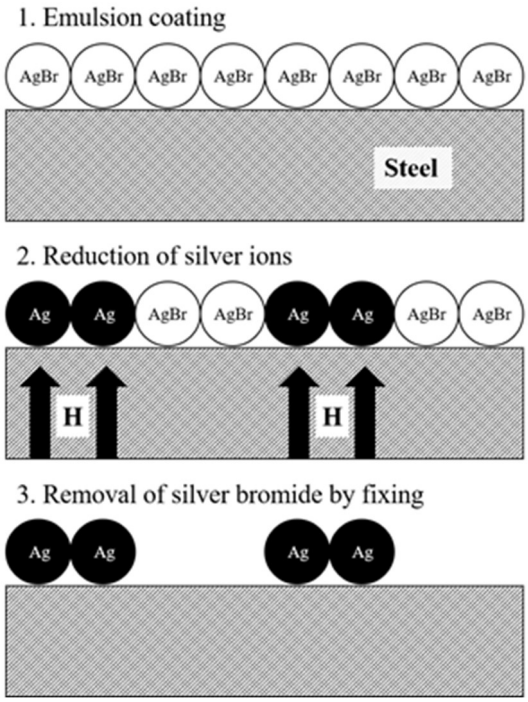

Figure 2.42 Schematic of the hydrogen microprint technique (adapted from ([190])).

A good example of this application is shown by Ichitani et al. [190], who combined the technique with the charging half of a permeation cell. They were able to show that for low carbon steel there were no preferential diffusion paths observed, but for a higher carbon steel containing pearlite localisation of silver particles was observed at ferrite/carbide interfaces prior to reaching steady-state, and upon reaching steady-state silver particles also covered the eutectoid ferrite lamellae within the pearlite and the proeutectoid grains comprising the rest of the microstructure.

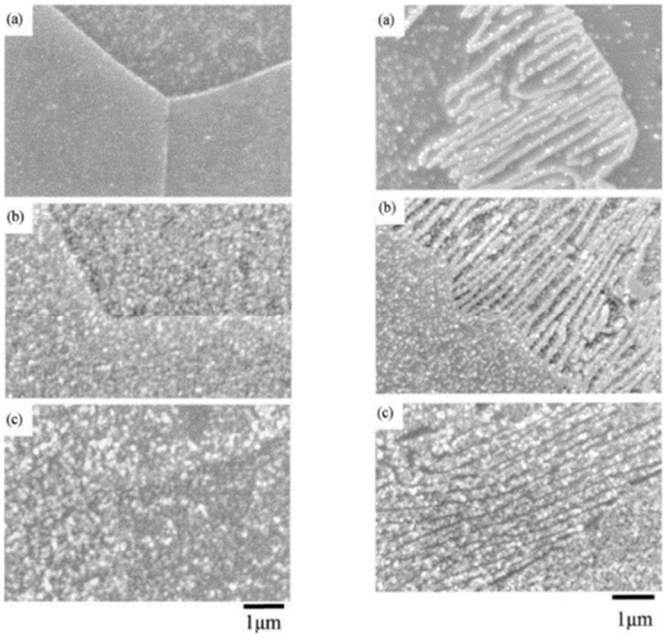

Figure 2.43 HMT results for left: 0.002% C steel, and right: 0.29% C steel, where letters refer to different charging times a) 5 minutes, b) 20 minutes, c) 40 minutes [190].

Whilst this technique has been used to elegantly present how hydrogen diffusion is affected by artefacts such as stress fields [189], dislocations [192], and trap distribution [193], it does however remain a qualitative technique. Furthermore, it is highly sensitive to changes in methodology, as shown by Ronevich et al. [191]. This sensitivity to preparation, which can be laborious and should be undertaken within a photographic dark room, can limit the application of this technique.

Another technique with the ability to provide a visual representation of hydrogen diffusion utilises scanning Kelvin probe force microscopy (SKPFM). Essentially an atomic force microscope (AFM) with a scanning Kelvin probe (SKP) attached, this technique enables Volta potential difference measurements across the scanned surface of a metallic sample with the resolution of AFM [186].

More typically used for corrosion studies [194], SKP has been shown to be a reliable technique for inferring the presence of permeating hydrogen in iron by Williams et al. [195]. With the requirement to understand differences in hydrogen diffusion characteristics between microconstituents that may be sub-micron in diameter,

SKPFM is growing in popularity as a means of observing preferential hydrogen diffusion within metals, and is capable of providing a way of deriving semi-quantitative data on permeated hydrogen with high lateral resolution [196,197], although the lack of a reference electrode in SKPFM prevents actual quantification, as is possible in SKP [186]. At the very least, quantitative measurements of the relative differences in diffusion between different microconstituents are possible, as demonstrated by Senöz et al. [198], who observed significant differences in Volta potential between austenite and ferrite phases within a duplex stainless steel due to the emergence of hydrogen charged from the opposite surface (Figure 2.44).

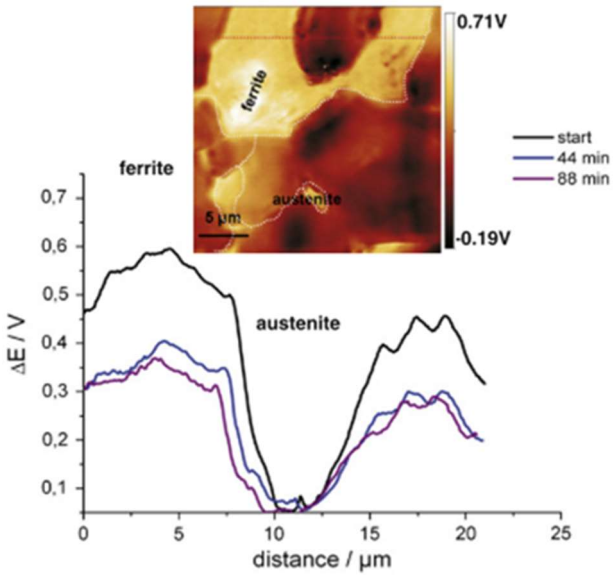

Figure 2.44 Potential evolution along red dotted line of AFM image upon commencement of hydrogen charging at opposite surface of a duplex stainless steel [198].

Again, there are some limitations to this technique. Constraints on lateral resolution due to probe tip diameter and tip-sample distance seen in macroscopic SKP [199] still apply for SKPFM [198,200], although for the most part the greatly reduced probe tip size and much smaller tip-sample distance means that the resolution is still several orders of magnitude more refined in SKPFM [201]. However, lateral resolution in SKPFM hydrogen permeation measurements are affected by noise from oxidation currents at the sample surface [197]. This is minimised by a variety of strategies, chiefly application of a Pd coating [202,203], although Tohme et al. [204] suggests application of a Pd layer may actually hinder detection of effusing hydrogen from particular steel microstructures, and Burgstaller et al. [203] points out that keeping

humidity levels low is crucial to avoid inducing damage in Pd membranes that can lead to significant trapping of hydrogen within the membranes, and Schimo et al. [205] show that oxygen concentrations in the scanning environment greatly affect the rate at which hydrogen effuses from Pd. Despite these concerns, SKPFM provides an extremely useful means of assessing diffusion characteristics at the microstructural level. The ability to monitor diffusion over time, and under different atmospheric conditions, also gives it a clear edge over HMT (or equivalent silver decoration technique).

Diffusion of hydrogen, allowing it to concentrate at stress concentrations, triggers premature failure. A variety of techniques have emerged for characterising diffusion, with varying levels of resolution. This has allowed researchers to gain some good insights into how hydrogen interacts with particular microstructures, showing preferential diffusion through ferrite grains or along ferrite-cementite interfaces in pearlite. However, it has also shown that a sufficiently full picture of hydrogen-microstructure interactions may only be gained through use of multiple techniques operating at different scales.

The way hydrogen impacts upon different microstructures is also far from straightforward, even when diffusion characteristics are well-characterised, and depends not only on the inherent lattice diffusion and densities/binding energies of traps, but also on the processing of the alloys concerned. As an example of this, despite displaying lower overall diffusivity, martensitic microstructures are particularly susceptible to embrittlement due to their low ductility and high defect concentrations. The presence of traps, commonly thought of as a way of ‘inoculating’ steels against hydrogen degradation, has been shown to be a far more complex picture, and in certain cases may in fact exacerbate the problem by concentrating hydrogen at defects and initiating cracks, or continuing to release hydrogen to diffuse in the lattice even after the external supply of hydrogen has ceased. Retained austenite present in TRIP steels is a particularly deep trap for hydrogen, but upon deformation transforms into martensite that is then supersaturated with hydrogen. Conversely, there is evidence

that ‘reverted’ austenite that is not liable to further transform may provide some benefit. This complexity indicates that designing steels that are resistant to hydrogen embrittlement is far from trivial, and may be best treated as with the design of any particular alloy properties (e.g. strength, ductility) as a balance between different attributes.

We have seen from the literature that the study of hydrogen embrittlement in steels is a broad and complex undertaking, encompassing fundamental metallurgy, electrochemistry, and fracture mechanics, as well as atomistic and real-world service considerations. Ensuring that the data collected and the conclusions drawn from it is relevant, meaningful, and hopefully, useful, is a challenge in itself.

However, given what we have learned from the literature, the critical pathway for this project necessitates a fundamental understanding of the microstructures of the steels in question, as it is from this that the differences in hydrogen evolution, diffusion, and mechanical degradation, follow, including determining the severity and mechanism of each of these processes. Alloying and microstructural considerations therefore underpin all of the work described subsequently, and the choices regarding techniques used in this work have been made with this as the prime concern.

3 Experimental methods

3.1 Material

Six commercially available strip steels commonly used in vehicle construction were studied. These were 2 ferritic nanoprecipitate steels designed for use in suspension components, XPF800 and XPF1000, 2 ferrite-martensite dual-phase steels utilised for a range of parts both in the BiW and chassis, DP800 and DP1000, and 2 fully-martensitic (in service) hot-stamping boron steels commonly used in safety cage anti-intrusive structures within the BiW, 22MnB5 and 27MnB5+Nb.

As these steels are also widely-utilised with the presence of a galvanic zinc coating (galvanised), the effect of galvanic corrosion due to damage to a zinc coating upon hydrogen evolution was undertaken. In the absence of galvanised UHSS samples, for the work on galvanic corrosion, a coupon of GI-coated DX51 steel was used. DX51 is a low carbon, aluminium-killed steel with a relatively wide specification for alloy chemistry and mechanical properties, and is considered a 'base' galvanised product within the low-alloy strip range. As such, it is considered to be sufficiently similar to the UHSS that are the primary focus of this work that it can be considered as representative.

3.1.1 Alloy chemistry

Selected alloy chemistry of each of the steels is displayed in Table 3-1, with 'carbon equivalent value' (CEV), a value which has been typically used to estimate the strengthening effects of various alloying elements with respect to carbon additions, calculated according to [20]:

$$\%CEV = C + \frac{Mn}{6} + \left(\frac{Cr + Mo + V}{5}\right) + \left(\frac{Ni + Cu}{15}\right) in\ wt.\% \qquad (38)$$

Table 3-1 Alloy chemistry of investigated steels.

Steel	C	Si	Mn	Cr	Mo	Nb	Ti	V	B	CEV
DP800	0.136	0.236	1.692	0.553	0.003	0.024	0.021	0.003	0.0002	0.532
XPF800	0.0611	0.189	1.373	0.016	0.141	0.061	0.002	0.212	0.0002	0.366
DP1000	0.149	0.041	2.222	0.548	0.005	0.014	0.026	0.006	0.0001	0.634
XPF1000	0.1037	0.201	1.396	0.023	0.292	0.05	0.003	0.286	0.0002	0.459
22MnB5	0.22	0.165	1.228	0.288	0.001	0.001	0.023	0.003	0.0032	0.485
27MnB5+Nb	0.27	0.29	1.18	0.046	0.001	0.029	0.05	0.003	0.0025	0.478

Specific alloy chemistry for the galvanised DX51 is unavailable, but the specification is shown below in Table 3-2.

Table 3-2 Alloy chemistry specification of DX51D+Z galvanised steel [206].

	C Max.	**Mn** Max.	**P** Max.	**S** Max.	**Al** Min.	**N** Max.	**Ti** Max.
DX51D+Z	0.18	1.2	0.12	0.045	-	-	0.3

Historically, a higher CEV would be thought to correlate to higher strength/lower ductility, and hence an increased risk of hydrogen embrittlement, although this is a generalisation and ignores the effects of different thermomechanical treatments. It can be seen that within the distinct 'families' of UHSS being studied in this work there are common features concerning alloying additions. The two hot-forming steels, 22MnB5 and 27MnB5+Nb, both have boron additions to increase hardenability [180], with the 22MnB5 also having a deliberate chromium addition, as opposed to the 27MnB5+Nb, which has a different carbide-forming addition in the form of niobium. This niobium addition causes some grain refinement both in the austenite phase during heat-treatment or hot rolling, and in the final microstructure. Both of these hot forming steels have similar manganese additions, however the 27MnB5 has a significantly greater silicon addition. The increase in carbon in the 27MnB5+Nb should also increase the strength of the final product, though this remains to be seen.

For the dual-phase steels, a similar difference in manganese and silicon levels is observed. In small amounts these elements perform a similar role within strip steels as substitutional solid-solution strengthening additions, although Mn also acts as an austenite stabiliser as opposed to Si which promotes ferrite formation. The chromium additions in both dual-phase steels is almost identical and is used to retard pearlite (and/or bainite) formation.

Finally, the XPF steels both have similar additions, with the higher strength XPF1000 generally having increased levels of molybdenum and vanadium (both strong carbide-forming elements for grain refinement and precipitation hardening), as well as double the level of carbon, for strengthening, although the carbon levels for this range are notably low for steels of this strength.

3.1.2 Strip processing

All steels in this work were manufactured via the blast furnace and basic oxygen furnace (BOF) process and were fully aluminium-killed. Each steel was subsequently reheated to >1150 ºC and rolled through a hot strip mill (HSM).

The DP steels and boron steels were further processed through pickling, cold rolling (~55% reduction for all), and annealing via a continuous annealing and processing line (CAPL).

3.1.3 Heat treatments

Prior to mechanical testing or microstructural assessment, two of the steels (22MnB5 and 27MnB5+Nb) required some heat-treatment to achieve the properties they would require of their in-service condition. To best replicate the processing conditions that they would undergo, hot-stamping simulations (Figure 3.1), whereby sample strips of 225 x 25mm are heated in a furnace (with unprotected atmosphere), soaked for a set time (

Table 3-3), and then transferred to a press where they are die-quenched for 15-20 seconds, were carried out at Tata Steel's Product Development Centre in Port Talbot, as undertaken by Taylor *et al*. [55]. This most closely replicates the hot-stamping cycle

at industrial plants in terms of cooling rates, achieving up to -150 ºC/s, well beyond the critical cooling rate to achieve a fully martensitic microstructure [55].

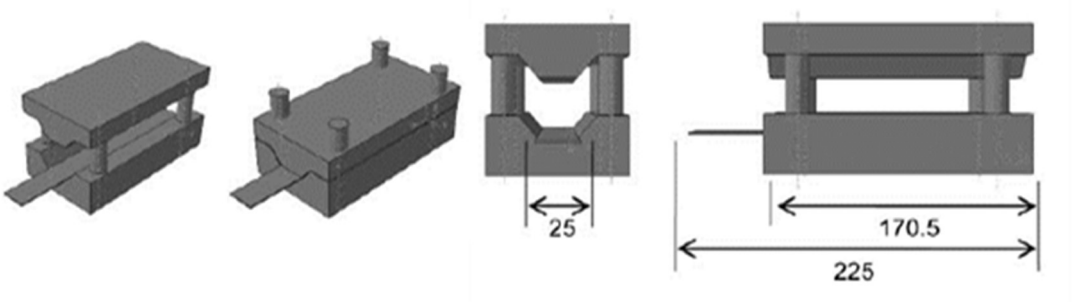

Figure 3.1 Laboratory hot-stamping tool and blank geometry in mm [55].

Table 3-3 Hot-stamping simulation cycle.

Steel	Ramp Time (s)	Soak Temperature (ºC)	Soak Time (s)	Air Cool (transfer time, s)	Press Quench (s)
22MnB5	120	900	180	~ 8	20
27MnB5+Nb	120	900	180	~ 8	20

3.1.4 Microstructural characterisation

Microstructural characterisation was undertaken primarily through quantitative metallographic analyses of images taken using a Zeiss Evo LS25 scanning electron microscope (SEM), operating with 20 kV accelerating voltage and probe current of 250 pA. Samples were prepared according to a standard metallographic procedure by first being sectioned using a circular abrasive cutting saw, mounted in conductive resin, ground with P120-, P600-, and P1200-grit silicon carbide paper with running water lubrication, followed by polishing with 6 µm, 3 µm and 1 µm polycrystalline diamond suspension, and finally etched using 3% nital for between ~8 and 20 seconds (repeated if necessary) to reveal the microstructure, example of which is displayed in Figure 3.2. Grain size analysis was performed via the linear intercept method [207] using a GUI-based (graphical user interface) plugin within Matlab software [208].

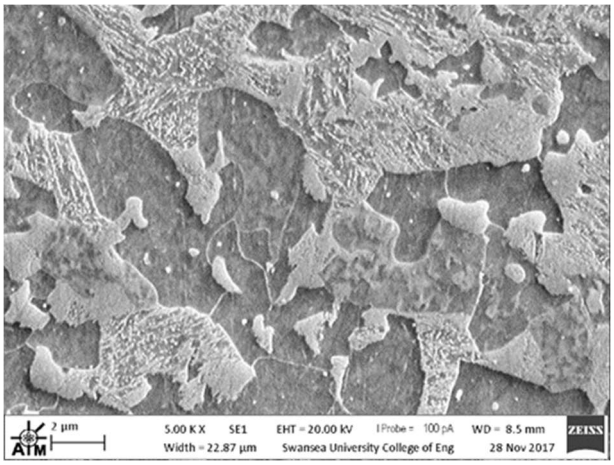

Figure 3.2 Example of DP microstructure revealed in SEM.

Phase quantification in the DP steels was performed using Weka trainable segmentation plugin within ImageJ software [209]. This plugin has a learning algorithm, so it can be trained to automatically recognise particular microconstituents. Once satisfied with how the software has classified each microconstituent, the 'classified' image undergoes a threshold analysis to quantify the volume fractions of each segment, and hence the volume fraction of the given phases within the image. In this work, phase fractions were estimated using images taken 'through thickness' (along the rolling direction), and perpendicular (normal) to the rolling direction in equal amounts. Quoted figures for phase fractions are area-averages of these quantifications.

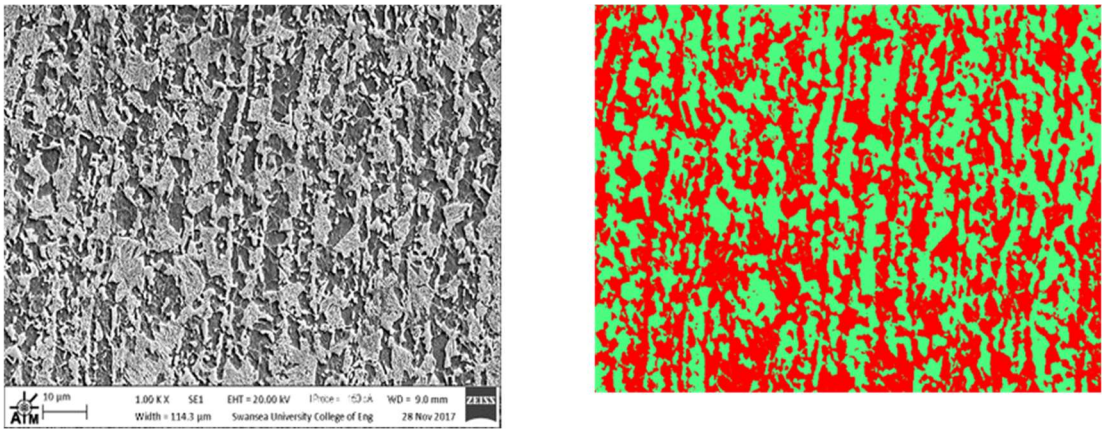

Figure 3.3 Example of phase classification in the Weka ImageJ plugin.

3.1.5 Electron Backscatter Diffraction (EBSD)

EBSD analyses in this work were undertaken with an Oxford Instruments Nordlys Nano EBSD detector fitted to a JEOL 7800F SEM equipped with a field emission gun (FEG), with an accelerating voltage of 20 kV, beam spot size of 7 nm, and step size of 0.2 μm. Sample preparation was as for the standard metallographic analysis outlined above, with the added step of ~ 3 minutes final polishing with 0.05 μm colloidal silica. Within the SEM, this carefully-prepared sample is tilted through 70°, creating an intersection angle of 20° between the electron beam and sample surface. A fluorescent screen then detects the electron backscatter patterns (EBSP, formed from 'Kikuchi bands') generated from electrons diffracted by the first few atomic layers of the sample. Each pattern is characteristic of the crystal structure and orientation, and can be used to characterise phases (confirmed by user), misorientations, morphologies, textures, and grain boundaries within the scanned region.

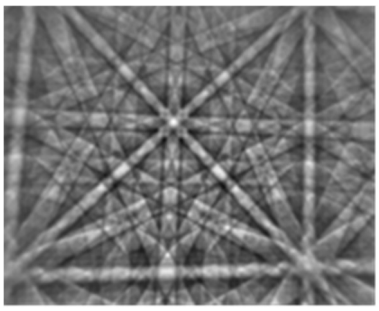

Figure 3.4 Characteristic Kikuchi bands in an EBSP ([www.EBSD.com]).

Post-processing data analysis was undertaken with Oxford Instruments Channel 5 HKL software suite, and the open-source Matlab plugin MTEX [210]. For the fully-martensitic boron steels, EBSD data was further processed to reconstruct orientation relationships (OR) between martensite 'packets' and parent austenite grains using an iterative algorithm freely provided by Nyyssönen *et al*. for the Matlab MTEX plugin [211,212].

3.1.6 Energy-dispersive X-ray Spectroscopy (EDS)

To characterise the elemental proportions (and to a lesser extent, confirm the published chemistry composition) of the steels under study, EDS analysis was performed using an Oxford Instruments XMax50n EDS detector fitted to both the JEOL 7800F FEG-

SEM, and Zeiss Evo LS25 SEM. Scans were performed with an accelerating voltage of 20 kV, and a step size of 0.2 µm. The EDS detector intercepts the X-rays that are emitted from the sample due to interactions with the electron beam. These X-rays ionise the detector's absorbing crystal, which in turn generates free electrons, producing an electrical charge that is proportional to the energy level of the generated X-ray, and characteristic of the element that emitted the X-ray [213]. Energy spectra and elemental maps were constructed to show the relative abundance of elements within the scanned area of the sample (Figure 3.5) using Oxford Instruments 'AZtec' software. It should be noted that extra care must be taken when attempting to quantify carbon with EDS as, even after plasma cleaning, significant surface carbon contamination can be present on an SEM sample, as well as within the SEM chamber. For this reason, in most cases, the values for carbon are generally excluded from any further analysis.

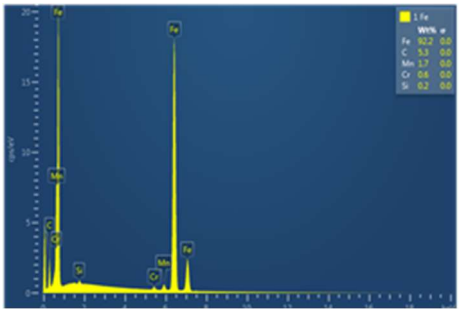

Figure 3.5 Characteristic EDS spectrum.

3.1.7 Powder X-ray Diffraction (XRD)

To determine lattice parameters and get a bulk sample measurement of phase fractions, particularly the fractions of retained austenite (γ) within the heat-treated (hot-stamped) samples, powder X-ray diffraction (XRD) scans were undertaken.

To perform this, a Bruker D8 Discover XRD machine was used with copper anode radiation source, λ=1.5406 Å, operating in parallel beam mode, with voltage set at 40 kV and scans performed between 40 – 100° with a 0.02° step size. Post-scan peak analyses were performed using Bruker DiffracEva software, with identified peaks used to calculate estimated lattice parameters for all of the steel samples. Following this, quantitative phase analyses were performed by Rietveld refinement method [214] using the open-source MAUD software [215]. Estimates for dislocation densities, δ,

were obtained utilising methods adapted from those outlined by Williamson and Smallman in [216] based on the 'full width at half maximum' of the diffraction peaks:

$$\delta = \frac{1}{D^2} \tag{39}$$

where δ is the dislocation density (no./$m^2 \times 10^{15}$), and D is the 'crystallite size' (in nm), which is itself calculated from:

$$D = \frac{K_s \lambda}{\beta \cos \theta} \tag{40}$$

where K_s is Scherrer's constant (taken as 0.9), λ is the wavelength of Cu Kα X-rays in nm (0.15406), β is the full width at half maximum of the X-ray peak (in radians), and θ is Bragg's angle (in radians). This is the Scherrer equation [217].

3.1.8 Gauge standardisation

Prior to undertaking any further characterisation (except for conventional tensile tests, described in Chapter 3.4.1), the investigated steel samples were reduced in thickness to 0.1 mm and 0.8 mm by wire electro-discharge machining (EDM), provided by an external company. Microstructures were compared between 'as received' (or heat-treated) and machined samples to ensure there were no residual effects, such as the presence of different phases, contamination, or indications of mechanical strain, seen in the microstructures from the reduction in thickness.

Standardising the gauges minimises variation in measured parameters due to sample dimensions, allowing for a more straightforward comparison between the effects of different microstructures.

3.2 Electrochemistry

The investigated steels were subjected to a variety of electrochemical measurements to discern their corrosion characteristics. Further tests were run to examine the effects of different environmental conditions that these steels may encounter in service. The methods for these tests are described here. All electrolytes described herein were prepared using laboratory-grade reagents from Sigma Aldrich Chemical Co. and distilled water.

3.2.1 Open circuit potential (OCP) measurements

To assess the relative susceptibilities of the different steels to corrosion, open circuit potential experiments were undertaken. For this, samples of dimensions roughly 26 × 34 mm were cut with a circular abrasive saw, and ground with P120-, P600- and P1200-grit silicon carbide paper, both to remove any scale present from heat-treatment and to ensure that each sample had the same surface conditions. Following grinding, each sample was cleaned thoroughly with detergent, water, ethanol, and acetone to minimise any remaining contaminants, though this was not undertaken for hot-dipped galvanised samples tested for reference. Prior to submersion, all faces and edges of the samples were covered with extruded Polytetrafluoroethylene (PTFE) tape (5490 HD, 3M) to ensure a repeatable exposed surface area of 10 mm × 10 mm.

Samples were then submerged within a 3.5% NaCl electrolyte with exposed face placed opposite a saturated calomel reference electrode (SCE, +244 mV versus standard hydrogen electrode), and the relative open circuit potentials (OCP) of the various samples measured (against SCE) by a Solartron Analytical SI1286 potentiostat. The time taken for the experiment to complete was largely dependent on the stability of the measured potentials, as tests were terminated once it appeared to have stabilised at a maximum. A schematic of the experimental setup is in Figure 3.6.

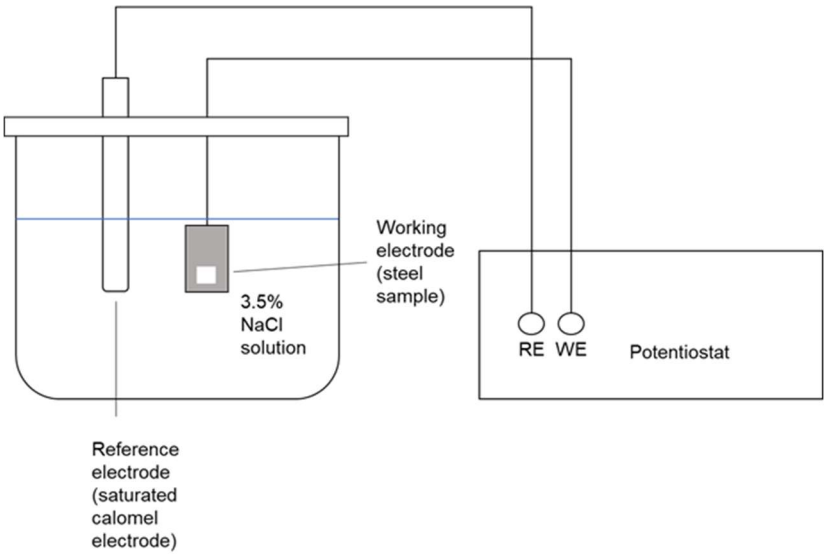

Figure 3.6 Schematic of the experimental setup for OCP measurements.

3.2.2 Potentiodynamic cathodic polarisation

To identify suitable current densities and potentials for future experiments involving hydrogen charging (i.e. the potential that the hydrogen evolution reaction becomes dominant), as well as assessing corrosion potentials and cathodic electrochemical reaction rates, cathodic polarisation experiments were undertaken on all of the steels, in the heat-treated and un-heat-treated states in the case of the boron-bearing steels (to assess the extent that electrochemical response is dependent on microstructure or chemistry – here we have 2 chemistries with 2 microstructures each, with the martensitic microstructure common to both chemistries in the heat-treated condition). In this experiment a 3-electrode cell was setup in pH 5.9, 3.5% NaCl solution, at 293 K (+/- 0.5 K). Samples of dimensions 26 × 34 mm were cut, and ground with P120- and P600-, and P1200-grit silicon carbide paper, both to remove scale from heat-treatment and to ensure that each sample had the same surface conditions. Following grinding, each sample was cleaned thoroughly with detergent, water, ethanol, and acetone to minimise any remaining contaminants (this was not undertaken for the hot-dipped galvanised samples tested for reference). Prior to submersion, all faces and edges of the samples were covered with 3M 5490 PTFE tape to ensure a repeatable exposed surface area of 10 mm x 10 mm. A saturated calomel electrode (SCE) was used as the reference electrode (RE), and platinum (Pt) foil acted as a counter electrode (CE), with the steel samples acting as the working electrode (WE). All 3 electrodes

were connected to a Solartron Analytical SI1286 potentiostat, which was setup to 'sweep' the potential of the cell from a potential just above (anodic to) the open circuit potential of the cell (-0.5V SCE) to a set potential cathodic to (below) the open circuit potential (-1.4V SCE) at a specified rate of 0.167 mV/s, measuring the current density at each step. A schematic of the setup for this experiment is shown in Figure 3.7.

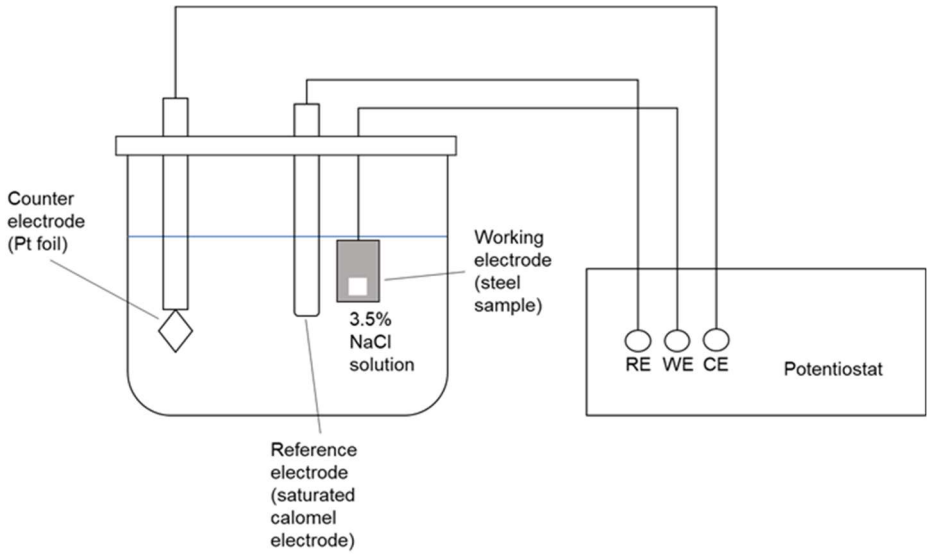

Figure 3.7 Schematic of the experimental setup for potentiodynamic cathodic polarisation experiments.

Output plot is of the logarithm of the (absolute) current density as a function of the swept potential, providing data on the nature of corrosion reactions occurring across the potential range, in this case identifying potentials at which a hydrogen evolution reaction becomes apparent and/or dominant. Post-processing of this data was done using Scribner Associates CorrView software, and involved fitting of (cathodic) Tafel slopes. Further statistical post-processing was undertaken to ascertain whether there were any significant differences in the reaction rates between individual steels in the heat-treated and un-heat-treated conditions, namely by the use of Student's t-test, described later.

3.2.3 Scanning Kelvin Probe Force Microscope (SKPFM)

Where it was considered appropriate, scanning Kelvin probe force microscope (SKPFM) scans were performed in air to assess the relative differences in work function between different microconstituents, in this case between ferrite and martensite phases in DP1000. In this work, this technique allows for a semi-quantitative assessment of the inherent differences in electrochemical response between the ferrite and martensite phases present within the dual-phase steels. In the XPF and boron steels the microstructures contained very little in the way of secondary phases, and it was thus considered that there would be insufficient contrast to provide useful data by using this technique on those steels with the limited time available upon the equipment.

For these measurements, the surface for scanning was prepared by standard metallographic procedures (Chapter 3.1.5) to a 0.05 μm finish, followed by etching in 3% nital for 5-10 seconds to create a discernible topography of the sample microstructures, allowing comparison between microconstituents. Scans were performed using a JKP NanoWizard 3 atomic force microscope (AFM) in contact mode, at a resolution of 50 × 50 μm (with higher resolution scans on areas of interest 15 × 15 μm, and 3 × 3 μm), every 20 minutes, for a total of 2 hours per sample. Kelvin probe measurements were undertaken via a 're-trace' of topographical scans performed by the AFM, thereby limiting the effect of topography for introducing artificial differences in work function measurements as distance between tip and sample surface should remain constant using this method.

3.2.4 Scanning Vibrating Electrode Technique (SVET)

As seen from Chapter 2.2.1.2, galvanic corrosion can lead to a hydrogen evolution reaction upon the steel surface as it becomes the cathode in a galvanic cell. This in turn implies the prospect of embrittlement should this hydrogen enter the steel in sufficient quantities. The steels studied throughout this work are also widely-utilised in the galvanised condition, and it is therefore important to understand how the presence of a zinc coating affects response to a corrosive environment, particularly where the coating may be damaged.

To examine the impact of galvanic corrosion of a zinc coating on a strip steel substrate with particular regards to the evolution of hydrogen, a scanning vibrating electrode technique (SVET) was used to quantify the local anodic and cathodic current densities during immersion within a 0.1 M NaCl solution.

For this, a coupon of GI-coated DX51-grade steel of approximately 30 × 30 mm was cut with a circular abrasive saw, and manually ground using P1200-grit silicon carbide paper with ethanol lubricant (to avoid corrosion during preparation) across half of one surface to remove the zinc coating, exposing the steel substrate across one half of the surface. The sample was then rinsed thoroughly with ethanol to remove any remaining debris and dried with warm air. All faces and edges of the samples were then covered with 5490 PTFE tape to ensure a repeatable exposed surface area of approximately 11 mm × 11 mm.

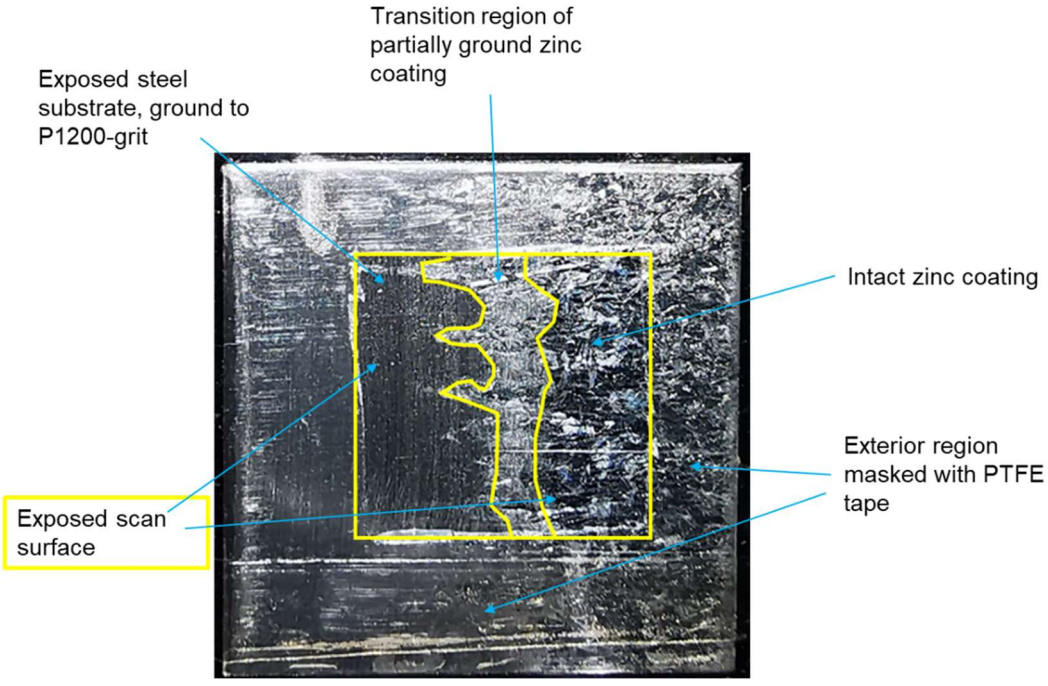

Figure 3.8 Prepared sample for SVET scan, showing regions of exposed steel substrate and intact zinc coating within the scan region.

The SVET measurements were undertaken using a probe containing a platinum wire of 125 µm diameter, sealed within a glass tube to leave a 125 µm diameter Pt microdisk electrode and total probe tip diameter of approximately 250 µm. This is mounted on a moving coil electromagnetic driver connected via a glass push rod to vibrate the probe at a frequency of 140 Hz. This is achieved via lock-in amplifier (EG&G model 7260)

which is also responsible for detecting and digitising SVET signal. Probe, driver, and push-rod are housed in a μ-metal enclosure and aluminium cylinder to prevent flux leakage, with bearing mounted at the base of the cylinder constraining probe vibration to a direction perpendicular to the plane of scan, in the z direction [218].

Prior to calibration the tip was cleaned by ~ 5 minutes immersion in aqueous 2 M HCl, before being rinsed thoroughly with distilled water. Position of the probe is controlled through stepper motors driving an orthogonal arrangement of linear bearings [219], with probe movement and data logging controlled via PC. Vibration frequency and drive voltage produce an amplitude of probe vibration of 25 μm [220]. A schematic of the SVET tip and housing is shown in Figure 3.9.

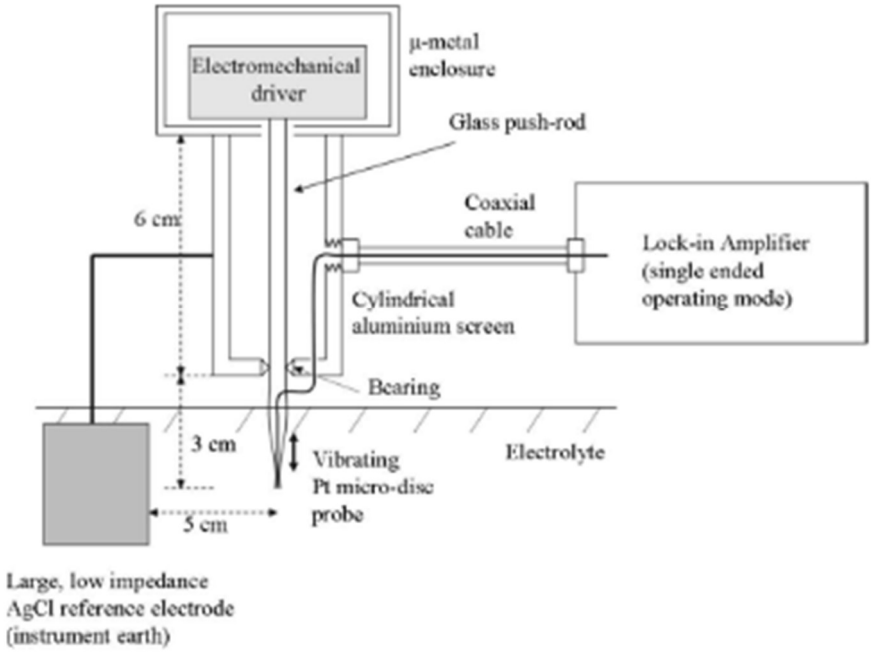

Figure 3.9 Schematic of SVET setup [218].

Calibration of the SVET was done galvanostatically in the test electrolyte (neutral-buffered 0.1 M NaCl, pH 7) using a 2-compartment cell. In one compartment, a bespoke nylon beaker containing a Pt electrode of 100 mm^2 is affixed to the base of a glass tank (300 mm diameter, 100 mm depth). The other compartment consisted of the remaining volume of the tank, filled with the test electrolyte, and also containing a 100 mm^2 Pt electrode, approximately 200 mm from the Pt electrode contained within the nylon beaker. A glass tube of internal diameter 4.8 mm and length 60 mm affixed in vertical orientation to one side of the nylon beaker, and also filled with test electrolyte,

connected the 2 cell compartments. The SVET probe was inserted approximately 5 mm into this tube, and a low impedance Ag/AgCl reference electrode of 25 × 25 mm area connected to the aluminium probe housing of the SVET was immersed within the electrolyte contained within the tank. Both Pt electrodes were then connected to a nano-galvanostat, which was used to pass a range of currents (5 -50 nA), subsequently calculated for current density using the known internal cross-sectional area of the glass tube (radius = 2.4 mm). The tube ensures current flux aligns vertically along its length, meaning the SVET tip vibrates in a region of uniform current density. SVET voltage was measured at each current density, and was found to vary linearly. The gradient of this linear plot of current density versus voltage provides a calibration factor, which in this case was 12,000 A/m^2/V. This calibration factor is subsequently used to convert SVET data into current density data.

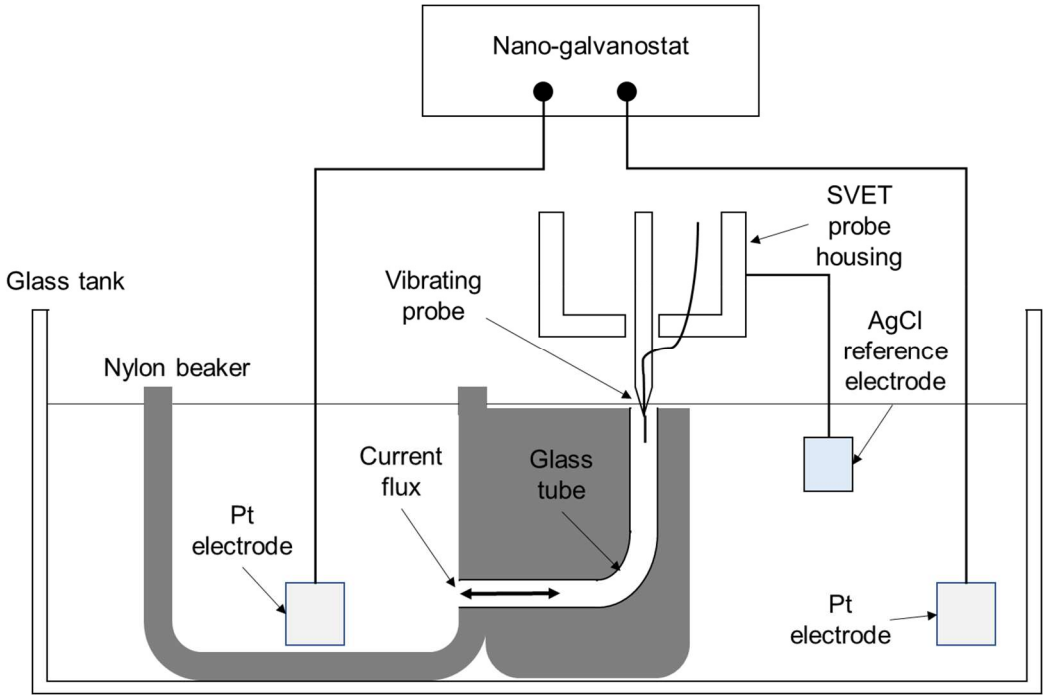

Figure 3.10 Schematic of SVET calibration setup (adapted from [218]).

After completing calibration, the tip was again cleaned as before, and rinsed. The sample was placed inside a shallow glass beaker with exposed surface area facing upwards, and secured in place by additional PTFE tape. The probe was then lowered to the surface of the sample to gauge any height variations across the surface, then withdrawn to a scan height of 100 µm. The test electrolyte was then added to the beaker ensuring that the sample, probe tip, and Ag/AgCl reference electrode were fully

submerged, and scans commenced over a 10 × 10 mm surface, with 100 µm step sizes, to give a 100 × 100 array of measurements. Scans were undertaken every 30 minutes over the course of 24 hours to provide a series of spatial and time-resolved current density measurements along the axis of measurement, J_z, across the surface. Post-processing of data was performed and current density maps created using Golden Software Surfer10 program, and integrals of area-averaged current density calculated using Matlab software.

3.2.5 Time-lapse photography (TLP) of simulated crevice corrosion

The process of crevice corrosion is widely regarded to be a particularly damaging form of environmental corrosion that can cause a rapid dissolution of metal at the anode [70]. The mechanism is described in Chapter 2.2.1.3, but importantly, it is accompanied by a decrease in pH within the crevice (and an accompanying increase in pH adjacent to the crevice due to production of hydroxyl ions). Decreases in pH can have a dramatic impact on the mechanism of hydrogen evolution in steels, as seen in the Pourbaix diagram for iron in water (Figure 2.21).

To visualise the crevice corrosion process, and gain some insight to its possible severity, a time-lapse photography experiment was devised, inspired by the simulated crevice corrosion setup in [73]. A sample of XPF800 steel of dimensions roughly 26 × 34 mm were cut with a circular abrasive saw, and ground with P120-, P600- and P1200-grit silicon carbide paper. Following grinding, the sample was cleaned thoroughly with detergent, water, ethanol, and acetone to minimise any remaining contaminants.

Prior to submersion, all faces and edges of the samples were covered with extruded PTFE tape (5490 HD, 3M) to leave an exposed surface area of 20 mm x 20 mm.

The sample was then affixed to the base of a shallow glass dish (150 mm diameter × 10 mm depth), and placed into a photographic light box upon a support stand with adjustable height to assist focussing of the camera, which in this case was a Canon EOS 250D digital SLR attached to a laptop running Canon EOS Utility software. A schematic of the experimental setup is shown in Figure 3.11. After optimising the height of the stage and camera focus, an electrolyte consisting of neutral-buffered 0.1

M NaCl (pH 7) + Unisol 113 universal pH indicator (Carl Roth Ltd.) was added to the sample dish. A small, 10 mm × 10 mm × 1 mm glass was extracted from a microscope slide by use of a diamond scribe, and after this was cleaned, rinsed, and dried thoroughly was affixed to the centre of the exposed surface of the steel sample with a piece of double-sided tape (3M), roughly 8 × 4 mm, to leave an artificial 'crevice' between the glass and steel around the perimeter of the double-sided tape. The transparent nature of the glass allowed for observation of the changes occurring beneath the glass, within the artificial crevice.

Upon closure of the photographic light box, the EOS software was instructed to commence photographing the sample every 5 minutes for a duration of 2 hours. Through this, localised changes in pH over time due to crevice corrosion can be visualised and tracked.

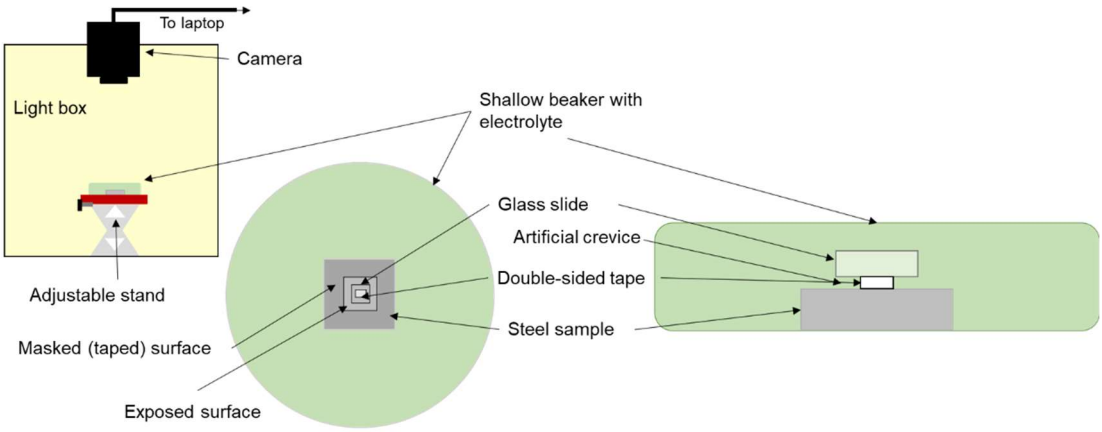

Figure 3.11 Schematic of simulated crevice corrosion experiment. Left: view of setup inside light box; centre: top-down view of sample; right: side-on view of sample showing setup of artificial crevice.

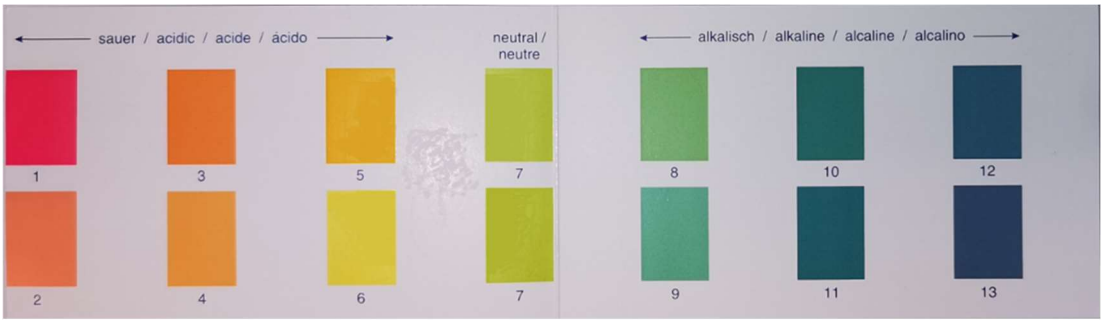

Figure 3.12 Colour key for Unisol 113 universal pH indicator.

3.3 Hydrogen diffusion

Hydrogen diffusion characteristics were discerned through the use of permeation experiments, details of which are presented here.

3.3.1 Hydrogen permeation

Hydrogen diffusion properties for each of the steels was assessed via the potentiostatic permeation method. For the permeation experiments undertaken in this work, a bespoke Devanathan-Stachurski cell [167] was manufactured from PTFE. Samples for permeation were prepared from small sheets of roughly 150 × 240 mm size, with thickness of 0.8 mm and 1.2 mm. For the material available a thickness of 1.2 mm (22MnB5) was the lightest gauge of any product, however, in order to ensure that the sample conditions were as uniform as possible between steels it was deemed necessary that all of the steels received some thickness reduction, therefore all steels also had some samples where thickness was reduced to a ‘standardised' nominal thickness of 0.8 mm. These gauges (0.8 mm and 1.2 mm) are quite typical of cold-reduced UHSS used within automotive structures, and so were suitably representative of real-world applications. For looking at the effects of membrane thickness upon permeation, a further reduction to a nominal thickness of 0.1 mm was performed, however this is not representative of real-world applications, and for reasons discussed later in this work is not optimal for gaining reliable permeation data.

These small sheets were subsequently cut into 30 mm × 30 mm × thickness coupons using a circular abrasive cutting saw, and both surfaces were prepared as per the samples for metallographic analysis to 1 μm diamond finish (without etching in nital). The samples were then rinsed with de-ionised water and ethanol to ensure there was no surface contamination from grinding and polishing, and dried with warm air. Five thickness measurements were taken using a digital micrometer and averaged, and the samples were then placed between a PTFE flange protector and a natural rubber washer, mounted between the two connecting tubes of the permeation cell, and clamped into place using a wing nut clamp, forming a tight seal against both surfaces. The exposed surface area was 2.011 cm^2 on each side of the sample. A 0.1 M NaOH solution, pH 13.15, was added to the oxidation cell, and a desorption cycle run for a minimum of 14 hours. To achieve this a Gamry 1010 potentiostat was used to fix the

potential at -0.094 V versus a saturated calomel electrode (SCE) with platinum foil acting as a counter electrode. Once the current density in the oxidation cell attained a steady-state background level, a 3.5% NaCl + 3 g/L NH_4SCN (to act as a recombination poison) electrolyte, pH 4.56 (the addition of the recombination poison lowered the pH from ~5.9), was added to the charging cell, and a charging potential of -1050 mV vs SCE applied immediately using a Gamry Interface 1000 potentiostat, with a Pt foil counter electrode. Both cells were covered using bespoke acrylic lids, with specific ports for insertion of reference and counter electrodes. For simplicity, electrolytes and cell conditions were kept identical for all steels, except where the specific effects of altering charging potential were investigated. The lag time method was used in this work to calculate values for the effective diffusion coefficient according to equation (31). Additionally, an estimate for the charging surface concentration was calculated according to the equation:

$$C_0 = \frac{J_\infty L}{D} \tag{41}$$

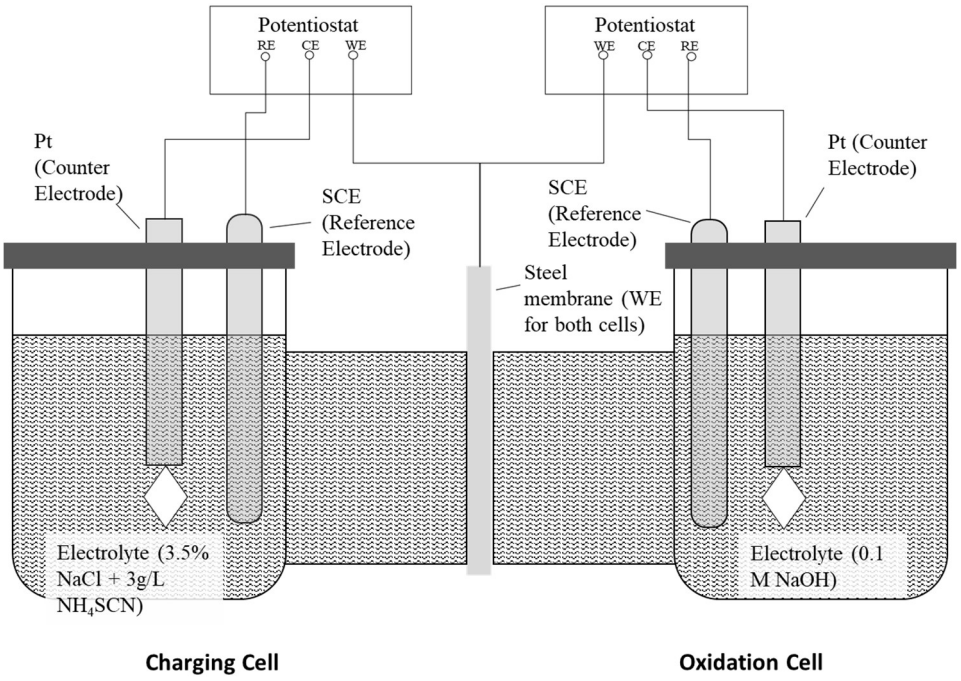

Figure 3.13 Schematic of permeation cell experimental setup.

Once tests had been completed, the data was analysed using a bespoke Matlab script I created specifically for this work (Appendix I), which loaded and analysed the

experimental data, then calculated and extracted specific parameters. These parameters were in turn used to simulate the perfect ‘Fickian’ curve using equation (28). By comparing this simulated curve with that obtained from the test data, a qualitative assessment can be made about what characteristics may be affecting the hydrogen diffusion.

3.4 Mechanical properties

A range of techniques have been used to characterise mechanical properties, and the degradation of these properties due to hydrogen ingress. Alongside this, a number of supplementary techniques were applied to interpret the data gleaned, and infer mechanisms of degradation occurring under the given test conditions. The methods utilised are described here.

3.4.1 Tensile test

Baseline mechanical properties were assessed by means of conventional strain-rate tensile tests, personally conducted as per BS EN ISO 6892-1:2016 [221] with a gauge-length of 50 mm (A50 sample geometry) at a nominal strain rate of 3×10^{-4}/s (rising to 3×10^{-3}/s upon reaching 0.2% proof stress), using a Zwick 1474 tensile testing machine located in Tata Steel's Technical Development Centre, Port Talbot. This strain-rate is the standard rate used for all tensile tests on production material in Tata Steel's strip production facilities in the UK. Results were output directly from the Zwick TestExpert control software used to run the tests.

3.4.2 Slow strain-rate tests (SSRT)

Mechanical degradation due to hydrogen was assessed by means of slow strain-rate tensile tests. For this, samples were machined via wire EDM at the University engineering workshop containing 2 sets of radii, with a gauge length of 3 mm × 10 mm × nominal thickness of 0.8 mm. Total sample length was 64 mm Figure 3.14.

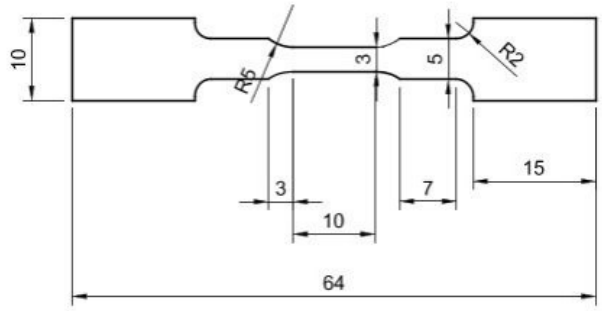

Figure 3.14 Sample geometry for SSRT (dimensions in mm).

Samples were placed between the grips of an Instron 8516 universal testing machine and deformed at a crosshead separation rate of 0.005 mm/min, a nominal strain-rate of 8.33×10^{-6}/s. For tests involving hydrogen charging, a bespoke polyethylene cell was placed around the sample gauge length prior to mounting the sample between the grips, and approximately 30 mL of 3.5% NaCl + 3g/L NH_4SCN solution introduced to the cell. To generate hydrogen at the sample surface, the sample was polarised potentiostatically using a PalmSens 4 potentiostat at -1050 mV versus a saturated calomel reference electrode (SCE), with platinum foil acting as a counter electrode. *In situ* hydrogen charging was either commenced simultaneously upon straining (henceforth referred to as 'charged' tests), or for 2 hours' pre-charging prior to straining (referred to as 'pre-charged' tests), with charging maintained throughout the duration of the test (i.e. until fracture) in both cases. 2 hours' pre-charging was selected as the minimum time to reach maximum hydrogen content within 0.8 mm specimens, as determined from maximum flux in permeation experiments, with the aim of discerning differences in performance at 'maximum' hydrogen concentration. Further tests were also undertaken at a 10 × higher strain-rate (i.e. 8.33×10^{-5}/s), with *in situ* charging (but no pre-charging), to further discern the impacts of charging duration and strain-rate upon the performance of the various products ('higher strain-rate' tests). (Note, for DP800 and XPF800, no tests were undertaken at 10^{-6}/s strain-rate without pre-charging due to shortage of material and the emergence of a trend seen in the other steels that indicated little difference between the 'pre-charged' and 'charged' (without pre-charging) conditions at 10^{-6}/s.)

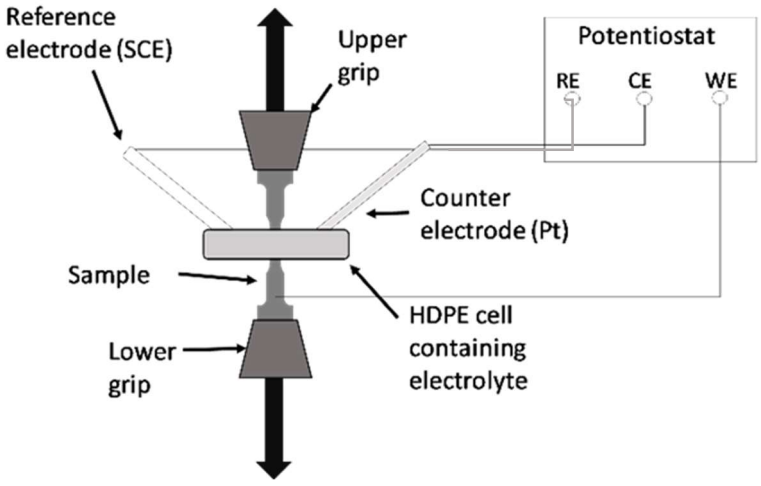

Figure 3.15 SSRT test setup.

In this work, embrittlement was assessed according to two measurements: i) the decrease in time-to-failure (TTF) in the presence of hydrogen, used for the lower strain-rate tests; ii) the decrease in total elongation in the presence of hydrogen – this is used for the higher strain-rate tests. Each was calculated according to equation (42):

$$Embrittlement\ Index = \frac{Performance\ in\ air - Performance\ in\ hydrogen}{Performance\ in\ air} \quad (42)$$

where 'Performance' refers to either the time-to-failure in seconds, or % total elongation, depending on the analysis (in both cases a higher number is a better performance).

Results for ultimate tensile strength (UTS, R_m), 0.2% proof stress ($R_{p0.2}$), % uniform elongation (A_g), and % total elongation were computed using Microsoft Excel using the relative equations from BS EN ISO 6892-1:2016. All other data analysis regarding SSRT data was performed using OriginLab OriginPro 2016 software.

3.4.3 Concentration profiles

To compliment the permeation experiments, mechanical tests, and more specifically, fractographic analyses, hydrogen concentration distributions within the sample gauge lengths were modelled within Matlab using Finite Element Method (FEM). Model dimensions were specified according to measurements of specimen geometry input to stress and strain calculations within slow strain-rate test data (or according to exposed surfaces and membrane thickness of a permeation specimen), with default mesh (typically 3×8291 nodes, but dependent on sample geometry), maximum element size (long axis) 0.35 mm, applied in each case. Values for effective diffusion coefficients were obtained from permeation test data acquired previously, based on the 'lag time' method. An example script for these analyses can be found in Appendix II.

Matlab does not contain a FEM partial differential equation solving function to simulate mass diffusion directly, but the equation for one-dimensional heat diffusion, for which Matlab does have functionality, is of identical form ($\frac{dT}{dt} = a \times \frac{d^2T}{dx^2}$, where T is temperature, and a is the thermal diffusivity), with the concentration parameter of the mass diffusion equation replaced by a temperature parameter and 'mass' diffusion

coefficient replaced with thermal diffusivity (itself calculated as $a = \frac{\lambda}{C\rho}$, with λ being thermal conductivity, C specific heat capacity, and ρ mass density) [222,223]. With that in mind, and thermal conductivity being a requirement for the simulation to run, the model was set to substitute hydrogen diffusion coefficient with an appropriate thermal conductivity coefficient by rearranging the equation for thermal diffusivity, and therefore calculated according to the following:

$$\text{Thermal conductivity } (\lambda) = D_{\text{eff}} \text{ (from permeation data, analogous to } a) \times \text{Mass density } (\rho, \text{fixed at } 7800\ \text{kg/m}^3) \times \text{Specific Heat Capacity } (C, \text{fixed at } 420\ \text{J/kg.K}) \quad (43)$$

Using this equation, heat diffusion coefficient (thermal conductivity) is varied directly according to the hydrogen diffusion coefficient (the other parameters are fixed). Boundary conditions included fixed hydrogen concentration (in mass ppm), also calculated from permeation data specific to the steel in question, substituted for external temperature at the charging surfaces of the specimen (for time = 0 to ∞). Unlike the SSRT specimens, for permeation specimens this boundary condition only applied at one surface, with the other surfaces fixed at 0 ppm concentration for all times. Concentration within the specimen at time = 0 was set to 0 ppm (substituted as 0 K). No allowances were made for the effects of traps, dimensional changes, or imparted stresses and strains.

Output data consisted of 3D plotted 'heat distribution' maps of the specimen, plus graphical concentration profiles through a central section of the specimen geometry (i.e. through the centre of the specimen in a direction normal to the loading direction).

3.4.4 Nanoindentation

Nanoindentation experiments were undertaken to determine the relative embrittlement responses between different microconstituents. Whilst attempts were made to construct a charging cell that could charge the sample *in situ* from the surface opposite the indented surface without introducing 'compliance', this was abandoned, and charging took place *ex situ*.

In this work, a Bruker Hysitron TI950 Triboindenter was used, with a standard Berkovich diamond tip, using the high load head. Samples were sectioned from 0.8

mm gauge materials, with charging/indenting surface prepared by standard metallographic procedure (as outlined in Chapter 3.1.4) to 0.05 μm finish (no nital etch). As no significant heterogeneity was observed in the microstructure of any of the steels tested, no specific allowances were made in the setup of the indent arrays, meaning that they were sampled according to geometric constraints, rather than microstructural, allowing a statistical comparison to be computed.

After a single 3 × 3 indent array was performed on the un-charged specimen (300 μN load, 20-second load time, 40-second dwell, 30-second unload), the specimen was then removed from the indenter, inserted as a working electrode into a 3-electrode electrochemical cell setup (as shown for potentiodynamic experiments, Figure 3.7), with saturated calomel reference electrode and platinum foil counter electrode, and potentiostatically polarised for 6 hours at -1050 mV (SCE) in 3.5% NaCl + 3g/L NH_4SCN electrolyte to charge the sample with hydrogen using a Gamry 1010 potentiostat.

Upon removal from the electrolyte, the specimen was then washed thoroughly with detergent, rinsed with tap water and ethanol, and dried thoroughly in warm air. As cathodic potential was applied almost immediately upon immersion, no corrosion product was visible upon the sample surface. Nonetheless, to remove any surface artefacts induced by the hydrogen-charging process, a short extra final polishing procedure with 0.05 μm colloidal silica was performed to ensure the best possible surface finish. The sample was then returned to the nanoindenter. Total time between hydrogen charging and return of the specimen to the nanoindenter was no more than 10 minutes. Indents were made according to pre-programmed 3 × 3 arrays (according to the previous parameters) at 30-minute time intervals, with each time interval selected to represent key points in the measured permeation curve for each steel. From this comparisons could be drawn regarding the average response to indentation, such as changes in hardness, as hydrogen is desorbed from the specimen.

3.4.5 Fractographic analysis

3.4.5.1 Optical-topographical microscopy

Fracture surfaces were analysed for evidence of different failure mechanisms by optical-topographical microscopy using a Keyence VHX-1000 microscope, chiefly for identifying macro features of ductile or brittle failure modes. Stacked images at multiple stage heights controlled by the microscope software were taken at 200× magnification, and stitched within the same software to create composite images of the entire fracture surface. These were in turn colour-coded according to focus height to create a 3-dimensional colour-coded topographical map of the fracture surface.

3.4.5.2 Scanning Electron Microscope (SEM)

Fracture surface analysis was also undertaken by SEM (Zeiss Evo LS25 operating at 20 kV accelerating voltage, 200 pA probe current) for a more detailed analysis of the fracture surface features. Images were then stitched using ImageJ software. Regions of the fracture surface were then assigned a colour (using Microsoft PowerPoint) depending on the dominant features observed in a particular location - fracture mechanisms depend upon hydrogen concentrations around crack tips and the associated stress intensity factors at these locations. Typically, quasi-cleavage (QC) facets (highly-localised 'flat' features indicative of failure via cleavage, but not on typical slip plane) and regions of intergranular (IG) fracture (fracture along grain boundary) are thought to represent a more 'brittle' fracture mode (low-energy, analogous to a decohesion-based mechanism), whereas microvoid coalescence (MVC), shear voids, and tear ridges (TR) occur in more 'ductile' failures (analogous to a plasticity-based mechanism). Transgranular (TG) cracks can be found in both ductile and brittle regions, and commonly occur where mechanisms are competing (key in Figure 4.101). From this a quantitative assessment was made in Matlab of the various fracture features observed by location on the fracture surface, and this is compared to the concentration distributions obtained from the FEM modelling outlined in Chapter 3.4.3.

3.4.5.3 Computed tomography (CT) scans

To visually assess what was going on beneath the fracture surfaces and towards the sample interior, 3D analysis of fractured 22MnB5 specimens was undertaken via computed tomography (CT), utilising a Zeiss Xradia Versa 520 (Carl Zeiss XRM, Pleasanton, CA, USA), equipped with a charge coupled device (CCD) detector and tungsten transmission target. X-ray tube voltage was set to 100 kV, tube current 80 μA, exposure time 12,000 ms, with voxel size of 0.5 μm [224]. Tomograms were reconstructed from 2D images using Zeiss XMReconstructor commercial software. This technique was used to assess differences in sub-surface features around fracture sites, particularly differences in crack morphology between hydrogen-charged specimens and specimens that were tested without charging. Further scans on XPF and DP steels were conducted externally at The Welding Institute (TWI) in Port Talbot through a partnership between Tata Steel and TWI, using similar setup (Zeiss Xradia Versa 520) with voxel size 0.7 μm.

3.5 Statistical analysis

3.5.1 Student's t-test

Student's t-test for small sample sizes was used to compute whether there were statistically significant differences between test populations. This applied to comparisons between different steels cathodic Tafel slopes from potentiodynamic polarisation experiments, and embrittlement indices calculated by time-to-failure and total elongation during slow strain-rate tests, both between different steels and between different test conditions. Where no significant difference is found between populations, quantitatively they may be considered to be part of the same overall population.

The test involves calculation of a test statistic, t, by comparing the means of the two data populations through the equation:

$$t = \frac{(m_1 - m_2)}{s\sqrt{(1/n_1\ 1/n_2)}} \tag{44}$$

where m_1 and m_2 represent the means of the two data sets, and n_1 and n_2 the number of measurements in each set. s is calculated from the standard deviations of the two populations:

$$s^2 = \frac{s_1^2 + s_2^2}{2} \tag{45}$$

where s_1 and s_2 represent the standard deviations of the two data sets. Test statistic, t, is then compared with tabulated values for a 95% confidence level with ((n_1 -1) + (n_2 -1)) degrees of freedom. If the test statistic is lower than the t-distribution, then it can be concluded with a 95% confidence level that the datasets belong to the same population, i.e. acceptance of the null hypothesis [93].

In this work, t-tests were carried out using the data analysis facilities in Microsoft Excel (for potentiodynamic data) and OriginLab Origin Pro 2016 (for SSRT data).

3.5.2 Weibull model

As SSRT data for tests occurring at 10^{-6}/s strain-rate were compared according to 'time-to-failure', it was useful to utilise Weibull statistics to calculate the probability

of survival of a group of specimens before failure through hydrogen embrittlement. These plots provide a helpful visual tool for comparing different populations and test variables.

For this, the time-to-failure data for each set of product-test condition pairs was evaluated, and compared with a mean time-to-failure of the un-charged condition for each of the steels, to give a comparison between products/conditions in terms of 'premature failure'.

The Weibull distribution has probability density function (pdf) according to:

$$P_{(f)} = \frac{\beta}{\alpha}\left(\frac{x}{\alpha}\right)^{\beta-1} e^{-\left(\frac{x}{\alpha}\right)^{\beta}} \tag{46}$$

where (in this case) f is time-to-failure, β is the shape parameter, and α is the scale parameter.

The cumulative distribution function (cdf) is as follows:

$$F_{(f)} = 1 - e^{-\left(\frac{x}{\alpha}\right)^{\beta}} \tag{47}$$

i.e. $F_{(f)}$ is the probability that time-to-failure is at most, f.

In steels, the Weibull model was adapted for analysis through brittle failure by Yokobori [225], showing that the probability of a specimen 'surviving' (i.e. not failing) within a specified time, t, is calculated according to (a rearrangement of the cumulative distribution function):

$$P_{(s)} = 1 - F_{(f)} = e^{-\beta t} \tag{48}$$

where $P_{(s)}$ is the 'probability of survival'. In this work, x is the probability per unit time that a crack forms of sufficient severity to cause failure of the specimen, and is deduced from the negative gradient of a plot of $\ln P_{(s)}$ versus t. As there is a minimum time for a critical crack to initiate (due to requirement of sufficient application of stress), the graph is displaced along the time axis by this amount, as shown by Robinson [226], modifying equation (48) to become:

$$P_{(s)} = 1 - P_{(f)} = e^{-\beta(t-t_i)} \tag{49}$$

where t_i is the time required for initiation of a crack of sufficient severity to cause failure [93]. This provides for a much simpler analysis, and allows the visualisation of time-to-failure data in simplified Weibull plots, with $P_{(f)}$ estimated according to:

$$P_{(f)} = \frac{n}{(n+1)} \tag{50}$$

where n is the number of specimens under consideration at any particular time (i.e. 1 to 3) [227].

4 Results

4.1 Material characterisation

The ‘dual-phase’ nature of the microstructures of the two DP steels can be seen clearly in the SEM micrograph examples given in Figure 4.1, with the darker regions being the ferrite (α) phase, and the lighter regions being the martensite (α′) phase. The relative differences in volume fraction are also clear, and qualitatively, more apparent ‘clustering’ of ferrite grains seen in the DP800, i.e. the martensite phase is less dispersed. Furthermore, in the DP1000 at higher magnification, the martensite packets can be clearly made out within the α′ colonies. Quantitatively, both volume fractions and ferrite grain size for each of the products are comparable with the figures obtained from the literature [228,229], with DP800 showing a 39% volume fraction of martensite, and DP1000 having a 55% martensite fraction.

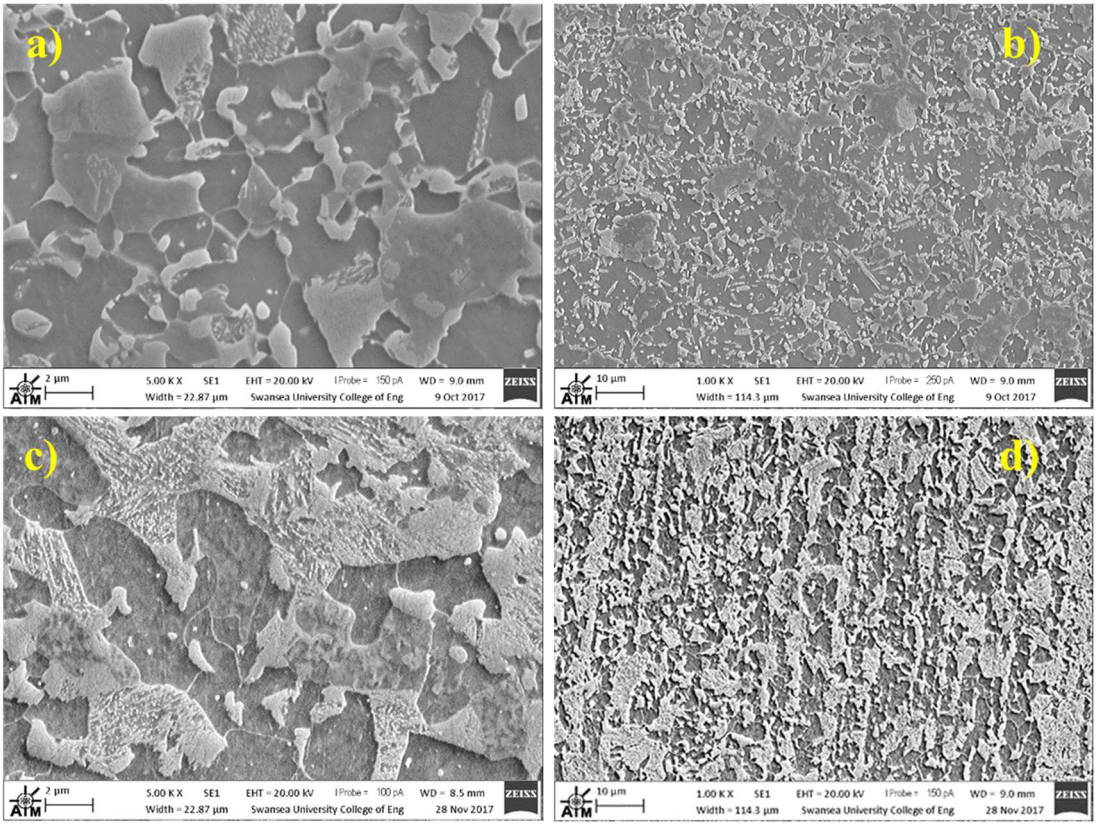

Figure 4.1 SEM micrographs of a) and b) DP800; c) and d) DP1000, at left: 5000×, and right: 1000× magnification.

The XPF steels appear to have a much less complex microstructure from the SEM images, with a nominally 100% ferrite microstructure and fine grain size (for a ferritic steel). There is little evidence of any Fe_3C formations, either lamellar or globular, as may be expected from the chemistry and processing conditions of the steels. However for both XPF800 and XPF1000 grain size appears somewhat bi-modal, with grains appearing either consistently larger, or consistently smaller, with little in the way of intermediate sizes. This is borne out in the mean and standard deviation for grain diameter, with XPF800 having mean grain diameter of 2.3 (±1.45) µm, and XPF1000 mean grain diameter of 2.21 (±1.73) µm (determined via linear intercept method on both planar and longitudinal micrographs).

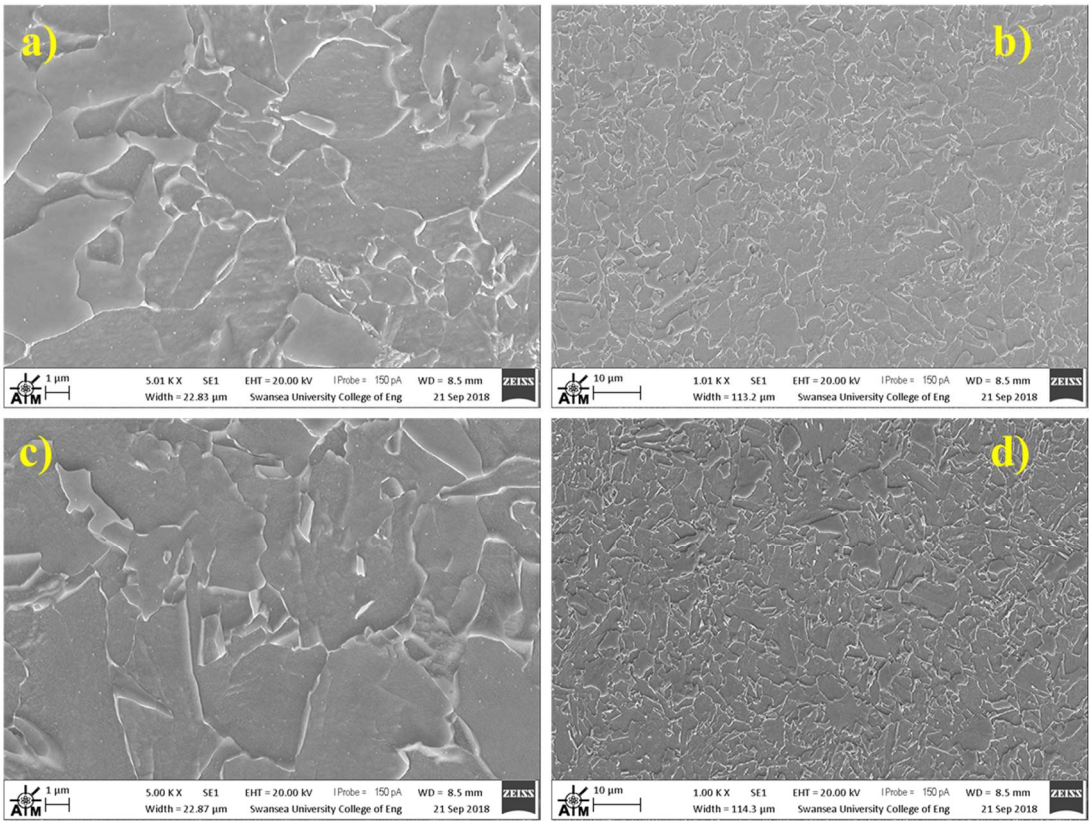

Figure 4.2 SEM micrographs of a) and b) XPF800; c) and d) XPF1000, at left: 5000×, and right: 1000× magnification.

22MnB5 and 27MnB5+Nb have the added complexity of heat treatment prior to use in service. In the un-heat-treated condition, 22MnB5 has a ferritic microstructure, with globular particles of Fe_3C primarily decorating the grain boundaries. 27MnB5+Nb has a more typical ferrite-pearlite microstructure, with relatively equiaxed ferrite grains and pearlite colonies. After laboratory hot-stamping, both achieve a nominally fully-martensitic microstructure, with metallographic analysis revealing the laths, packets, and prior austenite grain boundaries contained within.

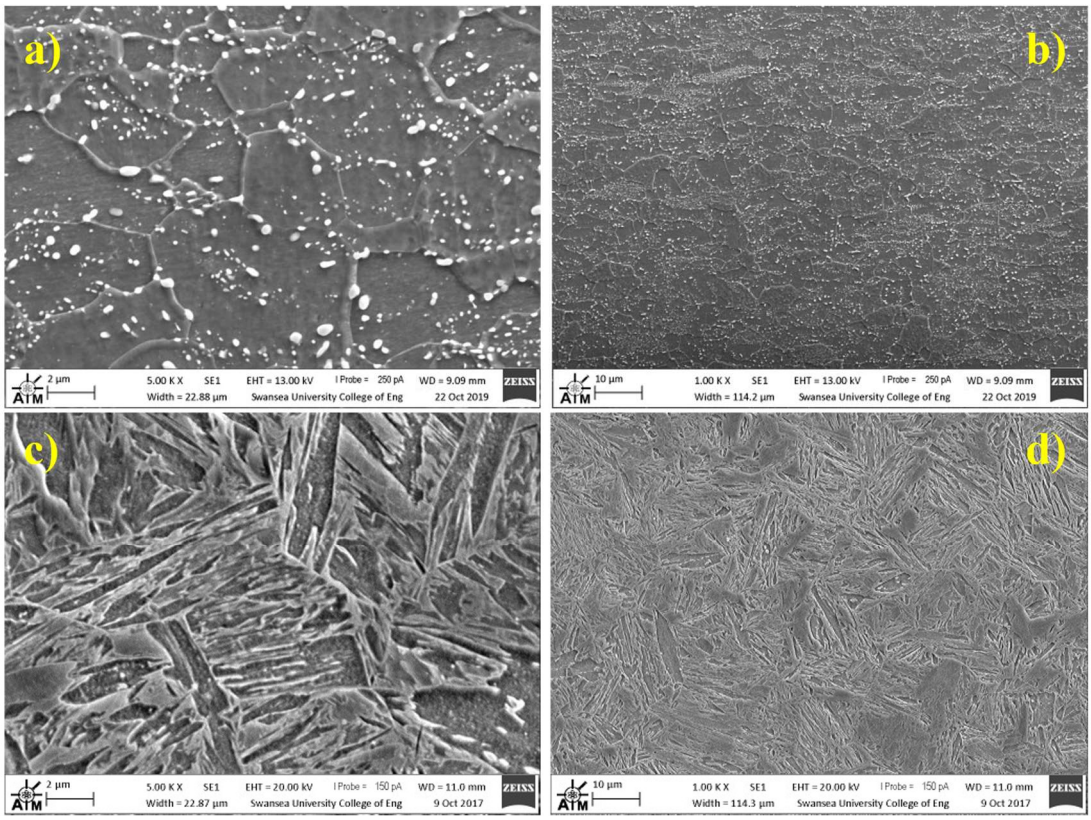

Figure 4.3 SEM micrographs of a) and b) 22MnB5 (UHT); c) and d) 22MnB5 (900C), at left: 5000×, and right: 1000× magnification.

To achieve the fully-martensitic microstructure required in the part, the increased hardenability obtained from a boron addition needs to be fully realised, meaning the steel must be fully-austenitised during heat-treatment. If that is not the case then there is the possibility that not all of the boron would be taken into solution, and therefore not contributed to the hardenability during quenching as fully as possible. Unlike the 27MnB5+Nb, however, 22MnB5 has relatively low levels of carbide-forming elements (Ti, Nb, V), and may encounter grain growth during the soak at high temperature (typically 900 – 950^{o} C). This in turn would also lead to a marginal

increase in martensite packet size due to the Kurdjumov-Sachs relationship between prior austenite grains and subsequent martensite formation that occurs for steels with < 0.6% carbon [20]. This is indeed what has been found for these steels, when prior austenite grain boundaries are reconstructed from EBSD maps of the heat-treated samples, 22MnB5 shows a mean prior austenite grain size (PγGS) of 10.37 (±9.16) µm, compared to 27MnB5+Nb having PγGS of 7.74 (±5.20) µm, despite having the smaller ferrite grain size in the un-heat-treated condition. This appears to translate to a larger martensite packet size (as seen in Table 4-1), although the range of measurement involves mean this cannot be concluded with high confidence.

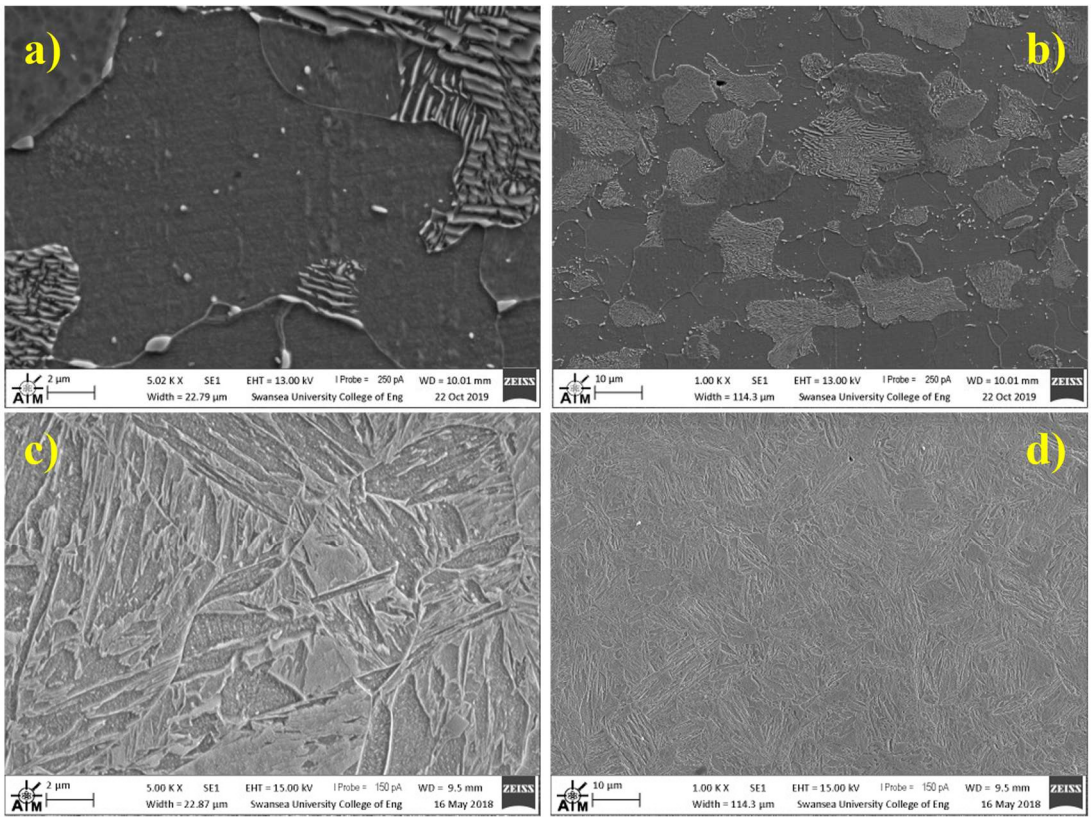

Figure 4.4 SEM micrographs of a) and b) 27MnB5+Nb (UHT); c) and d) 27MnB5 (900C), at left: 5000×, and right: 1000× magnification.

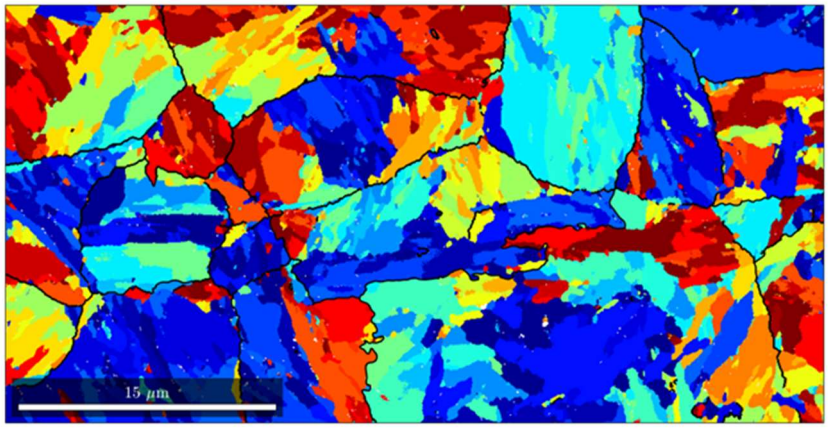

Figure 4.5 Example of EBSD map of 22MnB5 (900C), reconstructed to show the prior austenite grains, grain boundaries, and the orientation relationships occurring between the different martensite packets within the 'parent' austenite grains.

Table 4-1 Volume fractions of martensite and grain size measurements from quantitative metallographic measurements. Datasets feeding into this table are included in Appendix IV.

Product	Estimated martensite fraction f_m	Phase Size Measured	Mean Diameter, d_f, µm	Estimated Mean Area µm^2
DP800	0.39	Ferrite	3.49 (±1.77)	9.58
XPF800	0	Ferrite	2.30 (±1.45)	4.14
DP1000	0.55	Ferrite	2.32 (±1.37)	4.23
XPF1000	0	Ferrite	2.21 (±1.73)	3.84
22MnB5 (900C)	1	Martensite Packet Size	1.87 (±1.06)	2.73
	0	Prior Austenite	10.37 (±9.16)	84.47
27MnB5+Nb (900C)	1	Martensite Packet Size	1.56 (±1.04)	1.92
	0	Prior Austenite	7.74 (±5.20)	46.99

X-ray diffraction (XRD) measurements carried out according to the method described in Chapter 3.1.7, also allowed the calculation of an estimated volume fraction of retained austenite (via the Rietveld refinement software MAUD [215]), and dislocation density using the 45° (110), 65° (200), and 82° (211) 2θ peaks as input to the calculations. Detailed calculations of dislocation densities for all of the steels is included in Appendix V.

Table 4-2 Values for dislocation density calculated from XRD data as outlined in Chapter 3.1.7, and retained austenite phase fraction calculated via Rietveld refinement.

Steel	Dislocation density, δ/m^2	Retained γ percentage
DP800	1.337×10^{15}	1.659 (±0.96)
XPF800	1.992×10^{15}	0.000 (±0)
DP1000	1.327×10^{15}	1.988 (±0.829)
XPF1000	4.432×10^{15}	0.000 (±0)
22MnB5 (UHT)	1.380×10^{15}	0.022 (±0.19)
22MnB5 (900C)	6.400×10^{15}	2.529 (±1.01)
27MnB5+Nb (UHT)	2.003×10^{15}	0.000 (±0)
27MnB5+Nb (900C)	5.546×10^{15}	1.871 (±1.04)

Table 4-2 shows that for the boron steels, quenching to achieve fully-martensitic microstructure imparts a substantial strain to the individual grains, with an accompanying high dislocation density, at least 25% higher than the steel with the next highest density, XPF1000. This is despite the boron steels in the un-heat-treated condition having very comparable dislocation densities to the other steels. The DP steels both have similar dislocation densities, lower than that of all of the other steels. This is due to the fact that, despite a significant phase fraction of martensite, they are fully-annealed, with the martensite within having formed during a slow cool section within the annealing furnace. A lack of quenching in this case has allowed some 'recovery' within the martensite crystals.

Also notable is the amount of retained austenite present within the DP steels, which is comparable to the quenched boron steels (the fully-ferritic XPFs are not calculated to have any retained austenite). Whilst there is a substantial uncertainty about the precision of these estimates, the martensite finish temperature (M_f) is below room temperature for the chemistry of these steels – transformation to other phases is not possible at such lower temperatures and austenite will persist in a meta-stable condition.

Of the 2 boron steels, whilst 22MnB5 may have had a larger PγGS, it has both higher calculated dislocation density and (35%) higher estimated retained austenite fraction.

4.2 Electrochemistry characteristics

This section has been divided in to 3 parts. Chapter 4.2.1 shows results for each of the steels with regards to open circuit potential, as well as the open circuit potential measurements for a standard hot-dip galvanised sample, described with reference to the rate of change of the measured potential. This part also includes potentiodynamic cathodic polarisation curves to illustrate different reactions taking place as the steels are polarised from the free corrosion potential, with fitted Tafel slopes illustrating expected differences in hydrogen evolution reaction rate between the steels.

Chapter 4.2.2 displays the results of a scanning vibrating electrode technique (SVET) scan on a damaged hot-dip galvanised coating sample where the substrate steel is exposed, demonstrating the effects of the sacrificially anodic corrosion of the zinc coating upon the substrate surface reactions.

Finally, Chapter 4.2.3 shows the results of a time-lapse photography experiment monitoring the change in local pH over time in simulated crevice corrosion conditions.

4.2.1 Product corrosion characteristics

This section displays the results of open circuit potential (OCP) and potentiodynamic cathodic polarisation experiments for the steels studied.

4.2.1.1 DP800

Figure 4.6 shows the OCP curve for DP800 in 3.5% NaCl electrolyte (pH 5.9). After an initial relatively rapid voltage drop averaging -3.14×10^{-5} V/s during the first 20 minutes of immersion, this rate of change gradually reduces, reaching -2.03×10^{-6} V/s after 2 hours. Measured OCP value had reached -0.606 V (SCE) after 20 minutes, and -0.645 V (SCE) after 2 hours.

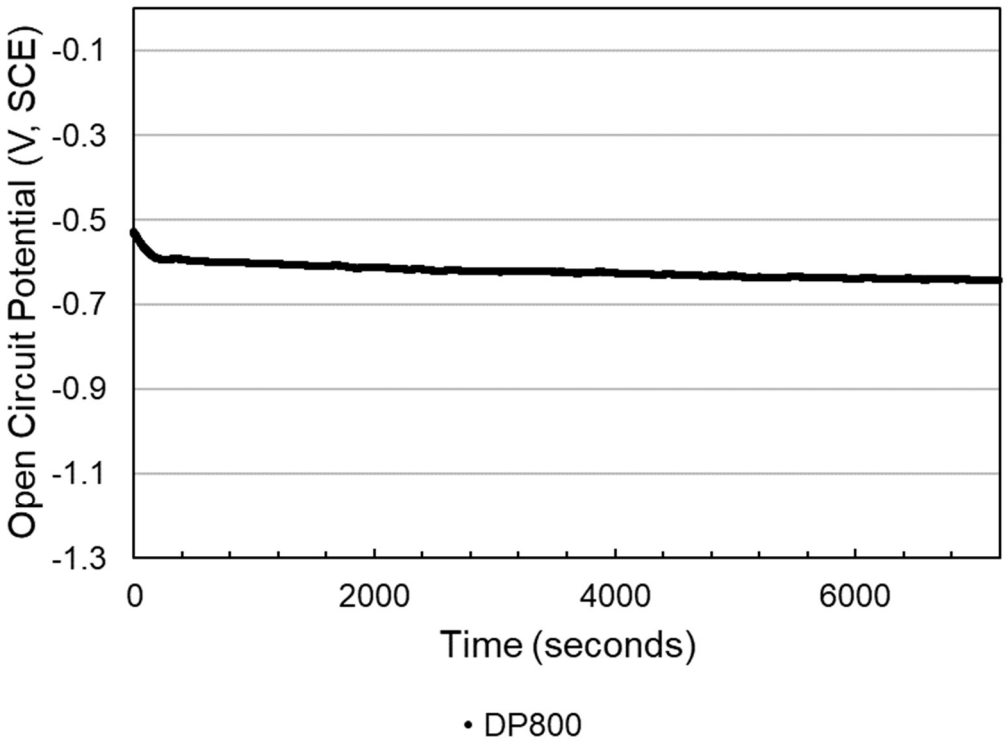

Figure 4.6 Open circuit potential versus time for DP800 in 3.5% NaCl solution.

A typical cathodic potentiodynamic curve for DP800 in 3.5% NaCl solution (pH 5.96) from the 5 tests undertaken under these conditions is shown in Figure 4.7. Between potentials of around -0.70 V and -0.95 V the oxygen reduction rection (ORR) is occurring according to equation (9). This changes at around -1.05 V with a clear transition to the hydrogen evolution reaction (HER, equation (8) or (11)) becoming dominant. The slope (Tafel fit, ß) of this region over 5 potentiodynamic sweeps (measured between -1.05 V and -1.20 V (SCE)) was -151 mV.

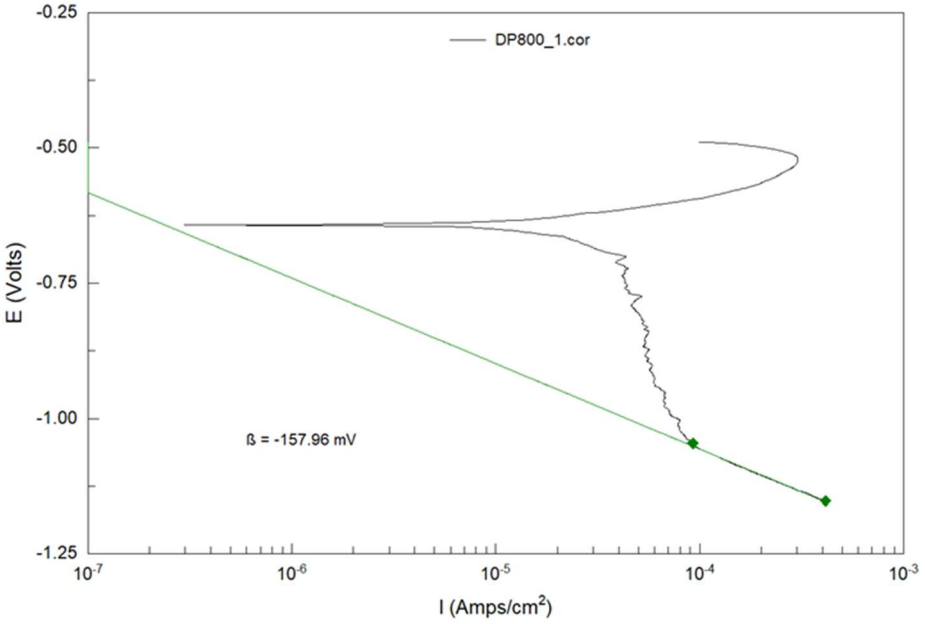

Figure 4.7 Typical cathodic potentiodynamic curve for DP800 in 3.5% NaCl.

4.2.1.2 XPF800

The OCP curve for XPF800 is shown in Figure 4.8. Voltage drop during the first 20 minutes of immersion in 3.5% NaCl solution averaged -5.73×10^{-5} V/s, reaching a value of -0.573 V (SCE), reducing to a rate of -7.00×10^{-7} V/s after 2 hours reaching a value of -0.631 V (SCE).

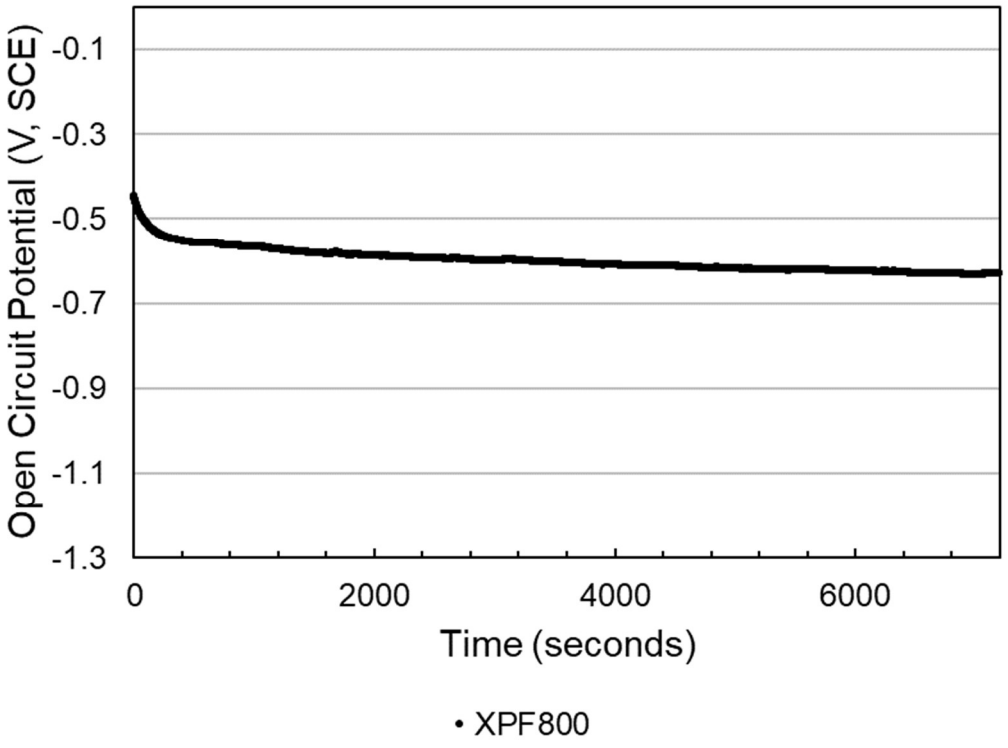

Figure 4.8 Open circuit potential versus time for XPF800 in 3.5% NaCl solution.

Figure 4.9 shows a typical cathodic potentiodynamic curve for XPF800. As with DP800, the region between -0.70 V and -0.95 V shows the presence of the oxygen reduction cathodic reaction, with a marked transition at around -1.05 V to a region where HER is dominant. The averaged ß over 5 potentiodynamic sweeps for XPF800 was -168 mV.

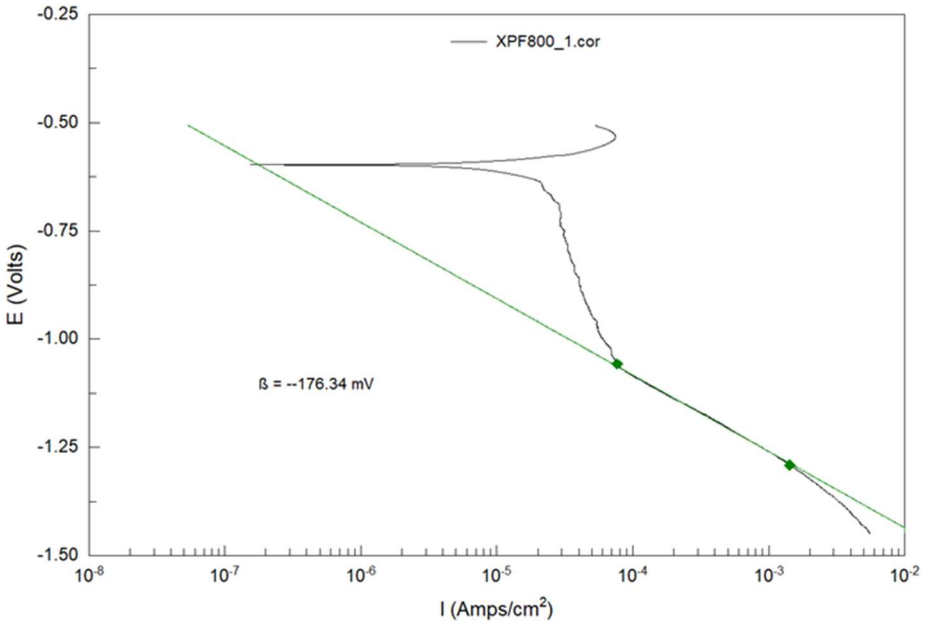

Figure 4.9 Typical cathodic potentiodynamic curve for XPF800 in 3.5% NaCl.

4.2.1.3 DP1000

Figure 4.10 illustrates the OCP versus time plot for DP1000 in 3.5% NaCl. During the first 20 minutes of immersion, the potential decreased at an average rate of -1.06×10^{-5} V/s, reaching a potential of -0.591 V (SCE). After 2 hours, the rate of decrease in potential had slowed to -2.72×10^{-6} V/s, with the potential reaching -0.658 V (SCE).

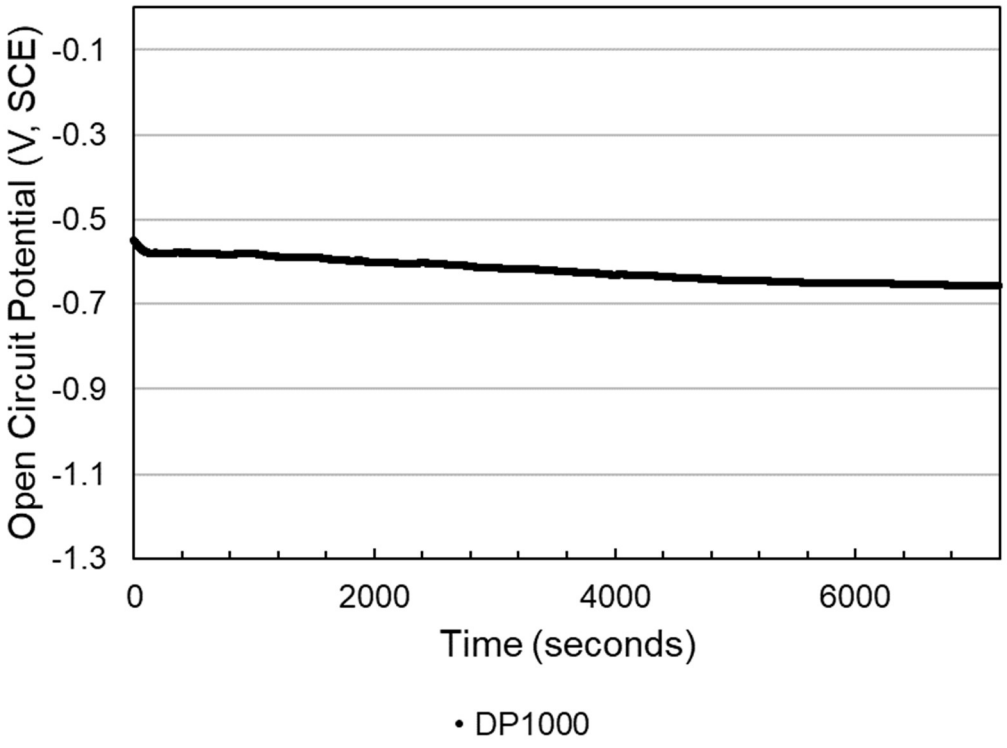

Figure 4.10 Open circuit potential versus time for DP1000 in 3.5% NaCl solution.

For DP1000, a typical cathodic potentiodynamic curve is shown in Figure 4.11. Once again it can be seen that the ORR occurs between ~ -0.70 V and -0.95 V, with the clear transition to HER at ~ -1.00 to -1.05 V, beyond which this reaction is dominant until the tests are ended (at -1.45 V). Averaged ß over 5 potentiodynamic sweeps for DP1000 was -148 mV.

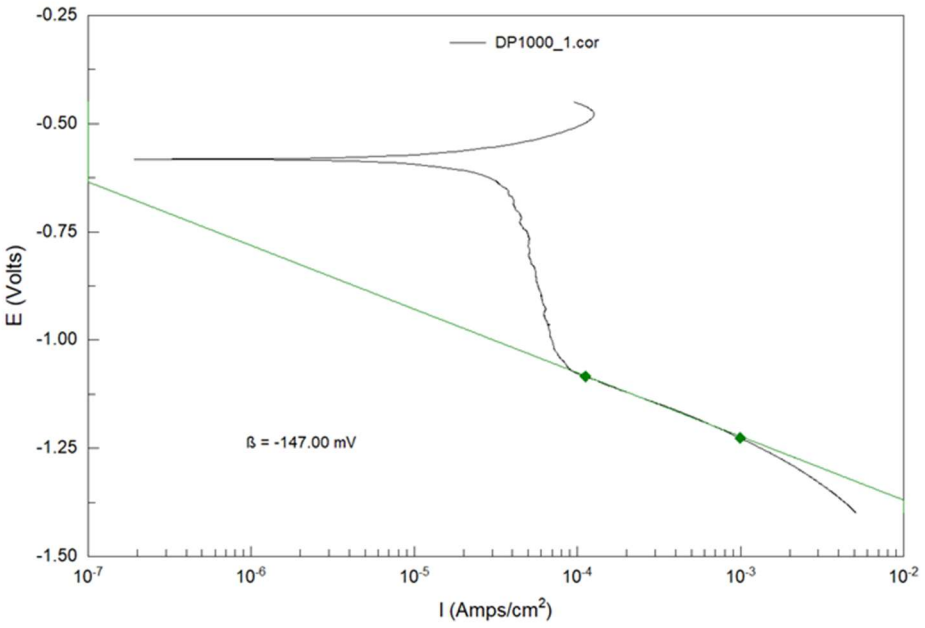

Figure 4.11 Typical cathodic potentiodynamic curve for DP1000 in 3.5% NaCl.

4.2.1.4 XPF1000

The OCP curve for XPF1000 in 3.5% NaCl solution is shown in Figure 4.12. The first 20 minutes of immersion saw the potential drop at a rate of -3.34×10^{-5} V/s, reaching a potential of -0.584 V (SCE). After 2 hours the potential had dropped to -0.660 V (SCE) at an average rate of decrease of -3.64×10^{-6} V/s.

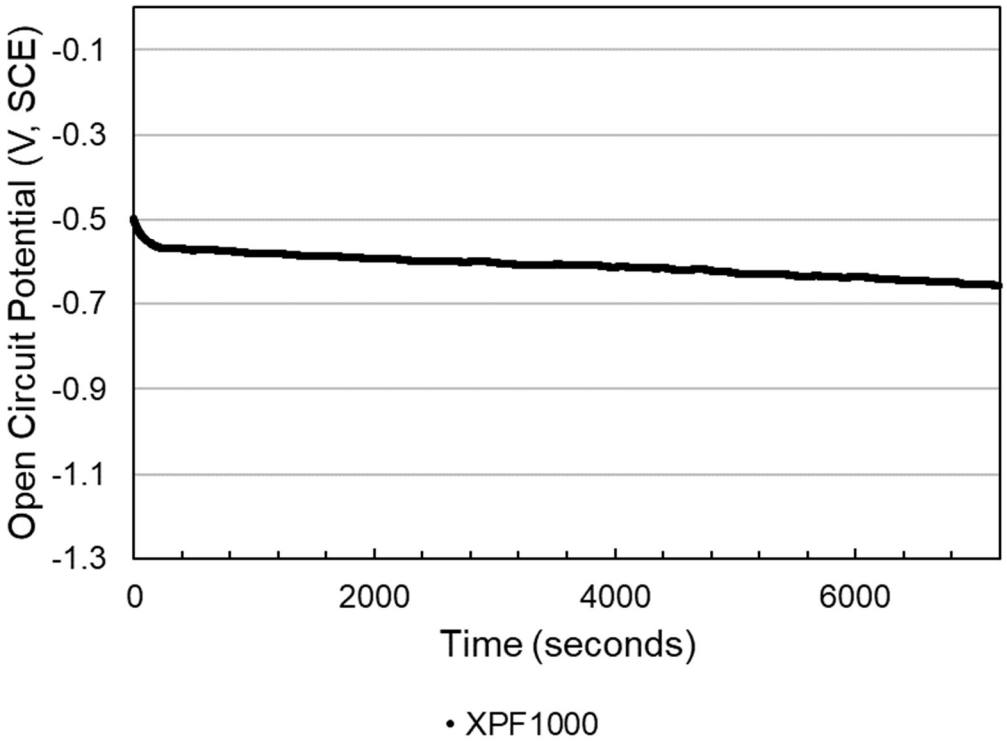

Figure 4.12 Open circuit potential versus time for XPF1000 in 3.5% NaCl solution.

Figure 4.13 demonstrates a typical cathodic potentiodynamic curve for XPF1000. As for all the products, below ~ -0.90 V (SCE) the ORR occurs, whereas above ~ -1.05 V (SCE) the HER becomes dominant. Average ß for XPF1000 was -158 mV.

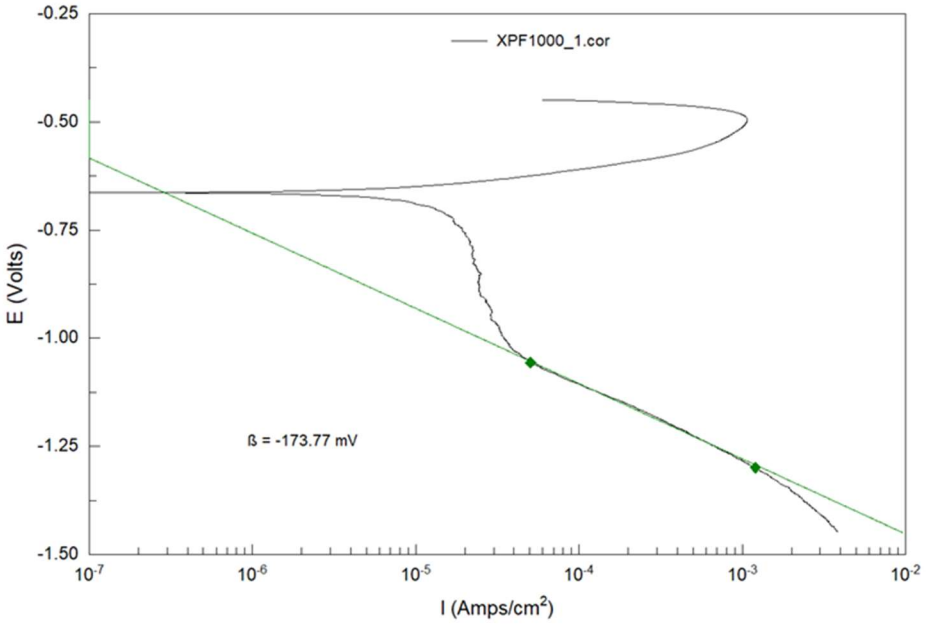

Figure 4.13 Typical cathodic potentiodynamic curve for XPF1000 in 3.5% NaCl.

4.2.1.5 22MnB5

Figure 4.14 shows the OCP curves in 3.5% NaCl solution for 22MnB5 in the un-heat-treated (UHT, solid line) and heat-treated (900C, dashed line) conditions. Little difference is observed between the conditions. During the first 20 minutes, the UHT sample saw a drop in potential to -0.608 V (SCE) at a rate of -5.83×10^{-5} V/s, whilst the 900C sample reached a potential of -0.618 V (SCE) at a rate of -6.05×10^{-5} V/s. After 2 hours the UHT sample was experiencing a drop in potential of -4.09×10^{-6} V/s and had reached a measured potential of -0.652 V (SCE), whereas the 900C sample saw a drop in potential at a rate of -5.62×10^{-7} V/s, reaching a measured potential of -0.643 V (SCE).

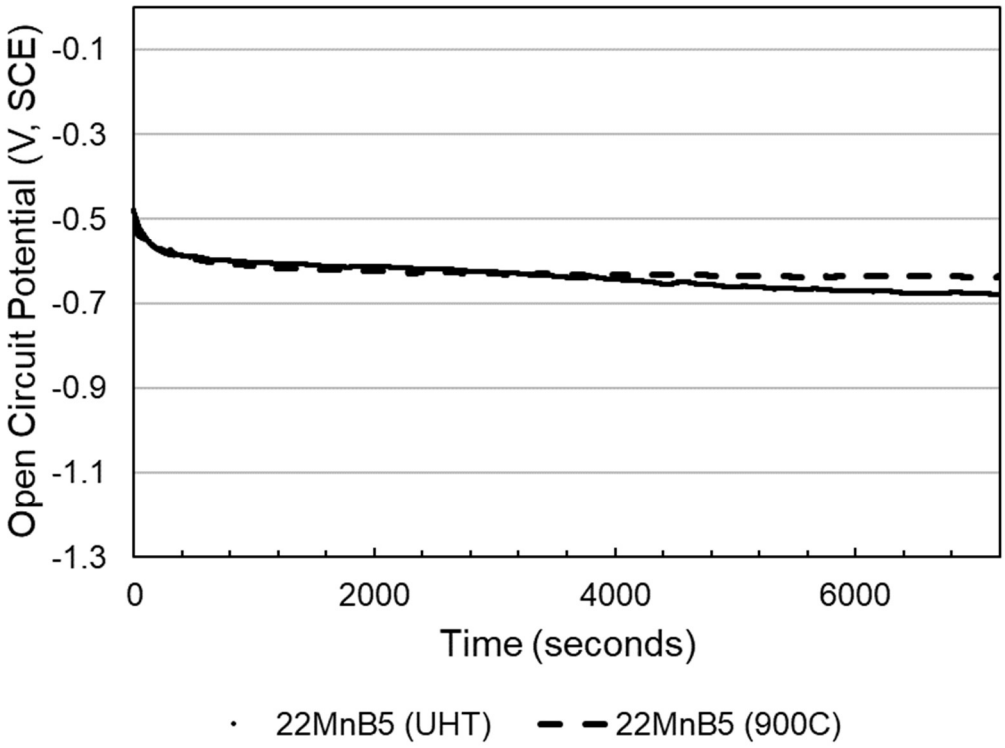

Figure 4.14 Open circuit potential versus time for 22MnB5 (UHT – solid line, 900C – dashed line) in 3.5% NaCl solution.

Figure 4.15 shows the cathodic potentiodynamic curve for 22MnB5 in the un-heat-treated condition, with average ß between -1.05 V and -1.20 V of -167 mV. Figure 4.16 shows the curve for 22MnB5 in the heat-treated condition (900C soak). Average ß for these samples was -163 mV.

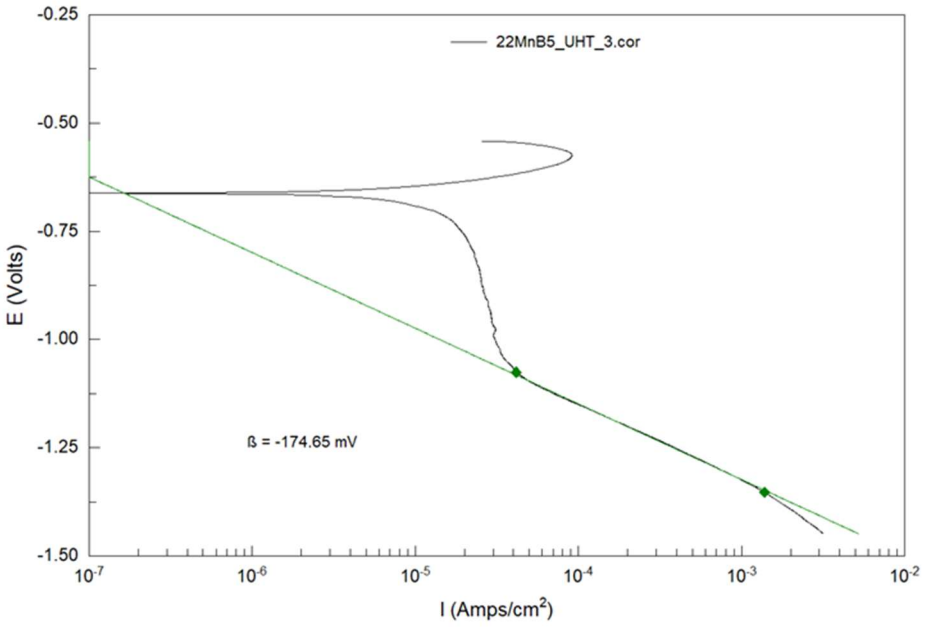

Figure 4.15 Typical cathodic potentiodynamic curve for 22MnB5 (UHT) in 3.5% NaCl.

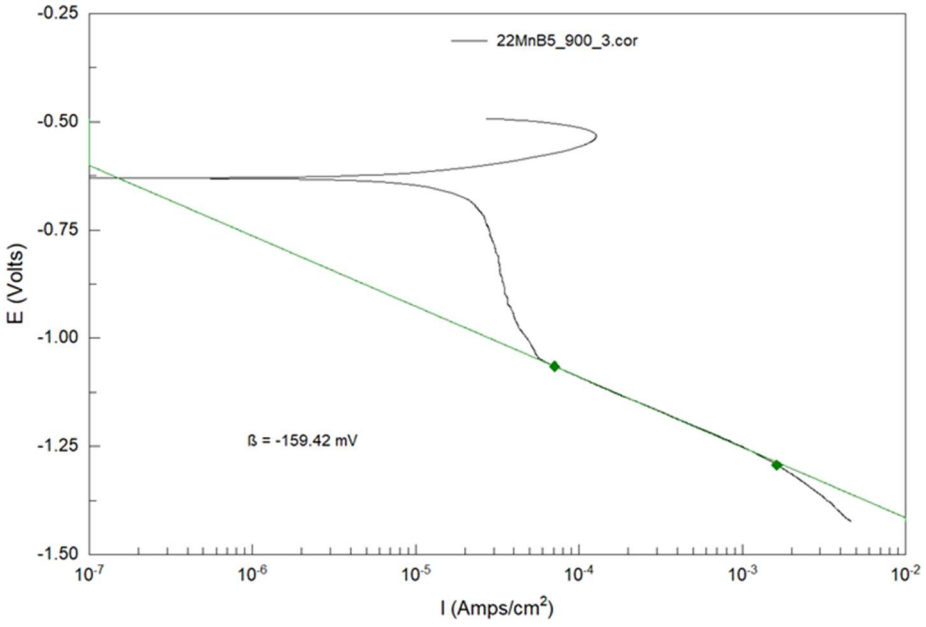

Figure 4.16 Typical cathodic potentiodynamic curve for 22MnB5 (900C) in 3.5% NaCl.

4.2.1.6 27MnB5+Nb

OCP curves for 27MnB5+Nb in the un-heat-treated (UHT, solid line) and heat-treated (900C, dashed line) conditions are displayed in Figure 4.17. During the first 20 minutes, the UHT sample saw the potential decrease by an average of -4.23×10^{-5} V/s to reach -0.619 V (SCE), whilst the 900C sample's potential decreased by an average of -3.90×10^{-5} V/s and reached -0.575 V (SCE). After 2 hours the UHT sample's rate of decrease in potential had reduced to -4.35×10^{-6} V/s, with a measured potential of -0.662 V (SCE), whereas the decrease in potential for the 900C sample was -2.15×10^{-6} V/s with a measured potential of -0.647 V (SCE) after 2 hours.

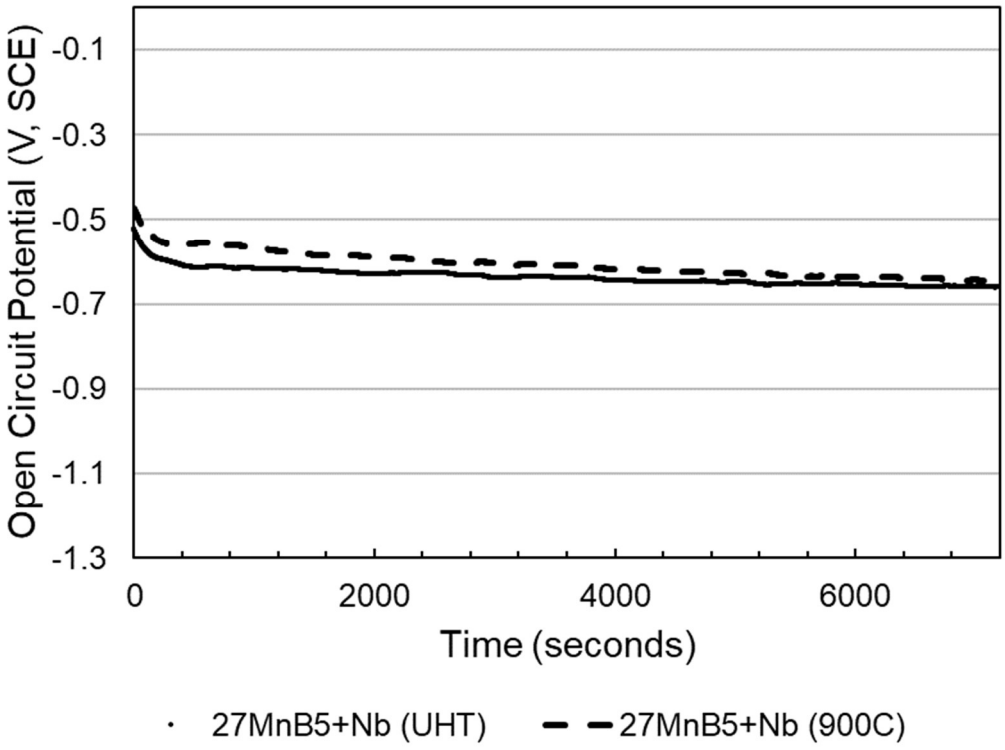

Figure 4.17 Open circuit potential versus time for 27MnB5+Nb (UHT – solid line, 900C – dashed line) in 3.5% NaCl solution.

Typical cathodic potentiodynamic curves are shown for 27MnB5+Nb in the un-heat-treated (UHT) in Figure 4.18, and the heat-treated (900C) condition in Figure 4.19. Both show the transition between presence of the ORR and dominance of HER at around -0.90 V to -1.00 V seen for all of the other products shown so far. For the UHT samples, average ß was -159 mV. For the 900C samples, average ß was also -159 mV.

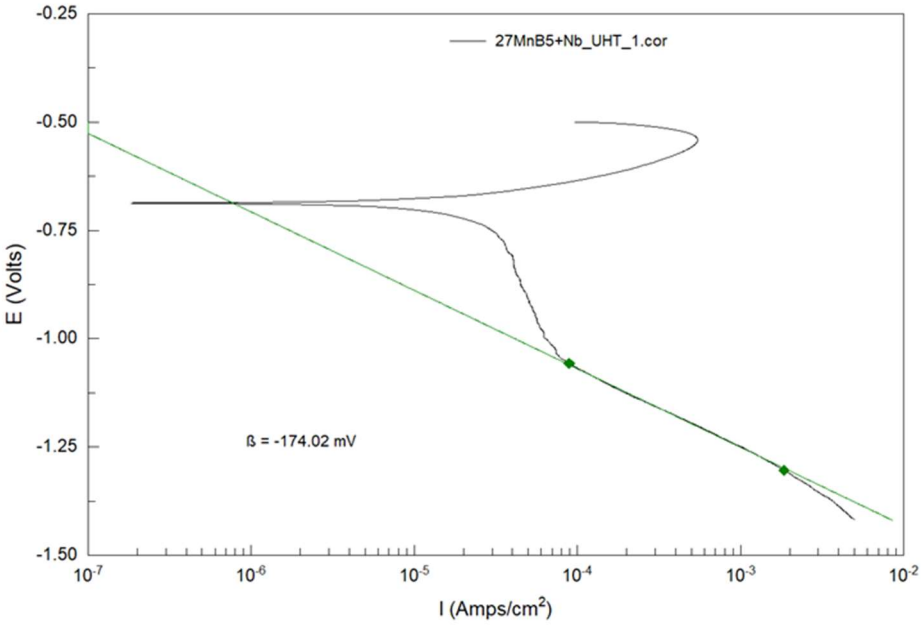

Figure 4.18 Typical cathodic potentiodynamic curve for 27MnB5+Nb (UHT) in 3.5% NaCl.

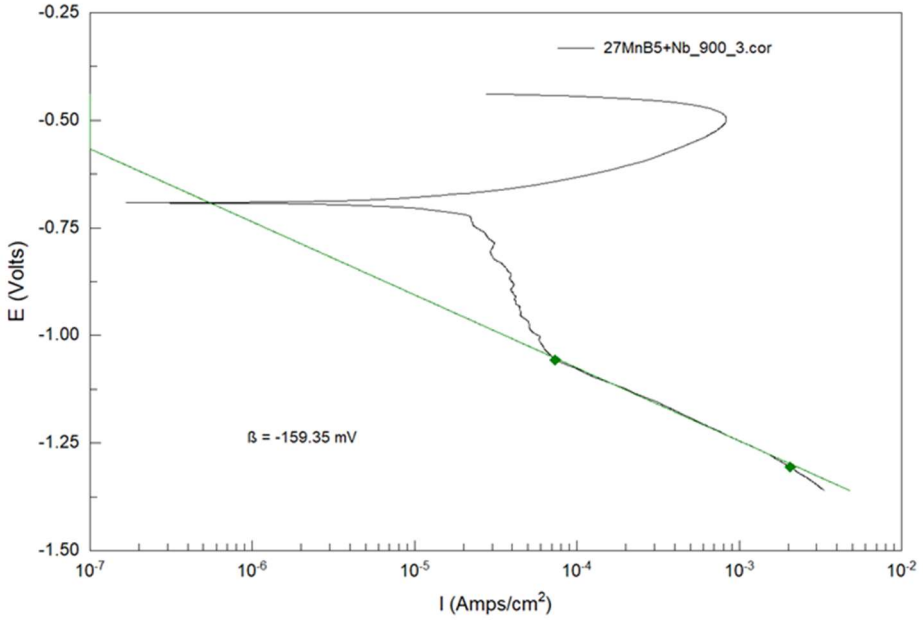

Figure 4.19 Typical cathodic potentiodynamic curve for 27MnB5+Nb (900C) in 3.5% NaCl.

4.2.1.7 Hot-dip galvanised (DX51D formable steel substrate)

The work characterising the corrosion behaviour of the studied steels is done with consideration of how this compares with the corrosion characteristics of coatings that are commonly utilised on steel automotive structures. Overwhelmingly, the most-utilised coating for this application is hot-dip galvanised (HDG) zinc coating, or 'GI' coating. The OCP versus time curve for a HDG coated mild steel sample (DX51D product) is shown below in Figure 4.20.

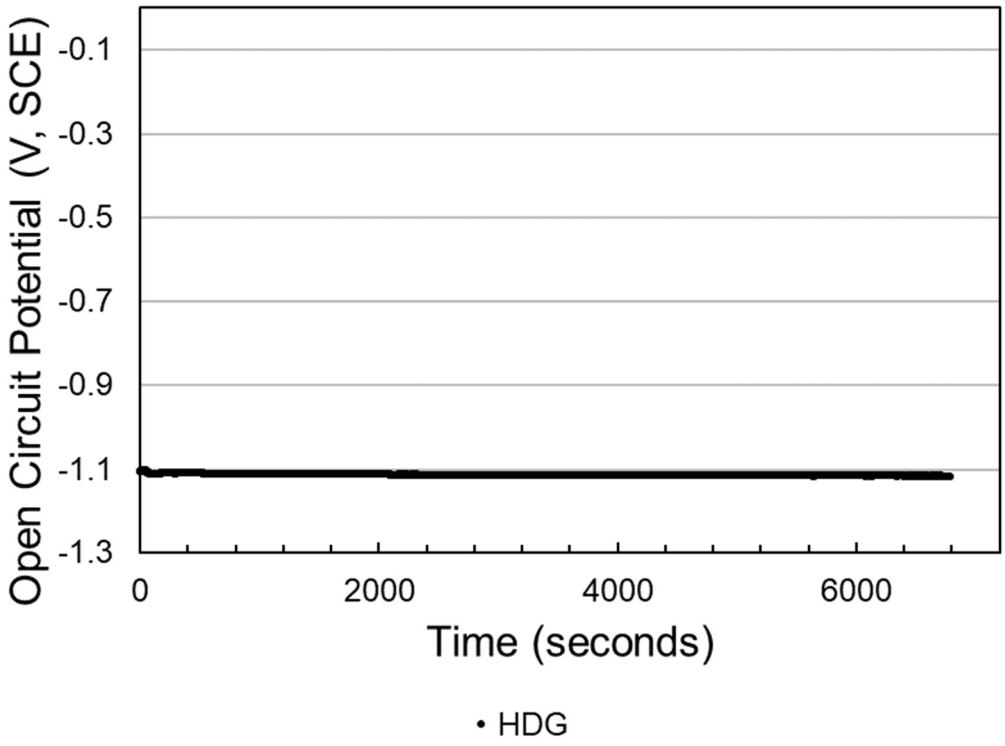

Figure 4.20 Open circuit potential versus time for hot-dipped galvanised zinc coating in 3.5% NaCl solution.

In the first 20 minutes of immersion, the potential decreases by -3.76×10^{-6} V/s, reaching a measured OCP of -1.113 V (SCE). This does not change very much up until 2 hours of immersion, reaching a measured potential of -1.117 V (SCE), with a change in rate of decrease to -4.68×10^{-7} V/s.

4.2.2 Damaged coating corrosion characteristics

To determine the effects of a damaged (in this case 'partially ground away') coating upon the corrosion characteristics of an automotive part, half-hourly scans were performed using a scanning vibrating electrode technique (SVET) to measure the local normalised current densities (J_z) across the surface of a steel sample with a damaged hot-dipped galvanised zinc coating in a neutral buffered 0.1 M NaCl solution over the course of 24 hours. Figure 4.22, shows a selection of contour plots of scans taken every 2 hours (i.e. every fourth scan), demonstrating regions of cathodic (blue) and anodic (red) activity upon the sample surface, and how this progresses as corrosion processes proceed.

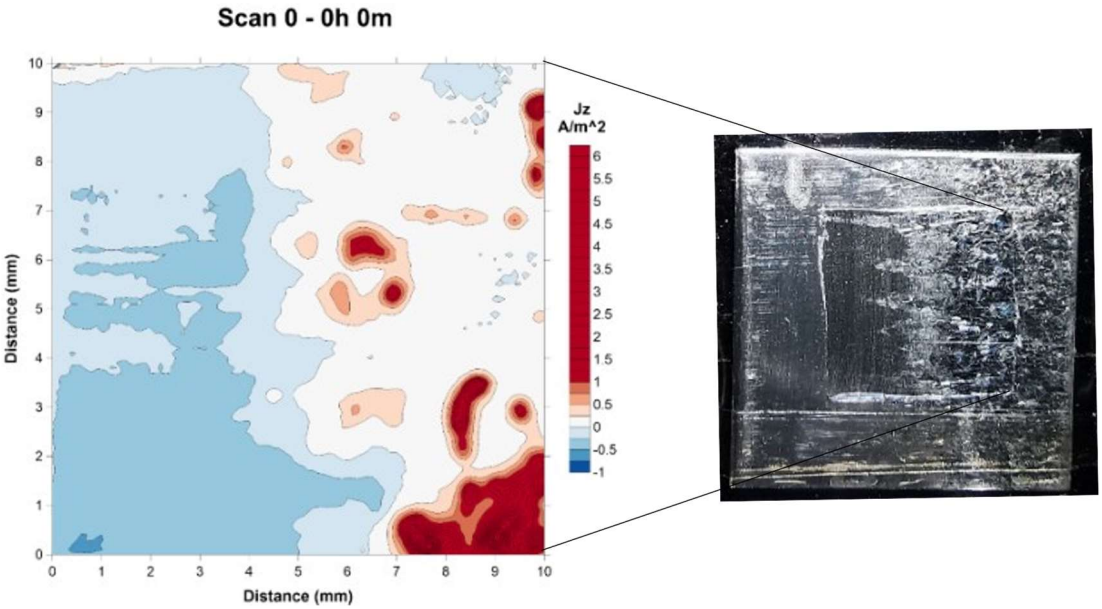

Figure 4.21 SVET contour plot of a galvanised steel sample with coating partially ground away to expose substrate, with corresponding optical image of the prepared specimen prior to submersion to illustrate correspondence between SVET measurements and surface condition. Displayed contour plot shows scan at time = 0s (i.e. the first scan). Contour lines every ±0.25 A/m^2 current density.

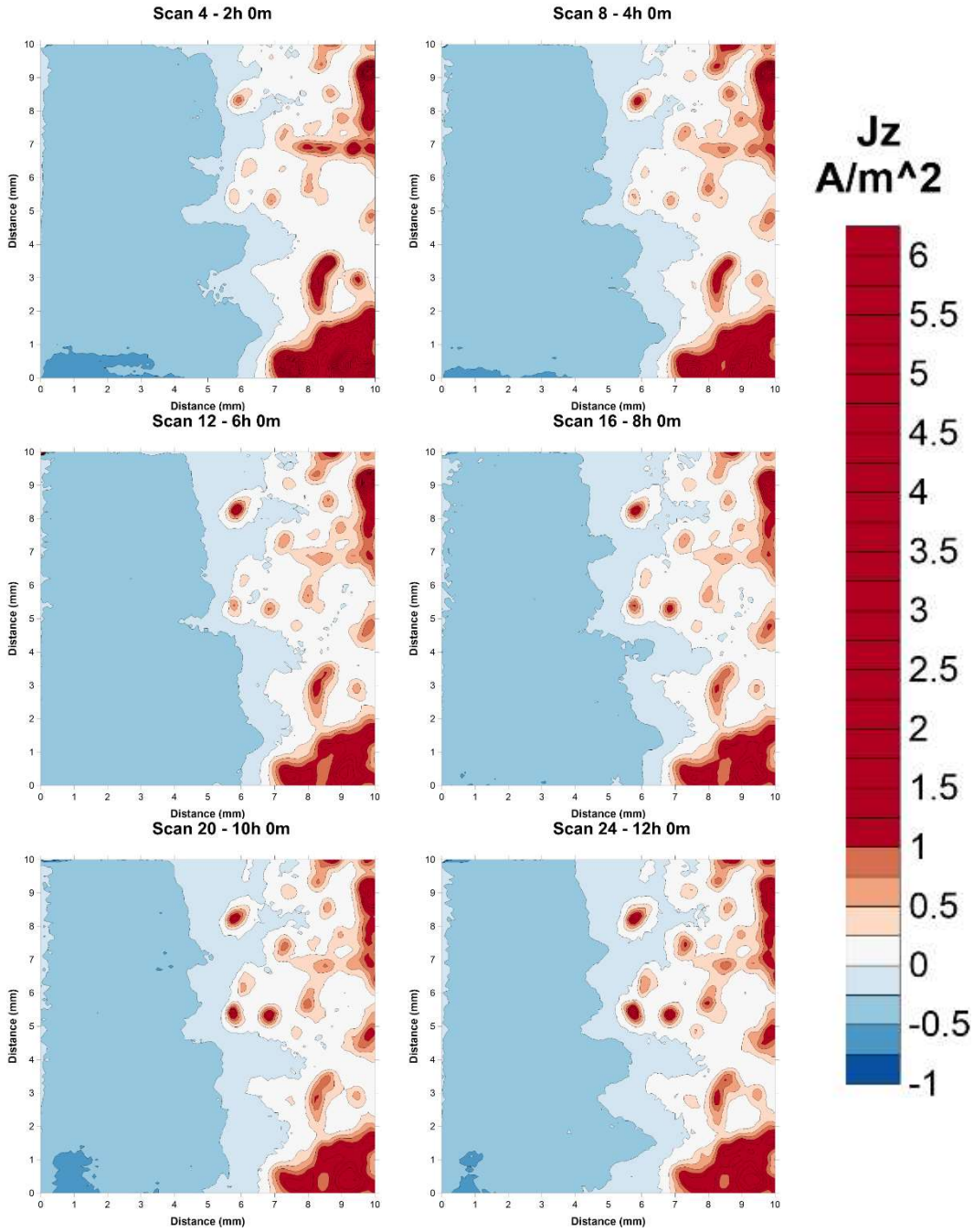

Figure 4.22 SVET contour plots of a galvanised steel sample with coating partially ground away to expose substrate. Displayed images show scans 2 hours apart from 2 hours – 12 hours into the experiment.

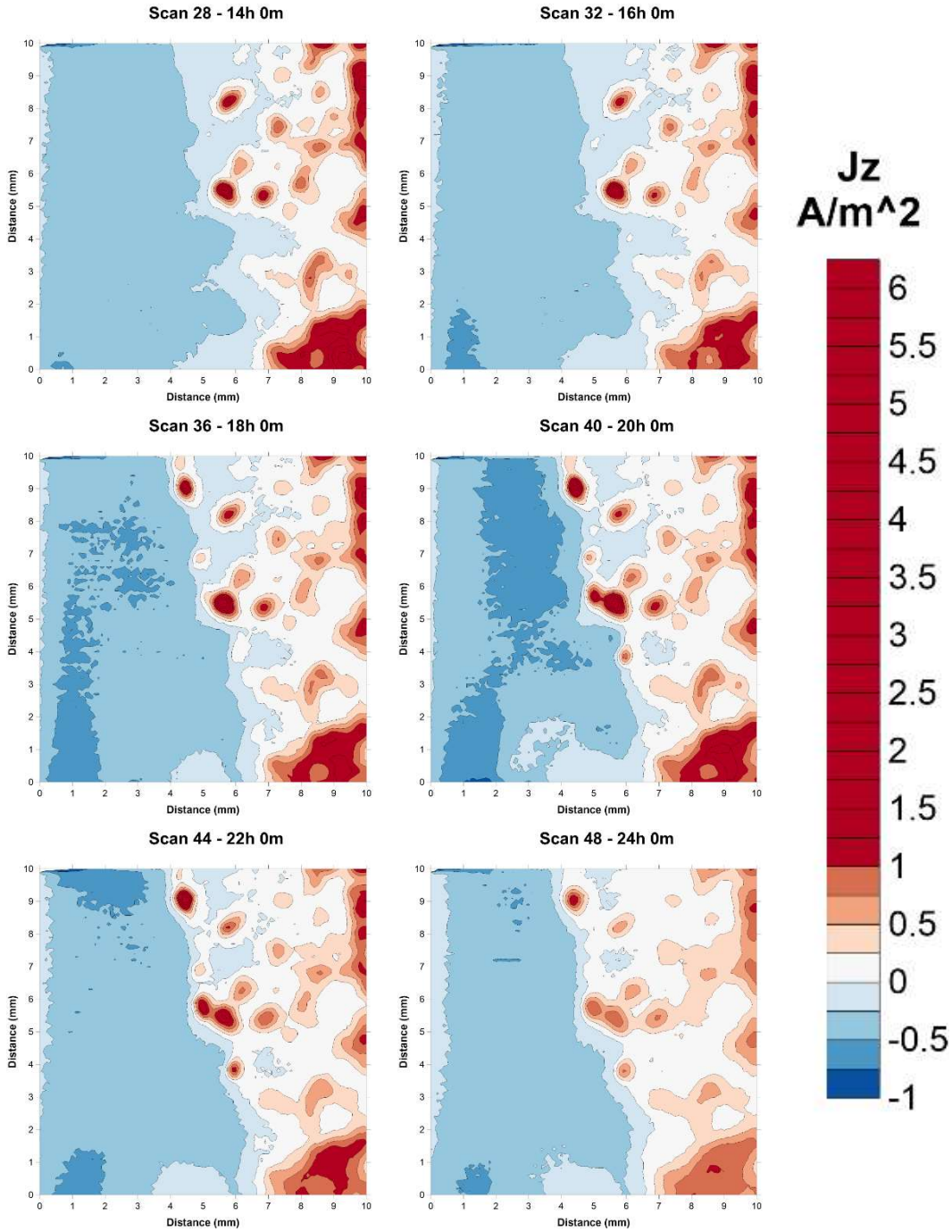

Figure 4.23 SVET contour plots of a galvanised steel sample with coating partially ground away to expose substrate. Displayed images show scans 2 hours apart from 14 hours – 24 hours into the experiment.

Figure 4.21 shows how early on, even in the relatively weak 0.1 M NaCl solution, regions of intense and acutely localised anodic activity (current density up to +6.01 A/m^2) occurs in the coated region as soon as the corrosive electrolyte is introduced. As a balance to this, a wide region of relatively consistent cathodic current densities is shown for the exposed substrate, with a maximum cathodic current density of -0.53

A/m^2. This current density is indicative of cathodic polarisation at the steel surface such that a substantial evolution of hydrogen may be expected, albeit in competition with a diffusion-limited oxygen reduction reaction, as found by Akiyama and Li [171].

As the surface reactions proceed, the anodic regions begin to become more widespread, but with a lower intensity. Conversely, cathodic regions now periodically develop some localised regions of increased cathodic current density, particularly after about 15 hours, peaking around 20 hours. After 24 hours, both anodic and cathodic activity had reduced intensity from peak current densities in these localised, previously high-intensity regions.

4.2.3 Changes in local pH during crevice corrosion

As shown in the Pourbaix diagram in Figure 2.21., a decrease in pH of an electrolyte during corrosion of steels (or iron) makes occurrence of a hydrogen evolution reaction more favourable, i.e. it becomes more prominent at smaller overpotentials. Conditions during crevice corrosion may therefore accelerate hydrogen entry into steels, as found by Liu [73]. The following results attempt to visualise the magnitude and progression of the changes in pH during crevice corrosion.

Figure 4.24 shows photographs taken every 5 minutes during the first half hour of corrosion on an XPF800 sample ground to 1200-grit surface finish, in simulated crevice corrosion conditions, as described in Chapter 3.2.5 (0.1 M NaCl + Unisol 113 universal pH indicator).

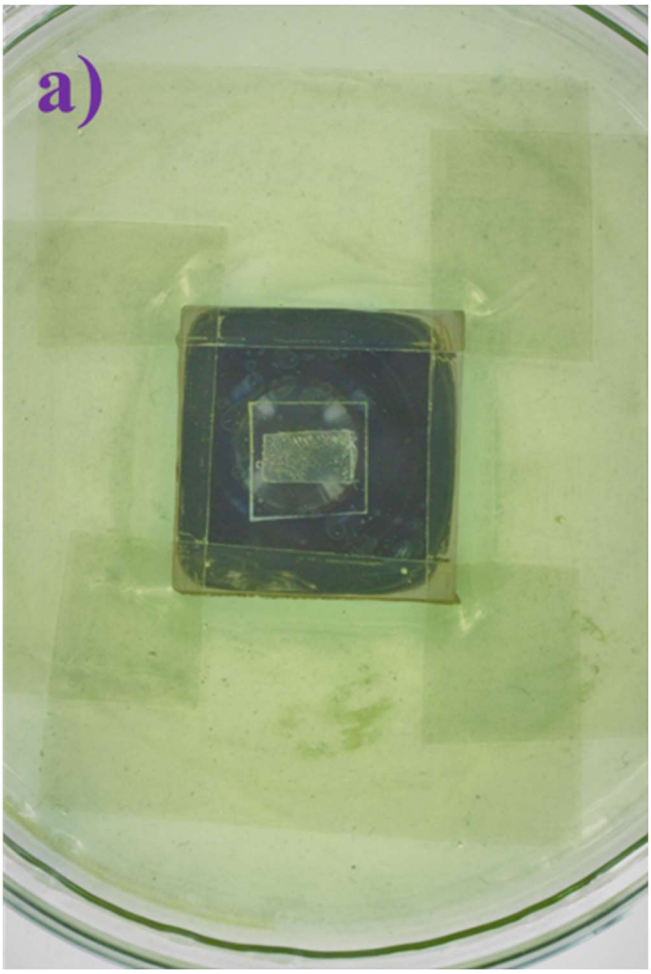

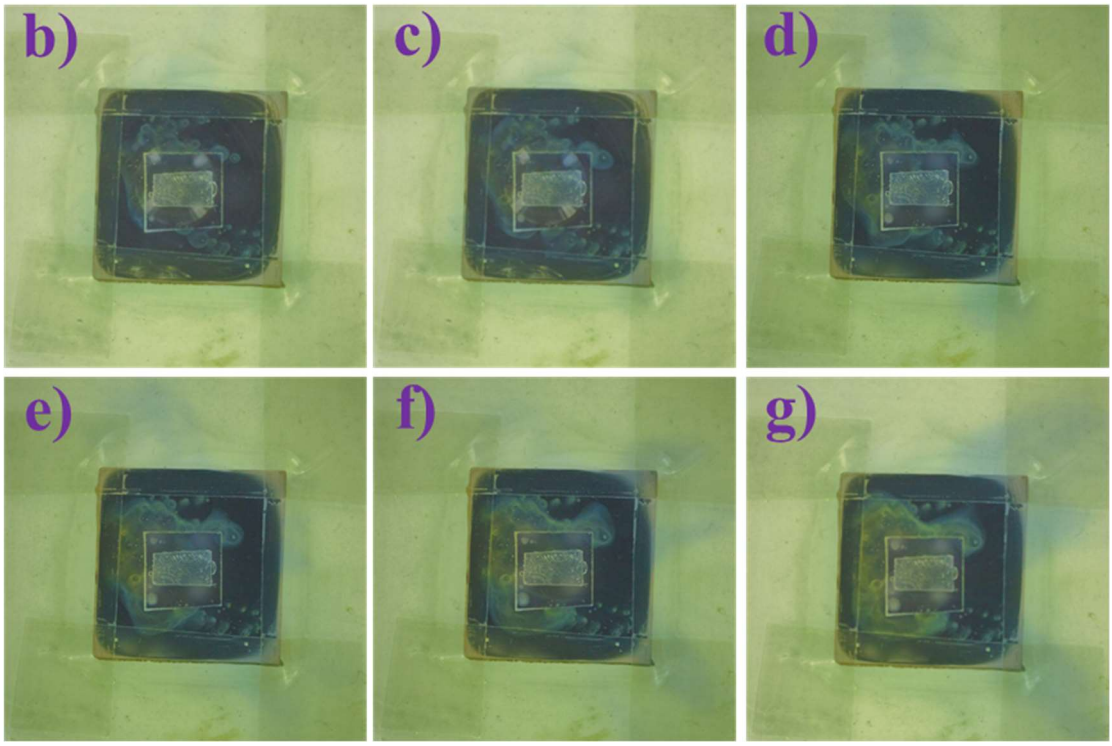

Figure 4.24 Time-lapse images taken at 5-minute intervals during simulated crevice corrosion. a) t=0 min.; b) t=5 min. →g) t=30 min.

It can be seen from Figure 4.24b) that changes in local pH occur almost immediately after immersion, with clear evidence of a rapidly increasing pH adjacent to the simulated crevice, particularly to the left-hand side, where there are regions with estimated pH $\geq$ 11. This is indicative of the production of hydroxyl ions, OH^-, at these locations. There is also some evidence of pitting corrosion occurring away from the crevice towards the bottom-right corner of the exposed area of the sample.

After 20 minutes' immersion, Figure 4.24e), the pH increase adjacent to the crevice has become extensive, with evidence also becoming apparent of the decrease in pH at the location of the crevice, with some increase in the amount of orange and red visible beneath the glass slide at the left hand side (although it remains difficult to quantify). After half an hour, Figure 4.24g), the visibility of red shades is becoming increasingly apparent, but the regions of high pH adjacent to the crevice now appear less intense. Furthermore, it appears that some drift of corrosion product from within the crevice is now modifying the pH in these cathodic regions (or adding 'noise' to the image).

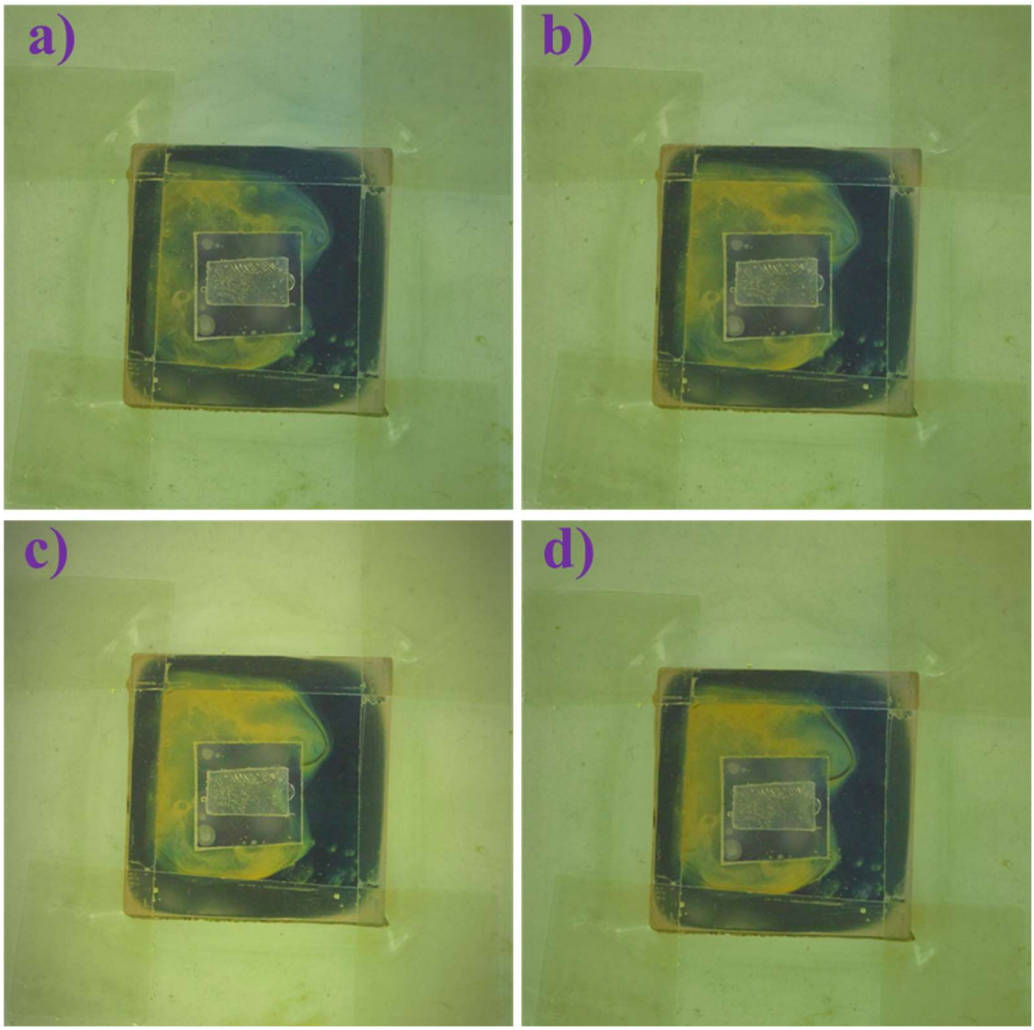

Figure 4.25 Time-lapse images taken at 20-minute intervals during simulated crevice corrosion. a) t=50 min. →d) t=110 min.

As corrosion proceeds, the pH within the crevice appears to become increasingly low, though remains difficult to quantify without high magnification, though certainly some regions in the crevice, particularly along its left edge, appear to be as low as pH 1. The regions of high pH adjacent to the crevice also now appear more difficult to quantify due to in-flow of corrosion product, and associated low-pH electrolyte from within the crevice, giving the appearance in this region that was previously pH $\geq$ 11, that pH is now around 4. The amount of pitting that was apparent at the beginning of the experiment is also either reduced or obscured by corrosion product from inside the crevice.

4.3 Hydrogen Diffusion

This section has been divided in to 3 parts. The first part shows the permeation curves and associated output parameters from the hydrogen permeation tests as described in Chapter 3.3.1 for each of the tested steels at a nominal membrane thickness of 0.8 mm and consistent charging potential. The second shows results from permeation tests undertaken at different charging potentials. Finally, the results of permeation tests undertaken at a constant charging potential with membranes of different thickness are shown.

4.3.1 Hydrogen Permeation Tests – Effect of Microstructure

4.3.1.1 DP800

Results from hydrogen permeation tests undertaken on a DP800 membrane of 0.8 mm thickness, with charging potential of -1050 mV versus a saturated calomel reference electrode (SCE) are shown below in Figure 4.26.

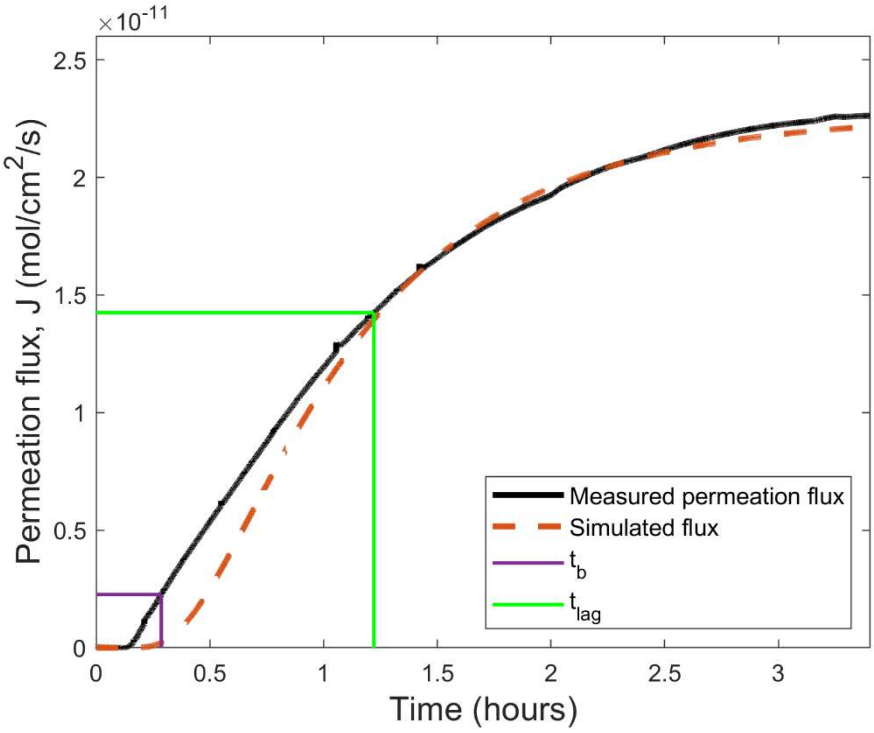

Figure 4.26 Hydrogen permeation flux (black line) for DP800 membrane with 0.8 mm nominal thickness, charged at -1050 mV (SCE) in 3.5% NaCl + 3 g/L NH_4SCN. Dashed orange line is curve simulated using Fick's 2nd law with input parameters calculated from experimental curve.

In this experimental setup, DP800 had a breakthrough time, t_b, of 1,033 seconds, a lag time, $t_{lag,}$, of 4,397 seconds, a maximum flux, J_∞, of 2.26×10^{-11} mol/cm^2/s, effective diffusion coefficient, D_{eff}, of 1.87×10^{-7} cm^2/s, and a maximum concentration at the charging surface, C_0, of 8.51×10^{-6} mol/cm^2. Simulated curve shows a longer 'breakthrough' time than seen experimentally, indicated by the extended 'flat' portion of the curve at the beginning of the test in comparison to the experimental curve. This divergence is discussed in the context of reversible/irreversible trapping phenomenon in Chapter 5.2.3.

4.3.1.2 XPF800

Results from hydrogen permeation tests undertaken on a XPF800 membrane of 0.8 mm thickness, with charging potential of -1050 mV versus SCE are shown below in Figure 4.27.

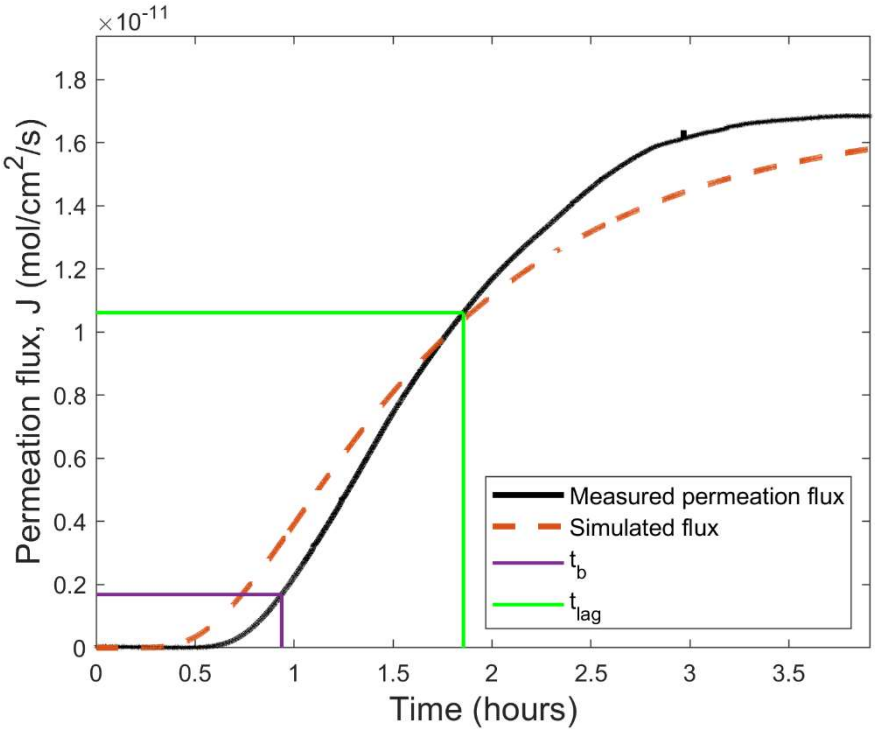

Figure 4.27 Hydrogen permeation flux (black line) for XPF800 membrane with 0.8 mm nominal thickness, charged at -1050 mV (SCE) in 3.5% NaCl + 3 g/L NH_4SCN. Dashed orange line is curve simulated using Fick's 2nd law with input parameters calculated from experimental curve.

In this experimental setup, XPF800 had t_b of 3,373 seconds, a t_{lag} of 6,682 seconds, J_∞ of 1.68×10^{-11} mol/cm^2/s, D_{eff} of 1.68×10^{-7} cm^2/s, and C_0 of 8.21×10^{-6} mol/cm^2.

4.3.1.3 DP1000

Results from hydrogen permeation tests undertaken on a DP1000 membrane of 0.8 mm thickness, with charging potential of -1050 mV versus SCE are shown below in Figure 4.28.

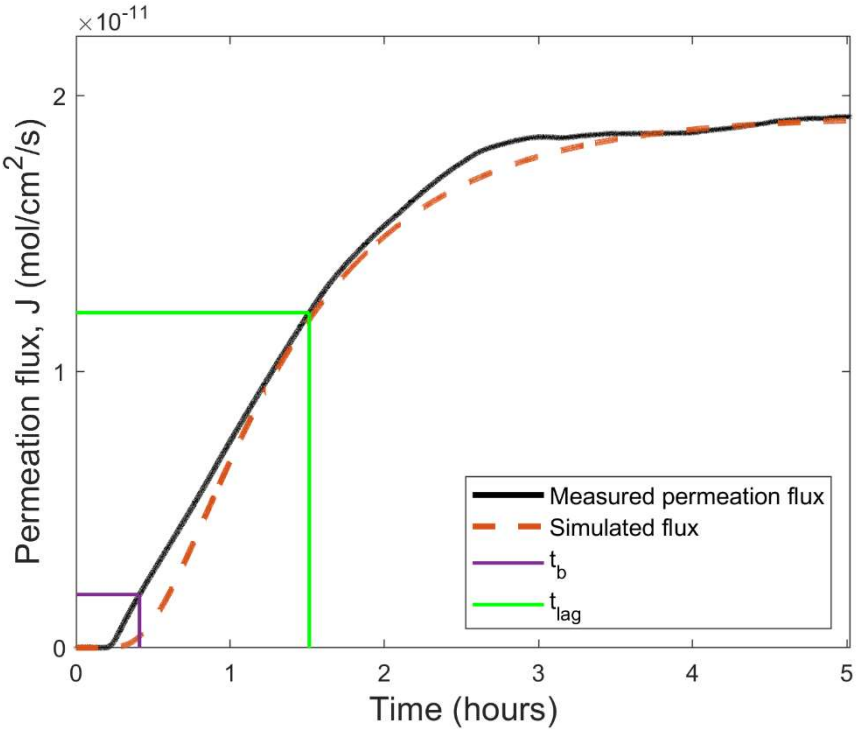

Figure 4.28 Hydrogen permeation flux (black line) for DP1000 membrane with 0.8 mm nominal thickness, charged at -1050 mV (SCE) in 3.5% NaCl + 3 g/L NH_4SCN. Dashed orange line is curve simulated using Fick's 2nd law with input parameters calculated from experimental curve.

In this experimental setup, DP1000 had t_b of 1,481 seconds, a t_{lag} of 5,445 seconds, J_∞ of 1.93×10^{-11} mol/cm^2/s, D_{eff} of 1.45×10^{-7} cm^2/s, and C_0 of 9.14×10^{-6} mol/cm^2.

4.3.1.4 XPF1000

Results from hydrogen permeation tests undertaken on a XPF1000 membrane of 0.8 mm thickness, with charging potential of -1050 mV versus SCE are shown below in Figure 4.29.

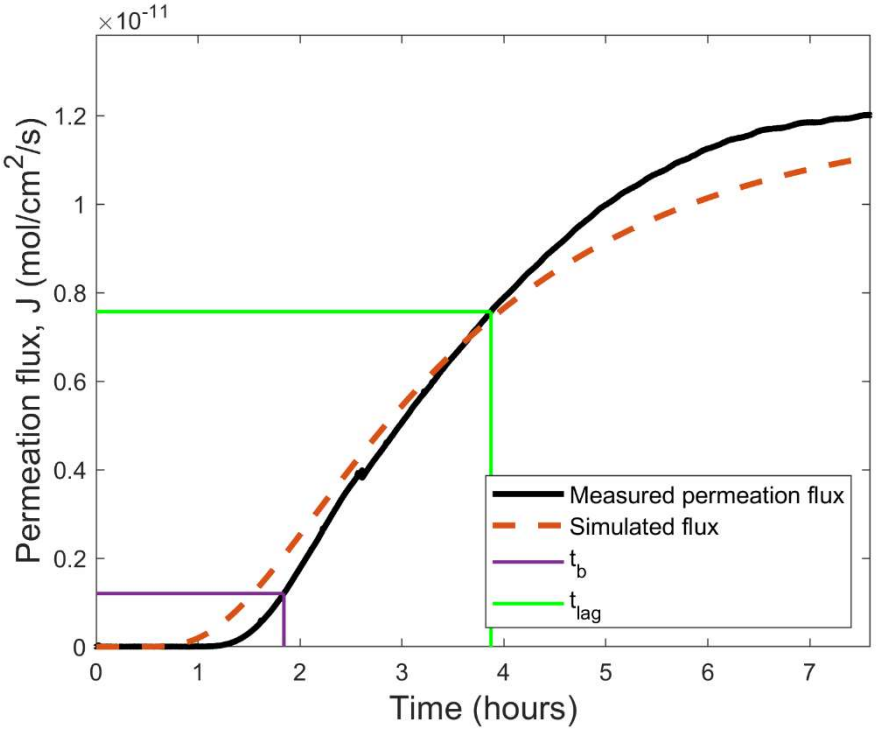

Figure 4.29 Hydrogen permeation flux (black line) for XPF1000 membrane with 0.8 mm nominal thickness, charged at -1050 mV (SCE) in 3.5% NaCl + 3 g/L NH_4SCN. Dashed orange line is curve simulated using Fick's 2nd law with input parameters calculated from experimental curve.

In this experimental setup, XPF1000 had t_b of 6,628 seconds, a t_{lag} of 13,944 seconds, J_∞ of 1.20×10^{-11} mol/cm^2/s, D_{eff} of 7.45×10^{-8} cm^2/s, and C_0 of 1.54×10^{-5} mol/cm^2.

4.3.1.5 22MnB5 – un-heat-treated (UHT)

Results from hydrogen permeation tests undertaken on a 22MnB5 membrane in the un-heat-treated condition (UHT) of 0.8 mm thickness, with charging potential of -1050 mV versus SCE are shown below in Figure 4.30.

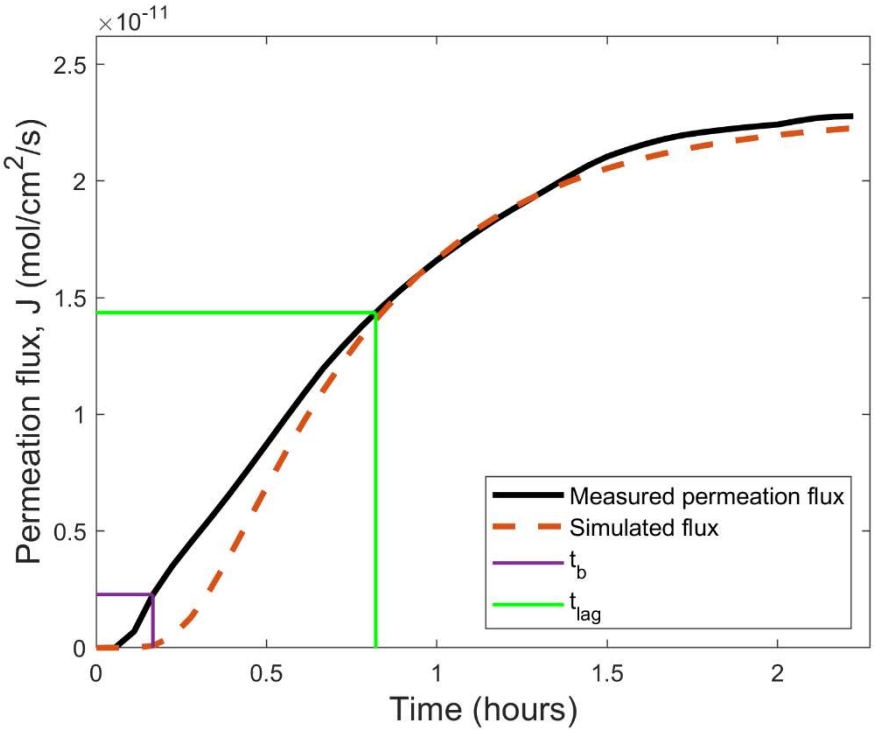

Figure 4.30 Hydrogen permeation flux (black line) for 22MnB5 (UHT) membrane with 0.8 mm nominal thickness, charged at -1050 mV (SCE) in 3.5% NaCl + 3 g/L NH_4SCN. Dashed orange line is curve simulated using Fick's 2nd law with input parameters calculated from experimental curve.

In this experimental setup, 22MnB5 (UHT) had t_b of 1,126 seconds, a t_{lag} of 5,544 seconds, J_∞ of 2.28×10^{-11} mol/cm^2/s, D_{eff} of 1.70×10^{-7} cm^2/s, and C_0 of 1.01×10^{-5} mol/cm^2.

4.3.1.6 22MnB5 – heat-treated (900° C soak temperature)

Results from hydrogen permeation tests undertaken on a 22MnB5 membrane in the heat-treated condition (900C) of 0.8 mm thickness, with charging potential of -1050 mV versus SCE are shown below in Figure 4.31.

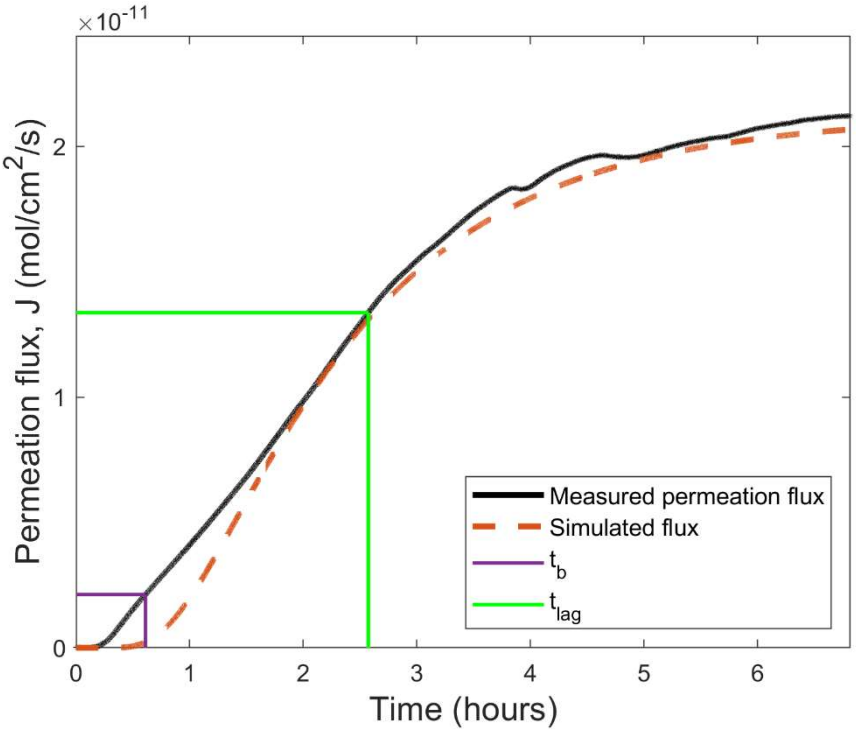

Figure 4.31 Hydrogen permeation flux (black line) for 22MnB5 (900C) membrane with 0.8 mm nominal thickness, charged at -1050 mV (SCE) in 3.5% NaCl + 3 g/L NH_4SCN. Dashed orange line is curve simulated using Fick's 2nd law with input parameters calculated from experimental curve.

In this experimental setup, 22MnB5 (900C) had t_b of 2,196 seconds, a t_{lag} of 9,261 seconds, J_∞ of 2.12×10^{-11} mol/cm^2/s, D_{eff} of 9.81×10^{-8} cm^2/s, and C_0 of 1.60×10^{-5} mol/cm^2.

4.3.1.7 27MnB5+Nb – un-heat-treated (UHT)

Results from hydrogen permeation tests undertaken on a 27MnB5+Nb membrane in the un-heat-treated condition (UHT) of 0.8 mm thickness, with charging potential of -1050 mV versus SCE are shown below in Figure 4.32

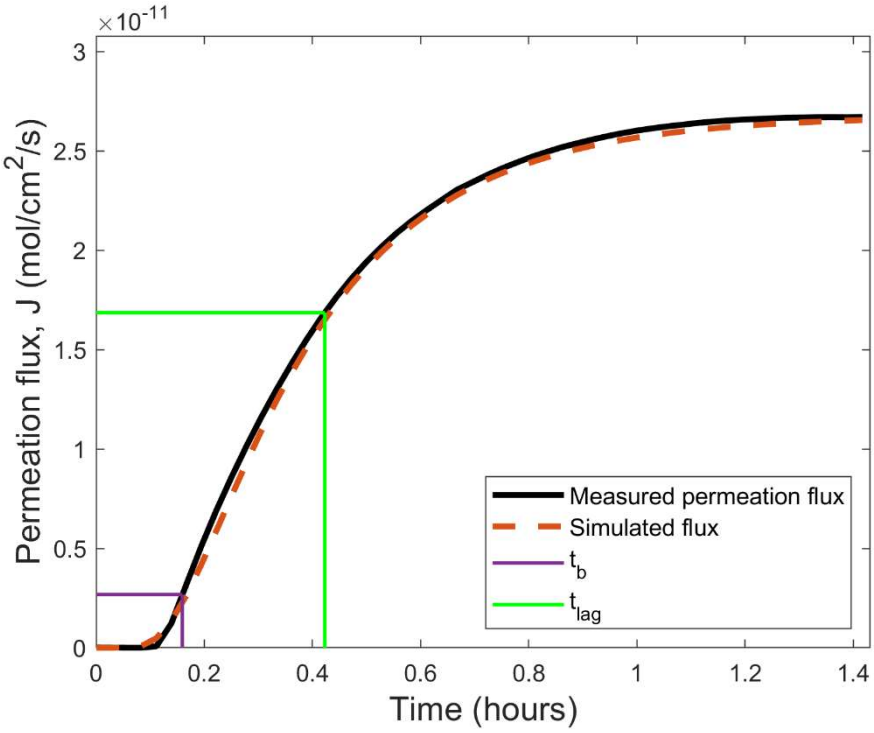

Figure 4.32 Hydrogen permeation flux (black line) for 27MnB5+Nb (UHT) membrane with 0.8 mm nominal thickness, charged at -1050 mV (SCE) in 3.5% NaCl + 3 g/L NH_4SCN. Dashed orange line is curve simulated using Fick's 2nd law with input parameters calculated from experimental curve.

In this experimental setup, 27MnB5+Nb (UHT) had t_b of 574 seconds, a t_{lag} of 1,522 seconds, J_∞ of 2.68×10^{-11} mol/cm^2/s, D_{eff} of 5.45×10^{-7} cm^2/s, and C_0 of 3.46×10^{-6} mol/cm^2.

4.3.1.8 27MnB5+Nb – heat-treated (900° C soak temperature)

Results from hydrogen permeation tests undertaken on a 27MnB5+Nb membrane in the heat-treated condition (900C) of 0.8 mm thickness, with charging potential of -1050 mV versus SCE are shown below in Figure 4.33.

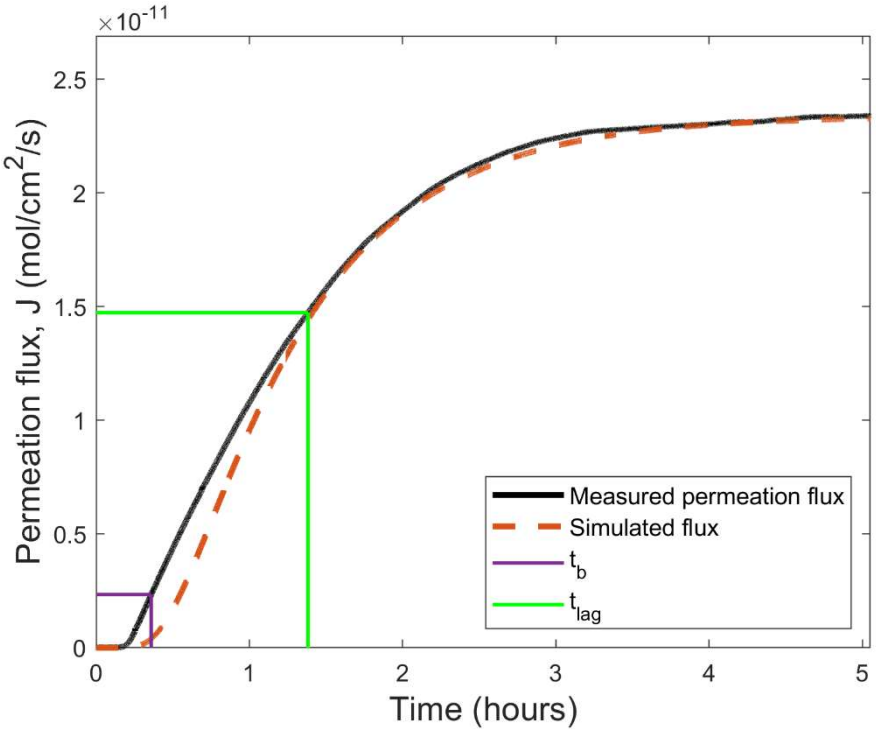

Figure 4.33 Hydrogen permeation flux (black line) for 27MnB5+Nb (900C) membrane with 0.8 mm nominal thickness, charged at -1050 mV (SCE) in 3.5% NaCl + 3 g/L NH_4SCN. Dashed orange line is curve simulated using Fick's 2nd law with input parameters calculated from experimental curve.

In this experimental setup, 27MnB5+Nb (900C) had t_b of 1,294 seconds, a t_{lag} of 4,976 seconds, J_∞ of 2.34×10^{-11} mol/cm^2/s, D_{eff} of 2.03×10^{-7} cm^2/s, and C_0 of 8.96×10^{-6} mol/cm^2.

4.3.2 Hydrogen Permeation Tests – Effect of Charging Potential

Results from hydrogen permeation tests undertaken on a 22MnB5 membranes in the heat-treated condition (900C) of 1.2 mm thickness, with charging potentials of -850 mV, -950 mV, and -1050 mV versus SCE, respectively are shown below in Figure 4.34 and output values summarised in Table 4-3. These tests were undertaken to determine whether differing charging surface concentrations have an effect upon hydrogen transport characteristics, and if so, what these effects may be.

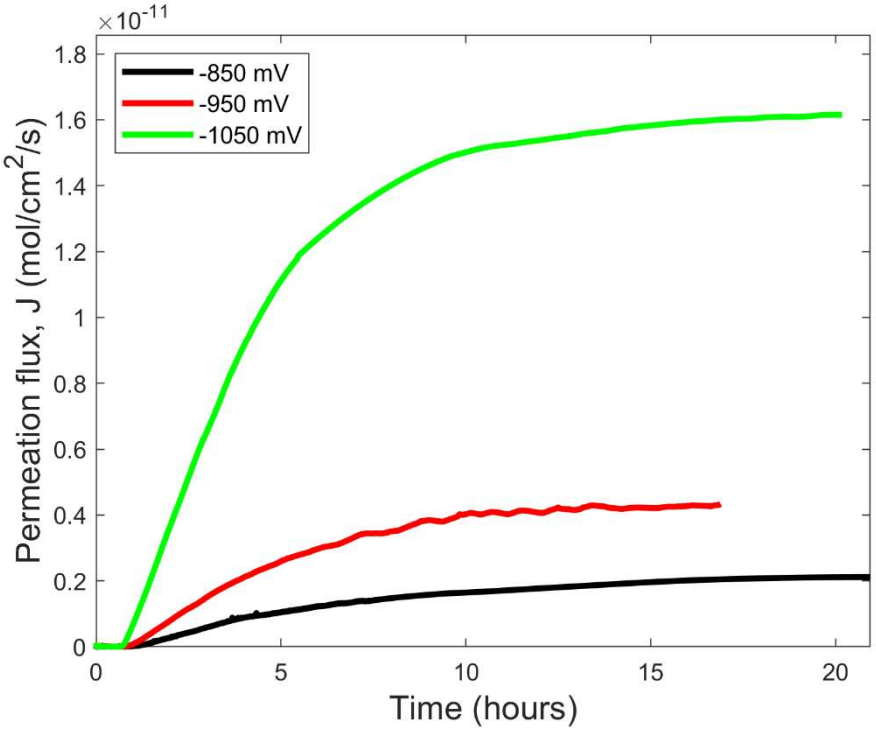

Figure 4.34 Hydrogen permeation curves for 22MnB5 (900C) membranes with 1.2 mm nominal thickness, charged at -850 mV (black line), -950 mV (red line) and -1050 mV (green line) (SCE) in 3.5% NaCl + 3g/L NH_4SCN.

Table 4-3 Summary of output parameters calculated from hydrogen permeation tests on 22MnB5 (900C) of nominal membrane thickness 1.2 mm, with increasing charging potential in 3.5% NaCl + 3g/L NH_4SCN electrolyte.

Charging potential (mV SCE)	t_b (seconds)	t_{lag} (seconds)	J_∞ (mol/cm^2/s)	D_{eff} (cm^2/s)	C_0 (mol/cm^2)
-850	6,337	24,367	2.11×10^{-12}	1.05×10^{-7}	2.50×10^{-6}
-950	5,577	20,529	4.52×10^{-12}	1.18×10^{-7}	4.61×10^{-6}
-1050	4,790	16,156	1.62×10^{-11}	1.54×10^{-7}	1.28×10^{-5}

4.3.3 Hydrogen Permeation Tests – Effect of Membrane Thickness

Hydrogen permeation curves for tests undertaken on membranes of DP800 material at *nominal* thicknesses of 0.1 mm (true thickness for both dual-phase '0.1 mm' membranes was higher upon receipt after thickness reduction), 0.8 mm, and 1.5 mm, with a common charging potential of -1050 mV (SCE) in 3.5% NaCl + 3g/L NH_4SCN, are shown in Figure 4.35, below.

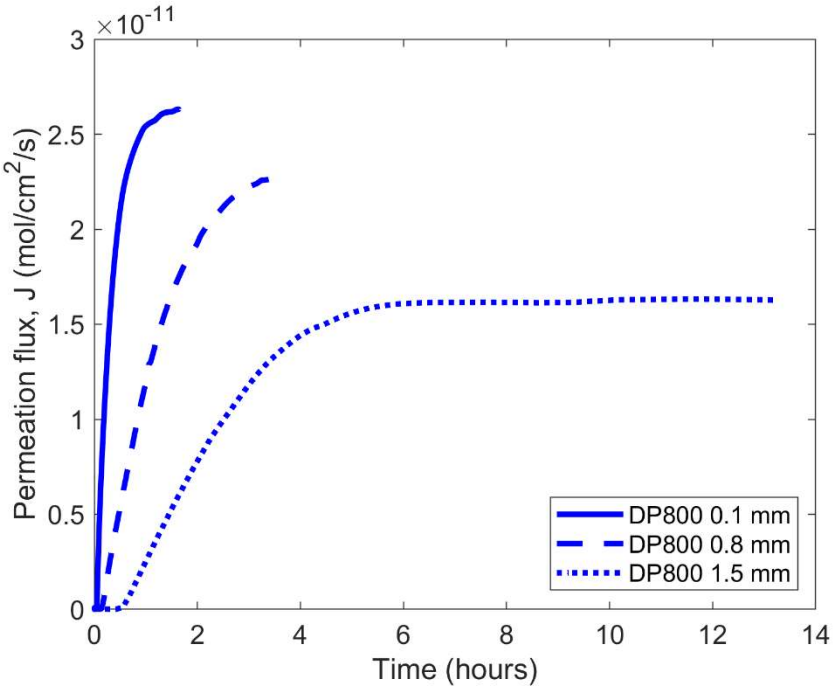

Figure 4.35 Hydrogen permeation curves for DP800 membranes of 0.1 mm (plain line), 0.8 mm (dashed line), and 1.5 mm (dotted line) nominal thickness, charged at -1050 mV (SCE) in 3.5% NaCl + 3g/L NH_4SCN.

From the curves shown in Figure 4.35, values for t_b, t_{lag}, J_∞, D_{eff} and C_0 were calculated, summarised in Table 4-4, below.

Table 4-4 Summary of output parameters calculated from permeation tests undertaken upon DP800 membranes of differing thicknesses at a constant charging potential of -1050 mV (SCE) in 3.5% NaCl + 3g/L NH_4SCN charging solution.

Membrane thickness (mm)	t_b (seconds)	t_{lag} (seconds)	J_∞ (mol/cm^2/s)	D_{eff} (cm^2/s)	C_0 (mol/cm^2)
0.1	275	1,209	2.63×10^{-11}	4.79×10^{-8}	1.02×10^{-5}
0.8	1,033	4,397	2.26×10^{-11}	1.87×10^{-7}	8.51×10^{-6}
1.5 (as received)	3,050	9,433	1.65×10^{-11}	4.55×10^{-7}	6.42×10^{-6}

Hydrogen permeation curves for tests undertaken on membranes of DP1000 material at nominal thicknesses of 0.1 mm, 0.8 mm, and 1.5 mm, with a common charging potential of -1050 mV (SCE) in 3.5% NaCl + 3g/L NH_4SCN, are shown in Figure 4.36, below.

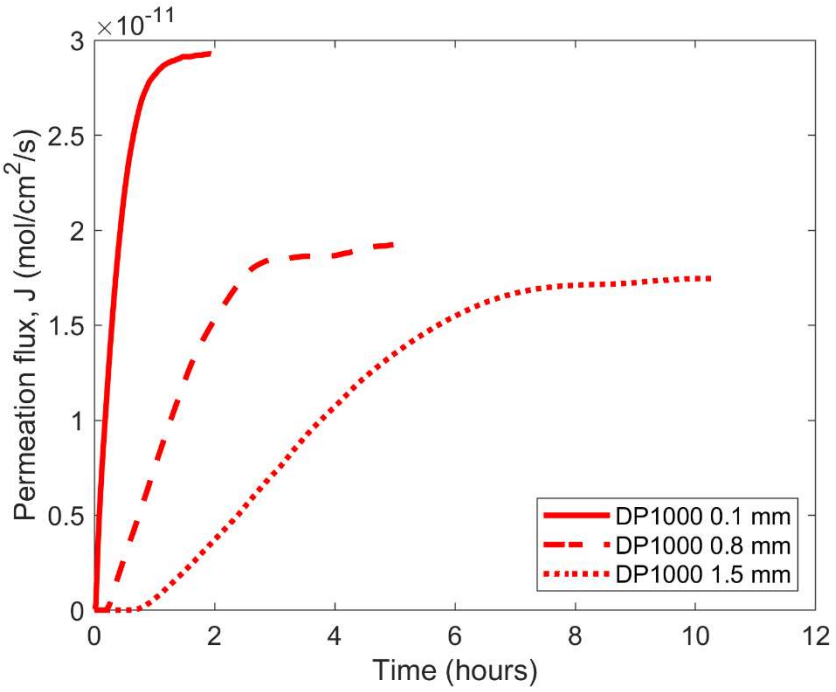

Figure 4.36 Hydrogen permeation curves for DP1000 membranes of 0.1 mm (plain line), 0.8 mm (dashed line), and 1.5 mm (dotted line) nominal thickness, charged at -1050 mV (SCE) in 3.5% NaCl + 3g/L NH_4SCN.

From the curves shown in Figure 4.36, values for t_b, t_{lag}, J_∞, D_{eff} and C_0 were calculated, summarised in Table 4-5, below.

Table 4-5 Summary of output parameters calculated from permeation tests undertaken upon DP1000 membranes of differing thicknesses at a constant charging potential of -1050 mV (SCE) in 3.5% NaCl + 3g/L NH_4SCN charging solution.

Membrane thickness (mm)	t_b (seconds)	t_{lag} (seconds)	J_∞ (mol/cm^2/s)	D_{eff} (cm^2/s)	C_0 (mol/cm^2)
0.1	200	1,383	2.93×10^{-11}	4.34×10^{-8}	1.28×10^{-5}
0.8	1,481	5,445	1.93×10^{-11}	1.45×10^{-7}	9.14×10^{-6}
1.5	5,026	14,731	1.75×10^{-11}	2.73×10^{-7}	9.93×10^{-6}

Figure 4.37 (below) shows the hydrogen permeation curves for tests undertaken on membranes of 22MnB5 (900C) material at nominal thicknesses of 0.1 mm, 0.8 mm, and 1.2 mm, with a common charging potential of -1050 mV (SCE) in 3.5% NaCl + 3g/L NH_4SCN.

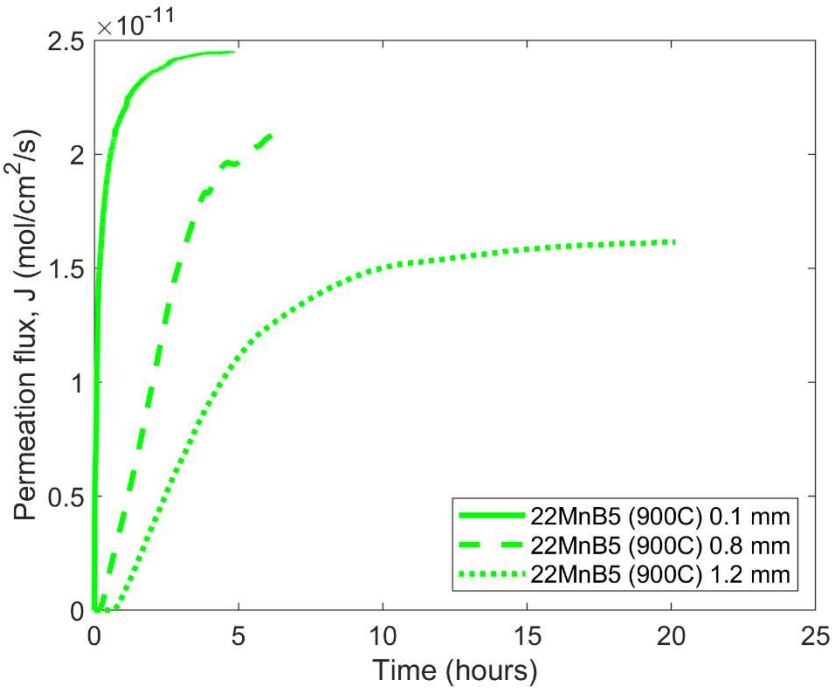

Figure 4.37 Hydrogen permeation curves for 22MnB5 (900C) membranes of 0.1 mm (plain line), 0.8 mm (dashed line), and 1.2 mm (dotted line) nominal thickness, charged at -1050 mV (SCE) in 3.5% NaCl + 3g/L NH_4SCN.

From the curves in Figure 4.37, values for t_b, t_{lag}, J_∞, D_{eff} and C_0 were calculated. These are summarised in Table 4-6, below.

Table 4-6 Summary of output parameters calculated from permeation tests undertaken upon 22MnB5 (900C) membranes of differing thicknesses at a constant charging potential of -1050 mV (SCE) in 3.5% NaCl + 3g/L NH_4SCN charging solution.

Membrane thickness (mm)	t_b (seconds)	t_{lag} (seconds)	J_∞ (mol/cm^2/s)	D_{eff} (cm^2/s)	C_0 (mol/cm^2)
0.1	27	737	2.45×10^{-11}	1.60×10^{-8}	1.29×10^{-5}
0.8	2,196	9,261	2.12×10^{-11}	9.81×10^{-8}	1.60×10^{-5}
1.2	4,790	16,156	1.62×10^{-11}	1.54×10^{-7}	1.28×10^{-5}

The effect of membrane thickness on the maximum flux attained, J_∞, for DP800, DP1000, and 22MnB5 (900C), is represented graphically in Figure 4.38.

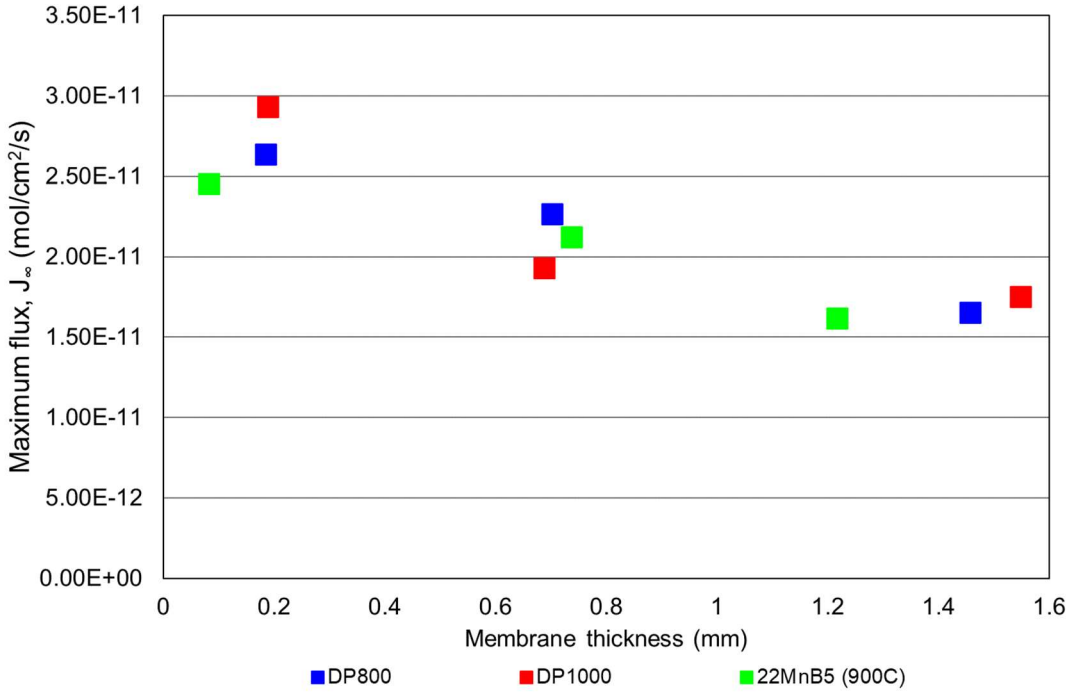

Figure 4.38 Effect of membrane thickness on maximum flux for DP800, DP1000, and 22MnB5 (900C).

From Figure 4.38 we see that J_∞, a measured parameter, shows a clear trend of reduction in magnitude as membrane thickness increases. Mathematically, this follows from equation (28) which shows that measured flux, J, scales with the square of the thickness, L. Conceptually, flux through the membrane is dependent on the diffusion coefficient, D, and the concentration gradient $\frac{dc}{dx}$, between $x = 0$ and $x = L$. Therefore, as membrane thickness increases (i.e. increase in the value of L), the concentration gradient becomes more shallow (i.e. lower magnitude), assuming charging concentration is consistent and concentration at desorption surface is maintained at zero.

4.4 Mechanical Testing

This section has been divided in to 3 parts. The first part shows the typical mechanical properties from conventional strain-rate (7×10^{4}/s rising to 3×10^{-3}/s after reaching proof stress) tensile tests using BS EN ISO6892-1:2016 A50 samples. The second shows results from slow strain-rate testing using sample geometry described in Figure 3.14. To statistically evaluate the differences between product performance under different test conditions, Student's t-test has been applied to the measured values for time-to-failure, and total elongation. These t-tests show whether a set of tests under a given condition can be considered to be part of a separate population, or whether there is no significant difference between conditions. Finally, the fractographic analyses for the various charging conditions during slow strain-rate testing are shown.

4.4.1 Baseline Mechanical Properties

Results from conventional strain-rate tensile tests for DP800 are shown in Figure 4.39. This shows a mean 0.2% proof strength, $R_{p0.2}$, of 488 (± 2) MPa, ultimate tensile strength, R_m, of 782 (± 4) MPa, uniform (plastic) elongation, A_g, of 12.5% (± 0.1%), and total (plastic) elongation at fracture, A_{50}, of 19.7% (± 0.3%).

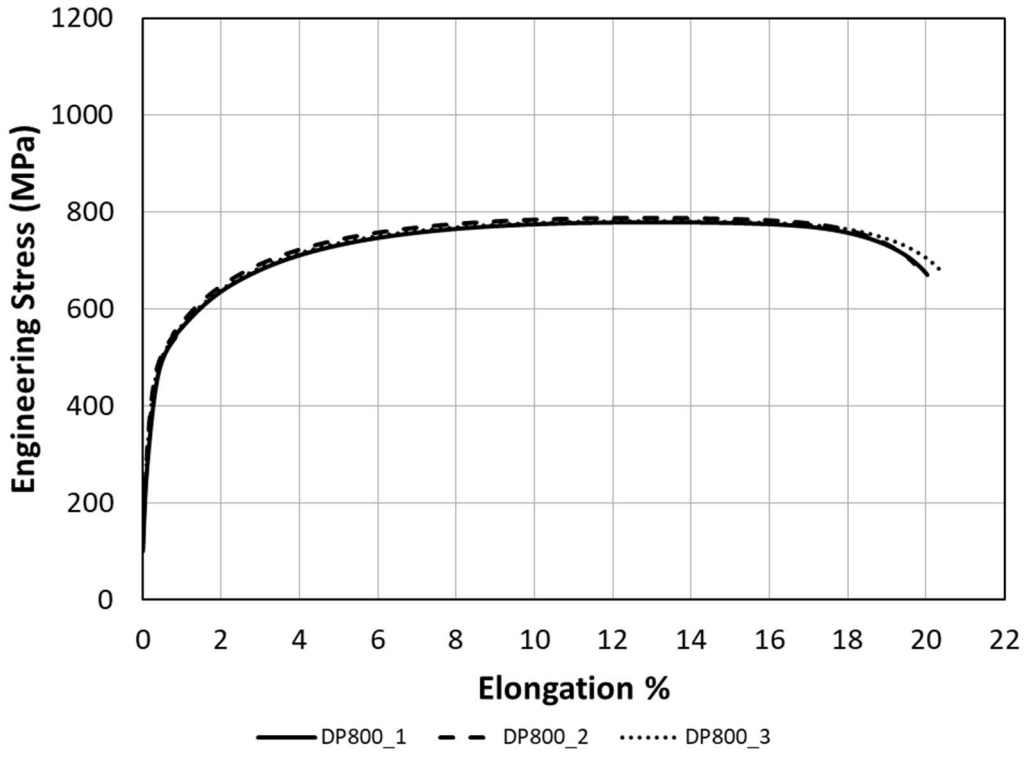

Figure 4.39 Engineering stress-elongation curves for conventional tensile tests performed on DP800.

Results from conventional strain-rate tensile tests for XPF800 are shown in Figure 4.40. Mean $R_{p0.2}$ is 747 (± 12) MPa, R_m 825 (± 5) MPa, A_g 9.3% (± 0.3%), and A_{50} 17.2% (± 1.5%).

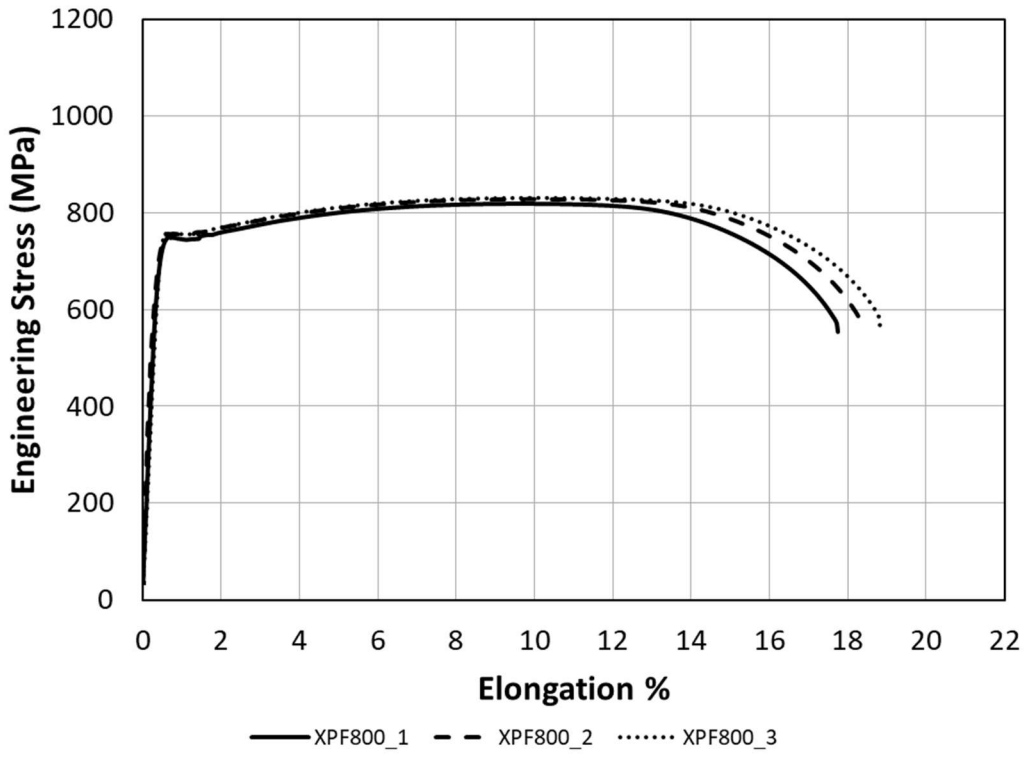

Figure 4.40 Engineering stress-elongation curves for conventional tensile tests performed on XPF800.

Results from conventional strain-rate tensile tests for DP1000 are shown in Figure 4.41. Mean value for $R_{p0.2}$ is 700 (± 5) MPa, R_m is 1027 (± 9) MPa, A_g is 7.8% (± 0.3%), and A_{50} is 13.5% (± 0.4%).

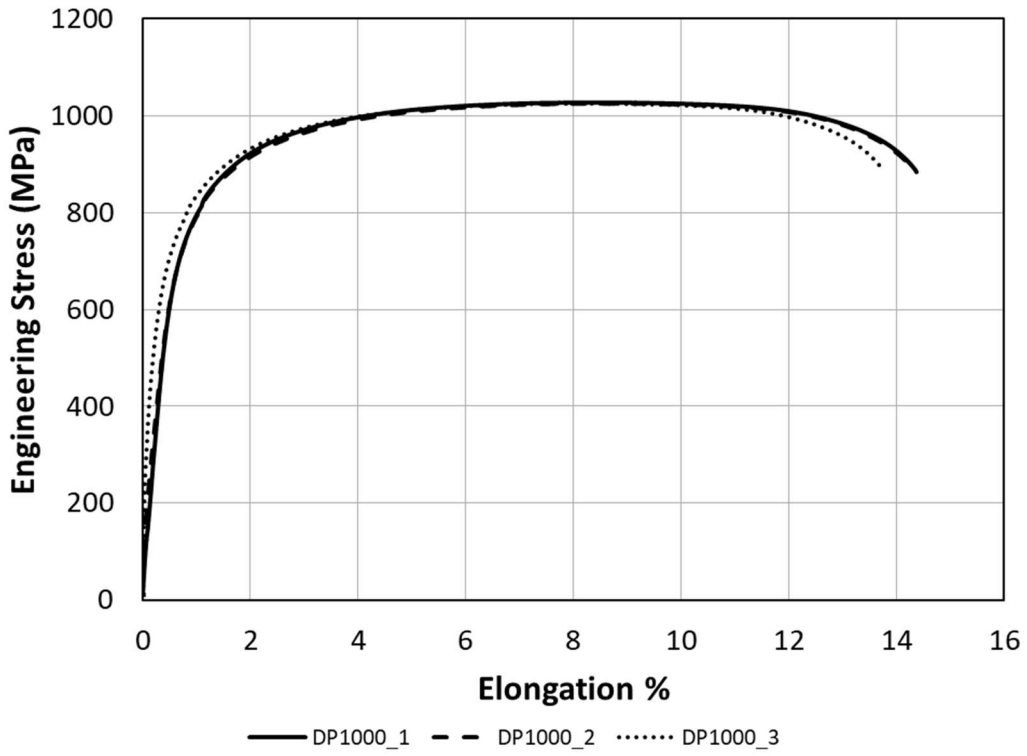

Figure 4.41 Engineering stress-elongation curves for conventional tensile tests performed on DP1000.

Results from conventional strain-rate tensile tests for XPF1000 are shown in Figure 4.42. It can be seen that mean $R_{p0.2}$ is 864 (± 8) MPa, mean R_m is 964 (± 4) MPa, mean A_g is 8.2% (± 0.1%), and mean A_{50} is 16.7% (± 0.3%).

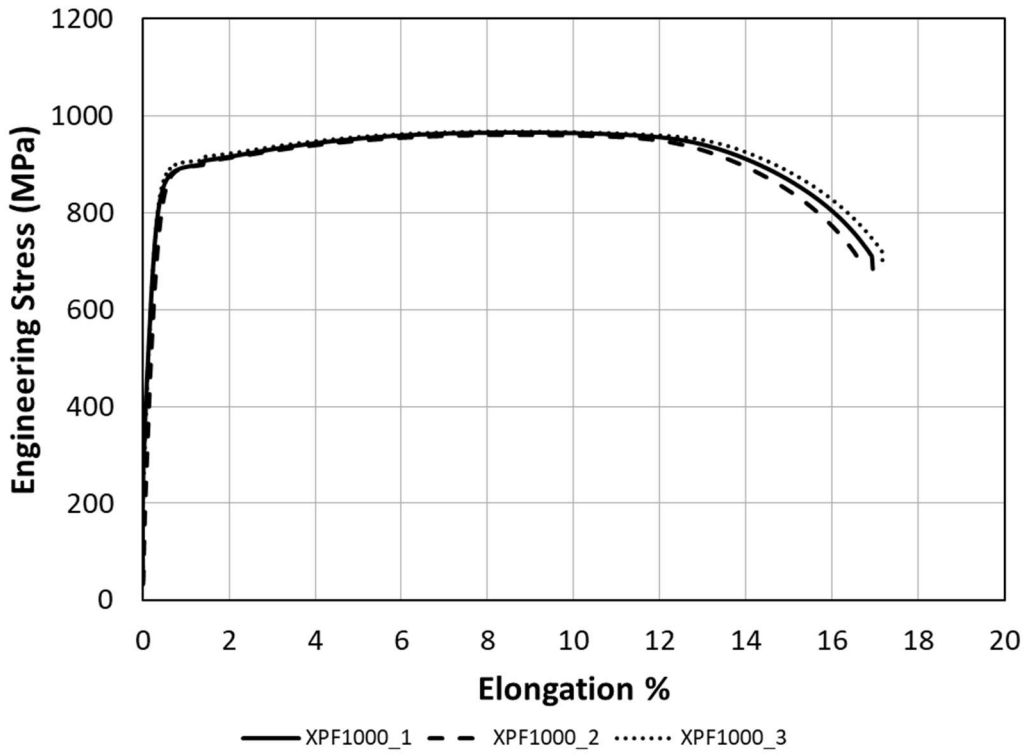

Figure 4.42 Engineering stress-elongation curves for conventional tensile tests performed on XPF1000.

Results from conventional strain-rate tensile tests for 22MnB5 are shown in Figure 4.43. In the un-heat-treated condition mean values for $R_{p0.2}$ is 404 (± 2) MPa, R_m is 587 (± 0.1) MPa, A_g is 13.1% (± 0.1%), and A_{50} is 22.7% (± 0.4%). In the heat-treated condition (soak temperature 900 °C, die quenched), strength is increased, and ductility decreased dramatically, with mean $R_{p0.2}$ 1245 (± 8) MPa, mean R_m 1589 (± 2) MPa, mean A_g 2.7% (± 0.1%), and A_{50} 4.7% (± 0.2%).

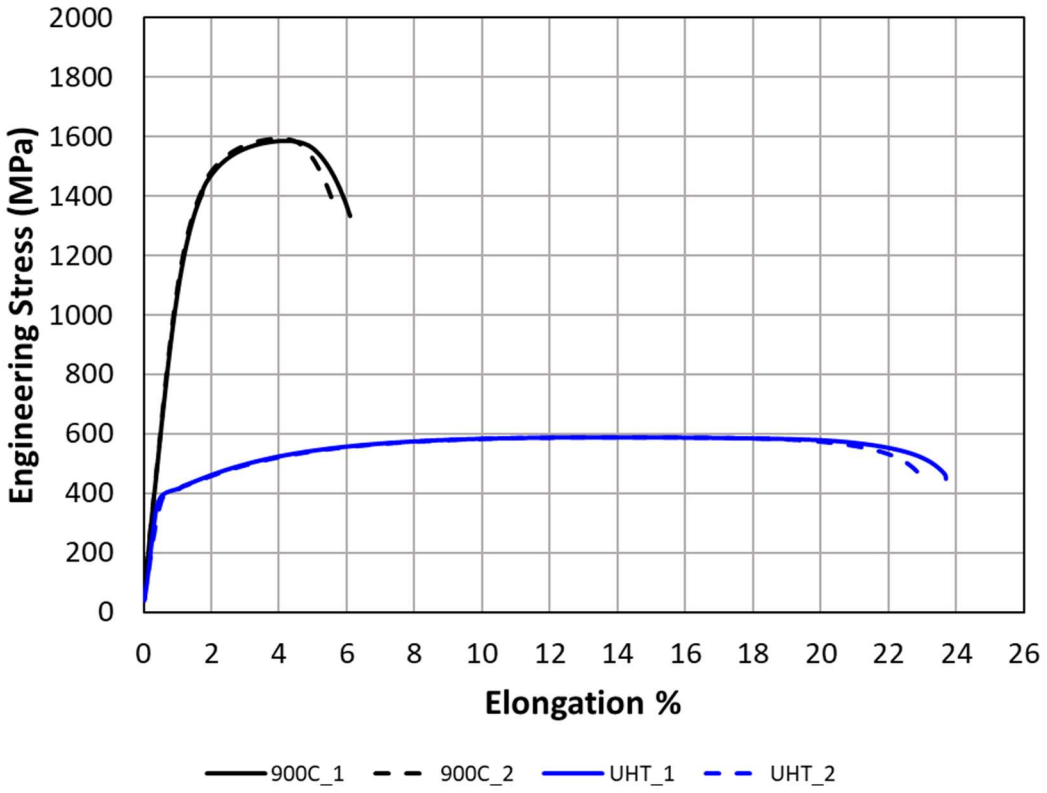

Figure 4.43 Engineering stress-elongation curves for conventional tensile tests performed on 22MnB5 in un-heat-treated (UHT) condition, and heat-treated with a 900 °C soak temperature.

Results from conventional strain-rate tensile tests for 27MnB5+Nb are shown in Figure 4.44. In the un-heat-treated condition 27MnB5+Nb has mean $R_{p0.2}$ of 378 (± 1) MPa, R_m of 601 (± 2) MPa, A_g of 12.4% (± 0.0%), and A_{50} of 17.1% (± 0.4%). As with the 22MnB5, in the heat-treated condition (soak temperature 900 °C, die quenched), strength is increased, and ductility decreased dramatically, with mean $R_{p0.2}$ of 1238 (± 13) MPa, mean R_m 1703 (± 2) MPa, mean A_g 3.7% (± 0.3%), and A_{50} 7.6% (± 0.2%).

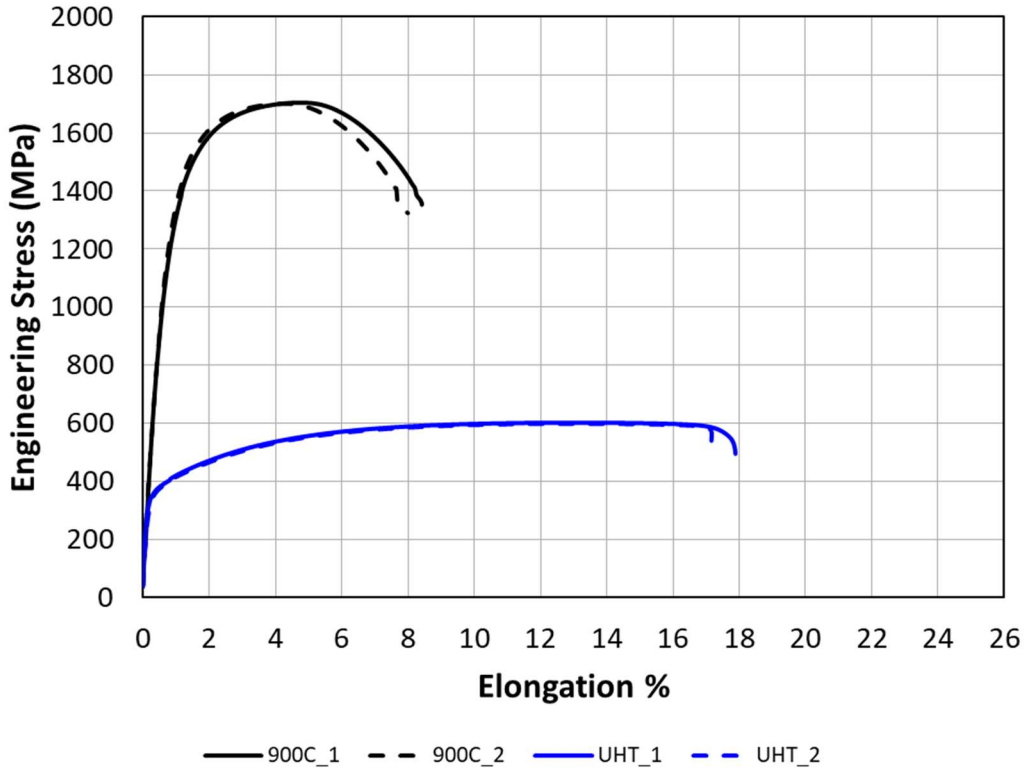

Figure 4.44 Engineering stress-elongation curves for conventional tensile tests performed on 27MnB5+Nb in all heat-treatment conditions.

A summary of the tensile test results is given in Table 4-7, below.

Table 4-7 Summary of results of conventional tensile tests for all products.

Product	Average			
	$R_{p0.2}$ MPa	R_m MPa	A_g %	A_{50} %
XPF800	747 (±12)	825 (± 5)	9.3 (± 0.3)	17.2 (± 1.5)
DP800	488 (± 2)	782 (± 4)	12.5 (± 0.1)	19.7 (± 0.3)
XPF1000	862 (± 8)	982 (± 3)	8.2 (± 0.1)	16.7 (± 0.3)
DP1000	700 (± 5)	1027 (± 9)	7.8 (± 0.3)	13.5 (± 0.4)
22MnB5 (900C soak)	1245 (± 8)	1589 (± 2)	2.7 (± 0.1)	4.7 (± 0.2)
22MnB5 (UHT)	404 (± 1.5)	587 (± 0)	13.1 (± 0.1)	22.7 (± 0.4)
27MnB5+Nb (900C soak)	1238 (± 13)	1703 (± 2)	3.7 (± 0.3)	7.6 (± 0.2)
27MnB5+Nb (UHT)	378 (± 0.8)	601 (± 2)	12.4 (± 0)	17.1 (± 0.4)

It can be seen that the tensile curves for both XPF800 and XPF1000 show a difference in shape to the other tensile curves except the un-heat-treated boron steels, with a sharp transition between the 'elastic' and 'plastic' portions of the curve that is not observed for the steels with significant volume fractions of martensite. This is due to the yield point phenomenon present in the predominantly ferritic microstructure of the XPF steels (and the un-heat-treated borons), which is not present in the steels containing martensite (and would not be present if tests were conducted on material in the fully temper-rolled condition).

This phenomenon occurs as an effect of room temperature diffusion of interstitial carbon and nitrogen atoms. At the onset of dislocation motion (slip), interstitials can diffuse to the dislocation cores to form 'atmospheres' (much like that described in bake hardening, Chapter 2.1.4.1), lowering the overall strain energy, and hence 'pinning' the dislocations in place, effectively preventing further plastic deformation involving the pinned dislocations. However, as the sample is further deformed, fresh dislocations are formed, which in turn become locked in place by diffusing carbon and nitrogen atoms. This cycle repeats, showing as an almost straight line parallel to the strain axis on the stress-strain curve (the yield point extension, or 'Luders extension'), until the

whole specimen (gauge length) has yielded, at which point the material begins to work harden as normal and the tensile curve rises smoothly.

In steels containing martensite, the high dislocation density of the martensite provides ample positions for any carbon or nitrogen atoms to form atmospheres, even prior to straining, hence limiting the effects upon fresh dislocations formed during deformation, and in turn minimising the appearance of a sharp yield point. This effect is replicated in non-martensitic strip steels via temper rolling, which introduces large amounts of mobile dislocations at the strip surface through very low levels of cold reduction (generally < 2%), though this yield-point-limiting effect will diminish over time due to the room temperature diffusion of solute carbon and nitrogen [20].

4.4.2 Slow Strain-Rate Tests (SSRT)

The effect of 3 different conditions (described in Table 4-8, below) are presented. Complementary to the SSRT curves for each of the products, embrittlement indices (EI) for a variety of parameters are calculated. Corresponding Weibull plots are displayed to show time-to-failure (TTF) for each condition (where applicable), and summary tables of results from Student's t-test are displayed to show the significance of the different charging and straining conditions upon different measures of embrittlement for each of the products.

Table 4-8 Summary of test conditions and parameters for slow strain-rate tests.

		Condition			
		Dry	**Pre-charged**	**Charged**	**Higher strain-rate**
Parameter	Hydrogen Pre-charging × 2 hours	No	Yes	No	No
	Strain-rate	10^{-6}/s	10^{-6}/s	10^{-6}/s	10^{-5}/s
Product	DP800	✓	✓	-	✓
	XPF800	✓	✓	-	✓
	DP1000	✓	✓	✓	✓
	XPF1000	✓	✓	✓	✓
	22MnB5 (900C)	✓	✓	✓	✓
	27MnB5+Nb (900C)	✓	✓	✓	✓

No 'charged' tests (10^{-6}/s strain-rate, *in situ* charging, no pre-charging) were undertaken on DP800 or XPF800, as there was insufficient material for a full test matrix on these products, and it was clear by the time these were tested that there was little difference in performance in hydrogen-charged specimens in the slowest strain-rate tests whether pre-charging had been undertaken or not. Therefore, for DP800 and XPF800 comparison is made between degradation with 'maximum' hydrogen content and 'hydrogen-free' tests at the slowest strain-rate, with wider comparisons concerning the relative differences between all of the steels with hydrogen concentrations below the maximum made in the 'higher strain-rate' condition.

4.4.2.1 DP800

Figure 4.45 shows the SSRT curves for each test condition for DP800. A large reduction in ductility from the 'Dry' condition (no hydrogen charging, strain-rate 10^{-6}/s) can be seen for both the 'Pre-charged' (2 hours' pre-charging, *in situ* charging maintained throughout testing, strain-rate 10^{-6}/s) and the 'Higher strain-rate' conditions (*in situ* charging maintained throughout testing, no pre-charging, strain-rate 10^{-5}/s), with the average total elongation dropping from 18.85% in the 'dry' condition, to 9.41% and 11.46% in the pre-charged and higher strain-rate conditions, respectively.

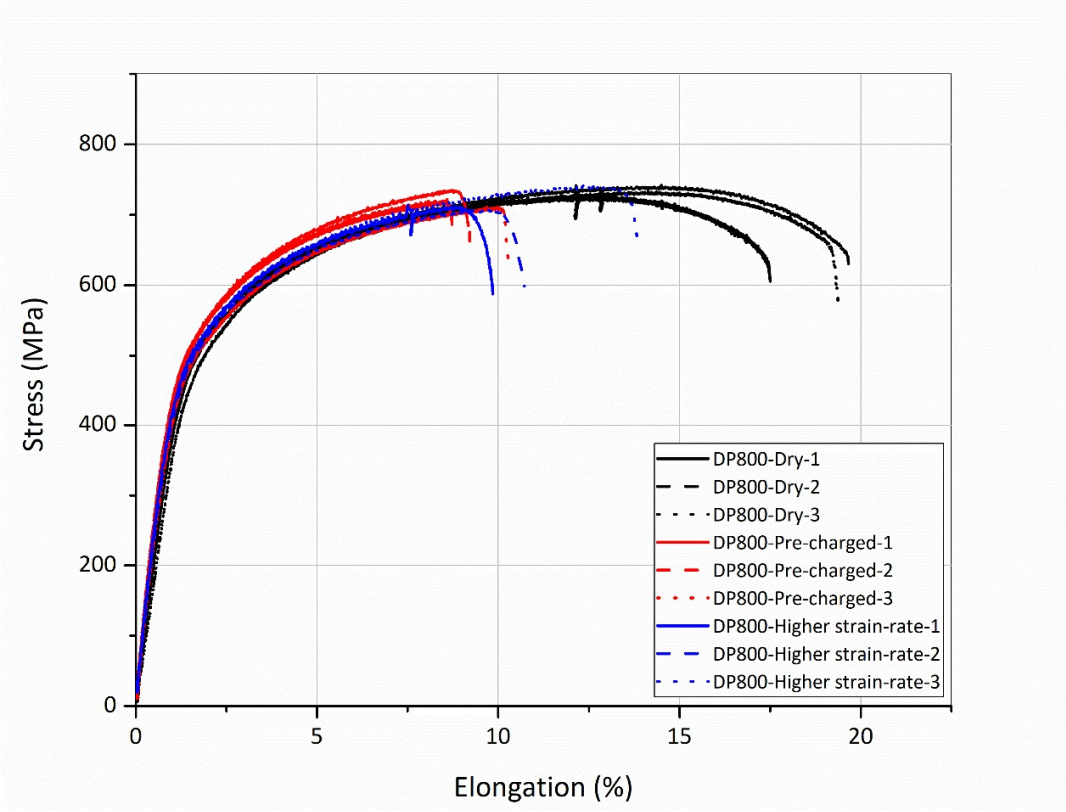

Figure 4.45 Engineering stress-elongation curves for slow strain-rate tests for DP800 under each charging condition.

Time-to-failure on DP800 was more consistent for each test condition, as illustrated in the Weibull plot in Figure 4.46, showing the differences in apparent 'survival' rates of the specimens between different charging conditions (i.e. hydrogen concentrations). In this case the plot shows 2 clearly distinct populations. Mean TTF for the dry condition was 22,553 seconds (6.26 hours), reducing to 11,206 seconds (3.11 hours) for the pre-charged condition.

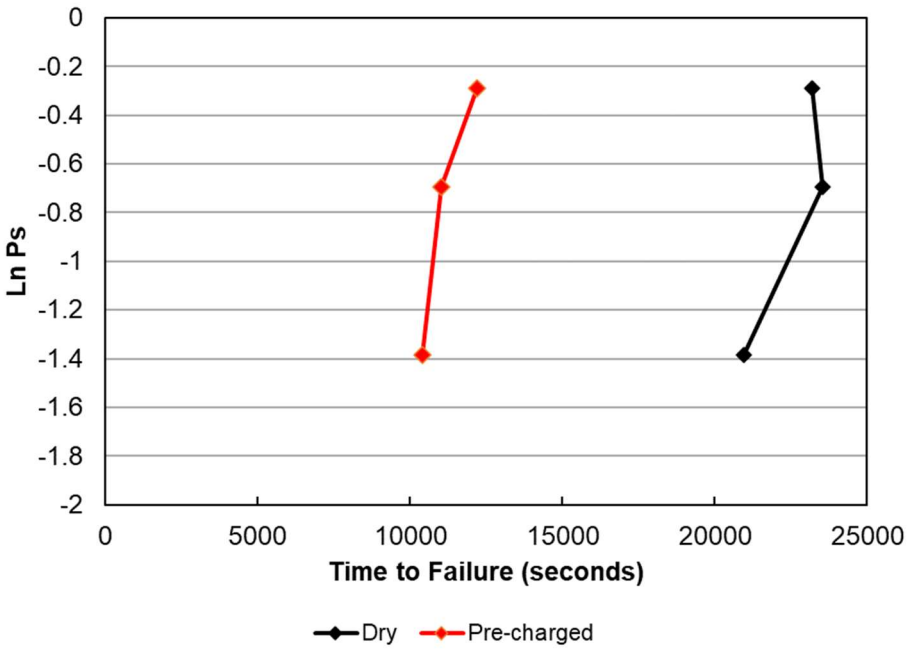

Figure 4.46 Weibull plots for DP800 slow strain-rate tests, showing differences in 'survival' times for the test specimens. Changes in gradient reflect the range of times that a DP800 specimen could be expected to 'survive' under the specified test conditions.

Student's t-test statistics, displayed in Table 4-9 (below), show that for DP800 there are significant differences between the dry tests and those involving hydrogen charging by any of the utilised embrittlement parameters, with 95% confidence. However, no significant difference is measured between the pre-charged tests and the higher strain-rate tests.

Table 4-9 Student's t-tests analysis of DP800 slow strain-rate tests, according to different parameters.

Product	Parameter	Mean Measurement	Mean Embrittlement Index %	t-statistic	p-value	Power	Statistically Different from Dry
Dry (10^{-6}/s SR, no charging)	TTF	22,552s (± 1,138s)	-	-	-	-	-
	Total Elongation	18.9% (± 1%)	-	-	-	-	-
Pre-charged (10^{-6}/s SR, charged, 2 hours' pre-charging)	TTF	11,205s (± 751s)	50.30%	11.773	2.98×10^{-4}	1	Yes
	Total Elongation	9.4% (± 0.7%)	50.05%	11.5	3.25×10^{-4}	1	Yes
Higher strain-rate (10^{-5}/s SR, charged, no pre-charge)	TTF	-	-	-	-	-	-
	Total Elongation	11.5% (± 1.7%)	39.20%	5.3	0.006	0.97	Yes

4.4.2.2 XPF800

Figure 4.47 shows the SSRT curves for XPF800. It can be seen that mean total elongation dropped from 18.93% in the dry condition to 12.81%, in the 'pre-charged' condition, although one of the tests (pre-charged test 3) appears to have persisted to a significantly higher elongation than the others for the same conditions. It appears that at the higher strain-rate (10^{-5}/s), where charging commenced at the beginning of straining, the reduction in ductility is potentially within the scatter of the 'un-charged' tests, with a mean total elongation of 16.61%.

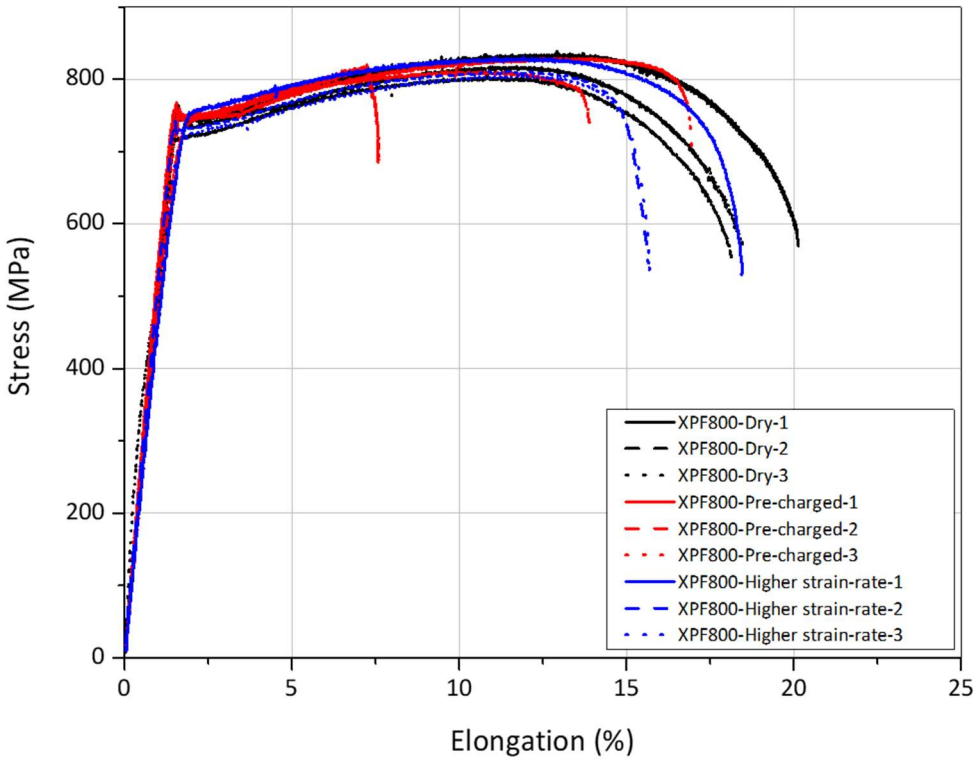

Figure 4.47 Engineering stress-elongation curves for slow strain-rate tests for XPF800 under each charging condition.

The Weibull plots shown in Figure 4.48 for XPF800 in each condition show that there is a degree of scatter that may indicate significant overlap between populations. Mean TTF for the dry population is 22,655 seconds (6.29 hours), and for the pre-charged condition it is 15,323 seconds (4.26 hours).

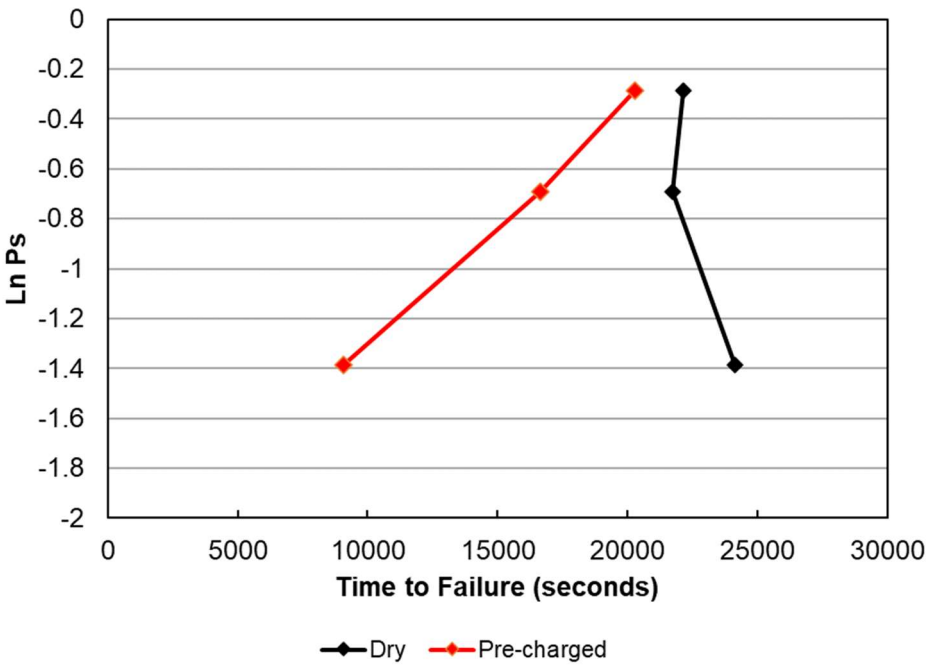

Figure 4.48 Weibull plots for XPF800 slow strain-rate tests.

The statistical analysis using Student's t-test, presented in Table 4-10, show that there is no statistically significant difference between any of the conditions with a 95% confidence, when evaluated by SSRT results only.

Table 4-10 Student's t-tests analysis of XPF800 slow strain-rate tests, according to different measures of embrittlement.

Product	Parameter	Mean Measurement	Mean Embrittlement Index %	t-statistic	p-value	Power	Statistically Different from Dry
Dry (10^{-6}/s SR, no charging)	TTF	22,655s (± 1,043s)	-	-	-	-	-
	Total Elongation	18.9% (± 1%)	-	-	-	-	-
Pre-charged (10^{-6}/s SR, charged, 2 hours' pre-charging)	TTF	15,323s (± 4,668s)	32.4%	2.168	0.096	0.38	No
	Total Elongation	12.8% (± 3.9%)	32.3%	2.167	0.096	0.38	No
Higher strain-rate (10^{-5}/s SR, charged, no pre-charge)	TTF	-	-	-	-	-	-
	Total Elongation	16.6% (± 1.3%)	12.3%	2.091	0.105	0.36	No

4.4.2.3 DP1000

The SSRT curves for DP1000 are shown in Figure 4.49. A severe loss of ductility is readily apparent for each of the test conditions involving hydrogen charging. Mean total elongation in the 'dry' tests is 18.50%, but this is reduced to 4.60% for pre-charged tests, 4.55% for charged tests (at 10^{-6}/s strain-rate), and 8.28% for the higher (10^{-5}/s) strain-rate tests.

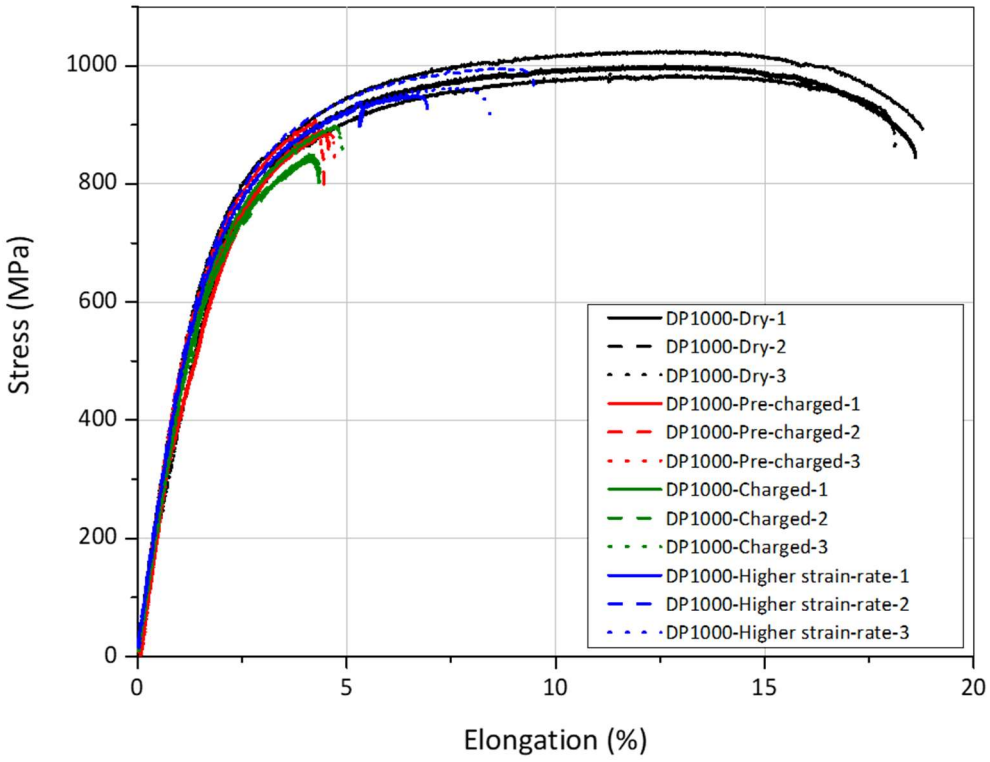

Figure 4.49 Engineering stress-elongation curves for slow strain-rate tests for DP1000 under each charging condition.

Mean TTF values for DP1000 see a similar reduction when the test specimens are charged with hydrogen, with little measured impact of 2 hours' pre-charging. Mean TTF can be seen to drop from 22,158 seconds (6.16 hours) for tests in the dry condition, to 5,417 seconds (1.51 hours), and 5,397 seconds (1.50 hours), for the 'pre-charged', and 'charged' tests (both with strain-rate 10^{-6}/s) , respectively. This is illustrated by the Weibull plots for DP1000 shown in Figure 4.50.

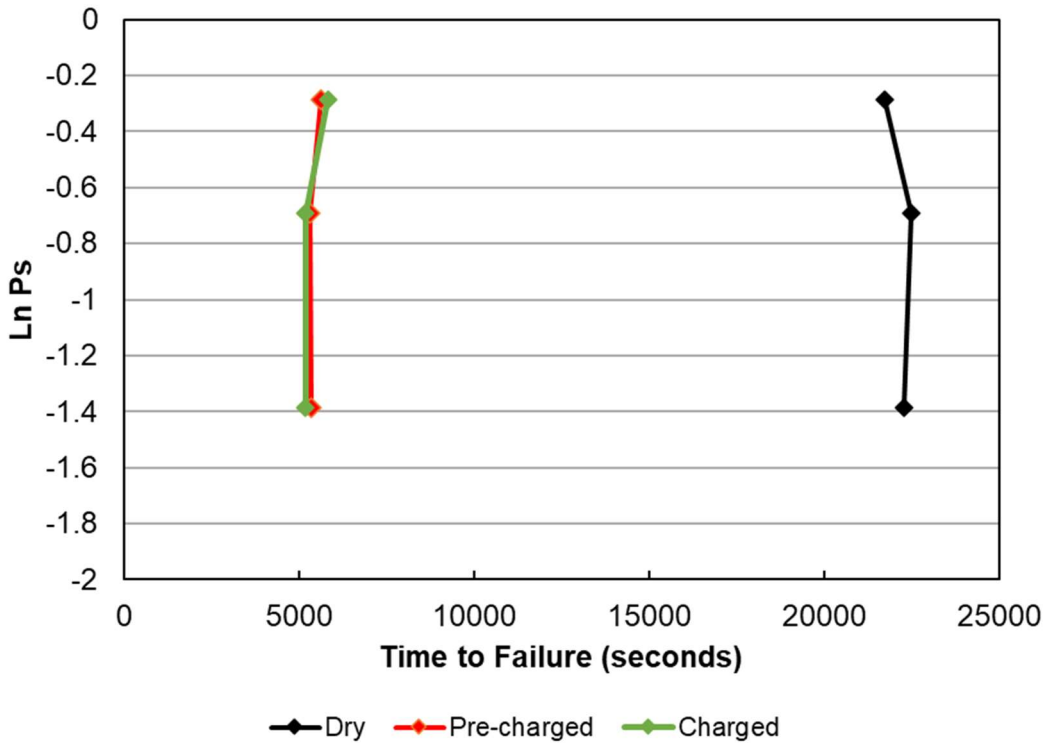

Figure 4.50 Weibull plots for DP1000 slow strain-rate tests.

Student's t-test analysis for DP1000, shown in Table 4-11, shows statistically significant differences (with 95% confidence) between the dry tests and all of the conditions involving hydrogen charging. As can be seen from the tensile curves in Figure 4.49, DP1000 suffered a large drop in performance in the presence of hydrogen, and this is validated in the output of the t-tests.

Table 4-11 Student's t-tests analysis of DP1000 slow strain-rate tests, according to different measures of embrittlement.

Product	Parameter	Mean Measurement	Mean Embrittlement Index %	t-statistic	p-value	Power	Statistically Different from Dry
Dry (10^{-6}/s SR, no charging)	TTF	22,158s (± 328s)	-	-	-	-	-
	Total Elongation	18.5% (± 0.3%)	-	-	-	-	-
Pre-charged (10^{-6}/s SR, charged, 2 hours' pre-charging)	TTF	5,418s (± 135s)	75.60%	66.706	3.03×10^{-7}	1	Yes
	Total Elongation	4.6% (± 0.1%)	75.10%	66.491	3.07×10^{-7}	1	Yes
Charged (10^{-6}/s SR, charged, no pre-charge)	TTF	5,398s (± 301s)	75.60%	55.223	7.46×10^{-7}	1	Yes
	Total Elongation	4.6% (± 0.3%)	75.40%	51.83	8.29×10^{-7}	1	Yes
Higher strain-rate (10^{-5}/s SR, charged, no pre-charge)	TTF	-	-	-	-	-	-
	Total Elongation	8.3% (± 1%)	55.30%	13.402	1.79×10^{-4}	1	Yes

4.4.2.4 XPF1000

SSRT curves for each test condition for XPF1000 are shown in Figure 4.51. Like the XPF800, some scatter is observed when specimens are charged with hydrogen. However, differences are apparent between conditions. Mean total elongation in the dry condition is 17.36%. This reduces to 9.99% for the pre-charged condition, 7.92% for the 'charged' condition (whereby hydrogen charging only commences at the beginning of mechanical testing), and 13.69% for the higher strain-rate condition.

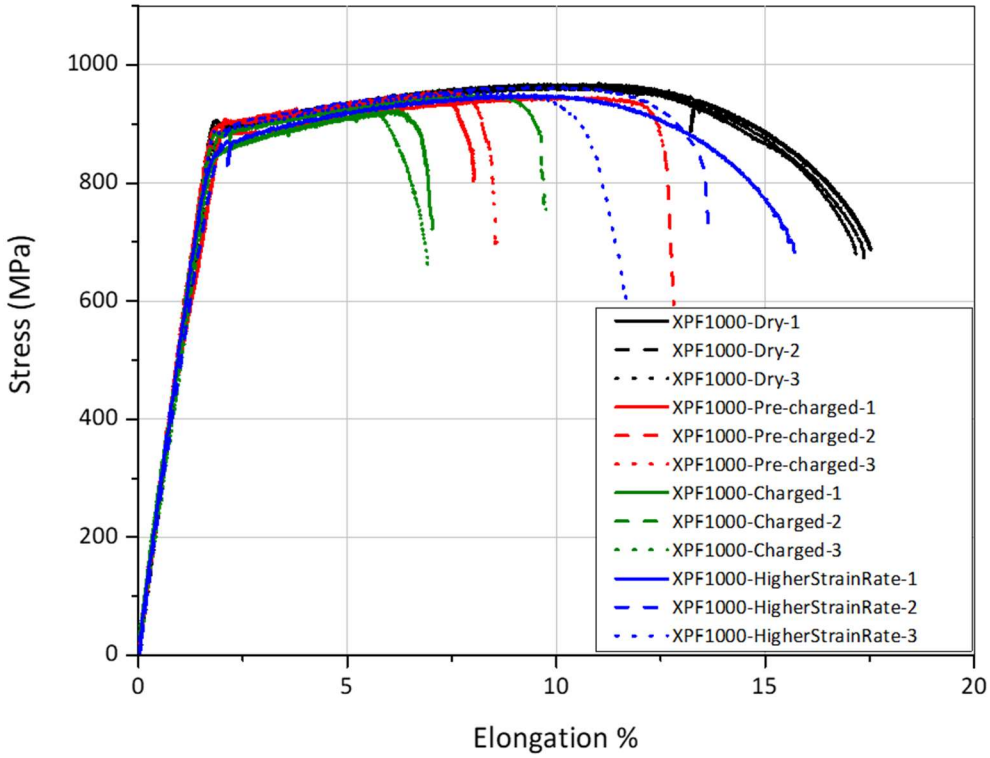

Figure 4.51 Engineering stress-elongation curves for slow strain-rate tests for XPF1000 under each charging condition.

Weibull plots for XPF1000, shown in Figure 4.52, shows substantial decrease in TTF between the dry and hydrogen-charged conditions (with and without pre-charging) at the lower strain-rate, with mean TTF decreasing from 20,763 seconds (5.77 hours) in the dry condition, to 11,633 seconds (3.23 hours) and 9,402 seconds (2.61 hours) for the pre-charged and charged conditions (10^{-6}/s strain-rate), respectively. Of all the steels tested, XPF1000 showed the greatest variability in test performance for given conditions (XPF800 also showed relatively large variation, overall). These steels incurred the largest reduction in thickness from the as-received condition, and as such there is the potential that this may have led to inconsistencies in surface condition, known to introduce variation to SSRT results [230]. This is also a particular problem for introducing variation if these inconsistencies introduce any compressive stresses to the surface [231,232]. Whilst every effort has been made to ensure condition sample condition, it is possible that such differences have introduced some inconsistencies to SSRT for the XPF steels.

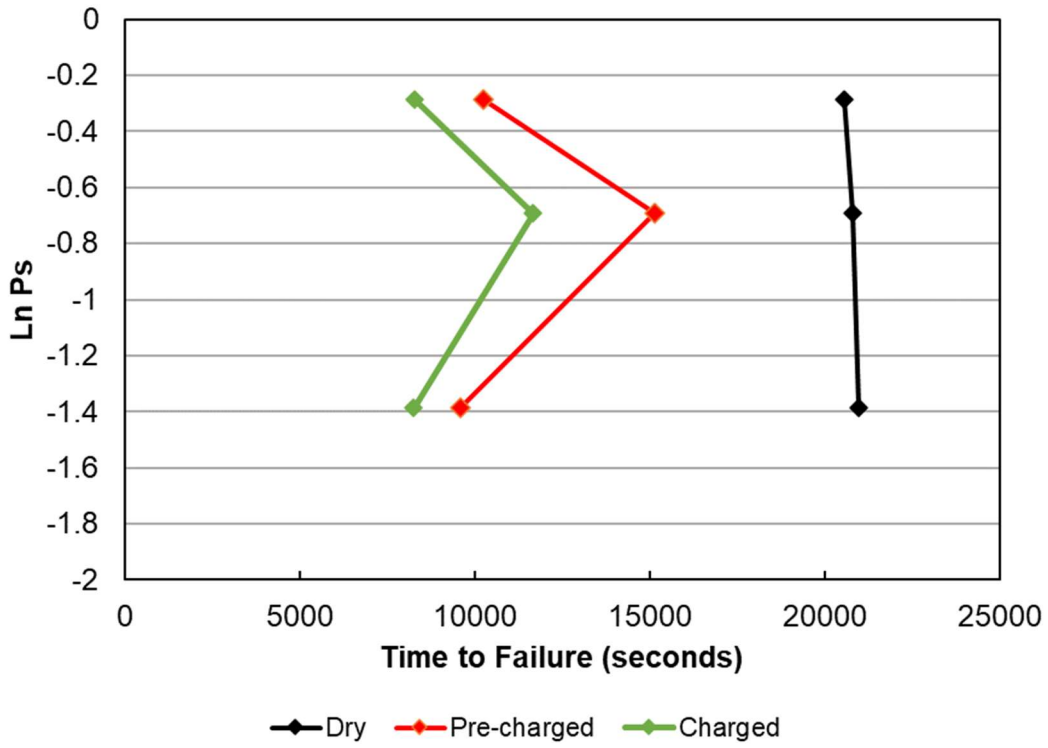

Figure 4.52 Weibull plots for XPF1000 slow strain-rate tests.

The significance of the differences in performance under the different conditions is clear from the t-test summaries in Table 4-12, which demonstrates that the pre-charged and charged conditions are significantly different from the dry condition by any of the utilised parameters for calculating embrittlement indices, as is the higher strain-rate condition. However, the lower power values for the higher strain-rate condition imply that this effect is less pronounced in these much (10×) quicker tests.

Table 4-12 Student's t-tests analysis of XPF1000 slow strain-rate tests, according to different measures of embrittlement.

Product	Parameter	Mean Measurement	Mean Embrittlement Index %	t-statistic	p-value	Power	Statistically Different from Dry
Dry (10^{-6}/s SR, no charging)	TTF	20,762s (± 173s)	-	-	-	-	-
	Total Elongation	17.4% (± 0.2%)	-	-	-	-	-
Pre-charged (10^{-6}/s SR, charged, 2 hours' pre-charging)	TTF	11,663s (± 2,475s)	43.80%	5.186	6.58×10^{-3}	0.97	Yes
	Total Elongation	10% (± 2%)	42.50%	5.207	6.49×10^{-3}	0.97	Yes
Charged (10^{-6}/s SR, charged, no pre-charge)	TTF	9,402s (± 1,598s)	54.70%	9.998	5.62×10^{-4}	1	Yes
	Total Elongation	7.9% (± 1.3%)	54.40%	10.186	5.23×10^{-4}	1	Yes
Higher strain-rate (10^{-5}/s SR, charged, no pre-charge)	TTF	-	-	-	-	-	-
	Total Elongation	13.7% (± 1.6%)	21.20%	3.153	3.40×10^{-2}	0.64	Yes

4.4.2.5 22MnB5 (heat-treated condition)

Figure 4.53 shows the SSRT curves for 22MnB5 (in the 900 ºC soak heat-treated condition) for each test condition. Mean total elongation in the dry condition is 11.34%. Where hydrogen is charged to the test specimens, mean total elongation is 3.39% for the pre-charged condition, 3.71% for the charged condition, and 6.58% for the higher strain-rate condition, demonstrating a significant and readily-apparent loss of ductility in this product due to hydrogen charging, at both the tested strain-rates.

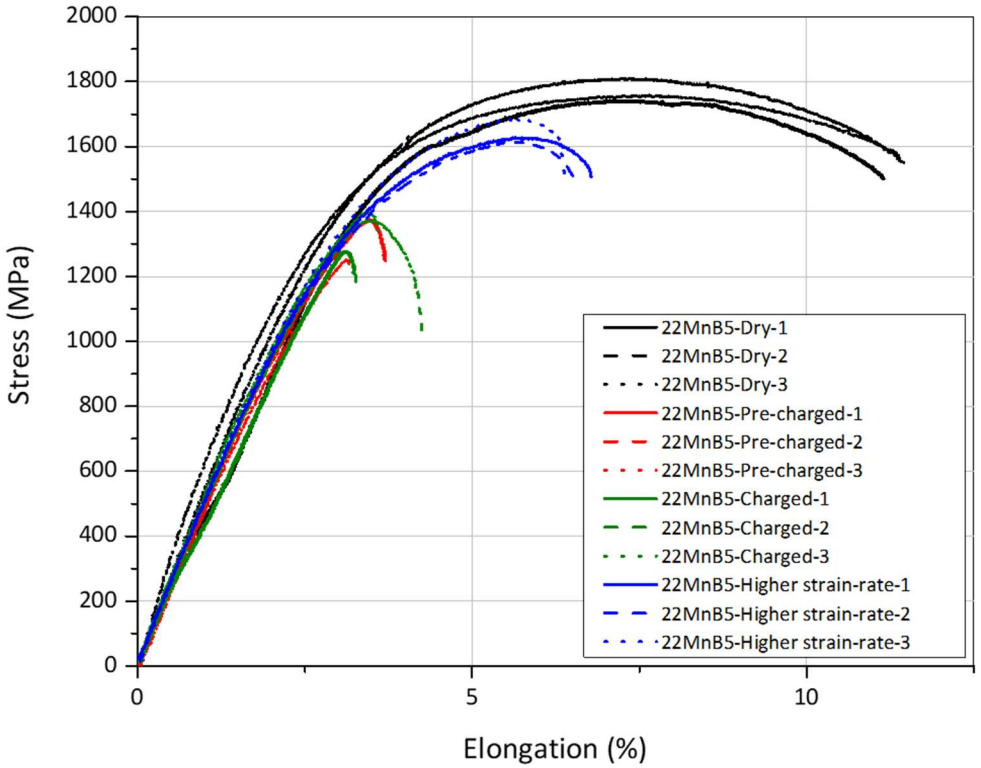

Figure 4.53 Engineering stress-elongation curves for slow strain-rate tests for 22MnB5 (900C) under each charging condition.

As with the DP1000, 22MnB5 also sees a similar reduction in performance due to hydrogen when measured against the time-to-failure, with little effect of 2 hours of pre-charging apparent on the overall degradation, as seen from the Weibull plots in Figure 4.54. Mean TTF for the dry condition is 13,547 seconds (3.76 hours), but this is reduced to 4,020 seconds (1.12 hours) for the pre-charged condition, and 4,406 seconds (1.22 hours) in the charged condition (both 10^{-6}/s strain-rate).

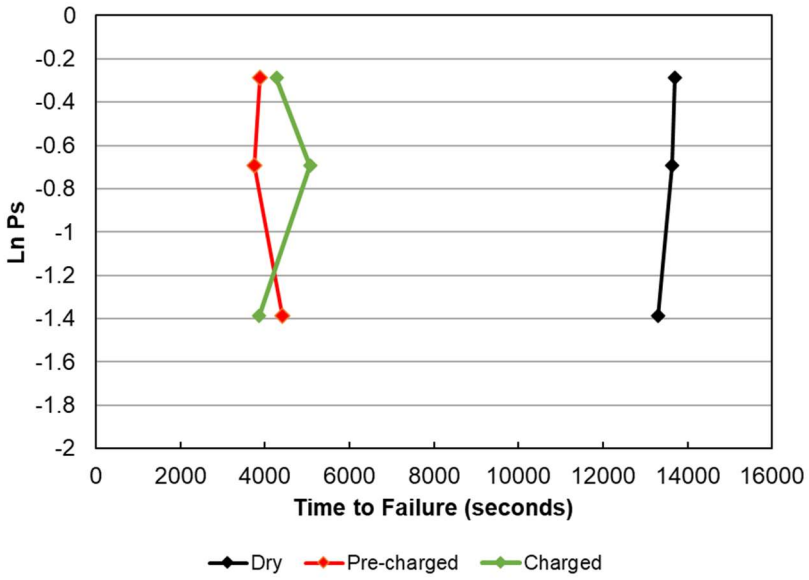

Figure 4.54 Weibull plots for 22MnB5 (900C) slow strain-rate tests.

The t-tests for 22MnB5 (Table 4-13) showed that there were statistically significant differences between the mean values for TTF and total elongation for dry tests and all conditions involving hydrogen charging.

Table 4-13 Student's t-tests analysis of 22MnB5 (900C) slow strain-rate tests, according to different measures of embrittlement.

Product	Parameter	Mean Measurement	Mean Embrittlement Index %	t-statistic	p-value	Power	Statistically Different from Dry
Dry (10^{-6}/s SR, no charging)	TTF	13,547s (± 171s)	-	-	-	-	-
	Total Elongation	11.3% (± 0.1%)	-	-	-	-	-
Pre-charged (10^{-6}/s SR, charged, 2 hours' pre-charging)	TTF	4,020s (± 277s)	70.30%	41.365	2.04×10^{-6}	1	Yes
	Total Elongation	3.4% (± 0.2%)	70.10%	42.212	1.88×10^{-6}	1	Yes
Charged (10^{-6}/s SR, charged, no pre-charge)	TTF	4,406s (± 500s)	67.50%	24.465	1.66×10^{-5}	1	Yes
	Total Elongation	3.7% (± 0.4%)	67.30%	24.699	1.59×10^{-5}	1	Yes
Higher strain-rate (10^{-5}/s SR, charged, no pre-charge)	TTF	-	-	-	-	-	-
	Total Elongation	6.6% (± 0.2%)	42.00%	33.337	5.45×10^{-6}	1	Yes

4.4.2.6 27MnB5+Nb (heat-treated condition)

SSRT curves for 27MnB5+Nb (in the 900 °C soak heat-treated condition) for each test condition are shown in Figure 4.55. As with both 22MnB5 and DP1000, a large loss of ductility due to hydrogen charging is readily apparent, with mean total elongation reducing from 11.36% in the dry condition, to 3.15%, 3.62%, and 6.07% for the pre-charged (10^{-6}/s), charged (10^{-6}/s), and higher strain-rate (10^{-5}/s) conditions, respectively.

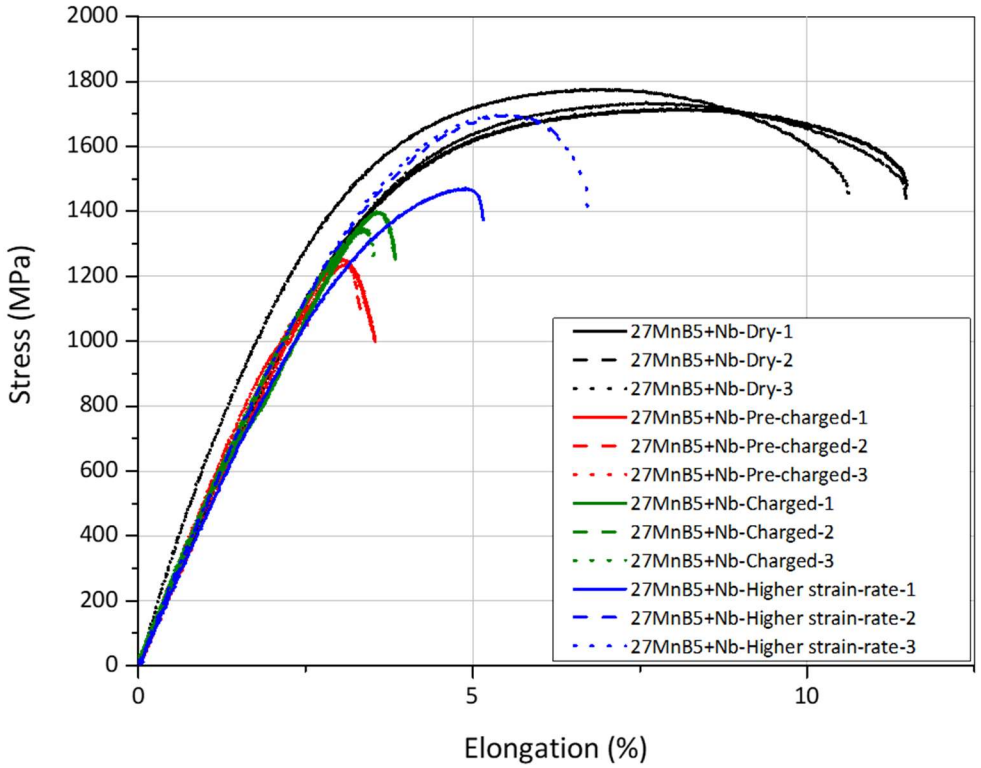

Figure 4.55 Engineering stress-elongation curves for slow strain-rate tests for 27MnB5+Nb (900C) under each charging condition.

Likewise, as can be seen from the Weibull plots in Figure 4.56, mean time-to-failure is reduced in a similar fashion, dropping from 13,399 seconds (3.72 hours) in the dry condition, to 3,711 seconds (1.03 hours), and 4,183 seconds (1.16 hours), for the pre-charged, and charged conditions, respectively.

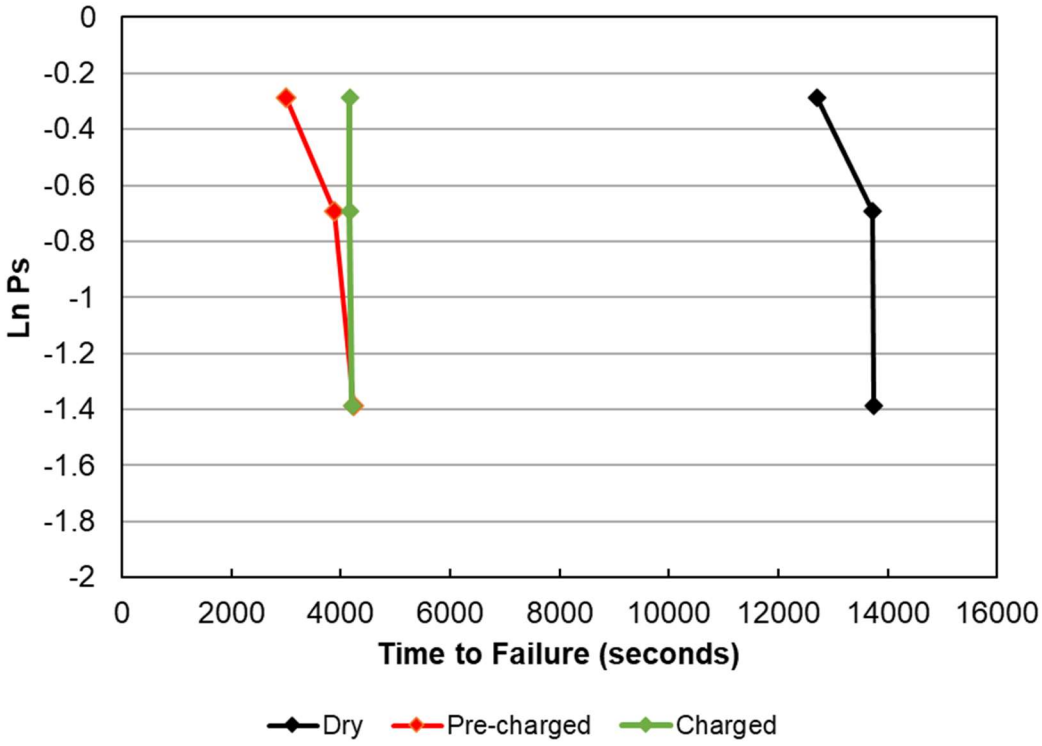

Figure 4.56 Weibull plots for 27MnB5+Nb (900C) slow strain-rate tests.

For the 27MnB5+Nb, Student's t-test analyses (Table 4-14) show that, like for the 22MnB5 and the DP1000, across all parameters evaluated, mean values for the dry tests belong to different statistical populations than the pre-charged, charged, and higher strain-rate tests.

Table 4-14 Student's t-tests analysis of 27MnB5+Nb (900C) slow strain-rate tests, according to different measures of embrittlement.

Product	Parameter	Mean Measurement	Mean Embrittlement Index %	t-statistic	p-value	Power	Statistically Different from Dry
Dry (10^{-6}/s SR, no charging)	TTF	13,399s (± 488s)	-	-	-	-	-
	Total Elongation	11.4% (± 0.5%)	-	-	-	-	-
Pre-charged (10^{-6}/s SR, charged, 2 hours' pre-charging)	TTF	3,711s (± 518s)	72.30%	19.253	4.29×10^{-5}	1	Yes
	Total Elongation	3.2% (± 0.4%)	72.30%	16.658	7.61×10^{-5}	1	Yes
Charged (10^{-6}/s SR, charged, no pre-charge)	TTF	4,183s (± 23s)	68.80%	26.683	1.17×10^{-5}	1	Yes
	Total Elongation	3.6% (± 0.2%)	68.10%	19.263	4.28×10^{-5}	1	Yes
Higher strain-rate (10^{-5}/s SR, charged, no pre-charge)	TTF	-	-	-	-	-	-
	Total Elongation	6.1% (± 0.7%)	46.50%	8.624	9.94×10^{-4}	1	Yes

4.4.3 Fractographic Analyses

In this section, fractographic analysis of the products in each of the test conditions is presented. In addition to qualitative characterisation of the fracture surfaces, quantitative analysis has been undertaken to contrast the prevalence of specific fracture features in each product, for each test condition. Electrochemical hydrogen charging occurred at all of the exterior surfaces visible (as edges in the SEM images).

4.4.3.1 DP800 Specimens

The optical-topographical images of Figure 4.57 a) and b) shows a typically ductile fracture mode for the DP800 specimen tested in air at 10^{-6}/s strain-rate ('dry' condition), with evidence of significant necking, and a conventional 45^{o} fracture angle along plane of maximum shear (high amounts of energy absorption leading to plastic deformation, and eventually 'necking', prior to fracture; if no plastic deformation occurs – i.e. low energy absorption, brittle failure - the fracture angle would be close to 90^{o} as there is no deformation of the specimen prior to fracture).

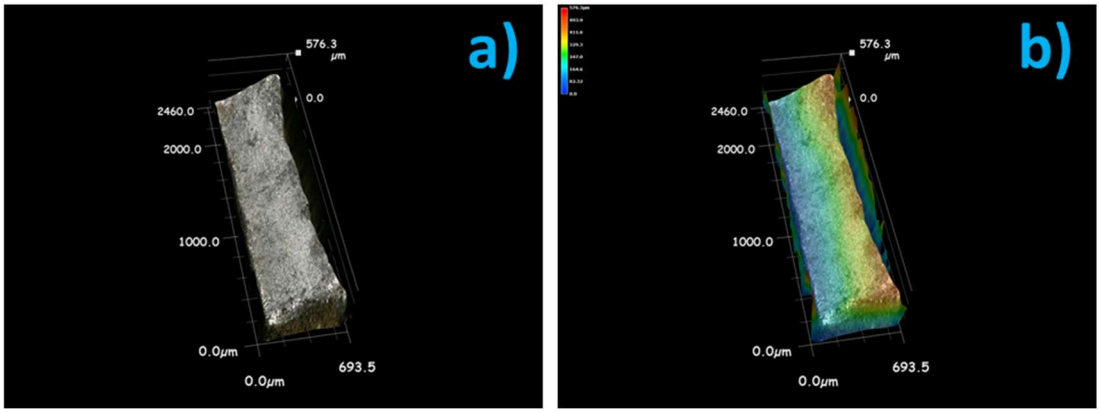

Figure 4.57 a) 3D-optical, and b) topographical images of DP800 specimen tested in the dry condition (without hydrogen charging) at 10^{-6}/s strain-rate.

Further evidence of a classically ductile failure for this sample is noted from the SEM images in Figure 4.58, with the reduction in cross-section apparent in the composite image of Figure 4.58 a), and the dominance of microvoid coalescence (MVC), whereby microvoids nucleated as a result of plastic flow during deformation coalesce

with adjacent microvoids, as the primary fracture surface feature shown by way of example in Figure 4.58 b).

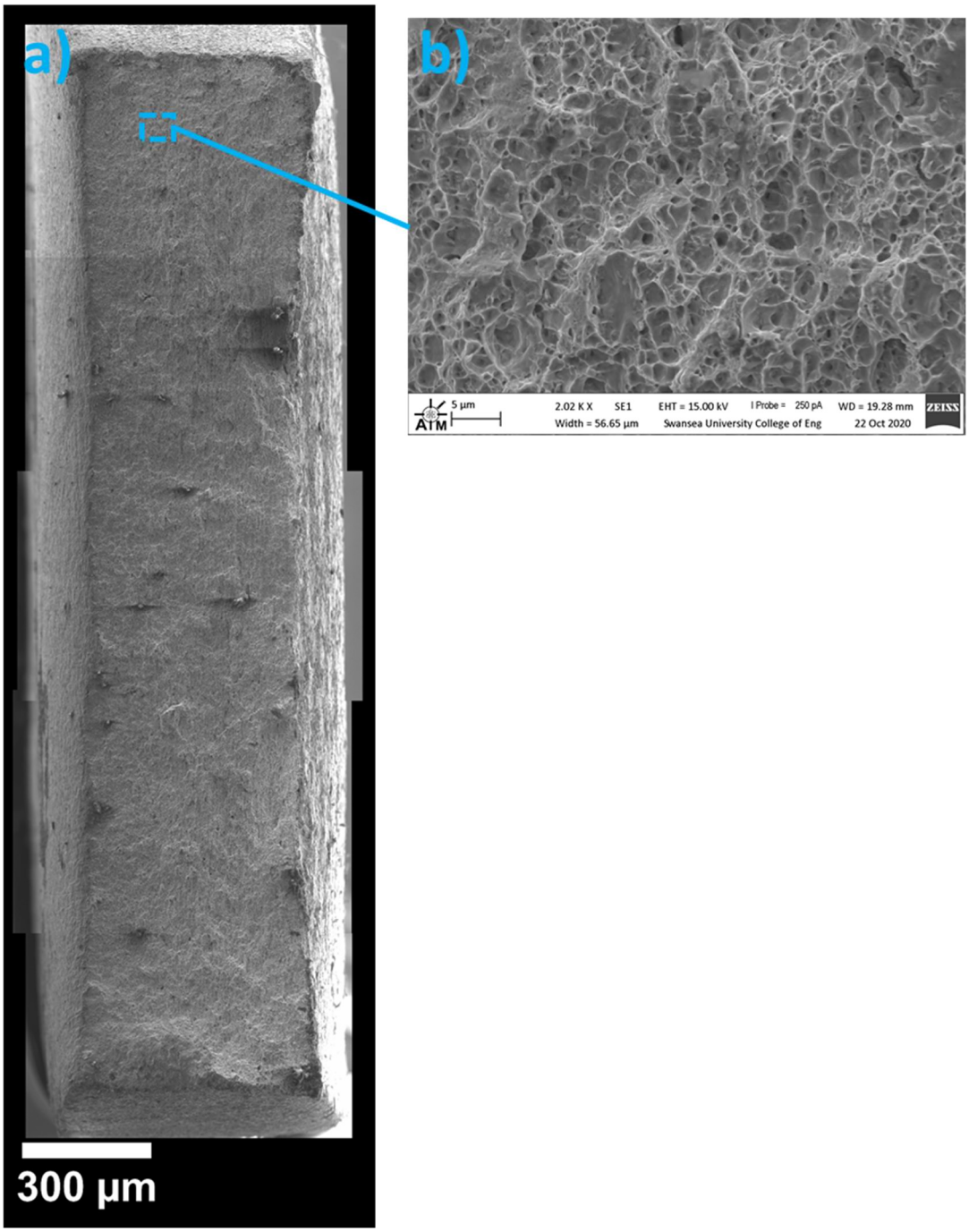

Figure 4.58 SEM images of DP800 specimen tested in the dry condition (without hydrogen charging) at a strain-rate of 10^{-6}/s at a) 150×, and b) 2000× magnification.

The pre-charged sample (strained at a rate of 10^{-6}/s) fracture surface for DP800 is far more mixed. The optical-topographical images in Figure 4.59 show changing fracture

angles across the surface, indicating that crack propagation occurred along different planes at different distances from the charging surface, and rapid failure along surfaces that sit 90° to the loading direction.

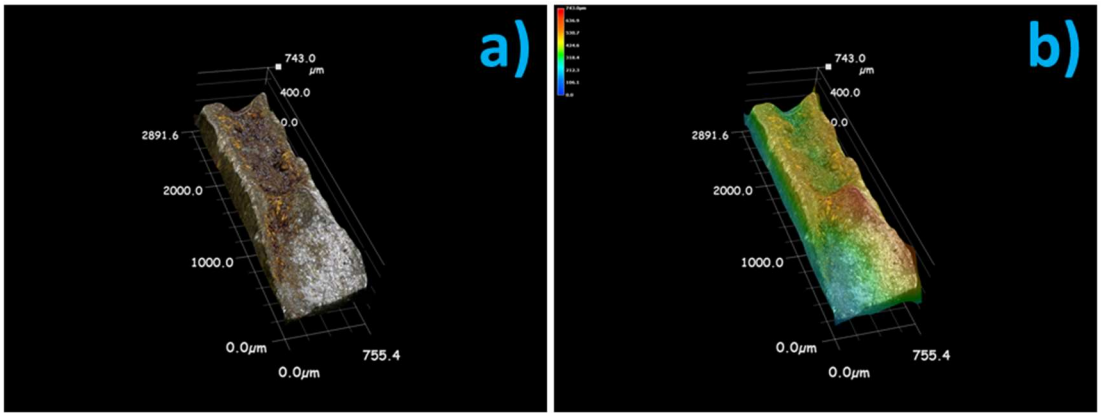

Figure 4.59 a) 3D-optical, and b) topographical images of DP800 specimen tested with 2 hours' hydrogen pre-charging at 10^{-6}/s strain-rate (charging maintained throughout test).

It can be seen from the SEM images in Figure 4.60, that the dominant fracture features for the pre-charged DP800 specimen are dependent on location, with some MVC observed towards the centre of the sample where hydrogen concentration is lowest, albeit with some transgranular (TG) cracks (Figure 4.60 c)). Far greater prominence of 'quasi-cleavage' (QC) facets (d)), and some QC facets alongside some IG cracks (b) and e)), more typically brittle fracture features, are occurring closer to the charging surfaces, where hydrogen concentration is highest.

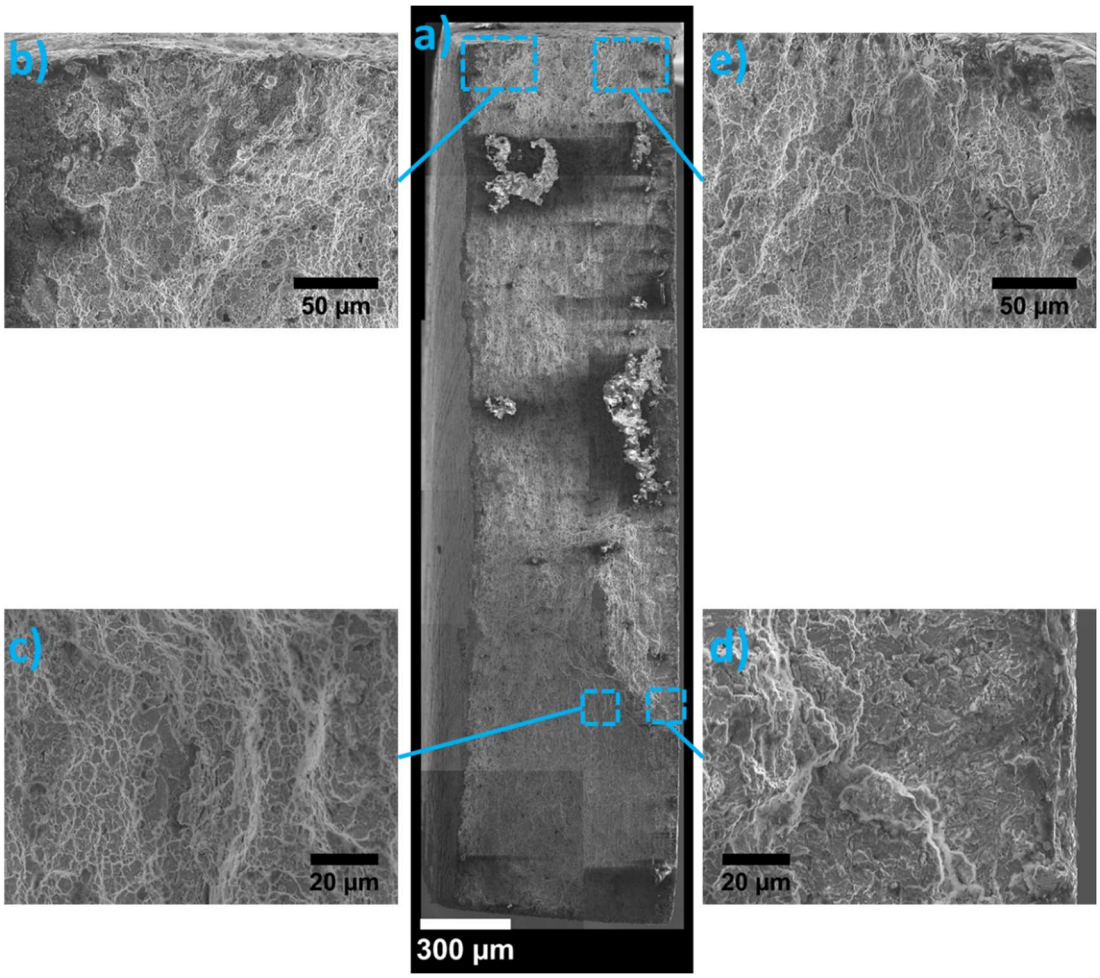

Figure 4.60 SEM images of DP800 specimen tested with 2 hours' hydrogen pre-charging (charging maintained throughout test) at a strain-rate of 10^{-6} at a) 150×, b) and e) 500×, and c) and d) 1000× magnification.

Optical-topographical images of the DP800 specimen tested in the higher strain-rate (10^{-5}/s, *in situ* charging throughout, no pre-charging) condition are shown in Figure 4.61. It can be seen, particularly from the topographical map in Figure 4.61 b), that the fracture angle bears more similarity to that seen in Figure 4.58 for the DP800 specimen tested in the dry condition. The caveat to this is that at the two 'edges' (as it appears in the image), there does appear to be a fracture angle that is perpendicular (normal) to the loading direction, indicative of transverse cracking in the regions in closest proximity to hydrogen charging surfaces.

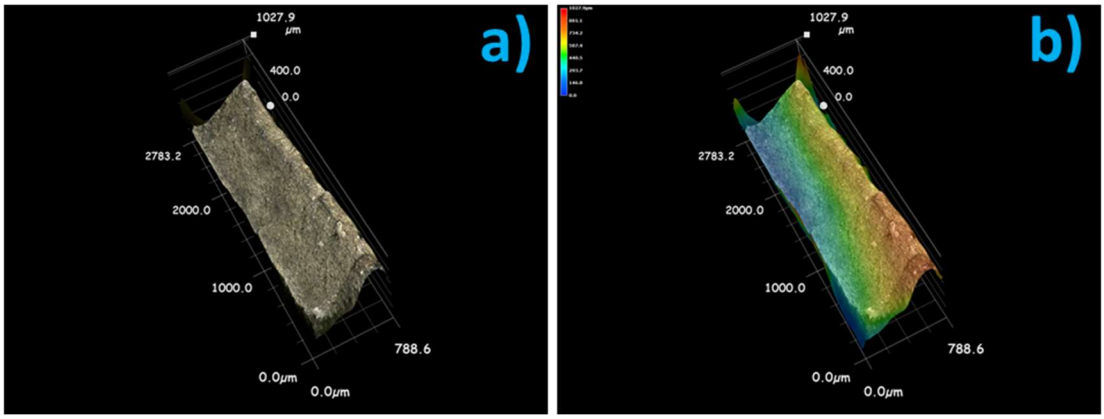

Figure 4.61 a) 3D-optical, and b) topographical images of DP800 specimen tested at 10^{-5}/s strain-rate with simultaneous hydrogen charging (charging maintained throughout test; no pre-charging).

Again, for the SEM images seen in Figure 4.62, it can be seen that around the edges of the fracture surface, adjacent to the charging surfaces, brittle features such as QC (c) and d)), as well as IG cracks (e)) dominate. However, b) shows that there is some transition from a 'fully' brittle mode (QC and IG) to a predominantly ductile mode (MVC + TG), in the region furthest from the charging surface (and hence with the lowest hydrogen concentration).

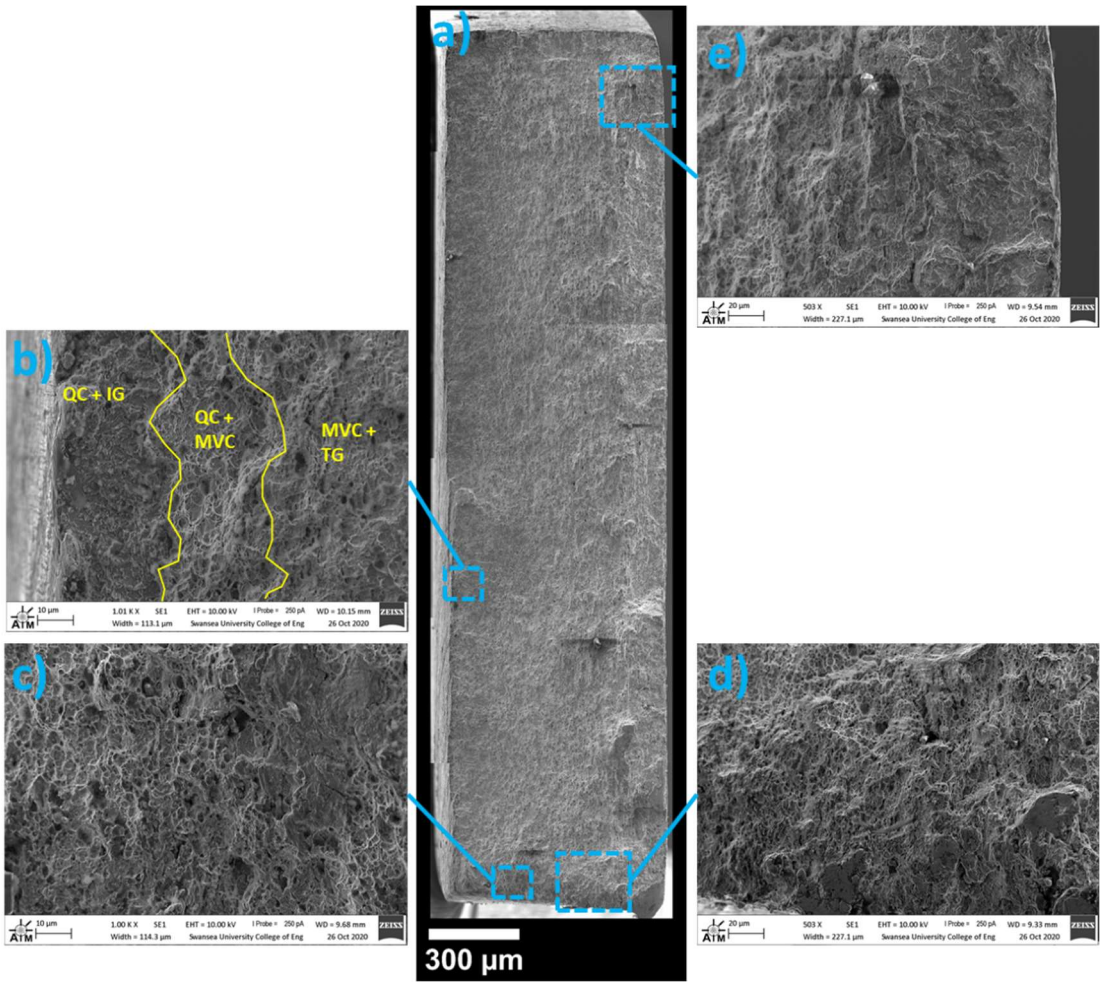

Figure 4.62 SEM images of DP800 specimen tested at a strain-rate of 10^{-5}/s with simultaneous hydrogen charging (charging maintained throughout test; no pre-charging). a) 150×, b) and c) 1000×, and d) and e) 500× magnification.

4.4.3.2 XPF800 Specimens

The topographical image and map in Figure 4.63 a) and b) show that this specimen displayed significant reduction in cross-sectional area (necking). A typical ductile fracture surface is seen for XPF800 tested in air ('dry' condition, 10^{-6}/s strain-rate) in the stitched SEM image in Figure 4.64 a), with clearly visible 'tear ridges' indicative of microvoid coalescence (MVC) in a fine grain size microstructure shown in close up in Figure 4.64 b).

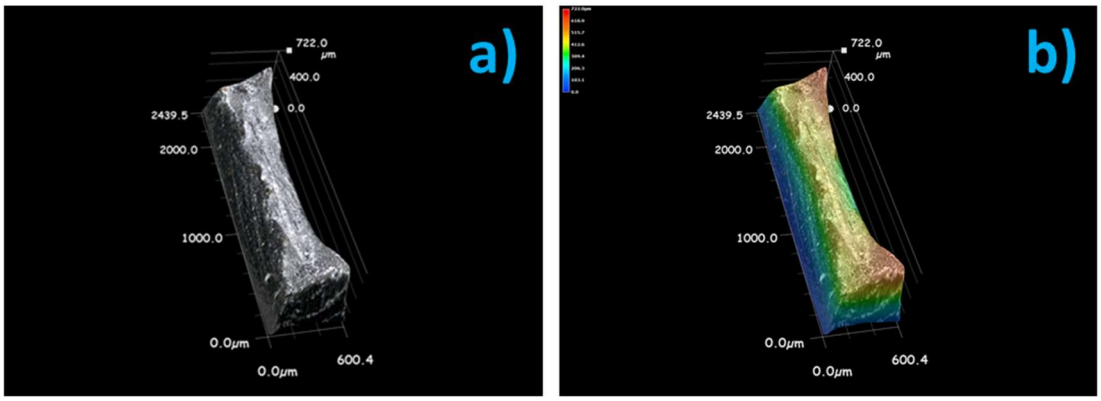

Figure 4.63 a) 3D-optical, and b) topographical images of XPF800 specimen tested in the dry condition (without hydrogen charging) at 10^{-6}/s strain-rate.

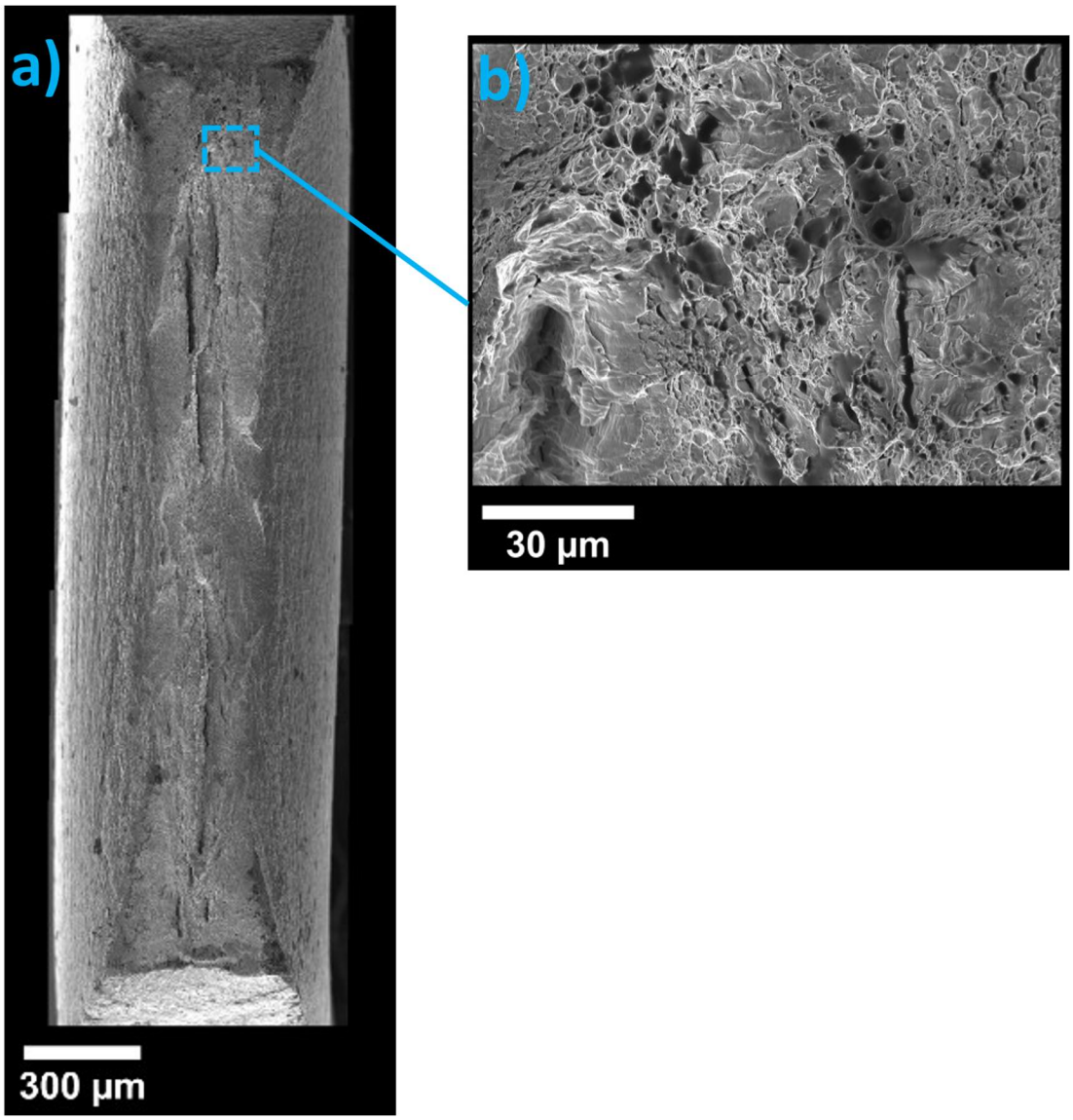

Figure 4.64 SEM images of XPF800 specimen tested in the dry condition (without hydrogen charging) at a strain-rate of 10^{-6}/s at a) 150×, and b) 1000× magnification.

The introduction of hydrogen to the XPF800 specimens when testing at a strain-rate of 10^{-6}/s was seen to lead to a marked difference in fracture surface morphology, with a mix of features present on the surface. The topographical images in Figure 4.65 show that for a test involving 2 hours' pre-charging (with continuing charging throughout the test), whilst a portion of the sample displays a classic 45° fracture, much of the fracture surface is at 90° to the loading direction, indicative of rapid brittle failure.

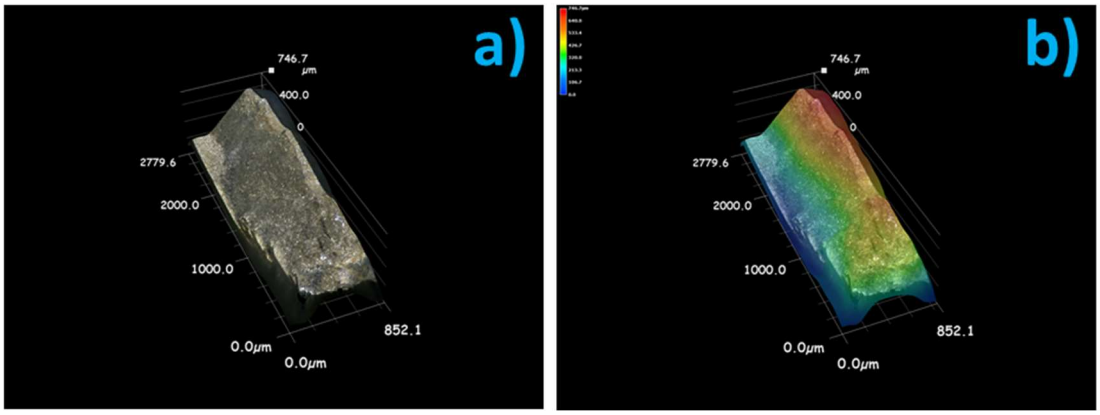

Figure 4.65 a) 3D-optical, and b) topographical images of XPF800 specimen tested with 2 hours' hydrogen pre-charging at 10^{-6}/s strain-rate (charging maintained throughout test).

This mixture of fracture modes is also apparent at higher magnifications displayed in the SEM images of Figure 4.66. Figure 4.66 b) (top left) shows clear intergranular fracture, typical of a brittle fracture mode. Figure 4.66 d) (bottom left) is more mixed, with the intergranular (IG) fracture still present, but evidence of some transgranular (TG) fracture and MVC further towards the middle of the fracture surface, in a region of lowest hydrogen concentration. Again, in Figure 4.66 c) (left middle), the features are mixed, with quasi-cleavage (QC) features (typically associated with brittle failure) interspersed among evidence of MVC.

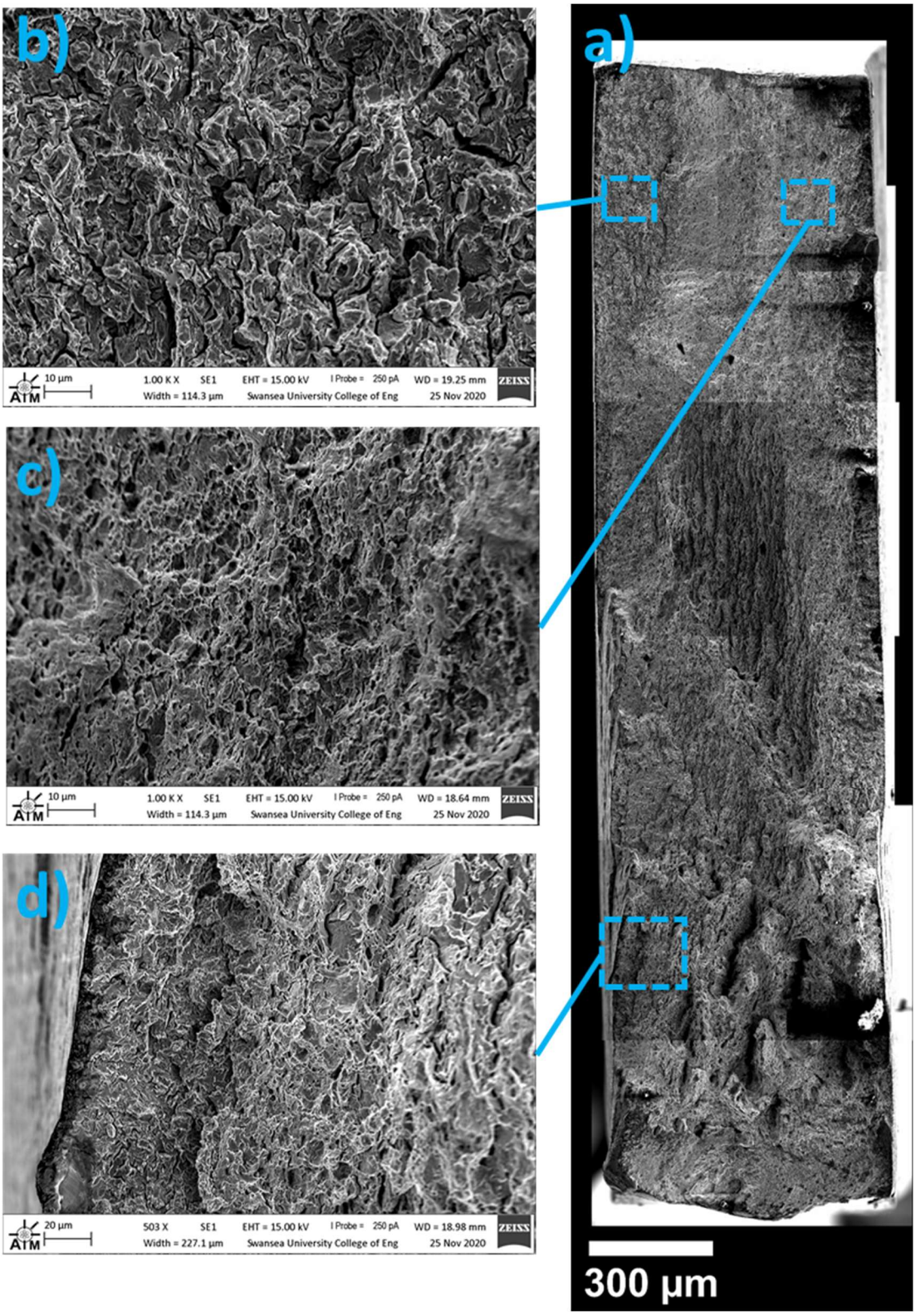

Figure 4.66 SEM images of XPF800 specimen tested with 2 hours' hydrogen pre-charging (charging maintained throughout test) at a strain-rate of 10^{-6}/s at a) 150×, b) and c) 1000×, and d) 500× magnification.

Fracture surfaces for XPF800 samples tested at the higher strain-rate (10^{-5}/s) and with no pre-charging are shown in Figure 4.67 (optical-topographical) and Figure 4.68 (SEM).

Despite the lower charging duration, the mixed modes of fracture seen in the pre-charged specimen are still apparent in the higher strain-rate sample from the optical-topographical images in Figure 4.67, with clear regions of rapid failure particularly notable around the perimeter of the sample.

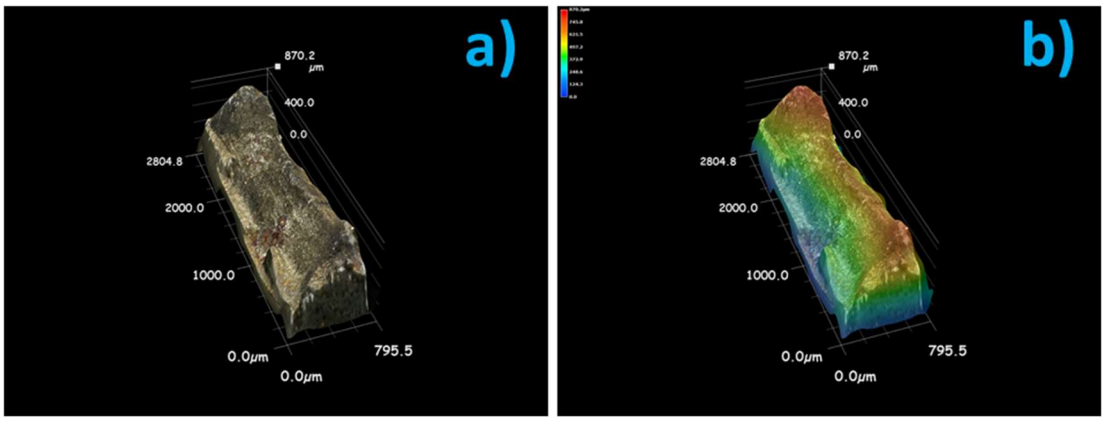

Figure 4.67 a) 3D-optical, and b) topographical images of XPF800 specimen tested at 10^{-5}/s strain-rate with simultaneous hydrogen charging (charging maintained throughout test; no pre-charging).

The composite SEM fractograph of Figure 4.68 a) does however show that the central region (bar the corrosion incurred due to pandemic-induced delay to imaging post-test – samples were stuck in the laboratory as lockdown ensued, and were not retrieved for over 4 months, by which time they had incurred significant corrosion) has much in common with the fracture surface seen for the specimen tested in the dry condition, with evidence of widespread MVC and tear ridges. This region had little time for hydrogen to accumulate. Closer inspection of regions nearer the sample surface, however, show extensive brittle features. The region shown in Figure 4.68 b) shows specific different modes are dominant as we traverse towards the centre of the specimen, with QC and IG facets dominant at the edge (specimen surface), progressing to a mixture of QC and shear microvoids, and finally a region where MVC is dominant. IG cracks alongside QC initiation points are widespread in the 'top-right' corner region of the composite image (Figure 4.68 c)), indicative of rapid failure at this point.

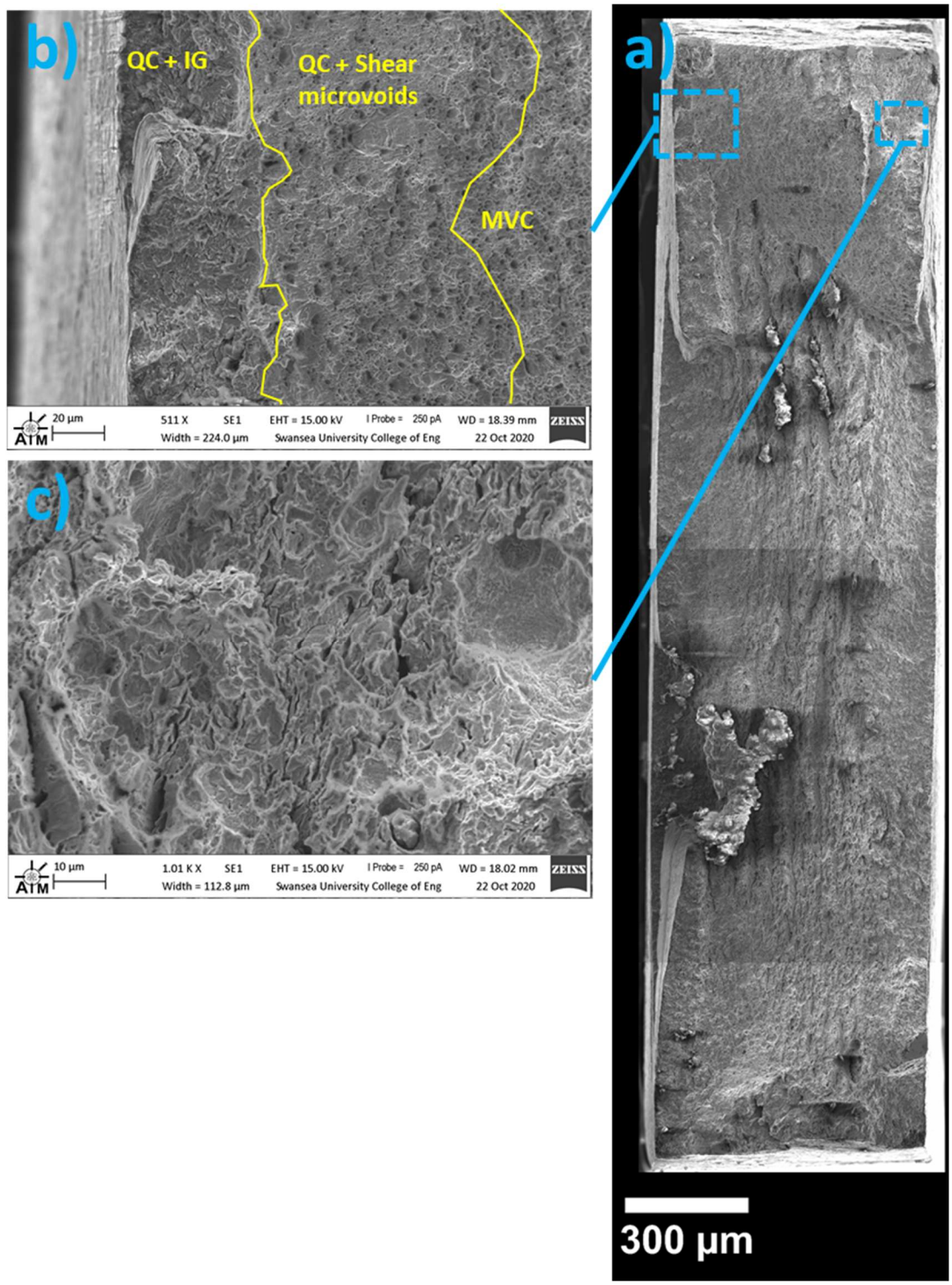

Figure 4.68 SEM images of XPF800 specimen tested at a strain-rate of 10^{-5}/s with simultaneous hydrogen charging (charging maintained throughout test; no pre-charging). a) 150×, b) 500×, and c) 1000× magnification.

4.4.3.3 DP1000 Specimens

The DP1000 specimen tested in the dry condition shows a consistent angle across the fracture, with some evidence of necking towards the 'highest' edge, indicative of a relatively ductile fracture, as seen in the optical-topographical images in Figure 4.69.

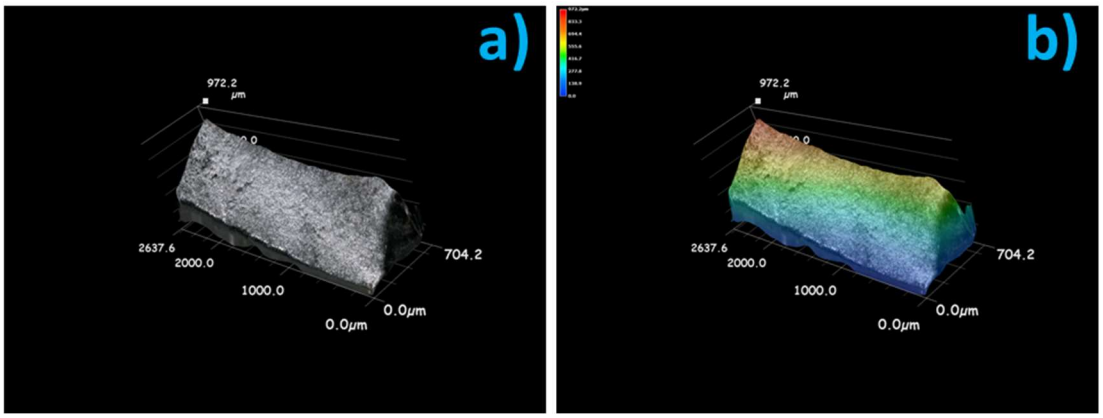

Figure 4.69 a) 3D-optical, and b) topographical images of DP1000 specimen tested in the dry condition (without hydrogen charging) at 10^{-6}/s strain-rate.

Likewise, the composite SEM image shown in Figure 4.70 shows a consistent MVC fracture mode across the fracture surface (not accounting for the contamination visible in the top third of the image), with clear evidence of necking on what is the right edge. No obvious cracking is visible, but none of the visible tear ridges or shear microvoids visible for the dry XPF samples are seen for DP1000, indicative of the different deformation characteristics between these two steel types.

Figure 4.70 SEM image of DP1000 specimen tested in the dry condition (without hydrogen charging) at a strain-rate of 10^{-6}/s at 150× magnification.

For the pre-charged DP1000 specimens, a radical change in the appearance of the fracture surface compared to the dry specimen is observed. Figure 4.71 shows a fracture angle much more perpendicular to the loading direction, as well as a change in the angle across the surface near one edge of the sample.

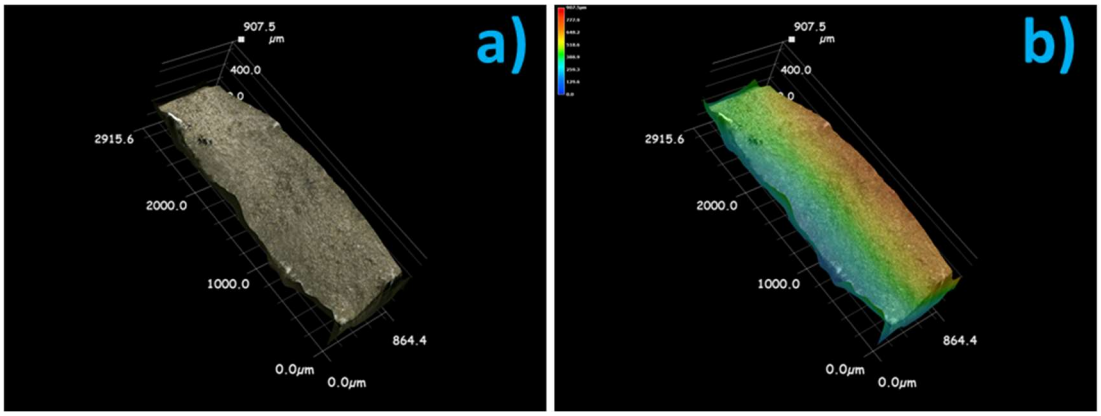

Figure 4.71 a) 3D-optical, and b) topographical images of DP1000 specimen tested with 2 hours' hydrogen pre-charging at 10^{-6}/s strain-rate (charging maintained throughout test).

The SEM images shown in Figure 4.72 demonstrate another mixture of fracture features, with b) and f) showing extensive QC and TG micro-cracks, as well as some larger IG cracks. Towards the centre of the specimen (c)) MVC becomes more apparent, however in this instance there is still some evidence of QC and TG cracks. Further towards the bottom of the image in d) and e), the brittle features become more severe with proliferation of IG and inter-phase (IP) cracks.

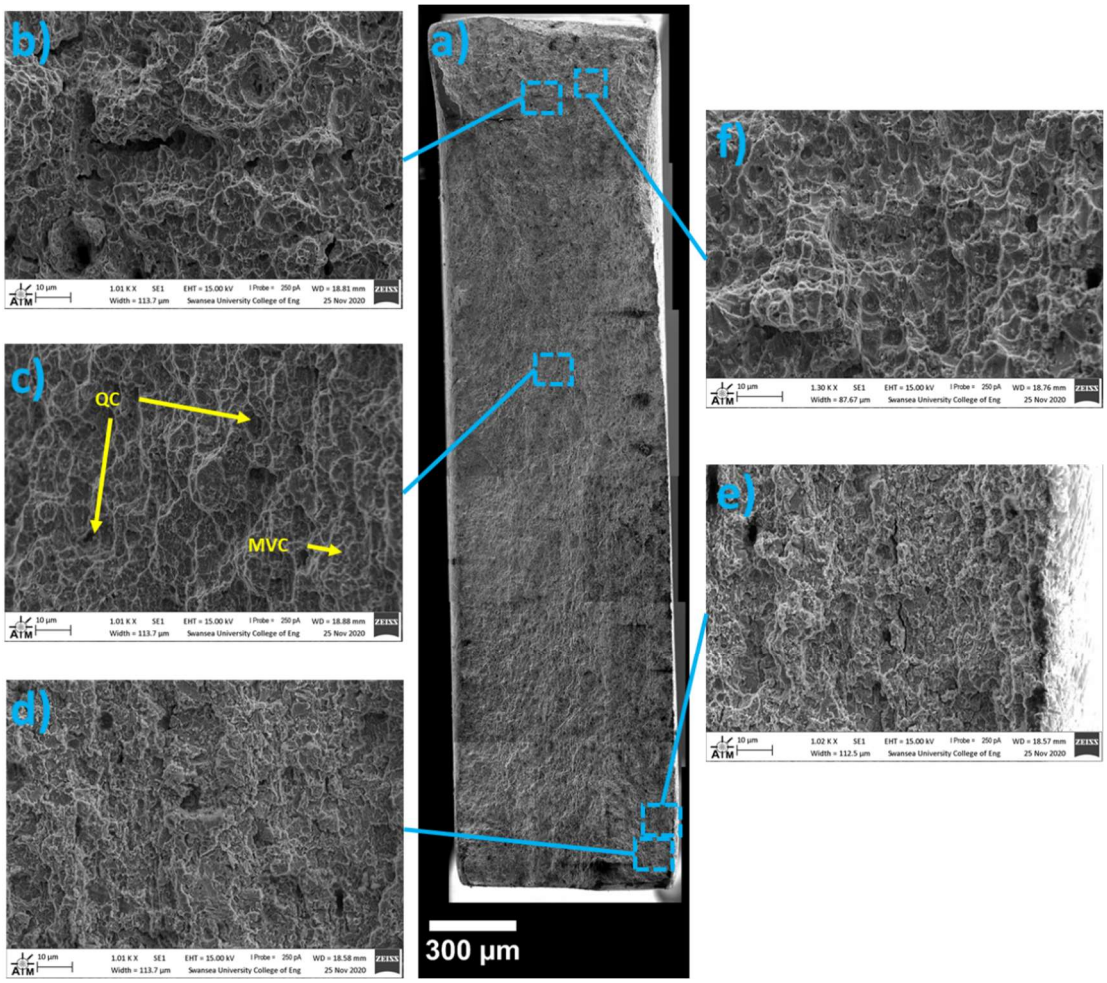

Figure 4.72 SEM images of DP1000 specimen tested with 2 hours' hydrogen pre-charging (charging maintained throughout test) at a strain-rate of 10^{-6}/s at a) 150×, and b) to f) 1000× magnification.

The fracture surface of the charged DP1000 sample (no pre-charging) tested at a strain-rate of 10^{-6}/s showed similar 'macro' features to the sample that had received 2 hours of hydrogen pre-charging. A relatively shallow fracture angle across the surface is observed, transitioning to an even more 'flat' profile towards the leftmost and bottom edges of the image, indicative of rapid failure at these points, and evidenced from the uniformity of the colour in these regions in the profile map of Figure 4.73 b).

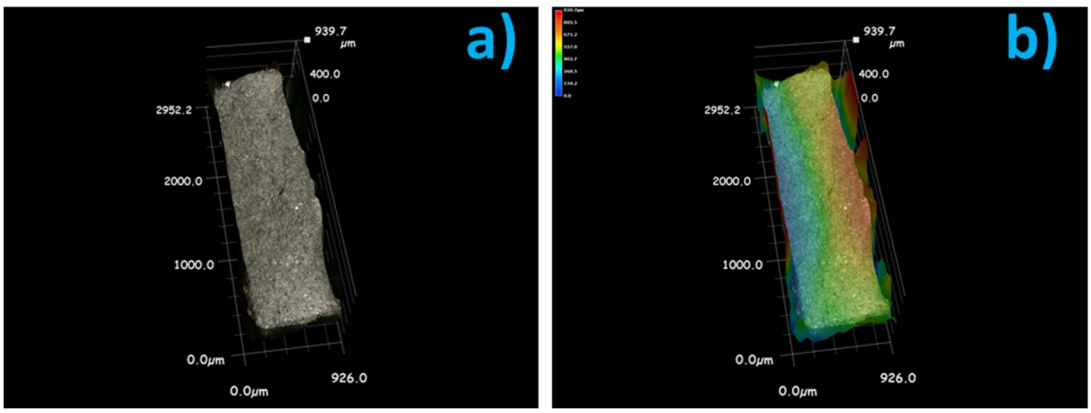

Figure 4.73 a) 3D-optical, and b) topographical images of DP1000 specimen tested at 10^{-6}/s strain-rate with simultaneous hydrogen charging (charging maintained throughout test; no pre-charging).

It can be seen from the SEM images in Figure 4.74 b) and c) that these 'flatter' regions along the left (at charging surface) and bottom of the image (in a region of hydrogen charging from 3 surfaces) have relatively large, smooth facets. The image in b) shows that this larger facet is adjacent to a region of extensive QC facets, as well as some IG cracks (or, more likely inter-phase (IP) cracks). Similarly, the larger facet seen in c) sites in a region of similar features of smaller size. Evidence of MVC or other typically ductile features is absent.

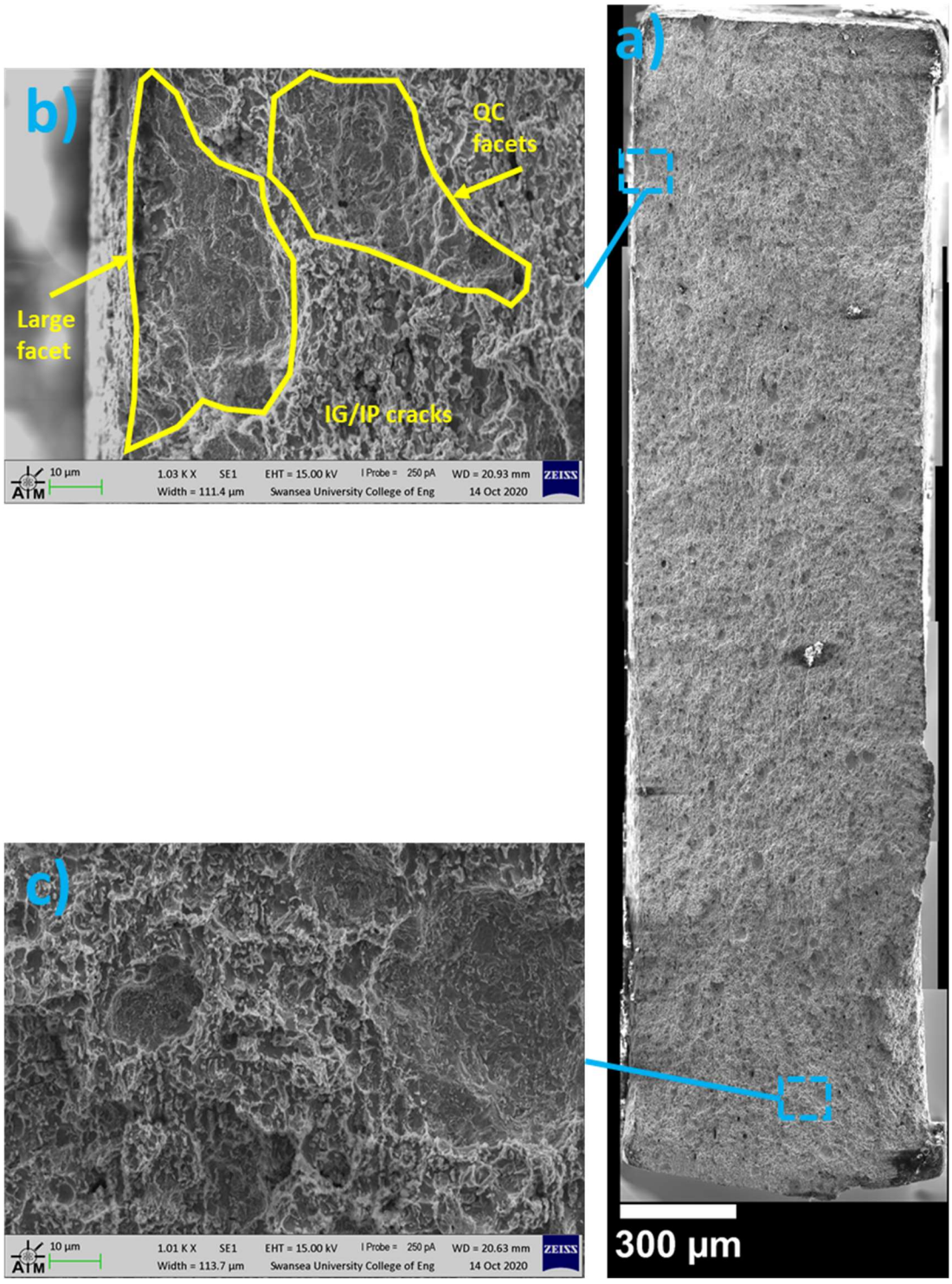

Figure 4.74 SEM images of DP1000 specimen tested at a strain-rate of 10^{-6}/s with simultaneous hydrogen charging (charging maintained throughout test; no pre-charging). a) 150×, b) and c) 1000× magnification.

The macro fracture surface features for the DP1000 tested in the higher strain-rate condition (Figure 4.75) shows a significant transition of angle across the fracture surface, with angles perpendicular to the loading direction at the sample edges, and a

steep gradient along the middle of the sample. This indicates a rapid failure occurring at the sample edges (regions of hydrogen charging at three surfaces), with a more gradual failure at the sample centre, although this region is still not displaying a typically ductile angle lying between 45 – 60° to the loading direction (i.e. it is not in a plane of maximum shear), suggesting that the presence of hydrogen is altering the stress states in different regions of the specimen during the test.

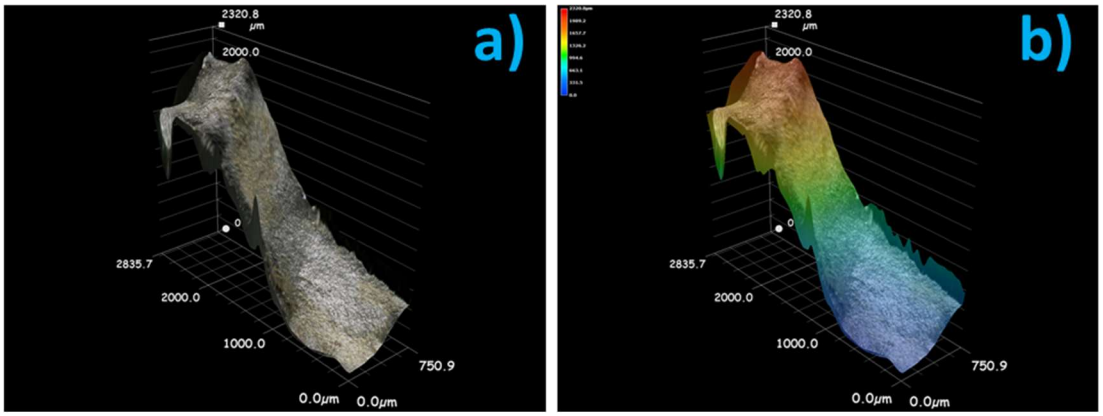

Figure 4.75 a) 3D-optical, and b) topographical images of DP1000 specimen tested at 10^{-5}/s strain-rate with simultaneous hydrogen charging (charging maintained throughout test; no pre-charging).

The SEM image in Figure 4.76 also shows some of the differences in features by location, or distance from the charging surfaces. b) shows IG cracks at the sample edge, and a smooth region of rapid failure adjacent to it. Towards the top-right corner of b), moving further inwards from the charging surfaces, there is evidence of MVC. This is more apparent from c), further towards the centre of the sample, where the dominant feature is MVC, though some QC facets are still apparent and some TG microcracks can be observed along some of the perimeters of the microvoid features. Towards the bottom edge of the image, shown in d), a mixture of features is apparent, with some evidence of MVC overlayed with quite severe IG/IP cracks and QC facets.

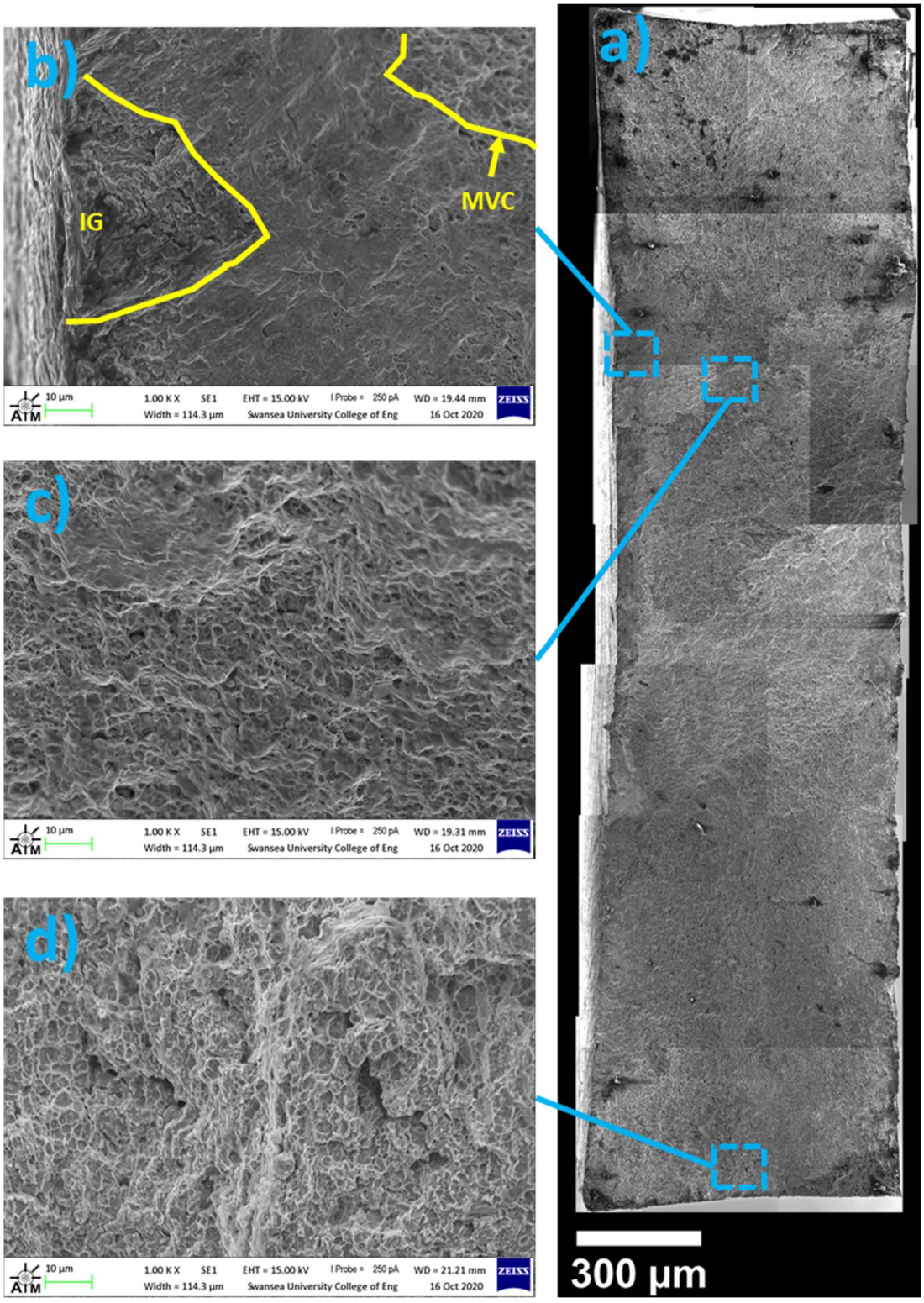

Figure 4.76 SEM images of DP1000 specimen tested at a strain-rate of 10^{-5}/s with simultaneous hydrogen charging (charging maintained throughout test; no pre-charging). a) 150×, b) 500×, and c) 1000× magnification.

4.4.3.4 XPF1000 Specimens

Similar to the fracture surface observed for XPF800, the XPF1000 specimen tested in the 'dry' condition (10^{-6}/s strain-rate) shows clear reduction in cross-sectional area (necking), as seen in the optical-topographical images of Figure 4.77.

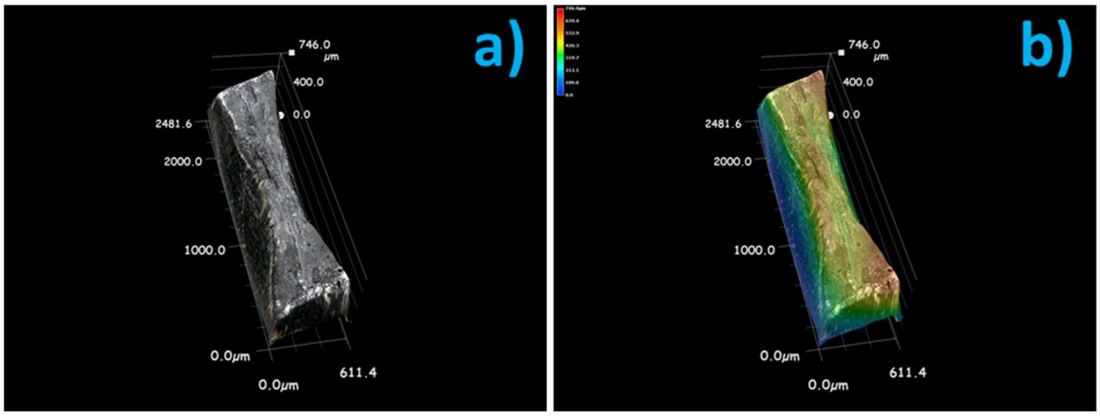

Figure 4.77 a) 3D-optical, and b) topographical images of XPF1000 specimen tested in the dry condition (without hydrogen charging) at 10^{-6}/s strain-rate.

The SEM images in Figure 4.78 show numerous tear-ridges (b)) and shear microvoids (c)) indicative of ductile fracture in fine-grained or significantly deformed material, as well as the more typical MVC (d)) observed for ductile fracture more widely. Again, the significant necking is readily apparent from the composite image in a).

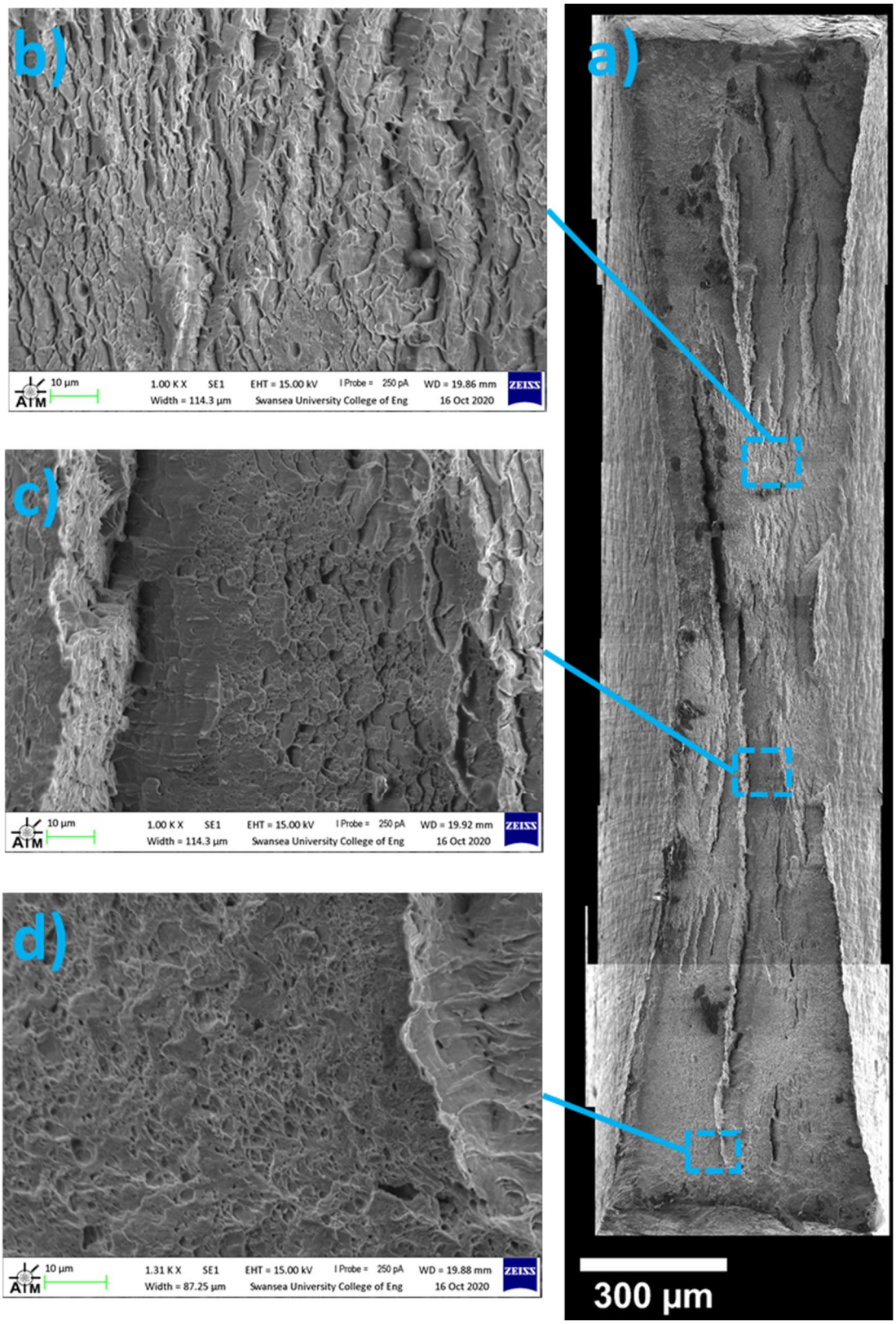

Figure 4.78 SEM images of XPF1000 specimen tested in the dry condition (without hydrogen charging) at a strain-rate of 10^{-6}/s at a) 200×, and b) to d) 1000× magnification.

The pre-charged XPF1000 specimen shows significant divergence in fracture features from that tested in the dry condition, with no necking apparent from the optical-topographical images (Figure 4.79), and significantly shallower fracture angles suggesting a much more ‘brittle’ fracture at the macro scale.

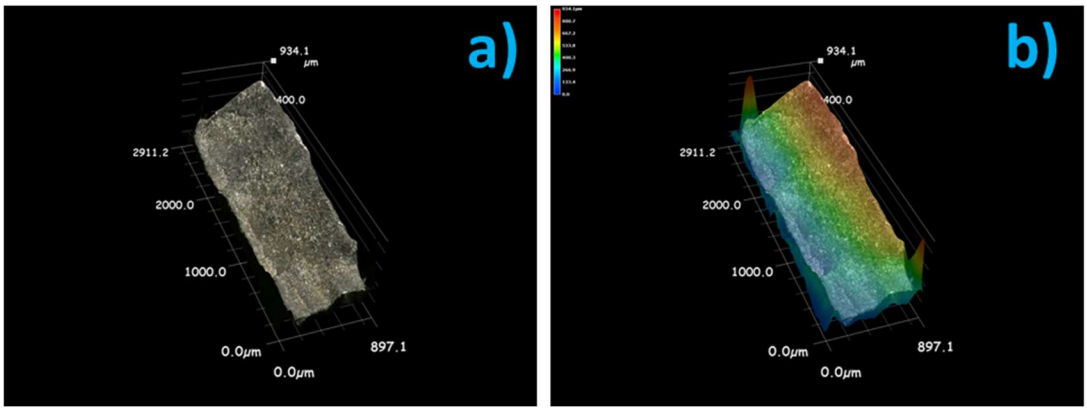

Figure 4.79 a) 3D-optical, and b) topographical images of XPF1000 specimen tested with 2 hours’ hydrogen pre-charging at 10^{-6}/s strain-rate (charging maintained throughout test).

The SEM images in Figure 4.80 shows that whilst there is still some evidence of ductile features, such as tear ridges (b)), these are interspersed among widespread QC facets. Furthermore, it can be seen in c) that adjacent to the charging surface is the presence of IG cracks, a significant departure from the fracture modes observed for the dry sample.

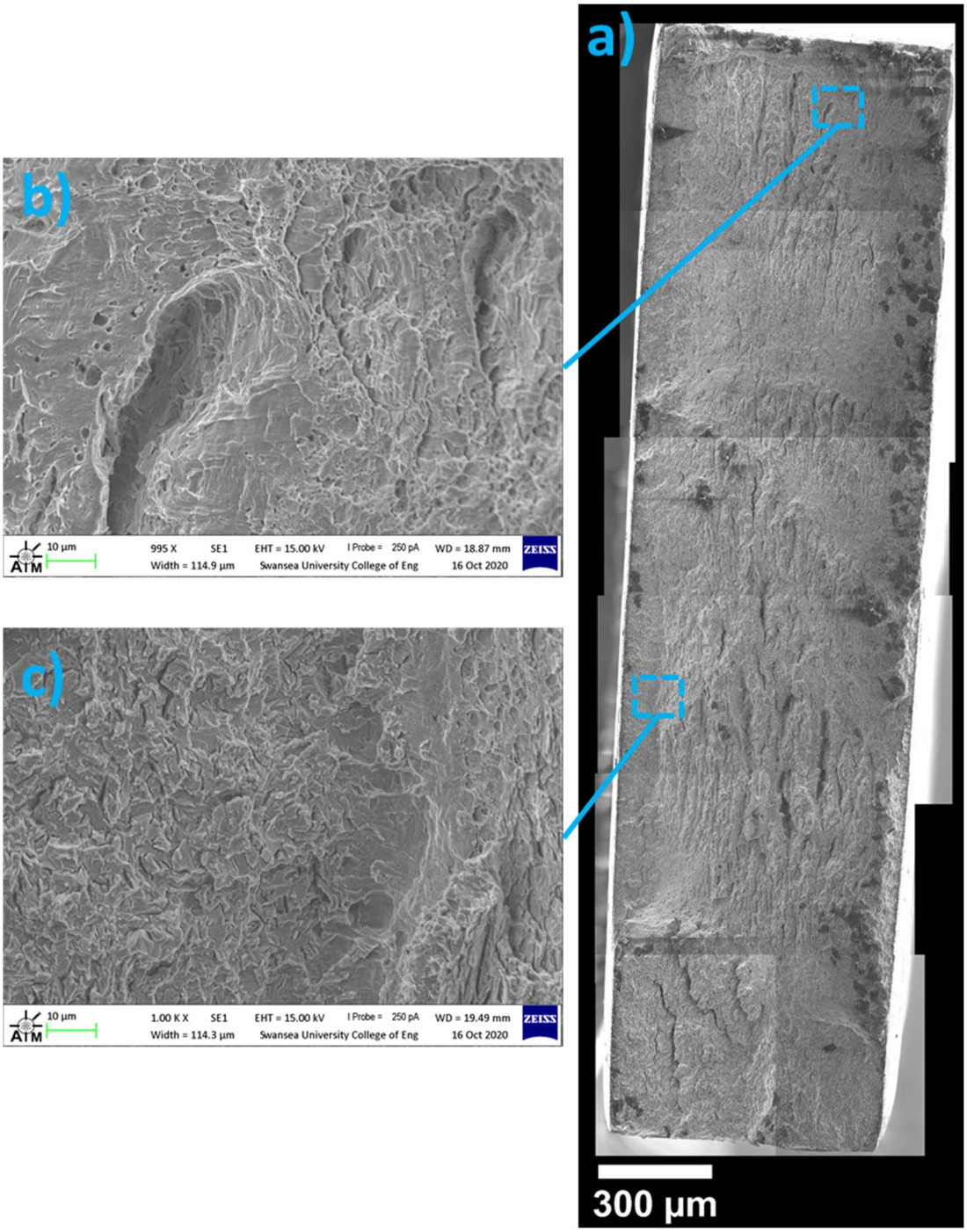

Figure 4.80 SEM images of XPF1000 specimen tested with 2 hours' hydrogen pre-charging (charging maintained throughout test) at a strain-rate of 10^{-6}/s at a) 150×, and b) and c) 1000× magnification.

The XPF1000 charged specimen (without 2 hours' pre-charging) has somewhat chaotic fracture features at the macro scale as seen in Figure 4.81, with multiple fracture angles across the surface, and clear evidence of rapid failure adjacent to the charging surfaces.

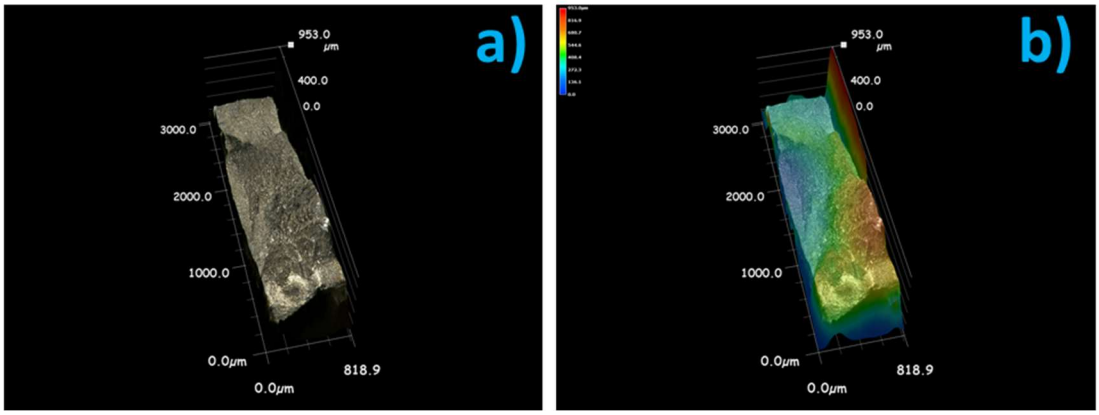

Figure 4.81 a) 3D-optical, and b) topographical images of XPF1000 specimen tested at 10^{-6}/s strain-rate with simultaneous hydrogen charging (charging maintained throughout test; no pre-charging).

The composite SEM image in Figure 4.82 a) further illustrates the complexity of the fracture surface, with some highly localised reduction in cross-sectional area visible, but clear transverse cracks even at this relatively low magnification.

The large crack visible in b) is present in a region of TG cracking and QC facets, yet this is one of the regions which showed some evidence of necking. Likewise, c) shows a small amount of shear microvoids among widespread QC facets, whereas d) shows more extensive shear microvoids with little evidence of more brittle fracture features. The region shown in Figure 4.82 e) shows severe brittle IG cracking among extensive QC facets, with no evidence of any ductile fracture features.

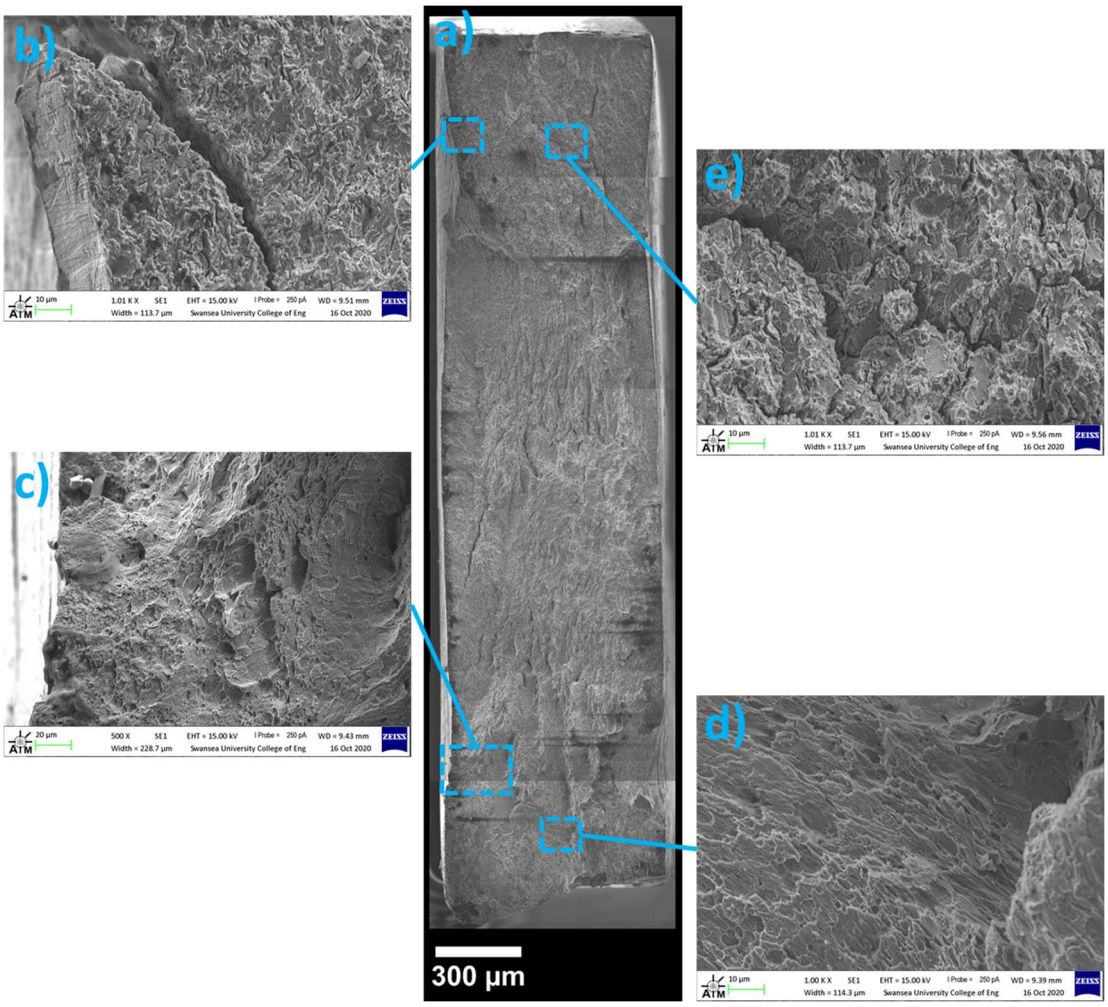

Figure 4.82 SEM images of XPF1000 specimen tested at a strain-rate of 10^{-6}/s with simultaneous hydrogen charging (charging maintained throughout test; no pre-charging). a) 150×, b) 1000× c) 500×, and d) and e) 1000× magnification.

At the higher strain-rate (10^{-5}/s), XPF1000 retains a mixture of fracture features, with Figure 4.83 showing that there is less proliferation of fracture angles in such highly-localised regions than for the 'charged' specimen shown in Figure 4.81. Instead, a clear 'ridge' is seen to extend across approximately half the transverse length (actually parallel to the longer axis of the image), with a planar region perpendicular to the loading direction apparent at the bottom of the images indicative of a rapid fracture at this point. Furthermore, a distinct 'pillar' feature at the right of the images is shown.

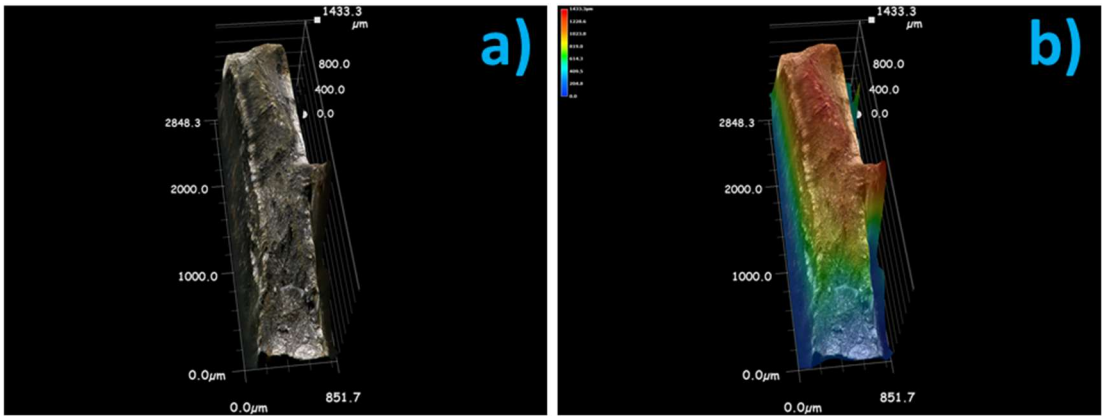

Figure 4.83 a) 3D-optical, and b) topographical images of XPF1000 specimen tested at 10^{-5}/s strain-rate with simultaneous hydrogen charging (charging maintained throughout test; no pre-charging).

The composite image shown in Figure 4.84 a) shows more widespread evidence of necking than seen for the charged specimen shown in Figure 4.82, although this is clearly not as extensive as for the dry condition (e.g. Figure 4.78 a)), demonstrating that hydrogen is still having a significant effect upon the fracture mode. This juxtaposition is striking in Figure 4.84 d), where evidence of several local, stepwise, necking 'events' is apparent, whilst the dominant features in this region are actually IG cracks. The region highlighted in c) from the central portion of the specimen where hydrogen concentration will be lowest shows more typically ductile shear microvoids as well as a tear ridge at the right of the image. Figure 4.84 b) shows TG cracks alongside some QC facets, with some large ridges suggesting a stepwise deformation in this region, similar to that seen with the necking events in d).

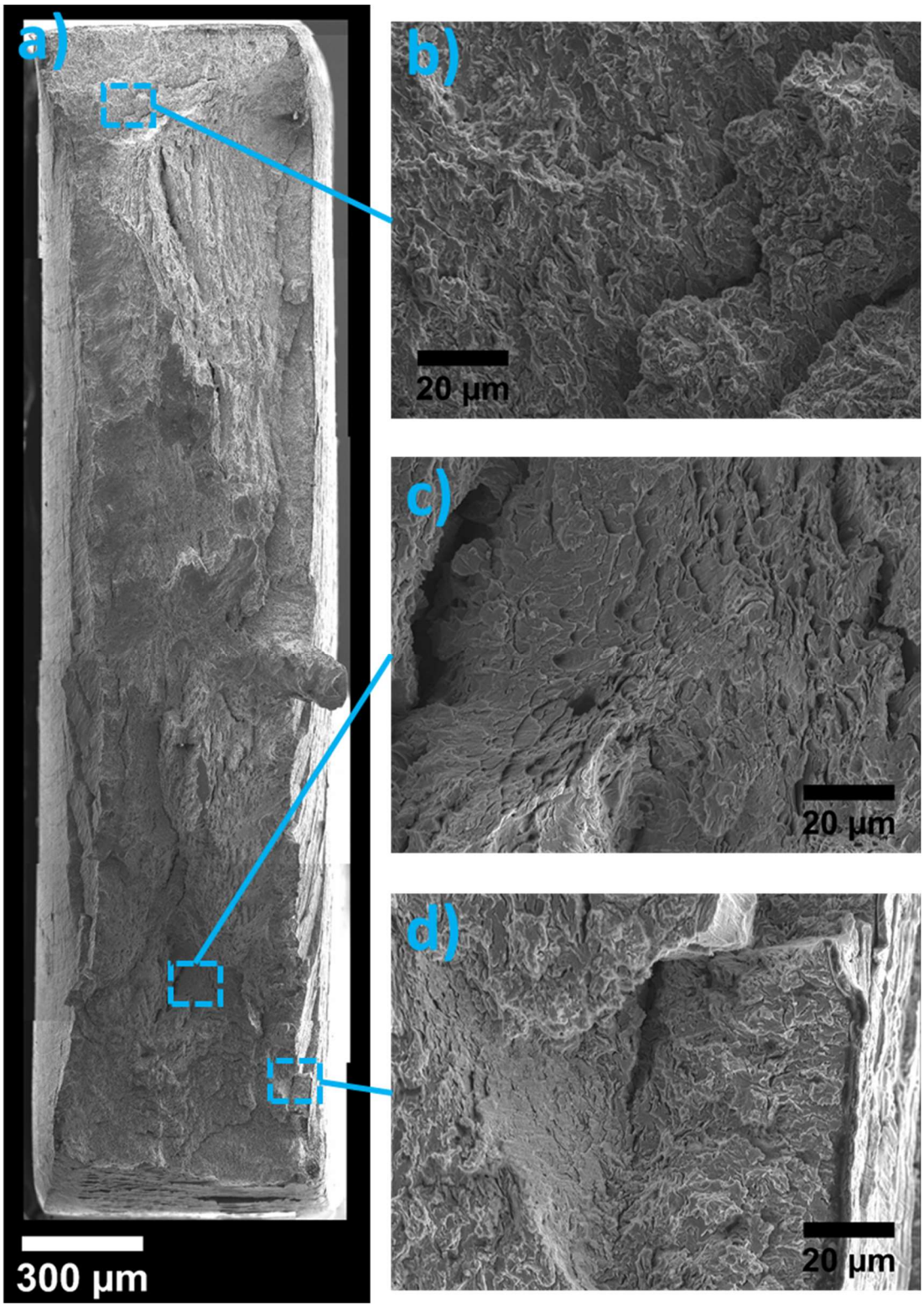

Figure 4.84 SEM images of XPF1000 specimen tested at a strain-rate of 10^{-5}/s with simultaneous hydrogen charging (charging maintained throughout test; no pre-charging). a) 150×, and b) and c) 1000× magnification.

4.4.3.5 22MnB5 (900C) Specimens

The optical-topographical images of Figure 4.85 show the macro-scale fracture features for a fully-martensitic 22MnB5 sample (heat-treated at 900C) tested in the dry condition. It can be seen that across most of the width of the specimen there is a roughly 45° fracture angle, typical of a ductile mode of failure. There is a change in this angle towards the left side of the image, though this also represents a 45° fracture angle to the loading direction, but is indicative of a transition in the nature of the stresses present in the sample during the test.

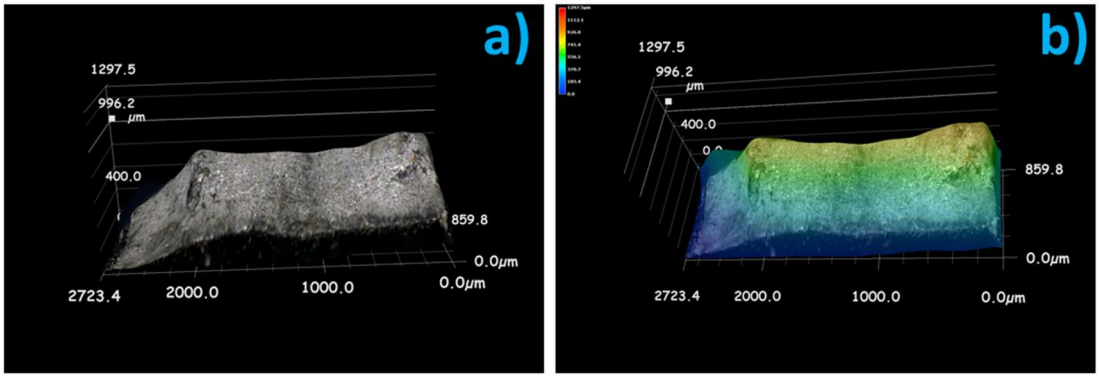

Figure 4.85 a) 3D-optical, and b) topographical images of 22MnB5 (900C) specimen tested in the dry condition (without hydrogen charging) at 10^{-6}/s strain-rate.

Figure 4.86 shows SEM images of the same fracture surface. Some evidence of necking is present on the left-hand side of the compound image of a), though this is not extensive as failure occurred after only ~ 4% elongation after reaching the ultimate tensile stress. The dominant fracture feature across the surface is MVC with some evidence of microvoid shearing, illustrated by way of example with a closer view of the region in b). No typically 'brittle' fracture features were observed in this hydrogen-free condition.

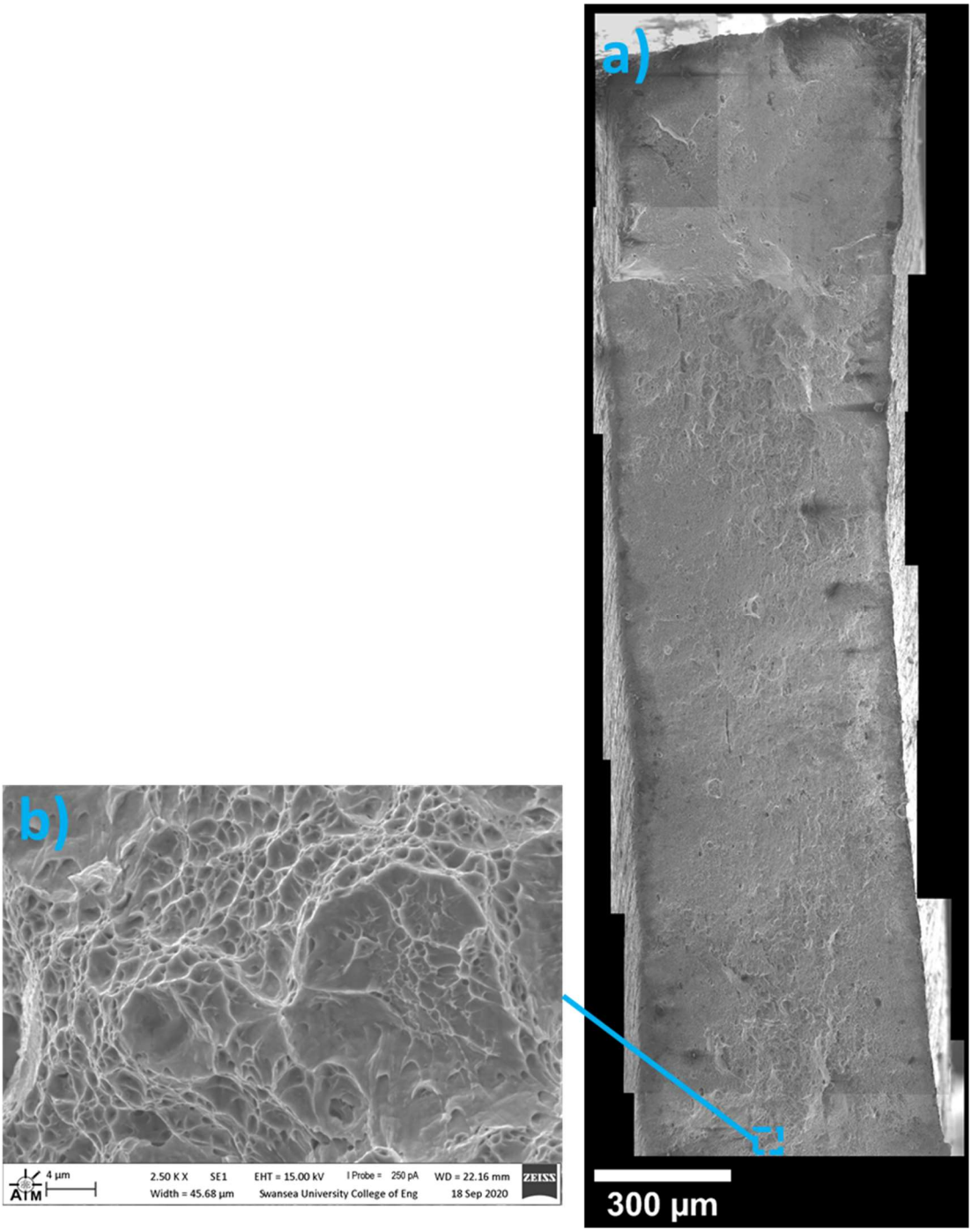

Figure 4.86 SEM images of 22MnB5 (900C) specimen tested in the dry condition (without hydrogen charging) at a strain-rate of 10^{-6}/s at a) 150×, and b) 2500× magnification.

For the pre-charged 22MnB5 specimen, the optical-topographical images in Figure 4.87 show a fracture angle much more perpendicular to the loading direction than observed for the dry specimen, indicative of rapid fracture across the width of the sample.

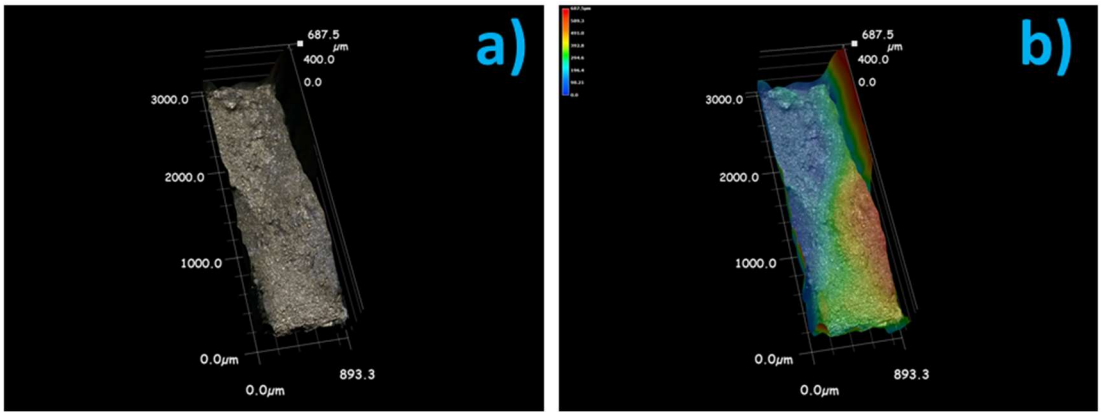

Figure 4.87 a) 3D-optical, and b) topographical images of 22MnB5 (900C) specimen tested with 2 hours' hydrogen pre-charging at 10^{-6}/s strain-rate (charging maintained throughout test).

The SEM images of the pre-charged 22MnB5 specimen in Figure 4.88 show a mixture of fracture features in different locations across the fracture surface. The compound image in a) shows a clear direction of rapid crack propagation from the 'top-right' of the image in the form of a region that appears as a localised 'depression'. Conversely, the selected region in b) shows features that are not dissimilar to those observed for the dry 22MnB5 sample, with MVC dominant. However, closer inspection of these features reveals the presence of TG microcracks that indicate that even in this region fracture was not wholly ductile in nature. The inset images in c), d), and e) all show significant IG cracking along prior austenite grain boundaries, evidence of highly brittle fracture behaviour due to weakening of grain boundaries by hydrogen accumulation to the extent that this mode of localised failure becomes energetically favourable compared to intragranular cracking or slip-based mechanisms.

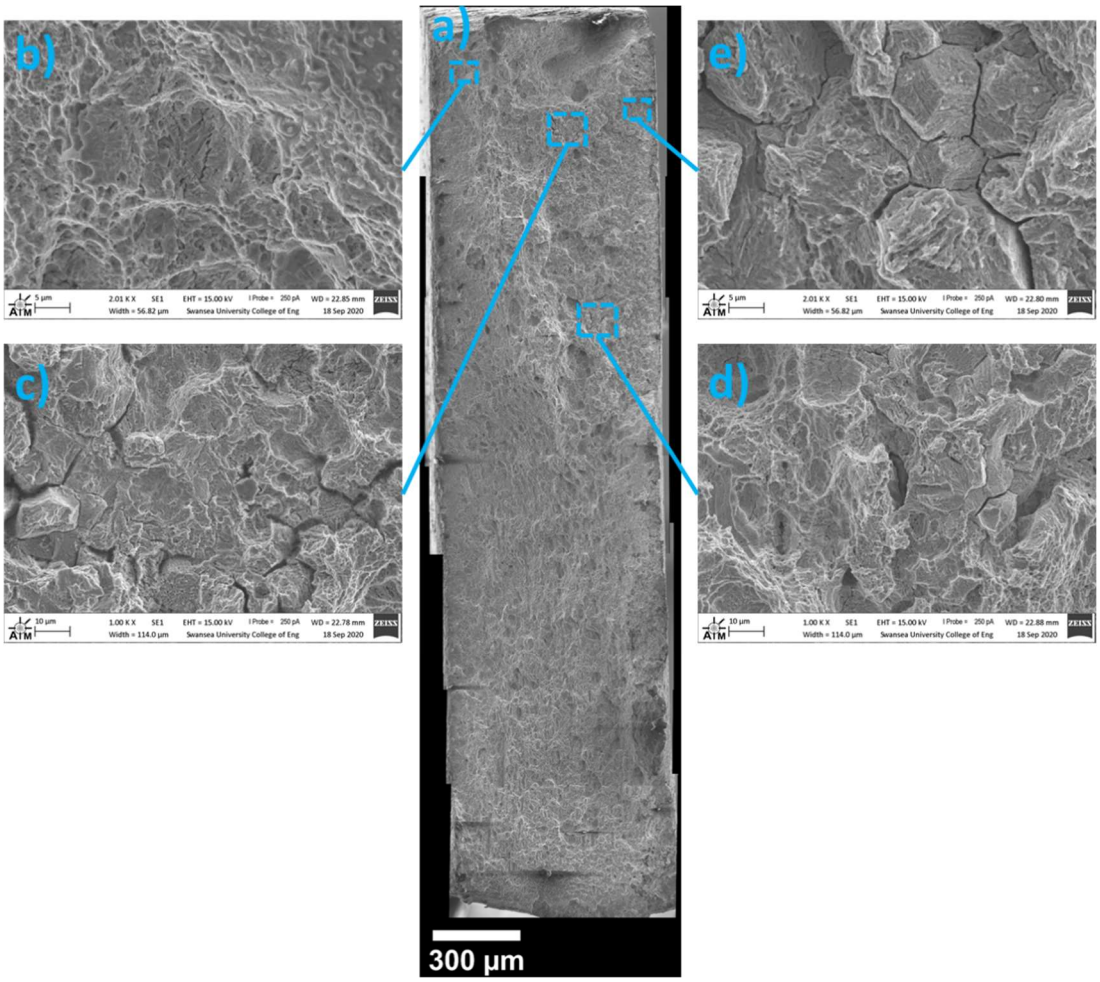

Figure 4.88 SEM images of 22MnB5 (900C) specimen tested with 2 hours' hydrogen pre-charging (charging maintained throughout test) at a strain-rate of 10^{-6}/s at a) 150×, b) and e) 2000×, and c) and d) 1000× magnification.

The optical-topographical images of the 22MnB5 charged specimen tested at 10^{-6}/s without 2 hours' pre-charging shown in Figure 4.89 display a clearly defined ridge, roughly along the centreline of the specimen. To the left side of this ridge the macro features of this fracture surface appear to show a consistent fracture angle of ~ 45° found typically in ductile failure modes. To the right side of the ridge lies a region that has a fracture angle much more perpendicular to the loading direction, with relatively large crater-like features indicative of rapid failure in this region.

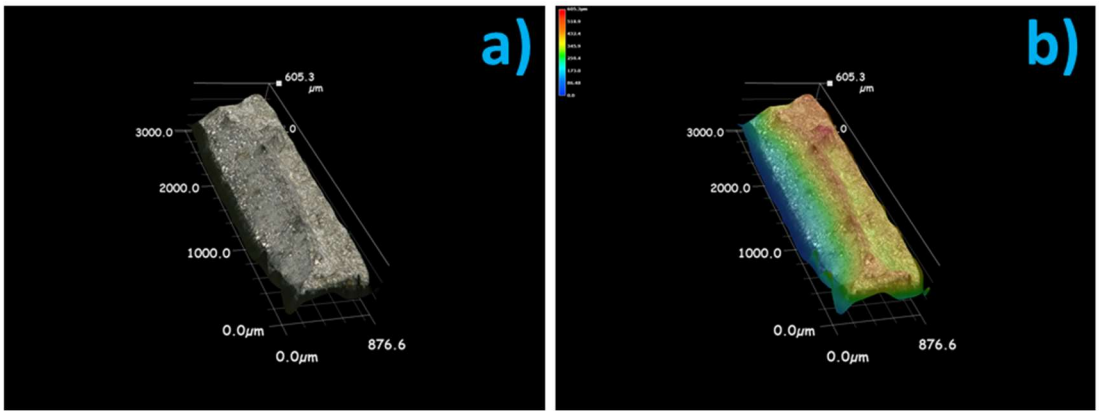

Figure 4.89 a) 3D-optical, and b) topographical images of 22MnB5 (900C) specimen tested at 10^{-6}/s strain-rate with simultaneous hydrogen charging (charging maintained throughout test; no pre-charging).

The apparent differences between these regions are even more clearly demarked in the SEM image in Figure 4.90 a), where even at the relatively low magnification of 200×, widespread cracking is readily-apparent within the 'right' region of the image, including one crack network that appears to span the whole width of the sample (top-to-bottom in the image, indicated by the yellow arrows), transverse to the loading direction. Within this region, widespread IG cracks (e) and f)) and QC facets (d)) can be seen.

To the 'left' side, more typically ductile MVC features can be seen in c), however in the region adjacent to the specimen surface highlighted in b), more evidence of QC facets can be seen amongst the dimpled features that characterise MVC.

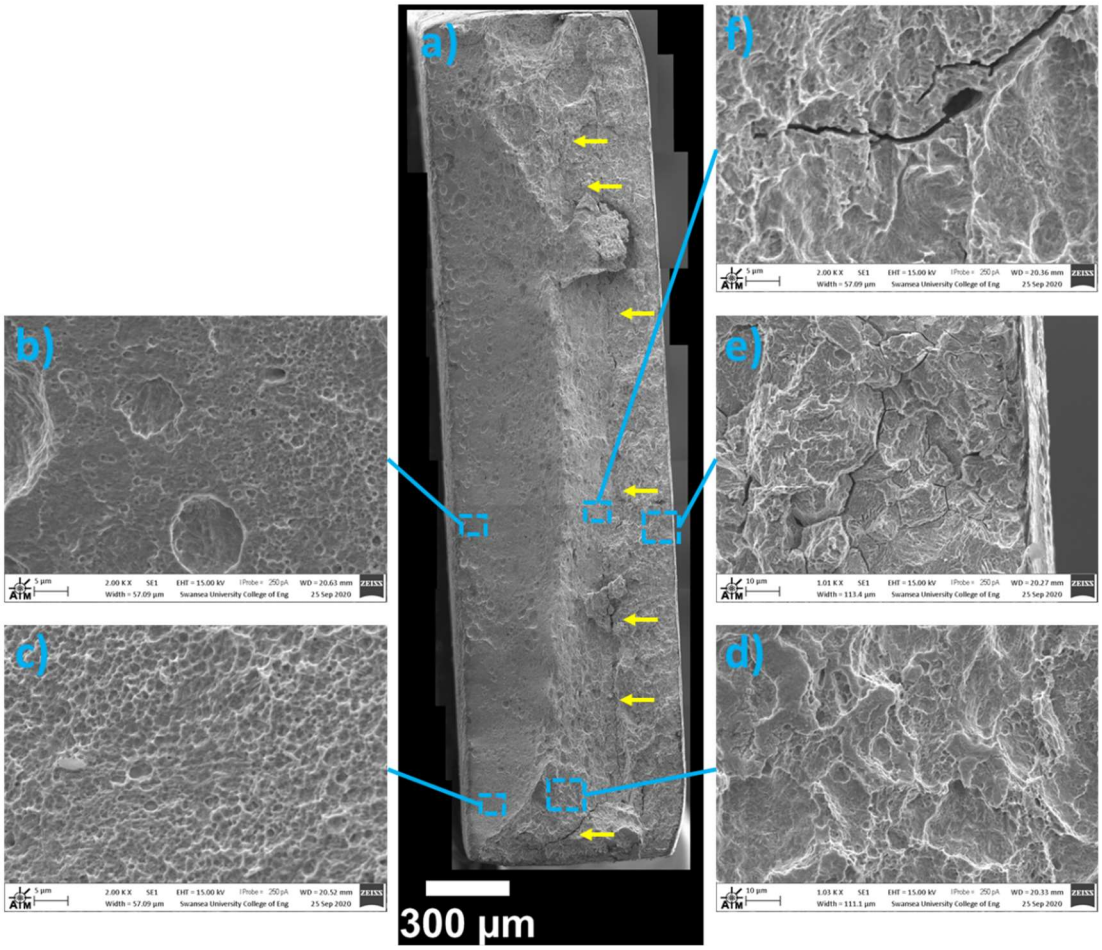

Figure 4.90 SEM images of 22MnB5 (900C) specimen tested at a strain-rate of 10^{-6}/s with simultaneous hydrogen charging (charging maintained throughout test; no pre-charging). a) 150×, b), c) and f) 2000×, and d) and f) 1000× magnification

The charged specimen strained at a rate of 10^{-5}/s has a somewhat complex fracture surface topography, as seen in Figure 4.91. Fracture angles appear to alter rapidly across the fracture surface, with little consistency apart from a small region adjacent to one edge of the sample (towards the bottom of the images), which appears to be a region of rapid failure characterised by a fracture angle ~ 90° to the loading direction.

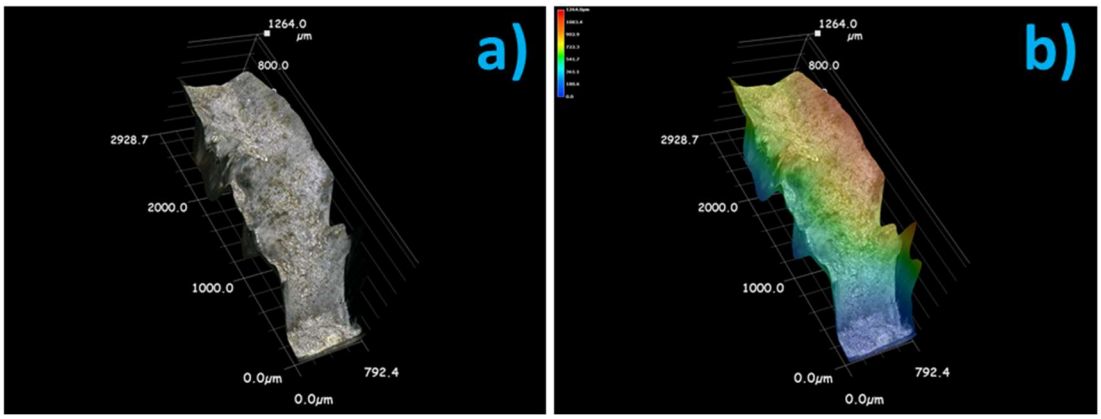

Figure 4.91 a) 3D-optical, and b) topographical images of 22MnB5 (900C) specimen tested at 10^{-5}/s strain-rate with simultaneous hydrogen charging (charging maintained throughout test; no pre-charging).

This apparent complexity is also visible in the microscopic features seen in the SEM images in Figure 4.92. The transitions in topography seen in Figure 4.91 are still clearly apparent within the stitched image of the whole fracture surface in a). Furthermore, large cracks are clearly visible extending from the charging surface across the sample in a direction between transverse and normal to the loading direction, one of which is highlighted by yellow arrows. As with the 'charged' condition, these large cracks are considered to have contributed to, but not caused, the failure of the specimen, and the 'step-wise' character of the cracks indicate that propagation was not instantaneous, potentially indicative of a plasticity-based mechanism.

In the central region highlighted in b), MVC is dominant, similar to the features seen across the surface for the dry 22MnB5 specimen strained at a rate of 10^{-6}/s. Some MVC features are also still visible as we move away from the charging surface in the region highlighted in c), however at the charging surface the dominant features are IG cracks along prior austenite grain boundaries. Regions highlighted in d) and e) show the features apparent as the large crack originating at the circled area propagates across the specimen. In d), it can be seen that there is still widespread evidence of MVC, particularly on the 'lower' side of the crack. On the 'upper' side of the crack, however, is a small region of QC facets, indicating that fracture in this region was not in a straightforward 'ductile' or 'brittle' fashion. In e), the crack appears to propagate through a region where MVC is dominant, though closer inspection shows that the crack is progressing via intergranular means.

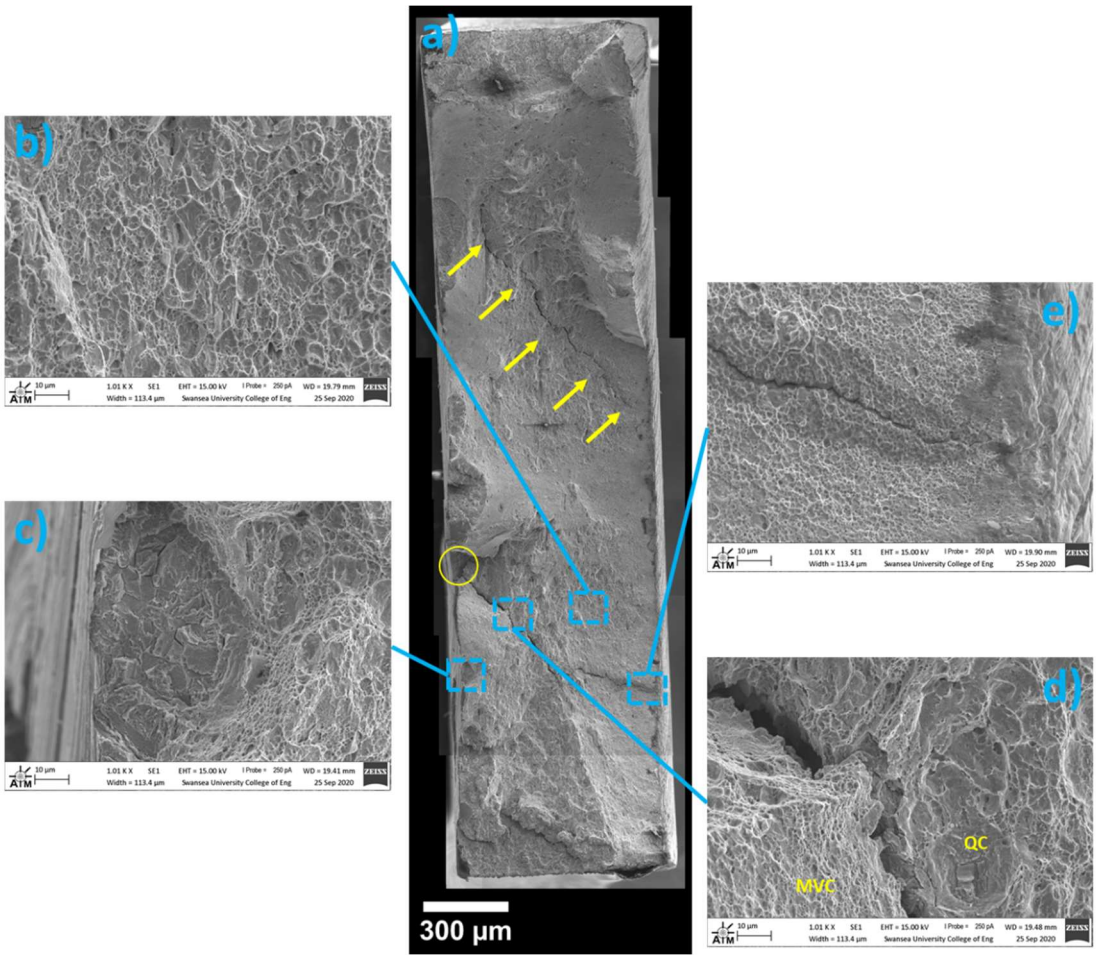

Figure 4.92 SEM images of 22MnB5 (900C) specimen tested at a strain-rate of 10^{-5}/s with simultaneous hydrogen charging (charging maintained throughout test; no pre-charging). a) 150×, and b) to e) 1000× magnification.

4.4.3.6 27MnB5+Nb (900C) Specimens

Figure 4.93 shows the topographical characteristics of the fracture surface of a 27MnB5+Nb specimen tested at a strain-rate of 10^{-6}/s in the dry condition (absence of hydrogen charging). Apart from small, isolated protrusions visible at the edges of the specimen, the topography of the sample is consistent, with the typically ductile fracture angle of 45° to the loading direction apparent across the width of the sample (along the transverse direction), though this reaches a minimum about one-third of the way in from the sample edge at the top of the image as seen in Figure 4.93, where it reverses direction.

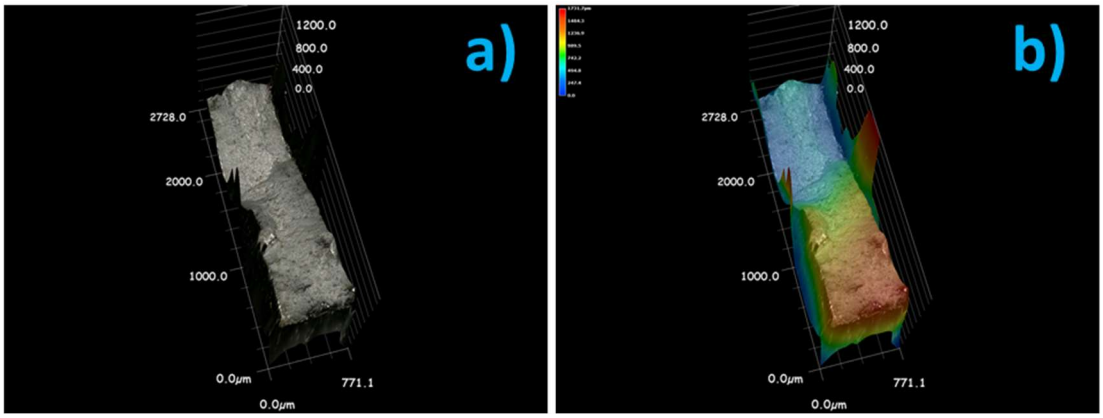

Figure 4.93 a) 3D-optical, and b) topographical images of 27MnB5+Nb (900C) specimen tested in the dry condition (without hydrogen charging) at 10^{-6}/s strain-rate.

Each of the SEM images in Figure 4.94 show the dominance of MVC across the fracture surface, plus some evidence of a reduction in cross-sectional area, particularly in the middle portion of the sample. Caveats to this include a region of shear fracture (SF) indicated in c), plus some cleavage facets interspersed among MVC dimples most apparent in d), often seen to centre around precipitates (or inclusions).

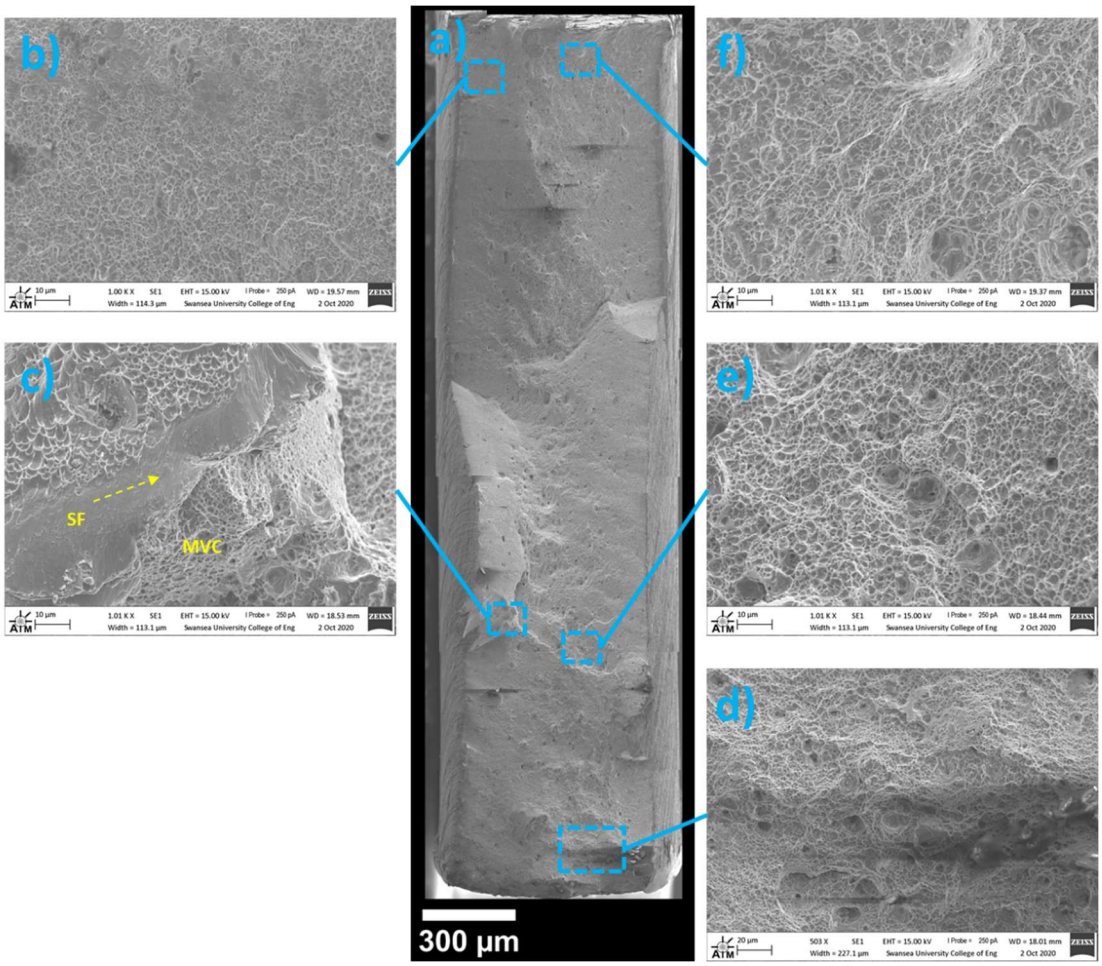

Figure 4.94 SEM images of 27MnB5+Nb (900C) specimen tested in the dry condition (without hydrogen charging) at a strain-rate of 10^{-6}/s at a) 150×, b) and c) 1000×, d) 500×, and e) and f) 1000× magnification.

For the pre-charged 27MnB5+Nb specimen strained at a rate of 10^{-6}/s, the topography of the fracture surface shown in Figure 4.95 appears mixed, with a clear demarcation between failure regimes roughly along the centreline of the sample. To the right hand side of the specimen the topography appears fairly consistent, with a fracture angle of between 45º and 60º to the loading direction. To the left hand side, and extending around the 'top' and 'bottom' regions (actually what would be the sample edges), the topography appears relatively flat, perpendicular to the loading direction, and has readily visible crack networks apparently emanating inward from the specimen surface.

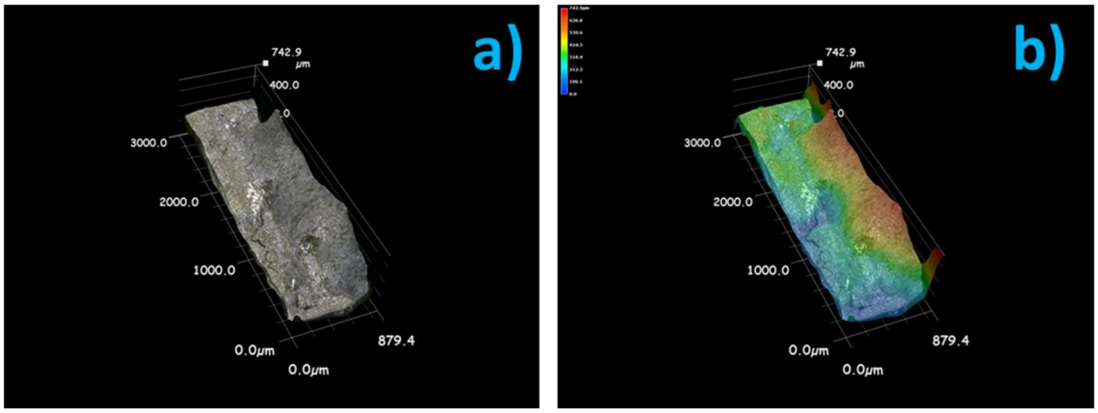

Figure 4.95 a) 3D-optical, and b) topographical images of 27MnB5+Nb (900C) specimen tested with 2 hours' hydrogen pre-charging at 10^{-6}/s strain-rate (charging maintained throughout test).

These stark differences in morphology are illustrated further through the SEM images shown in Figure 4.96, with the more central region expanded in g), and to a lesser extent the region expanded in f), showing a transition from large QC facets and visible transverse cracks to a more MVC-dominated fracture mode. The region highlighted in d) shows MVC dimples surrounding QC facets, adjacent to a large IG crack. The other two images of b) and c) show widespread IG cracks initiated from QC facets, indicating a highly embrittled region.

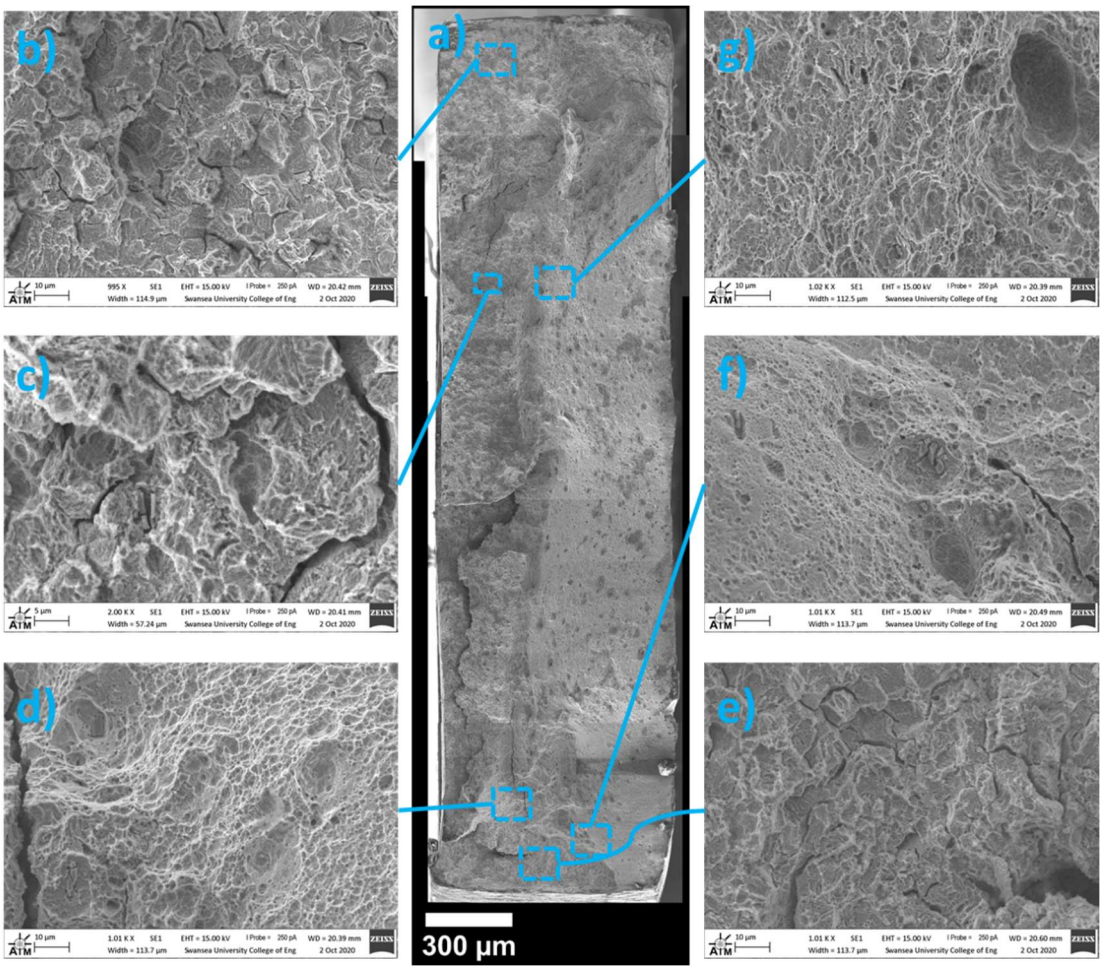

Figure 4.96 SEM images of 27MnB5+Nb (900C) specimen tested with 2 hours' hydrogen pre-charging (charging maintained throughout test) at a strain-rate of 10^{-6}/s at a) 150×, b) and d) to g) 1000×, and c) 2000× magnification.

A not dissimilar topography is seen for the 'charged' (no pre-charging) 27MnB5+Nb specimen tested at a strain-rate of 10^{-6}/s. Two distinct regions are apparent, with an angled region towards the left-hand side of the image (Figure 4.97), and to the right a 'flatter' region, more perpendicular to the loading direction.

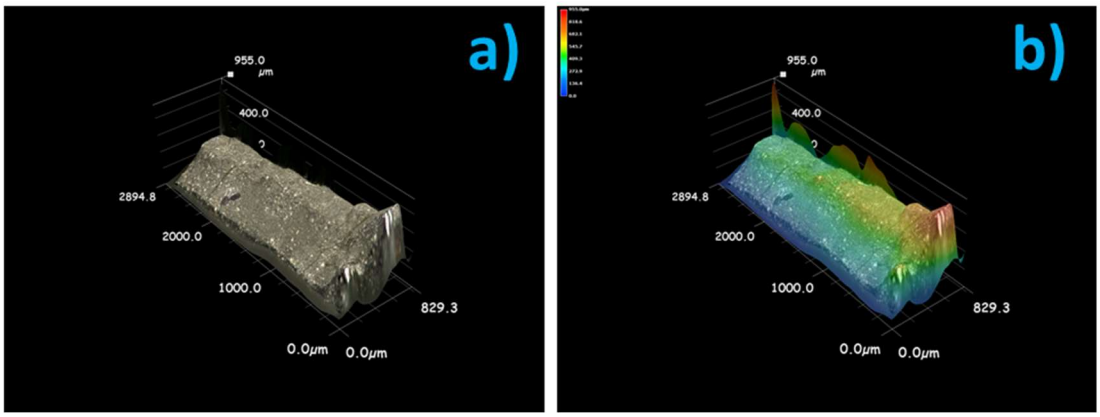

Figure 4.97 a) 3D-optical, and b) topographical images of 27MnB5+Nb (900C) specimen tested at 10^{-6}/s strain-rate with simultaneous hydrogen charging (charging maintained throughout test; no pre-charging).

Again, the SEM images (Figure 4.98, rotated ~160^{o} from Figure 4.97) show a clear contrast in fracture features between the two regions previously highlighted in Figure 4.97, with extensive IG cracking originating from QC events visible in the regions highlighted in b) and c), whereas whilst QC facets are still visible in d), the dominant features are MVC dimples. In e), some MVC dimples are apparent, but there are many QC facets, and a large crack is seen running normal to the loading direction (a similar crack is visible about one-third of the way up from the bottom edge of the specimen). This implies that even in the more 'ductile' region, the fracture modes cannot be thought of as being wholly ductile for this specimen.

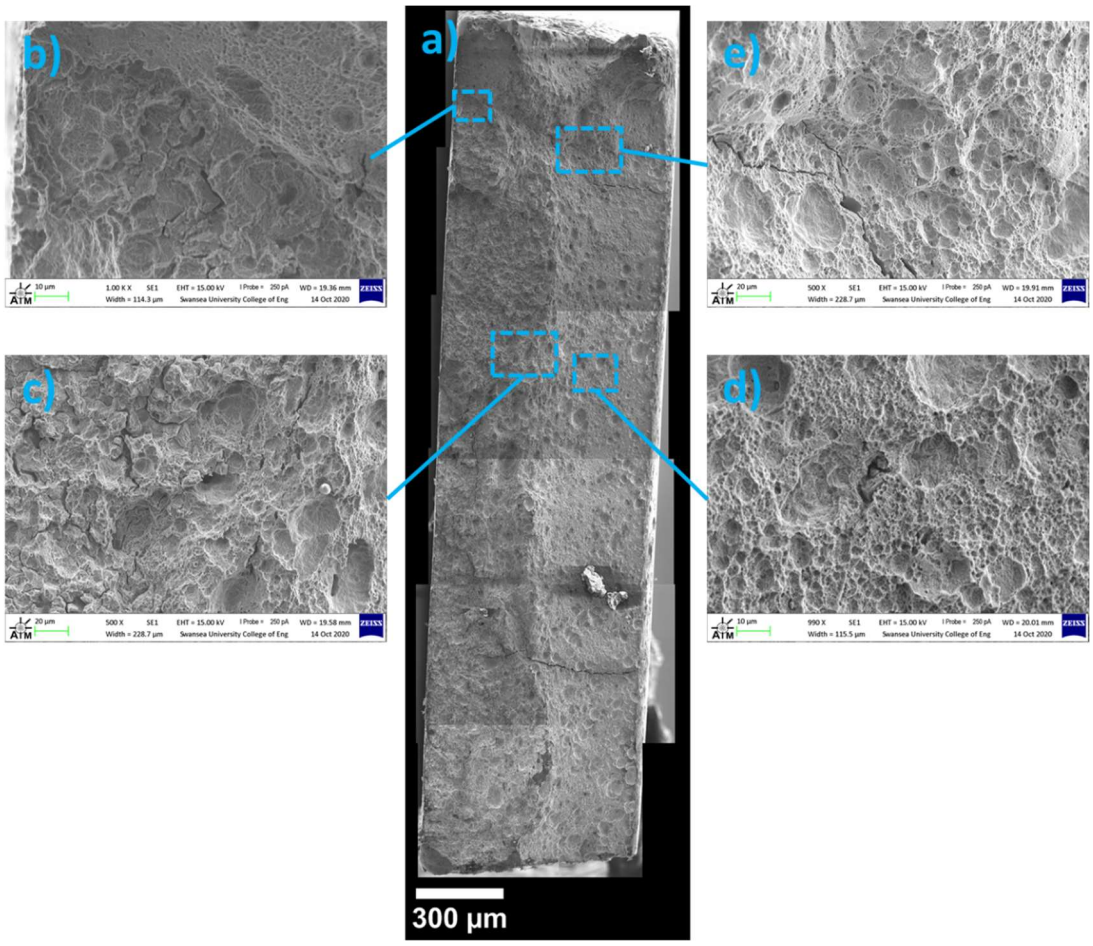

Figure 4.98 SEM images of 27MnB5+Nb (900C) specimen tested at a strain-rate of 10^{-6}/s with simultaneous hydrogen charging (charging maintained throughout test; no pre-charging). a) 150×, b), and d) 1000×, and c) and e) 1000× magnification

Finally, the charged 27MnB5+Nb sample (no pre-charging) tested at the higher (10^{-5}/s) strain-rate again shows a bi-modal topography. However, this specimen shows a much-reduced 'brittle' region which runs largely adjacent to one face (long axis) and the two edges (shorter axes of the image) of the specimen, as seen in Figure 4.99. The other region of the specimen shows a relatively consistent fracture angle, roughly 45° to the loading direction.

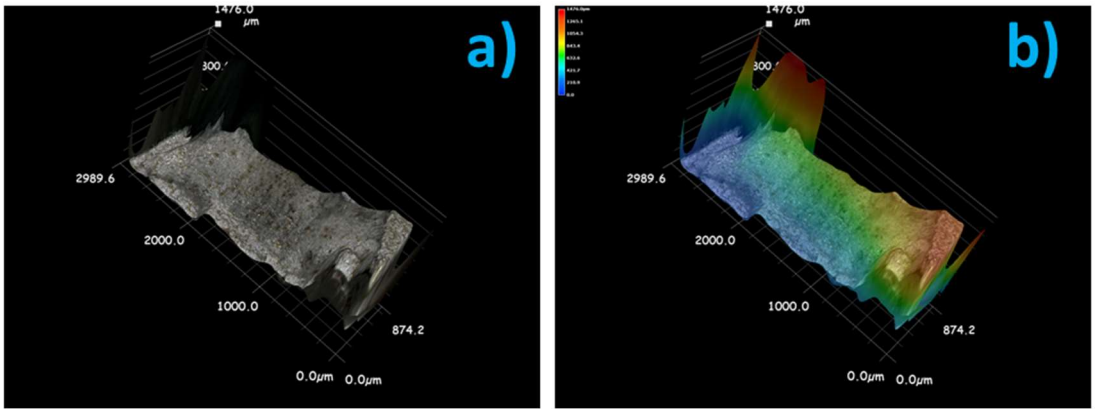

Figure 4.99 a) 3D-optical, and b) topographical images of 27MnB5+Nb (900C) specimen tested at 10^{-5}/s strain-rate with simultaneous hydrogen charging (charging maintained throughout test; no pre-charging).

The SEM image of the specimen (Figure 4.100, rotated ~160° to the optical-topographical images of Figure 4.99) shows several regions with mixed features. The compound image in a) shows a clear demarcation between the typically 'ductile-dominant' and 'brittle-dominant' regions identified in Figure 4.99, plus several cracks visible running transverse and normal to the loading direction. The region highlighted in b) shows a quite rapid transition between QC and IG cracks to MVC dimples as we proceed from the sample surface towards the sample interior, and a similar transition is observed in c) and d), although d) shows a crack propagating into the MVC-dominant region. The region highlighted in e) further away from the sample surfaces shows almost entirely MVC dimples, indicating that at this point the failure mode is predominantly of a 'ductile' nature.

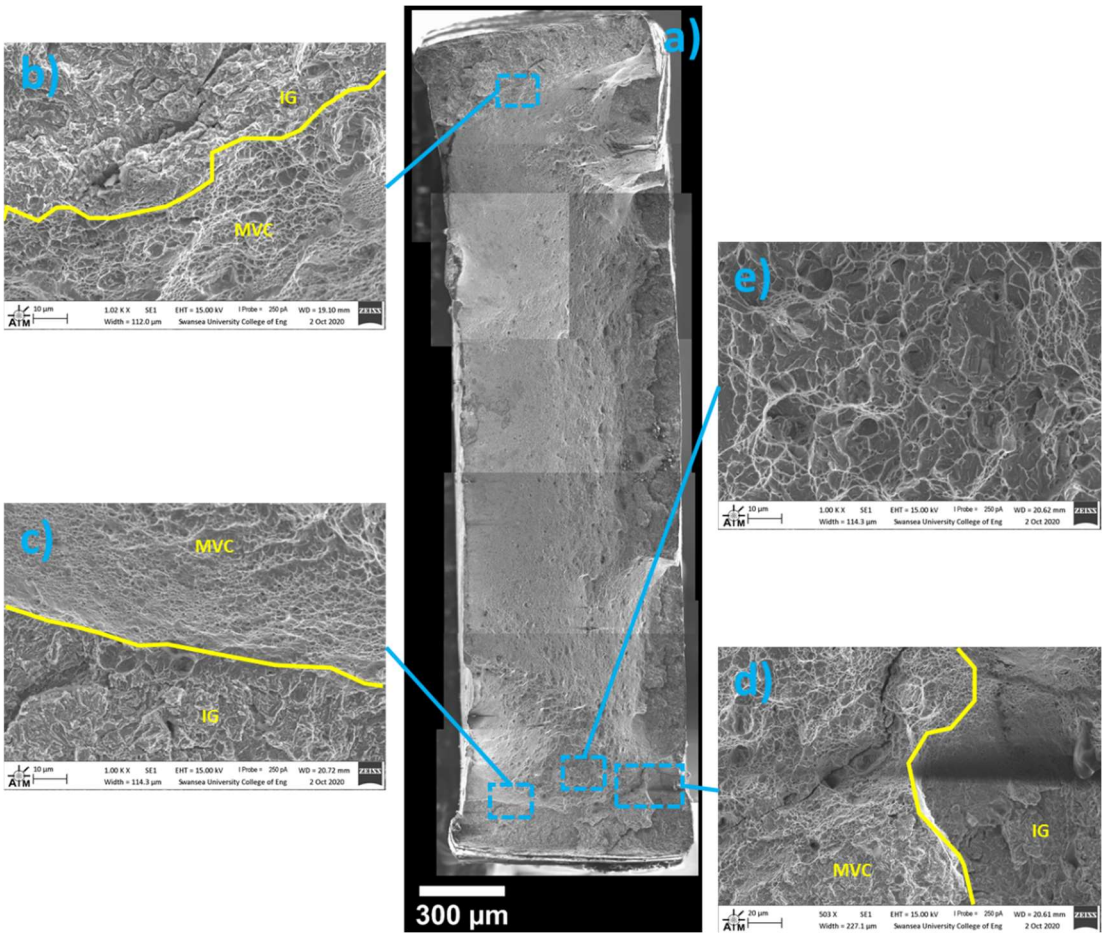

Figure 4.100 SEM images of 27MnB5+Nb (900C) specimen tested at a strain-rate of 10^{-5}/s with simultaneous hydrogen charging (charging maintained throughout test; no pre-charging). a) 150×, b), c) and e) 1000×, and d) 500× magnification.

4.4.3.7 Quantitative analysis

Fracture mechanisms depend upon hydrogen concentrations around crack tips and the associated stress intensity factors at these locations. Simplistically, quasi-cleavage (QC) facets, river-like cleavage (RC) and regions of intergranular (IG) fracture are thought to represent a more brittle fracture mode, whereas microvoid coalescence (MVC), ductile dimples (DD, singular microvoids that are not coalesced and only visible at high magnification), shear voids, and tear ridges (TR) occur in more ductile failures. Transgranular (TG) cracks can be found in both ductile and brittle regions, and commonly occur where mechanisms are competing or where the grain structure is very refined.

Fracture surface features were categorised and assigned colours according to the logic in Figure 4.101, below, whereupon the compound fractographs (150× magnification) were manually segregated into separate colour 'regions' according to the relative prevalence of fracture features in those regions (essentially by utilising the drawing tools in Microsoft PowerPoint). These classifications were subsequently analysed quantitatively (percentage of the surface belonging to each classification) for comparison between embrittlement indices and relative prevalence of fracture surface features. This comparison is tabulated in Table 4-15.

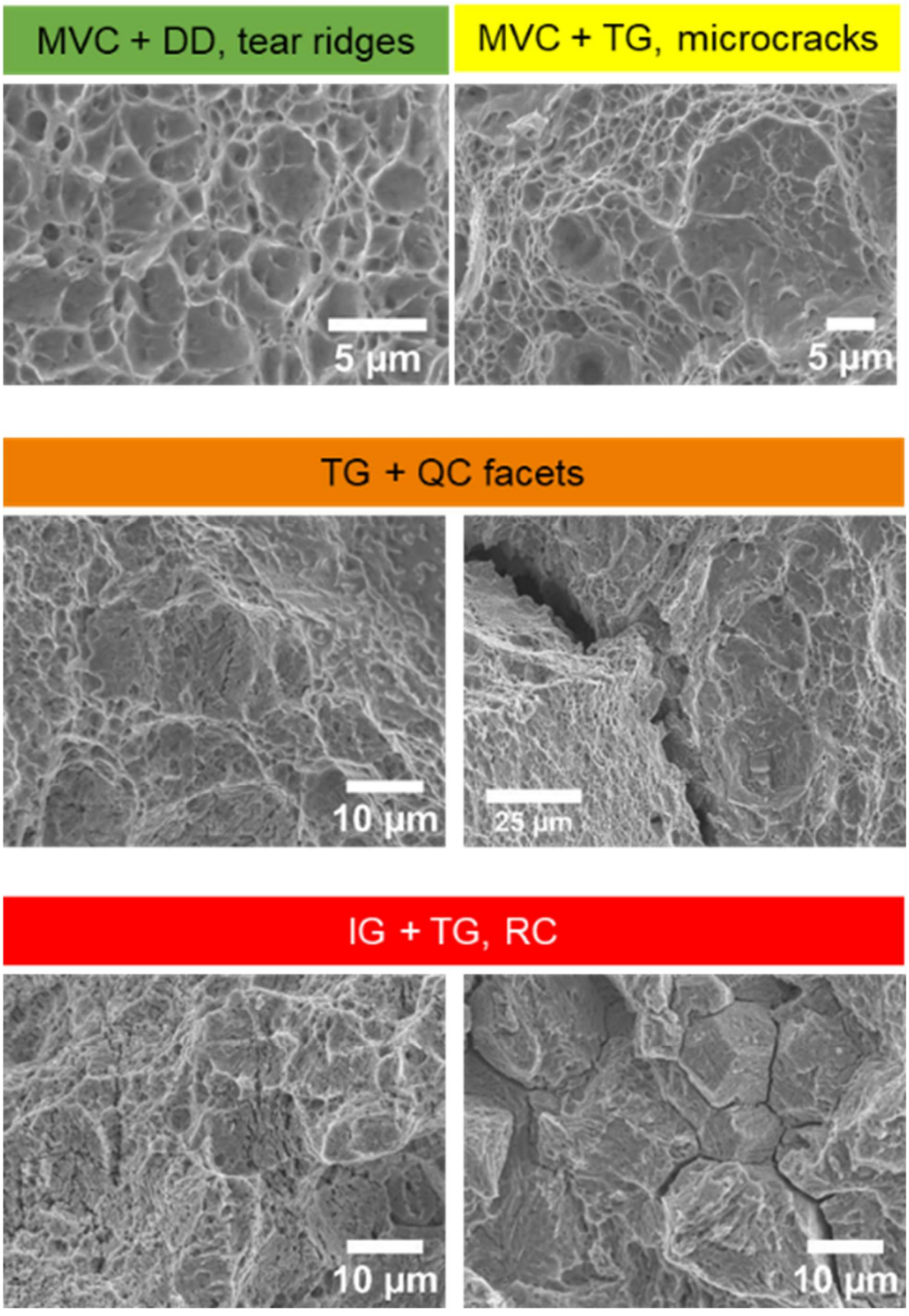

Figure 4.101 Classification of fracture surface features.

Table 4-15 Summary of fractographic classification analysis for all of the products and conditions tested.

Product	Dry 10^{-6}/s	Pre-charged 10^{-6}/s	Charged 10^{-6}/s	Higher Strain-rate 10^{-5}/s
	Classif.	Classif.	Classif.	Classif.
DP800		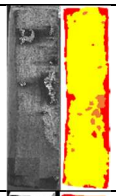	-	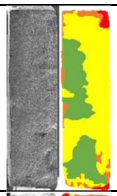
XPF800		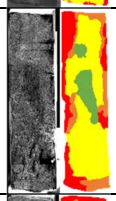	-	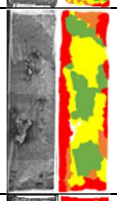
DP1000	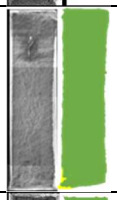	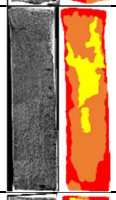	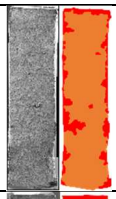	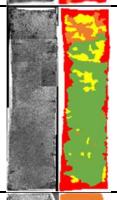
XPF1000		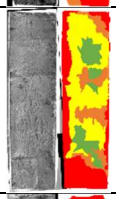	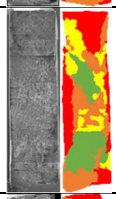	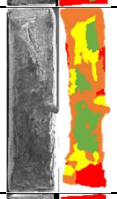
22MnB5 (900C)	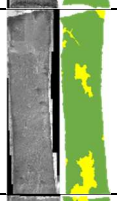	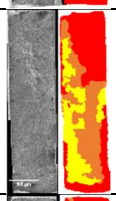	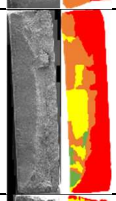	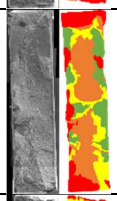
27MnB5+Nb (900C)	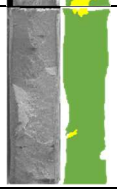	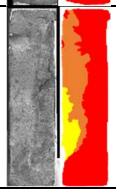	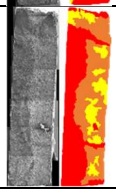	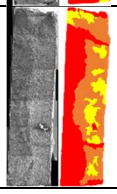

Table 4-16 Percentage of classified fracture features for each steel and test condition, and embrittlement index ($=\frac{Elongation\ in\ air - Elongation\ when\ charged}{Elongation\ in\ air}$) for each examined specimen.

Product	Condition	'Ductile' →→→→→→→→→→'Brittle'				Specimen Embrittlement Index %
DP800	Dry	100%	0%	0%	0%	-
	10-6/s, Pre-charged	0%	79%	4%	17%	46%
	10-5/s, In situ	34%	56%	7%	2%	27%
XPF800	Dry	100%	0%	0%	0%	-
	10-6/s, Pre-charged	11%	53%	15%	21%	27%
	10-5/s, In situ	29%	35%	9%	28%	17%
DP1000	Dry	99%	1%	0%	0%	-
	10-6/s, Pre-charged	0%	2%	79%	19%	75%
	10-6/s, In situ	0%	0%	82%	18%	77%
	10-5/s, In situ	57%	12%	7%	24%	54%
XPF1000	Dry	99%	1%	0%	0%	-
	10-6/s, Pre-charged	14%	38%	16%	30%	51%
	10-6/s, In situ	24%	18%	29%	29%	60%
	10-5/s, In situ	23%	21%	45%	11%	33%
22MnB5	Dry	87%	13%	0%	0%	-
	10-6/s, Pre-charged	0%	26%	32%	42%	72%
	10-6/s, In situ	4%	17%	29%	51%	71%
	10-5/s, In situ	20%	20%	39%	21%	44%
27MnB5+Nb	Dry	98%	2%	0%	0%	-
	10-6/s, Pre-charged	0%	9%	27%	64%	78%
	10-6/s, In situ	0%	15%	39%	46%	69%
	10-5/s, In situ	35%	9%	15%	42%	41%

Table 4-15 and Table 4-16 show a general trend that the higher the embrittlement index, the higher the prevalence of brittle fracture features. This is particularly the case for the steels containing a high phase-fraction of martensite. It is also apparent from Table 4-15 that the highest prevalence of the most typically brittle features is found generally closer to the charging surfaces, particularly for specimens charged at the higher strain-rate of 10^{-5}/s. More generally, several of the hydrogen-charged specimens appear to have distinct differences between one side of the sample and the other.

4.5 Simulations

This section describes results of simulations undertaken to explore two themes – hydrogen distribution in a membrane during permeation experiments, and hydrogen distribution in tensile test pieces during charging in slow strain-rate tests. This is done with the aim of achieving a greater understanding through visualisation of how, conceptually, sample thickness, differences in diffusivity due to microstructure, concentration and concentration gradients affect both hydrogen flux and susceptibility to premature failure. Details of the simulation methods and parameters are described in Chapter 3.4.3.

4.5.1 Hydrogen distribution within permeation membranes during testing

To visualise hydrogen distribution within permeation membranes, a finite-element method (FEM) was used to simulate the hydrogen distribution, with input parameters (charging surface concentration, effective diffusion coefficient, dimensions) obtained from the actual test data. Alongside this, where parameters were varied between a set of tests (e.g. observing the effect of charging potential), concentration profiles were calculated and presented in graphical form. In each case, for FEM and concentration profiles, Fick's 2nd Law was taken to apply.

4.5.1.1 Hydrogen concentration where nominal thickness and charging potential are equal

Table 4-17, below, shows the simulated hydrogen distribution for the different steels for permeation tests undertaken at 0.8 mm nominal membrane thickness, and -1050 mV (SCE) charging potential, with distributions displayed for each test's measured t_b, t_{lag}, and steady-state. Each scale is calibrated to the calculated charging surface concentration in mass parts-per-million (ppm) of hydrogen for each particular test, i.e. it is not a normalised measure.

Table 4-17 Simulated hydrogen distributions for hydrogen permeation membranes undertaken at 0.8 mm nominal membrane thickness, and -1050 mV (SCE) charging potential.

Steel	
DP800	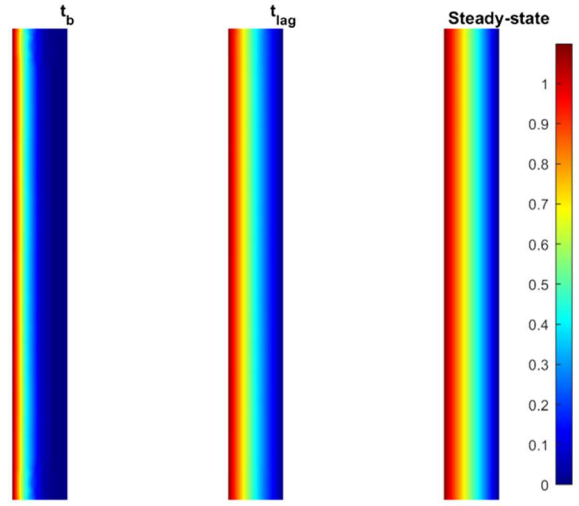
XPF800	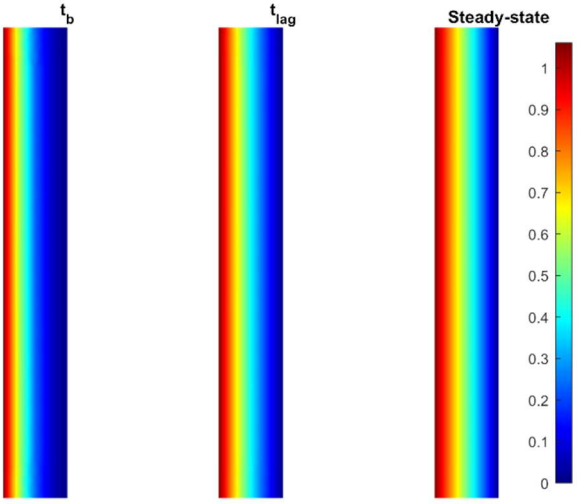

DP1000	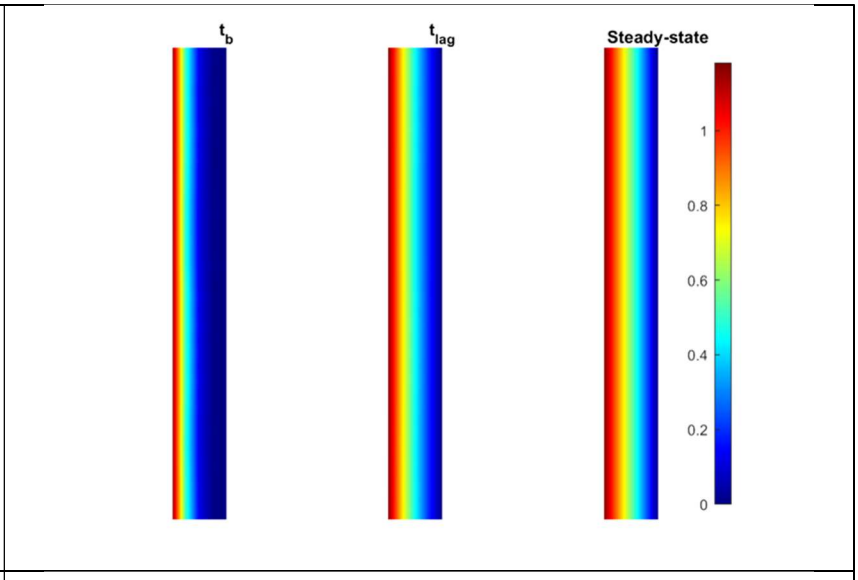
XPF1000	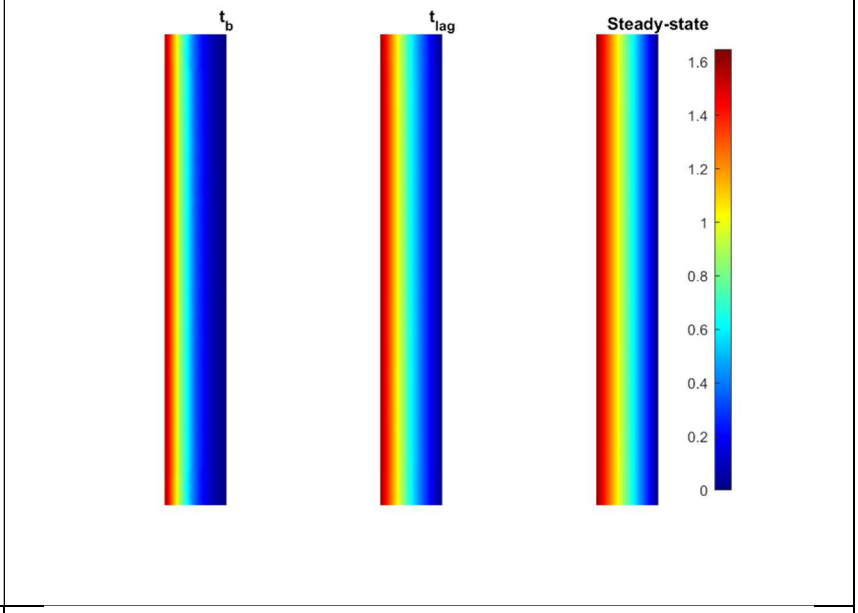
22MnB5 (UHT)	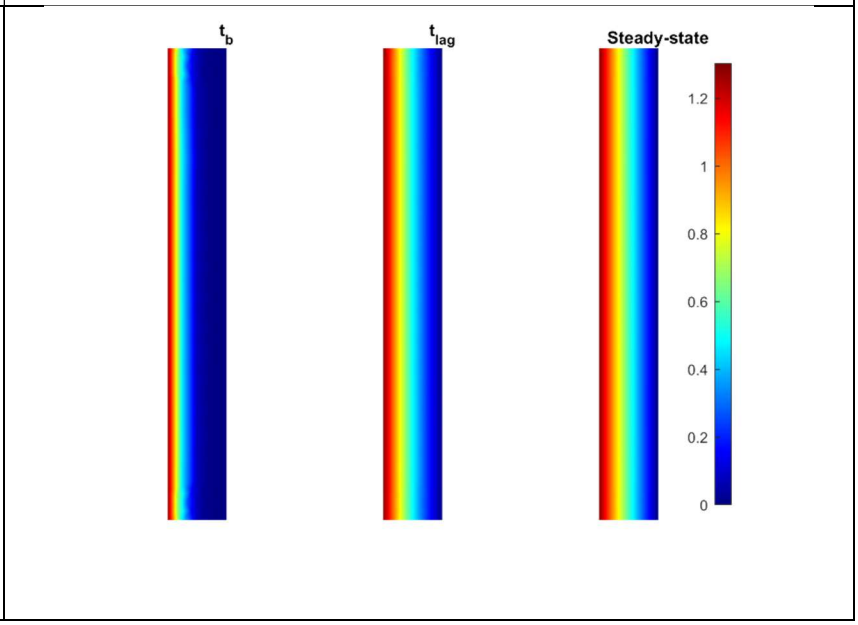

22MnB5 (900C)	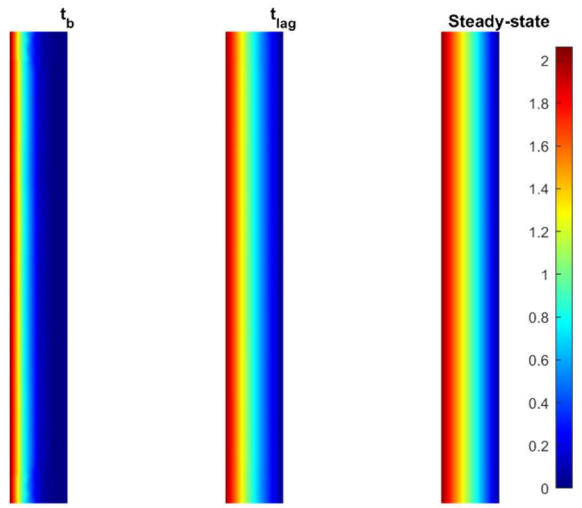
27MnB5+Nb (UHT)	
27MnB5+Nb (900C)	

From Table 4-17 it is clear that, assuming Fick's 2nd Law applies in each case, the distribution of hydrogen throughout the membranes differs very little between the different microstructures for each of the time intervals, particularly as the intervals chosen (t_b, t_{lag}, and steady-state) are specific to the tests in question.

To better visualise the effect of differences in effective diffusion coefficient upon the distribution of hydrogen, it is necessary to run the same simulations with fixed time intervals, and normalise the membrane thickness and charging concentration parameters to remove any subtle differences between the tests. This essentially means that the only parameter being varied is the value of D_{eff}. This is shown in Table 4-18, below.

Table 4-18 Simulated hydrogen distributions for hydrogen permeation tests undertaken at 0.8 mm nominal membrane thickness, and -1050 mV (SCE) charging potential, with time intervals fixed at 200, 2000, and 10000 seconds, and normalised charging concentration.

Steel	
DP800 $D_{eff} = 3.75\times10^{-7}$ cm^2/s	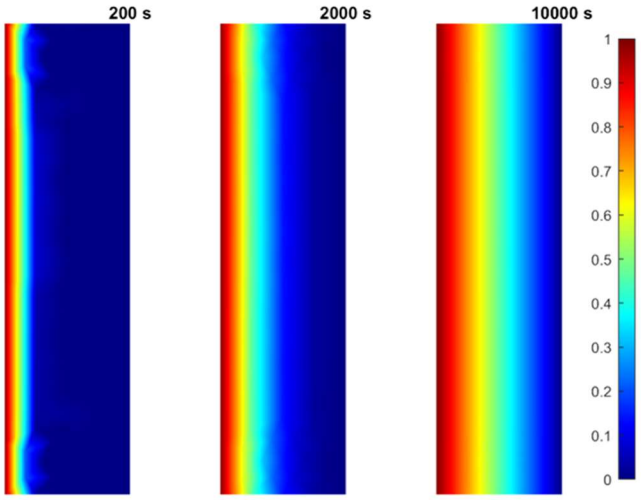

XPF800 $D_{eff} = 1.68\times10^{-7}$ cm^2/s	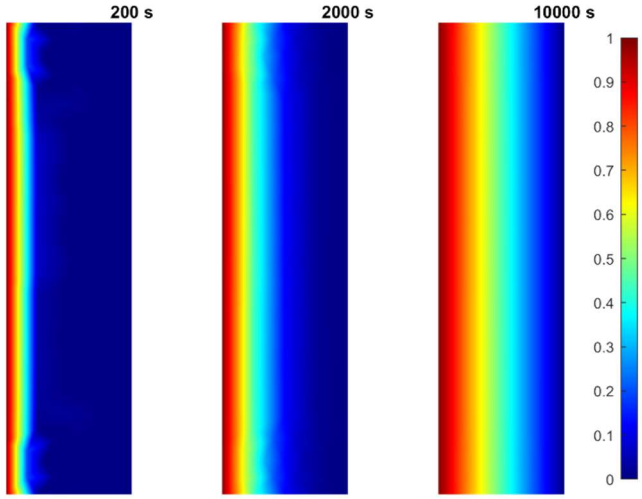
DP1000 $D_{eff} = 1.45\times10^{-7}$ cm^2/s	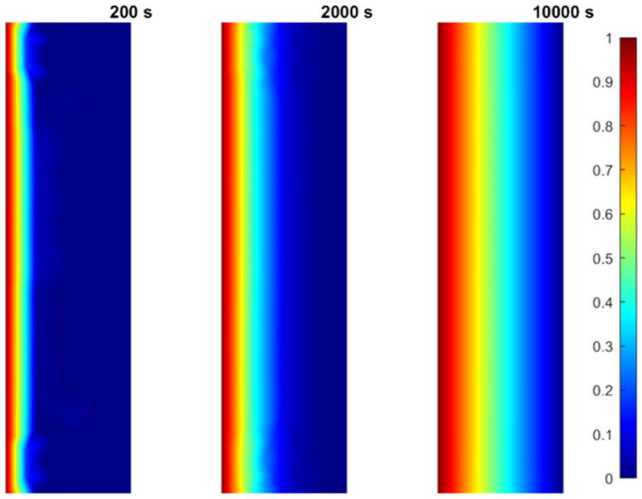
XPF1000 $D_{eff} = 7.45\times10^{-8}$ cm^2/s	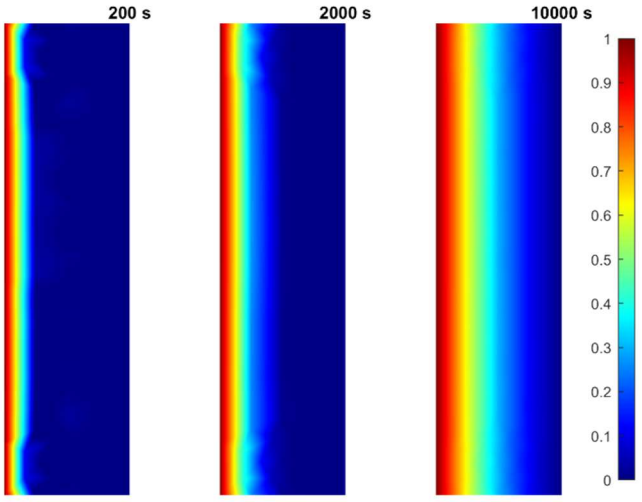

22MnB5 (UHT) $D_{eff} = 1.70\times10^{-7}$ cm^2/s	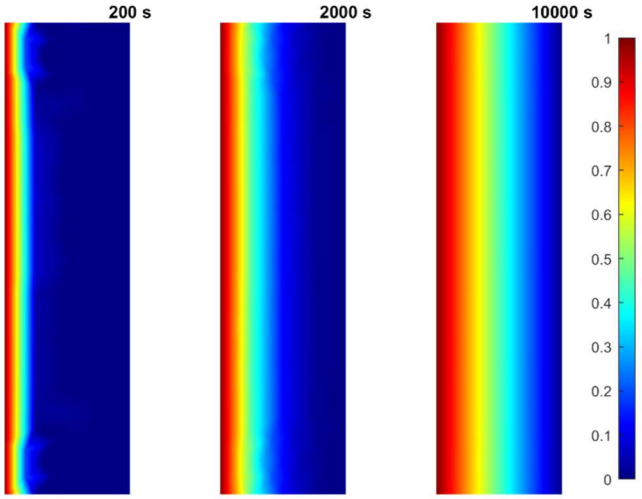
22MnB5 (900C) $D_{eff} = 9.81\times10^{-8}$ cm^2/s	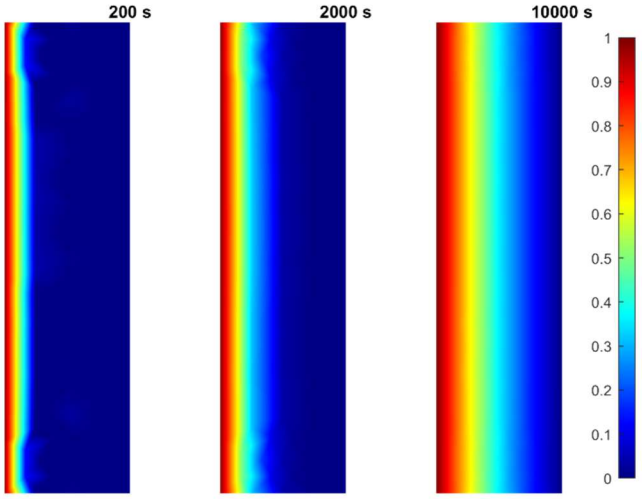
27MnB5+Nb (UHT) $D_{eff} = 5.45\times10^{-7}$ cm^2/s	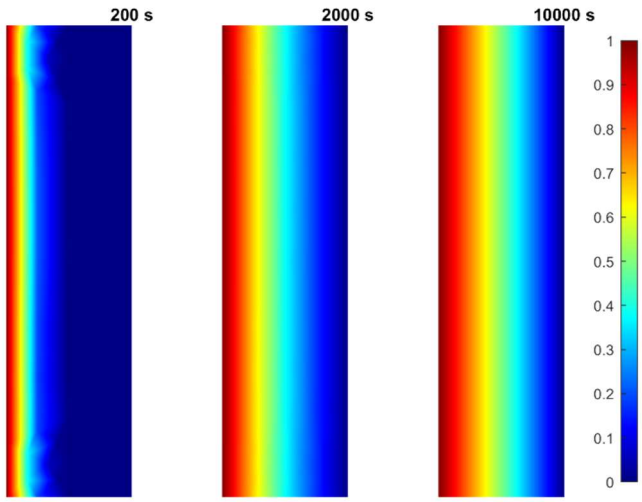

27MnB5+Nb (900C) $D_{eff} = 2.03 \times 10^{-7}$ cm^2/s	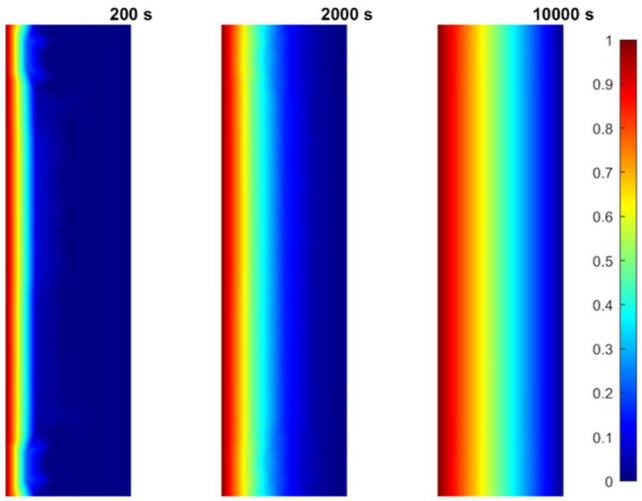

Table 4-18 shows how, for a given charging concentration and membrane thickness, the steel with the largest effective diffusivity, 27MnB5+Nb (UHT), will reach maximum hydrogen concentration through the membrane much earlier than e.g. the heat-treated equivalent (27MnB5+Nb (900C)). It is also apparent from Table 4-18 that differences in effective diffusivity seen between all of these steels do not appear to have a large impact on the hydrogen distribution over short time periods (200 seconds, in this instance).

4.5.1.2 Hydrogen distribution with the same membrane microstructure and thickness, varying charging potential

Table 4-19 shows the effect of varying charging potential on the hydrogen distribution during hydrogen permeation tests undertaken on membranes of 22MnB5 (900C) of nominal thickness 1.2 mm, with charging potentials of -850 mV, -950 mV, and -1050 mV (SCE). Scale bars for each simulation show the full range of concentrations at the charging surfaces for all of the tests undertaken, in mass ppm (i.e. 0ppm to 1.65ppm, calculated according to $\left(\frac{C_0 \times Atomic\ mass\ of\ hydrogen}{Mass\ density\ of\ iron\ (g.cm^{-3})}\right) \times 10^6$), to visualise the effect of charging potential on hydrogen concentration. In essence this means that simulated output for tests undertaken at -850 mV and -950 mV (SCE) are visually compared to tests undertaken at -1050 mV (SCE).

Table 4-19 Simulated hydrogen distributions for hydrogen permeation tests undertaken on 22MnB5 (900C) membranes of 1.2 mm nominal thickness, at -850, -950, and -1050 mV (SCE) charging potential, with time intervals fixed at 5000, 15000, and 25000 seconds. Colour axes relative to the -1050 mV charging condition.

Charging potential (mV SCE)	
-850	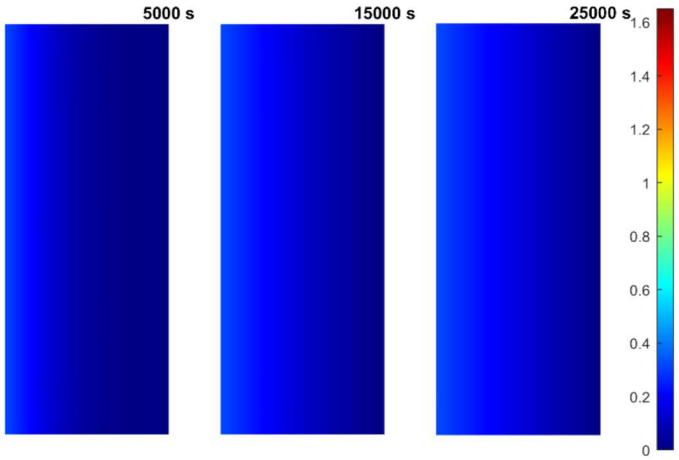

-950	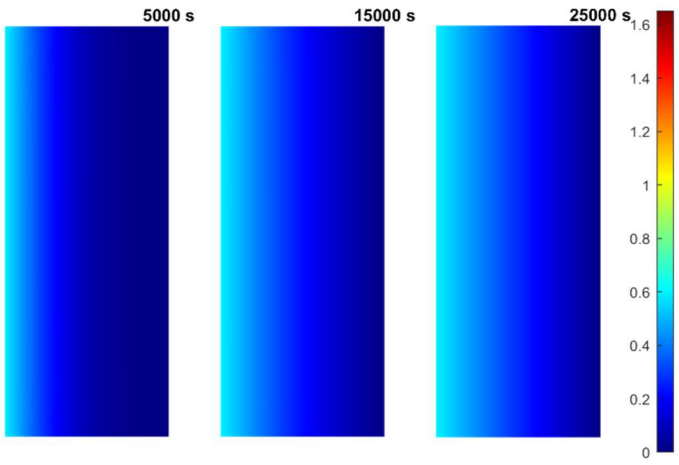
-1050	

Whilst Table 4-19 clearly illustrates the differences in hydrogen concentration overall, it does not readily impart information about whether differences in concentration at the charging surface have an effect on the overall relative distribution within the membrane.

To address this, the same data is shown in Table 4-20, but with the colour axes now specific to the test conditions.

Table 4-20 Simulated hydrogen distributions for hydrogen permeation tests undertaken on 22MnB5 (900C) membranes of 1.2 mm nominal thickness, at -850, -950, and -1050 mV (SCE) charging potential, with time intervals fixed at 5000, 15000, and 25000 seconds. Colour axes relative to specific tests.

Charging potential (mV SCE)	
-850	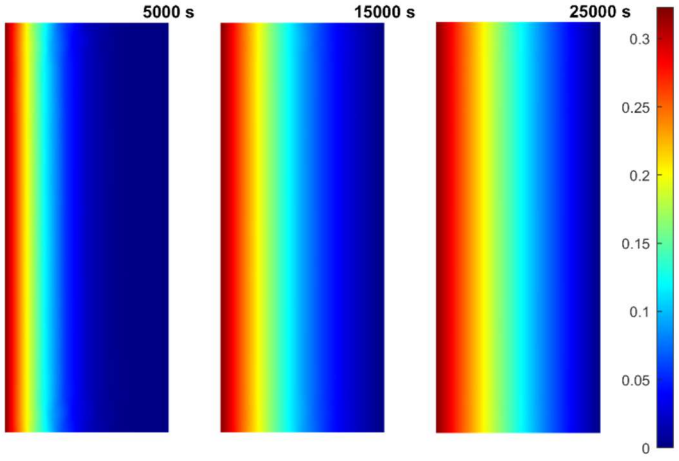
-950	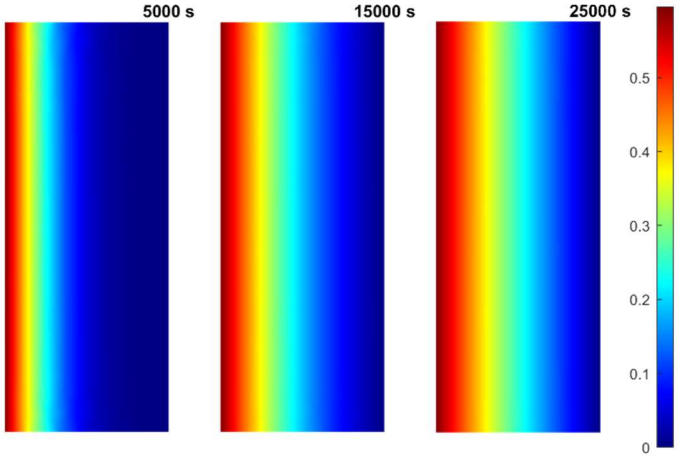

-1050	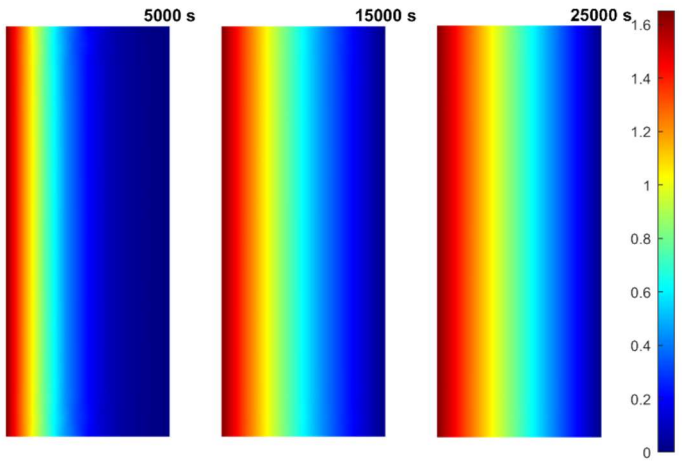

Table 4-20 shows that despite varying the charging potential, minimal impact on the *relative* distribution of hydrogen within the permeation membrane is observed. This is further demonstrated by plotting the hydrogen concentration profiles, C_H, across the membranes for the specified time intervals. These concentration profiles across the membrane are shown in Figure 4.102, below.

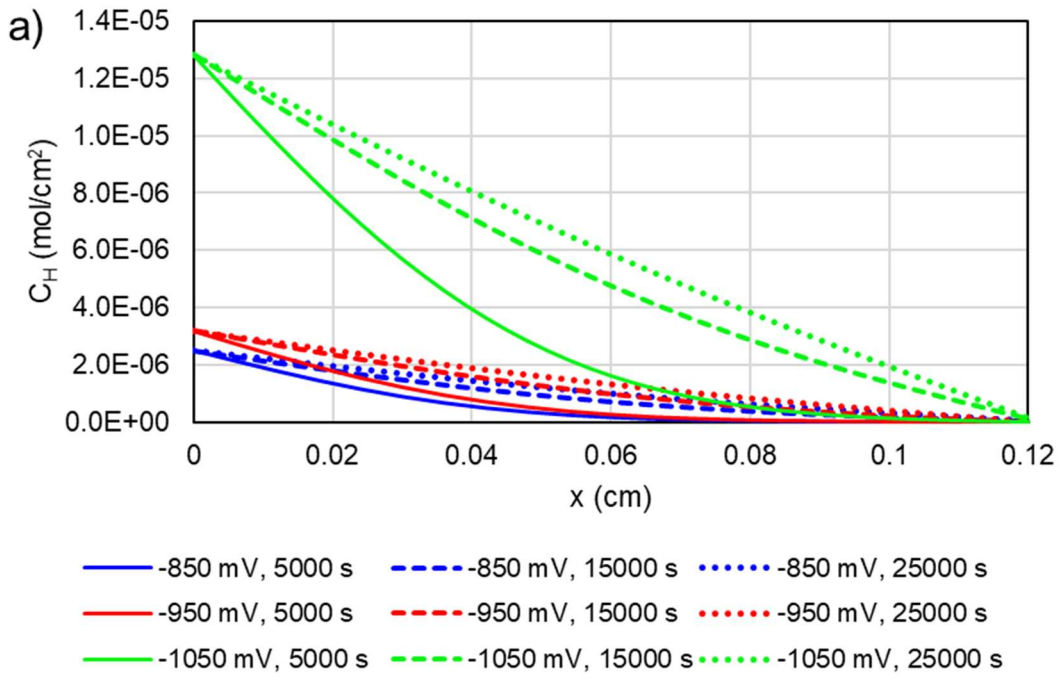

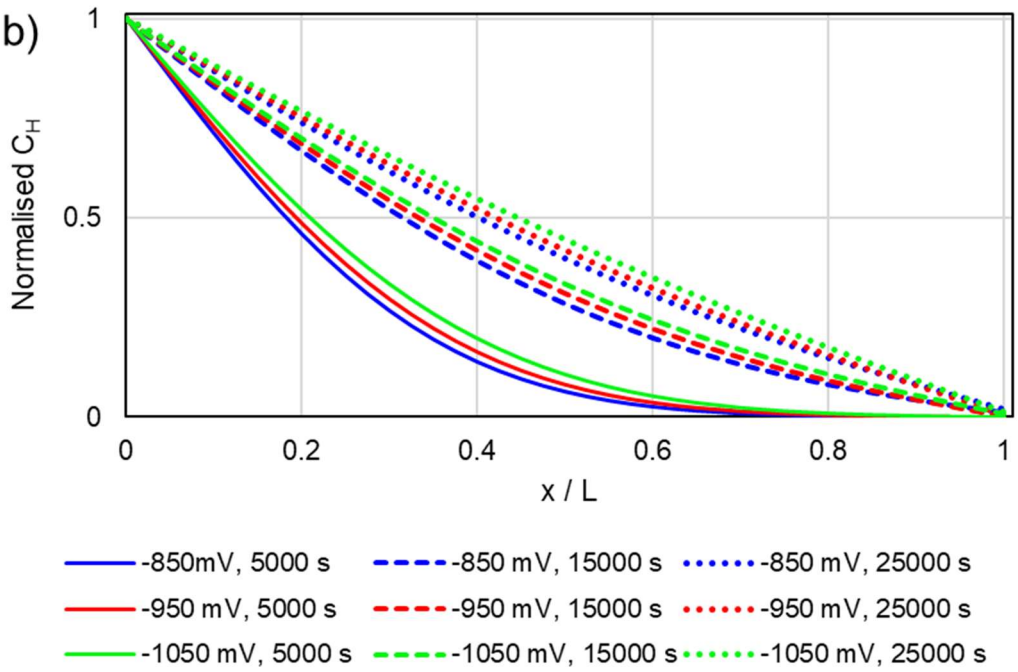

Figure 4.102 a) Absolute, and b) normalised, hydrogen concentration profiles across permeation membranes during permeation tests undertaken at -850, -950, and -1050 mV (SCE) charging potentials.

Figure 4.102 a) shows the magnitude of the increase in hydrogen concentration with increasing charging potentials, illustrating the relatively similar hydrogen concentration distributions obtained with charging potentials of -850 mV and -950 mV (SCE), as opposed to the marked increase seen from charging at -1050 mV (SCE). However, to illustrate any effects of relative differences in hydrogen concentration, the plots must be normalised with respect to the charging surface concentrations, as displayed in Figure 4.102 b). The close fit between each of the profiles at the specified intervals clearly demonstrates that where the membrane thickness is kept constant, for the 22MnB5 (900C) membranes tested, there is minimal difference in the relative hydrogen concentration profiles across the membrane for different charging potentials.

4.5.2 Hydrogen distribution within slow strain-rate test specimens

To visualise hydrogen distribution within test specimens during slow strain-rate testing (SSRT), a finite-element method was used to simulate the hydrogen distribution, with input parameters (charging surface concentration, effective diffusion coefficient, dimensions) taken from the results of permeation tests for the equivalent steels at the same nominal thickness (in this case, 0.8 mm), with dimensional parameters taken from measurements of the specimens taken prior to testing. Concentration profiles along a linear-section through the thickness (i.e. normal to the direction of loading) were also calculated and presented in graphical form. In each case, for FEM and concentration profiles, Fick's 2nd Law was taken to apply. Charging surface concentration in ppm for each of the following figures is calculated from C_0 values obtained from permeation experiments on equivalent product/thickness (e.g. for Figure 4.103 the maximum ppm is calculated from the C_0 values calculated from DP800 permeation experiment on membrane of 0.8 mm nominal thickness). Subsequently, the calculated concentration profiles were used to estimate 'critical' hydrogen concentrations by overlaying the profiles upon the fractographs, and (after normalising the 'distance' axis of the concentration profile to the scale bar of the fractograph) observing where the transition (if present) between ductile and brittle fracture features occurs on the concentration profile. This last aspect is presented as part of the Discussion.

The following Figures show the simulated hydrogen distributions within SSRT specimens at the time of failure, for specimens tested at strain rate of 10^{-6}/s with (all steels) and without (all but DP800 and XPF800) 2 hours' hydrogen pre-charging, and for specimens tested at 10^{-5}/s without pre-charging (all steels). In all cases hydrogen charging was taken to be constant throughout the duration of the test, as was the case.

4.5.2.1 DP800

Figure 4.103 a) and c) show the hydrogen distribution within the SSRT specimens for tests labelled as DP800-Pre-charged-3 (10^{-6}/s strain-rate, 2 hours pre-charging), and DP800-Higher strain-rate-3 (10^{-5}/s strain-rate, no pre-charging), respectively. Figure

4.103 b) and d) show the concentration profiles through-thickness at the time of failure for the same tests. Colour axes measured in mass ppm.

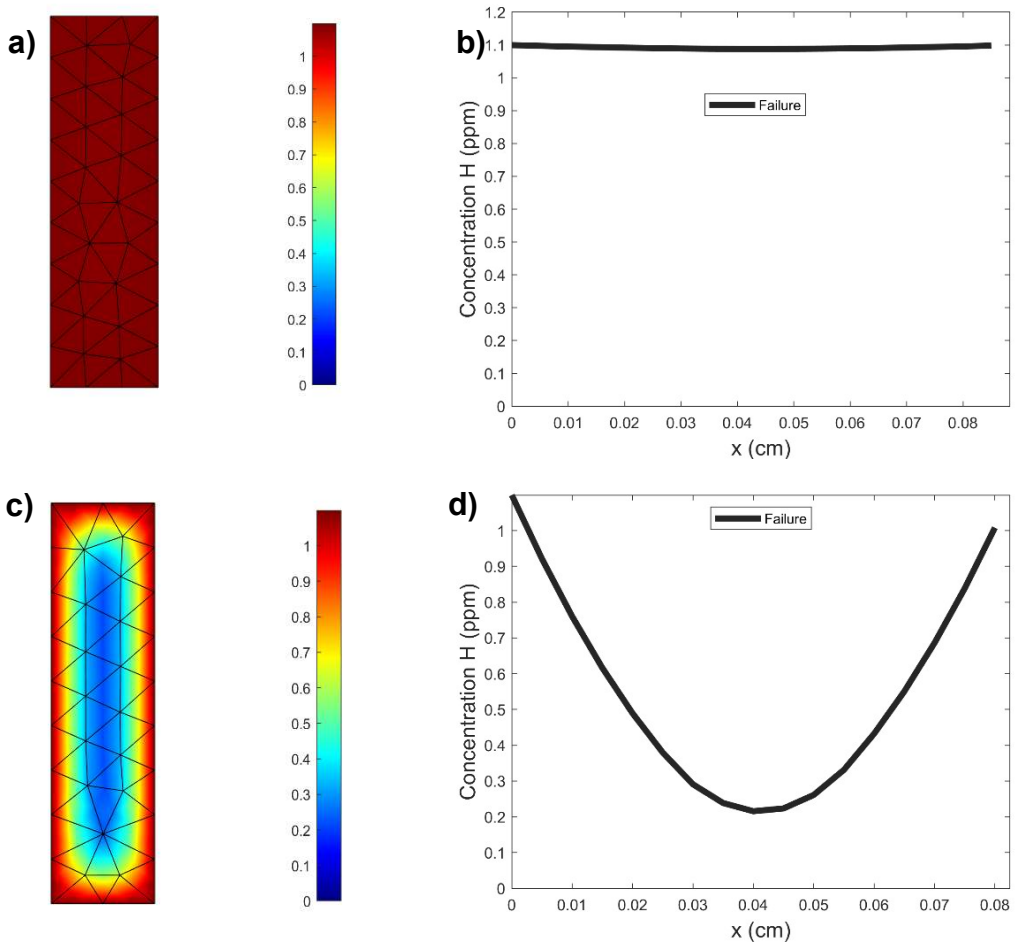

Figure 4.103 a) hydrogen distribution and b) through-thickness hydrogen concentration profile at failure of DP800 SSRT test undertaken at 10^{-6}/s strain-rate with 2 hours' pre-charging; c) and d) hydrogen distribution and concentration profile at failure of DP800 SSRT tested at 10^{-5}/s without pre-charging.

Figure 4.103 a) and b) show how at failure after 2 hours of pre-charging and charging throughout the duration of the test, the DP800 SSRT specimen tested at 10^{-6}/s strain-rate had an almost uniform distribution of hydrogen of ~1.1 ppm. c) and d) however, show that for the test at the higher strain-rate of 10^{-5}/s and without pre-charging, the distribution of hydrogen ranged from ~1.1 ppm at the charging surfaces to ~0.2 ppm at the centre of the sample.

4.5.2.2 XPF800

Figure 4.104 (below) shows the hydrogen distribution and concentration profiles within the SSRT specimens for tests labelled as XPF800-Pre-charged-1 (10^{-6}/s strain-rate, 2 hours pre-charging, a) and b)), and XPF800-Higher strain-rate-2 (10^{-5}/s strain-rate, no pre-charging, c) and d)), respectively.

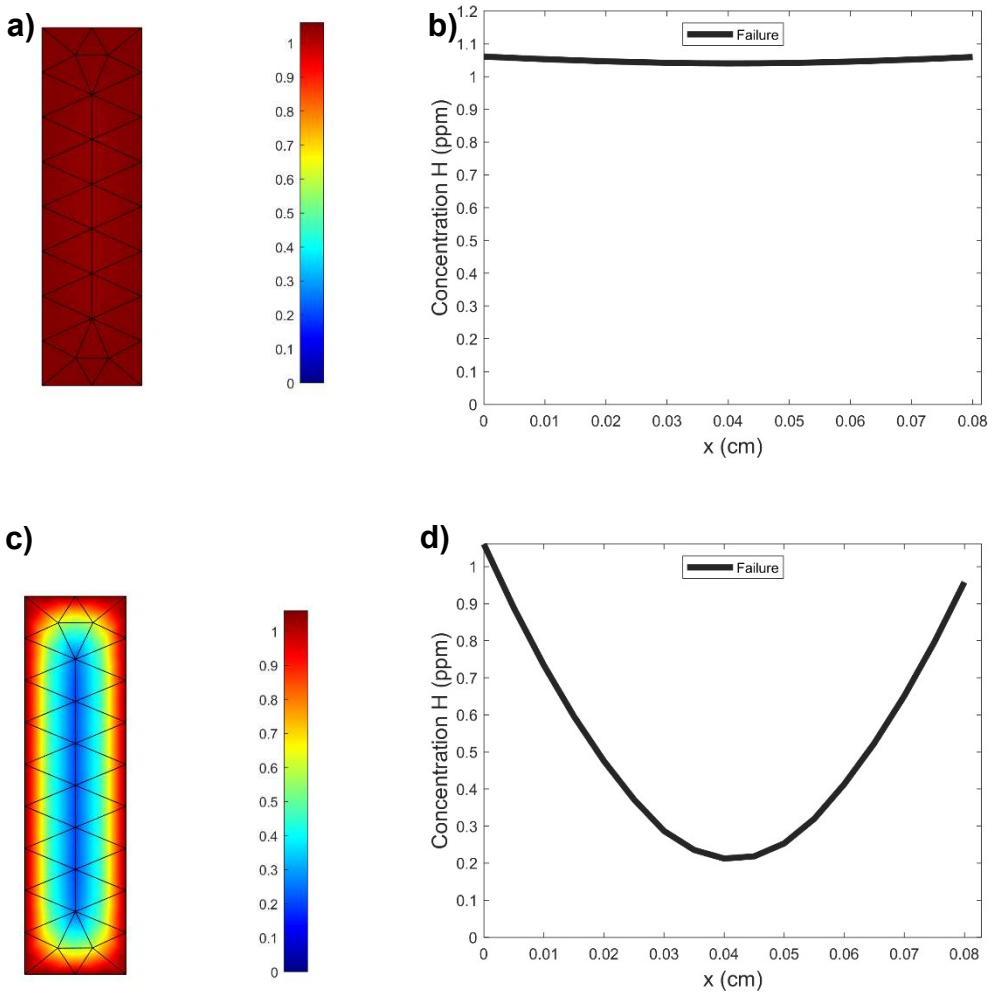

Figure 4.104 a) hydrogen distribution and b) through-thickness hydrogen concentration profile at failure of XPF800 SSRT test undertaken at 10^{-6}/s strain-rate with 2 hours' pre-charging; c) and d) hydrogen distribution and concentration profile at failure of XPF800 SSRT tested at 10^{-5}/s without pre-charging.

The pre-charged XPF800 sample tested at 10^{-6}/s strain-rate, like that for the DP800, shows an almost uniform hydrogen concentration throughout the specimen of ~1.1 ppm, as seen from Figure 4.104 a) and b). For the XPF800 specimen tested at 10^{-5}/s strain-rate without pre-charging, hydrogen concentration ranged from ~1.1 ppm at the charging surface to ~0.2 ppm at the centre of the sample.

4.5.2.3 DP1000

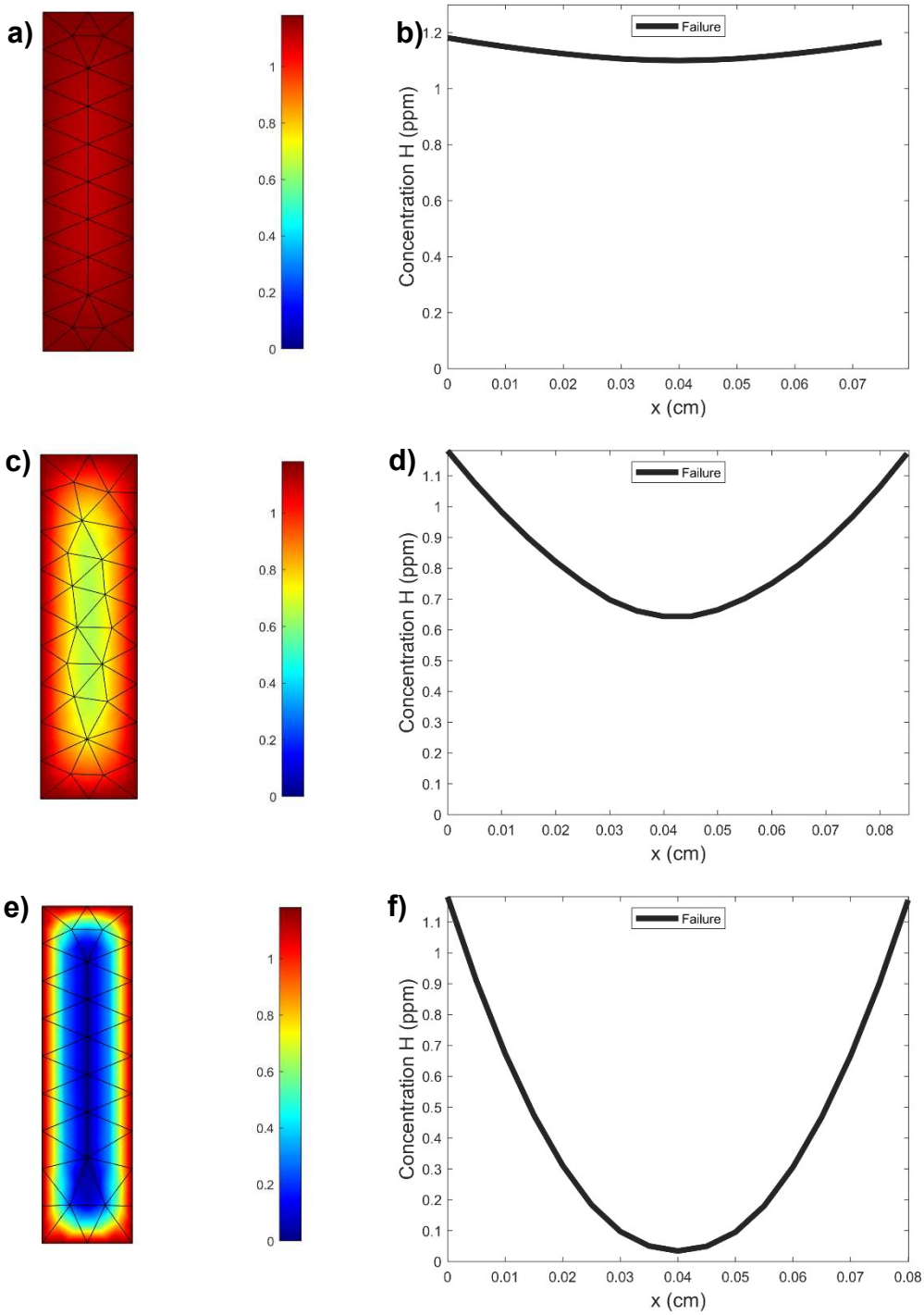

Figure 4.105 Hydrogen distribution and through-thickness hydrogen concentration profile at failure of DP1000 SSRT test undertaken at 10^{-6}/s strain-rate with 2 hours' pre-charging a) and b)); 10^{-6}/s strain-rate with no pre-charging c) and d)); 10^{-5}/s strain-rate with no pre-charging e) and f)).

Figure 4.105 (above) shows the hydrogen distribution and concentration profiles within the SSRT specimens for tests labelled as DP1000-Pre-charged-3 (10^{-6}/s strain-rate, 2 hours pre-charging, a) and b)), DP1000-Charged-2 (10^{-6}/s strain-rate, no pre-

charging, c) and d)), and DP1000-Higher strain-rate-3 (10^{-5}/s strain-rate, no pre-charging, e) and f)), respectively.

For the pre-charged specimen tested at 10^{-6}/s strain-rate (Figure 4.105 a) and b)), again we see an almost uniform hydrogen concentration between 1 and 1.2 ppm, with only a very slight difference between the concentration at the charging surface and that at the centre of the sample. Conversely, the sample tested at 10^{-6}/s strain-rate without pre-charging seen in c) and d) shows a concentration gradient where the hydrogen concentration at the centre of the sample is about half that seen at the charging surface. Finally, the sample tested at 10^{-5}/s strain-rate without pre-charging shows a steep surface-to-centre concentration gradient, with an almost 0 ppm concentration at the centre of the specimen.

4.5.2.4 XPF1000

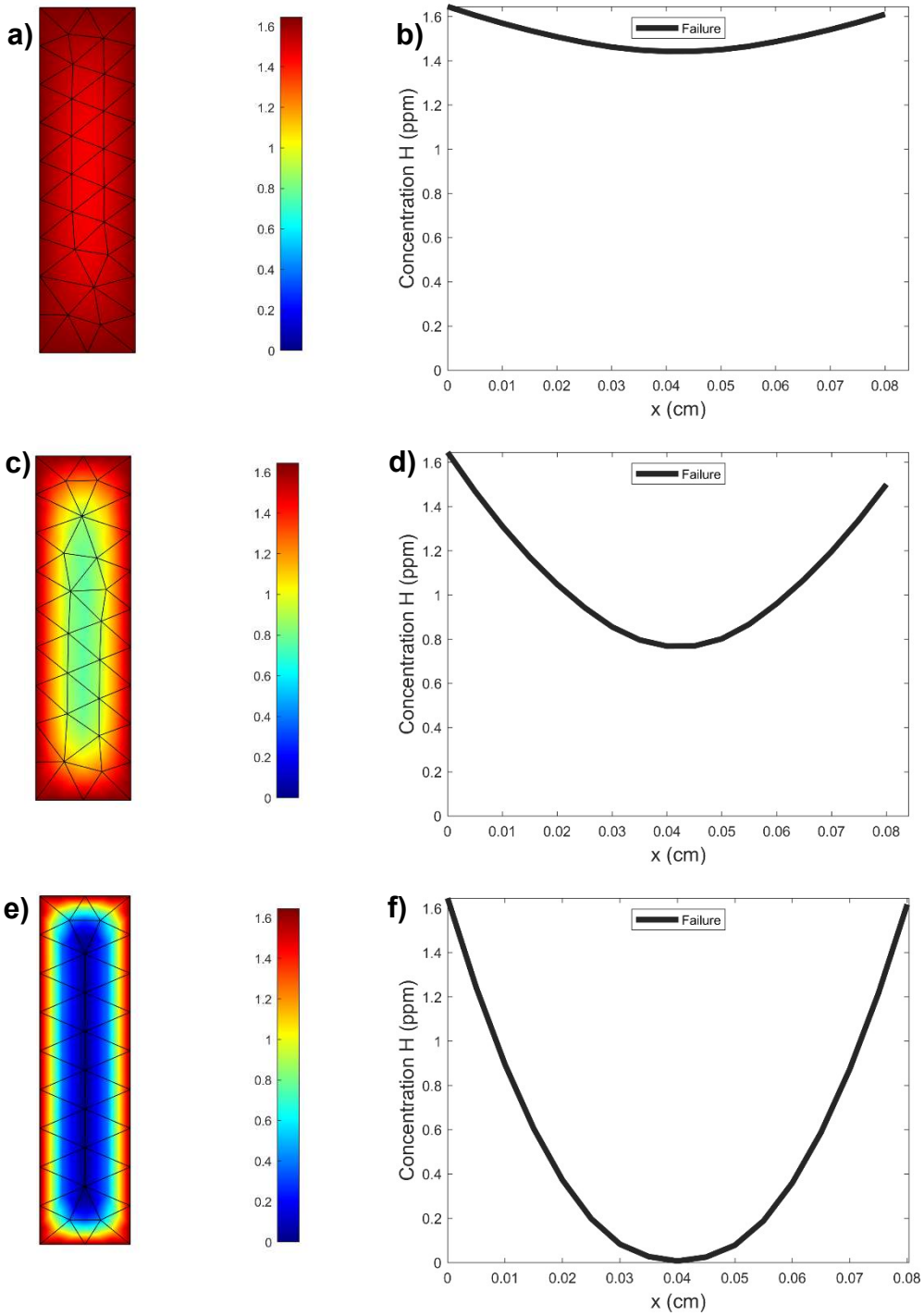

Figure 4.106 Hydrogen distribution and through-thickness hydrogen concentration profile at failure of XPF1000 SSRT test undertaken at 10^{-6}/s strain-rate with 2 hours' pre-charging (a) and b)); 10^{-6}/s strain-rate with no pre-charging (c) and d)); 10^{-5}/s strain-rate with no pre-charging (e) and f)).

Figure 4.106 (above) shows the hydrogen distribution and concentration profiles within the SSRT specimens for tests labelled as XPF1000-Pre-charged-3 (10^{-6}/s strain-rate, 2 hours pre-charging, a) and b)), XPF1000-Charged-3 (10^{-6}/s strain-rate, no pre-charging, c) and d)), and XPF1000-Higher strain-rate-2 (10^{-5}/s strain-rate, no pre-charging, e) and f)), respectively.

For the pre-charged specimen tested at 10^{-6}/s strain-rate (Figure 4.106 a) and b)), hydrogen concentration varies between ~1.7 ppm at the charging surfaces to ~ 1.4 ppm at the sample centre. The sample tested at 10^{-6}/s strain-rate without pre-charging seen in c) and d) shows a concentration gradient where again the hydrogen concentration at the centre of the sample is about half that seen at the charging surface, as seen in the equivalent DP1000 specimen. Finally, the sample tested at 10^{-5}/s strain-rate without pre-charging shows a steep surface-to-centre concentration gradient, with an almost 0 ppm concentration at the centre of the specimen.

4.5.2.5 22MnB5 (900C)

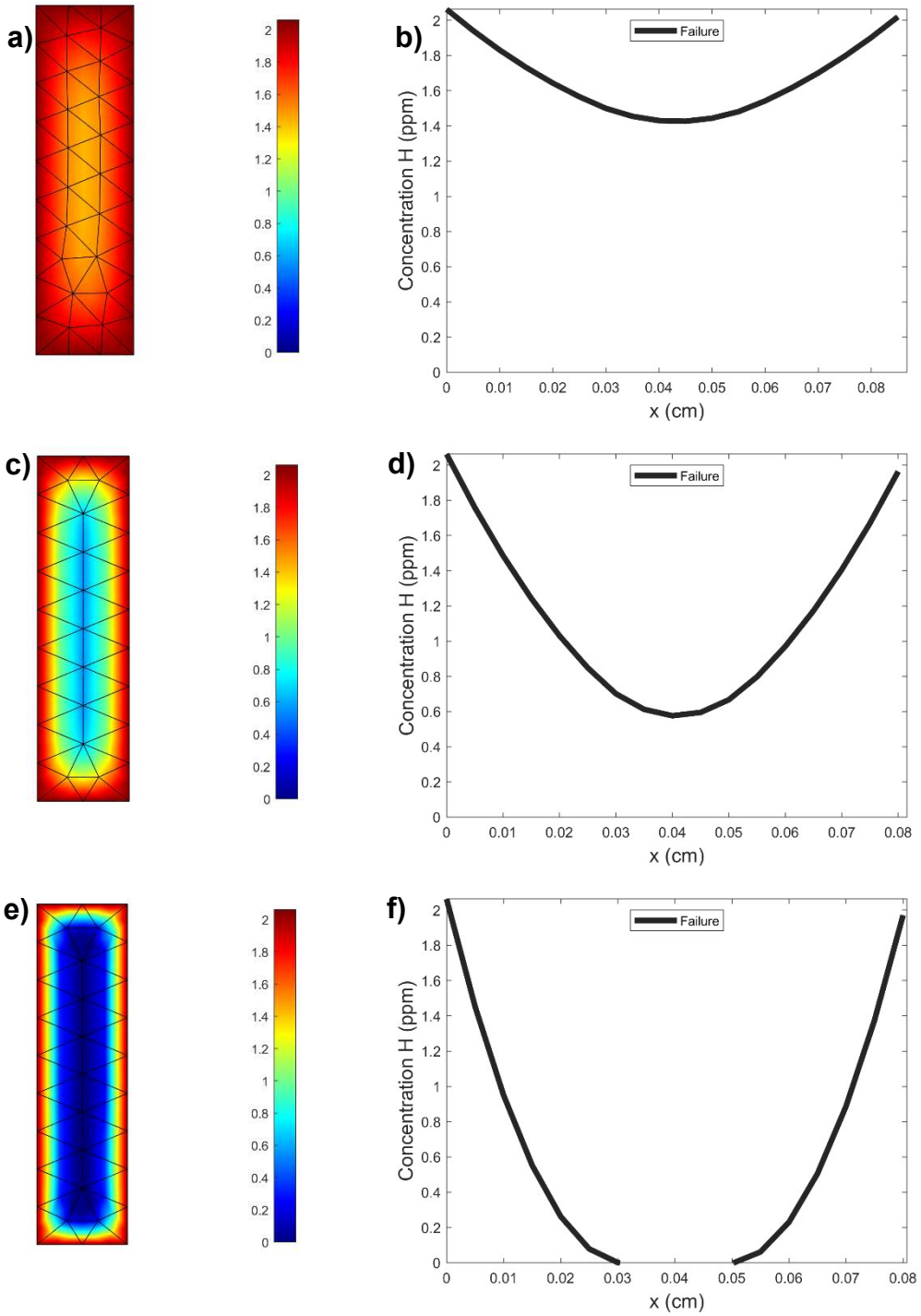

Figure 4.107 Hydrogen distribution and through-thickness hydrogen concentration profile at failure of 22MnB5 (900C) SSRT test undertaken at 10^{-6}/s strain-rate with 2 hours' pre-charging (a) and b)); 10^{-6}/s strain-rate with no pre-charging (c) and d)); 10^{-5}/s strain-rate with no pre-charging (e) and f)).

Figure 4.107 (above) shows the hydrogen distribution and concentration profiles within the SSRT specimens for tests labelled as 22MnB5-Pre-charged-2 (10^{-6}/s strain-rate, 2 hours pre-charging, a) and b)), 22MnB5-Charged-1 (10^{-6}/s strain-rate, no pre-charging, c) and d)), and 22MnB5-Higher strain-rate-3 (10^{-5}/s strain-rate, no pre-charging, e) and f)), respectively.

For the pre-charged specimen tested at 10^{-6}/s strain-rate (Figure 4.107 a) and b)), hydrogen concentration varies between ~2.1 ppm at the charging surfaces to ~ 1.4 ppm at the sample centre, a steeper gradient than we have seen so far from the equivalent tests on the other steels. The sample tested at 10^{-6}/s strain-rate without pre-charging seen in c) and d) shows a concentration gradient where the hydrogen concentration at the centre of the sample is less than one-third of that seen at the charging surface, again steeper than seen in the equivalent specimens for the steels shown prior. Finally, the sample tested at 10^{-5}/s strain-rate without pre-charging shows a steep surface-to-centre concentration gradient, with 0 ppm concentration at the centre of the specimen, reflecting the relatively short duration of the test, and hence charging time.

4.5.2.6 27MnB5+Nb (900C)

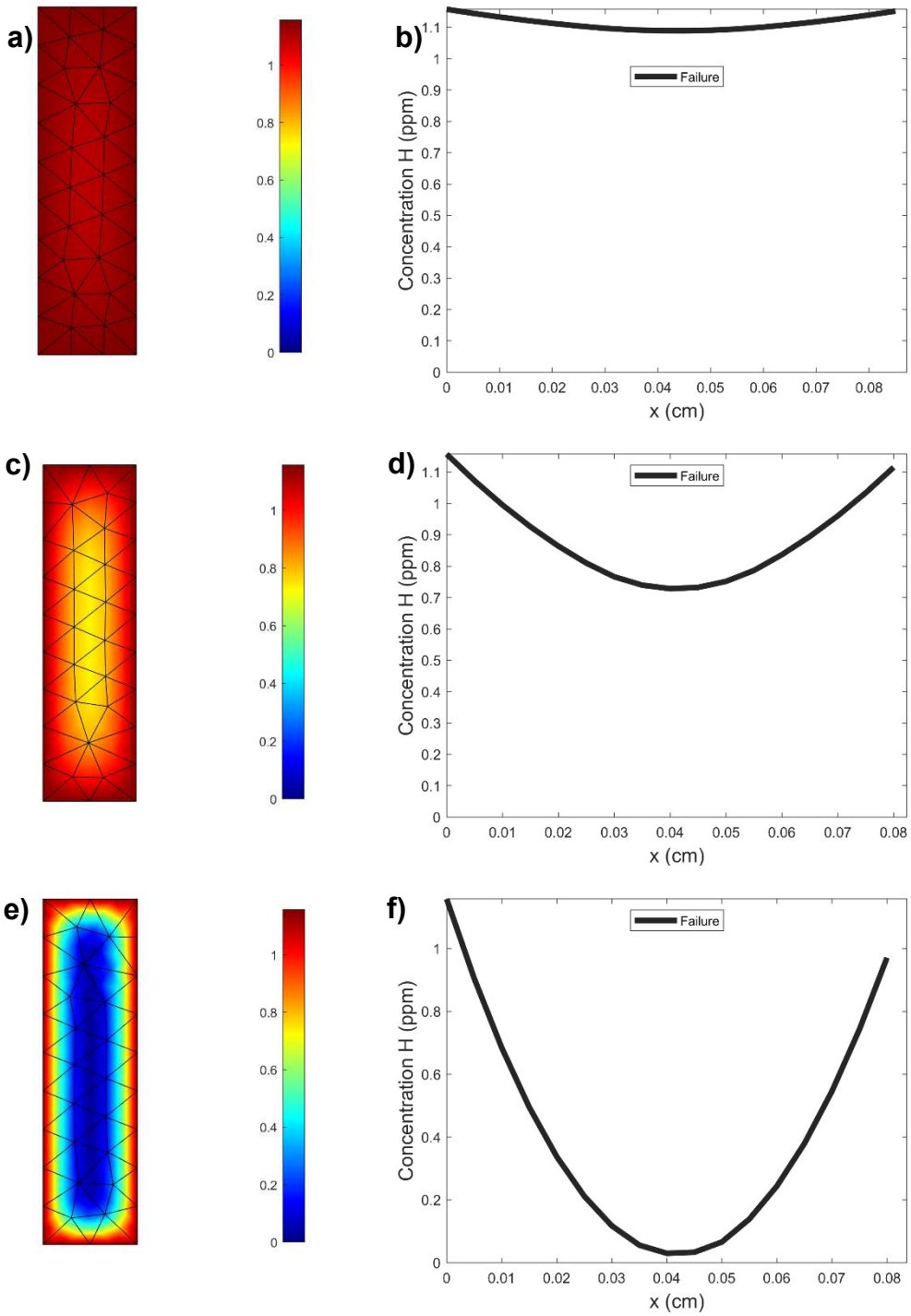

Figure 4.108 Hydrogen distribution and through-thickness hydrogen concentration profile at failure of 27MnB5+Nb (900C) SSRT test undertaken at 10^{-6}/s strain-rate with 2 hours' pre-charging (a) and b)); 10^{-6}/s strain-rate with no pre-charging (c) and d)); 10^{-5}/s strain-rate with no pre-charging (e) and f)).

Figure 4.108 (above) shows the hydrogen distribution and concentration profiles within the SSRT specimens for tests labelled as 27MnB5+Nb-Pre-charged-1 (10^{-6}/s

strain-rate, 2 hours pre-charging, a) and b)), 27MnB5+Nb-Charged-3 (10^{-6}/s strain-rate, no pre-charging, c) and d)), and 27MnB5+Nb-Higher strain-rate-3 (10^{-5}/s strain-rate, no pre-charging, e) and f)), respectively.

For the pre-charged specimen tested at 10^{-6}/s strain-rate (Figure 4.108 a) and b)), hydrogen concentration varies between ~1.2 ppm at the charging surfaces to ~ 1.1 ppm at the sample centre, much more uniformly distributed than for the equivalent 22MnB5 specimen. The sample tested at 10^{-6}/s strain-rate without pre-charging seen in c) and d) shows a slight concentration gradient where the hydrogen concentration at the centre of the sample is just over 0.7 ppm, again a much shallower gradient than that seen for the equivalent 22MnB5 specimen. Finally, the sample tested at 10^{-5}/s strain-rate without pre-charging shows a steep surface-to-centre concentration gradient, with a near-zero concentration at the centre of the specimen.

5 Discussion

This chapter is divided into 3 sub-chapters, which are in turn sub-divided as required. However, where a more holistic discussion is merited, subject-matter from various sections and sources is invoked to enhance the insights gained into this most complex of subjects.

In the first section, the results of the electrochemistry characterisation are analysed, with particular attention given to how the results translate into in-service corrosion performance, when the steels may be exposed to a range of unfavourable environmental conditions. This is particularly relevant when corrosion characteristics will increase the likelihood of hydrogen uptake.

Secondly, the hydrogen diffusion characteristics are compared and contrasted, with particular attention paid to the impact of microstructure upon effective diffusivity. Additional consideration is given to the effects of variation in a range of different experimental parameters on hydrogen diffusion measurements, in particular variation of charging potential, and the effect of recombination poison in the charging electrolyte.

Finally, the results of mechanical testing and subsequent fracture analysis are discussed. Critical consideration is given to the role of microstructure in imparting inherent mitigation or susceptibility to the studied steels, to what degree this is an effect of the relative diffusivity or an intrinsic material property, and how different microstructural features affect the mechanism of degradation. Consideration is also given to the notion of a ‘critical’ hydrogen concentration for brittle failure, and the relative importance of this parameter when assessing the overall susceptibility of a particular steel to hydrogen embrittlement.

5.1 Electrochemistry Characteristics

5.1.1 Product corrosion characteristics

Prior to any discussion about the deleterious effects of hydrogen ingress to investigated steels, it is helpful to discern any differences between the steels in terms of how they respond to the environmental conditions that may be encountered, particularly if there are differences that exist in terms of hydrogen generation due to corrosion processes at the steel surface. To this end, the product corrosion characteristics detailed in Chapter 4.2 are discussed further here, with the particular intention of addressing any characteristic mechanisms that may distinguish the steels in terms of corrosion performance.

5.1.1.1 Open circuit potential

The simplest way to compare the open circuit potential (OCP) measurements between different materials is to compare the values measured at fixed time intervals for each test. However, to characterise the differences in the development of the open circuit potential between steels (all low-alloy carbon steels in this instance), it is helpful to consider three aspects separately, each representing a separate mechanism. Firstly, the time period immediately after immersion until an inflection in the OCP curve, where the often rapid drop in potential is due to the dissolution of surface oxides that develop after surface preparation [77]. Secondly, the 'settled' open circuit potential, considered here to be reached after 2 hours' immersion time, representative of the more 'general' corrosion of the bare steel [233]. Finally, the difference (delta) between these values, as a proxy for the degree of protection being afforded to the bulk steel by its surface oxide layers. Each contributes to the overall corrosion characteristics of the alloy in question, and are plotted for each of the investigated steels in Figure 5.1.

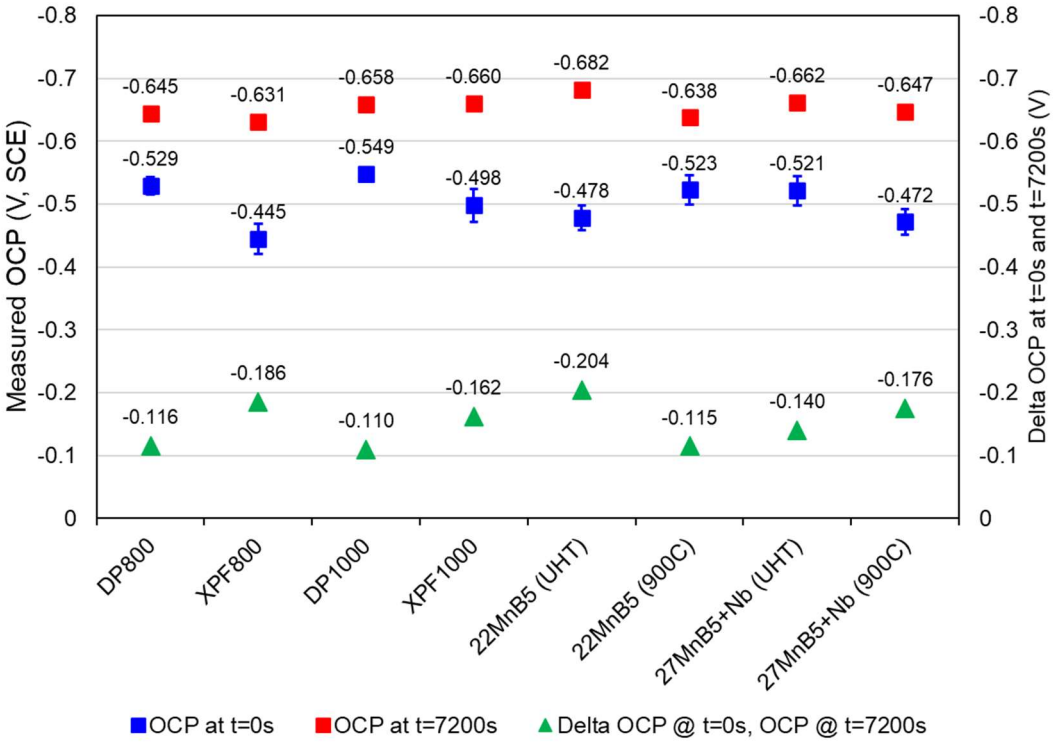

Figure 5.1 Measured open circuit potentials at t=0s and t=7200s, for the investigated steels in aerated 3.5% NaCl solution, and the difference between these values.

Upon immersion (at t=0s), the XPF800 shows the highest (most noble) value for OCP (-0.445 V, SCE), and remains the most noble after 2 hours (-0.631 V, SCE), though it does incur the second largest drop in potential of all of the steels in that time (-0.186 V). XPF800's microstructure is fine-grained, single-phase ferrite with a dispersion of very fine vanadium and molybdenum carbides. Molybdenum, whilst forming carbides that contribute substantially to precipitation hardening in this steel, has also been shown to form MoO_4^{2-} oxides within the rust layer for low-alloy steels of very similar composition immersed in NaCl electrolyte, which are capable of resisting aggressive chloride ions [234], as should also be the case for XPF1000. Where passivity is a consideration, grain refinement (XPF1000 has a smaller grain size than XPF800) is thought to provide a more protective film [235], however grain (or phase) boundaries tend to have higher energy (and electron activity) than occurs within grains, increasing the overall reactivity of the surface [236]. Furthermore, it has been shown recently that interphase (as opposed to random) precipitation of vanadium carbo-nitrides can decrease corrosion resistance in steels of a similar chemistry, and this detrimental effect scales with the levels of microalloy additions [237]; XPF1000 contains double

the carbon of XPF800, lowering the relative A_{r3} temperature, and the reduced transformation kinetics favour an interphase precipitation mode. With 36% more vanadium than XPF800, substantially more interphase precipitation of vanadium carbides is expected in XPF1000 than XPF800, and may be expected to contribute to the slightly more negative OCP measurements.

The boron steels (22MnB5 and 27MnB5+Nb) had almost a mirror-image of each other in terms of OCP results. For the 22MnB5, the un-heat-treated ferrite-segregated carbide microstructure had the third highest potential at t=0s (-0.478 V, SCE), yet had the least noble potential after 2 hours' immersion (-0.682 V, SCE), giving the greatest reduction in potential overall (-0.204 V). Conversely, the martensitic microstructure of the heat-treated condition had one of the least noble potentials at t=0s (-0.523 V, SCE), but the second-most noble potentials after 2 hours' immersion (-0.638 V, SCE), to give the second-lowest reduction in potential of the investigated steels (-0.115 V).

For the 27MnB5+Nb, it is the heat-treated, martensitic condition that has the most noble starting potential (-0.472 V, SCE), with a drop in potential of -0.176 V to reach -0.647 V (SCE) after 2 hours' immersion. The un-heat-treated ferrite-pearlite microstructure, conversely, had a much lower starting potential at t=0s (-0.521 V, SCE), but saw a much lower drop in potential of -0.140 V, so that at t=7200s (-0.662 V, SCE) it had a similar OCP as measured for the DP1000 (ferrite-martensite) and XPF1000 (fully-ferritic with dispersed microalloy nanoprecipitates).

Deconvoluting why the different heat-treatment conditions lead to different behaviours during open circuit potential experiments, plus discerning with any certainty why a particular heat-treatment has had opposing outcomes for two boron-containing low-alloy steels in terms of their corrosion responses, is difficult without further investigation. Nevertheless, for 22MnB5, the largely ferritic, microstructure of the un-heat-treated condition is likely to lead to a relatively homogeneous oxide layer, rich in chromium that has been shown to enhance corrosion resistance in low-alloy steels [233]. Once this oxide layer is removed, however, the grain boundaries are decorated with coarse carbide precipitates, further increasing the energy at the grain boundaries, and hence driving reduction in potential.

27MnB5+Nb in the un-heat-treated condition has a ferrite-pearlite microstructure, which in turn should lead to localised variations in the oxide layer formed after preparation. It also lacks any significant chromium addition, and lacks the extra barrier protection that this may provide. It does contain a considerable niobium addition that the 22MnB5 does not, and niobium carbides have been shown to aid corrosion resistance [237]. However, in the 'as-rolled' (un-heat-treated) condition, cooling is too slow to effectively utilise the precipitation of the NbC, and inferred from the larger grain size lower $R_{p0.2}/R_m$ ratio relative to the 22MnB5 (UHT). In the heat-treated condition, rapid cooling from the 900 ^oC soak temperature maintains the fine grain size obtained when NbC has assisted in retarding the austenite grain growth (Table 4-1), minimising interphase precipitation seen to be detrimental to corrosion properties, but increasing the overall energy due to increased grain boundary area, and hence a more sizeable drop in potential is observed once the surface oxides are dissolved.

Upon quenching from 900 ^oC, 22MnB5 no longer has the segregated carbides observed in the un-heat-treated condition. However, it is postulated that in the martensitic condition chromium is less able to enrich the surface oxide layer, but instead remains in the martensite matrix, leading to lower potential immediately upon immersion, but a relatively more noble potential after 2 hours.

The dual-phase steels behaved very similarly in terms of OCP, with the least noble starting potential upon immersion (-0.529 V (SCE), and -0.549 V (SCE), for DP800 and DP1000, respectively), but relatively low drops in measured potential after 2 hours (-0.116 V and -0.110 V, for DP800 and DP1000, respectively). The two-phase nature of these steels, plus the differences in carbon content between the two phases, means that there are different reactions, or rates of reaction [238], depending on whether the electrolyte contact is with ferrite, martensite, or a phase/grain boundary, and consequently inherently higher energy in the system overall. This is discussed further with regards to cathodic polarisation in the following section.

Mitigating against this inherent propensity for increased corrosion from the presence of multiple phases is a substantial chromium addition (~ 0.55 wt.% for both DP800 and DP1000). As discussed previously, chromium imparts enhanced corrosion

resistance to low-alloy steels, and in these quantities it is to be expected that this addition offers some benefit to the corrosion resistance of these steels.

5.1.1.2 Open circuit potential of zinc-coating

The OCP of the uncoated steels settled at an average of -0.653 V (SCE) (± 0.015 V), whilst the HDG sample settled at -1.116 V (SCE), a delta between the coated and uncoated steels of 0.464 V. Should a zinc coating become sufficiently damaged to expose the steel substrate, this potential difference is more than sufficient to create a galvanic cell, and is one of the reasons that zinc is used to coat steel, as it will be sacrificially anodically dissolved in the event of the steel substrate becoming exposed in a corrosive environment. As zinc becomes the anode, the steel becomes the cathode, with a variety of possible reactions occurring at the steel surface that depend on the ions present in the electrolyte, electrolyte pH (generally and locally), ratio of anode to cathode in terms of area exposed to the electrolyte, and therefore the intensity of the reactions at the anode and the cathode [60]. At sufficient intensity, or sufficiently low pH (such as in crevice corrosion conditions shown in Chapter 4.2.3), the galvanic corrosion of zinc will cause a hydrogen evolution reaction at the surface of the steel, as per equation (8).

Given the differences in 'settled' OCP between the steels, and the fact that during coating no surface oxides should have formed on the surface of the substrate, this galvanic effect can be expected to be most pronounced on the steels with the most 'noble' value for OCP, which in this case is XPF800 (should it be utilised with a hot-dipped zinc coating). This is discussed further with regards to the SVET scans undertaken on a damaged coated specimen.

5.1.1.3 Potentiodynamic cathodic polarisation

Figure 5.2 (below) shows that for these steels, the average values of the Tafel slopes taken from cathodic potentiodynamic polarisation sweeps are close together, and with significant standard deviation any differences cannot be concluded to be as a result of intrinsic differences in polarisation behaviour with 95% level of confidence.

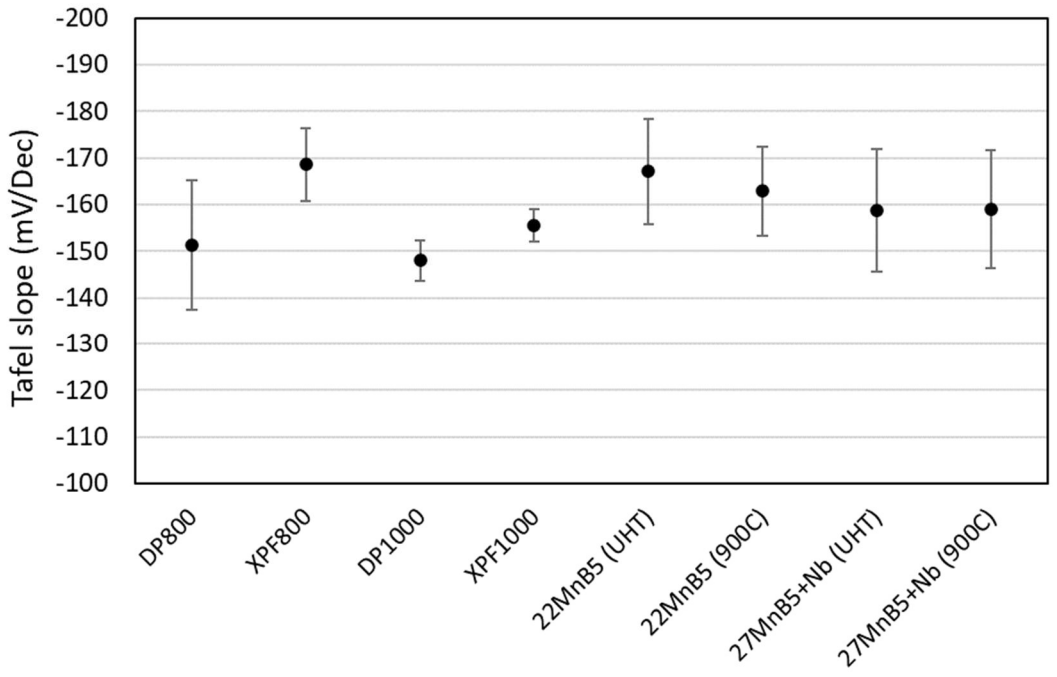

Figure 5.2 Average Tafel slopes from 5 cathodic potentiodynamic polarisation sweeps for each product (and condition) in 3.5% NaCl solution.

The cathodic potentiodynamic polarisation results showed that for the press-hardening boron steels (22MnB5 and 27MnB5+Nb) there was no statistically significant difference between the Tafel slopes whether the microstructure was ferrite-pearlite/ferrite-segregated carbide (as rolled) or martensitic (heat-treated), confirmed via Student's t-test for Tafel slope from 5 potentiodynamic curves.

With the exception of DP1000, which proved to be statistically significantly different (with 95% confidence) from 22MnB5 (both heat-treated and un-heat-treated conditions), XPF800, and XPF1000, the magnitude of the standard deviation in measured Tafel slopes for the majority of these steels means that there is significant overlap in the distributions of the Tafel slopes between almost all of the steels.

DP1000 is observed to have the lowest measured Tafel slope (-148 mV/Dec) of all the investigated steels (for the intervals measured), indicating that for a given increase in magnitude of polarisation, DP1000 would experience the greatest increase in current density of any of the investigated steels.

A closer look at the surface of DP1000 may provide some explanation as to why it may be i) inherently more sensitive to polarisation at these potentials; ii) respond differently to the other investigated steels upon immersion to a NaCl electrolyte. Figure 5.3 shows a series of scanning Kelvin probe force microscope (SKPFM) scans on the microstructure of DP1000.

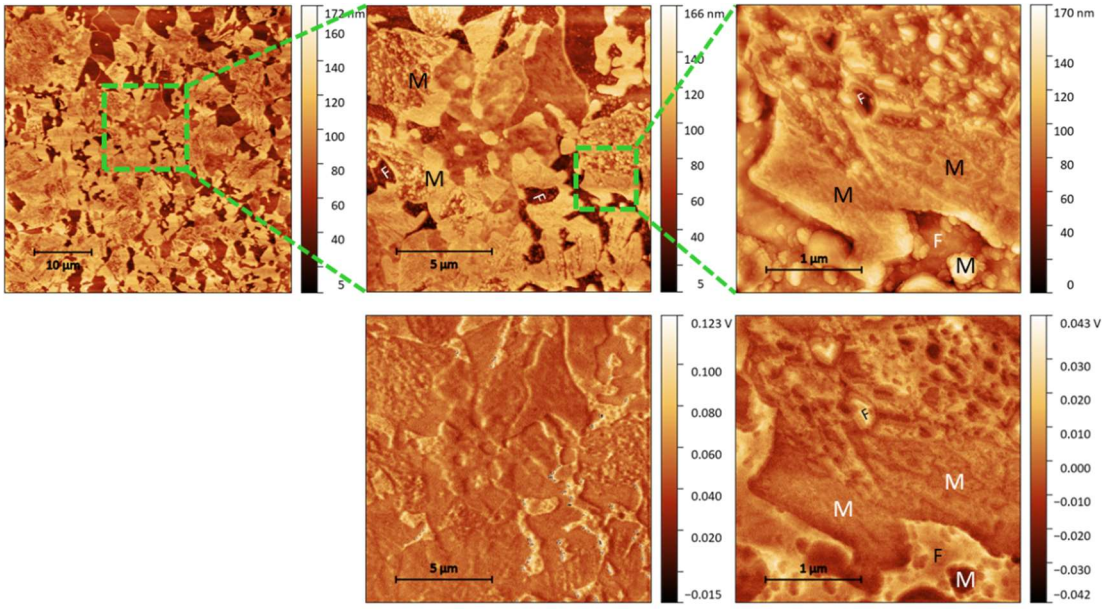

Figure 5.3 Scanning Kelvin probe force microscopy images of DP100 in air. The top row shows cascading images of the topographical scans. The bottom row images are of corresponding volta potential scans. Ferrite grains labelled 'F'; martensite grains labelled 'M'.

The images above show that there is an inherent potential difference between the ferrite and martensite phases in DP1000, on the order of around 85-138 mV, with the ferrite phase acting as the anode and the martensite phase acting as the cathode, and the contrast between the different potentials most acute at the phase boundaries. Again, this is a sufficiently large potential difference that under the right conditions would form a galvanic cell within the steel itself. Given that DP1000 has a roughly 45% / 55% mix between ferrite-phase and martensite-phase respectively, and that the phase distribution of the tested material is largely homogeneous, there is the possibility that

this is precisely what is happening, and that reactions at the sample surface are being made more complex by the inherently galvanic nature of the material itself, both during OCP experiments and during cathodic polarisation. DP800, another ferrite-martensite steel, but with a lower volume fraction of the 'cathodic' martensite phase (~40%), had the second lowest average Tafel slope (albeit with greater standard deviation) at -151 mV/Dec. For the remaining steels, including those that contain significant volume fractions of second phase Fe_3C, this potential difference will be less pronounced as the volume fractions of second phases are comparatively much smaller.

5.1.1.4 Damaged coating characteristics

The first thing observed from the SVET scans on the damaged zinc coating exposing the (DX51) steel substrate in 0.1 M NaCl electrolyte is that immediately after immersion, the anodic current density is highly concentrated in very small regions approximately adjacent to regions of weak cathodic activity, which is far more general in these early stages. This is an indication that corrosion of the zinc coating commences by pitting.

After ~ 2.5 hours, the anodic regions begin to become more general, but with lower intensity, indicating that pitting has ceased and corrosion of the zinc has become more general. Conversely, the cathodic regions periodically develop some localised regions of increased cathodic current density, particularly after about 15 hours, peaking around 20 hours. After 24 hours, both anodic and cathodic activity had reduced intensity from peak current densities in these localised, previously high-intensity regions. Plots of the maximum measured anodic and cathodic current densities are displayed in Figure 5.4, where a general trend of decreasing magnitude of maximum anodic activity over time, whilst maximum cathodic activity generally increases in magnitude (becomes more negative) over time, can be seen.

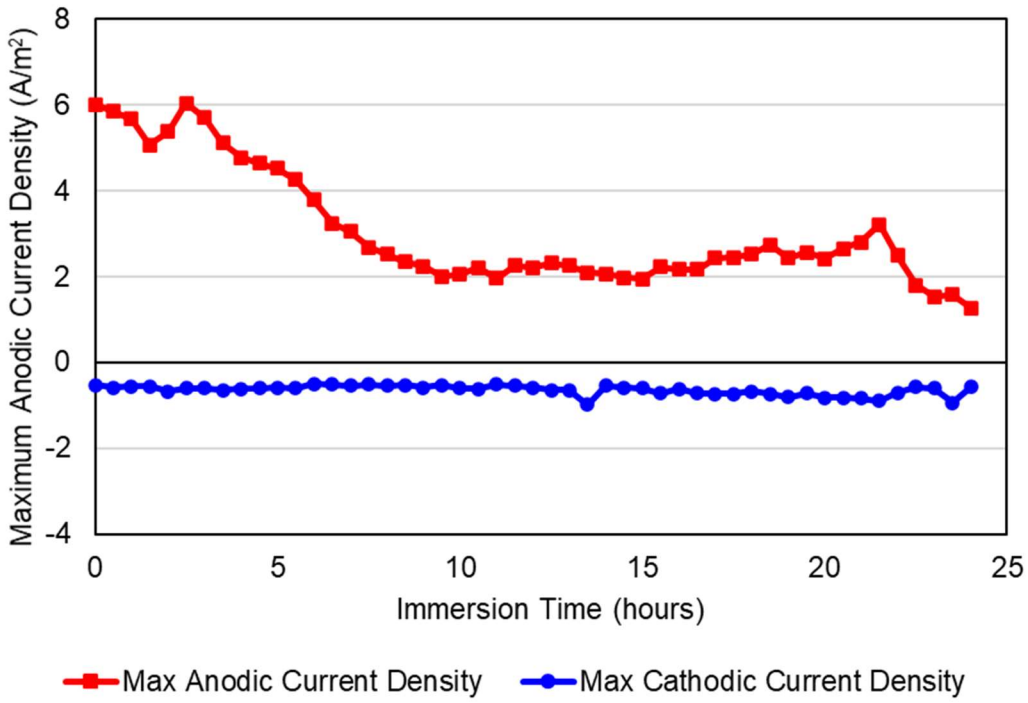

Figure 5.4 Maximum measured anodic and cathodic current densities over time.

Contrast this with the overall behaviour over the total surface in contact with the electrolyte. Figure 5.5 and Figure 5.6 show the area-averaged anodic and cathodic current densities, respectively, calculated according to equation (51) (the equivalent for anodic current density with respect to time, J_{at}, calculated using $J_{z(x,y)} > 0$).

$$I_c = A.J_{ct} \geq \int_0^y \int_0^x [J_{z(x,y)} < 0]\, dx\, dy \qquad (51)$$

Clearly, the measured total anodic current density shows much greater stability over the 24 hour duration of the test than the maximum current density plot would imply, showing that there is a sizeable amount of general corrosion of the zinc coating as the immediate pitting behaviour subsides, and continuing throughout. Conversely, the cathodic current density measurements show a great degree of fluctuation, but are consistently measuring at a higher magnitude than the anodic current density.

However, by utilising the area-averaged values for anodic or cathodic current, I_a and I_c, respectively (also calculated according to equation (51)), and by calculating the area of measured anodic or cathodic 'regions 'on the sample surface (red- or blue-coloured

in the SVET data presented in Figure 4.21 - Figure 4.23, respectively), it is possible to reconstruct values for 'true' anodic or cathodic current densities, applicable only to the relevant regions on the sample surface, and analogous to the calculation of 'true' stress, whereby the values obtained pertain to the measured area of a sample at the precise moment of measurement.

Of course, under open-circuit conditions such as these, cathodic regions, or anodic regions do not exist in isolation, and the presence of one necessitates the presence of the other. Nevertheless, these values for 'true' anodic or cathodic current densities show that in the specific regions (not averaged over the entire surface), current density in both regimes is substantially higher than when averaged over the entirety of the scan area.

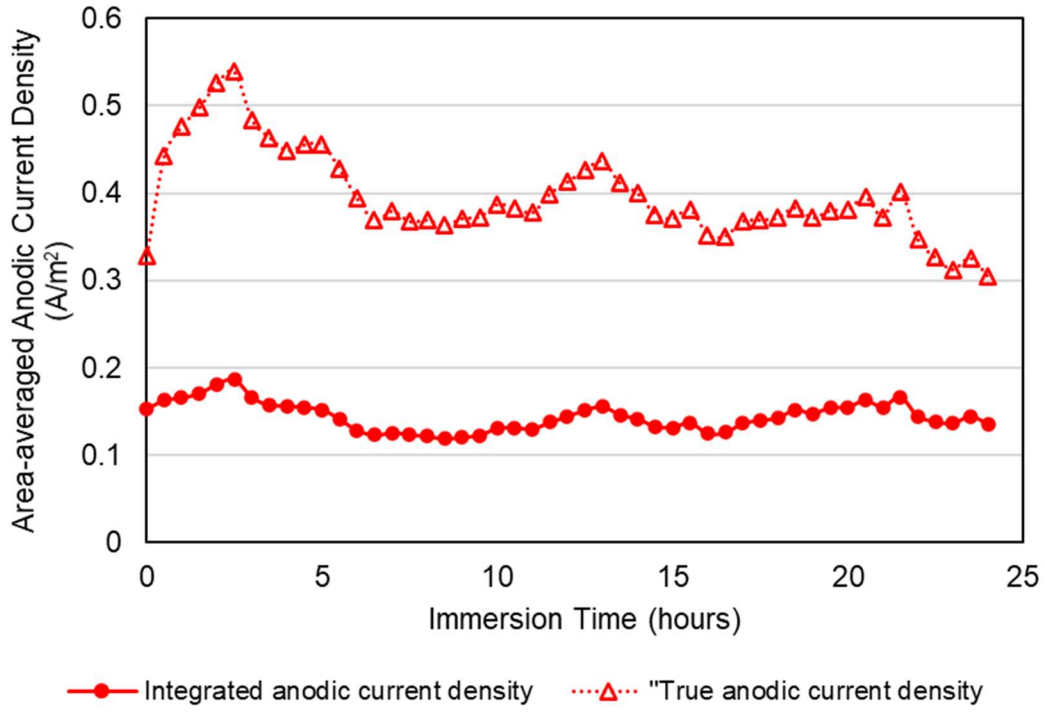

Figure 5.5 Integrated anodic current density, Ja_z, and calculated 'true' anodic current density based on the area of measured anodic current density, over time.

For the cathodic regions, the 'true' current density is actually close to -0.3 A/m^2 for most of the duration of the experiment, and generally increasing further after around 16 hours. At this cathodic current density, it may be expected that significant hydrogen evolution will occur at the exposed steel surface, as evidenced by the permeation

transient undertaken with potentiostatic charging polarisation of -850 mV (SCE) (Figure 4.37), in combination with potentiodynamic sweeps of the studied steels, which show that -0.3 A/m^2 is in the typical range of current densities that could be expected during polarisation at around -850 mV at a pseudo-potentiostatic scan rate of -0.167 mV/s.

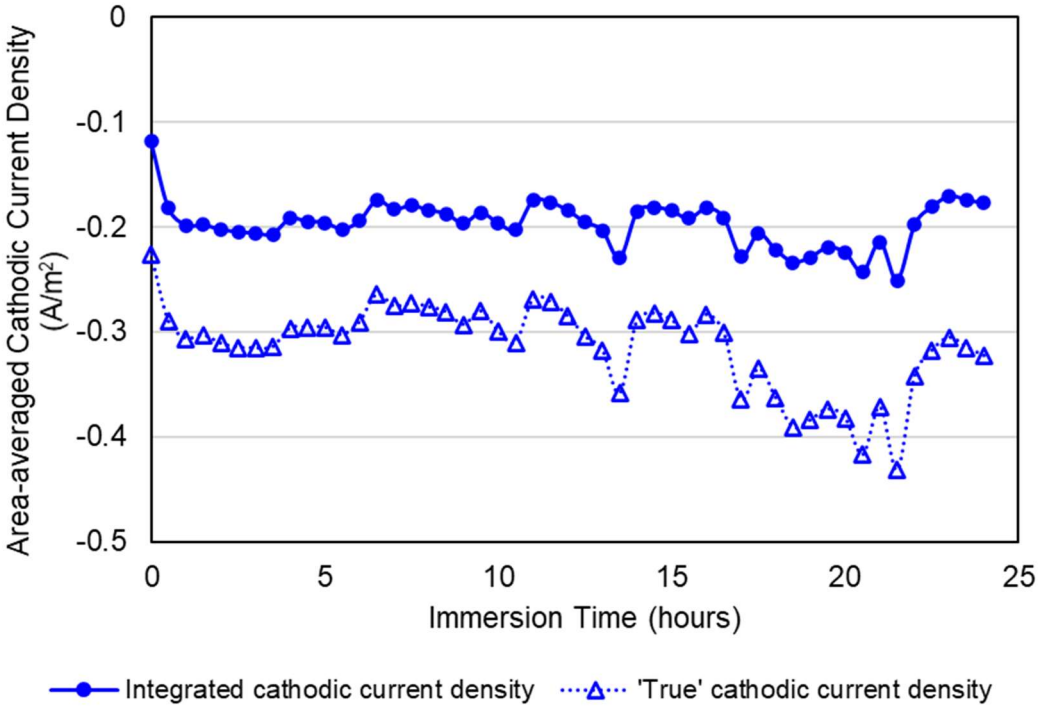

Figure 5.6 Integrated cathodic current density, Jc_z, and calculated 'true' cathodic current density based on the area of measured cathodic current density, over time.

Figure 5.7, below, shows the measured area coverage of regions with anodic measurements (Ja_z) and those with cathodic measurements (Jc_z), as well as regions with cathodic current densities measuring below -0.3 A/m^2. This shows how, in part, and as seen from the contour plots (Figure 4.21 - Figure 4.23) shown previously, that increased regions of cathodic activity of higher magnitude (i.e. measuring <= -0.3A/m^2) not only counterbalances the overall decrease in total cathodic area, but makes a sizeable contribution to the general increase in area-averaged (across the whole scan area) Jc_z.

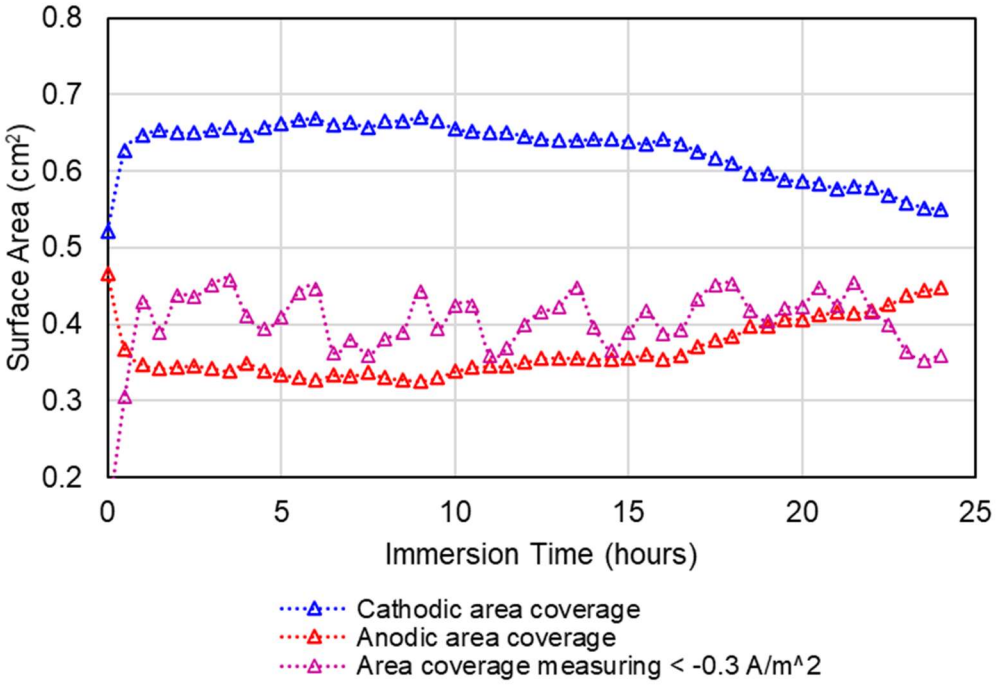

Figure 5.7 Surface area coverage for J_z values that are locally measured < 0 A/m^2 (cathodic, blue triangles), > 0 A/m^2 (anodic, red triangles), and <= -0.3 A/m^2 (cathodic, magenta triangles).

By utilising the SVET data and applying Faraday's Law, it is possible to calculate an estimate for the total hydrogen evolved at the exposed steel surface according to equation (52),

$$Q = \int_{t=0}^{t=t_m} J_{ct} \, . dt \tag{52}$$

where Q is the total charge in C/m^2 and t_m the scan time in seconds, with integration performed numerically and assuming that J_{ct} is constant between scans. A note of caution is merited as detection efficiency only approaches 100% when local anode-cathode spacing is significantly greater than scan height ($L_{ac} \gg h$) [239], which here is 100 µm. A cursory glance at the contour plots in Figure 4.21 - Figure 4.23 shows that strongly anodic and strongly cathodic regions are segregated by regions of weaker anodic, or cathodic, measurements that are greater than 100 µm in width, meaning this criteria can be taken to be effectively fulfilled for these purposes, as the weakest cathodic regions will make proportionally little contribution to the total charge.

Concern is also merited over the previous finding of Glover [240] of a tendency for the SVET to over-estimate the cathodic current density in the presence of hydrogen

bubbles adhered to the sample surface. However, in this study, no surface bubbles were observed, and work discussed later would indicate that no hydrogen bubbles are likely to form at the measured values we see here.

Figure 5.8, below, shows the values for hydrogen evolved at the exposed steel surface over the duration of the experiment, both considering all cathodic current density measurements as having a contribution, and when considering only measurements <= -0.3 A/m^2 as contributing to hydrogen evolution (which also has the effect of removing ambiguity due to detection efficiency).

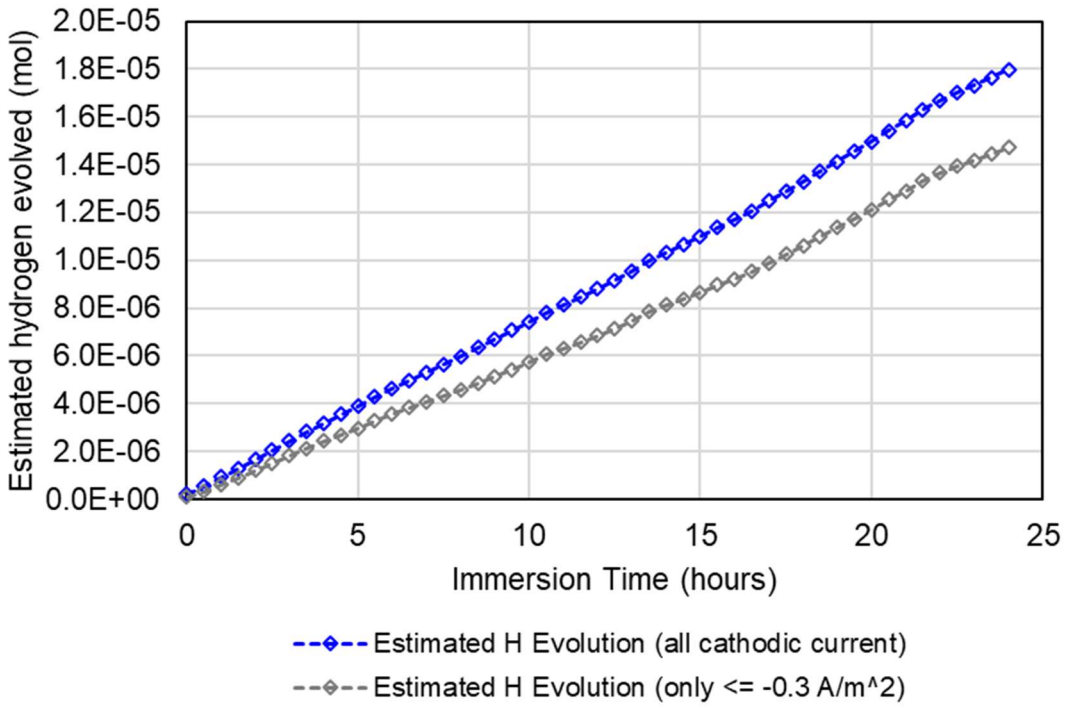

Figure 5.8 Estimated hydrogen evolution over the duration of the experiment. Blue diamonds represent hydrogen evolved if the hydrogen evolution reaction is taking place at all cathodic current densities; grey diamonds represent hydrogen evolution only where J_z measured below -0.3 A/m^2.

Figure 5.8 confirms that the weakly cathodic regions make little difference to the overall estimate of hydrogen evolution during the 24 hours of the experiment. Nonetheless, the total hydrogen evolved over 24 hours in these conditions is similar to that estimated from just over 3 hours' charging a surface area roughly three times larger in electrolyte with close to six times the molar concentration of NaCl, a recombination poison addition, and with an imposed cathodic polarisation of -1050

mV (SCE). This can be seen from Figure 5.9, where the hydrogen evolution during charging of a slow strain-rate test of heat-treated 22MnB5, calculated according to equation (52), is shown.

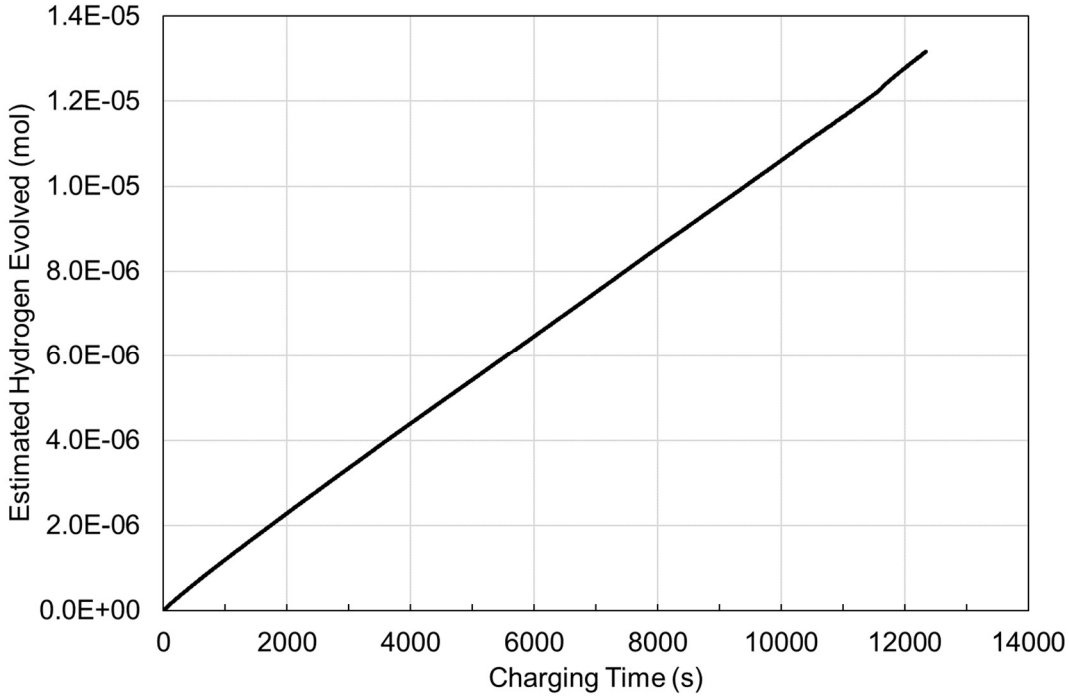

Figure 5.9 Estimated hydrogen evolved during charging of SSRT sample 22MnB5-Pre-charged-1 in 3.5% NaCl + 3g/L NH4SCN solution with an applied potential of -1050 mV (SCE).

Clearly, conditions during the SVET scans are much less severe in terms of hydrogen charging than those imparted during slow strain-rate tests. Despite this, and when considering that the worst-performing steels in SSRTs had only been exposed to an estimated total hydrogen evolution of ~ 7×10^{-7} mol.H to suffer a > 40% reduction in total elongation, it is reasonable to conclude that the anodic dissolution of a zinc coating in a chloride-containing electrolyte will be sufficient to induce a potentially damaging hydrogen evolution reaction at the exposed surface of the steel substrate. This is further strengthened when considering that the SVET scans were undertaken in a relatively low molarity NaCl solution. Numerous researchers [66,80] have shown a link between chloride-concentration and hydrogen uptake in steels, and Liu [73] showed that once a zinc coating becomes damaged or corroded during service, more hydrogen can enter the steel substrate than if the steel was not coated at all.

This presents a particular problem in coastal locations, or during winter months in temperate or colder climates where salt grit is regularly added to road surfaces to prevent freezing. Rivett [241] found chloride molar quantities exceeding that of the electrolyte used in the SVET study in this work in freshwater streams near to UK motorways that had been treated with salt. It is reasonable to infer that chloride concentrations in surface water along the highway will be substantially higher than this.

Under these conditions, steels with the most 'noble' open-circuit potentials (those furthest from that of the zinc coating), in this case XPF800 and heat-treated 22MnB5, will form the most potent galvanic cell (should they incur coating damage), driving reactions at both the zinc coating (anode) and steel substrate (cathode). The overall potential of a cell involving the galvanic corrosion of zinc on XPF800 in 3.5% NaCl (no allowance for ohmic drop) is plotted in Figure 5.10. In this respect, stronger inherent corrosion-resistance of a steel part is not necessarily an advantage. Liu [73] found that dissolution of zinc induced a cathodic polarisation at the steel surface, favouring reduction of water (or reduction of hydrogen at low pH). As the vast majority of coatings utilised for automotive steels are either Zn, Zn-Al, or Zn-Al-Mg, all of which have similar free corrosion potentials in sodium chloride solutions, this is an issue for most coated automotive steels.

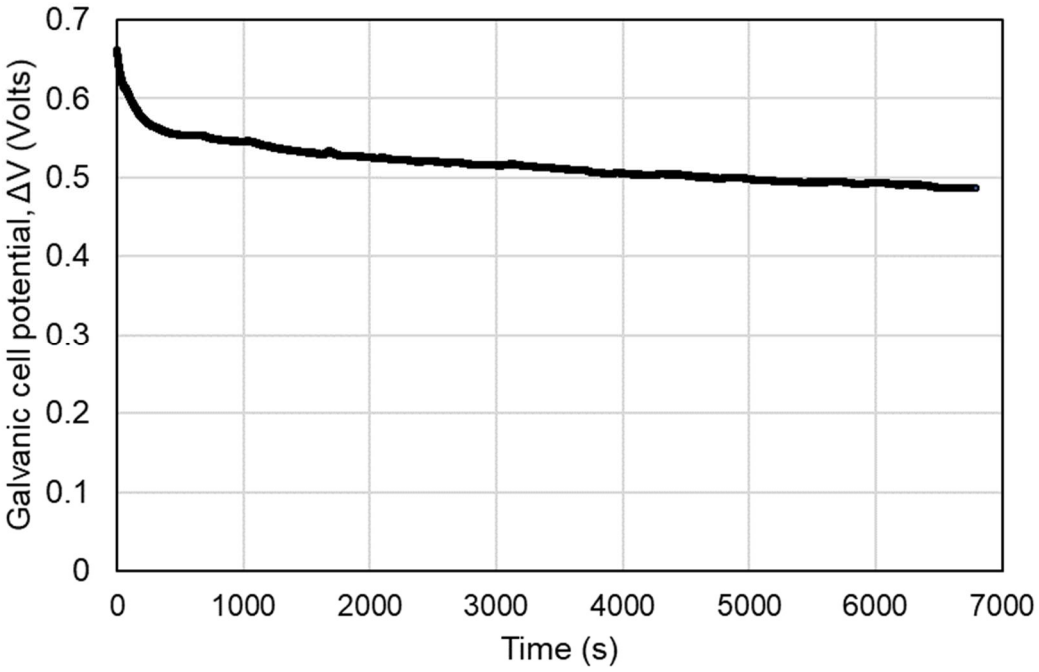

Figure 5.10 Theoretical galvanic cell potential, ΔV, of zinc coating corroding on XPF800 substrate.

More generally, resolving this issue, whilst maintaining the beneficial effects of these coatings, remains a significant challenge. It should be noted, however, that apart form XPF800 and XPF1000, the steels studied here are likely to be used within the body-in-white (BiW) structure, which has several further coatings deposited, each providing a different function, and limiting the opportunity for the steel parts to be exposed to corrosive environments. Nevertheless, to minimise the problems caused by hydrogen, it is preferable to design high-strength steels with effective means of resisting degradation due to hydrogen ingress, as part design, as well as environmental factors, are likely to continue to offer the possibility of subjecting these steels to corrosion, and in turn the prospect of exposure to hydrogen.

5.2 Hydrogen diffusion

In this section, the results of hydrogen permeation experiments displayed in Figure 4.26 to Figure 4.38 are analysed. Particular attention is paid to the impact that microstructural differences have upon the permeation curve, maximum flux, and diffusion coefficient. Adjustments in experimental parameters such as charging potential, recombination poison additions to charging electrolyte, and membrane thickness, are also discussed in terms of the impact they have upon diffusion measurements.

5.2.1 Effect of charging potential

Prior to undertaking permeation tests probing the effects of microstructure, preliminary tests were carried out at various charging potentials to probe the effects of the overpotential to the hydrogen evolution reaction on the permeation transient. This parameter has a direct effect upon overall hydrogen concentration at the charging surface, C_0, for a given charging electrolyte and surface condition [242]. The constant hydrogen concentration at the charging surface achieved at each charging potential is shown graphically below in Figure 5.11.

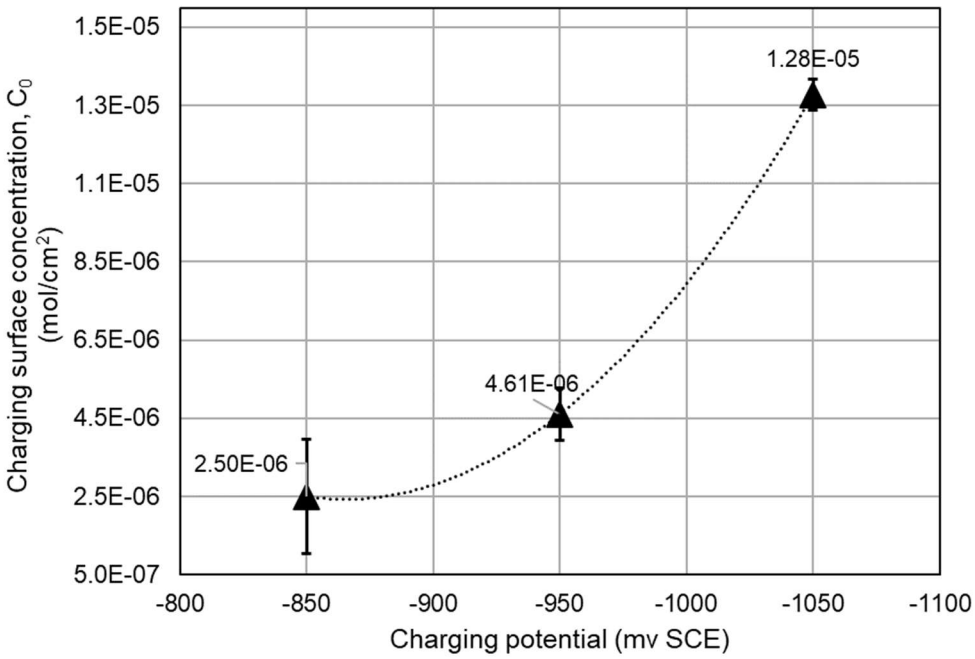

Figure 5.11 Differences in calculated charging surface concentration, C_0, achieved at different charging potentials during permeation tests undertaken on 22MnB5 (900C) membranes of 1.2 mm thickness.

It is clear from Figure 5.11 that, for these charging potentials, the relationship between charging potentials and charging surface concentration is not a strictly linear correlation, with a rapid increase when moving from -950 mV to -1050 mV (SCE) that is not seen for the equivalent transition when moving from -850 mV to -950 mV. This can be explained when considering the Butler-Volmer equation which relates the current density to the overpotential, and is expressed as :

$$i = i_0 \left(e^{\frac{(1-\beta)zF\eta}{RT}} - e^{\frac{-\beta zF\eta}{RT}} \right) \tag{53}$$

where η is overpotential ($\eta = E - E_{equilibrium}$), i_0 is exchange current density, β charge transfer coefficient, F is the Faraday constant, z the number of electrons involved in the electrode reaction, R is the gas constant, and T the absolute temperature. At low overpotentials, this equation approximates a linear relationship between overpotential, η, and current density, i [64]:

$$\eta = \frac{RT}{zFi_0} \times i = k \times i \tag{54}$$

where k is the rate constant. However, at higher overpotentials (polarisation further from equilibrium potential), the Butler-Volmer equation simplifies to the Tafel equation, which for cathodic reactions is:

$$\eta = a_c - b_c \log i \tag{55}$$

where:

$$a = -\frac{2.3RT}{\beta zF} \log i_0 \tag{56}$$

and:

$$b = \frac{2.3RT}{\beta zF} \tag{57}$$

which of course, when combined, equations (55)-(57) resemble equation (13b).

Hence, as overpotentials become increasingly cathodic, there is a transition between linear response of current density (and thus hydrogen evolution reaction rate, in this case) to applied overpotential, to an exponential one.

This pattern is also seen when plotting the calculated values for steady-state flux, J∞, versus charging potential, as can be seen from Figure 5.12, below.

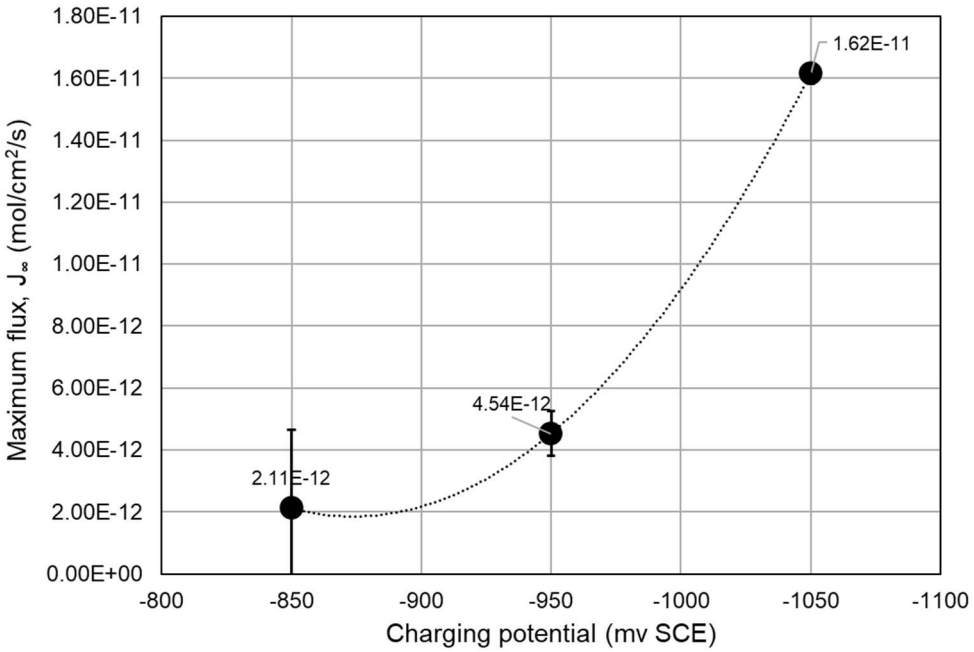

Figure 5.12 Differences in maximum flux, J∞, achieved at different charging potentials during permeation tests undertaken on 22MnB5 (900C) membranes of 1.2 mm thickness.

Hydrogen permeation transients seen in Figure 4.37 get noticeably steeper as the charging potential becomes more severe, and increase in parallel towards larger steady-state flux, 2.11×10^{-12}, 4.54×10^{-12}, and 1.62×10^{-11} mol/cm^2/s at -850, -950, and -1050 mV (SCE) respectively (Figure 5.12). This follows from the increase in hydrogen concentration (C_0 = 2.50×10^{-6}, 4.61×10^{-6}, and 1.28×10^{-5} mol/cm^3, respectively, Figure 5.11) obtained at the charging surface with increasing overpotential, which follows the same trend as the cathodic Tafel slope up to a limiting value [139], although using NH_4SCN as a recombination poison could significantly increase the Tafel slope in the cathodic region (compared to a 3.5% NaCl-only solution), as found by Akiyama and Li [172], and is discussed in Chapter 5.2.2.

The maximum flux, J_∞, increases by a higher proportion for potentials between -950 mV to -1050 mV, than that for the range -850 mV to -950 mV. This is due to a change in the balance of reactions at the charging surface at ~ -1040 mV, where the principal cathodic reaction in a 3.5% NaCl solution transitions from oxygen reduction at potentials around the open circuit potential, to the reduction of water [238].

This is better illustrated when considering the potentiodynamic curves of 22MnB5 (900C) recreated in Figure 5.13.

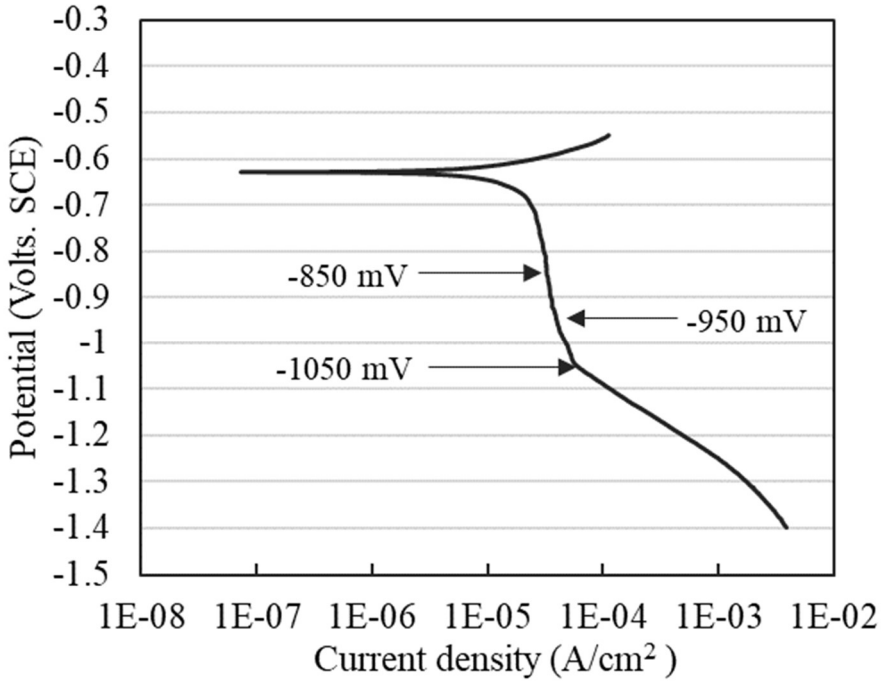

Figure 5.13 Typical potentiodynamic curves for 22MnB5 (900C) in heat-treated condition, 3.5% NaCl, 0.1667 mV/s.

It can be seen from Figure 5.13 that a potential of -1050 mV (SCE) is situated beyond the inflection point on the cathodic potentiodynamic curve that indicates a transition in the reactions at the sample surface (transitioning from linear to exponential response of change in current density to change in potential), whereas -850 mV and -950 mV lie prior to this inflection point in a region of competing cathodic reactions.

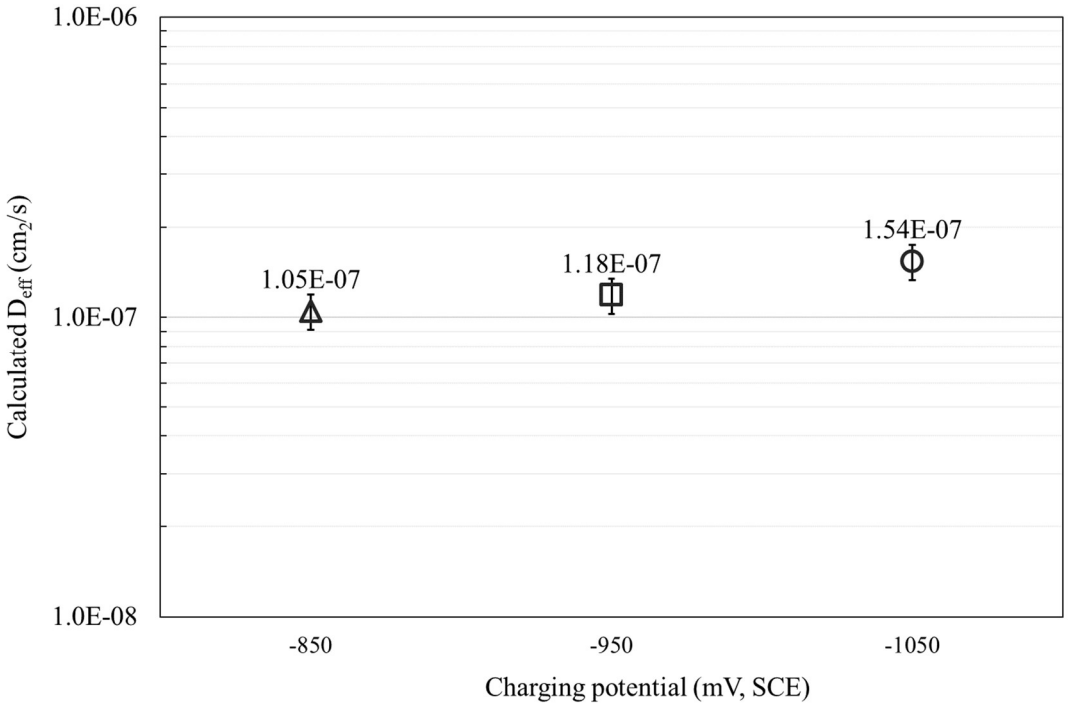

Figure 5.14 The effect of charging overpotential on D_{eff}, 22MnB5 (900C), 1.2 mm.

Despite the increase in J_∞ with increasing overpotential (as seen in Table 4-5), there is little difference between charging potentials in the time it takes to reach steady-state flux, and this is further emphasised when comparing the calculated values for D_{eff} for each potential, seen in Figure 5.14, with values increasing only by very small amounts with each increase in overpotential. This implies that there is, at most, a modest increase in diffusivity from increasing the overpotential in this range. This increase may not be significant considering the standard deviation values obtained at -1050 mV, and curves simulated according to Fick's laws provide a good fit to the test data indicating prevalence of 'ideal' lattice diffusion. Furthermore, whilst the concentration profiles simulated using input parameters from experimental data illustrate how the hydrogen concentration increases according to applied charging potential, when these are normalised there is very little apparent difference in the relative distribution of hydrogen across the membranes between the different charging potentials at any of the

sampled times. This is further visualised in the distribution maps from finite-element modelling shown in Table 4-20. Conversely, the small increase in D_{eff} *may* imply that with more severe charging potential (from -850 mV to -1050 mV), and hence increased C_0 (from 2.50×10^{-6} to 1.28×10^{-5} mol/cm^3), filling of any trap sites that may be present has proceeded more quickly, reaching a maximum occupancy at shorter times, and allowing lattice diffusion, i.e. J_∞, to be attained at a correspondingly shorter time [243].

Whilst it is recommended that where membranes of increasing thickness are not available, applied charging potential (or current) should be as high as possible to derive something close to 'intrinsic' diffusion properties [97], we have seen here that despite the increase in concentration at the charging surface, this has had minimal impact on the effective lattice diffusion measurements, implying that for 22MnB5 (900C) at 1.2 mm membrane thickness D_{eff} is not concentration-dependent.

5.2.2 Effect of recombination poison on charging severity

To assist determining optimal experimental parameters for studying the effects of microstructure upon effective diffusion properties, and prior to testing the effects of charging potential upon permeation characteristics, a separate experiment was undertaken to determine the maximum charging severity that should be imparted to permeation specimens involving periodic increases in fixed potential between a steel specimen and a saturated calomel reference electrode in 3.5% NaCl solution, and gauging the prominence of visual hydrogen bubbles upon the steels surface. Alongside this, the effect of ammonium thiocyanate, NH_4SCN as a recombination poison was investigated to look at how this influences hydrogen charging between -1050 mV and -1250 mV (SCE), and whether this could allow for the application of lower applied potentials.

It was found that at potentials negative of -1100 mV (SCE) inclusive, visible bubbles of hydrogen would form on the specimen surface, impairing the surface reactions and enabling the possibility of uneven hydrogen charging across the specimen surface. Furthermore, the inclusion of NH_4SCN did not appreciably lower the prevalence of visible bubbles at the charging surface. For this reason, an applied potential of -1050 mV was chosen as the optimal charging potential.

Despite there being no reduction in bubbles at the specimen surface, it was still determined that the addition of NH_4SCN was beneficial. Figure 5.15 shows plots of measured current densities versus time for each potentiostatic polarisation test between -1050 mV and -1250 mV (SCE).

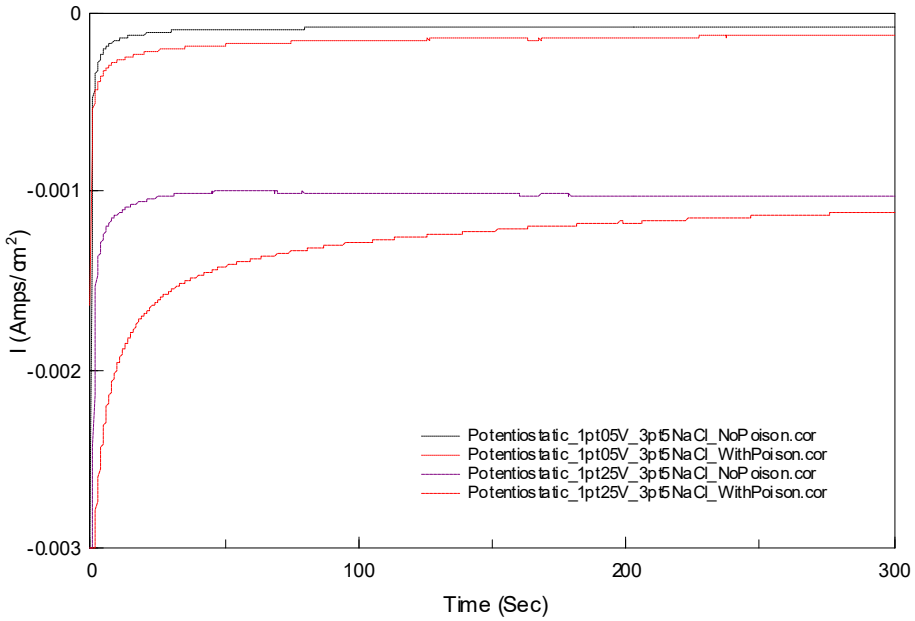

Figure 5.15 Current density (I) versus Time for the preliminary charging test undertaken between -1050 mV and -1250 mV (SCE). Graph only shows data for the highest and lowest applied potentials investigated as representation.

Figure 5.15 clearly shows that at a given potential there is an increase in current density when NH_4SCN is present compared to a 3.5% NaCl–only electrolyte. This means that for a given applied potential (and presence of visible hydrogen bubbles or otherwise), it is expected that there is an increase in 'uncombined' hydrogen at the charging surface, and hence greater availability of hydrogen ions to permeate the membrane. This is perhaps better illustrated when the same data is plotted as charge (Q) versus time, as in Figure 5.16, below.

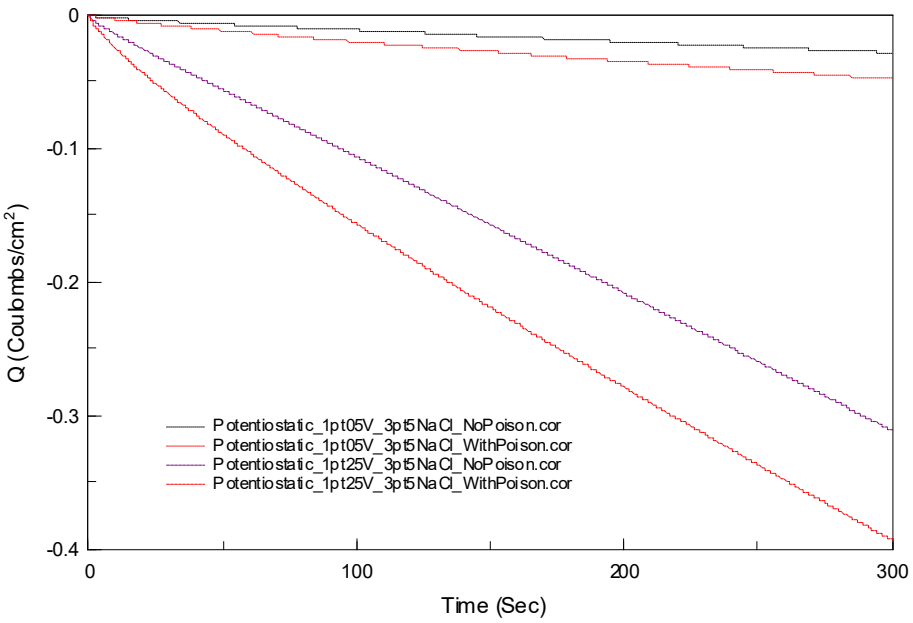

Figure 5.16 Charge (Q) versus Time for preliminary charging test undertaken between -1050 mV and -1250 mV (SCE). Graph only shows data for the highest and lowest applied potentials investigated as representation.

What Figure 5.15 and Figure 5.16 demonstrate is that the addition of NH_4SCN as a recombination poison increases the charge transfer for a given potential. This is not however due to it simply inhibiting recombination of hydrogen at the charging surface. In the non-buffered electrolytes used in this work, the 3.5% NaCl solution typically had a pH of ~ 5.9, whereas the addition of 3g/L NH_4SCN lowered the pH of the solution to 4.56. Cathodic reactions on the surface of steels include the reduction of both water and hydrogen, with the balance between the two dependent on pH. This has the effect that for a given *applied* potential an increase in the *overpotential* for the hydrogen evolution reaction is obtained, according to the Nernst equation, due to the relationship between pH and equilibrium potential, shown in the Pourbaix diagram for iron (Figure 2.21).

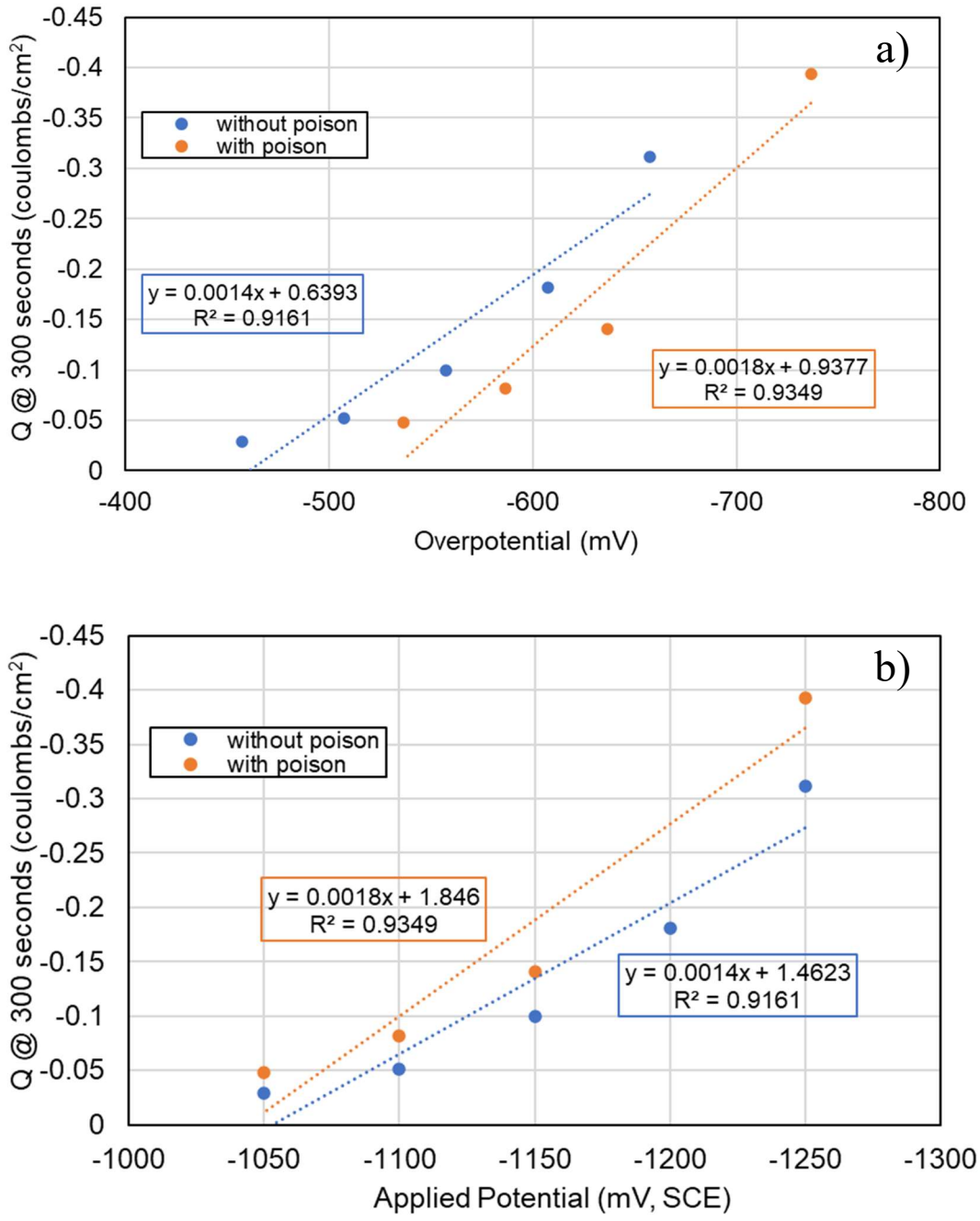

Figure 5.17 Effect of 3g/L NH_4SCN addition to 3.5% NaCl electrolyte on charge transfer during potentiostatic cathodic polarisation: a) plotted against overpotential, η; b) plotted against applied potential.

Counterintuitively, when overpotential is plotted against maximum charge transferred (i.e. after 300 seconds) as in Figure 5.17 a), the electrolyte containing NH_4SCN actually shows comparatively lower charge than that without the addition. For practical purposes however, because charge transfer is higher for a particular *applied* potential in the presence of NH_4SCN, as in Figure 5.17 b), for maximising hydrogen charging

it is beneficial for an addition to be made. In both analyses the gradient of increase in charge is greater when electrolyte contains NH_4SCN, implying that it becomes more beneficial as an addition as charging severity increases. It would be of value to further study these effects by using neutral-buffered 3.5% NaCl solutions (i.e. normalising the pH parameter), both with and without the addition of NH_4SCN.

5.2.3 Effect of microstructure

Perhaps the most pertinent question around observed differences in hydrogen diffusion is that of microstructure. The results of the hydrogen permeation tests described in Chapter 4.3 present an opportunity to discuss these differences in terms of both maximum flux and, critically, effective lattice diffusivity.

Figure 5.18 (below) shows the differences between the different steels in maximum steady-state hydrogen flux, J_∞, attained during permeation tests on membranes of 0.8 mm nominal thickness, charged at -1050 mV (SCE).

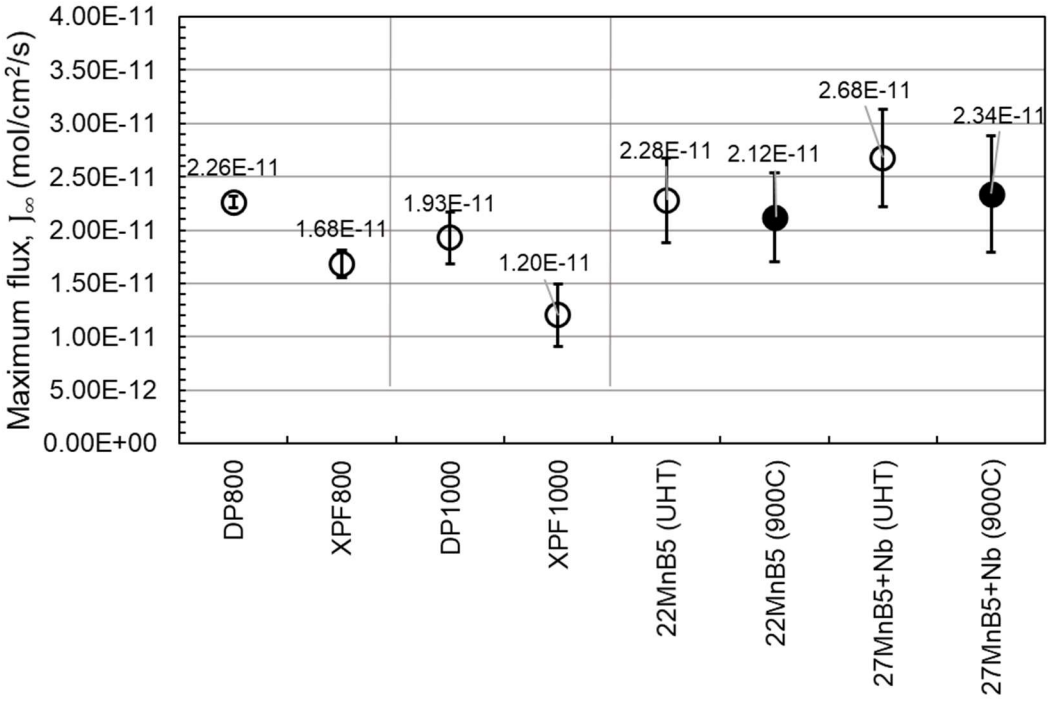

Figure 5.18 Comparison between steels of differences in maximum flux achieved during permeation tests on membranes of 0.8 mm thickness, -1050 mV (SCE) charging potential, 3.5% NaCl + 3 g/L NH_4SCN charging electrolyte (filled circle denotes steel which has been heat-treated).

For the fully-ferritic XPF 800 MPa and 1000 MPa steels, a lower maximum flux than the ferrite-martensite DP steels of equivalent strength was observed. For the press-hardenable boron steels, the fully-martensitic microstructure of the heat-treated condition showed a lower maximum flux than the ferritic-pearlitic microstructure of the 'as rolled', un-heat-treated condition, though these differences are less pronounced

than for the DP and XPF steels. However, whilst maximum flux indicates a state of lattice diffusion, it is a function of both effective diffusivity *and* membrane thickness. Whilst every effort has been taken to standardise membrane thicknesses, subtle variations still persist, and these must be considered when making comparisons.

A more precise comparison can be made when considering the effective diffusivity, D_{eff}, of the steels, particularly as calculation of which already accounts for membrane thickness. Figure 5.19 (below) shows the differences between the different steels in effective diffusion coefficient calculated from data obtained in permeation tests on membranes of 0.8 mm nominal thickness, charged at -1050 mV (SCE), using the lag time calculation.

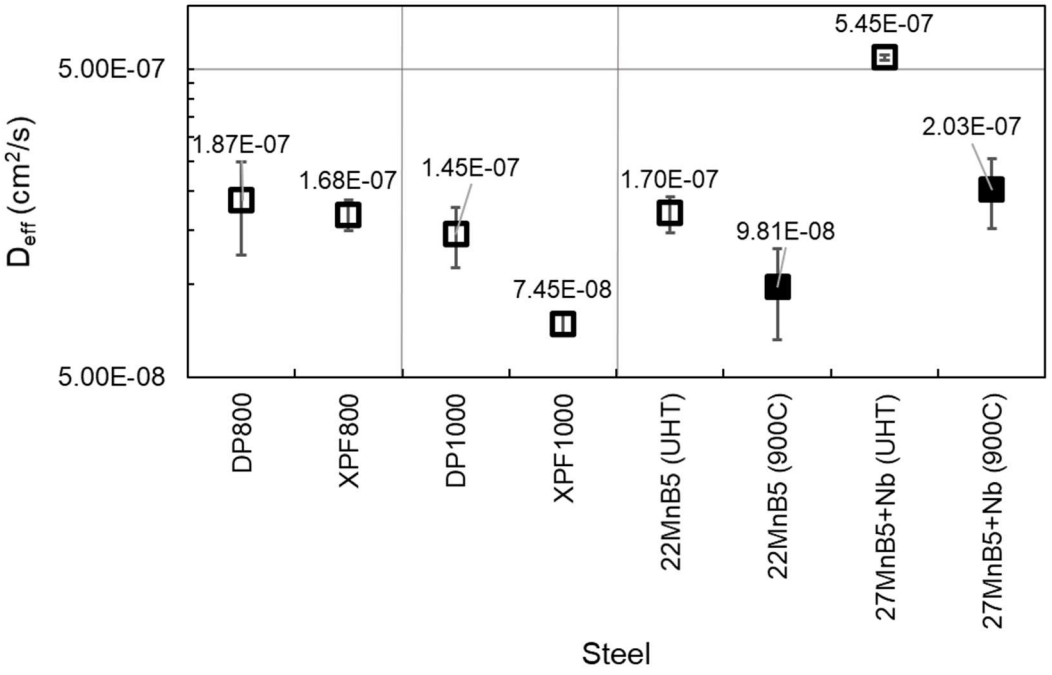

Figure 5.19 Comparison between steels of differences in effective diffusion coefficients, calculated from data obtained in permeation tests on membranes of 0.8 mm thickness, -1050 mV (SCE) charging potential, 3.5% NaCl + 3 g/L NH_4SCN charging electrolyte (filled square denotes steel which has been heat-treated; y-axis in logarithmic scale).

As with the maximum flux, the fully-ferritic XPF 800 MPa and 1000 MPa steels showed lower diffusivity than the ferrite-martensite DP steels of equivalent strength. For the press-hardenable boron steels, the fully-martensitic microstructure of the heat-treated condition showed lower diffusivity than the ferritic-pearlitic microstructure of

the un-heat-treated condition, though unlike for the maximum flux these differences are at least as pronounced, or more so, than for the DP and XPF steels.

That the fully-ferritic XPF steels have lower diffusivity than the equivalent ferrite-martensite DP steels is perhaps counter-intuitive. Martensite is known to have a high dislocation density [154], providing considerable opportunity for diffusing hydrogen to become 'trapped'. Furthermore, the multi-phase nature of the DP steels implies that hydrogen flux would be subject to increased tortuosity of diffusion path [6], both due to the differing solubilities between the phases, and the inherent variation in orientation relationship between both the martensite and ferrite phases, and within the martensite phase itself [20]. Whilst at the 800 MPa strength level it could be argued that, at ~ 10%, the differences in effective diffusivity may be within the range of testing error, XPF1000 was seen to have the lowest diffusivity of all the steels tested, and 49% lower than DP1000.

An indication as to why the XPFs exhibit lower overall diffusivity than the DPs can be seen by comparing the permeation curves in Figure 4.27 and Figure 4.29, for XPF800 and XPF1000, with Figure 4.26 and Figure 4.28, for DP800 and DP1000, respectively, paying particular attention to the relationship between the simulated flux and the measured permeation flux. For the DPs, the measured flux has a relatively shallow rising transient before the fit between simulated and measured flux converges and remains relatively coincident until the end of the test. Conversely, the XPFs show an initial rising transient that is displaced to a longer time (a delayed 'breakthrough time'), before rising more steeply than the simulated curves. Furthermore, convergence between simulated and measured curves is brief, with the measured flux exceeding the simulated flux after t_{lag}. Lan [244] and Van den Eeckhout [157] have shown that a delay in permeation curve, and therefore an increased breakthrough time, t_b, is caused by a higher overall trap density. This would indicate that the XPFs contain a greater trap density than the equivalent-strength DPs. Furthermore, as diffusible hydrogen saturates the strongest traps before filling the weaker traps or diffusing through the lattice [178], overall hydrogen diffusivity is impacted to a greater degree by the presence of strong, or 'irreversible', traps compared to weaker, or 'reversible', ones. Because strong traps fill quickly, the overall 'shape' of the permeation curve, including the time between 'breakthrough' and steady-state, is unlikely to be influenced by the presence of strong traps [158]. Reversible traps are therefore thought

to exert the greatest influence over the slope of the permeation curve [157]. This implies two things:

i) values for t_b, normalised to the membrane thickness (squared), can be used as a proxy for comparing the relative prevalence of irreversible traps between steels;

ii) the slope of the curve (normalised for flux and thickness) between t_b and $t_{steady\text{-}state}$ can be used as a proxy to compare the relative prevalence of reversible traps between steels.

In the case of the XPF and DP steels, the XPFs have longer breakthrough times (and lower overall diffusivity) for given strength levels, but steeper rising transients. This suggests that XPF steels contain a relatively high density of irreversible (strong) trap sites, but not necessarily equivalently high densities of reversible trap sites. Conversely, for given strength levels the opposite is true for the DP steels, with permeation transients suggesting low densities of irreversible trap sites and a comparatively higher density of reversible trap sites.

As described previously, XPF steels are alloyed with additions of niobium, vanadium, and molybdenum, which forms V, NbV, or NbVMo carbide/carbo-nitride precipitates, suppressing the formation of second-phase Fe_3C (by fully-consuming available carbon), and hence maintaining a fine-grained, essentially fully-ferritic microstructure [22]. It has been reported widely that such precipitates can be deep (irreversible) traps, i.e. with high magnitude binding energy [6], particularly if the precipitates are very fine. Depover [146,245,246] showed that microalloy carbides (and carbonitrides) of Ti, V, Mo are able to trap a significant amount of hydrogen in steels containing 0.1 – 0.3 wt% C, providing that the precipitates were not overly coarsened during tempering [140]. Using a cryogenic transfer method between hydrogen charging and atom probe tomography (APT), Chen [247] directly observed that hydrogen becomes trapped at cores of V/Mo/Nb-carbide precipitates embedded within a ferrite microstructure.

It would be beneficial to conduct further study using thermal desorption analysis. Nevertheless, based on the characteristics of the permeation curves, allied to the extensive literature pertaining to the trapping effects of precipitates that are present in the XPF steels, it is reasonable to conclude that the lower relative diffusivity of the XPF steels is primarily due to the irreversible trapping of hydrogen at microalloy

nanoprecipitates present in the microstructure. Furthermore, once the irreversible traps are filled, a relatively low density of reversible traps permits hydrogen to diffuse comparatively freely through the ferrite lattice.

The dual-phase steels, whilst having similar grain size to the XPF steels (they do contain a Nb addition that is ~ 50% lower than for the XPF steels), do not contain the same addition of vanadium or molybdenum, and are therefore not expected to have the same level of precipitation strengthening. Instead, second-phase martensite is the primary strengthening mechanism. Martensite is formed via a shear transformation rather than via a diffusive transformation (discussed in more detail with regards to the press-hardenable boron steels later), and as such is imbued with a relatively high dislocation density compared to ferrite. Dislocations have been shown in numerous studies (e.g. [188,248,249]) to act as reversible traps for diffusing hydrogen, thus decreasing the gradient of the rising transient, but not impacting the overall effective diffusivity, D_{eff}, to the same degree as irreversible traps. A further microstructural influence over hydrogen diffusion in the DP steels is the presence of multiple phases itself: as martensite and ferrite have different hydrogen diffusivity and solubility, this multi-phase microstructure will present a more tortuous diffusion path, delaying the permeation transient (delayed t_b), though the differences between ferrite and martensite in these DP steels are unlikely to increase tortuosity substantially as, other than carbon content, there are no substantial differences in alloy content or measurable lattice dilation between the phases, and the tortuosity effect would be far less than could be seen in a multi-phase steel containing significant volume fractions of austenite [250].

A similar analysis can be undertaken for the press-hardenable boron steels, 22MnB5 and 27MnB5+Nb. We can see from the permeation curves in Figure 4.30, Figure 4.31, Figure 4.32, and Figure 4.33 that for both steels the heat-treated samples had lower maximum flux, J_∞, and shallower curves, i.e. longer t_{lag}, reflected in the values for D_{eff}, seen in Figure 5.19, which show a 42% reduction in effective diffusivity for 22MnB5, and a 63% reduction for 27MnB5+Nb, after heat-treatment. This indicates comparatively less hindrance to hydrogen transport for the un-heat-treated condition both during the rising transient and at steady-state, in good agreement with other researchers [251–253].

There is a generally good fit between the curves simulated using Fick's laws and the experimental data, implying that lattice diffusion (plus effect of reversible traps) is largely responsible for observed differences in diffusion coefficients. For ferritic or ferritic-pearlitic microstructures as per the un-heat-treated condition, it has been previously reported that hydrogen transport is dominated by diffusion through ferrite grains [144,190] (further investigation via use of hydrogen microprint technique (HMT), or in situ scanning Kelvin probe force microscopy (SKPFM) would confirm this). As hydrogen atoms traverse the body-centred-cubic (bcc) lattice they are thought to favour tetrahedral interstitial sites [151], with the octahedral sites being occupied by carbon atoms. Whilst this interstitial carbon does cause some lattice dilation, the transformation from austenite to ferrite proceeds via diffusion, minimising strain on the lattice and in turn limiting the numbers of vacancies and dislocations retained within the lattice [20]. Consequently, where alloy chemistry is the same, the path through the ferrite lattice for diffusing hydrogen atoms should be comparatively straightforward when compared to the martensitic structure of the heat-treated condition.

For the heat-treated steels the adjustment in the orientation relationship between martensite (α') and the parent austenite (γ), coupled with tetragonality induced in the bcc lattice from super-saturation of carbon atoms, leads to significant strain residing within the lattice [20], and an accompanying high dislocation density [154]. Furthermore, even with the boron addition to improve hardenability [55], the completion of the martensitic transformation takes place below room temperature, and consequently there is a residual amount ($<\approx 1.5\%$) of 'retained' austenite within the as-quenched microstructure. Austenite has considerably higher hydrogen solubility, and notably lower diffusivity than martensite or ferrite [6,44]. This combination of high dislocation density, the orientation relationship between martensite 'packets' within the parent grain, and difference in solubility of the retained austenite, provides a higher level of complexity to the path of diffusing hydrogen within the martensitic microstructure compared to the un-heat-treated microstructures. Added to this, dislocations themselves have been shown to act as 'reversible' hydrogen traps, whereby hydrogen atoms become trapped at dislocations with a characteristic binding energy, such that when the concentration of hydrogen in the lattice decreases (or there is an increase in thermal energy in the system), trapped hydrogen is released back into

the lattice once more [147,155], maintaining an equilibrium between reversibly-trapped hydrogen and hydrogen in the lattice, as described by Oriani [156]. As discussed for the XPF and DP steels, this would explain the effect of making the permeation curve shallower, which is what we find for the heat-treated conditions in Figure 4.31 [157,158]. In this respect dislocations can be thought to act like a 'sieve' upon the hydrogen flux (as shown in Figure 5.20). The magnitude of J_{∞}, and the duration of the rising transient between breakthrough and steady-state, can therefore be thought to derive from the combination of lattice diffusion (with its inherent complexity), and the effects of reversible traps [243].

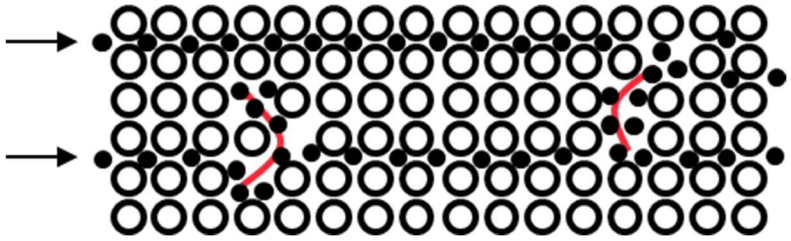

Figure 5.20 Illustration of the effect of dislocations upon hydrogen diffusion through a cubic lattice.

Table 5-1 Summary of permeation test results for heat-treated (900C) boron steel membranes of 0.8 mm thickness in 3.5% NaCl + 3 g/L NH_4SCN, with charging potential -1050 mV (SCE).

Alloy	Calculated C_0 (mol/cm^3)	t_{lag} (seconds)	Maximum Flux ($mol/cm^2/s$)	D_{eff} (cm^2/s)
22MnB5 (UHT)	1.01×10^{-5}	5,544	2.28×10^{-11}	1.70×10^{-7}
22MnB5 (900C)	1.60×10^{-5}	9,261	2.12×10^{-11}	9.81×10^{-8}
27MnB5+Nb (UHT)	3.46×10^{-6}	1,522	2.68×10^{-11}	5.45×10^{-7}
27MnB5+Nb (900C)	8.96×10^{-6}	4,976	2.34×10^{-11}	2.03×10^{-7}

It can be seen from the values in Table 5-1, above, that 27MnB5+Nb was found to have an increase in diffusivity greater than 50% in both conditions compared to the equivalent 22MnB5. Whilst it is clear from the results that the martensite lattice has lower diffusivity than the ferrite lattice for both steels, comparisons between steels with different chemistry is more difficult, as it is not necessarily the case that the reasons for higher or lower diffusivity are the same for each condition. For example, as seen from Table 4-1, in the un-heat-treated condition, grain size is smaller in 22MnB5 (hence larger grain boundary area). Grain boundary diffusion in steels is not

thought to be significantly accelerated [252,254], but in some instances may provide some reversible trapping effects [157]. Conversely, in the heat-treated condition 27MnB5+Nb has the larger grain boundary area, yet still has higher diffusivity.

What can be said with certainty is that the significant differences in alloying additions between the steels has certainly impacted upon the respective microconstituents, and this is reflected in the values obtained from X-ray diffraction (Table 4-2). In the heat-treated condition, 27MnB5+Nb has a 13.3% lower dislocation density (13.5% lower microstrain) than the 22MnB5, and 26% less retained (or reverted) austenite (though there is some spread in the retained austenite values). The combination of these two parameters goes some way to explaining lower effective diffusivity in 22MnB5, and the higher calculated hydrogen concentration at the charging surface, C_0, as shown by Sakamoto [253]. Whilst t_b is substantially displaced for both heat-treated steels relative to their un-heat-treated condition, 22MnB5 (900C) shows an absolute breakthrough time 70% longer than 27MnB5+Nb (900C), and when normalised to membrane thickness, breakthrough time (Norm.t_b) is 89% longer for the 22MnB5. This is a clear indication that there is a much greater effect of irreversible traps on the permeation transient of heat-treated 22MnB5 when compared not only to the un-heat-treated condition, but also to the heat-treated 27MnB5+Nb. Given that 27MnB5+Nb (900C) also had a displaced normalised t_b relative to 27MnB5+Nb (UHT), also indicating the presence of irreversible traps in the nominally fully-martensitic microstructure, it is reasonable to infer that, even if it does not account entirely for the differences between the two heat-treated boron steels, the volume fractions of retained austenite is affecting the overall diffusivity, with the effect being that with the higher fraction of retained austenite, 22MnB5 (900C) has a longer breakthrough time and a lower D_{eff} than 27MnB5+Nb (900C).

It is important at this juncture to point out that the discussion of retained austenite as an irreversible trap is strictly limited to comparisons between the two press-hardenable boron steels. Close examination of the permeation curves in Figure 4.30, Figure 4.31, Figure 4.32, and Figure 4.33 has already shown that there actually may be a greater prevalence of reversible trapping sites than irreversible, as reversible traps decrease the gradient of the permeation curve during the rising portion, and exist in equilibrium with the hydrogen concentration in the lattice, permitting a good fit between experimental and simulated data. In 3 out of the 4 transients shown for these steels,

experimental t_b actually occurs earlier than in the simulated data, but the gradient of the rising transient is reduced, allowing for a better fit with simulated data at later times. Despite this, 22MnB5 (900C) did have the second-lowest D_{eff} (after XPF1000), and as discussed previously, this is impacted more by the presence of irreversible traps than the presence of reversible traps.

In the un-heat-treated condition, interfaces between Fe_3C and ferrite are known to act as reversible trapping sites, and the 'segregated' nature of the carbide present in 22MnB5 (UHT) may well provide a more effective means of trapping hydrogen than the lamella structures present in pearlite within 27MnB5+Nb (UHT). Further investigation via permeation with *in situ* SKPFM, as well as analysis of trapping densities and energies via a thermal desorption technique would prove highly beneficial in characterising the exact differences between these steels and heat-treatments.

5.2.4 Effect of membrane thickness

The international standard for hydrogen permeation tests, ISO17081 [169], recommends performing tests on membranes of progressively increasing thickness to test for intrinsic diffusivity, as up to a limiting value, surface reaction kinetics and overly-rapid depletion can be rate-limiting (and hence unduly influential) on the measured flux. As membrane thickness increases, the influence of 'bulk' diffusion becomes ever-more prominent, and at a particular thickness the influence of the other mechanisms will become negligible. At this thickness (and above), the measured values can be said to be due to the intrinsic diffusivity of the material [97,177].

There is some recognition, however, that testing of thicker membranes is not always possible due to material availability [97]. In this work, studying strip steels destined for automotive applications, testing thicker membranes is not possible (these steels are not utilised at thicker gauges), and it can be argued that in terms of discerning performance in-service, 'intrinsic' diffusion properties are not actually relevant if they are only disclosed at thicknesses substantially greater than would be utilised in the parts for which they are destined :- we need to understand how these steels will perform at the sizes in which they are likely to be utilised, and we need to be able to make comparisons between them at a standardised size (i.e. normalised thickness) to determine their *relative* susceptibility or resistance to degradation due to hydrogen.

Despite this, it is still important to try and discern to what extent membrane thickness is affecting data gleaned from permeation experiments. To that end, permeation experiments were conducted across 3 different membrane thicknesses for DP800, DP1000, and 22MnB5 (900C), with the thickest gauge membranes reserved for specimens prepared from 'as-received' (or as heat-treated) material. Experimental data is shown in Figure 4.35, Figure 4.36, and Figure 4.37 with output parameters tabulated in Table 4-4, Table 4-5, and Table 4-6 for DP800, DP1000, and 22MnB5 (900C), respectively.

Results show that, as may be expected, as membrane thickness increases, maximum flux (J_∞) decreases, and t_b and t_{lag} are displaced to longer times. This displacement of t_{lag} is, however, not equivalent across membrane thicknesses, and leads to calculated values for D_{eff} that are not consistent between the different material gauges. This is shown graphically in Figure 5.21, below.

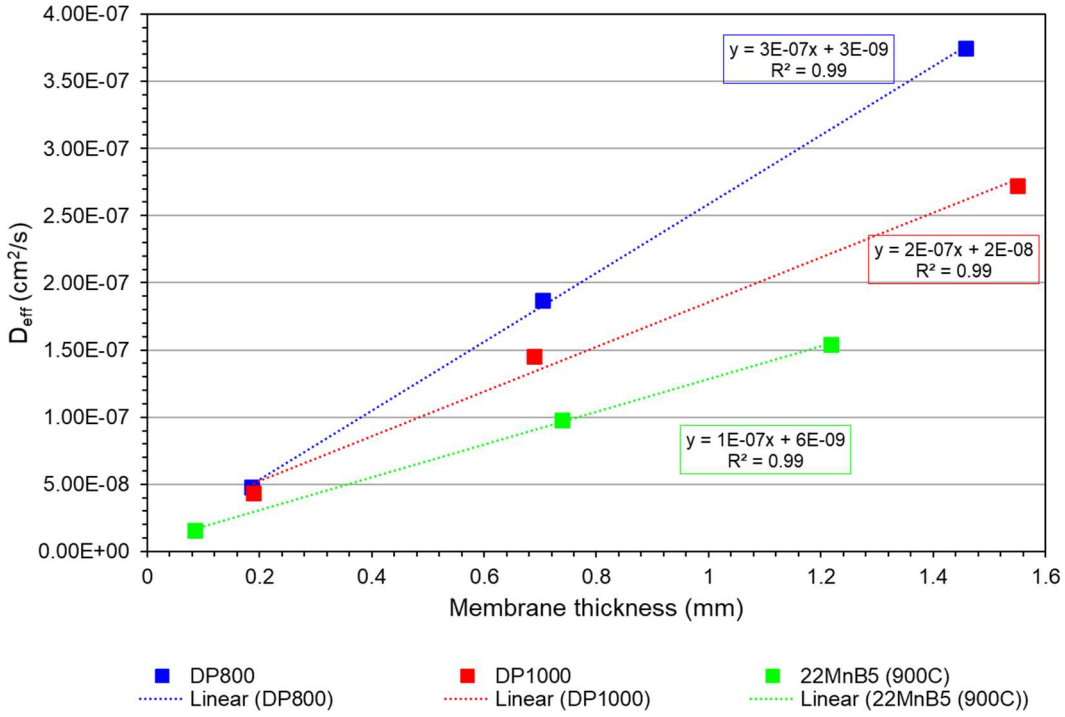

Figure 5.21 Effect of membrane thickness on effective diffusion coefficient for DP800, DP1000, and 22MnB5 (900C). Dotted lines represent curves fitted to the measured data.

Figure 5.21 shows that when plotting D_{eff} against membrane thickness for these steels, the response is linear for the material gauges available to us. For the three steels at which tests at multiple thicknesses were conducted, this means that *relative differences* in effective diffusivity are maintained across the range of thicknesses. This lends confidence to the notion that for the thicknesses available, where one steel shows a higher or lower D_{eff} than another, there is a high probability that this apparent difference will remain valid as membrane thickness increases across the entire range of material thicknesses. Indeed, in the case of these three steels, the magnitude of the differences between the steels increases as membrane thickness increases. In essence, bulk diffusion exerts enough influence over measured permeation parameters above a critical membrane thickness that observed relative differences between steels are valid and relevant. Where this threshold is may be different for each steel studied, but as long as the membrane thickness has exceeded the threshold for each of the steels being compared, the comparison will be legitimate.

Conversely, Figure 5.21 also demonstrates the legitimacy of testing membranes that are as thick as possible. At the thinnest gauges, differences in D_{eff} are small enough that they could be considered to be within the margin for error of the experiment, and without confirmation from experiments on thicker gauges it would be difficult to draw any conclusions regarding apparent differences in effective diffusivity between steels. This may be due to the mechanism proposed by Kittel [177], where hydrogen exits the depletion surface so rapidly that an equilibrium concentration, C_0, is never reached at the charging surface, essentially changing the boundary conditions for calculating permeation flux. In this work it is seen that this condition may be encountered when membranes are as thin as 0.1 mm nominal thickness. With greater material availability it may be possible to conduct many repeats at a variety of thicknesses in order to estimate a suitable minimum to avoid this phenomenon.

Another possibility raised by the permeation experiments run at different membrane thicknesses is that of extrapolating an estimate at which membrane thickness we could be sure of virtually eliminating the influence of rapid depletion or charging surface reaction kinetics on the permeation flux. Whilst the relationship between D_{eff} and membrane thickness appears linear (with high R^2) up to the 'as-received' gauge, there are hints that the relationship is actually parabolic (a second-order polynomial equation provides an even closer fit to the data), implying that there is a thickness beyond which there will be no change in D_{eff}. These values were calculated to be 8.9 mm, 2.9 mm, and 8.1 mm for DP800, DP1000, and 22MnB5 (900C), respectively, though there is limited validity to this analysis as there is a large degree of uncertainty when undertaking any kind of regression analysis, particularly when this analysis is based on only 3 data points. Furthermore, deriving these 'critical thickness' values may not actually add much value to the comparisons being made between the steels in this work either way, as (bar the XPFs) they tend to be utilised at gauges less than 1 mm. In essence, all of the confounding variables that exist at lower thicknesses are actually relevant under real-world conditions for these steels, so whilst at the thicknesses tested the intrinsic diffusion properties may not yet be revealed, the relevant diffusion characteristics for in-service conditions, are, under this experimental setup.

5.3 Degradation of mechanical properties

The results of slow strain-rate tests and the associated fracture analysis are discussed in this sub-chapter. Key to this discussion is how differences in microstructure affect relative susceptibility, how they affect the mechanism in which degradation is occurring, and whether this is primarily an effect of diffusion characteristics, or due to an inherent mechanical susceptibility imparted upon certain microstructural features. The concept of a critical hydrogen concentration for brittle failure is also discussed, with consideration given to what degree any single parameter can be given prominence as a crucial feature of hydrogen embrittlement, or whether a more 'holistic' analysis will always be more appropriate.

5.3.1 Response of different microstructures to hydrogen ingress

5.3.1.1 Fully-ferritic XPF and ferrite/martensite Dual-phase steels

Figure 4.45, Figure 4.47, Figure 4.49, and Figure 4.51, and Table 4-9, Table 4-10, Table 4-11, and Table 4-12 show that at a given strength level, the fully-ferritic XPF steels have substantially lower hydrogen embrittlement indices (HEI), i.e. suffer substantially less embrittlement, than the ferrite-martensite DP steels of equivalent strength, whether this is measured via time-to-failure (TTF), or % total elongation. It should be noted that XPF1000 did still show a HEI > 40% at the slowest strain-rate, with and without 2 hours' pre-charging, indicating that although it performed better than DP1000, its mechanical properties are still significantly degraded under these test conditions.

It is clear that these apparent differences in resistance to mechanical degradation between XPFs and DPs is due to microstructure, and critically, the underlying chemistry that is used to achieve these microstructures. As part of the discussion around differences in effective diffusivity between these steels, it was established that XPF steels contain numerous potential irreversible traps in the form of microalloy carbide (and carbonitride) nanoprecipitates. During slow strain-rate testing (SSRT), these traps act in a way that lowers the amount of diffusible hydrogen available to converge at stress concentrations, limiting the opportunity for formation of critical concentrations of hydrogen to initiate or propagate cracks. This has been found in a number of studies on steels containing similar precipitates. For example, Depover and

Verbeken [255] found that tempered Mo_2C particles trap a considerable amount of hydrogen, and a correlation between hydrogen mobility and hydrogen embrittlement susceptibility was confirmed. Secondly, Chen's use of APT showed hydrogen trapped at V/Mo/Nb carbide precipitates embedded within a ferrite microstructure [247], and this is backed up through thermokinetic modelling work undertaken by Stopher [256] that calculated NbC (and TiC) to be effective trapping sites. Conversely, when considering the trapping effects of VC precipitates, Turk [257] concluded that when embedded in a 'fully-annealed' ferrite matrix that trapping capacity may actually be comparatively low, and as these findings contradicted the vast majority of other literature on the subject, Turk considered that it may be the interaction between VC precipitates and dislocations that enhance trapping capacity. Analysis of XRD data showed dislocation densities, δ, of $2.0 \times 10^{15}/m^2$ and $4.4 \times 10^{15}/m^2$ for XPF800 and XPF1000, respectively. This is not remarkably high, yet with the presence of the other microalloy nanoprecipitates, plus the notion acknowledged by Turk that trapping efficacy increases with reduction in precipitate size (and allied to the majority of other researchers' findings that microalloy carbides are very effective hydrogen traps), it is reasonable to conclude that precipitates are imparting a considerable mitigation against the effects of hydrogen in XPF steels. Conceptually, this is not strictly through the lowering of overall effective diffusivity, but in restriction of the rapid enrichment of hydrogen to critical concentrations within high-stress regions.

Conversely, several studies on dual-phase steels have shown that the ferrite-martensite microstructure may be inherently susceptible to hydrogen embrittlement. Koyama [165] found that hydrogen charging reduces incubation time, and facilitates the nucleation of cracks in the martensite phase via the hydrogen enhanced decohesion (HEDE) mechanism by decreasing the critical strain required for such an initiation. It was also found that there was a parallel mechanism whereby hydrogen promoted cracking at the ferrite/martensite boundaries, as well as transgranular cracking in the ferrite phase, which is insufficiently strong to resist rapid propagation. This was also noted by Takashima [164], who found that where stress is sufficiently high (i.e. well above the yield strength), cracks will propagate through the martensite, avoiding the ferrite phase and causing a unique fracture surface with irregular roughness. Transgranular cracking in the ferrite phase and cracking at ferrite/martensite boundaries are mechanisms more commonly associated with hydrogen enhanced

localised plasticity (HELP), and this presents a particular problem for DP steels in that to design against hydrogen embrittlement, both the decohesion and the plasticity regimes must be mitigated against.

Evidence for these mechanisms in the DP steels studied in this work is present when comparing the fractographs of the DP specimens tested in the un-charged 'dry' condition (Figure 4.46 and Figure 4.50), and those that have been charged with hydrogen. For specimens tested without charging, virtually the entire surface shows the presence of the 'dimples' that indicate microvoid coalescence (MVC), considered to be typical of plastic deformation. This contrasts with the SEM fractographs shown in e.g. Figure 4.62 and Figure 4.72, which demonstrate that in regions with the highest hydrogen concentrations closest to the charging surfaces, there is widespread quasi-cleavage (QC) and intergranular cracking (IG), both indicative of a decohesion initiation and propagation, whereas in regions further from the charging surfaces there is still the presence of MVC, but with widespread transgranular (TG) cracks. In the most severely embrittled DP1000 (Figure 4.72), QC facets are still apparent even at the very centre of the specimen. In all of the tests done at 10^{-6}/s strain-rate with simultaneous hydrogen charging (with and without pre-charging) DP1000 failed at stress values short of the 0.2% proof stress, $Rp_{0.2}$, that were measured in the un-hydrogen-charged samples. Ordinarily, this limits the opportunity for processes associated with truly plastic deformation to occur (which will dominate subsequent to yielding), and explains the prevalence of features indicating rapid failure. However, the presence of TG cracks and MVC in regions also containing QC goes some way to supporting the notion that hydrogen may be lowering the critical stress for dislocation motion, i.e. the HELP mechanism, in the manner described by Koyama [165]. Typically 'brittle' fracture features are more prevalent in the dual-phase steels than the XPFs of equivalent strength, with increased visible damage near the charging surfaces, greater prevalence of visible damage towards the specimen centres, and comparatively more widespread transverse cracks. This damage can be seen in computed tomography (CT) images shown in Figure 5.23 and Figure 5.25 for DP800 and DP1000, respectively, as well as SEM images of the fractured specimen cross-sections in Figure 5.22 and Figure 5.24 for DP800 and DP1000, respectively.

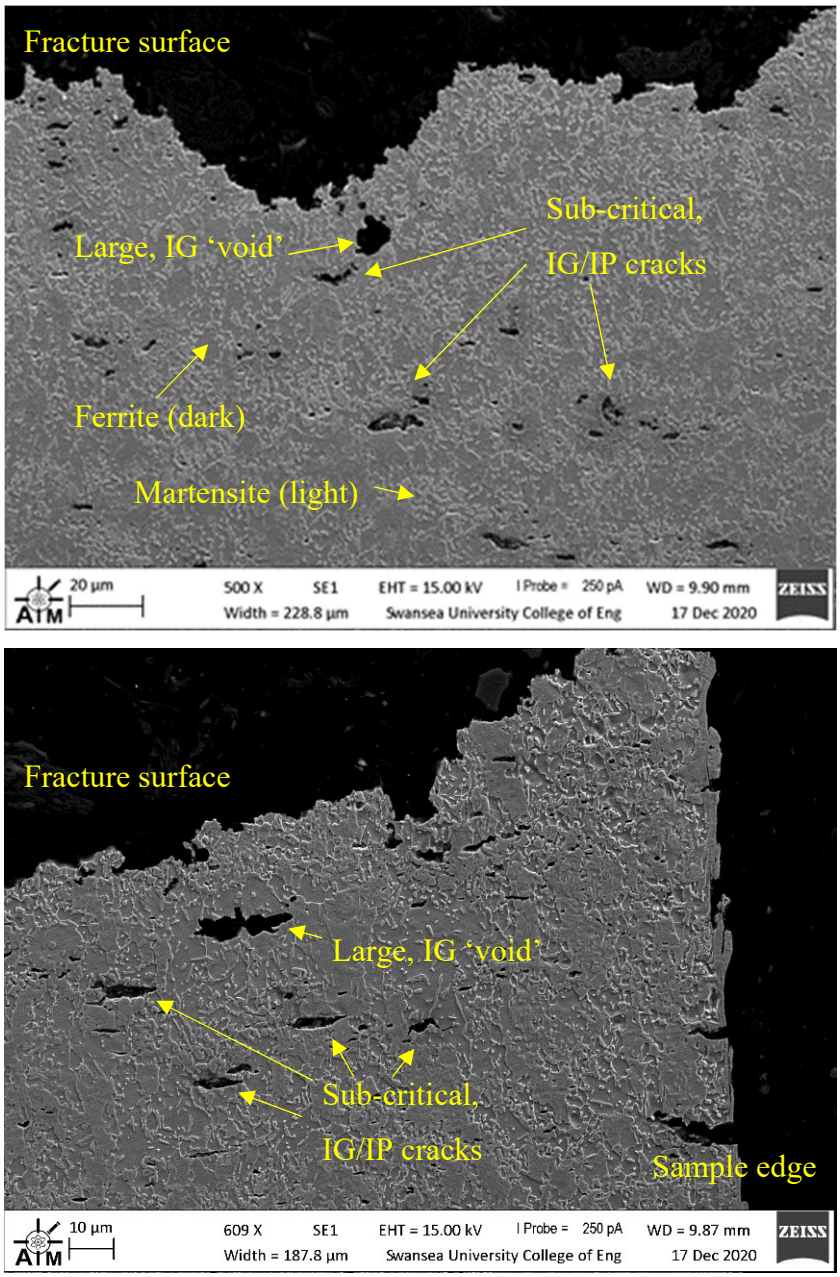

Figure 5.22 SEM images of fracture surface cross-section of DP800 tested at 10^{-6}/s strain-rate, with in situ hydrogen charging including 2 hours' pre-charging, showing intergranular 'voids' (sub-critical cracks).

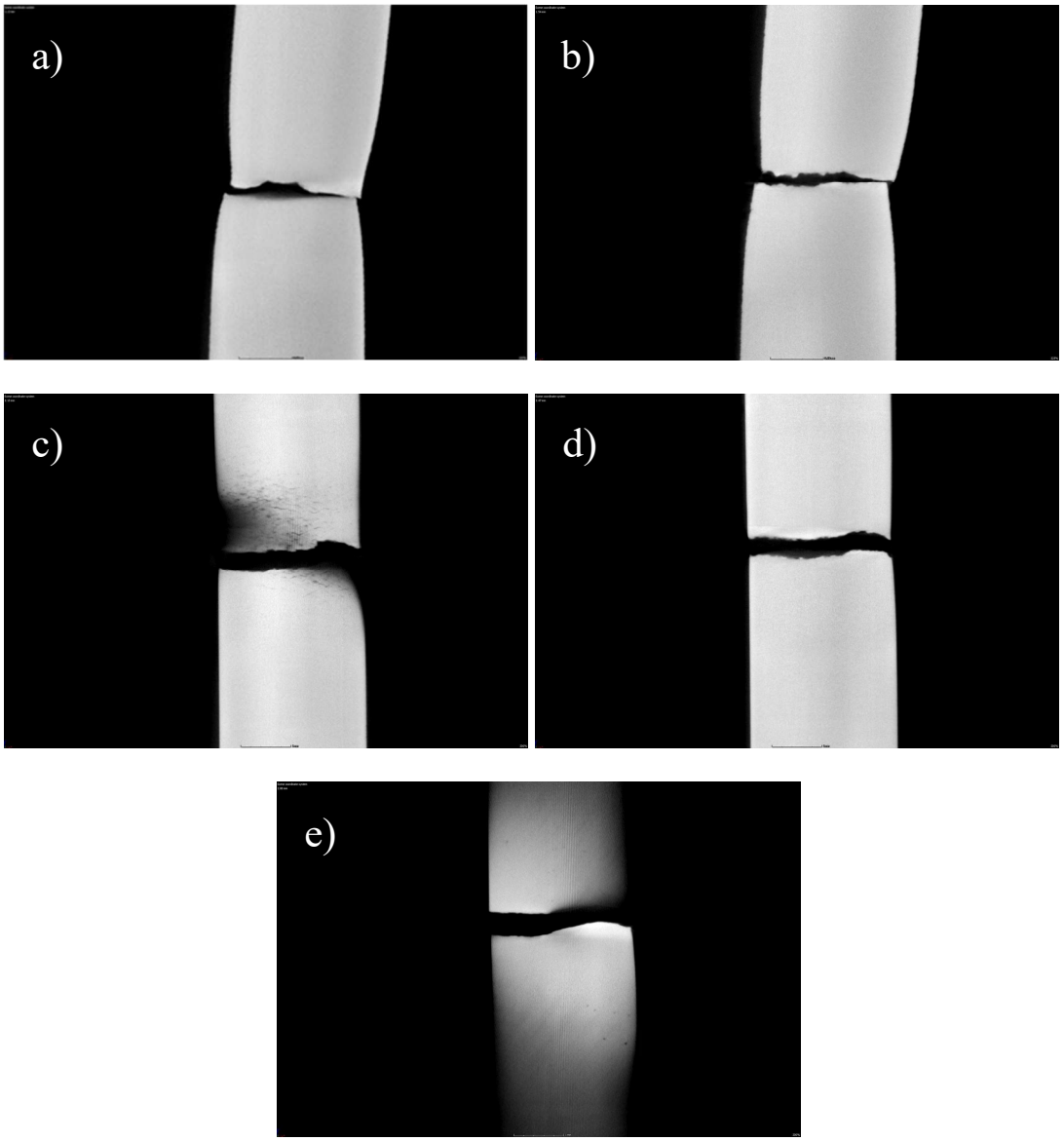

Figure 5.23 Micro computed tomography images of fractured DP800 SSRT specimens: a) and b) tested at 10^{-6}/s strain-rate without hydrogen charging, view close to exposed specimen surface; c) - e) tested at 10^{-6}/s strain-rate, with *in situ* hydrogen charging including 2 hours' pre-charging prior to straining, with c) and e) close to exposed specimen surface and d) at specimen centre.

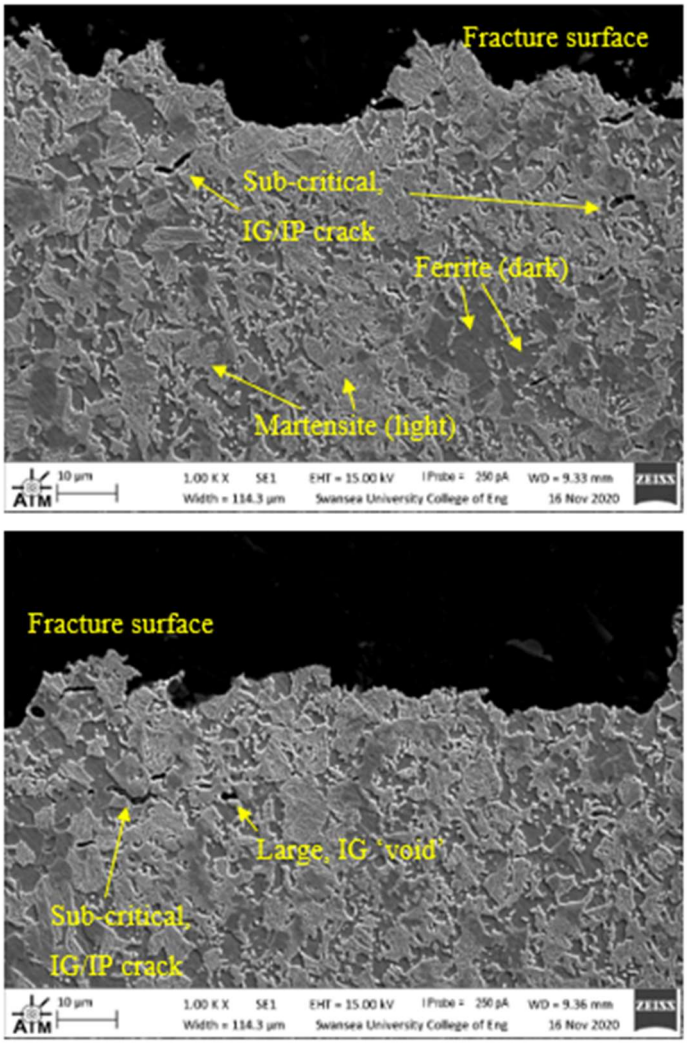

Figure 5.24 SEM images of fracture surface cross-section of DP1000 tested at 10^{-6}/s strain-rate, with in situ hydrogen charging including 2 hours' pre-charging, showing intergranular 'voids' (sub-critical cracks).

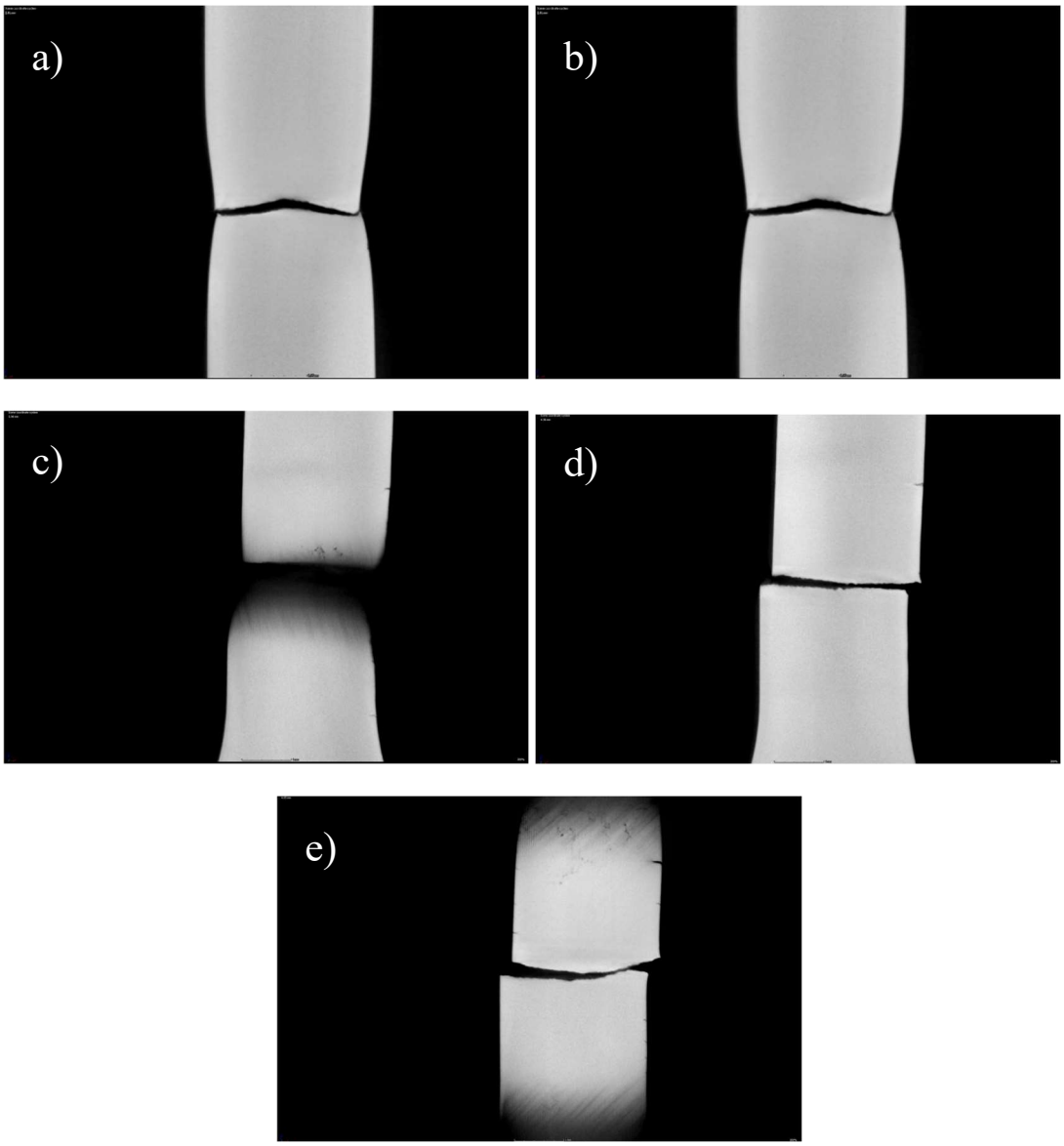

Figure 5.25 Micro computed tomography images of fractured DP1000 SSRT specimens: a) and b) tested at 10^{-6}/s strain-rate without hydrogen charging, view close to exposed specimen surface; c) – e) tested at 10^{-6}/s strain-rate, with in situ hydrogen charging including 2 hours' pre-charging prior to straining, with c) and e) close to exposed specimen surface and d) at specimen centre.

Mixed modes of fracture are also observed in the single-phase XPF steels, however, though not to the extent observed in the dual-phase steels. Without hydrogen charging both XPF800 and XPF1000 show extensive MVC, 'shear microvoids' (SM), and 'tear ridges' (TR), the latter two of which are associated in particular with quite severe reduction in cross-section (necking) of the tensile specimen and final failure along the centre of the specimen. Macro fracture features (Figure 4.63 and Figure 4.77) show this reduction in area clearly, demonstrating an entirely ductile mode of failure incurred when tensile specimens continue to extend well beyond reaching the ultimate

tensile strength (UTS or R_m). In this case this extension was 8% and 6% for the XPF800 and XPF1000, respectively.

With HEI of 27% and 51% for XPF800 and XPF1000 respectively, specimens tested at 10^{-6}/s strain-rate with pre-charging see typically brittle fracture features become far more prominent. There is no longer evidence of necking in the macro-scale fractographs, though a fracture angle along the plane of maximum shear between 45^o and 60^o is still visible in both steels (though substantially less for the XPF1000). In both cases, as can be seen from the 'classified' fracture surfaces shown for these specimens in Table 4-16, there are still significant regions in the pre-charged XPF specimens where there is no evidence of any typically 'brittle' features associated with hydrogen ingress. Only at the regions adjacent to the charging surfaces where hydrogen concentrations are at a maximum, are features such as QC and IG prevalent, in stark contrast to the equivalent DP specimens. Further evidence of the degradation in the region immediately adjacent to the charging surfaces is apparent from CT images, shown in Figure 5.27 and Figure 5.28 for XPF800 and XPF1000, respectively. At the outer surface visible 'pores', as well as sub-critical transverse cracks that are not present further towards the sample centre, can be seen in the pre-charged samples that are not apparent in the scans of the 'dry' samples for either XPF800 or XPF1000. SEM images of the cross-sections of the pre-charged XPF specimens (Figure 5.26 and Figure 5.29 for XPF800 and XPF1000, respectively) also reveal more of these 'pores', large sub-critical transverse cracks at the sample edges that appear to have further deformed during plastic straining, plus intergranular cracks, particularly towards the eventual fracture surface.

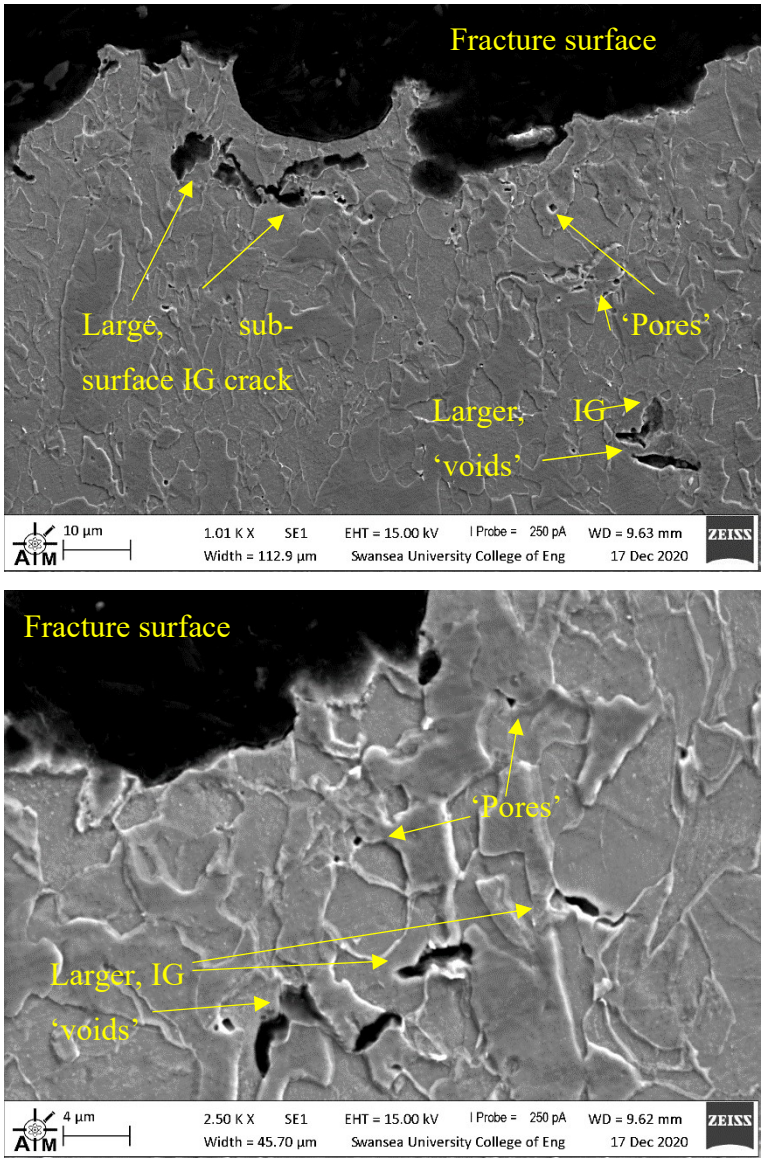

Figure 5.26 SEM images of fracture surface cross-section of XPF800 tested at 10^{-6}/s strain-rate, with *in situ* hydrogen charging including 2 hours' pre-charging, showing intergranular 'voids' (sub-critical cracks).

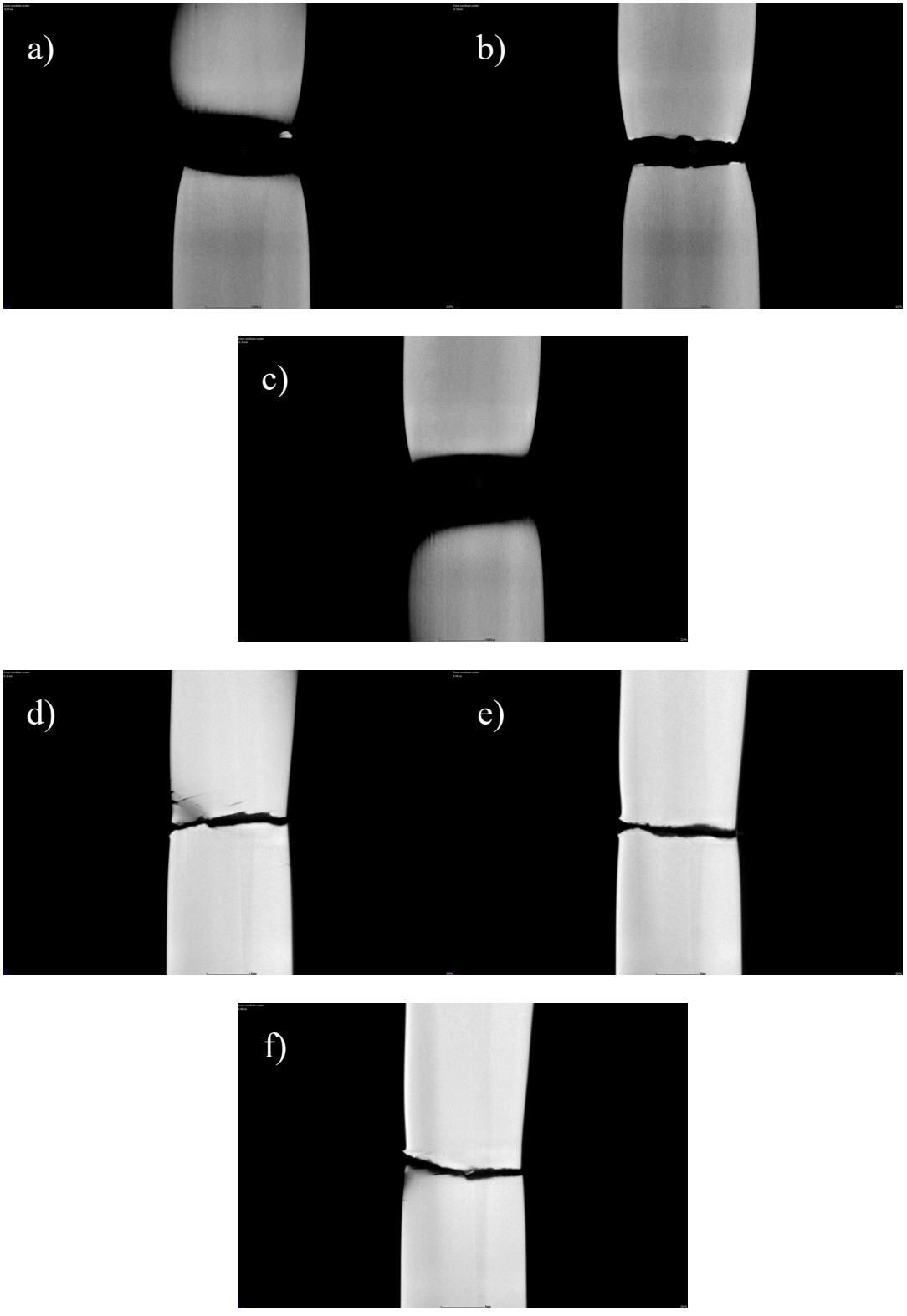

Figure 5.27 Micro computed tomography images of fractured XPF800 SSRT specimens: a) – c) tested at 10^{-6}/s strain-rate without hydrogen charging, with a) and c) close to exposed specimen surface and b) at specimen centre; d) – f) tested at 10^{-6}/s strain-rate with *in situ* hydrogen charging including 2 hours' pre-charging prior to straining, with d) and f) close to exposed specimen surface and e) at specimen centre.

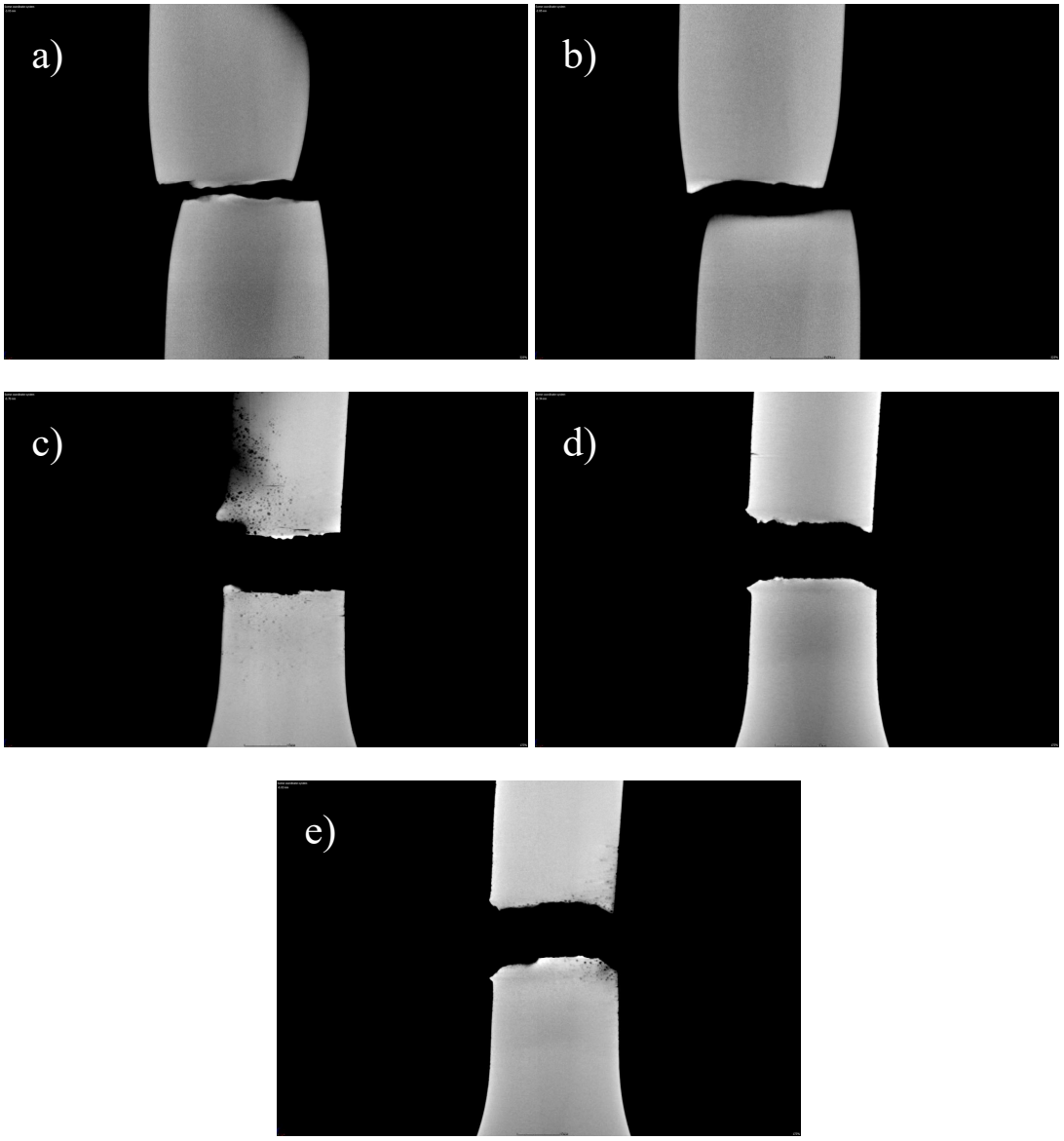

Figure 5.28 Micro computed tomography images of fractured XPF1000 SSRT specimens: a) and b) tested at 10^{-6}/s strain-rate without hydrogen charging, view close to exposed specimen surface; c) – e) tested at 10^{-6}/s strain-rate with *in situ* hydrogen charging including 2 hours' pre-charging prior to straining, with c) and e) close to exposed specimen surface and d) at specimen centre.

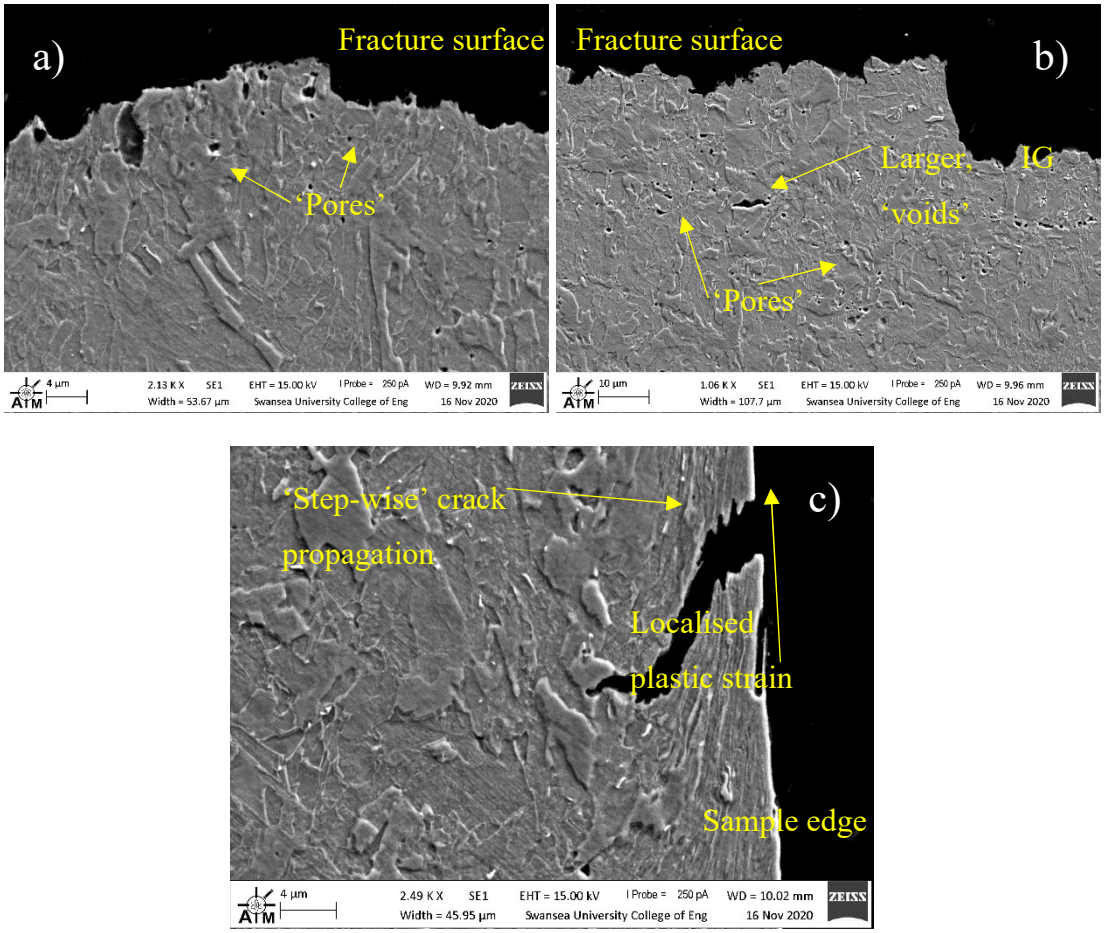

Figure 5.29 SEM images of fracture surface cross-section of XPF1000 tested at 10^{-6}/s strain-rate, with in situ hydrogen charging including 2 hours' pre-charging, showing intergranular cracks, (a) and b)), and a sub-critical transverse crack that has been plastically deformed after forming (c).

Allied to the differences in embrittlement index between the fully-ferritic XPFs and ferrite-martensite DPs, the differences in fracture features observed between them are a clear indication of the inherently better performance of the XPF microstructure when confronted with the ingress of diffusible hydrogen. This is almost certainly due to both the inherent 'trapping' effects of the microalloy carbide nanoprecipitates present in the XPF microstructure, as well as the presence of martensite that can act as crack initiation sites via the HEDE mechanism in the DP microstructure. As the DP microstructure is also sensitive to the enhanced plasticity effects of hydrogen (HELP), it suffers a comparatively large degradation due to hydrogen.

5.3.1.2 Fully-martensitic press-hardenable boron steels

Across the entire range of tests, DP1000 incurred the highest level of embrittlement of any of the products, including the fully-martensitic boron steels 22MnB5 (900C) and 27MnB5+Nb (900C), albeit of a similar order for hydrogen-charged specimens tested at 10^{-6}/s strain-rate. This is despite the UTS being around 500 MPa lower in the DP1000 than for the press-hardenable boron steels. At the higher strain rate of 10^{-5}/s with hydrogen charging, even the DP800 incurred a similar level of embrittlement to the 22MnB5 (900C).

5.3.1.3 The role of martensite in degradation mechanism

Clearly, the steels containing significant volume fractions of martensite are at a disadvantage with regards to mechanical degradation due to hydrogen – SSRT results demonstrate this, and as found in the preceding sub-chapter, the presence of martensite can act as a nucleation site for cracks to develop in the presence of hydrogen. This sub-chapter discusses how this characteristic affects the mechanism of degradation in microstructures containing (nominally) 100% martensite, as well as what differences may affect performance between the two fully-martensitic boron steels.

Figure 4.53 and Figure 4.55, and Table 4-13 and Table 4-14 show that for each test condition 22MnB5 and 27MnB5+Nb have very similar hydrogen embrittlement indices (HEI). HEI for all of the steels studied are summarised graphically in Figure 5.30, below.

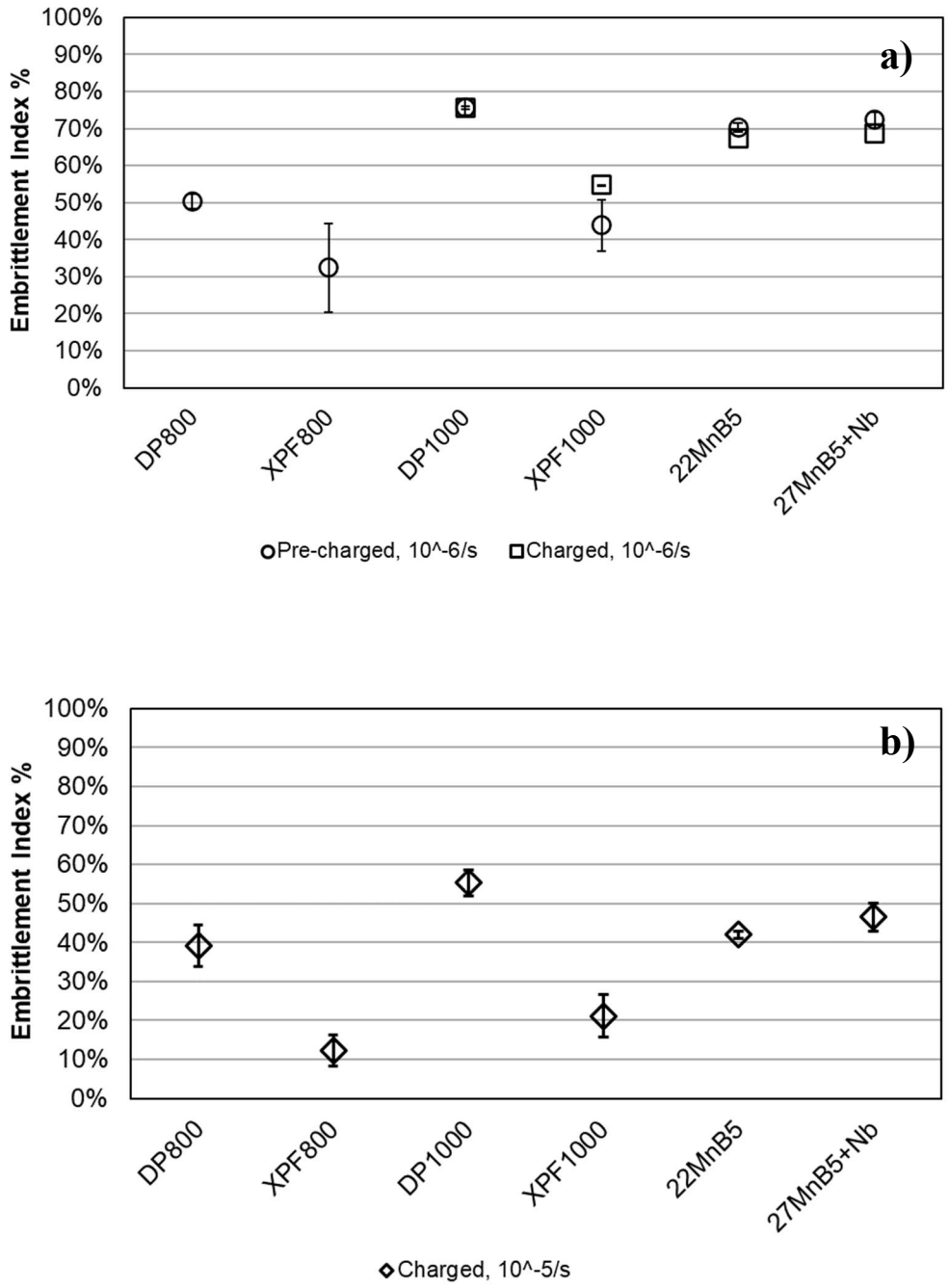

Figure 5.30 Hydrogen embrittlement indices for a) tests at 10^{-6}/s strain-rate (measured by time-to-failure), b) tests at 10^{-5}/s strain-rate (measured by total elongation), for each of the steels studied.

There is no statistically significant difference (with 95% confidence) between the 22MnB5 or 27MnB5+Nb, regardless of pre-charging or strain-rate. Nevertheless, mean embrittlement for 27MnB5+Nb is marginally higher under each test condition.

There are several possible factors in this. Firstly, and perhaps the most simple explanation, is that 27MnB5+Nb has the higher effective diffusivity of the two steels,

meaning within a given time-frame hydrogen is able to reach a greater concentration in higher-stress regions than in the 22MnB5. Evidence of this is apparent when we compare the quantified fracture features for the charged specimens tested at the higher 10^{-5}/s strain-rate, especially when viewed alongside the FEM hydrogen distribution for the samples in question. (At the lower 10^{-6}/s strain-rate specimens were essentially saturated and little apparent effect of diffusivity could be separated from the inherent resistance or susceptibility to embrittlement of the microstructures.) Figure 5.31 and Figure 5.32 show these quantifications and distributions for 22MnB5 and 27MnB5+Nb, respectively.

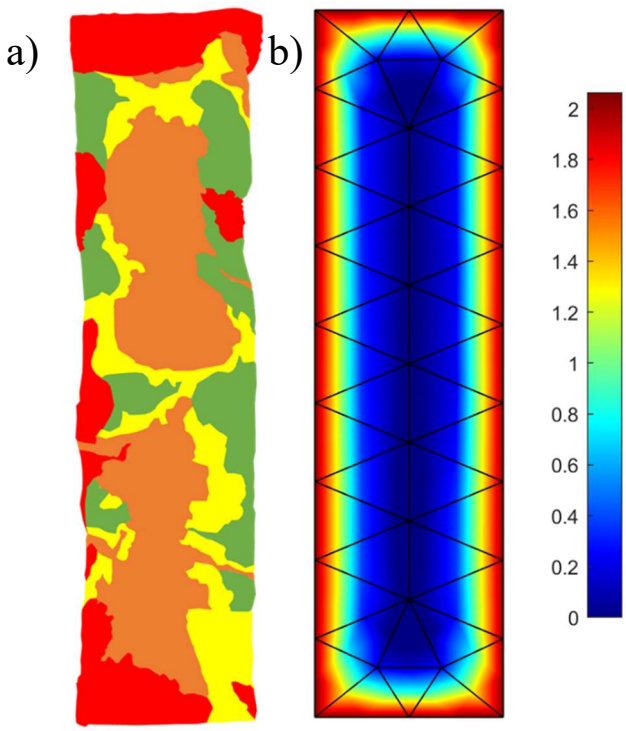

Figure 5.31 a) Quantified fracture surface features and b) finite-element modelled hydrogen distribution for sample 22MnB5-Higher strain-rate-3 (EI 43.69%). Scale of hydrogen concentration in ppm.H).

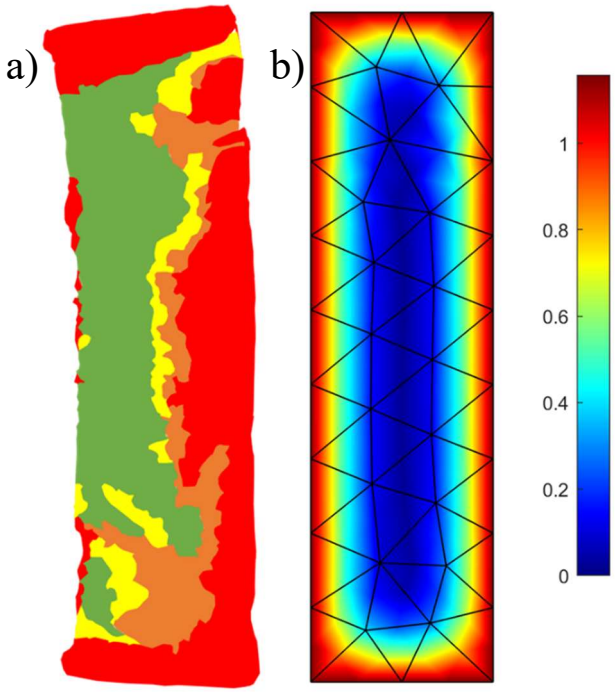

Figure 5.32 a) Quantified fracture surface features and b) FEM hydrogen distribution for sample 27MnB5+Nb-Higher strain-rate-3 (EI 40.56%).

For the 22MnB5 specimen shown in Figure 5.31, the most brittle fracture surface features are only observed immediately adjacent to the charging surface, i.e. in regions of the highest hydrogen concentration. This is to some extent also true of the 27MnB5+Nb specimen shown in Figure 5.32, but the most brittle features (red regions) are observed far more towards the centre of the specimen in the 27MnB5+Nb specimen than for the 22MnB5. As the FEM hydrogen distribution shows that hydrogen has reached higher *relative* concentration throughout as we travel further towards the sample centre, this is a good indication that where diffusivity is higher, so too is the availability of hydrogen to concentrate to levels that will propagate brittle failure in the material. As discussed in Chapter 5.2.3, 22MnB5 is estimated to contain slightly higher volume fractions of retained austenite which are capable of acting as irreversible traps which will become preferentially enriched with hydrogen over lattice diffusion, offering some constraint on the speed at which critical concentrations of hydrogen can be reached to cause brittle failure (when compared to 27MnB5+Nb). Furthermore, the higher density of dislocations in 22MnB5 also lowers overall effective diffusivity (manifested as shallower permeation curve), again limiting the speed at which hydrogen can reach the centre of the specimen.

Nevertheless, despite these differences in diffusivity (the effective diffusion coefficient, D_{eff}, was calculated to be ~2.07× lower in 22MnB5), and a very general lower average embrittlement index seen in the 22MnB5, there is still no statistically significant difference in the embrittlement indices of these two steels. This should perhaps not be unexpected as they both have nominally similar microstructures and have undergone similar thermomechanical processing prior to testing. It should be noted at this point, however, that the estimated concentration of hydrogen at the charging surfaces is 1.78× higher for 22MnB5, meaning the overall availability of hydrogen is higher for this steel. Despite the findings of Venezuela [258] that for martensitic steels there is no correlation between hydrogen uptake and level of mechanical degradation, given the prevalence of brittle fracture regions in the 27MnB5+Nb fractographs, it also suggests that lower diffusivity has necessarily offered a small amount of mitigation for 22MnB5, relative to 27MnB5+Nb, in terms of degradation in mechanical properties. It is implicit, therefore, that the critical concentration of hydrogen required for brittle fracture is lower for 27MnB5+Nb than it is for 22MnB5.

To test this assertion, scaled plots of hydrogen concentration profiles were simulated using parameters obtained from permeation experiments, equivalent to halved plots of those shown in Figure 4.107 and Figure 4.108. These plots were then overlayed onto fractographs with x-axes (specimen thickness) matched to the scale bar of the fractographs, and overlayed onto the fracture surface image. Where there is a clear delineation between 'brittle' fracture features and mixed or 'ductile' features, the intersection between this delineation and the plotted hydrogen concentration provides an estimate of the critical concentration of hydrogen required to induce failure via a brittle fracture mechanism. This method is similar to the one outlined by Brown [259]. An example of this is shown in Figure 5.33.

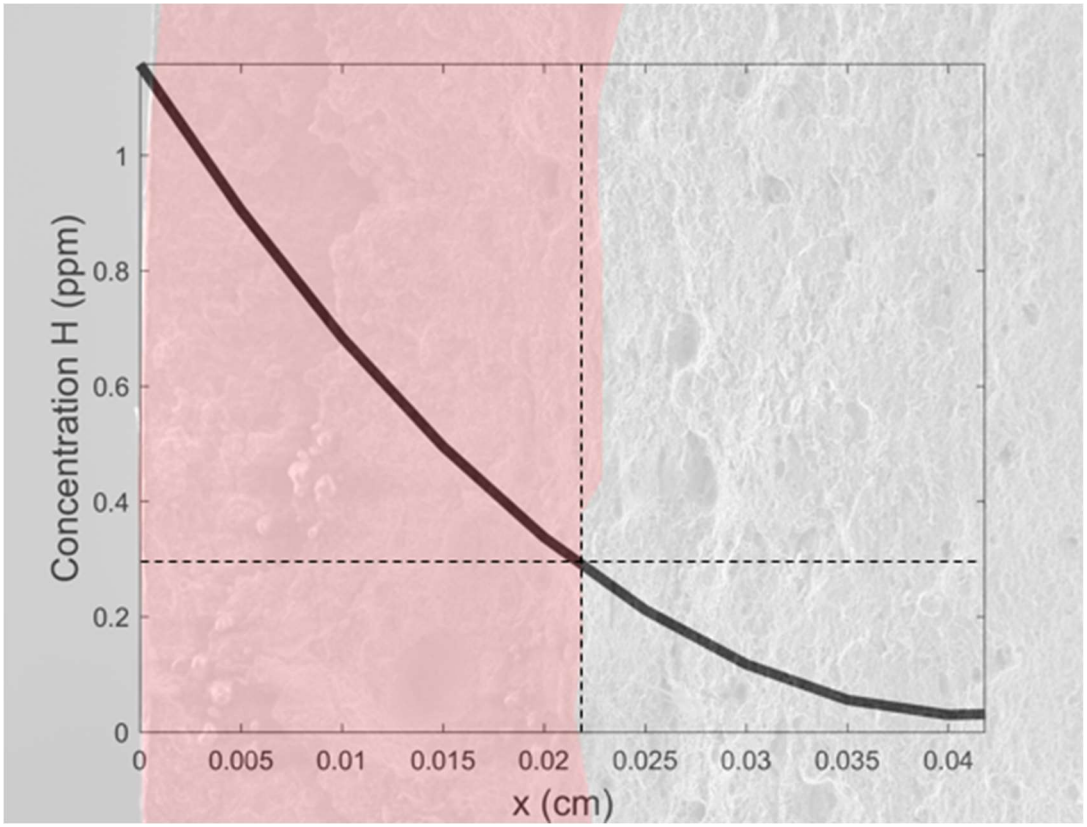

Figure 5.33 Fractograph of 27MnB5+Nb-Higher strain-rate-3 (EI 40.56%) specimen, with transition from brittle to ductile (or mixed) fracture modes clearly delineated (brittle region coloured red). Simulated hydrogen concentration profile for this specimen is overlayed (solid line). Intersection between concentration profile and dashed lines gives estimate of concentration at this point and distance towards the specimen centre.

This analysis, undertaken on numerous fractographs, provided estimated critical concentrations of hydrogen (C_{Hcrit}) of 0.648 (±0.064) ppm.H for 22MnB5, and 0.288 (±0.023) ppm.H for 27MnB5+Nb. This shows that for brittle failure to occur in

22MnB5, a hydrogen concentration that is 2.25× that required for brittle failure to occur in 27MnB5+Nb is required.

These results also showed 27MnB5+Nb to have the lowest critical hydrogen concentration of any of the steels studied, including DP1000. Given what is known about the effects of microalloy carbides in similar steels [260], and for the XPF steels studied in this work, this finding is unexpected. W. Chen [261] found that hot-stamped boron steels benefitted from the addition of vanadium as it formed dispersive precipitates (irreversible traps) and increased grain boundary area (from refinement of austenite grains), imparting an increased resistance to hydrogen embrittlement over non-vanadium-containing steels that were otherwise identical, through restriction of the ability of hydrogen to agglomerate to critical concentrations. Y. Chen [262], also found via APT that hydrogen is effectively trapped at the interfaces between the lattice and NbC precipitates. This would suggest that a similar benefit may come from the niobium addition present in 27MnB5+Nb. However, Mohrbacher [260] found that it is the interaction between the microalloy carbides and lattice defects, such as vacancies and dislocations, that imparts resistance to hydrogen degradation, indicating that for hot-stamping steels microalloy carbide precipitates actually supress degradation mechanisms involving these defects, such as HELP and HESIV, rather than directly reducing the concentration of diffusible hydrogen available through direct trapping effects. In the 27MnB5+Nb studied here, the smaller grain size implies that NbC has been effective at grain refinement, but the higher overall effective diffusivity would indicate that there is little in the way of irreversible trapping occurring as a result of the niobium addition in the heat-treated condition. This is consistent with the TDA results reported by Y. Chen [262], where a large peak in desorbed hydrogen attributed to NbC acting as traps present in the ferritic condition was greatly reduced in the martensitic condition, and dwarfed by the peak attributed to hydrogen trapped at dislocations. It would seem that in this study, there are very limited effects of irreversible traps at all for 27MnB5+Nb, either on overall effective diffusivity, in limiting opportunity for reaching critical concentrations, or in mitigating hydrogen degradation mechanisms. As noted for the DP1000, martensite acts as a crucial site for initiation of cracks, and without mitigation this fully-martensitic microstructure is highly susceptible to degradation.

From Figure 5.32 it is notable that away from the region of brittle fracture (red), there is a relatively low amount of 'mixed' fracture features observed (orange and yellow) for 27MnB5+Nb tested at 10^{-5}/s strain-rate, indicating that away from the brittle region deformation proceeds in a ductile manner. This is an indication that for 27MnB5+Nb, below the critical hydrogen concentration there is little effect upon mechanical degradation. The brittle nature of the fracture close to the ultimate fracture surface can be seen from the micrographs of cross-sections taken of the fractured sample from test 27MnB5+Nb-Charged-3, shown in Figure 5.34, where large cracks are propagating almost entirely inter-granularly along the prior austenite grain boundaries, alongside a number of other smaller, sub-critical intergranular cracks, can be seen.

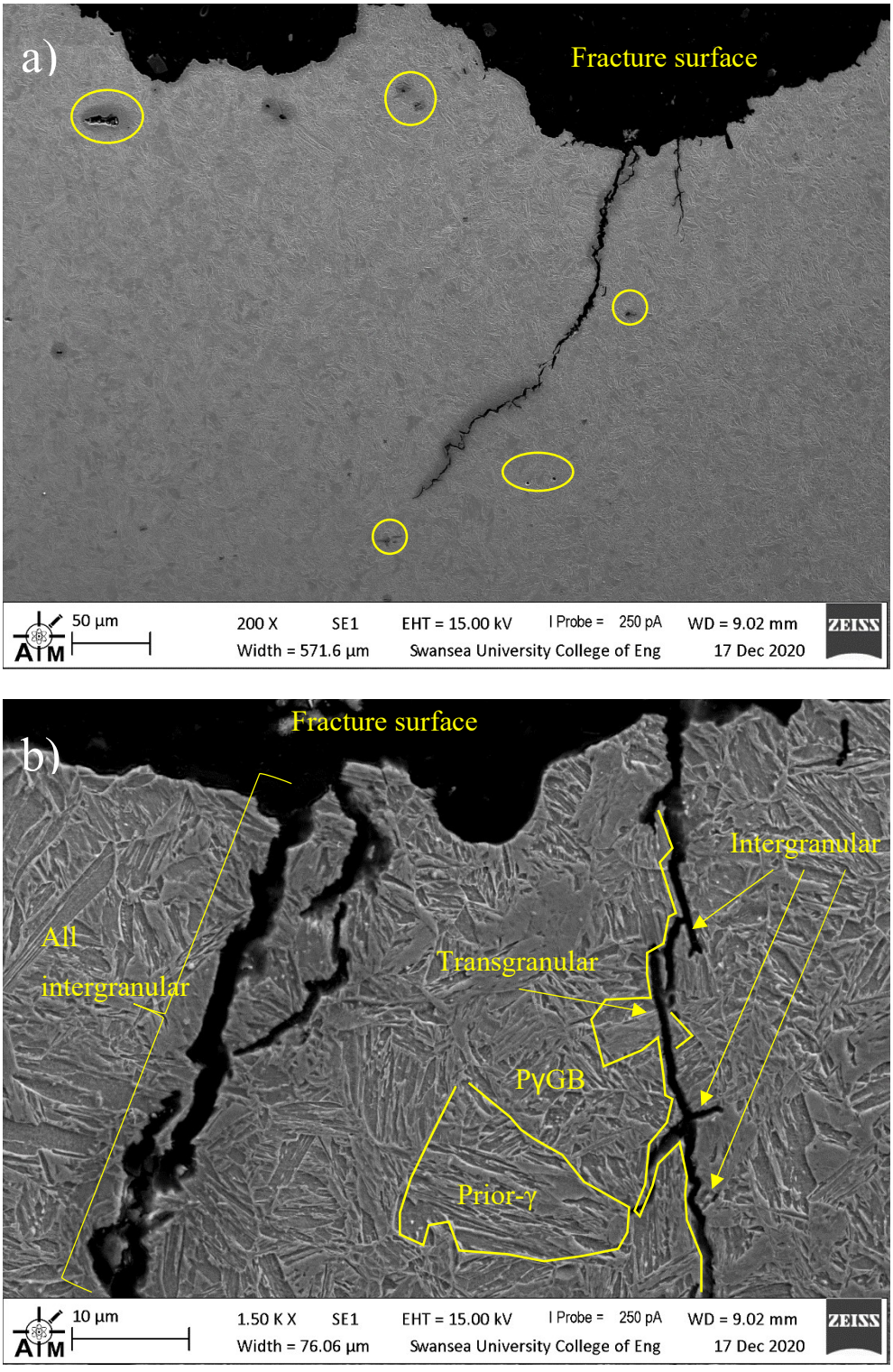

Figure 5.34 SEM images of fracture surface cross-section of 27MnB5+Nb tested at 10^{-6}/s strain-rate, with in situ hydrogen charging, showing intergranular cracks, and a number of sub-critical intergranular cracks (circled in yellow) at a) 200×, and b) 1500× magnification.

At 10^{-5}/s strain-rate regions of mixed fracture features are generally more prevalent in the 22MnB5 specimens, indicating that below the critical concentration, hydrogen is still affecting fracture mode. This implies that in 22MnB5, hydrogen concentrations below that needed for brittle fracture mechanisms can still affect mechanical performance through enhanced plasticity, i.e. HELP and HESIV. This is an important finding, as 22MnB5 had the second-lowest effective diffusivity of all the steels in this work, and third-highest C_{Hcrit} for brittle failure, yet the propensity for high C_0 allied to susceptibility to plasticity-mediated degradation mechanisms at hydrogen concentrations below C_{Hcrit} make 22MnB5 almost as susceptible overall as both DP1000 and 27MnB5+Nb, regardless of retained austenite or dislocation density. Furthermore, higher dislocation density has the potential to increase the prevalence of plasticity-related fracture features, as hydrogen facilitates the motion of dislocations [246].

Boron content apparently offers little effect upon hydrogen degradation either way – 22MnB5 has 28% higher boron addition than 27MnB5+Nb - although Komazazki [137] found boron could lower adsorption of hydrogen to the steel surface (it was found in the same study that boron had no effect on mechanical degradation due to hydrogen). Although boron nitride has been found to be a highly effective hydrogen trap, ‘free’ boron is thought to compete with hydrogen for residence at trap sites such as retained austenite, thus lowering the effectively 'safe' hydrogen concentration within a given steel [179], though quantifying ‘free’ boron is extremely challenging. For these steels, despite the higher boron addition for the 22MnB5, 27MnB5+Nb has substantially higher additions of strong nitride-forming elements such as Ti, Al, and Nb, with a ratio of Ti+Nb+V+S.Al to N (Table 3-1) that is around 2.3 times higher than that for 22MnB5. Whilst boron itself is a very strong nitride former (it is often used in low carbon formable grades as a ‘scavenger’ of free nitrogen to limit room temperature ageing), it may well be that 27MnB5+Nb actually has higher ‘free’ boron as a result of these other additions, and hence may have a lower ‘safe’ hydrogen concentration than for the 22MnB5.

Either way, the difference in fracture characteristics between 27MnB5+Nb and 22MnB5 is marked, as seen by further comparing Figure 5.34 and Figure 5.35, with 22MnB5 showing many small ‘cracks’ at frequent intervals extending ~ 2 μm below the ultimate fracture surface, and an increase in the prevalence of ‘pores’, some of

which are not intergranular in location. Nevertheless, CT scan images (Figure 5.36 and Figure 5.37) of 22MnB5 tested at 10^{-6}/s strain-rate with *in situ* hydrogen charging including 2 hours' pre-charging show the formation of several large cracks initiated from the specimen surface, propagating transverse to the tensile load. These cracks are not the point of ultimate failure in the sample, but do imply rapid intergranular propagation from regions of highest concentration towards the region of lowest.

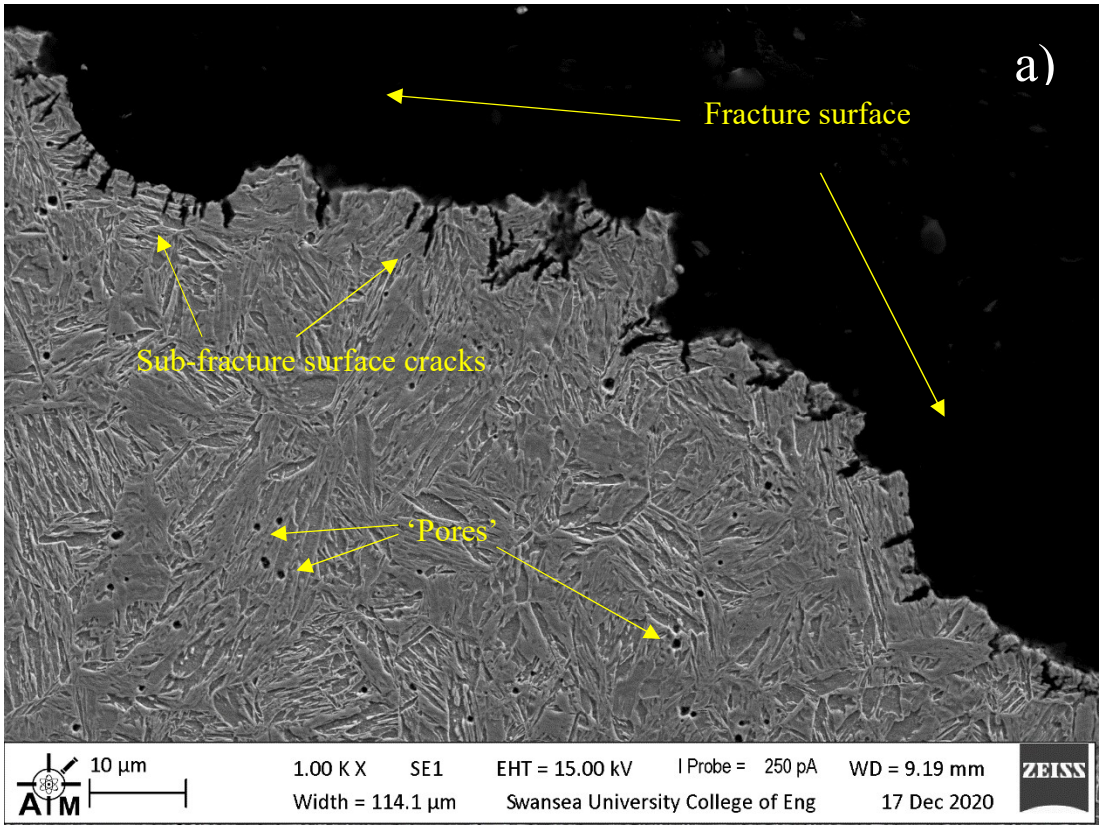

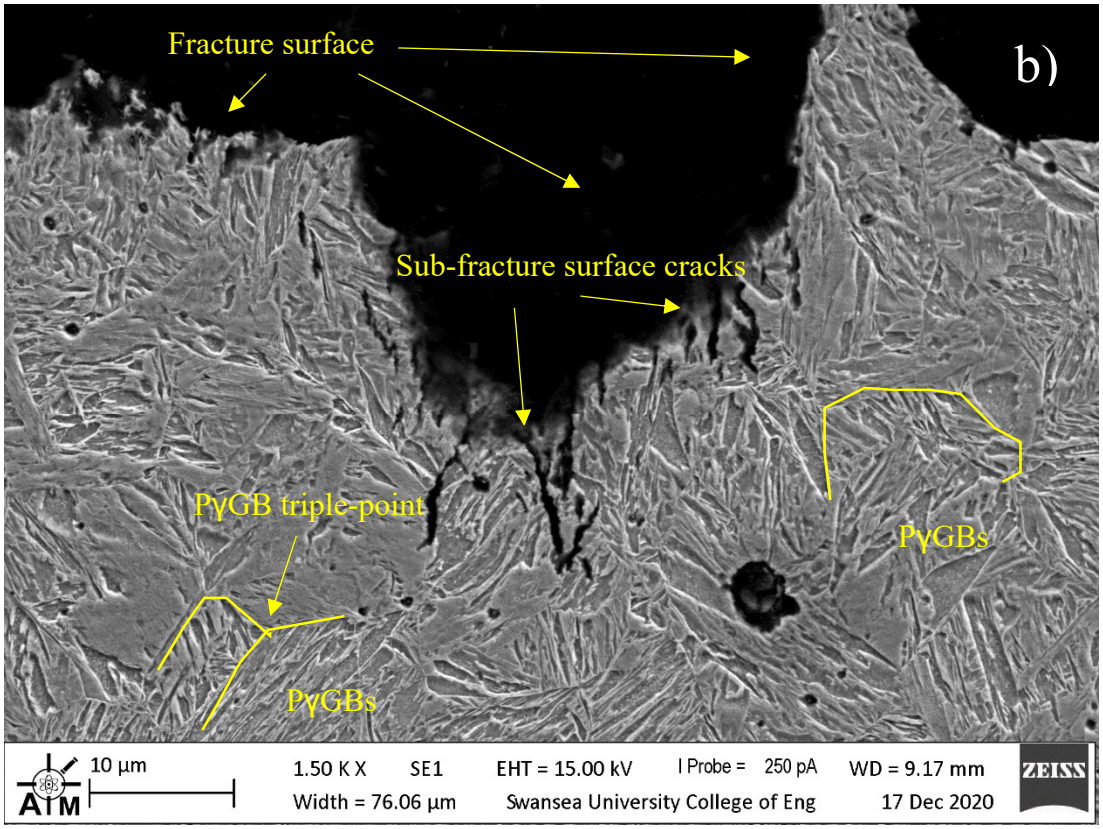

Figure 5.35 SEM images of fracture surface cross-section of 22MnB5 tested at 10^{-6}/s strain-rate, with in situ hydrogen charging, showing cracks at the fracture surface and sub-surface 'pores' at a) 1000×, and b) 1500× magnification.

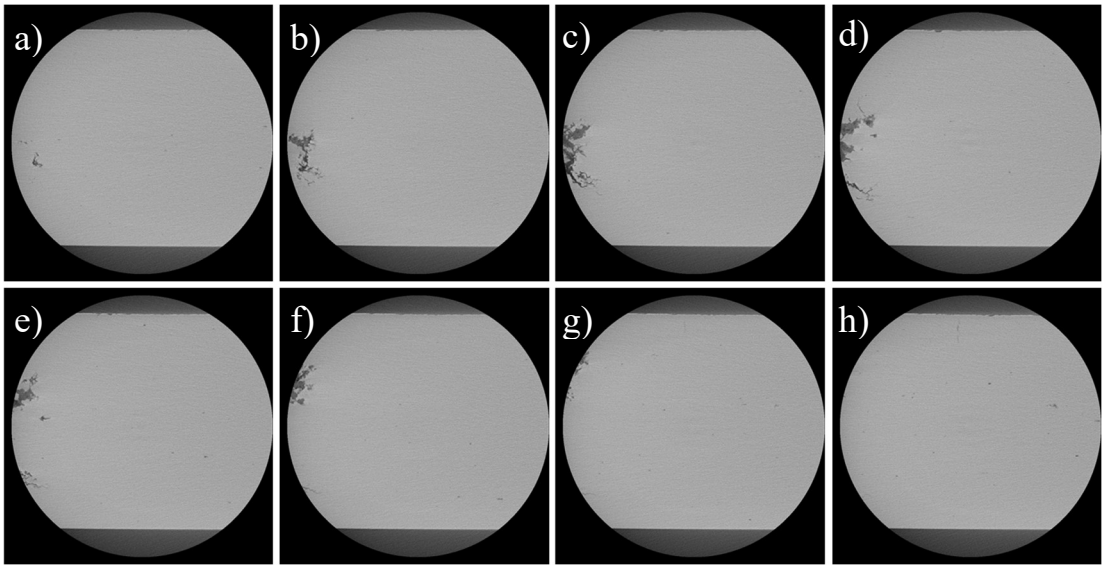

Figure 5.36 Computed tomography images of 22MnB5 (900C) tested at 10^{-6}/s strain-rate with 2 hours' pre-charging with hydrogen. Aspect is down along the tensile axis, rising by 1 µm with each image, showing the presence of a sub-critical crack transverse to the loading direction approximately 30 µm below the fracture surface.

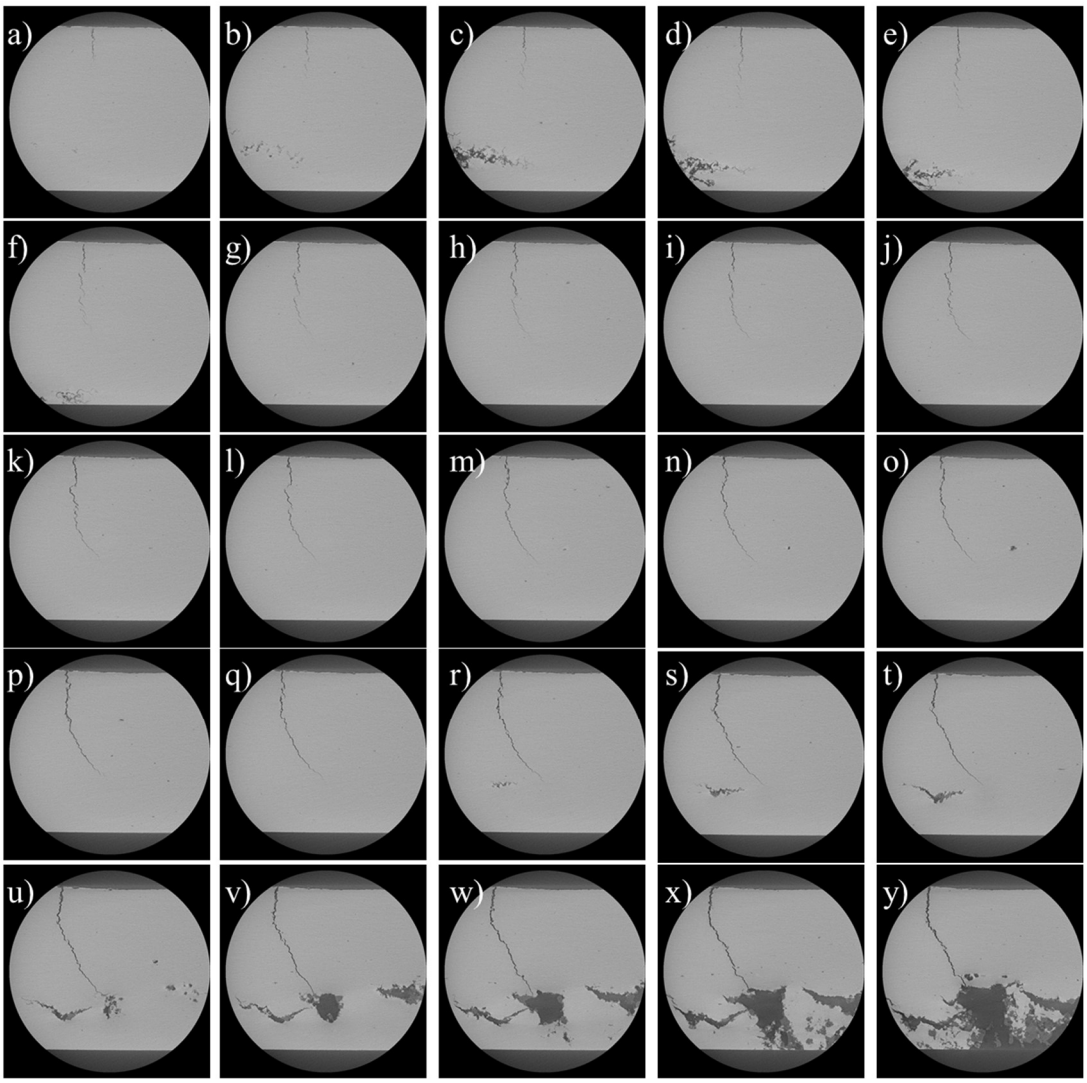

Figure 5.37 Computed tomography images of the same 22MnB5 (900C) tested at 10^{-6}/s strain-rate with 2 hours' pre-charging with hydrogen. Aspect is down along the tensile axis, rising by ~1 µm with each image, showing the presence of an increasing number of cracks approximately 25 µm below the fracture surface, coalescing at the fracture surface.

The response of 22MnB5 to hydrogen, like that of the dual-phase steels, appears to be multi-faceted in terms of fracture mechanism. Whilst some mitigation is provided by a trace amount of retained austenite that can provide some irreversible trapping to diffusible hydrogen, lowering the amount available to agglomerate to critical concentrations at high-stress regions, its high dislocation-density provides ample opportunity for low concentrations of hydrogen to facilitate motion of said dislocations via the HELP mechanism, and its nominally fully-martensitic microstructure is highly susceptible to initiation of cracks through the HEDE mechanism.

A further clue as to the behaviour of 22MnB5 (900C) under hydrogen-charged conditions comes from data obtained via nanoindentation. Detailed experimental setup is described in Chapter 3.4.4, but in essence this involved charging 0.8 mm samples with hydrogen for 6 hours and then indenting the sample in 3 × 3 arrays, every 20 minutes (at pre-defined locations). Results are then compared against values obtained from un-charged conditions on the same specimen. Figure 5.38 shows the values for nano-hardness across 6 hours' testing.

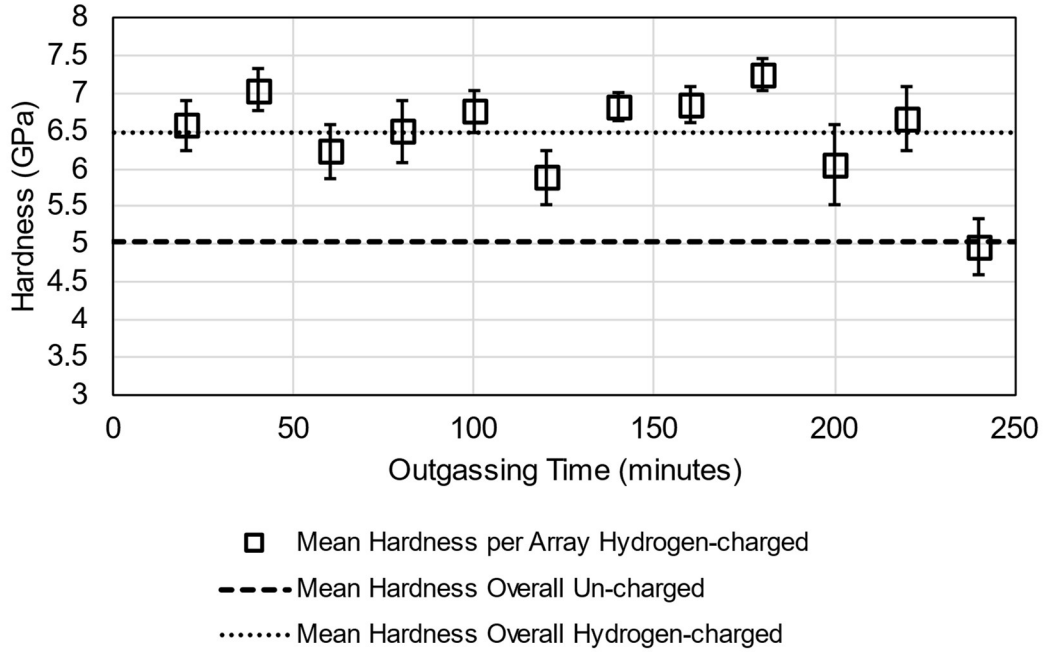

Figure 5.38 Nano-hardness measurements on a 22MnB5 (900C) specimen charged with hydrogen at -1050 mV (SCE) in 3.5% NaCl + 3g/L NH_4SCN, for 6 hours prior to nanoindentation. Dashed line represents mean hardness obtained when the specimen was in the 'un-charged' condition.

This method provides an estimate for how mechanical properties are 'recovered' as hydrogen is desorbed from the specimen. In the case of 22MnB5, Figure 5.38 demonstrates how the martensitic microstructure incurs an increase in hardness as a result of being charged with hydrogen. This increased hardness is maintained until the hydrogen is essentially fully-desorbed (or below a critical threshold) after ~ 6 hours (which actually corresponds to the duration of hydrogen charging), whereby the mechanical properties (hardness in this case) return to levels measured prior to charging the specimen with hydrogen. This step-change is due to the nature of nanoindentation, where only a few tens of nanometres are deformed by the probe tip [110] – as hydrogen has to desorb through the specimen surface, this region will

always have the highest hydrogen concentration, and will therefore be affected until the hydrogen concentration becomes negligible. This implies that mechanical property degradation is not irreversible, and with enough time, or with an appropriate ‘baking out’ procedure, fully-martensitic 22MnB5 will recover its mechanical properties after incurring an ingress of hydrogen, provided that desorption reduces levels below the critical concentration.

5.3.1.4 The role of effective diffusivity in mechanical degradation

As discussed above, where strength levels are equivalent, steels with microstructures affording them lower effective diffusion coefficients, D_{eff}, generally tend to incur less degradation in mechanical property performance than those with higher D_{eff}. This can be seen graphically when D_{eff} values are overlayed upon the embrittlement indices displayed in Figure 5.30, shown below in Figure 5.39.

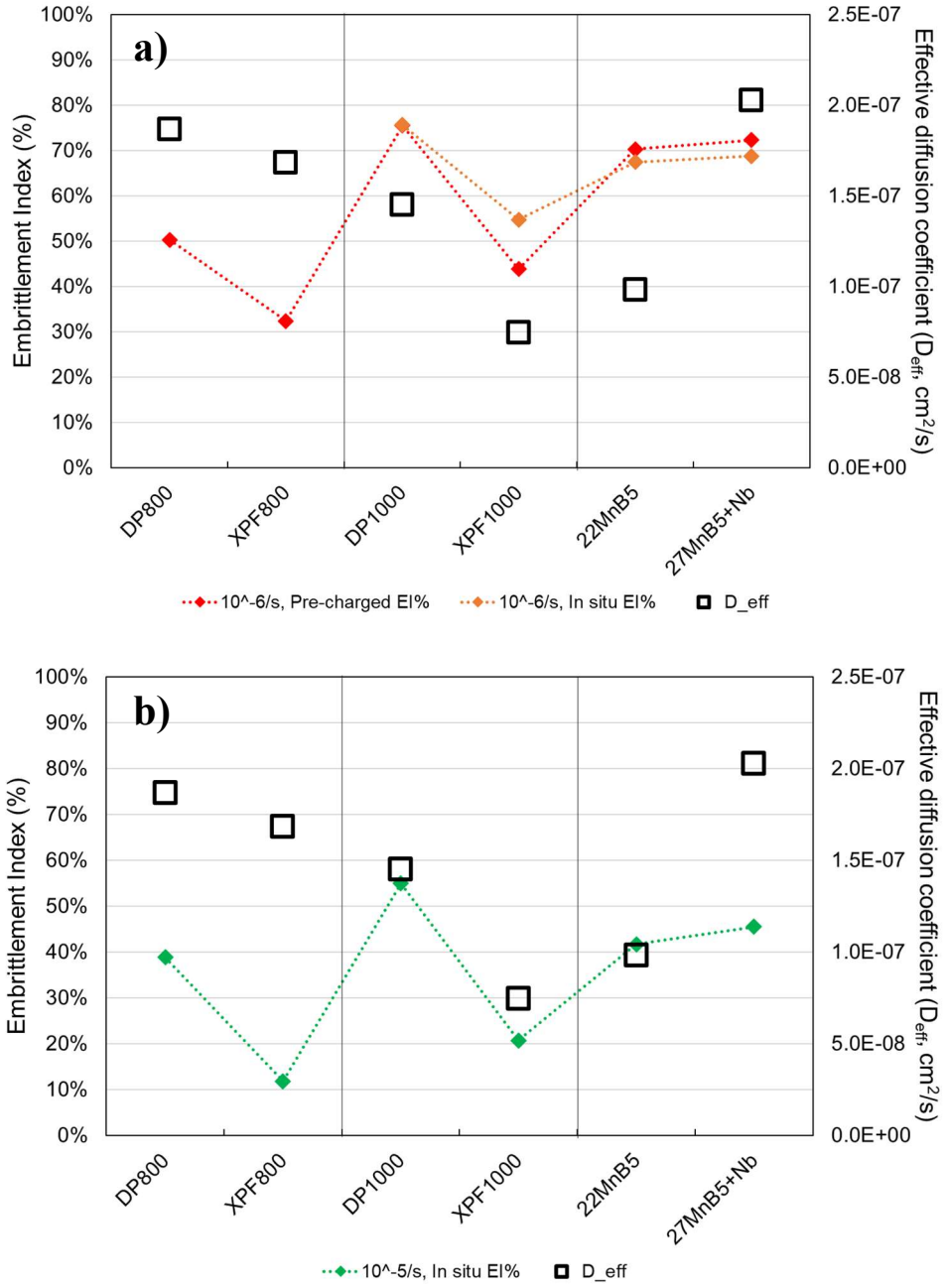

Figure 5.39 Embrittlement indices for each test condition (markers with dotted lines), with effective diffusion coefficient (black-border squares) overlayed. a) tests at 10^{-6}/s strain-rate, b) test at 10^{-5}/s strain-rate.

For each ‘group’ of strength levels, the trend in level of embrittlement under each condition matches the trend in diffusivity, regardless of strain-rate. This correlates with the work of many other researchers, for example Depover [246,263], and the review paper on the subject by Bhadeshia [6], found higher diffusivity to correlate with higher levels of mechanical degradation. Furthermore, Depover and Verbeken [264] found that although diffusible hydrogen content was higher for quench-and-tempered materials, embrittlement was more pronounced in as-quenched material due to its higher hydrogen diffusivity, implying that diffusivity may be a more critical parameter than absolute hydrogen concentration where levels of degradation are concerned. Diffusivity of hydrogen allows it to concentrate at regions of high stress triaxiality, initiating (or propagating) highly-localised cracking mechanisms, or enhancing local plasticity.

In this work, there is also a correlation between embrittlement index and proportion of fracture features that can be categorised as ‘brittle’, such as quasi-cleavage and intergranular cracking. Figure 5.40 shows the links between embrittlement index and fracture features.

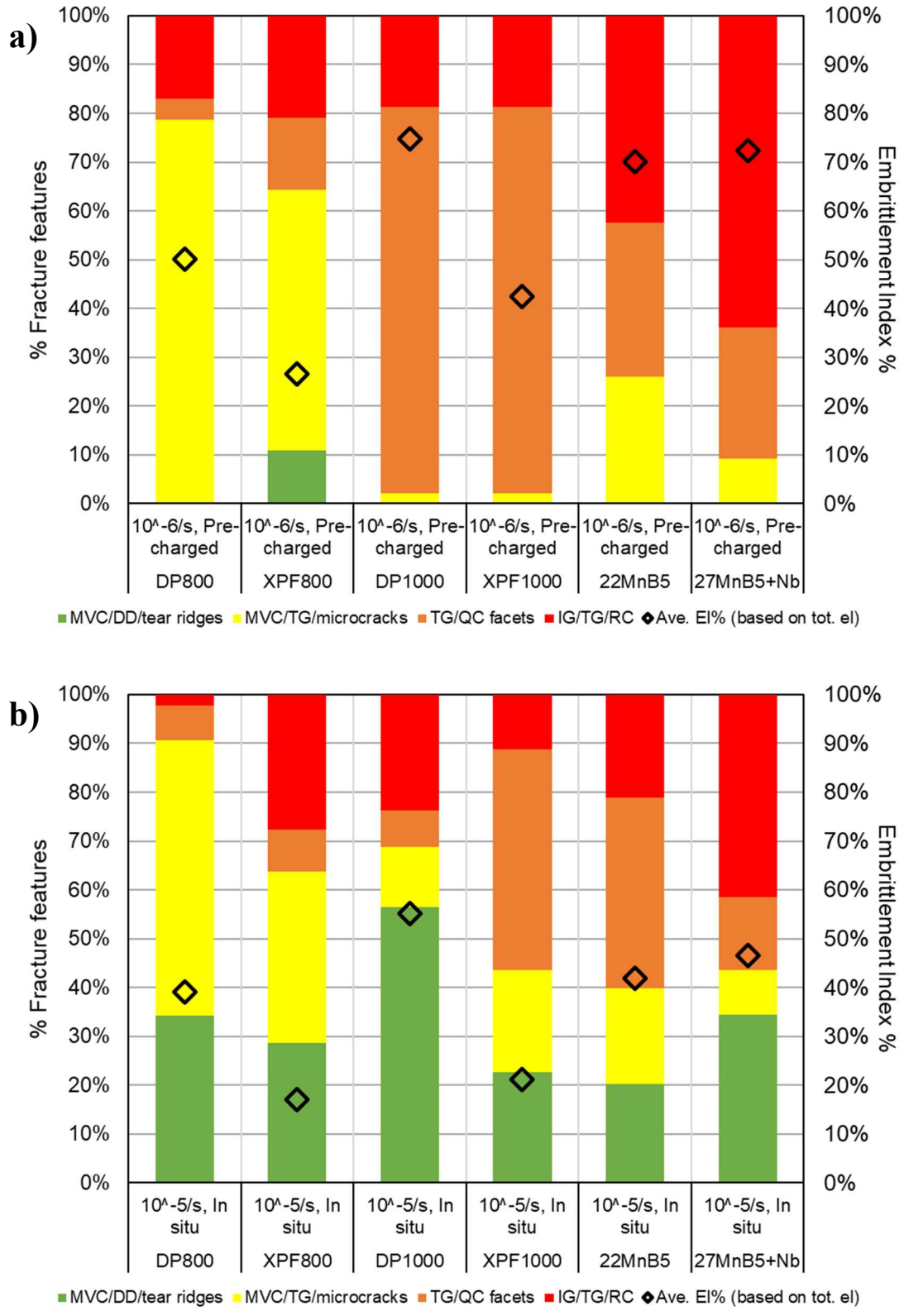

Figure 5.40 Percentage classified fracture features for each steel and test condition involving hydrogen charging, and embrittlement index. a) Pre-charged + *in situ* charging 10^{-6}/s strain-rate, b) *In situ* charging only at 10^{-5}/s strain-rate.

Despite embrittlement index correlating with both D_{eff} and prevalence of brittle fracture features, this correlation does not strictly translate to correlation between brittle fracture features and effective diffusivity, based on this work. Furthermore, as can be seen from the results for XPF800 in Figure 5.40, lower levels of embrittlement does not necessarily translate to lower levels of 'brittle' features. It is this characteristic of hydrogen embrittlement that led to the development of the HELP mechanism to explain fracture surface features.

However, there is a strong correlation between D_{eff} and the critical concentration of hydrogen to induce brittle fracture features, C_{Hcrit}. Figure 5.41 shows clearly how at a given strength level, steels with a higher D_{eff} have a lower C_{Hcrit}.

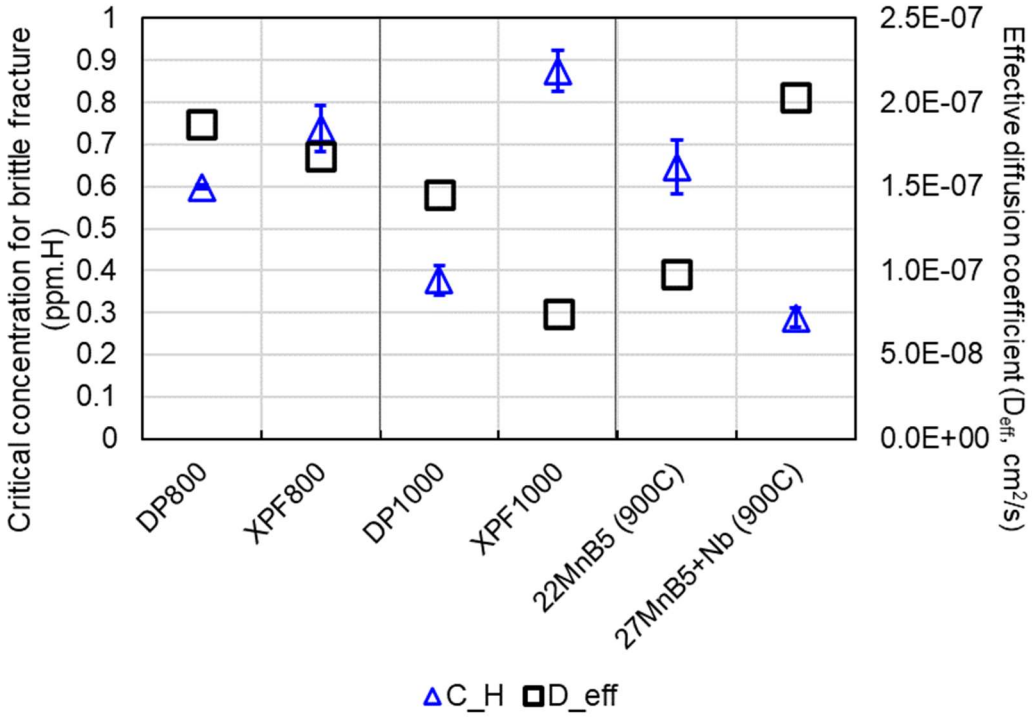

Figure 5.41 Critical hydrogen concentrations for brittle failure in specimens tested at 10^{-5}/s strain-rate, and effective diffusion coefficients.

This presents a serious problem for the steels in question. If critical concentration is low and effective diffusivity is high, the time taken to reach this critical concentration is going to be short, particularly if charging conditions are severe, such as in conditions of low pH during crevice corrosion (Figure 4.24, and [73]). This is observed for the worst performing steels in this work, and in the work of Depover [264], who found

that DP1000 would suffer a measurable loss of ductility after only 1 minute of hydrogen charging. Exposure to chloride-containing aqueous environments has been shown to lead to hydrogen uptake [66,80], an environment that can be expected in coastal locations, or during winter months with salt-treated highways, and should a part be under stress during service when exposed to this environment it could be cause for serious concerns for the integrity of the part.

Figure 5.30 and Figure 5.39 show that the relative differences in degradation between the steels are maintained, regardless of the presence of 2 hours' pre-charging, or the strain-rate at which testing was undertaken. It also shows that there is no statistically significant difference between embrittlement indices for tests performed at 10^{-6}/s strain-rate, with and without pre-charging, as confirmed by Student's t-test for each of the steels. This is interpreted as being a result of the testing speed itself: 10^{-6}/s strain-rate meant tests ran for a sufficient time to allow the specimens to easily reach critical concentration throughout, even without 2 hours of charging prior to straining. Evidence for this is in the simulated hydrogen distributions and concentration profiles, which show that for all of the steels across almost the whole specimen thickness (save for a narrow region at the very centre of the specimens) the hydrogen concentration exceeds the critical values plotted in Figure 5.41. For the tests undertaken at the higher strain-rate of 10^{-5}/s with in situ hydrogen charging, this critical concentration is only reached in regions close to the charging surfaces, correlating with regions of brittle fracture features, and ultimately leading to much lower levels of embrittlement overall. At higher strain-rates hydrogen is unable to keep pace with dislocation motion meaning it is less able to concentrate at defects or high-stress regions [265], whereas at lower strain-rates dynamic strain-aging will increase dislocation density [266]. Nonetheless, the relative performance of each of the steels remains consistent, leading to the conclusion that for a given strength level, the steels with the higher effective diffusivity will incur higher levels of mechanical degradation due to hydrogen ingress. In turn, it suggests that designing steel alloys to have lower effective diffusivity should be an effective way to mitigate against the damaging effects of hydrogen.

6 Conclusions

From the work detailed throughout this document, the following conclusions have been drawn:

- For a given strength level, XPF steels were substantially more resistant to hydrogen embrittlement than DP steels of equivalent strength. The XPF800 and XPF1000, with their ferrite + nanoprecipitate microalloy carbide microstructure, showed embrittlement indices of 32% and 42%, respectively, when tested at 10^{-6}/s with *in situ* hydrogen charging including 2 hours' pre-charging. DP800 and DP1000 had embrittlement indices of 50% and 75%, respectively, under the same conditions. Similar differences were found for the other test conditions involving hydrogen charging. These differences in susceptibility are attributed to the lower diffusivity found in XPF steels, and the inherent susceptibility to brittle fracture of the martensite phase.

- DP1000 had the highest embrittlement indices of any of the tested steels, at 75%, 75%, and 55% for the tests performed at 10^{-6}/s strain-rate with 2 hours' pre-charging, 10^{-6}/s strain-rate with *in situ* charging only, and 10^{-5}/s strain-rate with *in situ* charging only, respectively. This is despite the fully-martensitic boron steels having a hydrogen-free UTS ~ 500 MPa higher than DP1000. Analysis of the fracture surfaces found propagation of cracks nucleated in martensite were not resisted by the softer ferrite phase, and significant sub-surface cracking in the region beneath the fracture surface. Hydrogen also increased the plasticity in the ferrite phase, leading to increased prevalence of typically 'ductile' fracture features, even when failure occurred prematurely.

- Of the boron steels, 22MnB5 had a consistently lower embrittlement index at 70%, 67.5%, and 42%, than 27MnB5+Nb at 72.3%, 68.8%, and 46.5% for the tests performed at 10^{-6}/s strain-rate with 2 hours' pre-charging, 10^{-6}/s strain-rate with *in situ* charging only, and 10^{-5}/s strain-rate with *in situ* charging only, respectively. Whilst this is within the margin of error, analysis of the fracture surfaces alongside simulated hydrogen concentration profile of the two steels found that 22MnB5 had a higher critical hydrogen concentration required for brittle fracture than 27MnB5+Nb.

- There is a correlation between embrittlement index (EI%) and effective diffusion coefficient, D_{eff}. Relative differences in embrittlement index were found to follow the same pattern as the relative differences in effective diffusivity. Higher diffusivity is therefore a risk factor for increased susceptibility to mechanical property degradation due to hydrogen ingress. Minimising hydrogen diffusion is a key parameter when designing microstructures to be resistant to hydrogen embrittlement.

- The highest proportion of typically 'brittle' fracture features, such as intergranular cracks and quasi-cleavage facets, were observed on the specimens with the highest embrittlement indices, e.g. specimen labelled 27MnB5+Nb-Pre-charged-1, which had embrittlement index of 68.6% and a fracture surface showing 64% brittle features. However, for specimens with a comparatively lower embrittlement index, e.g. XPF800-Pre-charged-2, which had embrittlement index 26.5% and only 20.9% brittle features, there was significantly more evidence of features such as microvoid coalescence than in the XPF800 specimens tested in air, which had deformed via severe, but uniform, necking (localised strain). Analysis of hydrogen concentrations on fracture surfaces shows at the regions of highest hydrogen concentration, hydrogen is inducing brittle crack formation and failure via cleavage, whereas at lower concentrations hydrogen is increasing the appearance of 'ductile' fracture features at lower stresses than would be expected. This is indicative of the activity of both decohesion-based and plasticity-based mechanisms.

- There is no statistically significant difference between the degradation occurring after 2 hours' pre-charging (maintaining charging *in situ* throughout the test), or when hydrogen charging is commenced at the beginning of straining, in tests conducted at 10^{-6}/s strain-rate. This indicates that the test duration is sufficiently long at this strain-rate to allow hydrogen to be charged to critical concentrations, even without 2 hours' pre-charging. Modelling of hydrogen distributions for the two conditions (pre-charged/not pre-charged) shows that at the time of fracture the hydrogen distributions in the specimens are very similar, in most cases. Modelling of the hydrogen distributions for the higher strain-rate tests (10^{-5}/s, no pre-charging) shows a good correlation

between higher hydrogen concentrations towards the charging surfaces of the specimens, and regions of brittle fracture features.

- XPF steels have lower diffusion coefficients than DP steels of equivalent strength level. XPF800 and XPF1000 had D_{eff} of 1.68×10^{-7} and 7.45×10^{-8} cm^2/s, respectively, whereas DP800 and DP1000 had D_{eff} of 1.87×10^{-7} and 1.45×10^{-7} cm^2/s, respectively. XPF1000 had the lowest D_{eff} of any of the investigated steels. This is attributed to the 'irreversible' trapping effects of the microalloy carbide nanoprecipitates present in the XPF steels, which had the effect of displacing the breakthrough time to longer times, and steepening the gradient of the rising transient during hydrogen permeation experiments.

- For all of the steels apart from the XPFs, hydrogen permeation curves simulated according to Fick's laws provided a reasonable fit to all of the permeation transients from membranes of 0.8 mm nominal thickness. This indicates that for all bar the XPF steels, lattice diffusion is dominant, even if there is a presence of 'reversible' traps.

- For the boron steels, the heat-treated martensitic microstructure had a >40% lower diffusion coefficient (9.81×10^{-8} cm^2/s for 22MnB5, 2.03×10^{-7} cm^2/s for 27MnB5+Nb) than the ferritic-pearlitic or ferritic + segregated carbide microstructures of the as-received material (1.70×10^{-7} cm^2/s for 22MnB5, and 5.54×10^{-7} cm^2/s for 27MnB5+Nb). This is interpreted as an effect of the high dislocation density providing 'reversible' traps for diffusing hydrogen (in equilibrium with the lattice diffusion), the complex orientation relationship of martensite packets, and small amounts of retained austenite in the martensitic microstructure providing a much more convoluted transport path for diffusing hydrogen.

- A greater increase in steady-state flux is achieved when reducing charging potential from -950 mV (SCE) to -1050 mV, than the increase achieved when moving from -850 mV to -950 mV. This is due to a greater increase in hydrogen concentration at the charging surface (C_0) between -950 mV and -1050 mV, in turn caused by a change in the dominance of reactions occurring at the charging

surface in favour of hydrogen evolution through the reduction of water at a potential of around -1040 mV (SCE). This change is reflected in a change in Tafel slope at an inflection point in the potentiodynamic curve as a result of the Butler-Volmer relationship.

- However, reducing the charging potential from -850 mV to -1050 mV (SCE) for the same steel (22MnB5) of the same membrane thickness (1.2 mm) has only a very modest impact upon diffusion coefficient, increasing it from 1.05×10^{-7} to 1.54×10^{-7} cm^2/s, despite the increase in maximum flux, J_∞, from 2.11×10^{-12} $mol/cm^2/s$ at -850 mV (SCE) to 1.62×10^{-11} $mol/cm^2/s$ at -1050 mV (SCE). This implies that diffusion is not concentration-dependent, but bulk diffusion-dependent at 1.2 mm thickness for heat-treated 22MnB5, a finding supported by the nearly-identical normalised concentration profiles at each charging potential.

- The introduction of ammonium thiocyanate, NH_4SCN, as a recombination poison to a 3.5% NaCl electrolyte increases hydrogen uptake to a polarised steel surface by increasing the current density for a given applied potential (i.e. a shallower gradient Tafel slope), whilst suppressing the formation of bubbles at the charging surface. This is achieved in part by a reduction in electrolyte pH.

- 0.8 mm is a typical gauge for these products, therefore the *relative* differences in diffusion between them at this thickness is pertinent, rather than 'intrinsic' properties, as the diffusion characteristics at thicker gauges is of limited relevance to in-service performance.

- SVET scans of a damaged GI coating exposing mild steel substrate to 0.1 M NaCl solution causes a galvanic cell of sufficient average net reduction potential to cause substantial hydrogen evolution at the surface of the exposed steel substrate via a cathodic reduction of water. Hydrogen evolution at the most strongly cathodic regions was at an average of 1.69×10^{-10} $mol/cm^2/hr$, a rate of similar order as potentiostatic charging at -850 mV (SCE) in a 3.5% NaCl + 3g/L NH_4SCN solution. Part design and coating practices must ensure

that hot-dip zinc layers are sufficiently protected from damage to avoid problematic hydrogen evolution at the steel surface.

- SVET scans of a damaged GI coating exposing a mild steel substrate in 0.1 M NaCl solution show a high magnitude of maximum anodic current density (reaction rate) early on, 6 A/m^2, before reducing to a more settled level after about 10 hours at ~ 2 A/m^2. This is indicative of highly localised sacrificial anodes (pits) immediately after immersion. These are depleted over time, and the anodic current settles, indicating a more general form of corrosion. Conversely, cathodic activity begins in a highly generalised way before periodic formation of localised cathodes of comparatively higher intensity. This demonstrates that even short exposure of a damaged coating to a corrosive electrolyte can cause considerable long-term flaws in the integrity of the part.

- There is about 450 - 500 mV difference between the open circuit potential of GI coated mild steels and all of the uncoated steels (average net reduction potential). This is more than enough to drive a galvanic reaction in the presence of an aqueous electrolyte.

- There is sufficient difference in equilibrium potential of the ferrite and martensite phases in DP1000 to drive galvanic corrosion without coupling to another steel or metallic coating. The 80-120 mV difference in equilibrium potential was revealed by use of scanning Kelvin probe force microscopy (SKPFM). Any exposure of a component manufactured using DP1000 to a corrosive electrolyte could induce galvanic corrosion within the part.

- Crevice corrosion leads to a rapid drop in electrolyte pH in the region within the crevice, as observed during time-lapse photography of simulated crevice corrosion. This leads to a decrease in required overpotential for the hydrogen evolution reaction according to the Nernst equation and Pourbaix diagrams. A concurrent increase in pH in the region immediately adjacent to the crevice is also observed. It is essential that part designs avoid the possibility of crevice formation to minimise the opportunity for such reactions to occur.

- No statistically significant differences were seen in the cathodic Tafel slopes generated during cathodic polarisation between any of the steels except DP1000. This is interpreted as being due to insufficient differences between the alloy chemistry and microstructures of the steels to invoke differences in response to cathodic polarisation.

7 Appendices

7.1 Appendix I – MATLAB code for analysing permeation data and simulating Fickian permeation curves

```
% Program to analyse DS Permeation Data and compare with simulated
curves


% BEFORE RUNNING THIS PROGRAM, PLEASE ENSURE YOU HAVE
% THE RAW DATA SAVED IN THE CORRECT FOLDER
%% First Section
% Step 1 is to import the data

clear % Clear memory to avoid variable contamination
help Permeation_Analysis1 % Print header

Name = input('Enter name of product (in single inverted commas): ');
Permdata = readtable(uigetfile);
TimeStart = input('What time did charging begin (in seconds)? ');
SurfaceArea = input('What was the oxidation surface area (cm2)? ');
Thickness1 = input('What was the first thickness measurement (mm)?
');
Thickness2 = input('What was the second thickness measurement (mm)?
');
Thickness3 = input('What was the third thickness measurement (mm)?
');

% Calculate average thickness and variation (warn if outside spec)

Lmm = (Thickness1 + Thickness2 + Thickness2)/3;
L = Lmm/10;

% Check gauge variation
ThickRatio1 = abs((Thickness1 - Thickness2)/Thickness1);
ThickRatio2 = abs((Thickness2 - Thickness3)/Thickness2);
ThickRatio3 = abs((Thickness1 - Thickness3)/Thickness3);

if ThickRatio1 >= 0.05
    warning('Gauge variation exceeds 5%. Please check tolerances.');
end
if ThickRatio2 >= 0.05
    warning('Gauge variation exceeds 5%. Please check tolerances.');
end
if ThickRatio3 >= 0.05
    warning('Gauge variation exceeds 5%. Please check tolerances.');
end

%% Begin analysing data by calculating columns as workspae variables
% Delete rows of data prior to charging cycle
toDelete = Permdata.T < TimeStart;
Permdata(toDelete,:) = [];
clear toDelete;

% Identify time to max flux and use for indexing graph
[M,I] = max(Permdata.Im);
```

```
if (I + 300) > max(Permdata.T)
    PlotEnd = max(Permdata.T);
else
    PlotEnd = I + 900;
end

% Clean time after max flux to avoid calculation contamination
toDelete = Permdata.T > (PlotEnd + TimeStart);
Permdata(toDelete,:) = [];
clear toDelete;

% Clean time data to start at 1 second
TestTime = Permdata.T - (TimeStart - 1);

% Add 'hour' column
Hours = TestTime / 3600;

% Identify minimum current value then subtract it from the ongoing
data
MinCurr = min(Permdata.Im);
Current = Permdata.Im - MinCurr;

% Identify maximum current value (steady-state)
MaxCurr = max(Current);

% Add 'normalised' current column
NormCurr = Current / MaxCurr;

% Add calculated 'flux' column and identify max
Flux = (Current / SurfaceArea) / 96485;
MaxFlux = max(Flux);

% Add 'normalised' flux column
NormFlux = Flux / MaxFlux;




%% Begin analysing data properly
% Breakthrough and lag times:
Fluxtb = 0.1 * MaxFlux;
Fluxtlag = 0.63 * MaxFlux;

% Breakthrough time
[~,idx1] = min(abs(Fluxtb - Flux)); % Identifies time for 0.1 x Jinf
Testtb = idx1
TestDtb = L^2/(15.3*Testtb) % Calculates D based on breakthrough
time

% Lag time
[~,idx2] = min(abs(Fluxtlag - Flux)); % Identifies time for 0.63 x
Jinf
Testtlag = idx2
TestDtlag = L^2/(6*Testtlag)
```

```
% Create new variable of normalised time
% Based on the lattice diffusion coefficient from Hagi 1994
TestTau = ((5.5e-4 * TestTime) / L^2);
TauEnd = floor(max(TestTau));

% Calculate C0 value based on whichever Dtlag is larger
 TestC0 = (MaxFlux * L) / TestDtlag;


PlotStep = round(PlotEnd/100); % Find a cleverer way of doing this

% Plot permeation data
figure(1)
plot(Hours(1:PlotStep:PlotEnd),Flux(1:PlotStep:PlotEnd),...
    'Marker','x','LineStyle','none');
xlabel('Time (hours)','FontName','Times New Roman');
ylabel('Permeation flux, J (mol/cm^2/s)','FontName','Times New
Roman',...
    'FontSize',12.5);
title(sprintf('Potentiostatic permeation flux of %s', Name));
hold on

% Plot normalised flux against normalised time
figure(2)
semilogx(TestTau(1:PlotStep:PlotEnd),NormFlux(1:PlotStep:PlotEnd),..
.
    'LineWidth',2);
title(sprintf('Normalised Flux vs Normalised Time %s', Name));

% Create ylabel
ylabel({'Normlised Flux J(t)/J(ss)'},'FontSize',16,...
    'FontName','Times New Roman');

% Create xlabel
xlabel({'Tau (Dt/L^2)'},'FontSize',16,'FontName','Times New Roman');

hold on


%% Simulate permeation using Fick's laws and Deff from test data
% Based on breakthrough time calculation
%* Set initial and boundary conditions.
C = 0; % Overall concentration set to zero
t = 1; % Time parameter set to zero
C0 = (MaxFlux * L) / TestDtb; % Set concentration based on
breakthrough
BrkJinf = ((TestDtb*C0)/L); % Steady-state flux
BrkJtb = 0.1*BrkJinf; % 'Breakthrough' flux
BrkJtlag = 0.63*BrkJinf; % 'Lag' flux


%* Set up loop.
iplot = 1; % Counter to count plots
tstep = PlotEnd; % Max number of seconds (t)
tlim = round(tstep*0.04);

syms n % Initialize symbolic n for sum over series
J = zeros(tstep,1); % Sets up matrix for accepting values for J
H2 = zeros(tstep,1); % Sets up matrix for recording time values
```

```
Tplot = zeros(tstep,1); % Sets up matrix for recording time values

%* Loop for set no. time-steps.
fprintf('%d', C0);
fprintf('\nCounter: ')



for t = 1:tstep %% MAIN LOOP %%

    %* Compute flux @ exit surface for each time-step.
    % Start with sigma calculation (1 to 5000):
    S1 = symsum((cos(pi*n)*exp((-
TestDtb*(n^2)*(pi^2)*t)/L^2)),n,1,5000);

    J(t) = BrkJinf*(1+(2*S1)); % Calculates flux for this time value
    Tplot(iplot) = t; % Record t for plotting
    H2(iplot) = t/3600;
    fprintf('\r'); % new line for counter
    fprintf('%d', t); % counter (time) value
    if round(max(J(t)),16) >= round(BrkJinf,16)
        break
    end
    iplot = iplot+1;

end

fprintf('\r'); % extra new line at end of counter

%%* Output calculated values for diffusion coefficients and steady-
state
% Values can be compared to input value of D as validation of
simulation

% Breakthrough time
[~,idx3] = min(abs(BrkJtb - J)); % Identifies time for 0.1 x Jinf
Brktb = idx3
BrkDtb = L^2/(15.3*Brktb) % Calculates D based on breakthrough time

% Lag time
[~,idx4] = min(abs(BrkJtlag - J)); % Identifies time for 0.63 x Jinf
Brktlag = idx4
BrkDtlag = L^2/(6*Brktlag)

%% Add 'breakthrough' simulation to graphs
% Tau value based on the lattice diffusion coefficient from Hagi
1994
BrkTau = ((5.5e-4 * Tplot) / L^2);
% Add 'normalised' flux column
BrkNormJ = J / BrkJinf;
% And a value for current
BrkCurrent = J * 96485 * SurfaceArea;



% Standard plot
figure(1)
plot(H2(1:PlotStep:PlotEnd),J(1:PlotStep:PlotEnd),'Marker','^',...
    'LineStyle','none');
```

```
hold on

% Log Tau plot
figure(2)
semilogx(BrkTau,BrkNormJ,'LineWidth',2);
hold on

% Save J and t as different variable
BrkFlux = J;
BrkTime = t;


%% Simulation part 2
% Based on lag time calculation
% Clear variables to be re-used
clear J iplot t tlim S1 Tplot C C0

%* Set initial and boundary conditions.
C = 0; % Overall concentration set to zero
t = 1; % Time parameter set to zero
C0 = (MaxFlux * L) / TestDtlag; % Set concentration based on lag
LagJinf = ((TestDtlag*C0)/L); % Steady-state flux
LagJtb = 0.1*LagJinf; % 'Breakthrough' flux
LagJtlag = 0.63*LagJinf; % 'Lag' flux


%* Set up loop.
iplot = 1; % Counter to count plots
tlim = round(tstep*0.04);

syms n % Initialize symbolic n for sum over series
J = zeros(tstep,1); % Sets up matrix for accepting values for J
H3 = zeros(tstep,1); % Sets up matrix for recording time values
Tplot = zeros(tstep,1); % Sets up matrix for recording time values

%* Loop for set no. time-steps.
fprintf('\nCounter: ')



for t = 1:tstep %% MAIN LOOP %%

    %* Compute flux @ exit surface for each time-step.
    % Start with sigma calculation (1 to 5000):
    S1 = symsum((cos(pi*n)*exp((-
TestDtlag*(n^2)*(pi^2)*t)/L^2)),n,1,5000);

    J(t) = LagJinf*(1+(2*S1)); % Calculates flux for this time value
    Tplot(iplot) = t; % Record t for plotting
    H3(iplot) = t/3600;
    fprintf('\r'); % new line for counter
    fprintf('%d', t); % counter (time) value
    if round(max(J(t)),16) >= round(LagJinf,16)
        break
    end
    iplot = iplot+1;

end
```

```
fprintf('\r'); % extra new line at end of counter

%%* Output calculated values for diffusion coefficients and steady-
state
% Values can be compared to input value of D as validation of
simulation

% Breakthrough time
[~,idx5] = min(abs(LagJtb - J)); % Identifies time for 0.1 x Jinf
Lagtb = idx5
LagDtb = L^2/(15.3*Lagtb) % Calculates D based on breakthrough time

% Lag time
[~,idx6] = min(abs(LagJtlag - J)); % Identifies time for 0.63 x Jinf
Lagtlag = idx6
LagDtlag = L^2/(6*Lagtlag)

%% Add 'lag' simulation to graphs
% Tau value based on the lattice diffusion coefficient from Hagi
1994
LagTau = ((5.5e-4 * Tplot) / L^2);
% Add 'normalised' flux column
LagNormJ = J / LagJinf;
% And a value for current
LagCurrent = J * 96485 * SurfaceArea;


% Standard plot
figure(1)
plot(H3(1:PlotStep:PlotEnd),J(1:PlotStep:PlotEnd),'Marker','o',...
    'LineStyle','none');
legend({'Test Data','Sim Data based on t_b',...
    'Sim Data based on t_l_a_g'},'Location','southeast',...
    'Orientation','vertical');
hold off

% Log Tau plot
figure(2)
semilogx(LagTau,LagNormJ,'LineWidth',2);
legend({'Test Data','Sim Data based on t_b',...
    'Sim Data based on t_l_a_g'},'Location','southwest',...
    'Orientation','vertical');
hold off


% Save J and t as different variable
LagFlux = J;
LagTime = t;

% Clear variables that are of no more use
clear idx1 idx2 idx3 idx4 idx5 idx6 J iplot t tlim S1
% End of program
```

7.2 Appendix II - MATLAB code for simulating hydrogen concentration distributions and plots

```
% ChargingSimulation - program to simulate H concentration in SSRT
% Hijacks thermal diffusion equation as substitue for mass
diffusion...
% ...the equation is of the same form
% You just need to derive values for mass density, specific heat
capacity
% and thermal conductivity that will give you an equivalent value
for the
% diffusion coefficient. In this case the only one of these that I
will
% vary is thermal conductivity

close
clc
clear

%% Assign values to variables to create geometry, D, and
concentration
Ln = 1; % Gauge length in cm (keep constant)
Wd = 0.31077; % Average width along gauge length in cm
Gge = 0.08673; % Average thickness along gauge length in cm
TC = 0.3213953; % Thermal conductivity (calculated) in W/K.m
MD = 7800; % Mass density in kg/m3
SHC = 420; % Specific heat capacity in J/kg.K
C_H = 2.062895953; % Concentration at charging surface in ppm (from
perm. data)
Fail = 10960; % Total time of charging and testing to failure in s

% Calculated maximum array value
MxFail = ceil(Fail / 5);

%% Create model, import test piece geometry and assign properties
gm = multicuboid(Wd, Ln, Gge);
thermalmodel = createpde('thermal','transient');
thermalmodel.Geometry = gm;
thermalProperties(thermalmodel,'ThermalConductivity',TC,...
                               'MassDensity',MD,...
                               'SpecificHeat',SHC);

%% Specify initial and boundary conditions and generate mesh

% Boundary conditions of hydrogen concentration
% ... at faces exposed to charging electrolyte
thermalBC(thermalmodel,'Face',3,'Temperature',C_H);
thermalBC(thermalmodel,'Face',5,'Temperature',C_H);
thermalBC(thermalmodel,'Face',[1,2],'Temperature',C_H);

% Initial state - everything at 0 degrees (equivalent to 0 ppm H)
thermalIC(thermalmodel,0);

% Create default mesh
generateMesh(thermalmodel,'Hmax',0.035);
figure(1)
subplot(2,2,1)
pdemesh(thermalmodel)
```

```
hold on
subplot(2,2,2)
pdemesh(thermalmodel)
hold on

% Specifiy solution time 0 to failure, 5 second step time
tlist = 0:5:Fail;

% Calculate solution
thermalresults = solve(thermalmodel,tlist);


%Interpolate and plot temperature along the face.
zg = 0:0.005:Gge;
xg = zeros(size(zg));
yg = zeros(size(zg));
TfaceTwentymin =
interpolateTemperature(thermalresults,xg,yg,zg,241);
% TfaceOnehour =
interpolateTemperature(thermalresults,xg,yg,zg,721);
% TfaceFinal = interpolateTemperature(thermalresults,xg,yg,zg,1441);
TfaceFail = interpolateTemperature(thermalresults,xg,yg,zg,MxFail);


%% Output
% Plot solution
figure(1)
subplot(2,2,1)
pdeplot3D(thermalmodel,'ColorMapData',thermalresults.Temperature(:,2
41))
title({'Hydrogen distribution',' after 20 minutes of charging'})
set(subplot(2,2,1),'Clim',[0 C_H]);
colorbar off
colorbar('southoutside');
xlim([-0.3 0.3])
ylim([-0.8 0.8])
zlim([-0.05 0.25])
view(5,5)
zoom(2)
hold on
subplot(2,2,2)
pdeplot3D(thermalmodel,'ColorMapData',thermalresults.Temperature(:,e
nd))
title({'Hydrogen distribution',' at failure'});
set(subplot(2,2,2),'Clim',[0 C_H]);
colorbar off
colorbar('southoutside');
xlim([-0.3 0.3])
ylim([-0.8 0.8])
zlim([-0.05 0.25])
view(5,5)
zoom(2)
hold on

% Plot cross-section
subplot(2,2,[3 4])
plot(zg,TfaceTwentymin,'Marker','none','LineStyle','-
','LineWidth',...
    2,'Color',[0.15,0.15,0.15])
```

```
title({'Hydrogen concentration through thickness',' for different
charging duration'})
xlabel('x (cm)')
ylabel('Concentration H (ppm)')
hold on
% plot(zg,TfaceOnehour,'Marker','none','LineStyle','-
.','LineWidth',...
%     2,'Color',[0.15,0.15,0.15])
% hold on
% plot(zg,TfaceFinal,'Marker','none','LineStyle',':','LineWidth',...
%     2,'Color',[0.15,0.15,0.15])
% hold on
plot(zg,TfaceFail,'Marker','none','LineStyle','--','LineWidth',...
    2,'Color',[0.15,0.15,0.15])
ylim([-0.001 C_H])
xlim([0 Gge])
legend({'20 minutes','Failure'},'Location','north',...
    'Orientation','vertical');
hold off



% End of program
```

7.3 Appendix III – MATLAB code for assessing relative percentages of fracture surface features (prior coloured images)

```
% Clear previous
clc
clear


% Read image
I = imread(uigetfile);

% Define RGB limits for brittle features
BrittleRedLowerLimit = 200;
BrittleRedUpperLimit = 255;
BrittleGreenLowerLimit = 0;
BrittleGreenUpperLimit = 80;
BrittleBlueLowerLimit = 0;
BrittleBlueUpperLimit = 5;

% Number of pixels of required colour
requiredColor1  = ( I(:,:,1) >= BrittleRedLowerLimit & I(:,:,1) <=
BrittleRedUpperLimit ) & ...
    ( I(:,:,2) >= BrittleGreenLowerLimit & I(:,:,2) <=
BrittleGreenUpperLimit ) & ( I(:,:,3) >= BrittleBlueLowerLimit &
I(:,:,3) <= BrittleBlueUpperLimit );
% Percentage of colour in the image
percentBrittle =
100*(sum(sum(requiredColor1))/(size(I,1)*size(I,2)))


% Define RGB limits for partially ductile features
PartialRedLowerLimit = 200;
PartialRedUpperLimit = 255;
PartialGreenLowerLimit = 90;
PartialGreenUpperLimit = 195;
PartialBlueLowerLimit = 0;
PartialBlueUpperLimit = 80;

% Number of pixels of required colour
requiredColor2  = ( I(:,:,1) >= PartialRedLowerLimit & I(:,:,1) <=
PartialRedUpperLimit ) & ...
    ( I(:,:,2) >= PartialGreenLowerLimit & I(:,:,2) <=
PartialGreenUpperLimit ) & ( I(:,:,3) >= PartialBlueLowerLimit &
I(:,:,3) <= PartialBlueUpperLimit );
% Percentage of colour in the image
percentPartial =
100*(sum(sum(requiredColor2))/(size(I,1)*size(I,2)))



% Define RGB limits for mostly ductile features
MostlyRedLowerLimit = 200;
MostlyRedUpperLimit = 255;
MostlyGreenLowerLimit = 196;
MostlyGreenUpperLimit = 255;
MostlyBlueLowerLimit = 0;
MostlyBlueUpperLimit = 5;
```

```
% Number of pixels of required colour
requiredColor3  = ( I(:,:,1) >= MostlyRedLowerLimit & I(:,:,1) <=
MostlyRedUpperLimit ) & ...
    ( I(:,:,2) >= MostlyGreenLowerLimit & I(:,:,2) <=
MostlyGreenUpperLimit ) & ( I(:,:,3) >= MostlyBlueLowerLimit &
I(:,:,3) <= MostlyBlueUpperLimit );
% Percentage of colour in the image
percentMostly =
100*(sum(sum(requiredColor3))/(size(I,1)*size(I,2)))


% Define RGB limits for ductile features
DuctileRedLowerLimit = 107;
DuctileRedUpperLimit = 190;
DuctileGreenLowerLimit = 125;
DuctileGreenUpperLimit = 220;
DuctileBlueLowerLimit = 25;
DuctileBlueUpperLimit = 95;

% Number of pixels of required colour
requiredColor4  = ( I(:,:,1) >= DuctileRedLowerLimit & I(:,:,1) <=
DuctileRedUpperLimit ) & ...
    ( I(:,:,2) >= DuctileGreenLowerLimit & I(:,:,2) <=
DuctileGreenUpperLimit ) & ( I(:,:,3) >= DuctileBlueLowerLimit &
I(:,:,3) <= DuctileBlueUpperLimit );
% Percentage of colour in the image
percentDuctile =
100*(sum(sum(requiredColor4))/(size(I,1)*size(I,2)))


percentIgnore =  100 - percentDuctile - percentMostly -
percentPartial - percentBrittle


% Compute relative % values after ignoring non-coloured pixels
Red = (percentBrittle / (percentBrittle + percentPartial +
percentMostly + percentDuctile))*100
Orange = (percentPartial / (percentBrittle + percentPartial +
percentMostly + percentDuctile))*100
Yellow = (percentMostly / (percentBrittle + percentPartial +
percentMostly + percentDuctile))*100
Green = (percentDuctile / (percentBrittle + percentPartial +
percentMostly + percentDuctile))*100



 % End of program
```

7.4 Appendix IV – Metallographic data

7.4.1 Volume fraction data for DP800 and DP1000

Table 7-1 Volume fraction estimates from threshold analysis performed on segmented SEM micrographs of DP800 and DP1000. In all cases the phase being estimated is martensite, with the balance taken to be ferrite.

Product	Aspect	Filename	Mag	Measured Volume %	Measured Volume Fraction	Area Assessed µm²	Phase Area um²
DP800	Thick	DP800 thick 1kx0	1 k	42.44%	0.4244	8550.71	3628.92
DP800	Thick	DP800 thick 1kx1	1 k	41.72%	0.4172	8661.46	3613.56
DP800	Planar	DP800 width 1kx0	1 k	36.71%	0.3671	8613.08	3161.86
DP800	Planar	DP800 width 2pt5kx0	2.5 k	33.50%	0.335	1401.63	469.55
DP1000	Thick	DP1000 thick 1kx3	1 k	52.61%	0.5261	8686.00	4569.71
DP1000	Thick	DP1000 width 1kx0	1 k	62.63%	0.6263	8684.97	5439.39
DP1000	Planar	DP1ksurf 1kx_2811_01	1 k	49.45%	0.4945	8694.15	4299.26
DP1000	Planar	DP1ksurf 1kx_2811_02	1 k	56.63%	0.5663	8760.87	4961.28
DP1000	Planar	DP1Ksurf2pt 5kx_2811_00	2.5 k	51.79%	0.5179	1390.76	720.27
DP1000	Planar	DP1Ksurf500 x_2811_03	0.5 k	53.42%	0.5342	35144.53	18774.21
DP1000	Thick	DP1Kthick1kx _2811_07	1 k	52.99%	0.5299	8671.35	4594.95
DP1000	Thick	DP1Kthick1kx _2811_08	1 k	62.41%	0.6241	8688.93	5422.76
DP1000	Thick	DP1kthick2pt 5kx_2811_09	2.5 k	52.04%	0.5204	1406.49	731.94
DP1000	Thick	DP1kthick2pt 5kx_2811_11	2.5 k	48.51%	0.4851	1408.77	683.39
DP1000	Thick	DP1Kthick5kx _2811_12	5 k	53.83%	0.5383	350.29	188.56
DP1000	Thick	DP1Kthick5kx _2811_13	5 k	54.57%	0.5457	350.29	191.15

7.4.2 Grain size data for all studied steels

Table 7-2 Summary statistics from grain size measurement using mean linear intercept method.

Product	Image Source	Mag	Aspect	Phase Measured	Mean Diam. µm	Median Diam. µm	Min µm	Max µm	StDv
DP800	SEM	1k/2.5k	1 x thick/1 x planar	Ferrite	3.49	2.82	1.71	14.91	1.77
XPF800	SEM	2.5k	1 x thick/1 x planar	Ferrite	2.30	2.10	0.08	5.92	1.45
DP1000	SEM	0.5k/1k /2.5k/5 k	1 x thick/1 x planar	Ferrite	2.32	1.93	0.78	8.51	1.37
XPF1000	SEM	2.5k	1 x thick/1 x planar	Ferrite	2.21	1.78	0.09	8.15	1.73
22MnB5_UHT	SEM	2.5k	1 x thick/1 x planar	Ferrite	5.05	4.87	0.04	13.77	3.34
22MnB5_900	SEM	2.5k	1 x thick/1 x planar	Martensite Packet Size	1.87	1.64	0.28	5.60	1.06
22MnB5_900_PAGB	EBSD	2.5k	1 x thick/1 x planar	Prior Austenite	10.37	8.91	0.07	33.88	9.16
27MnB5+Nb_UHT	SEM	2.5k	1 x thick/1 x planar	Ferr/Pearl	8.35	8.00	0.04	22.94	5.20
27MnB5+Nb_900	SEM	2.5k	1 x thick/1 x planar	Martensite Packet Size	1.56	1.33	0.20	9.21	1.04
27MnB5+Nb_900_PAGB	EBSD	2.5k	1 x thick/1 x planar	Prior Austenite	7.74	7.17	0.38	26.40	5.20

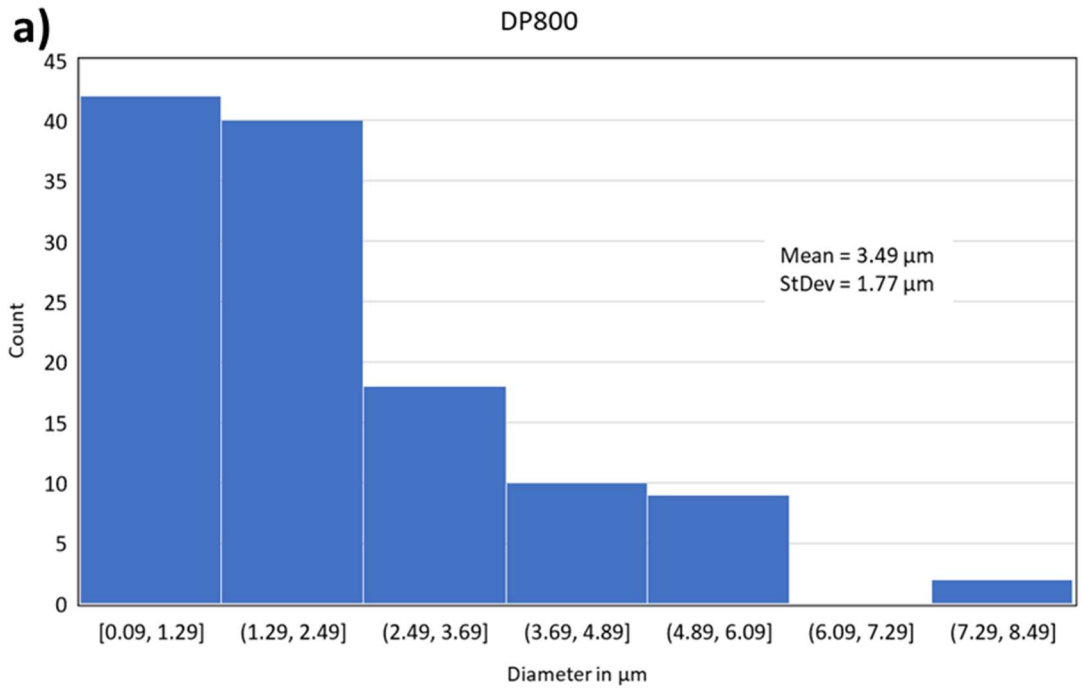

b)

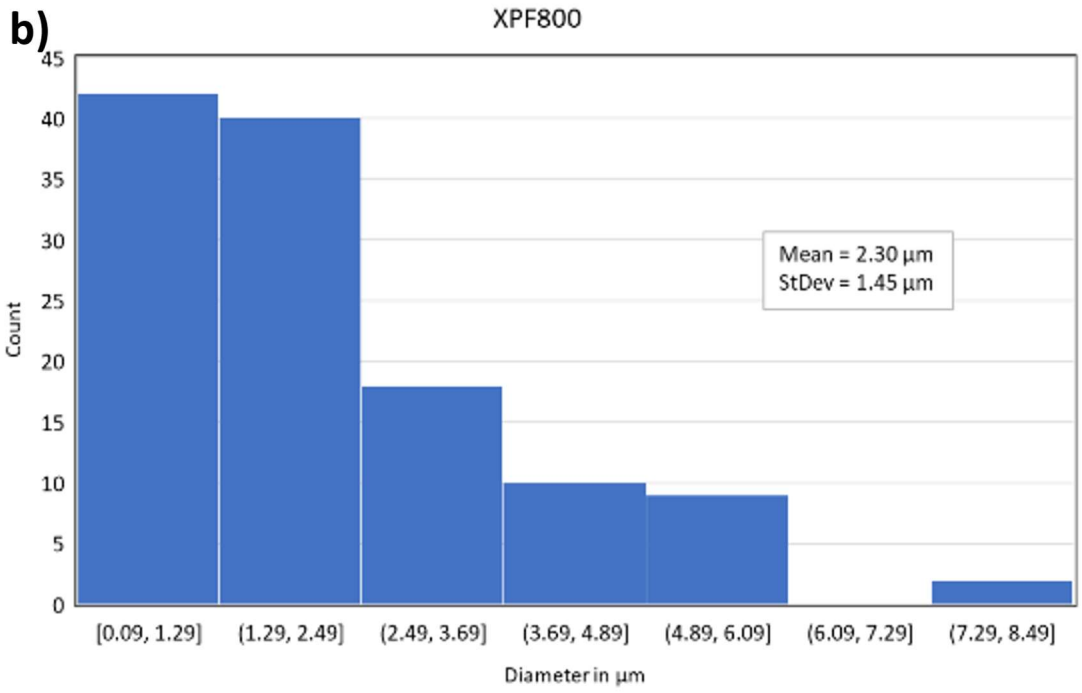
XPF800
Count
45
40
35
30
25
20
15
10
5
0
Mean = 2.30 µm
StDev = 1.45 µm
[0.09, 1.29]
(1.29, 2.49]
(2.49, 3.69]
(3.69, 4.89]
(4.89, 6.09]
(6.09, 7.29]
(7.29, 8.49]
Diameter in µm

c)

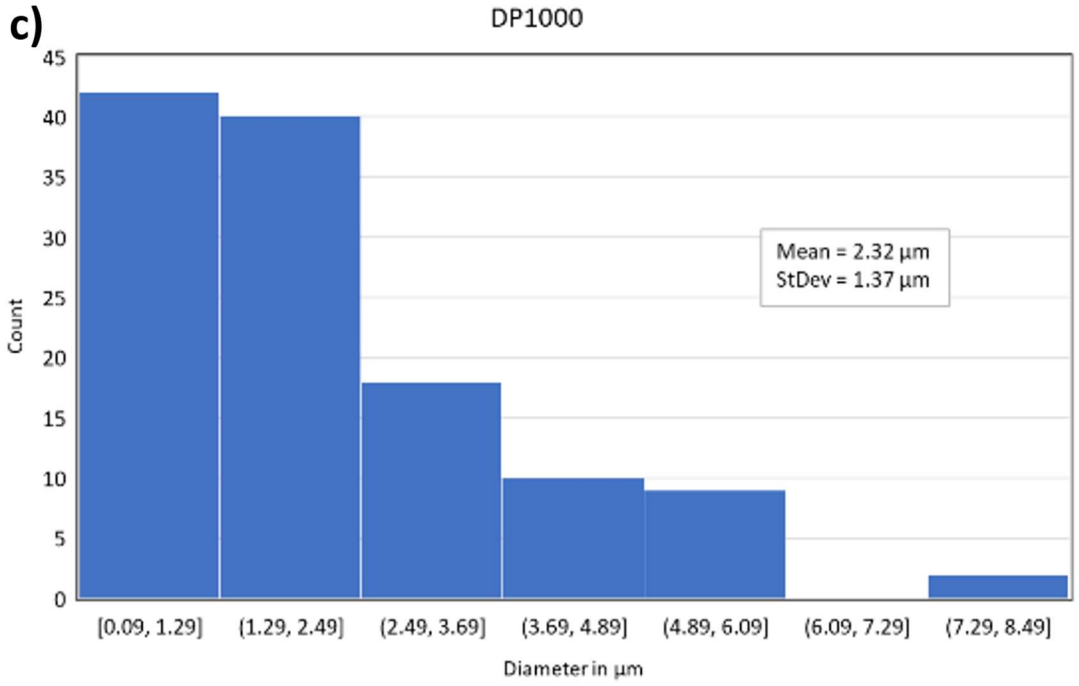
DP1000
Count
45
40
35
30
25
20
15
10
5
0
Mean = 2.32 µm
StDev = 1.37 µm
[0.09, 1.29]
(1.29, 2.49]
(2.49, 3.69]
(3.69, 4.89]
(4.89, 6.09]
(6.09, 7.29]
(7.29, 8.49]
Diameter in µm

d)

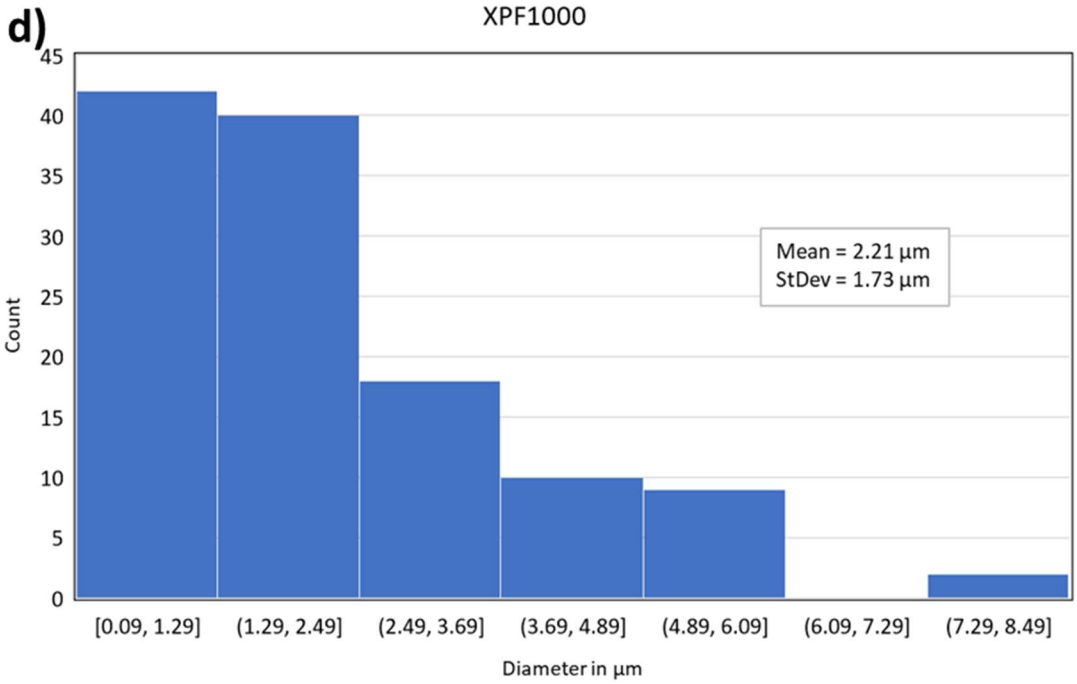
XPF1000
Mean = 2.21 µm
StDev = 1.73 µm
Count
45
40
35
30
25
20
15
10
5
0
[0.09, 1.29]
(1.29, 2.49]
(2.49, 3.69]
(3.69, 4.89]
(4.89, 6.09]
(6.09, 7.29]
(7.29, 8.49]
Diameter in µm

e)

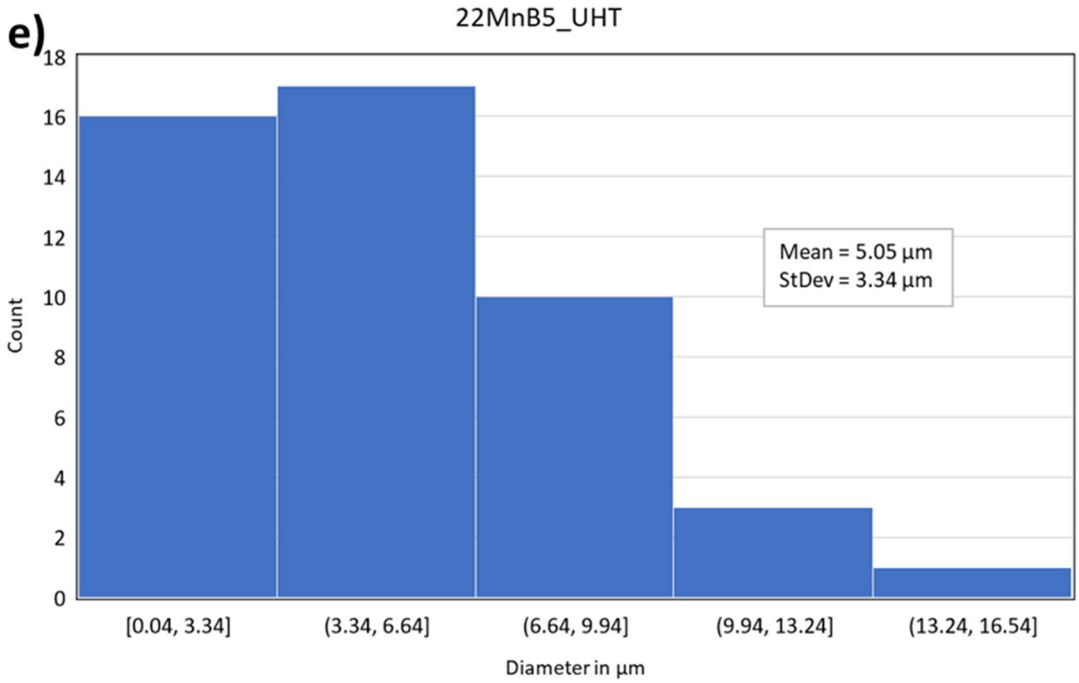
22MnB5_UHT
Mean = 5.05 µm
StDev = 3.34 µm
Count
18
16
14
12
10
8
6
4
2
0
[0.04, 3.34]
(3.34, 6.64]
(6.64, 9.94]
(9.94, 13.24]
(13.24, 16.54]
Diameter in µm

f)

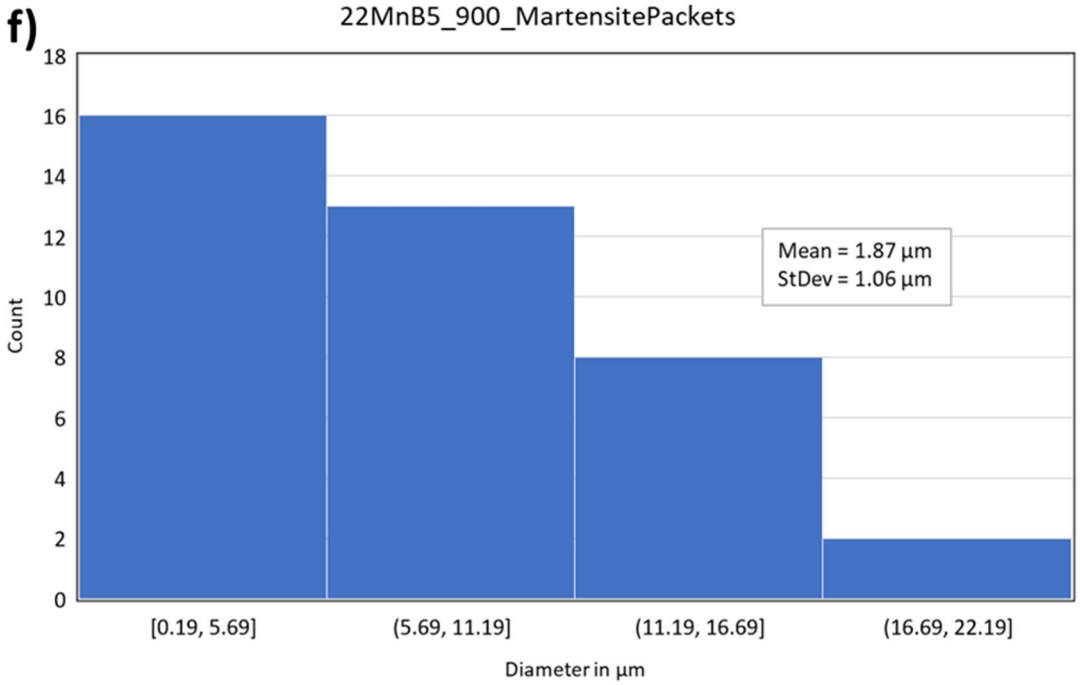
22MnB5_900_MartensitePackets
Count
Mean = 1.87 µm
StDev = 1.06 µm
[0.19, 5.69]
(5.69, 11.19]
(11.19, 16.69]
(16.69, 22.19]
Diameter in µm

g)

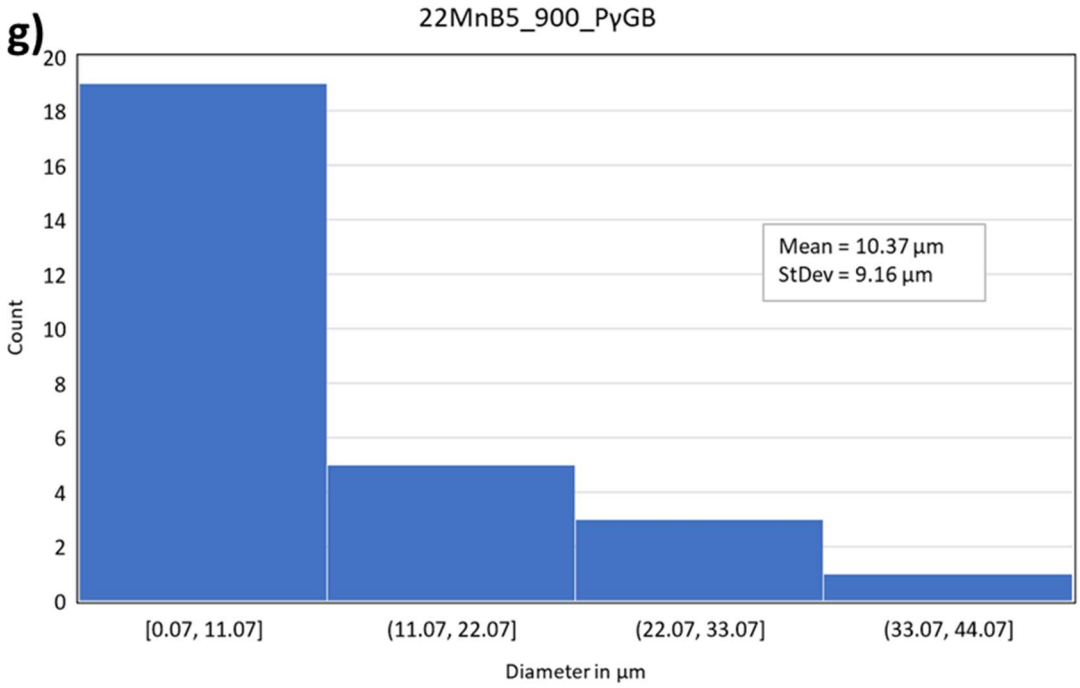
22MnB5_900_PγGB
Count
Mean = 10.37 µm
StDev = 9.16 µm
[0.07, 11.07]
(11.07, 22.07]
(22.07, 33.07]
(33.07, 44.07]
Diameter in µm

h)

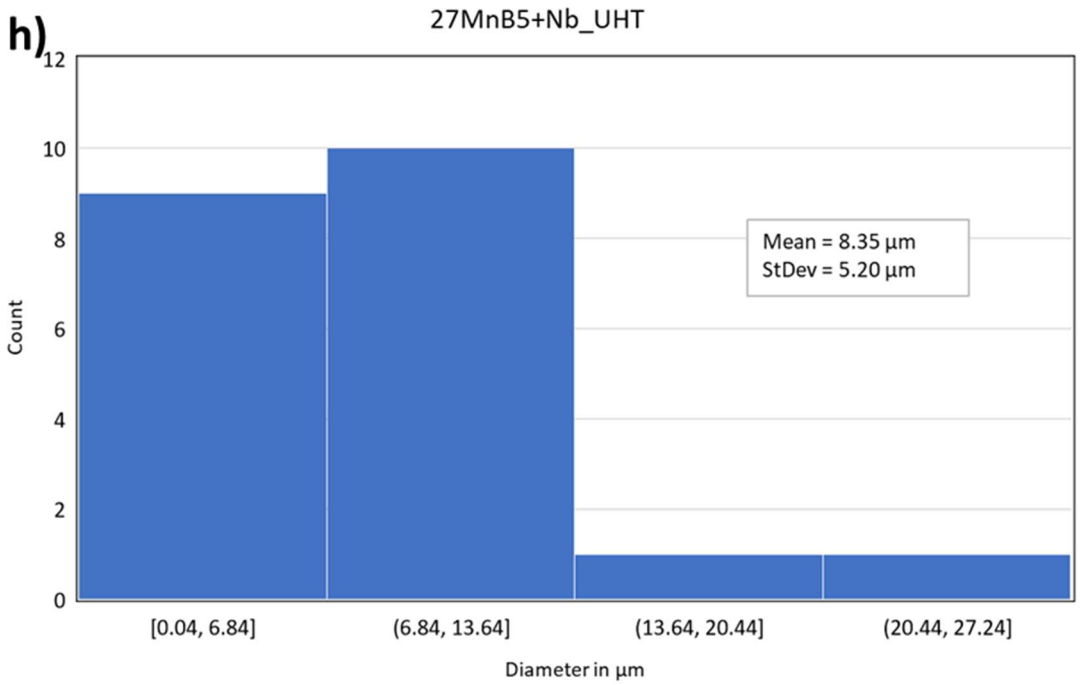
27MnB5+Nb_UHT
Count
Mean = 8.35 µm
StDev = 5.20 µm
[0.04, 6.84]
(6.84, 13.64]
(13.64, 20.44]
(20.44, 27.24]
Diameter in µm

i)

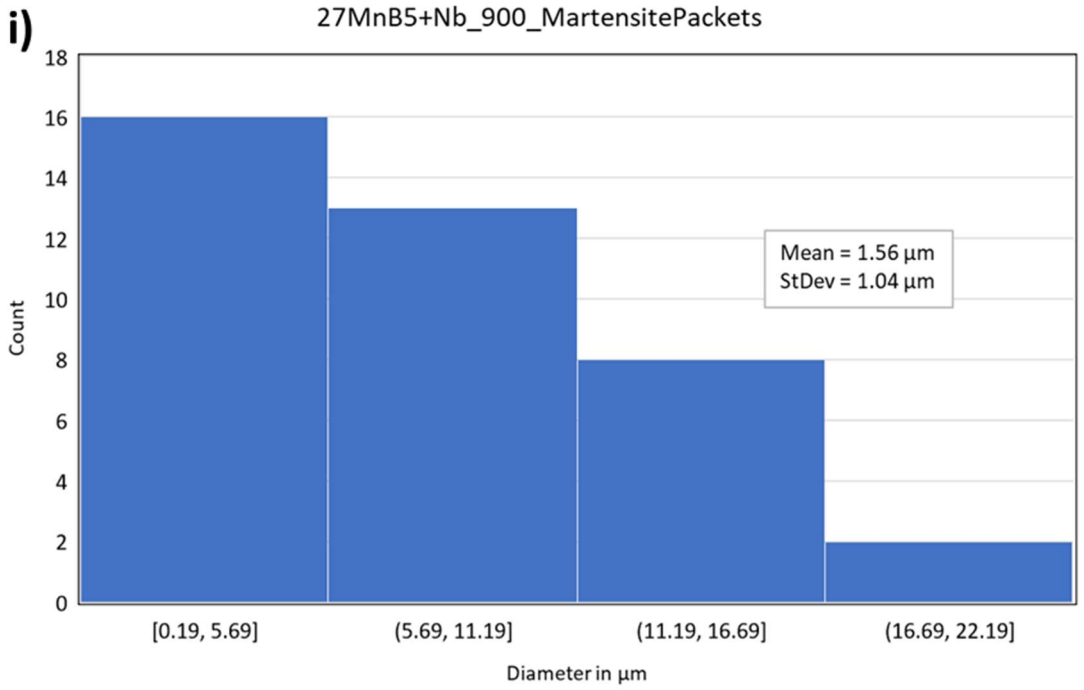
27MnB5+Nb_900_MartensitePackets
Count
Mean = 1.56 µm
StDev = 1.04 µm
[0.19, 5.69]
(5.69, 11.19]
(11.19, 16.69]
(16.69, 22.19]
Diameter in µm

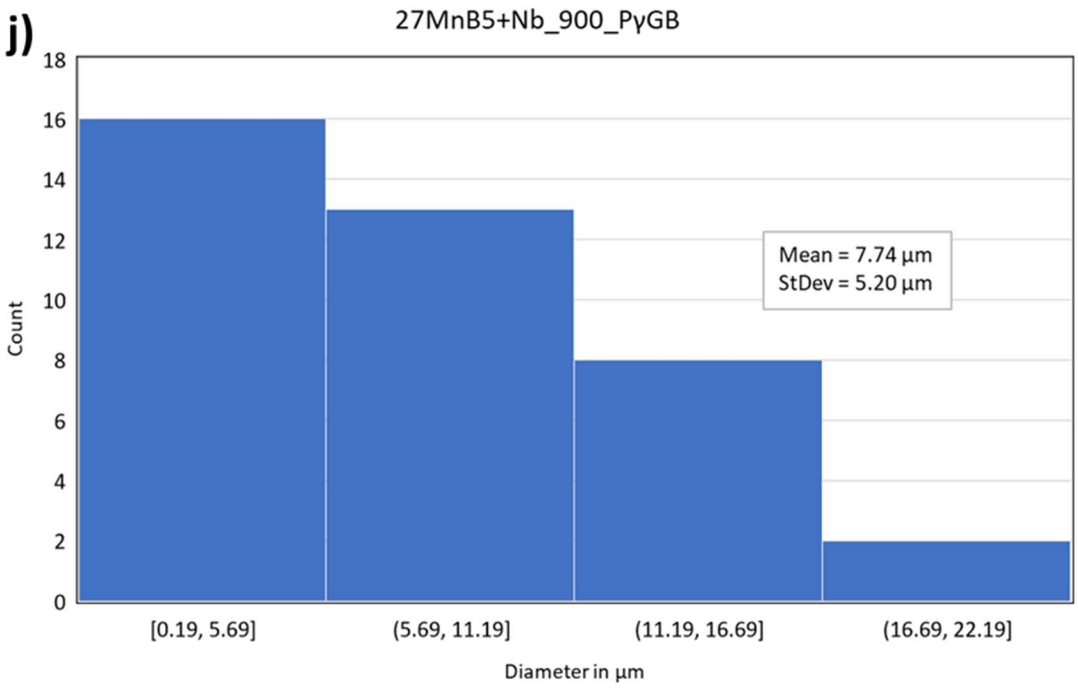

Figure 7.1 Histograms showing grain size frequency data for a) DP800, b) XPF800, c) DP1000, d) XPF1000, e) 22MnB5 (UHT, ferrite grains), f) 22MnB5 (900C, martensite packets), g) 22MnB5 (900C, prior austenite grains), h) 27MnB5+Nb (UHT, ferrite and pearlite grains), i) 27MnB5+Nb (900C, martensite packets), and j) 27MnB5+Nb (900C, prior austenite grains). Data collected via linear intercept method using SEM images.

7.5 Appendix V – X-ray Diffraction calculations

7.5.1 Dislocation density calculations

The following tables show how estimates for dislocation densities for each of the steels were calculated according to the methods of Williamson and Smallman, as described in Chapter 3.1.7, using the (110), (200), and (211) diffraction peaks for the calculations.

Table 7-3 Dislocation density calculations for DP800.

Peak location	Full-Width at Half-Maximum	"Crystallite size"	Dislocation density
2θ °	**β °**	**D (nm)**	**δ x 10^{-3} (nm^{-2})**
44.643	0.249	34.48914084	0.840688775
64.908	0.35	26.89898335	1.38206436
82.219	0.446	23.64085678	1.789260507
	Mean:	28.34299365	1.337337881
	StDev:	4.544974595	0.388542084

Table 7-4 Dislocation density calculations for XPF800.

Peak location	FWHM	"Crystallite size"	Dislocation density
2θ °	**β °**	**D (nm)**	**δ x 10^{-3} (nm^{-2})**
44.63207	0.274778094	31.25234507	1.023846331
64.86752	0.451421155	20.85088424	2.30012292
82.17854	0.542948161	19.41359383	2.653310782
	Mean:	23.83894105	1.992426678
	StDev:	5.274806178	0.699903009

Table 7-5 Dislocation density calculations for DP1000.

Peak location	FWHM	"Crystallite size"	Dislocation density
2θ °	**β °**	**D (nm)**	**δ x 10^{-3} (nm^{-2})**
44.61	0.249	34.48506492	0.840887515
64.907	0.348	27.05342507	1.366329633
82.203	0.444	23.74445422	1.773681421
	Mean:	28.42764807	1.326966189
	StDev:	4.491217073	0.381827386

Table 7-6 Dislocation density calculations for XPF1000.

Peak location	FWHM	"Crystallite size"	Dislocation density
2θ °	**β °**	**D (nm)**	**δ x 10^{-3} (nm^{-2})**
44.608	0.333659114	25.73500713	1.509911226
64.669	0.843541289	11.14609802	8.049229011
82.159	0.644253195	16.35848793	3.736919
	Mean:	17.74653103	4.432019746
	StDev:	6.036227574	2.714534099

Table 7-7 Dislocation density calculations for 22MnB5 (UHT).

Peak location	FWHM	"Crystallite size"	Dislocation density
2θ °	**β °**	**D (nm)**	**δ x 10^{-3} (nm^{-2})**
44.49319	0.26192	32.77029764	0.931191983
64.75715	0.432	21.77494749	2.109044617
82.11855	0.34943	30.15129433	1.099988335
	Mean:	28.23217982	1.380074978
	StDev:	4.689469168	0.520045256

Table 7-8 Dislocation density calculations for 22MnB5 (900C).

Peak location	FWHM	"Crystallite size"	Dislocation density
2θ °	**β °**	**D (nm)**	**δ x 10^{-3} (nm^{-2})**
44.5477	0.45072	19.04700866	2.756426658
64.74754	0.91291	10.30361936	9.41933813
82.12975	0.88313	11.93104517	7.024946481
	Mean:	13.76055773	6.400237089
	StDev:	3.796669706	2.755756846

Table 7-9 Dislocation density calculations for 27MnB5+Nb (UHT).

Peak location	FWHM	"Crystallite size"	Dislocation density
2θ °	**β °**	**D (nm)**	**δ x 10^{-3} (nm^{-2})**
44.58687	0.25642	33.48440207	0.891897412
64.81758	0.54461	17.2782821	3.349645747
82.21105	0.44323	23.78716208	1.767318146
	Mean:	24.84994875	2.002953768
	StDev:	6.658664416	1.017111868

Table 7-10 Dislocation density calculations for 27MnB5+Nb (900C).

Peak location	FWHM	"Crystallite size"	Dislocation density
2θ °	**β °**	**D (nm)**	**δ x 10^{-3} (nm^{-2})**
44.5717	0.4126	20.80854206	2.309493236
64.70869	0.86588	10.86092341	8.477474611
82.13099	0.80591	13.07436719	5.850037419
	Mean:	14.91461089	5.545668422
	StDev:	4.264477448	2.527248692

8 References

[1] J. Aylen, R. Ranieri, Ribbon of Fire: How Europe adopted and developed US strip mill technology (1920-2000), Pendragon, 2012.

[2] T. co. Team, Trends In Steel Usage In The Automotive Industry, 2017 (2015). http://www.forbes.com/sites/greatspeculations/2015/05/20/trends-in-steel-usage-in-the-automotive-industry/.

[3] R. Kuziak, R. Kawalla, S. Waengler, Advanced high strength steels for automotive industry, Arch. Civ. Mech. Eng. 8 (2008) 103–117. doi:10.1016/S1644-9665(12)60197-6.

[4] C.T. Broek, FutureSteelVehicle: leading edge innovation for steel body structures, Ironmak. Steelmak. 39 (2013) 477–492. doi:10.1179/0301923312z.000000000123.

[5] W.D. Callister, Materials science and engineering : an introduction, 7th editio, New York: John Wiley & Sons, New York, 2007.

[6] H.K.D.H. Bhadeshia, Prevention of Hydrogen Embrittlement in Steels, ISIJ Int. 56 (2016) 24–36. doi:10.2355/isijinternational.ISIJINT-2015-430.

[7] C.D. Beachem, A new model for hydrogen-assisted cracking (hydrogen “embrittlement”), Metall. Trans. 3 (1972) 441–455.

[8] I.M. Robertson, P. Sofronis, A. Nagao, M.L. Martin, S. Wang, D.W. Gross, K.E. Nygren, Hydrogen Embrittlement Understood, Metall. Mater. Trans. B. 46 (2015) 1085–1103. doi:10.1007/s11663-015-0325-y.

[9] W.H. Johnson, On some remarkable changes produced in iron and steel by the action of hydrogen and acids, Nature. 11 (1875) 393. doi:10.1038/011393a0.

[10] N. Silk, J. Wilkinson, K. Ridal, Development and application of high strength engineering alloys, Ironmak. Steelmak. 33 (2013) 372–378. doi:10.1179/174328106x118189.

[11] S. Keeler, M. Kimchi, Advanced high-strength steels application guidelines V6, WorldAutoSteel, 2015.

[12] J.N. Hall, J.R. Fekete, 2 - Steels for auto bodies: A general overview, in: R. Rana, S.B. Singh (Eds.), Automot. Steels, Woodhead Publishing, 2017: pp. 19–45. doi:https://doi.org/10.1016/B978-0-08-100638-2.00002-X.

[13] F.G. Caballero, M.K. Miller, C. Garcia-Mateo, C. Capdevila, C.G. de Andrés, Phase transformation theory: A powerful tool for the design of advanced steels, 2013. https://www.academia.edu/21117381/Phase_transformation_theory_A_powerful_tool_for_the_design_of_advanced_steels (accessed July 13, 2020).

[14] G. Szczęśniak, P. Nogowczyk, R. Burdzik, Some basic tips in vehicle chassis and frame design, J. Meas. Eng. 2 (2014) 208–214. https://www.jvejournals.com/article/15775 (accessed December 13, 2021).

[15] C.M. Tamarelli, AHSS 101: the evolving use of advanced high strength steels for automotive applications, 2011, Autosteel, 2011.

[16] N. Saeidi, A. Ekrami, Comparison of mechanical properties of martensite/ferrite and bainite/ferrite dual phase 4340 steels, Mater. Sci. Eng. A. 523 (2009) 125–129. doi:10.1016/J.MSEA.2009.06.057.

[17] M. Montoya-Rangel, N. Garza-Montes de Oca, C. Gaona-Tiburcio, R. Colás, J. Cabral-Miramontes, D. Nieves-Mendoza, E. Maldonado-Bandala, J. Chacón-Nava, F. Almeraya-Calderón, Electrochemical Noise Measurements of Advanced High-Strength Steels in Different Solutions, Metals (Basel). 10 (2020). doi:10.3390/met10091232.

[18] Autoshop, Buy Replacement Car & Truck Parts | 1 Auto Shop, (2020). https://1autoshop.com/ (accessed October 2, 2022).

[19] P. FB, Physical metallurgy and the design of steels, 1978. https://pascal-francis.inist.fr/vibad/index.php?action=getRecordDetail&idt=PASCALSOUDAGE7900081075 (accessed December 15, 2021).

[20] R.W.K. Honeycombe, H.K.D.H. Bhadeshia, Steels : microstructure and properties, 2nd ed., London : Edward Arnold, London, 1995. https://app.knovel.com/web/toc.v/cid:kpSMPE0001/viewerType:toc/root_slug:steels-microstructure.

[21] E. Hall, Yield point phenomena in metals and alloys, Macmillan, 1970. https://books.google.co.uk/books?hl=en&lr=&id=A0TUBwAAQBAJ&oi=fnd&pg=PA1&ots=p2tLCVWDh5&sig=NMaGaUa8BNPf4QIbVLX7e_7mwK0 (accessed December 15, 2021).

[22] A. Rijkenberg, A. Blowey, P. Bellina, C. Wooffindin, Advanced High Stretch-Flange Formability Steels for Chassis & Suspension Applications, in: Conf. Steels Cars Truck., 2014: pp. 426–433.

[23] T. Gladman, Precipitation hardening in metals, Mater. Sci. Technol. 15 (1999) 30–36. doi:10.1179/026708399773002782.

[24] Y. Funakawa, T. Shiozaki, K. Tomita, T. Yamamoto, E. Maeda, Development of High Strength Hot-rolled Sheet Steel Consisting of Ferrite and Nanometer-sized Carbides, ISIJ Int. 44 (2004) 1945–1951. doi:10.2355/ISIJINTERNATIONAL.44.1945.

[25] J.H. Jang, C.H. Lee, Y.U. Heo, D.W. Suh, Stability of (Ti, M)C (M = Nb, V, Mo and W) carbide in steels using first-principles calculations, Acta Mater. 60 (2012) 208–217. doi:10.1016/J.ACTAMAT.2011.09.051.

[26] T. Shimizu, Y. Funakawa, S. Kaneko, High Strength Steel Sheets for Automobile Suspension and Chassis Use — High Strength Hot-Rolled Steel Sheets with Excellent Press Formability and Durability for Critical Safety Parts, 2004.

[27] K. Sugimoto, M. Mukherjee, 8 - TRIP aided and complex phase steels, in: R. Rana, S.B. Singh

(Eds.), Automot. Steels, Woodhead Publishing, 2017: pp. 217–257. doi:https://doi.org/10.1016/B978-0-08-100638-2.00008-0.

[28] S. Sarkar, M. Militzer, Microstructure evolution model for hot strip rolling of Nb-Mo microalloyed complex phase steel, Mater. Sci. Technol. 25 (2009) 1134–1146. doi:10.1179/174328409X453271.

[29] MY Demeri, Advanced high-strength steels, ASM International, n.d. https://www.asminternational.org/documents/10192/1849770/05370G_TOC.pdf (accessed December 15, 2021).

[30] A. Kumar, S.B. Singh, K.K. Ray, Influence of bainite/martensite-content on the tensile properties of low carbon dual-phase steels, Mater. Sci. Eng. A. 474 (2008) 270–282. doi:http://dx.doi.org/10.1016/j.msea.2007.05.007.

[31] N. Fonstein, 7 - Dual-phase steels, in: R. Rana, S.B. Singh (Eds.), Automot. Steels, Woodhead Publishing, 2017: pp. 169–216. doi:https://doi.org/10.1016/B978-0-08-100638-2.00007-9.

[32] C.C. Tasan, M. Diehl, D. Yan, M. Bechtold, F. Roters, L. Schemmann, C. Zheng, N. Peranio, D. Ponge, M. Koyama, K. Tsuzaki, D. Raabe, An Overview of Dual-Phase Steels: Advances in Microstructure-Oriented Processing and Micromechanically Guided Design, Annu. Rev. Mater. Res. 45 (2015) 391–431. doi:10.1146/annurev-matsci-070214-021103.

[33] D. Barbier, L. Germain, A. Hazotte, M. Gouné, A. Chbihi, Microstructures resulting from the interaction between ferrite recrystallization and austenite formation in dual-phase steels, J. Mater. Sci. 50 (2015) 374–381. doi:10.1007/s10853-014-8596-2.

[34] M.K. Singh, Application of Steel in Automotive Industry, Int. J. Emerg. Technol. Adv. Eng. 6 (2016). http://www.ijetae.com/files/Volume6Issue7/IJETAE_0716_35.pdf.

[35] J.R. Fekete, J.N. Hall, 1 - Design of auto body: Materials perspective, in: R. Rana, S.B. Singh (Eds.), Automot. Steels, Woodhead Publishing, 2017: pp. 1–18. doi:https://doi.org/10.1016/B978-0-08-100638-2.00001-8.

[36] L.J. Baker, S.R. Daniel, J.D. Parker, D. Baker, Metallurgy and processing of ultralow carbon bake hardening steels, Mater. Sci. Technol. (2002). doi:10.1179/026708302225002452.

[37] A.H. Cottrell, B.A. Bilby, Dislocation Theory of Yielding and Strain Ageing of Iron, Proc. Phys. Soc. Sect. A. 62 (1949).

[38] E. Pereloma, I. Timokhina, 9 - Bake hardening of automotive steels, in: R. Rana, S.B. Singh (Eds.), Automot. Steels, Woodhead Publishing, 2017: pp. 259–288. doi:https://doi.org/10.1016/B978-0-08-100638-2.00009-2.

[39] S. Harper, Precipitation of Carbon and Nitrogen in Cold-Worked Alpha-Iron, Phys. Rev. 83 (1951) 709. doi:10.1103/PhysRev.83.709.

[40] S. Hartley, Strain-ageing in tantalum, Acta Metall. 14 (1966) 1237–1246. doi:10.1016/0001-6160(66)90241-0.

[41] A.K. De, S. Vandeputte, B.C. De Cooman, Kinetics of Strain Aging in Bake Hardening Ultra Low Carbon Steel-a Comparison with Low Carbon Steel, JMEPEG. 10 (2001) 567–575.

[42] D.M. Barnett, On nucleation of coherent precipitates near edge dislocations, Scr. Metall. 5 (1971) 261–266. doi:10.1016/0036-9748(71)90191-8.

[43] W. Chang Jeong, Effect of Prestrain on Aging and Bake Hardening of Cold-Rolled, Continuously Annealed Steel Sheets, (1998).

[44] A. Laureys, T. Depover, R. Petrov, K. Verbeken, Microstructural characterization of hydrogen induced cracking in TRIP-assisted steel by EBSD, Mater. Charact. 112 (2016) 169–179. doi:10.1016/j.matchar.2015.12.017.

[45] B.C. De Cooman, Structure-properties relationship in TRIP steels containing carbide-free bainite, Curr. Opin. Solid State Mater. Sci. 8 (2004) 285–303. doi:10.1016/j.cossms.2004.10.002.

[46] A.K. De, Micrograph 739 and full record, Dissem. IT Promot. Mater. Sci. (2003). https://www.doitpoms.ac.uk/miclib/micrograph_record.php?id=739 (accessed July 3, 2022).

[47] L. Durrenberger, X. Lemoine, A. Molinari, Effects of pre-strain and bake-hardening on the crash properties of a top-hat section, J. Mater. Process. Technol. 211 (2011) 1937–1947. doi:10.1016/J.JMATPROTEC.2011.06.015.

[48] N.J. Den Uijl, L.J. Carless, Advanced metal-forming technologies for automotive applications, Adv. Mater. Automot. Eng. (2012) 28–56. doi:10.1533/9780857095466.28.

[49] T. Taylor, G. Fourlaris, P. Evans, G. Bright, New generation ultrahigh strength boron steel for automotive hot stamping technologies, Mater. Sci. Technol. 30 (2014) 818–826. doi:10.1179/1743284713Y.0000000409.

[50] H. Karbasian, A.E. Tekkaya, A review on hot stamping, J. Mater. Process. Technol. 210 (2010) 2103–2118.

[51] M. Merklein, J. Lechler, Investigation of the thermo-mechanical properties of hot stamping steels, J. Mater. Process. Technol. 177 (2006) 452–455. doi:10.1016/J.JMATPROTEC.2006.03.233.

[52] G. V Kurdjumov, Phenomena occurring in the quenching and tempering of steels, (1960) 117–162.

[53] M. Naderi, M. Ketabchi, M. Abbasi, W. Bleck, Analysis of Microstructure and Mechanical Properties of Different Hot Stamped B-bearing Steels, Steel Res. Int. 81 (2010) 216–223. doi:10.1002/SRIN.200900125.

[54] P.D. Deeley, K.J.A. Kundig, H.R. Spendelow, Ferroalloys & alloying additives handbook, Shieldalloy Corp., 1981. http://amg-v.com/contents.html.

[55] T. Taylor, G. Fourlaris, A. Clough, Effect of carbon and microalloy additions on hot-stamped

boron steel, Mater. Sci. Technol. 33 (2017) 1964–1977. doi:10.1080/02670836.2017.1342018.

[56] E.J. Seo, L. Cho, B.C. De Cooman, Application of quenching and partitioning (Q&P) processing to press hardening steel, Metall. Mater. Trans. A Phys. Metall. Mater. Sci. 45 (2014) 4022–4037. doi:10.1007/s11661-014-2316-z.

[57] M. Tisza, Development of Lightweight Steels for Automotive Applications, Eng. Steels High Entropy-Alloys. (2020). doi:10.5772/INTECHOPEN.91024.

[58] R. Baboian, Corrosion tests and standards: application and interpretation, 1995. https://www.bcin.ca/bcin/detail.app?id=196229 (accessed December 20, 2021).

[59] A.J. Bard, L.R. Faulkner, Electrochemical Methods: Fundamentals and Applications, 2nd ed., John Wiley & Sons, Inc., New York, 2001.

[60] V.S. Bagot͡skiĭ, Fundamentals of electrochemistry, 2nd ed., Hoboken, N.J. : Wiley-Interscience, Hoboken, N.J., 2006.

[61] M. Pourbaix, H. Zhang, A. Pourbaix, Presentation of an Atlas of chemical and electrochemical equilibria in the presence of a gaseous phase, Mater. Sci. Forum. 251–254 (1974) 143–148. doi:10.4028/www.scientific.net/msf.251-254.143.

[62] D. Channei, S. Phanichphant, A. Nakaruk, S.S. Mofarah, P. Koshy, C.C. Sorrell, Aqueous and Surface Chemistries of Photocatalytic Fe-Doped CeO2 Nanoparticles, Catal. 2017, Vol. 7, Page 45. 7 (2017) 45. doi:10.3390/CATAL7020045.

[63] U. Evans, An introduction to metallic corrosion, 1963. https://www.bcin.ca/bcin/detail.app?id=47050&wbdisable=true (accessed December 21, 2021).

[64] P. Pedeferri, Corrosion Science and Engineering, 2018. doi:10.1007/978-3-319-97625-9_1.

[65] D. Talbot, J. Talbot, Corrosion Science and Technology, 1st ed., CRC Press, Boca Raton, FL, 1998.

[66] S. Ootsuka, S. Fujita, E. Tada, A. Nishikata, T. Tsuru, Evaluation of hydrogen absorption into steel in automobile moving environments, Corros. Sci. 98 (2015) 430–437. doi:10.1016/j.corsci.2015.05.049.

[67] H.P. Hack, Galvanic Corrosion, in: Shreir's Corros., Elsevier, 2010: pp. 828–856. doi:10.1016/B978-044452787-5.00033-0.

[68] N. Wint, J. Leung, J.H. Sullivan, D.J. Penney, Y. Gao, The galvanic corrosion of welded ultra-high strength steels used for automotive applications, Corros. Sci. 136 (2018) 366–373. doi:10.1016/J.CORSCI.2018.03.025.

[69] Y. Si, Investigation of Galvanic Corrosion Behavior of Dual Phase Steel, ECS Trans. 72 (2016) 13–21. doi:10.1149/07217.0013ECST/XML.

[70] M.G. Fontana, Corrosion Engineering, 3rd ed., McGraw-Hill Book Company, New York, 1986.

doi:10.1149/1.2411256/META.

[71] M. Nishimoto, J. Ogawa, I. Muto, Y. Sugawara, N. Hara, Simultaneous visualization of pH and Cl− distributions inside the crevice of stainless steel, Corros. Sci. 106 (2016) 298–302. doi:10.1016/j.corsci.2016.01.028.

[72] X.Y. Wu, J.K. Sun, J.M. Wang, Y.M. Jiang, J. Li, Crevice Corrosion Behaviors Between CFRP and Stainless Steel 316L for Automotive Applications, Acta Metall. Sin. (English Lett. 32 (2019) 1219–1226. doi:10.1007/S40195-019-00909-Z/FIGURES/11.

[73] Q. Liu, Q. Zhou, J. Venezuela, M. Zhang, A. Atrens, Hydrogen Concentration in Dual-Phase (DP) and Quenched and Partitioned (Q&P) Advanced High-Strength Steels (AHSS) under Simulated Service Conditions Compared with Cathodic Charging Conditions, Adv. Eng. Mater. 18 (2016) 1588–1599. doi:10.1002/adem.201600217.

[74] J.R. Galvele, Transport processes and the mechanism of pitting of metals, J. Electrochem. Soc. 123 (1976) 464–474.

[75] J.R. Galvele, Tafel's law in pitting corrosion and crevice corrosion susceptibility, Corros. Sci. 47 (2005) 3053–3067. doi:https://doi.org/10.1016/j.corsci.2005.05.043.

[76] M. Pourbaix, Significance of Protection Potential in Pitting and Intergranular Corrosion, Corrosion. 26 (1970) 431–438. doi:10.5006/0010-9312-26.10.431.

[77] U.R. Evans, The Corrosion of Metals, Edward Arnold, London, 1960.

[78] G. Williams, H. McMurray, Pitting Corrosion of Steam Turbine Blading Steels: The Influence of Chromium Content, Temperature, and Chloride Ion Concentration, Corros. 62 (2006) 231–242. doi:10.5006/1.3278269.

[79] S. Li, Z. Zhang, E. Akiyama, K. Tsuzaki, B. Zhang, Evaluation of susceptibility of high strength steels to delayed fracture by using cyclic corrosion test and slow strain rate test, Corros. Sci. 52 (2010) 1660–1667. doi:10.1016/j.corsci.2010.02.005.

[80] E. Akiyama, S. Li, T. Shinohara, Z. Zhang, K. Tsuzaki, Hydrogen entry into Fe and high strength steels under simulated atmospheric corrosion, Electrochim. Acta. 56 (2011) 1799–1805. doi:10.1016/j.electacta.2010.09.043.

[81] A. Drexler, C. Bergmann, G. Manke, V. Kokotin, K. Mraczek, S. Leitner, M. Pohl, W. Ecker, Local hydrogen accumulation after cold forming and heat treatment in punched advanced high strength steel sheets, J. Alloys Compd. (2020) 158226. doi:10.1016/j.jallcom.2020.158226.

[82] J. Robson, Steel Pickling: A Profile Draft Report Prepared for, 1993.

[83] A.R. Marder, The metallurgy of zinc-coated steel, Prog. Mater. Sci. 45 (2000) 191–271. doi:10.1016/S0079-6425(98)00006-1.

[84] J.B.O. Meré, A.G. Marcos, J.A. González, V.L. Rubio, Estimation of mechanical properties of steel strip in hot dip galvanising lines, Ironmak. Steelmak. 31 (2013) 43–50.

doi:10.1179/030192304225012060.

[85] Y. Morimoto, E. McDevitt, M. Meshii, Characterization of the Fe-AI Inhibition Stages of Hot-dip Galvannealing Layer Formed in the Initial, ISIJ Int. 37 (1997) 906–913.

[86] A.R.P. Ghuman, J.I. Goldstein, Reaction mechanisms for the coatings formed during the hot dipping of iron in 0 to 10 Pct Al-Zn baths at 450° to 700°C, Metall. Trans. 1971 210. 2 (1971) 2903–2914. doi:10.1007/BF02813270.

[87] P. Gogola, Z. Gabalcová, H. Suchánek, M. Kusý, Intermetallics formation during hot dip galvanizing of high carbon steel, IOP Conf. Ser. Mater. Sci. Eng. 723 (2020). doi:10.1088/1757-899X/723/1/012007.

[88] N. Tang, G. Adams, P. Kolisnyk, On determining effective aluminum in continuous galvanizing baths, in: Galvatech '95, 1995. https://scholar.google.com/scholar?q=Tang N-Y, Adams GR, Kolisnyk PS. On determining effective aluminum in continous galvanizing baths. GALVATECH 95. Chicago, IL: Iron and Steel Society, 1995. p. 777 (accessed December 27, 2021).

[89] V. Raghavan, Al-Fe-Zn (Aluminum-Iron-Zinc), J. Phase Equilibria. 24 (2003) 546–550. doi:10.1361/105497103772084606.

[90] B. Mintz, Hot dip galvanising of transformation induced plasticity and other intercritically annealed steels, Int. Mater. Rev. 46 (2001) 169–197. doi:10.1179/095066001771048754.

[91] Jordan CE, A model for galvanneal morphology development, in: A. Marder (Ed.), Phys. Metall. Zinc Coat. Steel, Minerals, Metals & Materials Society, San Francisco, 1994: pp. 1–333.

[92] C.S. Lin, M. Meshii, C.C. Cheng, Phase Evolutlon in Galvanneal Coatings on Steel Sheets, ISIJ Int. 35 (1995) 511.

[93] D. Figueroa, M.J. Robinson, Hydrogen transport and embrittlement in 300 M and AerMet100 ultra high strength steels, Corros. Sci. 52 (2010) 1593–1602. doi:http://dx.doi.org/10.1016/j.corsci.2010.01.001.

[94] S. Takagi, Y. Toji, M. Yoshino, K. Hasegawa, Hydrogen Embrittlement Resistance Evaluation of Ultra High Strength Steel Sheets for Automobiles, ISIJ Int. 52 (2012) 316–322. doi:10.2355/isijinternational.52.316.

[95] mechanicsupport.com: Hydrogen Embrittlement, (2011). http://mechanicsupport.blogspot.com/2011/02/hydrogen-embrittlement.html (accessed December 28, 2021).

[96] R.D. McCright, Effects of environmental species and metallurgical structure on the hydrogen entry into steel, Stress Corros. Crack. Hydrog. Embrittlement Iron Base Alloy. (1973) 306–325.

[97] A. Turnbull, Perspectives on hydrogen uptake, diffusion and trapping, Int. J. Hydrogen Energy. 40 (2015) 16961–16970. doi:10.1016/j.ijhydene.2015.06.147.

[98] J. Bockris, J. McBreen, L. Nanis, The Hydrogen Evolution Kinetics and Hydrogen Entry into a-Iron, J. Electrochem. Soc. 112 (1965) 1025–1031.

[99] D.G. Westlake, Generalized model for hydrogen embrittlement, Argonne National Lab., Ill., 1969.

[100] C.A. Zapffe, C.E. Sims, Hydrogen embrittlement, internal stress and defects in steel, Trans. AIME. 145 (1941) 225–271.

[101] N. Petch, P. Stables, A Decohesion Theory for Hydrogen-Induced Cracks Propagation, Nature. 169 (1952) 587.

[102] A.R. Troiano, The Role of Hydrogen and Other Interstitials in the Mechanical Behavior of Metals, Metallogr. Microstruct. Anal. 5 (1960) 557–569. doi:10.1007/s13632-016-0319-4.

[103] R. Oriani, A decohesion theory for hydrogen-induced crack propagation, Stress Corros. Crack. Hydrog. Embrittlement Iron Base Alloy. (1973) 351–358.

[104] J. Song, W.A. Curtin, A nanoscale mechanism of hydrogen embrittlement in metals, Acta Mater. 59 (2011) 1557–1569. doi:http://dx.doi.org/10.1016/j.actamat.2010.11.019.

[105] A. Tehranchi, X. Zhou, W.A. Curtin, A decohesion pathway for hydrogen embrittlement in nickel: Mechanism and quantitative prediction, Acta Mater. 185 (2020) 98–109. doi:10.1016/j.actamat.2019.11.062.

[106] J. Song, W.A. Curtin, Atomic mechanism and prediction of hydrogen embrittlement in iron, Nat Mater. 12 (2013) 145–151. doi:10.1038/nmat3479.

[107] S.P. Lynch, Hydrogen embrittlement (HE) phenomena and mechanisms, Stress Corros. Crack. Theory Pract. (2011) 90–130. doi:10.1533/9780857093769.1.90.

[108] X. Li, X. Ma, J. Zhang, E. Akiyama, Y. Wang, X. Song, Review of Hydrogen Embrittlement in Metals: Hydrogen Diffusion, Hydrogen Characterization, Hydrogen Embrittlement Mechanism and Prevention, Acta Metall. Sin. (English Lett. 33 (2020) 759–773. doi:10.1007/S40195-020-01039-7/FIGURES/1.

[109] I.M. Robertson, The effect of hydrogen on dislocation dynamics, Eng. Fract. Mech. 68 (2001) 671–692. doi:10.1016/S0013-7944(01)00011-X.

[110] A. Barnoush, H. Vehoff, Electrochemical nanoindentation: A new approach to probe hydrogen/deformation interaction, Scr. Mater. 55 (2006) 195–198. doi:10.1016/j.scriptamat.2006.03.041.

[111] A. Nagao, C.D. Smith, M. Dadfarnia, P. Sofronis, I.M. Robertson, Interpretation of Hydrogen-induced Fracture Surface Morphologies for Lath Martensitic Steel, Procedia Mater. Sci. 3 (2014) 1700–1705. doi:10.1016/J.MSPRO.2014.06.274.

[112] A. Nagao, M. Dadfarnia, B.P. Somerday, P. Sofronis, R.O. Ritchie, Hydrogen-enhanced-plasticity mediated decohesion for hydrogen-induced intergranular and “quasi-cleavage”

fracture of lath martensitic steels, J. Mech. Phys. Solids. 112 (2018). doi:10.1016/j.jmps.2017.12.016.

[113] S.P. Lynch, Hydrogen embrittlement and liquid-metal embrittlement in nickel single crystals, Scr. Metall. 13 (1979) 1051–1056. doi:http://dx.doi.org/10.1016/0036-9748(79)90202-3.

[114] J. Venezuela, Q. Zhou, Q. Liu, H. Li, M. Zhang, M.S. Dargusch, A. Atrens, The influence of microstructure on the hydrogen embrittlement susceptibility of martensitic advanced high strength steels, Mater. Today Commun. 17 (2018) 1–14. doi:10.1016/j.mtcomm.2018.07.011.

[115] S.P. Lynch, Environmentally assisted cracking: Overview of evidence for an adsorption-induced localised-slip process, Acta Metall. 36 (1988) 2639–2661. doi:http://dx.doi.org/10.1016/0001-6160(88)90113-7.

[116] R. Kirchheim, A. Pundt, R. Kirchheim, HYDROGEN IN METALS: Microstructural Aspects, Annu. Rev. Mater. Res. 36 (2006) 555–608. doi:10.1146/annurev.matsci.36.090804.094451.

[117] E. Protopopoff, P. Marcus, Surface effects on hydrogen entry into metals, in: P. Marcus (Ed.), Corros. Mech. Theory Pract., 2nd ed., Marcel Dekker, Inc., Basel, 2002: pp. 53–96.

[118] M.S. Daw, M.I. Baskes, Application of the Embedded Atom Method to Hydrogen Embrittlement, Chem. Phys. Fract. (1987) 196–218. doi:10.1007/978-94-009-3665-2_12.

[119] R.G. Hoagland, H.L. Heinisch, An atomic simulation of the influence of hydrogen on the fracture behavior of nickel, J. Mater. Res. 7 (1992) 2080–2088. doi:10.1557/JMR.1992.2080.

[120] M. Nagumo, M. Nakamura, K. Takai, Hydrogen thermal desorption relevant to delayed-fracture susceptibility of high-strength steels, Metall. Mater. Trans. A. 32 (2001) 339–347. doi:10.1007/s11661-001-0265-9.

[121] M. Nagumo, Hydrogen related failure of steels-a new aspect, Mater. Sci. Technol. 20 (2004) 940–950. doi:10.1179/026708304225019687.

[122] K. Sakaki, T. Kawase, M. Hirato, M. Mizuno, H. Araki, Y. Shirai, M. Nagumo, The effect of hydrogen on vacancy generation in iron by plastic deformation, Scr. Mater. 55 (2006) 1031–1034. doi:10.1016/j.scriptamat.2006.08.030.

[123] Y. Sugiyama, K. Takai, Quantities and distribution of strain-induced vacancies and dislocations enhanced by hydrogen in iron, Acta Mater. 208 (2021) 116663. doi:10.1016/j.actamat.2021.116663.

[124] M.B. Djukic, G.M. Bakic, V. Sijacki Zeravcic, A. Sedmak, B. Rajicic, The synergistic action and interplay of hydrogen embrittlement mechanisms in steels and iron: Localized plasticity and decohesion, Eng. Fract. Mech. 216 (2019). doi:10.1016/j.engfracmech.2019.106528.

[125] R. Kirchheim, On the solute-defect interaction in the framework of a defactant concept, Int. J. Mater. Res. 100 (2009) 483–487. doi:10.3139/146.110065.

[126] R. Kirchheim, Revisiting hydrogen embrittlement models and hydrogen-induced homogeneous

nucleation of dislocations, Scr. Mater. 62 (2010) 67–70. doi:http://dx.doi.org/10.1016/j.scriptamat.2009.09.037.

[127] A. Barnoush, H. Vehoff, Recent developments in the study of hydrogen embrittlement: Hydrogen effect on dislocation nucleation, Acta Mater. 58 (2010) 5274–5285. doi:10.1016/j.actamat.2010.05.057.

[128] A. Barnoush, N. Kheradmand, T. Hajilou, Correlation between the hydrogen chemical potential and pop-in load during in situ electrochemical nanoindentation, Scr. Mater. 108 (2015) 76–79. doi:10.1016/j.scriptamat.2015.06.021.

[129] G. Domizzi, G. Anteri, J. Ovejero-García, Influence of sulphur content and inclusion distribution on the hydrogen induced blister cracking in pressure vessel and pipeline steels, Corros. Sci. 43 (2001) 325–339. doi:10.1016/S0010-938X(00)00084-6.

[130] B.S. Institute, BS EN ISO 7539-4:1995 Corrosion of metals and alloys. Stress corrosion testing. Preparation and use of uniaxially loaded tension specimens, (1995).

[131] C. Georges, T. Sturel, P. Drillet, J.-M. Mataigne, Absorption/Desorption of Diffusible Hydrogen in Aluminized Boron Steel, ISIJ Int. 53 (2013) 1295–1304. doi:10.2355/isijinternational.53.1295.

[132] A. Barnoush, H. Vehoff, In situ electrochemical nanoindentation: A technique for local examination of hydrogen embrittlement, Corros. Sci. 50 (2008) 259–267. doi:10.1016/j.corsci.2007.05.026.

[133] N. Kheradmand, J. Dake, A. Barnoush, H. Vehoff, Novel methods for micromechanical examination of hydrogen and grain boundary effects on dislocations, Philos. Mag. 92 (2012) 3216–3230. doi:10.1080/14786435.2012.690939.

[134] T. Hajilou, Y. Deng, B.R. Rogne, N. Kheradmand, A. Barnoush, In situ electrochemical microcantilever bending test: a new insight into hydrogen enhanced cracking, Scr. Mater. 132 (2017) 17–21.

[135] A. Taha, P. Sofronis, A micromechanics approach to the study of hydrogen transport and embrittlement, Eng. Fract. Mech. 68 (2001) 803–837. doi:http://dx.doi.org/10.1016/S0013-7944(00)00126-0.

[136] S. Takagi, Y. Hagihara, T. Hojo, W. Urushihara, K. Kawasaki, Comparison of Hydrogen Embrittlement Resistance of High Strength Steel Sheets Evaluated by Several Methods, ISIJ Int. 56 (2016) 685–692. doi:10.2355/isijinternational.ISIJINT-2015-566.

[137] S. Komazazki, S. Watanabe, T. Misawa, Influence of Phosphorus and Boron on Hydrogen Embrittlement Susceptibility of High Strength Low Alloy Steel, 43 (2003) 1851–1857.

[138] H.J. Kim, M.G. Lee, S.C. Yoon, F. Vucko, C. wook Lee, D. Theirry, S.J. Kim, Diffusible hydrogen behavior and delayed fracture of cold rolled martensitic steel in consideration of automotive manufacturing process and vehicle service environment, J. Mater. Res. Technol. 9

(2020) 13483–13501. doi:10.1016/J.JMRT.2020.09.113.

[139] D. Figueroa, M.J. Robinson, The effects of sacrificial coatings on hydrogen embrittlement and re-embrittlement of ultra high strength steels, Corros. Sci. 50 (2008) 1066–1079.

[140] J. Lee, T. Lee, Y.J. Kwon, D.-J. Mun, J.-Y. Yoo, C.S. Lee, Effects of vanadium carbides on hydrogen embrittlement of tempered martensitic steel, Met. Mater. Int. 22 (2016) 364–372. doi:10.1007/s12540-016-5631-7.

[141] M. Loidl, O. Kolk, S. Veith, T. Göbel, Characterization of hydrogen embrittlement in automotive advanced high strength steels, Materwiss. Werksttech. 42 (2011) 1105–1110. doi:10.1002/mawe.201100917.

[142] D. Rudomilova, I. Traxler, J. Faderl, G. Luckeneder, G. Schimo-aichhorn, A. Muhr, Critical Assessment of the Effect of Atmospheric Corrosion, Metals (Basel). 11 (2021).

[143] T. Depover, D. Pérez Escobar, E. Wallaert, Z. Zermout, K. Verbeken, Effect of hydrogen charging on the mechanical properties of advanced high strength steels, Int. J. Hydrogen Energy. 39 (2014) 4647–4656. doi:10.1016/j.ijhydene.2013.12.190.

[144] C. Forot, E. Legrand, E. Roguet, J. Creus, J. Kittel, X. Feaugas, Impact of cementite on the tortuosity of the hydrogen diffusion paths in pearlitic steels, Eurocorr. (2015).

[145] B. Grysakowski, V. Optasanu, T. Montesin, S. Dejardin, T. Grunewald, P. Naas, G. Moll, Stress-assisted hydrogen diffusion in the presence of trapping sites in elasto-plastic materials, in: Congrès Français de Mécanique, AFM, Maison de la Mécanique, 39/41 rue Louis Blanc, 92400 Courbevoie, France …, 2013.

[146] T. Depover, K. Verbeken, The effect of TiC on the hydrogen induced ductility loss and trapping behavior of Fe-C-Ti alloys, Corros. Sci. 112 (2016) 308–326. doi:10.1016/j.corsci.2016.07.013.

[147] Q. Liu, J. Venezuela, M. Zhang, Q. Zhou, A. Atrens, Hydrogen trapping in some advanced high strength steels, Corros. Sci. 111 (2016) 770–785. doi:10.1016/j.corsci.2016.05.046.

[148] W.T. Geng, V. Wang, J.-X. Li, N. Ishikawa, H. Kimizuka, K. Tsuzaki, S. Ogata, Hydrogen trapping in carbon supersaturated α-iron and its decohesion effect in martensitic steel, Scr. Mater. 149 (2018) 79–83. doi:10.1016/j.scriptamat.2018.02.025.

[149] M. Iino, A more generalized analysis of hydrogen trapping, Acta Metall. 30 (1982) 367–375. doi:https://doi.org/10.1016/0001-6160(82)90216-4.

[150] A. Turnbull, Hydrogen diffusion and trapping in metals, in: Gaseous Hydrog. Embrittlement Mater. Energy Technol., Woodhead Publishing, 2012: pp. 89–128. doi:https://doi.org/10.1533/9780857095374.1.89.

[151] J. Svoboda, G. Mori, A. Prethaler, F.D. Fischer, Determination of trapping parameters and the chemical diffusion coefficient from hydrogen permeation experiments, Corros. Sci. 82 (2014) 93–100. doi:https://doi.org/10.1016/j.corsci.2014.01.002.

[152] S. Adolf, The absorption of gases by metals, ZeitschriftfürMetallkunde. 21 (1929) 37–46.

[153] G. Lovicu, M. Bottazzi, F. D'Aiuto, M. De Sanctis, A. Dimatteo, C. Santus, R. Valentini, Hydrogen Embrittlement of Automotive Advanced High-Strength Steels, Metall. Mater. Trans. A. 43 (2012) 4075–4087. doi:10.1007/s11661-012-1280-8.

[154] T. Maki, 2 - Morphology and substructure of martensite in steels, in: E. Pereloma, D. V Edmonds (Eds.), Phase Transform. Steels, Woodhead Publishing, 2012: pp. 34–58. doi:https://doi.org/10.1533/9780857096111.1.34.

[155] Q. Liu, A. Atrens, Reversible hydrogen trapping in a 3.5NiCrMoV medium strength steel, Corros. Sci. 96 (2015) 112–120. doi:10.1016/j.corsci.2015.04.011.

[156] R.A. Oriani, The diffusion and trapping of hydrogen in steel, Acta Metall. 18 (1970) 147–157. doi:https://doi.org/10.1016/0001-6160(70)90078-7.

[157] E. Van den Eeckhout, T. Depover, K. Verbeken, The Effect of Microstructural Characteristics on the Hydrogen Permeation Transient in Quenched and Tempered Martensitic Alloys, Metals (Basel). 8 (2018). doi:10.3390/met8100779.

[158] M. Iino, Trapping of hydrogen by sulfur-associated defects in steel, Metall. Trans. A. 16 (1985) 401–409.

[159] S.J. Lee, J.A. Ronevich, G. Krauss, D.K. Matlock, Hydrogen embrittlement of hardened low-carbon sheet steel, ISIJ Int. 50 (2010) 294–301. doi:10.2355/isijinternational.50.294.

[160] J.A. Ronevich, J.G. Speer, D.K. Matlock, Hydrogen Embrittlement of Commercially Produced Advanced High Strength Sheet Steels, Int. J. Mater. Manuf. 3 (2010) 255–267. doi:10.2307/26282905.

[161] K. Takashima, Y. Yoshioka, K. Yokoyama, Y. Funakawa, Hydrogen Embrittlement Behavior of Ultra-high Strength Dual Phase Steel Sheet under Sustained Tensile-loading Test, ISIJ Int. 58 (2018) 173–178. doi:10.2355/isijinternational.ISIJINT-2017-315.

[162] T. Schaffner, A. Hartmaier, V. Kokotin, M. Pohl, Analysis of hydrogen diffusion and trapping in ultra-high strength steel grades, J. Alloys Compd. 746 (2018) 557–566. doi:10.1016/j.jallcom.2018.02.264.

[163] P. Zhou, W. Li, H. Zhao, X. Jin, Role of microstructure on electrochemical hydrogen permeation properties in advanced high strength steels, Int. J. Hydrogen Energy. 43 (2018) 10905–10914. doi:10.1016/j.ijhydene.2018.04.241.

[164] K. Takashima, T. Nishimura, K. Yokoyama, Y. Funakawa, Role of Interface between Ferrite and Martensite in Hydrogen Embrittlement Behavior of Ultra-high Strength Dual-phase Steel Sheets, ISIJ Int. 59 (2019) 1676–1682. doi:10.2355/isijinternational.ISIJINT-2019-013.

[165] M. Koyama, C.C. Tasan, E. Akiyama, K. Tsuzaki, D. Raabe, Hydrogen-assisted decohesion and localized plasticity in dual-phase steel, Acta Mater. 70 (2014) 174–187. doi:10.1016/j.actamat.2014.01.048.

[166] N.K. van der Bij, The influence of AlSi and MagiZinc coatings on the susceptibility towards hydrogen embrittlement of press-hardening steel, TU Delft, 2016. https://repository.tudelft.nl/islandora/object/uuid%3A165b36db-c4d2-417f-ac69-605f0610283e (accessed December 30, 2021).

[167] M.A. V Devanathan, Z. Stachurski, The adsorption and diffusion of electrolytic hydrogen in palladium, Proc. R. Soc. Lond. A. 270 (1962) 90–102.

[168] L. Vecchi, D. Pecko, M.H. Mamme, D. Van Laethem, T. Depover, E. Van den Eeckhout, N. Van den Steen, B. Ozdirik, K. Verbeken, Y. Van Ingelgem, J. Deconinck, H. Terryn, Numerical interpretation to differentiate hydrogen trapping effects in iron alloys in the Devanathan-Stachurski permeation cell, Corros. Sci. 154 (2019) 231–238. doi:10.1016/j.corsci.2019.04.008.

[169] B.S. Institute, BS EN ISO 17081:2014. Method of measurement of hydrogen permeation and determination of hydrogen uptake and transport in metals by an electrochemical technique, (2014).

[170] J. Crank, The mathematics of diffusion, 2nd ed., Oxford university press, 1975.

[171] E. Akiyama, S. Li, Electrochemical hydrogen permeation tests under galvanostatic hydrogen charging conditions conventionally used for hydrogen embrittlement study, Corros. Rev. 34 (2016) 103–112.

[172] E. Akiyama, S. Li, Electrochemical Hydrogen Permeation Tests under Conventional Potentiostatic Hydrogen Charging Conditions Conventionally Used for Hydrogen Embrittlement Study, ECS Trans. 75 (2017) 23–31.

[173] M.D. Archer, N.C. Grant, Achievable Boundary Conditions in Potentiostatic and Galvanostatic Hydrogen Permeation through Palladium and Nickel Foils, Proc. R. Soc. A Math. Phys. Eng. Sci. 395 (1984) 165–183. doi:10.1098/rspa.1984.0096.

[174] A. McNabb, P.K. Foster, A new analysis of the diffusion of hydrogen in iron and ferritic steels, Trans. Met. Soc. AIME. 227 (1963) 618–627.

[175] L. Vecchi, H. Simillion, R. Montoya, D. Van Laethem, E. Van den Eeckhout, K. Verbeken, H. Terryn, J. Deconinck, Y. Van Ingelgem, Modelling of hydrogen permeation experiments in iron alloys: Characterization of the accessible parameters – Part II – The exit side, Electrochim. Acta. 262 (2018) 153–161. doi:10.1016/j.electacta.2017.12.173.

[176] R.M. Barrer, J.A. Barrie, M.G. Rogers, Permeation through a membrane with mixed boundary conditions, Trans. Faraday Soc. 58 (1962) 2473–2483.

[177] J. Kittel, F. Ropital, J. Pellier, Effect of Membrane Thickness on Hydrogen Permeation in Steels During Wet Hydrogen Sulfide Exposure, Corrosion. 64 (2008) 788–799. doi:10.5006/1.3278446.

[178] M. Dadfarnia, P. Sofronis, T. Neeraj, Hydrogen interaction with multiple traps: Can it be used to mitigate embrittlement?, Int. J. Hydrogen Energy. 36 (2011) 10141–10148.

doi:10.1016/j.ijhydene.2011.05.027.

[179] K. Randerson, H.C. Carey, K. Schomberg, A model for calculating solubility of hydrogen in steel, Ironmak. Steelmak. 30 (2003) 369–378. doi:10.1179/030192303225004060.

[180] G. Krauss, Steels: heat treatment and processing principles, ASM Int. 1990. (1990) 497.

[181] G. Mansilla, S. Hereñú, E. Brandaleze, Hydrogen effects on low cycle fatigue of high strength steels, Mater. Sci. Technol. 30 (2014) 501–505. doi:10.1179/1743284713Y.0000000328.

[182] Y. Momotani, A. Shibata, T. Yonemura, Y. Bai, N. Tsuji, Effect of initial dislocation density on hydrogen accumulation behavior in martensitic steel, Scr. Mater. 178 (2020) 318–323. doi:https://doi.org/10.1016/j.scriptamat.2019.11.051.

[183] A. Turnbull, R.B. Hutchings, D.H. Ferriss, Modelling of thermal desorption of hydrogen from metals, Mater. Sci. Eng. A. 238 (1997) 317–328. doi:http://doi.org/10.1016/S0921-5093(97)00426-7.

[184] K. Verbeken, Analysing hydrogen in metals: bulk thermal desorption spectroscopy (TDS) methods, in: Gaseous Hydrog. Embrittlement Mater. Energy Technol., Woodhead Publishing, 2012: pp. 27–55. doi:https://doi.org/10.1533/9780857095374.1.27.

[185] S. V Merzlikin, S. Borodin, D. Vogel, M. Rohwerder, Ultra high vacuum high precision low background setup with temperature control for thermal desorption mass spectroscopy (TDA-MS) of hydrogen in metals, Talanta. 136 (2015) 108–113. doi:http://dx.doi.org/10.1016/j.talanta.2015.01.014.

[186] M. Koyama, M. Rohwerder, C.C. Tasan, A. Bashir, E. Akiyama, K. Takai, D. Raabe, K. Tsuzaki, Recent progress in microstructural hydrogen mapping in steels: quantification, kinetic analysis, and multi-scale characterisation, Mater. Sci. Technol. 33 (2017) 1481–1496. doi:10.1080/02670836.2017.1299276.

[187] J. Takahashi, K. Kawakami, T. Tarui, Direct observation of hydrogen-trapping sites in vanadium carbide precipitation steel by atom probe tomography, Scr. Mater. 67 (2012) 213–216. doi:10.1016/j.scriptamat.2012.04.022.

[188] K. Takai, J. Seki, Y. Homma, Observation of Trapping Sites of Hydrogen and Deuterium in High-Strength Steels by Using Secondary Ion Mass Spectrometry, Mater. Trans. JIM. 36 (1995) 1134–1139. doi:10.2320/matertrans1989.36.1134.

[189] A. Nagao, S. Kuramoto, K. Ichitani, M. Kanno, Visualization of hydrogen transport in high strength steels affected by stress fields and hydrogen trapping, Scr. Mater. 45 (2001) 1227–1232. doi:http://dx.doi.org/10.1016/S1359-6462(01)01154-X.

[190] K. Ichitani, M. Kanno, Visualization of hydrogen diffusion in steels by high sensitivity hydrogen microprint technique, Sci. Technol. Adv. Mater. 4 (2003) 545–551. doi:10.1016/j.stam.2003.12.006.

[191] J.A. Ronevich, J.G. Speer, G. Krauss, D.K. Matlock, Improvement of the Hydrogen Microprint

Technique on AHSS Steels, Metallogr. Microstruct. Anal. 1 (2012) 79–84. doi:10.1007/s13632-012-0015-y.

[192] N. Ishikawa, H. Sueyoshi, A. Nagao, Hydrogen Microprint Analysis on the Effect of Dislocations on Grain Boundary Hydrogen Distribution in Steels, ISIJ Int. 56 (2016) 413–417. doi:10.2355/isijinternational.ISIJINT-2015-329.

[193] T. Ohmisawa, S. Uchiyama, M. Nagumo, Detection of hydrogen trap distribution in steel using a microprint technique, J. Alloys Compd. 356–357 (2003) 290–294. doi:http://dx.doi.org/10.1016/S0925-8388(03)00355-4.

[194] M. Rohwerder, F. Turcu, High-resolution Kelvin probe microscopy in corrosion science: Scanning Kelvin probe force microscopy (SKPFM) versus classical scanning Kelvin probe (SKP), Electrochim. Acta. 53 (2007) 290–299. doi:10.1016/j.electacta.2007.03.016.

[195] G. Williams, H.N. McMurray, R.C. Newman, Surface oxide reduction by hydrogen permeation through iron foil detected using a scanning Kelvin probe, Electrochem. Commun. 27 (2013) 144–147. doi:10.1016/j.elecom.2012.11.022.

[196] S. Evers, M. Rohwerder, The hydrogen electrode in the “dry”: A Kelvin probe approach to measuring hydrogen in metals, Electrochem. Commun. 24 (2012) 85–88. doi:10.1016/j.elecom.2012.08.019.

[197] S. Evers, C. Senoz, M. Rohwerder, Hydrogen detection in metals: a review and introduction of a Kelvin probe approach, Sci Technol Adv Mater. 14 (2013) 14201. doi:10.1088/1468-6996/14/1/014201.

[198] C. Senöz, S. Evers, M. Stratmann, M. Rohwerder, Scanning Kelvin Probe as a highly sensitive tool for detecting hydrogen permeation with high local resolution, Electrochem. Commun. 13 (2011) 1542–1545. doi:10.1016/j.elecom.2011.10.014.

[199] H.N. McMurray, G. Williams, Probe diameter and probe– specimen distance dependence in the lateral resolution of a scanning Kelvin probe, J. Appl. Phys. 91 (2002) 1673–1679. doi:10.1063/1.1430546.

[200] M. Wicinski, W. Burgstaller, A.W. Hassel, Lateral resolution in scanning Kelvin probe microscopy, Corros. Sci. 104 (2016) 1–8. doi:10.1016/j.corsci.2015.09.008.

[201] C. Örnek, C. Leygraf, J. Pan, On the Volta potential measured by SKPFM – fundamental and practical aspects with relevance to corrosion science, Corros. Eng. Sci. Technol. 54 (2019) 185–198. doi:10.1080/1478422X.2019.1583436.

[202] M. Koyama, A. Bashir, M. Rohwerder, S. V Merzlikin, E. Akiyama, K. Tsuzaki, D. Raabe, Spatially and Kinetically Resolved Mapping of Hydrogen in a Twinning-Induced Plasticity Steel by Use of Scanning Kelvin Probe Force Microscopy, J. Electrochem. Soc. 162 (2015) C638–C647. doi:10.1149/2.0131512jes.

[203] W. Burgstaller, G. Schimo, A.W. Hassel, Challenges in hydrogen quantification using Kelvin

probe technique at different levels of relative humidity, (2017). doi:10.1007/s10008-017-3541-3.

[204] E. Tohme, V. Barnier, F. Christien, C. Bosch, K. Wolski, M. Zamanzade, SKPFM study of hydrogen in a two phase material. Experiments and modelling, Int. J. Hydrogen Energy. 44 (2019) 18597–18605. doi:10.1016/j.ijhydene.2019.05.177.

[205] G. Schimo, W. Burgstaller, A.W. Hassel, Influence of atmospheric oxygen on hydrogen detection on Pd using Kelvin probe technique, J. Solid State Electrochem. (2017). doi:10.1007/s10008-017-3715-z.

[206] Tata Steel Europe, Strip products and services catalogue 2018 Metric Units, (2018) 1–232. https://www.tatasteeleurope.com/sites/default/files/tata-steel-engineering-strip-product-range-catalogue-en.pdf (accessed October 20, 2022).

[207] R.L. Higginson, C.M. Sellars, Worked examples in quantitative metallography, Maney Pub, 2003.

[208] S. Meister, Grain and particle analysis with line intersection method, (2012). https://uk.mathworks.com/matlabcentral/fileexchange/35203-grain-and-particle-analysis-with-line-intersection-method.

[209] E. Frank, M.A. Hall, I.H. Witten, The WEKA Workbench, Online Append. "Data Min. Pract. Mach. Learn. Tools Tech. 4th Edn. Morgan Kaufman, Burlingt. (2009).

[210] F. Bachmann, R. Hielscher, H. Schaeben, Texture Analysis with MTEX – Free and Open Source Software Toolbox, Solid State Phenom. 160 (2010) 63–68. doi:10.4028/www.scientific.net/SSP.160.63.

[211] T. Nyyssönen, M. Isakov, P. Peura, V.-T. Kuokkala, Iterative Determination of the Orientation Relationship Between Austenite and Martensite from a Large Amount of Grain Pair Misorientations, Metall. Mater. Trans. A. 47 (2016) 2587–2590. doi:10.1007/s11661-016-3462-2.

[212] H. Järvinen, M. Isakov, T. Nyyssönen, M. Järvenpää, P. Peura, The effect of initial microstructure on the final properties of press hardened 22MnB5 steels, Mater. Sci. Eng. A. 676 (2016) 109–120. doi:10.1016/j.msea.2016.08.096.

[213] D. Shindo, T. Oikawa, Energy Dispersive X-ray Spectroscopy, Japanese J. Tribol. 51 (2002) 81–102. doi:10.1007/978-4-431-66988-3_4.

[214] H. Rietveld, A profile refinement method for nuclear and magnetic structures, J. Appl. Crystallogr. 2 (1969) 65–71.

[215] L. Lutterotti, M. Bortolotti, G. Ischia, I. Lonardelli, H.R. Wenk, Rietveld texture analysis from diffraction images, Zeitschrift Fur Krist. Suppl. 1 (2007) 125–130. doi:10.1524/zksu.2007.2007.suppl_26.125.

[216] G.K. Williamson, R.E. Smallman, III. Dislocation densities in some annealed and cold-worked

metals from measurements on the X-ray Debye-Scherrer spectrum, Philos. Mag. 1 (1956) 34–46. doi:10.1080/14786435608238074.

[217] P. Scherrer, Bestimmung der inneren Struktur und der Größe von Kolloidteilchen mittels Röntgenstrahlen, in: R. Zsigmondy (Ed.), Kolloidchem. Ein Lehrb., Springer, 1912: pp. 387–409.

[218] G. Williams, H.N. McMurray, Localized corrosion of magnesium in chloride-containing electrolyte studied by a scanning vibrating electrode technique, J. Electrochem. Soc. 155 (2008) C340–C349.

[219] H.N. Mcmurray, D. Williams, D.A. Worsley, Artifacts Induced by Large-Amplitude Probe Vibrations in Localized Corrosion Measured by SVET, J. Electrochem. Soc. 150 (2003) 12–567. doi:10.1149/1.1623494.

[220] J. Sullivan, N. Cooze, C. Gallagher, T. Lewis, T. Prosek, D. Thierry, In-situ monitoring of corrosion mechanisms and phosphate inhibitor surface deposition during corrosion of Zinc Magnesium Aluminium (ZMA) alloys using novel time-lapse microscopy, Faraday Discuss. 180 (2015) 361–379. http://rsc.li/fd-upcoming-meetings (accessed July 14, 2020).

[221] B.S. Institute, BS EN ISO 6892-1:2016 - Metallic materials. Tensile testing. Method of test at room temperature, (2016). https://bsol.bsigroup.com/Bibliographic/BibliographicInfoData/000000000030268532.

[222] A. Díaz, J.M. Alegre, I.I. Cuesta, Coupled hydrogen diffusion simulation using a heat transfer analogy, Int. J. Mech. Sci. 115–116 (2016) 360–369. doi:10.1016/j.ijmecsci.2016.07.020.

[223] H.S. Carslaw, J.C. Jaeger, Conduction of heat in solids, 1959.

[224] R.L. Mitchell, M. Coleman, P. Davies, L. North, E.C. Pope, C. Pleydell-Pearce, W. Harris, R. Johnston, Macro-to-nanoscale investigation of wall-plate joints in the acorn barnacle Semibalanus balanoides: Correlative imaging, biological form and function, and bioinspiration, J. R. Soc. Interface. 16 (2019). doi:10.1098/RSIF.2019.0218.

[225] T. Yokobori, The strength, fracture, and fatigue of materials, P. Noordhoff, 1965.

[226] M.J. Robinson, R.M. Sharp, The Effect of Post-Exposure Heat Treatment on the Hydrogen Embrittlement of High Carbon Steel, Corrosion. 41 (1985) 582–586. doi:10.5006/1.3582987.

[227] D. Figueroa-Gordon, Hydrogen Re-Embrittlement Susceptibility of UHSS, Cranfield University, 2005. http://hdl.handle.net/1826/1433.

[228] A. Saai, O.S. Hopperstad, Y. Granbom, O.G. Lademo, Influence of Volume Fraction and Distribution of Martensite Phase on the Strain Localization in Dual Phase Steels, Procedia Mater. Sci. 3 (2014) 900–905. doi:10.1016/j.mspro.2014.06.146.

[229] Y. Bergström, Y. Granbom, D. Sterkenburg, A Dislocation-Based Theory for the Deformation Hardening Behavior of DP Steels: Impact of Martensite Content and Ferrite Grain Size, J. Metall. 2010 (2010) 1–16. doi:10.1155/2010/647198.

[230] M. Iannuzzi, Environmentally assisted cracking (EAC) in oil and gas production, in: Stress Corros. Crack. Theory Pract., Woodhead Publishing, 2011: pp. 570–607. doi:10.1533/9780857093769.4.570.

[231] O. Takakuwa, H. Soyama, Suppression of hydrogen-assisted fatigue crack growth in austenitic stainless steel by cavitation peening, (2012). doi:10.1016/j.ijhydene.2011.12.035.

[232] B.E. Wilde, I. Chattoraj, The effect of shot peening on hydrogen absorption by and hydrogen permeation through AISI 4130 steels, Scr. Metall. Mater. 26 (1992) 627–632. doi:10.1016/0956-716X(92)90296-Q.

[233] R. Wang, S. Luo, M. Liu, Y. Xue, Electrochemical corrosion performance of Cr and Al alloy steels using a J55 carbon steel as base alloy, Corros. Sci. 85 (2014) 270–279. doi:10.1016/j.corsci.2014.04.023.

[234] S.-B. Shin, S.-J. Song, Y.-W. Shin, J.-G. Kim, B.-J. Park, Y.-C. Suh, Effect of Molybdenum on the Corrosion of Low Alloy Steels in Synthetic Seawater, Mater. Trans. 57 (2016) 2116–2121. doi:10.2320/MATERTRANS.M2016222.

[235] K.D. Ralston, N. Birbilis, C.H.J. Davies, Revealing the relationship between grain size and corrosion rate of metals, Scr. Mater. 63 (2010). doi:10.1016/j.scriptamat.2010.08.035.

[236] K.D. Ralston, N. Birbilis, Effect of Grain Size on Corrosion: A Review, Corrosion. 66 (2010) 075005-075005–13. doi:10.5006/1.3462912.

[237] I. Rodionova, A. Amezhnov, E. Alekseeva, Y. Gladchenkova, I. Vasechkina, Effect of carbonitride precipitates on the corrosion resistance of low-alloy steels under operating conditions of oil-field pipelines, Metals (Basel). 11 (2021). doi:10.3390/met11050766.

[238] E. McCafferty, Validation of corrosion rates measured by the Tafel extrapolation method, Corros. Sci. 47 (2005) 3202–3215. doi:10.1016/j.corsci.2005.05.046.

[239] G. Williams, N. Birbilis, H.N. McMurray, The source of hydrogen evolved from a magnesium anode, Electrochem. Commun. 36 (2013) 1–5. doi:http://dx.doi.org/10.1016/j.elecom.2013.08.023.

[240] C.F. Glover, A. Barnes, I. Mabbett, R. Subramanian, G. Williams, The Scanning Vibrating Electrode Technique for the Study of Hydrogen Evolution from an Iron Electrode, ECS Trans. 64 (2015) 73–81.

[241] M.O. Rivett, M.O. Cuthbert, R. Gamble, L.E. Connon, A. Pearson, M.G. Shepley, J. Davis, Highway deicing salt dynamic runoff to surface water and subsequent infiltration to groundwater during severe UK winters, Sci. Total Environ. (2016). doi:10.1016/j.scitotenv.2016.04.095.

[242] J. Venezuela, E. Gray, Q. Liu, Q. Zhou, C. Tapia-Bastidas, M. Zhang, A. Atrens, Equivalent hydrogen fugacity during electrochemical charging of some martensitic advanced high-strength steels, Corros. Sci. 127 (2017) 45–58. doi:10.1016/j.corsci.2017.08.011.

[243] H.J. Grabke, E. Riecke, Absorption and diffusion of hydrogen in steels, Mater. Tehnol. 34 (2000) 331.

[244] L. Lan, X. Kong, Z. Hu, C. Qiu, D. Zhao, L. Du, Hydrogen permeation behavior in relation to microstructural evolution of low carbon bainitic steel weldments, Corros. Sci. 112 (2016) 180–193. doi:10.1016/J.CORSCI.2016.07.025.

[245] T. Depover, O. Monbaliu, E. Wallaert, K. Verbeken, Effect of Ti, Mo and Cr based precipitates on the hydrogen trapping and embrittlement of Fe–C–X Q&T alloys, Int. J. Hydrogen Energy. 40 (2015) 16977–16984. doi:https://doi.org/10.1016/j.ijhydene.2015.06.157.

[246] T. Depover, A. Laureys, D. Perez Escobar, E. Van den Eeckhout, E. Wallaert, K. Verbeken, Understanding the Interaction between a Steel Microstructure and Hydrogen, Mater. 11 (2018). doi:10.3390/ma11050698.

[247] Y.S. Chen, D. Haley, S.S. Gerstl, A.J. London, F. Sweeney, R.A. Wepf, W.M. Rainforth, P.A. Bagot, M.P. Moody, Direct observation of individual hydrogen atoms at trapping sites in a ferritic steel, Science (80-.). 355 (2017) 1196–1199. doi:10.1126/science.aal2418.

[248] H. Hagi, Y. Hayashi, Effect of Dislocation Trapping on Hydrogen and Deuterium Diffusion in Iron., Trans. Japan Inst. Met. 28 (1987) 368–374. doi:10.2320/matertrans1960.28.368.

[249] H. Hagi, Diffusion Coefficient of Hydrogen in Iron without Trapping by Dislocations and Impurities, Mater. Trans. JIM. 35 (1994) 112–117. doi:10.2320/matertrans1989.35.112.

[250] V. Olden, C. Thaulow, R. Johnsen, Modelling of hydrogen diffusion and hydrogen induced cracking in supermartensitic and duplex stainless steels, Mater. Des. 29 (2008) 1934–1948. doi:10.1016/j.matdes.2008.04.026.

[251] S.L.I. Chan, Hydrogen trapping ability of steels with different microstructures, J. Chinese Inst. Eng. 22 (1999) 43–53. doi:10.1080/02533839.1999.9670440.

[252] W.C. Luu, J.K. Wu, The influence of microstructure on hydrogen transport in carbon steels, Corros. Sci. 38 (1996) 239–245. doi:https://doi.org/10.1016/0010-938X(96)00109-6.

[253] Y. Sakamoto, T. Mantani, Effect of quenching and tempering on diffusion of hydrogen in carbon steel, Trans. Japan Inst. Met. 17 (1976) 743–748.

[254] B. Chew, F.T. Fabling, The Effect of Grain Boundaries on the Low-Temperature Diffusion of Hydrogen in Decarburized Mild Steel, Met. Sci. J. 6 (1972) 140–142. doi:10.1179/030634572790446055.

[255] T. Depover, K. Verbeken, Evaluation of the role of Mo2C in hydrogen induced ductility loss in Q&T Fe C Mo alloys, Int. J. Hydrogen Energy. 41 (2016) 14310–14329. doi:10.1016/j.ijhydene.2016.05.176.

[256] M.A. Stopher, P. Lang, E. Kozeschnik, P.E.J. Rivera-Diaz-del-Castillo, Modelling hydrogen migration and trapping in steels, Mater. Des. 106 (2016) 205–215. doi:10.1016/j.matdes.2016.05.051.

[257] A. Turk, D. San Martín, P.E.J. Rivera-Díaz-del-Castillo, E.I. Galindo-Nava, Correlation between vanadium carbide size and hydrogen trapping in ferritic steel, Scr. Mater. 152 (2018) 112–116. doi:10.1016/j.scriptamat.2018.04.013.

[258] J. Venezuela, Q. Zhou, Q. Liu, M. Zhang, A. Atrens, Hydrogen Trapping in Some Automotive Martensitic Advanced High-Strength Steels, Adv. Eng. Mater. 20 (2018). doi:10.1002/adem.201700468.

[259] M. Brown, On the Hydrogen Embrittlement of Oil and Gas Grade Alloy 718 and Alloy 945X, (n.d.).

[260] H. Mohrbacher, T. Senuma, Alloy Optimization for Reducing Delayed Fracture Sensitivity of 2000 MPa Press Hardening Steel, Metals (Basel). 10 (2020) 853. doi:10.3390/met10070853.

[261] W. jian Chen, P. fei Gao, S. Wang, H. zhou Lu, Z. zhi Zhao, Effect of vanadium on hydrogen embrittlement susceptibility of high-strength hot-stamped steel, J. Iron Steel Res. Int. (2020). doi:10.1007/s42243-020-00469-y.

[262] Y.-S. Chen, H. Lu, J. Liang, A. Rosenthal, H. Liu, G. Sneddon, I. McCarroll, Z. Zhao, W. Li, A. Guo, J.M. Cairney, Observation of hydrogen trapping at dislocations, grain boundaries, and precipitates, Science (80-.). 367 (2020) 171–175. doi:10.1126/science.aaz0122.

[263] T. Depover, E. Van den Eeckhout, K. Verbeken, The impact of hydrogen on the ductility loss of bainitic Fe–C alloys, Mater. Sci. Technol. 32 (2016) 1625–1631.

[264] T. Depover, E. Wallaert, K. Verbeken, Fractographic analysis of the role of hydrogen diffusion on the hydrogen embrittlement susceptibility of DP steel, Mater. Sci. Eng. A. 649 (2016) 201–208. doi:10.1016/j.msea.2015.09.124.

[265] T. Doshida, K. Takai, Dependence of hydrogen-induced lattice defects and hydrogen embrittlement of cold-drawn pearlitic steels on hydrogen trap state, temperature, strain rate and hydrogen content, Acta Mater. 79 (2014) 93–107. doi:10.1016/j.actamat.2014.07.008.

[266] B. Bal, M. Koyama, G. Gerstein, H.J. Maier, K. Tsuzaki, Effect of strain rate on hydrogen embrittlement susceptibility of twinning-induced plasticity steel pre-charged with high-pressure hydrogen gas, Int. J. Hydrogen Energy. 41 (2016) 15362–15372. doi:10.1016/J.IJHYDENE.2016.06.259.